Physics of the Solid State, Vol. 47, No. 10, 2005, pp. 1797–1804. Translated from Fizika Tverdogo Tela, Vol. 47, No. 10, 2005, pp. 1729–1736.

METALS AND SUPERCONDUCTORS

Simulation of α-Zr Structural Stability under Pressure Using the Molecular Dynamics Method

V. Yu. Trubitsyn, E. B. Dolgusheva, and E. I. Salamatov

Physicotechnical Institute, Ural Division, Russian Academy of Sciences, ul. Kirova 132, Izhevsk, 426001 Russia

e-mail: tvy@otf.fti.udmurtia.su

Received October 8, 2004; in final form, January 12, 2005

Abstract—The structural stability of α-Zr was studied using the molecular dynamics method in wide temperature and pressure ranges. The interatomic interaction was described by a pair potential calculated within the Animalu pseudopotential model. The potential parameters were selected using α-Zr phonon spectra. The features in the dynamics of the α–β and α–ω phase transitions at various temperatures and pressures were considered. The calculated hysteresis of forward and backward phase transitions and its pressure and temperature dependences are discussed. The data obtained were used to plot phase equilibrium lines in the *P–T* phase diagram. © *2005 Pleiades Publishing, Inc.*

1. INTRODUCTION

The development of methods for calculating the electron and phonon states within the electron density functional theory (EDFT) makes it possible to perform *ab initio* theoretical studies of the various properties of crystalline solids. One of the most important and actively developed applications of such calculations is the theoretical study of the structural stability of crystals under high pressures and temperatures.

Knowing the volume-dependent total energy $E(V)$ of the electronic subsystem of various crystals, one can obtain the sequence of structural transformations observed experimentally at low temperatures in both simple and complex materials. To describe the temperature dependence of the structural phase transitions, one needs to compare not the ground-state energies $E(V)$ but rather the thermodynamic potentials, more specifically, the free energy $F(V, T)$ or (if the pressure is given) the Gibbs potentials $G(P, T)$. Major problems in calculating the thermodynamic potentials arise when considering the contributions caused by lattice vibrations. In principle, the lattice dynamic properties can be calculated within the EDFT in the linear-response approximation [1]. Then, the structural phase diagram is completely determined from first principles. Despite the appeal of this approach, *ab initio* vibrational spectra sometimes cannot be used directly in calculating the temperature dependence of $F(V, T)$. Such a situation arises, in particular, when studying high-temperature crystal phases that do not exist at zero temperature and are characterized by strongly anharmonic lattice vibrations. In this case, in order to calculate the contribution of vibrational states to the thermodynamic potentials, one needs to use some approximate schemes. For example, using the Debye model for calculating the energy and entropy of lattice vibrations, we have calculated the phase diagrams of zirconium and some other metals, which agree well with known experimental data [2].

Currently, it is generally believed that the phase transition from the high-temperature β phase to the α phase, in which zirconium is under normal conditions ($T_{\beta \to \alpha}$ = 1136 K), is characterized by the soft-mode mechanism (see, e.g., [3]). Calculations of the effective potential carried out by Chen *et al.* [3] in the "frozen"-phonon model showed that, at low temperatures, the bcc lattice corresponding to the Zr β phase becomes unstable with respect to transverse vibrations with a wave vector $k = (1, 1, 0)$ (N phonon) and to longitudinal vibrations with $k = (2/3)(1, 1, 1)$ (L phonon).

There are several viewpoints on the mechanisms of high-temperature Zr β-phase stabilization. According to [3], the N-phonon frequency becomes real and comparable to the experimental value if the interaction of the N phonon with other phonon modes is considered. In [4], using a modified pseudoharmonic approximation [5], we showed that it is sufficient to consider the intrinsic anharmonicity of the N-phonon mode in order to accurately describe the temperature dependence of the N-phonon frequency. However, the authors of [6], by solving a Langevin-type nonlinear stochastic equation for describing the dynamics of an L or N photon placed in a thermostat, came to the conclusion that vibrations are complex and cannot be described in terms of phonons at all.

The calculations of the effective potential for L and N phonons carried out in [7] in the frozen-phonon model within the EDFT showed that there is a correlation between the potential anharmonicity and pressure: as the latter increases, the potential anharmonicity (and, therefore, the temperature at which bcc zirconium becomes stable) decreases. It was also shown in [7] that the α ⟶ ω phase transition observed experimentally

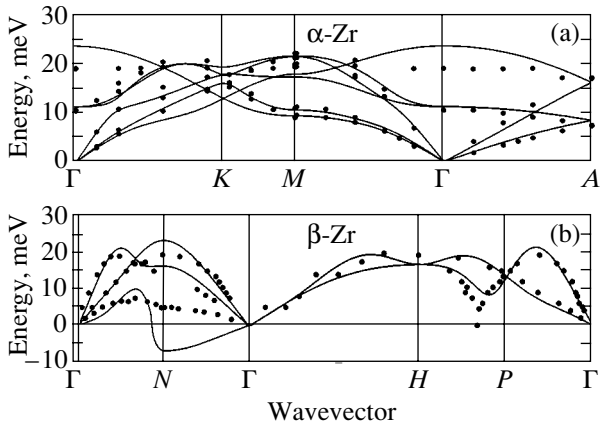

Fig. 1. Calculated phonon spectra of (a) α-Zr and (b) β-Zr. The imaginary frequencies corresponding to unstable phonons are shown as negative frequencies. Dots correspond to experimental values taken from [15, 16].

under pressure can be caused by an anomalous transverse optical mode E_{2g} at the Γ point of the hcp Brillouin zone. The effective potential of this mode becomes strongly anharmonic as the pressure increases, which brings about a decrease in the frequency of this mode and causes instability of the zirconium α phase. Such an abnormal behavior of the E_{2g} mode in α-Zr under pressure was experimentally observed in [8]. All these factors indirectly confirm the important role played by soft modes in *P–T* phase transitions.

Thus, on the one hand, many studies indicate that certain soft modes have a significant effect on the Zr structure stability. On the other hand, it is possible to describe the structural phase diagram well by applying the Debye model to the phonon subsystem. In principle, the role played by soft modes in zirconium phase transitions can be elucidated using the molecular dynamics (MD) method.

Calculations for the β ⟶ α transition in Zr using this method were carried out in [9–11], where the dynamics of this transition was studied at zero pressure using model pair potentials to describe the atomic interaction. In general, the results of those studies showed that the β ⟶ α phase transition is martensitic and is associated with atomic displacements corresponding to the *N* phonon. Unfortunately, it is rather difficult to determine the relative contribution from an individual vibrational mode in the MD simulation. The reason for this is that a huge number of interacting vibrational modes exist in the system at high temperatures. One possible way to determine the contribution from a soft mode is to simulate the structural transition at various pressures and temperatures.

In this study, we consider the results of MD simulation of the zirconium structural stability in wide ranges of temperatures and pressures using the Animalu pair pseudopotential of atomic interaction.

2. POTENTIAL AND PHONON SPECTRA

In this study, the atomic interaction was described by a pair potential calculated within the Animalu pseudopotential model for transition metals [12]. The Animalu pseudopotential has been repeatedly used to calculate various physical properties of simple and transition metals. For example, the total energies and equilibrium atomic volumes of the fcc, hcp, and bcc modifications of 24 transition elements were calculated in [13] to the second order of perturbation theory. In particular, it became possible to obtain the actual (hcp) low-temperature phase for zirconium. Calculations of the temperature dependence of the free energy of phases performed in [13] within the harmonic approximation yielded a temperature of the hcp ⟶ bcc phase transition in Zr (T_{calc} = 1080 K) that is close to the experimental temperature (T_{exp} = 1136 K). The application of Animalu pseudopotentials to MD simulation of the dynamics of complex lattices, such as those of high-temperature superconductors, is described in [14].

One of the advantages of this pseudopotential model is that it considers the set of natural physical parameters required to simulate structural transformations under pressure. The parameters A_i, which characterize the potential-well depth and are determined from spectroscopic data, were taken from paper [12], which was authored by Animalu, and were assumed to be fixed in our calculations. Only the unit volume Ω_0 and effective valence Z_{eff} were varied parameters. These two parameters were fitted using experimental phonon spectra of the zirconium α phase [15] and the value of the equilibrium unit volume Ω_0 = 23.3 Å of this phase.

Figure 1 shows the phonon dispersion curves of α- and β-Zr as calculated at Z_{eff} = 3 and Ω_0 = 23.3 Å. When calculating these curves, the dynamic matrix elements were found by summing over six coordination spheres. It follows from Fig. 1a that the largest disagreement with the experiment for the α phase is observed near the Γ point, where the calculated frequency of the optical branch is larger than the corresponding experimental value by approximately 4.5 meV. This overestimate of the optical phonon frequency at the Γ point of the Brillouin zone of hcp Zr, Ti, and Hf occurs in all calculations using the pair potential (see, e.g., [17, 18]). As shown in [19], the experimentally observed anomalous decrease [15] in the frequency of LO vibrations at the Γ point of hcp zirconium with a decrease in temperature is associated with features in the electronic band structure near the Fermi surface and cannot be adequately described in terms of the pseudopotential. In general, there is good agreement between the α-Zr phonon spectrum as calculated in the Animalu pseudopotential model and the experimental spectrum. Moreover, our results agree with the data calculated using many-particle interatomic potentials [17] and reproduce short-wavelength acoustic phonons rather well, which is important when considering the lattice stability.

When calculating the dispersion curves for the Zr β phase (Fig. 1b), the acoustic branch along the Γ–*N* (110) direction, corresponding to transverse vibrations, is found to have imaginary frequencies. Such a behavior of the acoustic branch agrees well with the experimental data from [16], in which an anomalous decrease in the frequency of β-Zr transverse vibrations along the [110] direction was observed as the temperature decreased. This also agrees with the results of *ab initio* calculations in the frozen-phonon model [3, 4], in which the T_{1N}-mode vibration frequency is purely imaginary. The appearance of soft modes in the vibration spectrum, as a rule, indicates structural instability of the lattice. The appearance of a branch of the vibrational spectrum for which all frequencies are imaginary explains the absence of the Zr β phase at normal pressure and low temperature. A similar result was obtained in [17]. In other respects, as can be seen in Fig. 1b, the Animalu pseudopotential fitted to the hcp phase also reproduces well the dynamic properties of bcc Zr. In particular, this is indicated by a dip in the calculated dispersion curve of the longitudinal vibrational *L*2/3 [111] mode. This mode plays an important role in the β ⟶ ω phase transformations of zirconium observed under high pressures.

Figure 2 shows the density of vibrational states of hcp Zr as calculated using the tetrahedron method with the involvement of 135 points in the irreducible part of the Brillouin zone. The calculated density of states fits that obtained on the basis of experimental data rather well [15].

Thus, we succeeded in selecting an Animalu pair pseudopotential that describes the dynamic properties of both α and β zirconium well. We did not calculate phonon dispersion curves for the third observed Zr phase (ω phase), since there are no experimentally measured phonon spectra for this structure.

In what follows, the selected potential was considered the same for all phases, temperatures, and pressures in the MD simulations.

3. MOLECULAR-DYNAMICS SIMULATION TECHNIQUE

As an initial atomic configuration, an hcp structure with 4500 atoms and cyclic boundary conditions was taken. After potential-energy minimization and system relaxation, the crystallite was exposed to a temperature $T = 0$ over a time no less than $t = 10^{-12}$ s. In all calculations, the time step was $\delta t = 0.5 \times 10^{-15}$ s. Crystallite heating and cooling were simulated by multiplying the atomic velocity components by the factor $\gamma_v = \sqrt{((T - T_s)\alpha_T + T_s)/T}$ every tenth time step. Here, T and T_s are the current and required temperatures, respectively, and α_T is a coefficient defining the rate of temperature change. In the calculation, we used values of α_T ranging from 0.995 to 0.999. Heating was carried out gradually in several steps. At each step, the new value of the temperature T_s differed from its preceding value by no more than 200 degrees. After reaching the temperature T_s, the system was exposed to this temperature and freely evolved to an equilibrium state. Thereafter, a new value of the temperature T_s was set if required.

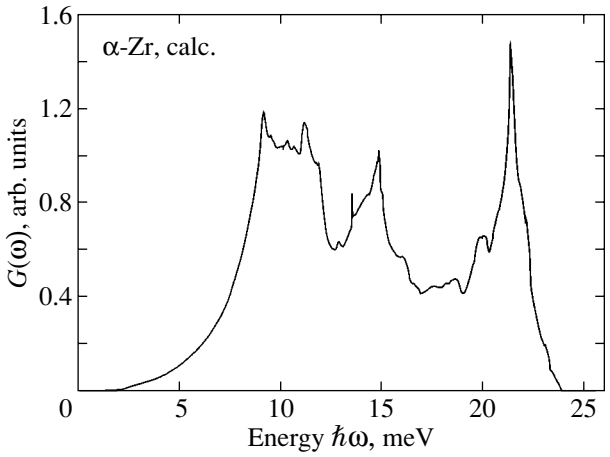

Fig. 2. Density of states of zirconium.

The α ⟶ ω transitions observed in zirconium under high pressures were simulated at a fixed temperature. Preliminarily, the crystallite was heated to a required temperature and brought to an equilibrium state; then, the external pressure P was changed stepwise (simulation at a fixed volume) or the lattice parameters a and c were changed by 1% (simulation at a fixed pressure). After each change in the parameters P or V, the system was brought to an equilibrium state at a fixed temperature.

The system was considered to be brought to equilibrium if the velocity-distribution function remained unchanged in time and if the main system parameters (the kinetic, potential, and total energy; the minimum interatomic distance; etc.) fluctuated, due to the finite size of the system, near average values that remained unchanged for a time of the order of 10^{-12} s.

The onset of a structural transformation, as a rule, was preliminarily determined by an abrupt change in the crystallite kinetic energy. The initial, final, and intermediate phases were traced by the evolution of the atomic radial distribution function (RDF).

4. CALCULATIONAL RESULTS

The dynamics of the α ⟶ β phase transition can be traced in Fig. 3, where the instantaneous atom positions are shown at various points in time of the MD simulation.

The upper left-hand panel shows the initial α phase with an hcp lattice before the temperature-driven phase transition. The upper right-hand panel shows the crys-

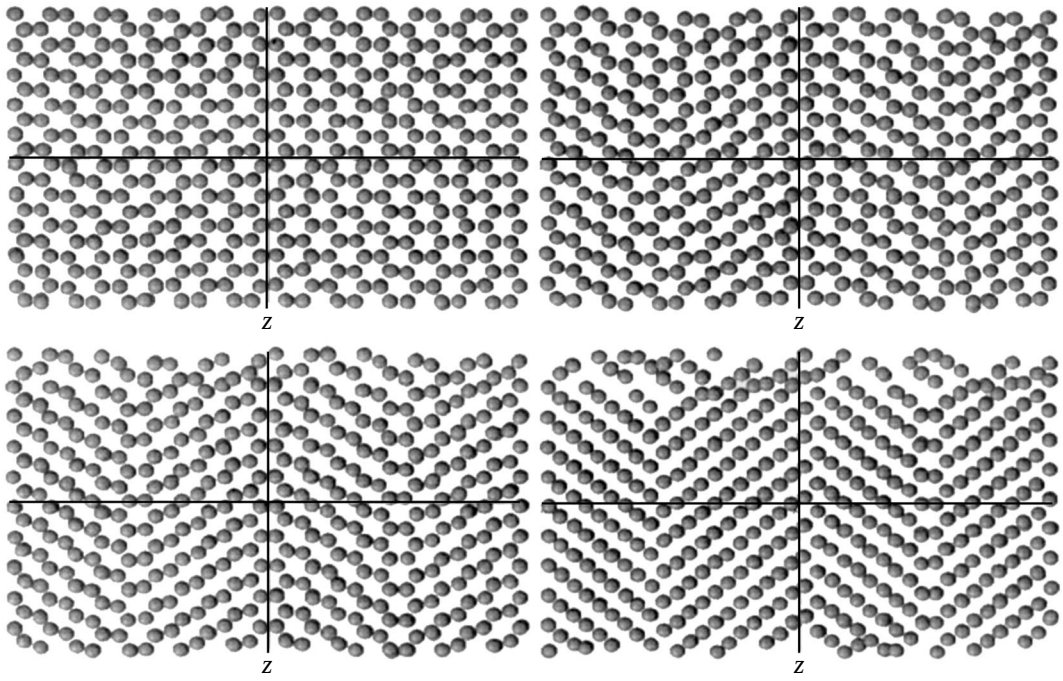

Fig. 3. Rearrangement of the Zr crystal structure during the α ⟶ β transition (see text for details).

tallite state after 300 time steps. We can see that the structure transformation begins almost simultaneously throughout the entire crystallite volume. In this case, atomic displacements correspond to two types of vibrations: short-wavelength vibrations that change the local structure and long-wavelength vibrations that give rise to a twin structure. The lower left-hand panel (Δt = 600 steps) shows the instant of time when the twin formation due to the structural transition to the β phase was mostly completed but the atoms arranged at interfaces retained the local neighborhood of the initial α phase. Finally, after 1000 steps (the lower right-hand panel), the rearrangement of atoms at twin boundaries is completed. Then, the formed β phase remains stable over the entire observation period.

As the temperature decreases, the reverse β ⟶ α transition is observed. Figure 4 shows the atomic RDF and the temporal variation of the crystallite kinetic energy (in temperature units). A decrease in the kinetic energy at the initial stage (Fig. 4b) corresponds to heat removal in the MD simulation. After reaching a temperature close to 750 K, the spatial rearrangement of atoms begins, which manifests itself in a sharp increase in kinetic energy. An analysis of the atomic structure (similar to the analysis made for the structure presented in Fig. 3) shows that the first main maximum in kinetic energy at the 180 000th step is caused by the rearrangement of atoms at the twin boundary; then, the transition to the hcp structure occurs in the other part of the crystallite for a short time. The start of this transition corresponds to the second peak in the kinetic-energy curve. Further cooling causes the formation of a homogeneous and stable α phase of zirconium. Figure 4a shows the RDFs in relation to the simulation time. The numerals near the curves denote the step numbers according to Fig. 4b.

The calculated kinetics of the β ⟶ α martensitic transition generally agrees with the results from [9–11]. In those papers, in contrast to the present study, the initial structure was chosen to be body-centered cubic and the emphasis was on simulation of the β ⟶ α transition. Under these initial conditions, a perfect bcc lattice transforms to an ordered system of twins with an hcp structure. In the case under consideration, the initial structure in the simulation of the β ⟶ α transition was a system of twins of a bcc lattice, which formed due to the temperature-driven transition from the α phase. Under these initial conditions, the newly restored α phase featured a homogeneous hcp lattice. This suggests that the forward and backward transitions occur via the same mechanism.

It should be noted that the authors of [10] failed to achieve the α ⟶ β transition using an ordinary simulation procedure. The transition became possible only after exciting the T_{1N}-phonon mode in the system. Even in this case, the final phase contained not only atoms with a bcc neighborhood but also a significant number of atoms with hcp ordering. The authors of [10] explain the impossibility of achieving the reverse α ⟶ β transition by the fact that the hcp phase does not contain vibrations exactly corresponding to the T_{1N} phonon of the bcc lattice. Our calculations agree better with the MD simulation results from [20], where the α ⟶ β

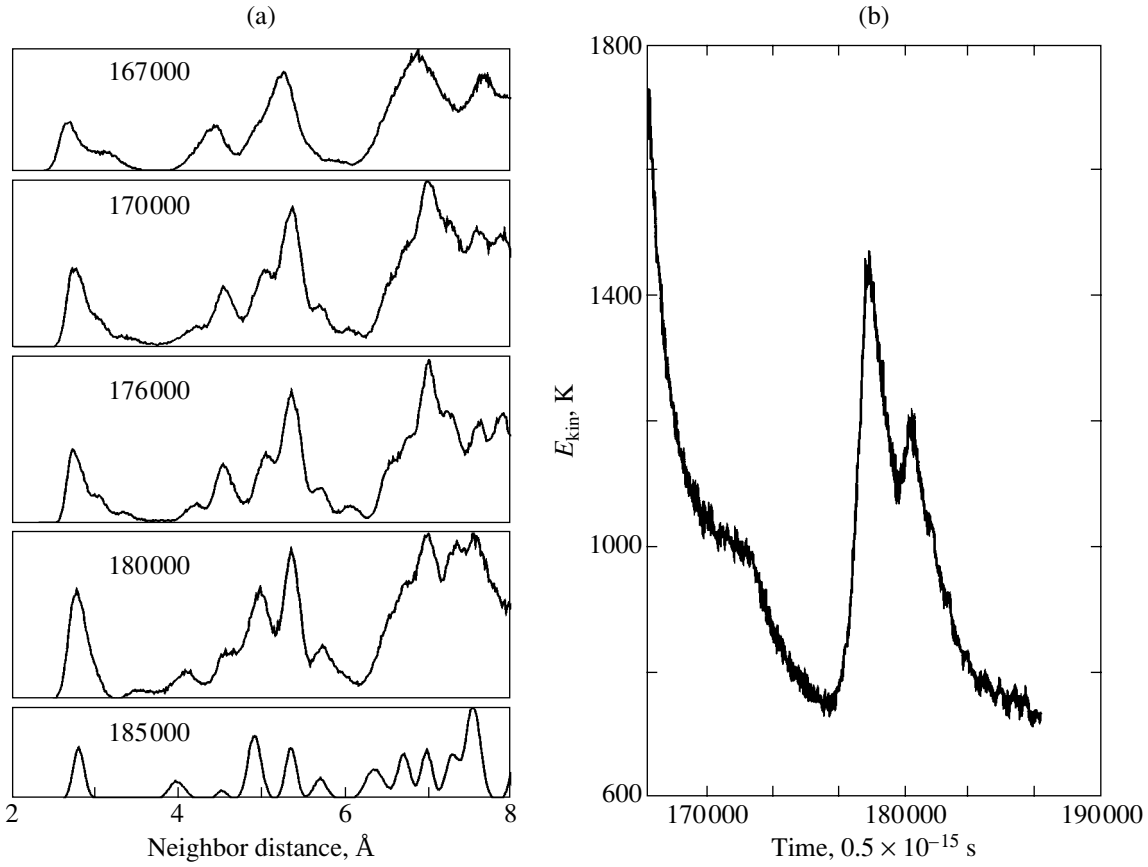

Fig. 4. Changes in (a) the atomic radial distribution function and (b) the crystallite kinetic energy during the β ⟶ α transition.

transformation occurs at $T > 1925$ K via the same mechanism as the β ⟶ α martensitic transition.

The typical change in the structure in the MD simulation of the α ⟶ ω transition is shown in Fig. 5. We can see that regions with a structure different from the hcp structure appear (upper right-hand panel) in the initial matrix of the α phase with the hcp lattice after 640 steps (upper left-hand panel). Then, the growth of new-phase nuclei is observed (lower left panel, $\Delta t = 640$) and, after 1820 steps, the new phase forms throughout the entire crystallite (lower right panel). Thus, the calculation shows that, in contrast to the α ⟶ β transformation, the mechanism of the transition to the ω phase is most likely the formation of new-phase nuclei and their further growth. In this case, the time required for a complete transformation is approximately two times longer than the time taken for the α ⟶ β transition. We also note that both α ⟷ β and α ⟷ ω transformations are displacive; i.e., the transformations occur only via small atomic displacements.

To determine the pressure and temperature ranges over which the α-Zr structure is stable, a series of MD calculations was carried out under various external conditions (P, T). The α ⟷ β transitions were simulated at a fixed pressure P_t with the temperature varying in steps as described above. The onset of a phase transition was also determined as an abrupt change in the kinetic energy and in the elementary volume and as a change in the atomic RDF. The α ⟷ ω transitions were simulated at a fixed temperature T_t and with stepped changes in pressure. The onset of a transition was also determined as an abrupt change in the kinetic energy and was monitored by changes in the elementary volume and atomic RDF. The results are shown in Fig. 6, where symbols indicate the values of P_t and T_t obtained by MD simulation; squares correspond to experimental data [21–25]. It should be noted that the experimental values of the pressure corresponding to the room-temperature transition to the ω phase differ significantly and are dependent on the experimental conditions. According to [21], the pressure of the α ⟷ ω transformation equilibrium as determined in experiments with shear deformations is 22 kbar. Experiments [22, 25] with resistivity measurements under quasi-hydrostatic compression of zirconium yield much larger pressures, from 50 to 70 kbar. Figure 6 shows the extreme experimental values. Thin solid lines conventionally separate the stability regions of the α, β, and ω phases of zirconium. Filled circles and filled triangles denote the forward transitions from the α phase to β and ω phases, respectively, obtained by MD simulation.

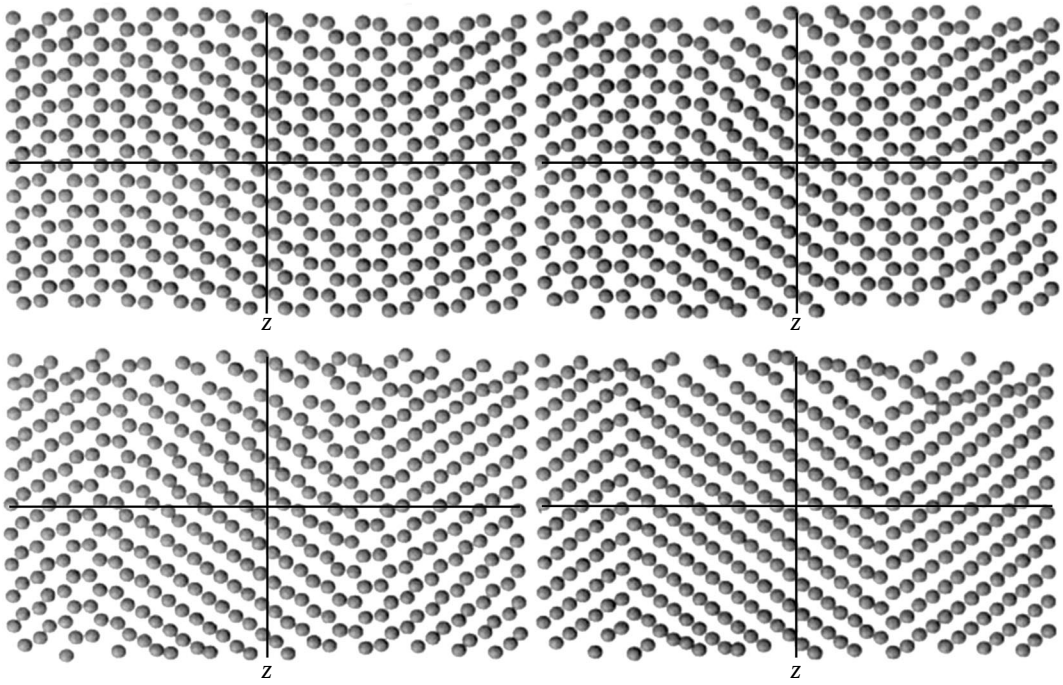

Fig. 5. Changes in the Zr crystal structure during the α ⟶ ω transition (see text for details).

Open circles and open triangles are points at which the backward transition to the α phase begins.

We can see in Fig. 6 that there is a significant hysteresis of forward and backward transformations for both the α ⇄ β and α ⇄ ω transitions. The hysteresis is almost independent of temperature and pressure for the α ⇄ β transition and is strongly dependent on temperature for the α ⇄ ω transition. The significant hysteresis at room temperature observed in our MD calculations agrees well with the experimental fact that the metastable ω phase exists at atmospheric pressure after the applied pressure is removed.

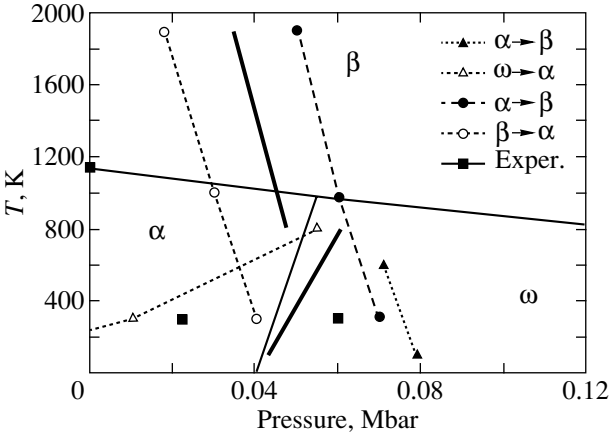

Fig. 6. Stability region of the Zr α phase obtained using molecular-dynamics simulation.

In contrast to experiment, the α ⟶ β transition was observed only under pressure, while the backward transition was observed at normal pressure as well. Figure 6 additionally shows the phase transition lines corresponding to the intermediate position between the forward and backward transitions (bold lines). We note that the α ⇄ β equilibrium line slope is much larger than that observed experimentally in all cases. This can be caused by the fact that the interatomic interaction potential was assumed not to change with pressure in the calculations and that it is impossible to consider the contribution from the electronic entropy in MD simulations. According to [26], the electronic entropy plays an important role in stabilizing the high-temperature bcc phase. *Ab initio* calculations [2] of the zirconium phase diagram show that the inclusion of the electronic entropy decreases the α ⇄ β transition temperature at atmospheric pressure by approximately 400 K. Since the difference between the entropies of the two phases $\Delta S = S_\alpha - S_\beta$ decreases in magnitude as the pressure increases, the role of the electronic entropy becomes insignificant under high pressures. In our opinion, this is the major cause for the α–β transition temperature we obtained by MD simulation being close to experimental data obtained under high pressures but significantly differing from them at low pressures.

An analysis of the changes in the hysteresis shows that the depth of the potential well for the initial α structure is inversely proportional to the applied pressure during the α–β transition; i.e., the height of the energy barrier separating the α structure from the β

phase decreases as the pressure increases. The barrier height for the β phase grows as the pressure decreases.

The height of the barrier to the α–ω transition changes in a very different manner. This transition is accompanied by a decrease in the energy barrier from the side of the β phase as the pressure increases. This follows from the fact that the slope of the phase transition line is negative (filled triangles in Fig. 6). The backward transition (open triangles in Fig. 6) is accompanied by a lowering of the barrier from the side of the ω phase as the pressure decreases. The different pressure dependences of the barrier height during the forward and backward transitions suggest that the lattice instability is associated with different combinations of vibrational modes even though both transitions are displacive.

5. CONCLUSIONS

The structural stability of α-Zr has been considered in wide temperature and pressure ranges using MD simulation. The simulation results show that the use of the pair potential makes it possible to describe the dynamics of the α–β and α–ω phase transitions sufficiently well. In particular, the $\alpha \rightleftharpoons \beta$ and $\alpha \rightleftharpoons \omega$ structural transformations are due to small atomic displacements associated with short-wavelength vibrations (which control the local structure after the transition) and with long-wavelength vibrations (which result in the formation of large-scale structures, such as twins). At the initial stage, the forward $\alpha \longrightarrow \beta$ transition occurs via the formation of a twin system in which the structure transforms in the volume of the twins. In this stage, the short-range order at the twin boundaries remains that corresponding to the initial hcp lattice. The further changes are due entirely to the transformation and to the boundary motion of twins. As the temperature decreases, the backward transition ($\beta \longrightarrow \alpha$) from the high-temperature bcc phase begins with the arrangement of twin boundaries and the formation of hcp lattice short-range order at interfaces, followed by a rapid transition to the α phase over the entire other region of the crystallite. The $\alpha \rightleftharpoons \beta$ transition temperature decreases as the pressure increases. However, the slope of the phase transition line in this case is much larger than the corresponding experimental value, which can be due to the fact that the contribution from the electronic entropy is not taken into account in the MD simulations.

The mechanism of the $\alpha \longrightarrow \omega$ transition is much different. In this case, the formation of a new phase also begins due to phonon instability; however, this process is multistage. First, small regions of a new phase appear in the crystallite volume and grow slowly with the formation of a stripe structure consisting of initial- and final-phase stripes. The stripes of the initial hcp structure decrease in size with time, and regions with a newly formed structure continue to grow. As a result, a new phase with a twin structure forms throughout the crystallite.

Our calculations carried out at various pressures have shown that the general pattern of the α–β and α–ω transitions remains unchanged and is caused by the same atomic displacements at various pressures.

It should be noted that, in this study, we assumed the interatomic interaction potential to be independent of pressure. However, we carried out test calculations using pseudopotentials with various values of the effective charge Z_{eff} and volume Ω_0 in order to trace the influence of the changes in the interatomic pair potential on the phase transition mechanisms. These calculations show that small changes in the potential do not change the general pattern of the transition mechanisms but rather affect only the position of the lines of equilibrium between various phases in the *P*–*T* diagram.

ACKNOWLEDGMENTS

This study was supported by the Russian Foundation for Basic Research, project no. 04-02-16680.

REFERENCES

1. S. Y. Savrasov, Phys. Rev. B: Condens. Matter **54** (23), 16 470 (1996).
2. S. A. Ostanin and V. Yu. Trubitsin, Phys. Rev. B: Condens. Matter **57** (21), 13 485 (1998).
3. Y. Chen, C.-L. Fu, K.-M. Ho, and B. N. Harmon, Phys. Rev. B: Condens. Matter **31** (10), 6775 (1985).
4. S. A. Ostanin, E. I. Salamatov, and V. Yu. Trubitsin, Phys. Rev. B: Condens. Matter **57** (9), 5002 (1998).
5. E. I. Salamatov, Phys. Status Solidi B **197**, 323 (1996).
6. Yu. N. Gornostyrev, M. I. Katsnelson, A. V. Trefilov, and S. V. Tret'jakov, Phys. Rev. B: Condens. Matter **54** (5), 3286 (1996).
7. S. A. Ostanin, E. I. Salamatov, and V. Yu. Trubitsin, High Pressure Res. **17**, 385 (2000).
8. H. Olijnyk and A. P. Jephcoat, Phys. Rev. B: Condens. Matter **56** (17), 10 751 (1997).
9. U. Pinsook and G. J. Ackland, Phys. Rev. B: Condens. Matter **58** (17), 11 252 (1998).
10. U. Pinsook and G. J. Ackland, Phys. Rev. B: Condens. Matter **59** (21), 13 642 (1999).
11. Yu. N. Gornostyrev, M. I. Katsnel'son, A. R. Kuznetsov, and A. V. Trefilov, Pis'ma Zh. Éksp. Teor. Fiz. **70** (6), 376 (1999) [JETP Lett. **70** (6), 380 (1999)].
12. A. O. Animalu, Phys. Rev. B: Solid State **8** (8), 3542 (1973).
13. A. A. Katsnel'son, O. M. Tatarinskaya, and M. M. Khrushchov, Fiz. Met. Metalloved. **64** (4), 655 (1987).
14. E. B. Dolgusheva, V. G. Chudinov, and A. G. Chirkov, Fiz. Tverd. Tela (St. Petersburg) **41** (10), 1729 (1999) [Phys. Solid State **41** (10), 1585 (1999)].
15. C. Stassis, J. Zarestky, D. Arch, O. D. McMasters, and B. N. Harmon, Phys. Rev. B: Condens. Matter **18** (6), 2632 (1978).

16. A. Heiming, W. Petry, J. Trampenau, M. Alba, C. Herzig, H. R. Schober, and G. Vogl, Phys. Rev. B: Condens. Matter **43** (13), 10 948 (1991).
17. F. Willaime and C. Massobrio, Phys. Rev. B: Condens. Matter **43** (14), 11 653 (1991).
18. V. G. Vaks, V. G. Kapinos, Yu. N. Osetskiĭ, G. D. Samolyuk, and A. V. Trefilov, Fiz. Tverd. Tela (Leningrad) **31** (3), 139 (1989) [Sov. Phys. Solid State **31** (3), 427 (1989)].
19. S. H. Liu, C. Stassis, and K.-M. Ho, Phys. Rev. B: Condens. Matter **24** (9), 5093 (1981).
20. F. Willaime and C. Massobrio, Phys. Rev. Lett. **63** (20), 2244 (1989).
21. V. A. Zil'bershteĭn, N. L. Chistotina, A. A. Zharov, N. S. Grishin, and É. I. Éstrin, Fiz. Met. Metalloved. **39** (2), 445 (1975).
22. Y. Akahama, M. Kobayashi, and H. Kawamura, J. Phys. Soc. Jpn. **59** (11), 3843 (1990).
23. Y. Akahama, M. Kobayashi, and H. Kawamura, J. Phys. Soc. Jpn. **60** (10), 3211 (1991).
24. E. Yu. Tonkov, *Phase Diagrams of Elements at High Pressures* (Nauka, Moscow, 1979), pp. 103–105 [in Russian].
25. A. Jayaraman, W. Klement, and G. C. Kennedy, Phys. Rev. **131** (2), 644 (1963).
26. E. G. Moroni, G. Grimvall, and T. Jarlborg, Phys. Rev. Lett. **76** (15), 2758 (1996).

Translated by A. Kazantsev

Physics of the Solid State, Vol. 47, No. 10, 2005, pp. 1805–1813. Translated from Fizika Tverdogo Tela, Vol. 47, No. 10, 2005, pp. 1737–1744.

METALS AND SUPERCONDUCTORS

Effect of Cherenkov Dissipation on Vortex Velocity in a Waveguide-Coupled Josephson Junction

A. S. Malishevskiĭ, V. P. Silin, S. A. Uryupin, and S. G. Uspenskiĭ

Lebedev Physical Institute, Russian Academy of Sciences, Leninskiĭ pr. 53, Moscow, 119991 Russia

e-mail: malish@sci.lebedev.ru

Received November 15, 2004

Abstract—A motion of slow and fast vortices in a waveguide-coupled Josephson junction induced by a transport current flowing through the entire structure is studied; the coupling is not assumed to be weak. For a fast vortex, conditions are established under which current oscillations due to energy dissipation via Cherenkov radiation of Swihart waves become comparable to the current compensating for ohmic losses in the Josephson junction, waveguide, and adjacent superconductors. For a slow vortex, it is proved that intermediate and strong couplings of the Josephson junction to the waveguide shift current oscillations to the velocity range below the Swihart velocity of the Josephson junction. © *2005 Pleiades Publishing, Inc.*

1. INTRODUCTION

Induced vortex motion in Josephson structures has been attracting the attention of scientists for a long time (see, for example, [1–9]). The laws of vortex motion are substantially dependent on the energy dissipation in both the Josephson junction itself and the other parts of the structure coupled with it. For a long time, it has been believed that the energy dissipation of a Josephson vortex is dominated by ohmic losses due to the finite conductance of the Josephson junction and the small resistance of the superconductors. Recently, it has been demonstrated that Cherenkov radiation of Swihart waves, which arises due to the spatial dispersion of superconductors, is an important channel of energy dissipation for a vortex [10, 11]. Vortex motion induced by the current flowing through an isolated Josephson junction was studied in [11] with allowance for both ohmic and Cherenkov losses. The transport current density required to sustain steady motion of a vortex was found. The Cherenkov losses manifest themselves as oscillations in the dependence of the transport current on the vortex velocity, which are superimposed on the monotonic variations corresponding to pure ohmic losses. The induced vortex motion in a Josephson junction with a spatially periodic time-delay line and the possible excitation of linear waves in such a line were studied in [7]. The induced vortex motion in a Josephson junction coupled with a planar waveguide was studied in [12, 13] under the assumption that the transport current flows through the Josephson junction only. The Cherenkov losses were neglected in [12]. In [13], the contributions to the current not only from ohmic losses in the Josephson junction and waveguide but also from the Cherenkov radiation of Swihart waves by the Josephson junction and waveguide were found. It was assumed that the Swihart velocity of the waveguide is much larger than that of the Josephson junction and that the coupling is weak. Progress in studying the Cherenkov losses became possible owing to the model relation of the Josephson current to the phase difference of the superconductor wave functions proposed by Sakai, Tateno, and Pedersen [14, 15].

In the present paper, we continue to study the influence of the Cherenkov losses on the induced vortex motion in a waveguide-coupled Josephson junction in the framework of the Sakai–Tateno–Pedersen approach. In order to find the conditions under which the Cherenkov losses are essential for the relation between the transport current and vortex velocity, we consider ohmic losses not only in the Josephson junction and the waveguide but also in the three superconductors forming the layered structure. In contrast to [13], we assume that the current flows through the entire layered structure and that the coupling between the Josephson junction and waveguide is not necessarily weak. As shown in [16], a current flowing through a waveguide can sustain steady motion of a fast vortex at a lower current density than a current flowing only through the Josephson junction. Giving up the weak coupling approximation, we can study conditions where the Cherenkov losses modify the relation between the current and velocity not only for a slow vortex but also for a fast vortex.

The paper is organized as follows. The main equations for the phase difference in the Josephson junction and waveguide are given in Section 2. Relations are found that make it possible to find the electric and magnetic fields created by a vortex in all space. In Section 3, we obtain expressions for vortex ohmic losses due to energy dissipation in the Josephson junction, waveguide, and superconductors. The dissipative and Lorentz forces acting on a uniformly moving vortex are

found. In Section 4, we obtain an expression for the Cherenkov losses of a moving vortex. The transport current densities required to sustain uniform motion of a slow and fast vortex are found in Sections 5 and 6, respectively. We also establish conditions under which the Cherenkov losses are comparable to ohmic losses and have a substantial effect on the relation between the transport current and velocities of slow and fast vortices.

2. THE FIELD OF A VORTEX IN THE SYSTEM OF A COUPLED JOSEPHSON JUNCTION AND WAVEGUIDE

Let us consider a structure consisting of a thin nonsuperconducting layer with dielectric constant ε_d and conductivity σ_d, placed inside the region $-d < x < d$, and a nonsuperconducting waveguide with dielectric constant ε_w and conductivity σ_w, placed inside the region $L + d < x < L + d + 2d_w$. In the regions $x < -d$ and $x > L + d + 2d_w$ and between the two nonsuperconducting layers ($d < x < d + L$), there are identical superconductors with a London penetration depth $\lambda \gg d_w, d$ and with a conductivity of normal electrons σ_n. As is well known (see, for example, [3]), the critical current density of an SIS junction can be estimated as $j_c \sim \exp(-2d/d_{\text{eff}})$, where the distance scale d_{eff} depends on the effective potential describing the tunnel junction. According to [13], the typical value for d_{eff} is ~5 Å. If $2d \sim d_{\text{eff}}$, the critical current can be sufficiently high for the Josephson effect to occur. The thickness of the second nonsuperconducting layer $2d_w$ is presumed to be much larger than d_{eff}. In this case, the critical current density through the second layer becomes exponentially small and this layer can be considered a waveguide without any Josephson current. So, we presume that the thickness of the waveguide satisfies the condition $d_{\text{eff}} \ll 2d_w \ll \lambda$. In the case where the London penetration depth of the superconductors is $\lambda \sim 10^3$ Å, the range of acceptable values of the waveguide thickness is sufficiently large. Under these conditions, the structure under study can be considered a Josephson junction magnetically coupled with a waveguide.

Let us assume that electromagnetic fields are independent of the y coordinate. We also presume that the characteristic scale of variation of a magnetic field along the z axis is large as compared to the London penetration depth λ. The magnetic field inside the nonsuperconducting layers is assumed to be independent of x. This assumption means that we will consider fields for which the typical scales across the Josephson junction ($\sim k_d^{-1}$) and across the waveguide ($\sim k_w^{-1}$) are much larger than the thicknesses $2d$ and $2d_w$, respectively:

$$2dk_d \ll 1, \quad 2d_w k_w \ll 1.$$

For a typical Josephson junction and fields that are of interest to us, the inequality $2dk_d \ll 1$ usually holds with a wide margin (see, for example, [17, 18]). Below, we show that, for the vortices under study, the condition $2d_w k_w \ll 1$ is also satisfied. The assumption of a small thickness of the waveguide and the condition that the vortex scales be small as compared to the London penetration depth make it possible to describe vortices in a system consisting of a Josephson junction and a waveguide in terms of weakly nonlocal electrodynamics, that is, to use the differential equation from Abrikosov's book [19] instead of a more complex integral equation similar to that used in [7].

Using the continuity of the x component of the generalized current at the interfaces between the superconducting and nonsuperconducting layers, we can write an equation that relates the wave-function phase differences over the Josephson junction, $\varphi(z, t)$, and over the waveguide, $\varphi_w(z, t)$, with the y components of the magnetic field in them, $H(z, t)$ and $H_w(z, t)$. Neglecting the currents due to the small conductivity of the nonsuperconducting layers, we get

$$\frac{\partial^2 \varphi_w(z, t)}{\partial t^2} = -\frac{4\pi}{\phi_0}\lambda V_{s,w}^2 \frac{\partial}{\partial z} H_w(z, t), \tag{1}$$

$$\omega_j^2 F[\varphi] + \frac{\partial^2 \varphi(z, t)}{\partial t^2} = -\frac{4\pi}{\phi_0}\lambda V_s^2 \frac{\partial}{\partial z} H(z, t), \tag{2}$$

where $\omega_j = 4\pi\sqrt{c j_c d/\varepsilon_d \phi_0}$ is the Josephson frequency; $\phi_0 = \pi\hbar c/|e|$ is the magnetic flux quantum; and V_s and $V_{s,w}$ are the Swihart velocities of the isolated Josephson junction and waveguide, respectively: $V_s^2 = c^2 d/(\varepsilon_d \lambda)$ and $V_{s,w}^2 = c^2 d_w/(\varepsilon_w \lambda)$. The function $F[\varphi]$ is the dimensionless tunnel current density through the Josephson junction. Equations (1) and (2) are similar, because the Josephson junction is a waveguide in itself with the distinction that there is a superconducting current flowing through it, whereas the superconducting current flowing through the waveguide is negligibly small.

A set of equations relating the fields and phase differences follows from the Maxwell equations and the continuity conditions for the magnetic field and the z component of the electric field at the layer boundaries. According to [20] (see also [21]), the equations linking the Fourier transforms of the fields $H(k, t)$ and $H_w(k, t)$ and the phase differences $\varphi(k, t)$ and $\varphi_w(k, t)$ have the form

$$H(k,t) = -ik\frac{\phi_0}{2\pi}\frac{1}{2\lambda^2\sqrt{k^2+\lambda^{-2}}}$$
$$\times[\varphi(k,t) + e^{-L\sqrt{k^2+\lambda^{-2}}}\varphi_w(k,t)],$$
$$H_w(k,t) = -ik\frac{\phi_0}{2\pi}\frac{1}{2\lambda^2\sqrt{k^2+\lambda^{-2}}} \quad (3)$$
$$\times[e^{-L\sqrt{k^2+\lambda^{-2}}}\varphi(k,t) + \varphi_w(k,t)].$$

If the typical scales of variation of the magnetic field and of the phase differences are large as compared to the London penetration depths, then the terms $\sim k\lambda$ can be neglected and from Eqs. (3) we obtain

$$H(z,t) = -\frac{\phi_0}{2\pi}\frac{1}{2\lambda}\frac{\partial}{\partial z}[\varphi(z,t) + e^{-L/\lambda}\varphi_w(z,t)],$$
$$H_w(z,t) = -\frac{\phi_0}{2\pi}\frac{1}{2\lambda}\frac{\partial}{\partial z}[e^{-L/\lambda}\varphi(z,t) + \varphi_w(z,t)]. \quad (4)$$

Substituting these approximate expressions for magnetic fields into Eqs. (1) and (2) describing the waveguide and Josephson junction, we get

$$\frac{\partial^2\varphi_w(z,t)}{\partial t^2} = V_{s,w}^2\frac{\partial^2\varphi_w(z,t)}{\partial z^2} + e^{-L/\lambda}V_{s,w}^2\frac{\partial^2\varphi(z,t)}{\partial z^2}, \quad (5)$$

$$\omega_j^2 F[\varphi] + \frac{\partial^2\varphi(z,t)}{\partial t^2}$$
$$= V_s^2\frac{\partial^2\varphi(z,t)}{\partial z^2} + e^{-L/\lambda}V_s^2\frac{\partial^2\varphi_w(z,t)}{\partial z^2}. \quad (6)$$

Notice that, if we disregard the coupling between the Josephson junction and waveguide, Eq. (5) reduces to the well-known equation for Swihart waves (see, for example, [19]).

Let us consider vortices moving freely along the z axis at a constant speed v. Equations (5) and (6) for them take the form

$$e^{-L/\lambda}V_{s,w}^2\psi''(\zeta) + (V_{s,w}^2 - v^2)\psi_w''(\zeta) = 0, \quad (7)$$

$$e^{-L/\lambda}V_s^2\psi_w''(\zeta) + (V_s^2 - v^2)\psi''(\zeta) = \omega_j^2 F[\psi]. \quad (8)$$

Here, $\psi(\zeta) = \varphi(z,t)$ and $\psi_w(\zeta) = \varphi_w(z,t)$, with $\zeta = z - vt$. Substituting ψ_w'' from Eq. (7) into Eq. (8), we get a single equation for $\psi(\zeta)$,

$$F[\psi] = \frac{2}{\pi}k_j^{-2}(v)\psi''(\zeta), \quad (9)$$

where the function $k_j(v)$ is defined as

$$k_j(v) = \sqrt{\frac{2}{\pi}}\omega_j\sqrt{\frac{V_{s,w}^2 - v^2}{(v_0^2 - v^2)(v_1^2 - v^2)}}. \quad (10)$$

Here, v_0 and v_1 ($v_0 < v_1$) are the roots of the equation

$$(V_s^2 - v^2)(V_{s,w}^2 - v^2) - e^{-2L/\lambda}V_s^2V_{s,w}^2 = 0.$$

To solve Eq. (9), we will use the Sakai–Tateno–Pedersen model, in which the function $F[\varphi]$ is given by

$$f[\varphi] = \begin{cases}(2/\pi)\varphi, & 0 < \varphi < \pi/2\\ (2/\pi)(\pi - \varphi), & \pi/2 < \varphi < 3\pi/2\\ (2/\pi)(\varphi - 2\pi), & 3\pi/2 < \varphi < 2\pi.\end{cases} \quad (11)$$

The solution to Eq. (9) corresponding to a stable elementary vortex (2π kink) moving at constant speed v is given by [11]

$$\psi(\zeta) = \frac{\pi}{2}\exp\left[k_j(v)\zeta + \frac{\pi}{4}\right], \quad \zeta < -\frac{\pi}{4k_j},$$
$$\psi(\zeta) = \pi + \frac{\pi}{\sqrt{2}}\sin[k_j(v)\zeta], \quad -\frac{\pi}{4k_j} < \zeta < \frac{\pi}{4k_j}, \quad (12)$$
$$\psi(\zeta) = 2\pi - \frac{\pi}{2}\exp\left[-k_j(v)\zeta + \frac{\pi}{4}\right], \quad \zeta > \frac{\pi}{4k_j}.$$

Using Eq. (12), we can write explicitly the condition that was used in deriving Eqs. (5) and (6)

$$k_j(v)\lambda \ll 1. \quad (13)$$

Condition (13) means that the spatial dimension of the vortex should be significantly larger than the London penetration depth. Also, it follows from Eq. (12) that the motion of a stable vortex is possible only if the function $k_j(v)$ is real. This imposes constraints on the vortex velocity v. It follows from Eq. (10) that an elementary vortex can move in two velocity ranges [12]. For example, if $V_{s,w} > V_s$, then one range corresponds to a slow vortex, $v < v_0 < V_s$, and the other corresponds to a fast vortex and extends from $V_{s,w}$ to v_1.

Let us show that the condition that the thickness of the waveguide $2d_w$ be small in comparison with k_w^{-1} can be satisfied for both slow and fast vortices. In the case under study, where the speed of light in the waveguide is large as compared to the Swihart velocities, we can, following [12], estimate k_w as

$$k_w = k_j(v)\sqrt{|1 - \varepsilon_w v^2/c^2|} \approx k_j(v).$$

With this estimate, we get $2d_wk_w \approx 2d_wk_j(v) = (2d_w/\lambda)(k_j(v)\lambda)$. Since we assume that condition (13) holds, the inequality $2d_wk_w \ll 1$ can easily be satisfied.

Let us consider the spatial distribution of the fields of a moving vortex described by Eq. (12). On substituting the derivative ψ_w' obtained from Eq. (7) by single

integration, Eqs. (4) for the magnetic fields in the nonsuperconducting layers become

$$H(\zeta) = -\frac{\phi_0}{4\pi\lambda}[v^2 - (1-e^{-2L/\lambda})V_{s,w}^2]\frac{\psi'(\zeta)}{v^2 - V_{s,w}^2},$$
$$H_w(\zeta) = -\frac{\phi_0}{4\pi\lambda}e^{-L/\lambda}\frac{v^2}{v^2 - V_{s,w}^2}\psi'(\zeta). \quad (14)$$

The magnetic fields in the superconductors are related to the fields in the Josephson junction and waveguide as follows:

$$H(x > d + L + 2d_w, z, t)$$
$$= H_w(z, t)\exp[-(x - L - d - 2d_w)/\lambda],$$
$$H(d < x < d + L, z, t) = H_w(z, t)\frac{\sinh[(x-d)/\lambda]}{\sinh(L/\lambda)} \quad (15)$$
$$- H(z, t)\frac{\sinh[(x-d-L)/\lambda]}{\sinh(L/\lambda)},$$
$$H(x < -d, z, t) = H(z, t)\exp[(x + d)/\lambda].$$

For moving vortices, the magnetic fields in the Josephson junction and waveguide entering into Eq. (15) are described by Eqs. (14). The electric field in the superconductors is related to the magnetic field as follows:

$$\mathbf{E}^{Sc} = \frac{\lambda^2}{c}\mathrm{curl}\frac{\partial \mathbf{H}^{Sc}}{\partial t}. \quad (16)$$

It follows from Eq. (16) and condition (13) that $|E_z^{Sc}| \gg |E_x^{Sc}|$ in the superconducting layers. Using this fact, the electric field in the superconductors can be approximated by

$$E_z^{Sc}(x < -d, \zeta) = v\frac{\psi_0}{4\pi c}[v^2 - (1-e^{-2L/\lambda})V_{s,w}^2]$$
$$\times \exp\left[\frac{x+d}{\lambda}\right]\frac{\psi''(\zeta)}{v^2 - V_{s,w}^2},$$
$$E_z^{Sc}(d < x < d + L + 2d_w, \zeta) = -v\frac{\psi_0}{4\pi c}\frac{1}{\sinh(L/\lambda)}$$
$$\times\{-e^{-2L/\lambda}v^2\cosh(L/\lambda) + [v^2 - (1-e^{-2L/\lambda})V_{s,w}^2]$$
$$\times \cosh\left[\frac{x-L-d}{\lambda}\right]\Bigg\}\frac{\psi''(\zeta)}{v^2 - V_{s,w}^2}, \quad (17)$$
$$E_z^{Sc}(x > d + L + 2d_w, \zeta) = -v\frac{\psi_0}{4\pi c}e^{-L/\lambda}\frac{v^2}{v^2 - V_{s,w}^2}$$
$$\times \exp\left[-\frac{x-L-d-2d_w}{\lambda}\right]\psi''(\zeta).$$

According to the Josephson equation, the fields in the nonsuperconducting layers are

$$E_x(-d < x < d, z, t) = \frac{\phi_0}{4\pi c}\frac{1}{d}\frac{\partial\varphi(z,t)}{\partial t},$$
$$E_x(L + d < x < L + d + 2d_w, z, t) \quad (18)$$
$$= \frac{\phi_0}{4\pi c}\frac{1}{d_w}\frac{\partial\varphi_w(z,t)}{\partial t}.$$

It is easily seen from Eqs. (18) and (13) that, inside the Josephson junction and waveguide, $|E_x| \gg |E_z|$.

The expressions derived in this section for the electric and magnetic fields in the Josephson junction and waveguide make it possible to calculate the energy losses due to the finite conductivity of the nonsuperconducting layers and the small resistance of the superconductors.

3. DISSIPATION OF VORTEX ENERGY

Let us consider ohmic energy losses of a vortex moving in a layered structure at a speed v. The variation in the vortex energy W because of the ohmic losses is given by

$$\frac{dW}{dt} = -\int dxdz\sigma E^2, \quad (19)$$

where integration is performed over the entire xz plane. The integral over x in Eq. (19) consists of five terms arising from the two nonsuperconducting layers with conductivities σ_d and σ_w and the three superconducting layers with normal electron conductivity σ_n. The latter conductivity arises because, at a nonzero temperature, some electrons of a superconductor are in the normal state. Using Eq. (18), we can find the contribution to Eq. (19) from the nonsuperconducting layers $-d < x < d$ and $L + d < x < L + d + 2d_w$

$$-\frac{dW_{d,d_w}}{dt} = \frac{\pi^2}{16}\left(1 + \frac{4}{\pi}\right)\left(\frac{\phi_0}{4\pi c}\right)^2$$
$$\times\left\{\beta + \beta_w e^{-2L/\lambda}\frac{V_s^2 V_{s,w}^2}{(V_{s,w}^2 - v^2)}\right\}\frac{\varepsilon_d}{d}v^2 k_j(v), \quad (20)$$

where $\beta = 4\pi\sigma_d/\varepsilon_d$ and $\beta_w = 4\pi\sigma_w/\varepsilon_w$. The contributions from each superconductor layer to the integral will be written separately. Using the first of Eqs. (17), we find losses in the region $x < -d$,

$$-\frac{dW_{Sc,1}}{dt} = \frac{\pi^3}{16}\sigma_n\left(\frac{\phi_0}{4\pi c}\right)^2$$
$$\times v^2\left[\frac{v^2 - V_{s,w}^2(1-e^{-2L/\lambda})}{v^2 - V_{s,w}^2}\right]^2\lambda k_j^3(v); \quad (21)$$

using the second of Eqs. (17), we find losses in the layer $d < x < d + L$,

$$-\frac{dW_{Sc,2}}{dt} = \frac{\pi^3}{16}\sigma_n\left(\frac{\phi_0}{4\pi c}\right)^2\left\{\left(\frac{L}{\lambda}+\frac{\sinh(2L/\lambda)}{2}\right)\right.$$
$$\times[v^4e^{-2L/\lambda}+(v^2-V_{s,w}^2(1-e^{-2L/\lambda}))^2]$$
$$\left.-2v^2e^{-L/\lambda}\left(\frac{L}{\lambda}+\frac{\sinh(2L/\lambda)}{2}\right)(v^2-V_{s,w}^2(1-e^{-2L/\lambda}))\right\}$$
$$\times\frac{v^2}{(v^2-V_{s,w}^2)^2}\frac{\lambda k_j^3(v)}{\sinh^2(L/\lambda)}; \quad (22)$$

and from the third of Eqs. (17), we obtain losses in the region $x > d + L + 2d_w$,

$$-\frac{dW_{Sc,3}}{dt} = \frac{\pi^3}{16}\sigma_n\left(\frac{\phi_0}{4\pi c}\right)^2\frac{v^6e^{-2L/\lambda}}{(v^2-V_{s,w}^2)^2}\lambda k_j^3(v). \quad (23)$$

Knowing the energy losses in the structure, we can find the dissipative force F_{diss} acting on a vortex moving at speed v:

$$\frac{dW}{dt} = \frac{dW_{d,d_w}}{dt}+\frac{dW_{Sc,1}}{dt}+\frac{dW_{Sc,2}}{dt}+\frac{dW_{Sc,3}}{dt} = -vF_{\text{diss}}. \quad (24)$$

If the uniform transport current density is j, the vortex is subjected to a Lorentz force whose magnitude per unit length along y axis is

$$F_z = -\int dxdz\frac{jH(x,z,t)}{c}, \quad (25)$$

where integration is performed over the entire xz plane. Using explicit expressions (14) and (15) for the magnetic field and Eqs. (12) for the phase differences, we can find from Eq. (25) that [16]

$$F_z = \frac{j}{c}\phi_0\left(1-e^{-L/\lambda}\frac{V_{s,w}^2}{V_{s,w}^2-v^2}\right). \quad (26)$$

Steady motion of the vortex is possible if the dissipative force F_{diss} is compensated by the Lorentz force that originates from the current flowing through the structure along the x axis. The transport current required to sustain the steady motion of the vortex can be found by equating the Lorentz force and the dissipative force.

4. CHERENKOV LOSSES FOR INDUCED VORTEX MOTION

Let us consider the effect of the Cherenkov losses on induced vortex motion. Assuming both ohmic and Cherenkov energy losses to be small, they can be taken into account independently. Therefore, when calculating the Cherenkov losses, we disregard the ohmic losses in the equations describing vortex motion in the system. As was shown in [11], in order to obtain the Cherenkov losses, it is necessary to take into account the spatial dispersion related to the higher order terms of expansion in the small ratio of the London penetration depth λ to the characteristic vortex dimension $\sim 1/k_j$. Assuming that the London penetration depth is small as compared to the vortex dimension, we retain the terms quadratic in $k\lambda$ in Eq. (3). Using this expansion in $k\lambda$, we get the following set of equations for the phase differences [cf. Eqs. (5) and (6)]:

$$\frac{\partial^2\varphi_w(z,t)}{\partial t^2}+\frac{(4\pi)^2\lambda V_{s,w}^2}{\phi_0 c}j = V_{s,w}^2\left[\frac{\partial^2\varphi_w(z,t)}{\partial z^2}+e^{-L/\lambda}\frac{\partial^2\varphi(z,t)}{\partial z^2}\right]$$
$$+\lambda^2\frac{V_{s,w}^2}{2}\left[\frac{\partial^4\varphi_w(z,t)}{\partial z^4}+e^{-L/\lambda}(1+L/\lambda)\frac{\partial^4\varphi(z,t)}{\partial z^4}\right], \quad (27)$$

$$\omega_j^2F[\varphi]+\frac{\partial^2\varphi_w(z,t)}{\partial t^2}+\omega_j^2\frac{j}{j_c} = V_s^2\left[\frac{\partial^2\varphi(z,t)}{\partial z^2}+e^{-L/\lambda}V_s^2\frac{\partial^2\varphi_w(z,t)}{\partial z^2}\right]$$
$$+\lambda^2\frac{V_s^2}{2}\left[\frac{\partial^4\varphi(z,t)}{\partial z^4}+e^{-L/\lambda}(1+L/\lambda)\frac{\partial^4\varphi_w(z,t)}{\partial z^4}\right]. \quad (28)$$

Let us consider vortices moving at a constant speed v. Using Eq. (7), we get [cf. Eq. (9)]

$$F[\psi] = \frac{2}{\pi}k_j^{-2}(v)\psi''(\zeta)-\frac{j}{j_c}\left(1-e^{-L/\lambda}\frac{V_{s,w}^2}{V_{s,w}^2-v^2}\right)$$
$$+\frac{\lambda_j^2\lambda^2}{2}\left[1+e^{-2L/\lambda}\frac{V_{s,w}^4}{(V_{s,w}^2-v^2)^2}\right.$$
$$\left.-2e^{-2L/\lambda}(1+L/\lambda)\frac{V_{s,w}^2}{V_{s,w}^2-v^2}\right]\psi^{IV}(\zeta), \quad (29)$$

where $\lambda_j = V_s/\omega_j$. An equation similar to Eq. (29) was solved in [11], where the Cherenkov losses in an isolated Josephson junction were studied. Equation (29) differs from the equation considered in [8] in terms of the coefficients of the current and of the derivatives. Thus, we can obtain a solution to Eq. (29) from the solution in [11] by substituting for the appropriate coefficients. With this substitution, we get the following

relation between the current and vortex velocity from Eq. (29):

$$\frac{j(v)}{j_c} = \frac{\varepsilon^4}{8}\left(\sin\frac{\pi}{2\varepsilon} - \frac{\varepsilon}{2}\cos\frac{\pi}{2\varepsilon}\right)^2 \times\left(1 - e^{-L/\lambda}\frac{V_{s,w}^2}{V_{s,w}^2 - v^2}\right)^{-1}, \quad (30)$$

where ε is defined as

$$\varepsilon = \sqrt{\pi}\lambda\lambda_j k_j^2(v)\left(1 + e^{-2L/\lambda}\frac{V_{s,w}^4}{(V_{s,w}^2 - v^2)^2} - 2e^{-2L/\lambda}(1 + L/\lambda)\frac{V_{s,w}^2}{V_{s,w}^2 - v^2}\right)^{1/2}. \quad (31)$$

Equation (30) is valid if $\varepsilon^2 \ll 1$ and $\lambda_j^2 k_j^2 \ll \varepsilon^2$ (for details, see [11]). Expression (30) differs from that obtained in [13] by the last parenthetical factor. This factor appears because the current is flowing through the entire structure rather than through the Josephson junction alone as in [13]. It is important that ε given by Eq. (31) and entering into Eq. (30) is obtained here without the assumption of weak coupling between the Josephson junction and waveguide, in contrast to [13].

5. SLOW VORTEX

Let us consider the case where the Swihart velocity in the waveguide is much larger than the Swihart velocity in the Josephson junction, $V_{s,w} \gg V_s$. As was shown in [12], the velocity of a moving vortex in this case has to lie in one of the two allowed ranges. In this section, we consider one of them, the slow-vortex region, where the velocity of a vortex is smaller than v_0:

$$0 < v < v_0 \approx V_s(1 - e^{-2L/\lambda})^{1/2}. \quad (32)$$

For this velocity range, the energy losses of a slow vortex in the Josephson junction and waveguide can be found from Eq. (20) to be

$$-\frac{dW_{d,d_w}}{dt} = \frac{1}{4}\left(\frac{\pi}{2}\right)^{3/2}\left(1 + \frac{4}{\pi}\right)\left(\frac{\phi_0}{4\pi c}\right)^2 \times\left\{\beta + \beta_w e^{-2L/\lambda}\frac{V_s^2}{V_{s,w}^2}\right\}\frac{\varepsilon_d}{d}v^2\frac{\omega}{\sqrt{v_0^2 - v^2}}, \quad (33)$$

and the total losses in the superconductors are

$$-\frac{dW_{Sc}}{dt} = \left(\frac{\pi}{2}\right)^{3/2}\sigma_n\left(\frac{\phi_0}{4\pi c}\right)^2\frac{v^2}{(v_0^2 - v^2)^{3/2}} \times\lambda\omega_j^3\left(1 - e^{-2L/\lambda} + 2\frac{L}{\lambda}e^{-2L/\lambda}\right). \quad (34)$$

Substituting Eqs. (33) and (34) into Eq. (24) and comparing it with Eq. (26), we obtain the transport current required to sustain slow vortex motion at a constant speed v:

$$\frac{j(v)}{j_c} = \frac{1}{4}\left(\frac{\pi}{2}\right)^{3/2}\left[\left(1 + \frac{4}{\pi}\right)\left(\beta + \beta_w e^{-2L/\lambda}\frac{V_s^2}{V_{s,w}^2}\right) + \eta\frac{2}{\pi}\frac{V_s^2}{v_0^2 - v^2}\left(1 - e^{-2L/\lambda} + 2\frac{L}{\lambda}e^{-2L/\lambda}\right)\right] \times\frac{v}{\omega_j}\frac{1}{\sqrt{v_0^2 - v^2}}\left(1 - e^{-L/\lambda}\frac{V_{s,w}^2}{V_{s,w}^2 - v^2}\right)^{-1}, \quad (35)$$

where $\eta = 2\pi\lambda^2\sigma_n\omega_j^2/c^2V_s^2$.

Now, let us consider the effect of Cherenkov losses on slow vortex motion. The corresponding contribution to the current is described by Eq. (30) with the difference that the quantity defined by Eq. (31) is now given by

$$\varepsilon = \frac{2}{\sqrt{\pi}}\frac{\lambda}{\lambda_j}\frac{V_s^2}{v_0^2 - v^2}\sqrt{1 - (+2L/\lambda)e^{-2L/\lambda}}. \quad (36)$$

Graphs of the current density as a function of slow vortex velocity are presented in Fig. 1. All three graphs are plotted for a region near the upper boundary of the allowed range of slow vortex motion; this region extends from the speed corresponding to $\lambda_j k_j/\varepsilon \approx 0.3$ up to the speed corresponding to $\varepsilon \approx 0.3$. For this velocity range, the contribution from the Cherenkov losses to the current can be described by Eq. (30). Figure 1a corresponds to the case of $L/\lambda = 3$, where $\exp(-L/\lambda) \approx 0.05$ and the coupling of the waveguide and Josephson junction is weak. Figure 1a is similar to Fig. 2 from [11], where an isolated Josephson junction was studied. As in [11], oscillations corresponding to Cherenkov losses, described by Eq. (30), are observed on a background of steadily increasing ohmic losses, given by Eq. (35). The amplitude of the oscillations grows as the vortex velocity approaches the upper boundary of the allowed velocity range. Notice that, for the coupled Josephson junction and waveguide, the allowed velocity range extends not to the Swihart velocity in the Josephson junction but rather to a smaller velocity $v_0 < V_s$. The dashed line in Fig. 1a corresponds to the case where there are no ohmic losses in the superconductors. Since the coupling of the Josephson junction to the waveguide is weak for $L/\lambda = 3$, the dashed curve coincides with the curve in Fig. 2 from [11]. The solid line in Fig. 1a includes the ohmic losses in the superconductors; so the values of the function $j(v)$ are increased as compared to those in [11].

The influence of the waveguide on induced vortex motion becomes substantial for lower values of L/λ. Figure 1b shows the dependence of the current on the

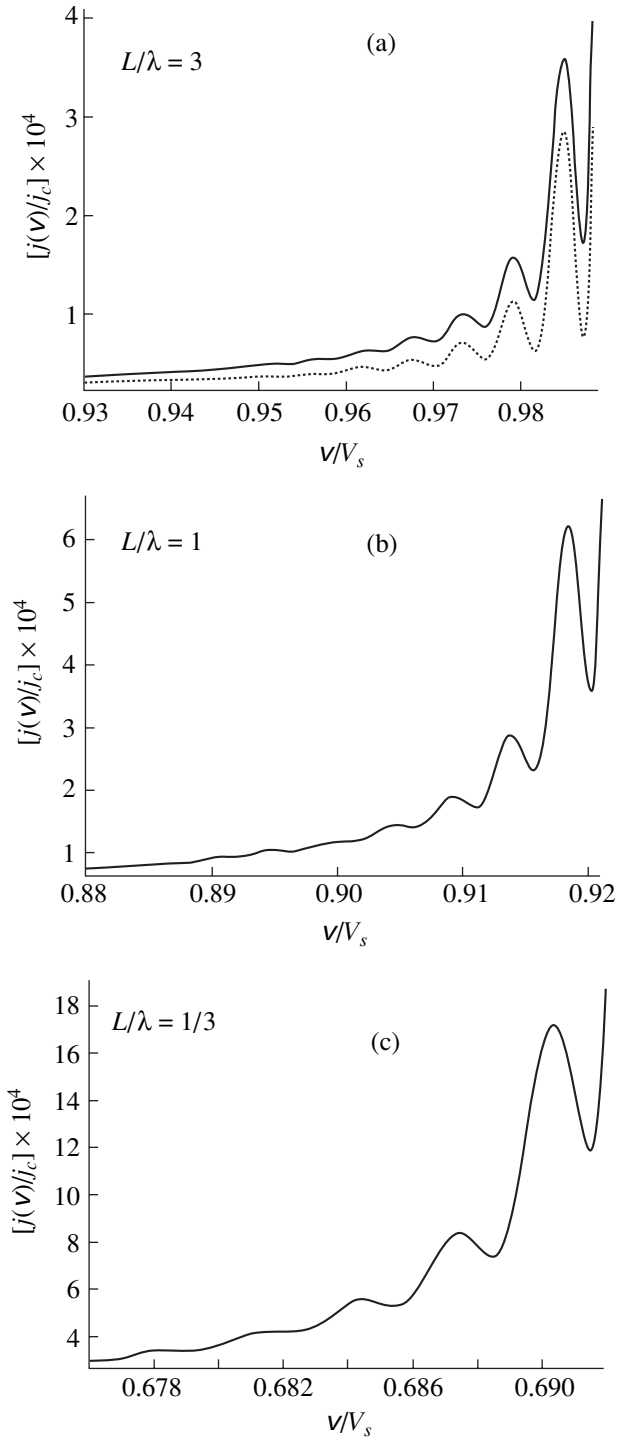

Fig. 1. Transport current density as a function of slow vortex velocity for $V_{s,w} = 5V_s$, $\lambda/\lambda_j = 5 \times 10^{-3}$, $\beta/\omega_j = 10^{-5}$, $\beta_w = \beta$, $\eta = \beta/10$, and various values of L/λ: (a) 3, (b) 1, and (c) 1/3. The dashed line corresponds to the case of $\eta = 0$.

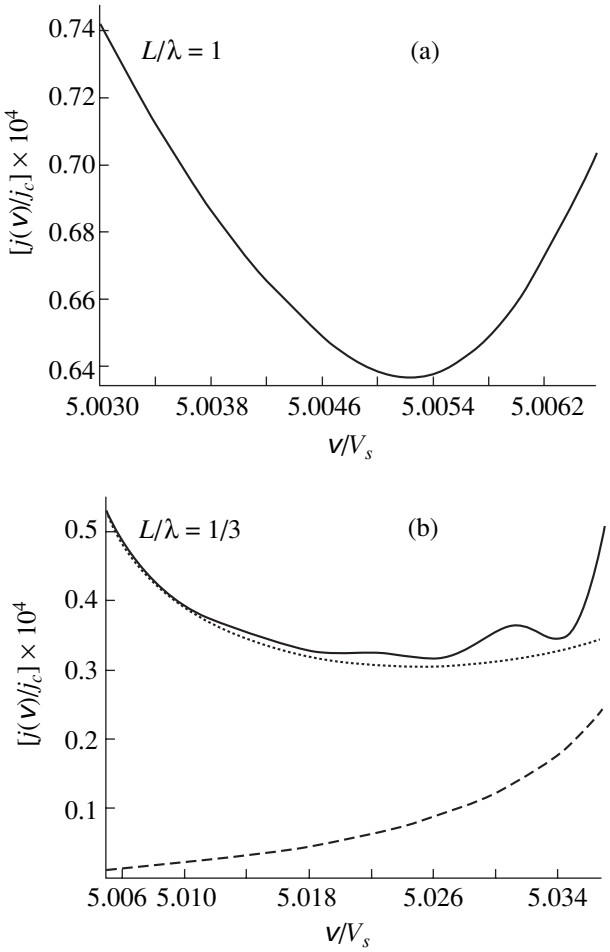

Fig. 2. Transport current density as a function of fast vortex velocity for $\lambda/\lambda_j = 5 \times 10^{-2}$; all other parameters are the same as those in Fig. 1. (a) $L/\lambda = 1$ and (b) $L/\lambda = 1/3$. The dotted line shows the contribution from dissipation in the nonsuperconducting layers to the current density. The dashed line is 10 times the contribution from dissipation in the superconductors to the current density.

vortex velocity for $L/\lambda = 1$. The influence of the waveguide contracts the allowed vortex velocity range in this case: $0 < v < v_0 \approx 0.93V_s$. As in the previous case, the graph is plotted up to $\varepsilon \approx 0.3$. As in Fig. 1a, as v increases, oscillations corresponding to Cherenkov losses appear and grow near the upper boundary of the allowed velocity range on the background of a steadily raising current corresponding to ohmic losses. In addition to the contraction of the allowed range, the influence of the waveguide causes the function $j(v)$ to increase in magnitude.

Finally, Fig. 1c shows the relation between the current and vortex velocity for the case of $L/\lambda = 1/3$, which corresponds to a relatively strong coupling of the Josephson junction to the waveguide. In this case, the width of the allowed velocity range of slow vortex motion is about $0.7V_s$. A significant contribution of the Cherenkov losses is evident in Fig. 1c, which is also plotted up to $\varepsilon \approx 0.3$. Comparing Figs. 1a–1c, we see that, as the coupling of the Josephson junction to the waveguide increases, the current oscillation shifts to velocities lower than V_s and $j(v)$ increases in magnitude.

6. FAST VORTEX

In this section, we consider a fast vortex that is a vortex moving at a speed v lying in the narrow range

$$V_{s,w} < v < v_1 \approx V_{s,w}\left(1 + \frac{1}{2}e^{-2L/\lambda}\frac{V_s^2}{V_{s,w}^2}\right). \quad (37)$$

For the velocity range (37), we get from Eq. (20)

$$-\frac{dW_{d,d_w}}{dt} = \frac{1}{4}\left(\frac{\pi}{2}\right)^{3/2}\left(1 + \frac{4}{\pi}\right)\left(\frac{\phi_0}{4\pi c}\right)^2$$

$$\times\left\{\beta + \beta_w e^{-2L/\lambda}\frac{V_s^2}{4(v - V_{s,w})^2}\right\}\frac{\varepsilon_d}{d}v^2\frac{\omega_j}{V_{s,w}}\sqrt{\frac{v - V_{s,w}}{v_1 - v}}, \quad (38)$$

and the total losses in the superconductors are

$$-\frac{dW_{Sc}}{dt} = \left(\frac{\pi}{2}\right)^{3/2}\sigma_n\left(\frac{\phi_0}{4\pi c}\right)^2$$

$$\times\lambda\omega_j^3\frac{v^2 e^{-2L/\lambda}}{4V_{s,w}(v_1 - v)^{3/2}(v - V_{s,w})^{1/2}}. \quad (39)$$

By substituting Eqs. (38) and (39) into Eq. (24) and making a comparison with Eq. (26), we obtain the transport current required to sustain steady motion of a fast vortex at speed v in the presence of ohmic losses:

$$\frac{j(v)}{j_c} = \frac{1}{4}\left(\frac{\pi}{2}\right)^{3/2}\left[\left(1 + \frac{4}{\pi}\right)\left(\beta + \beta_w e^{-2L/\lambda}\frac{V_s^2}{4(v - V_{s,w})^2}\right)\right.$$

$$\left. + \eta\frac{2}{\pi}e^{-2L/\lambda}\frac{V_s^2}{4(v - V_{s,w})(v_1 - v)}\right]$$

$$\times\frac{1}{\omega_j}\sqrt{\frac{v - V_{s,w}}{v_1 - v}}\left(1 - e^{-L/\lambda}\frac{V_{s,w}}{2(V_{s,w} - v)}\right)^{-1}. \quad (40)$$

The Cherenkov energy losses of a fast vortex are described by Eq. (30) with ε given by

$$\varepsilon = \frac{2}{\sqrt{\pi}}\frac{\lambda}{\lambda_j}\frac{V_s^2}{V_{s,w}^2}\frac{v - V_{s,w}}{v_1 - v}$$

$$\times\sqrt{1 + e^{-2L/\lambda}\frac{V_{s,w}^2}{4(v - V_{s,w})^2} - e^{-2L/\lambda}(1 + L/\lambda)\frac{V_{s,w}}{v - V_{s,w}}}. \quad (41)$$

The current density as a function of fast vortex velocity near the upper boundary of the allowed range (37) is shown in Fig. 2a. The graph is plotted for $L/\lambda = 1$ up to the velocity corresponding to $\varepsilon \approx 0.3$; small ohmic and Cherenkov losses are assumed to be additive. The Cherenkov losses cannot be distinguished from the background of ohmic losses even for relatively large ε. For stronger coupling of the Josephson junction to the waveguide, $L/\lambda = 1/3$, the picture is different. The current as a function of fast vortex velocity for $L/\lambda = 1/3$ is shown in Fig. 2b by a solid line. The limiting value of v in this figure corresponds to $\varepsilon \approx 0.3$. In Fig. 2b, the dotted line describes the contribution from the dissipation in the nonsuperconducting layers to the current density and the dashed line describes the contribution from the dissipation in the superconductors. It follows from Fig. 2b that oscillations due to Cherenkov losses can be observed if the coupling of the Josephson junction to the waveguide is relatively strong.

7. CONCLUSIONS

Cherenkov losses have been found for a vortex moving in a layered structure consisting of a Josephson junction and a waveguide magnetically coupled to it; the coupling of the Josephson junction to the waveguide is not assumed to be weak. We have demonstrated that, in the case where the coupling of the Josephson junction to the waveguide is strong, the current oscillation due to the Cherenkov losses of a fast vortex can be distinguished relatively easily from the contributions to the current from ohmic losses in the nonsuperconducting layers and superconducting terminals. For a slow vortex, the strong coupling shifts the peaks on the $j(v)$ curve to a velocity range below the Swihart velocity in the Josephson junction.

APPENDIX

Let us consider ohmic losses in the superconductors and nonsuperconducting layers for the case where the Josephson junction is described by an equation with a sine nonlinear term. In this case, Eq. (9) takes the form

$$\sin\psi(\zeta) = \frac{2}{\pi}k_j^{-2}(v)\psi''(\zeta), \quad (42)$$

and its solution describing a stable elementary vortex (2π kink) moving at a constant speed v is given by

$$\psi(\zeta) = 4\arctan\left\{\exp\left(\sqrt{\frac{\pi}{2}}k_j(v)\zeta\right)\right\}. \quad (43)$$

All formulas obtained for small ohmic losses in the model with sinusoidal nonlinearity differ from the expressions given above for the Sakai–Tateno–Pedersen model only in terms of their numerical coefficients. For example, energy dissipation in the nonsuperconducting layers is described by Eq. (20) in which the numerical factor $(\pi^2/16)(1 + 4/\pi)$ is replaced by $2 \times (2/\pi)^{1/2}$. Energy dissipation in the superconductors is described by Eqs. (21)–(23) with $\pi^3/16$ replaced by $(4/3)(\pi/2)^{3/2}$. In Eqs. (33) and (38) describing losses in the nonsuperconducting layers for slow and fast vortices, respectively, the factor $(1/4)(\pi/2)^{3/2}(1 + 4/\pi)$ should be replaced by $4/\pi$. For the dissipation of vortex energy

in the superconductors, Eqs. (34) and (39) are valid with $(\pi/2)^{3/2}$ replaced by 8/3. For the transport current required to sustain steady motion of the vortices, the current density as a function of the vortex velocity is given by Eqs. (35) and (40), where one should make the same substitutions in the coefficient of β as for Eqs. (33) and (38) and the same substitutions in the coefficient of η as for Eqs. (34) and (39).

ACKNOWLEDGMENTS

This work was supported by a grant from the president of the Russian Federation (project nos. NSh-1385.2003.2, MK-1809.2003.02) and the Foundation for High-Priority Research Programs (state contract no. 40.012.1.1.1357).

REFERENCES

1. I. O. Kulik and I. K. Yanson, *The Josephson Effect in Superconducting Tunneling Structures* (Nauka, Moscow, 1970; Halsted, Jerusalem, 1972).
2. M. B. Mineev and V. V. Shmidt, Zh. Éksp. Teor. Fiz. **79** (3), 893 (1980) [Sov. Phys. JETP **52**, 453 (1980)].
3. K. K. Likharev, *Dynamics of Josephson Junctions and Circuits* (Nauka, Moscow, 1985; Gordon and Breach, London, 1986), p. 27.
4. A. V. Ustinov, Physica D (Amsterdam) **123** (1–4), 315 (1998).
5. V. Kurin, A. Yulin, E. Goldobin, A. Klushin, H. Kohlstedt, M. Levichev, and N. Thyssen, IEEE Trans. Appl. Supercond. **9** (2), 3733 (1999).
6. J. Zitzmann, A. V. Ustinov, M. Levitchev, and S. Sakai, Phys. Rev. B: Condens. Matter **66** (6), 064 527 (2002).
7. V. V. Kurin and A. V. Yulin, Phys. Rev. B: Condens. Matter **55** (17), 11 659 (1997).
8. N. Martucciello, J. Mygind, V. P. Koshelets, A. V. Shchukin, L. V. Filipenko, and R. Monaco, Phys. Rev. B: Condens. Matter **57** (9), 5444 (1998).
9. E. Goldobin, A. Wallraff, N. Thyssen, and A. V. Ustinov, Phys. Rev. B: Condens. Matter **57** (1), 130 (1998).
10. R. G. Mints and I. B. Snapiro, Phys. Rev. B: Condens. Matter **52** (13), 9691 (1995).
11. V. P. Silin and A. V. Studenov, Zh. Éksp. Teor. Fiz. **117** (6), 1230 (2000) [JETP **90** (6), 1071 (2000)].
12. A. S. Malishevskii, V. P. Silin, and S. A. Uryupin, Phys. Lett. A **306** (2–3), 153 (2002).
13. A. S. Malishevskiĭ, V. P. Silin, and S. A. Uryupin, Zh. Éksp. Teor. Fiz. **125** (3), 673 (2004) [JETP **98** (3), 594 (2004)].
14. S. Sakai and H. Tateno, Jpn. J. Appl. Phys. **22** (9), 1374 (1983).
15. S. Sakai and N. F. Pedersen, Phys. Rev. B: Condens. Matter **34** (5), 3506 (1986).
16. A. S. Malishevskiĭ and S. A. Uryupin, Fiz. Tverd. Tela (St. Petersburg) **46** (7), 1165 (2004) [Phys. Solid State **46** (7), 1195 (2004)].
17. Yu. M. Aliev, V. P. Silin, and S. A. Uryupin, Sverkhprovodimost: Fiz., Khim., Tekh. **5** (2), 228 (1992).
18. A. Barone and G. Paterno, *Physics and Applications of the Josephson Effect* (Wiley, New York, 1982; Mir, Moscow, 1984).
19. A. A. Abrikosov, *Fundamentals of the Theory of Metals* (Nauka, Moscow, 1987; North-Holland, Amsterdam, 1988).
20. V. P. Silin and S. A. Uryupin, Zh. Éksp. Teor. Fiz. **108** (6), 2163 (1995) [JETP **81**, 1179 (1995)].
21. Yu. M. Aliev, K. N. Ovchinnikov, V. P. Silin, and S. A. Uryupin, Zh. Éksp. Teor. Fiz. **107** (3), 972 (1995) [JETP **80**, 551 (1995)].

Translated by G. Tsydynzhapov

Physics of the Solid State, Vol. 47, No. 10, 2005, pp. 1814–1822. Translated from Fizika Tverdogo Tela, Vol. 47, No. 10, 2005, pp. 1745–1753.

METALS AND SUPERCONDUCTORS

Critical Current of SFIFS Tunnel Junctions: Spin–Orbit Scattering Effects

V. N. Krivoruchko and R. V. Petryuk

Galkin Institute of Physics and Technology of Donetsk, National Academy of Sciences of Ukraine, ul. R. Lyuksemburg 72, Donetsk, 83114 Ukraine

e-mail: krivoruc@krivoruc.fti.ac.donetsk.ua

Received June 22, 2004; in final form, November 10, 2004

Abstract—The proximity effect of a bulk superconductor (S) and a thin normal ferromagnetic metal layer (F) containing spin–orbit scattering centers is studied. The weak and strong limits of the proximity effect in the SF bilayer are considered analytically in the framework of the microscopic model of the superconducting state of dirty metals. The critical current of an SFIFS tunnel junction (I stands for an insulating layer) whose sides are made of proximity-coupled SF layers is calculated. Effects of spin–orbit scattering in the F layers on tunneling current are studied for parallel and antiparallel magnetization vectors of the F layers. It is shown that there is a complex relation between the magnitude of the superconducting current flowing through the SFIFS junction and scattering: spin–orbit scattering suppresses the exchange field effect in a nonlinear way and, at a fixed concentration of scattering centers, depends on the SF boundary resistance and the strength of the proximity effect.

1. INTRODUCTION

Proximity effects are phenomena in which the order parameter of a particular state of a material penetrates into another material not possessing this kind of ordering intrinsically, due to direct contact between the materials. An example of the proximity effect is the penetration of superconducting correlations into a normal metal (N). To date, the proximity effect of a superconductor (S) and a nonmagnetic normal metal has been explored in detail [1–4].

In the case of an SN structure, one deals with one kind of ordering, namely, superconductivity. The phenomenon becomes much richer if the nonsuperconducting metal is a ferromagnet (F). The SF structure has two competing ordered states, superconducting and ferromagnetic. As a consequence, ferromagnetic correlations are induced in the superconductor [5–7] and the superconducting state generated in the F metal is qualitatively different from the superconductivity of an N metal. It is well known that the main distinction between nonsuperconducting nonmagnetic and nonsuperconducting ferromagnetic metals is the fact that conduction electrons in an F metal are spin polarized. As in an SN structure, superconducting correlations are induced in the F layer because of the proximity of the S layer; however, the polarization of electrons at the Fermi surface due to exchange interaction modifies the conditions of Cooper pairing. In the F layer, Cooper pairs are formed by quasiparticles in the states $\{\mathbf{p}\uparrow, (-\mathbf{p} + \Delta\mathbf{p})\downarrow\}$, $\{\mathbf{p}\downarrow, (-\mathbf{p} - \Delta\mathbf{p})\uparrow\}$; so the total momentum of a resulting pair is nonzero (here, $\Delta\mathbf{p} \sim H_{ex}/\hbar v_F$, where H_{ex} is the exchange field expressed in energy units and v_F is the Fermi velocity). If the spin–orbit scattering is sufficiently weak, there is almost no mixing between pairs belonging to different spin subbands. Therefore, the distinctive features of SFS junctions are associated with spatial oscillations ($\sim\cos(x\Delta p)$) of the induced superconducting order parameter in the F layer [8–10].

A state-of-the-art review of the thermodynamics of SF systems (including phase diagrams for superlattices) can be found in [11]. As for their transport properties, so-called π-phase superconductivity has been directly observed in recent experiments [12–18]. This kind of superconducting state is characterized by a spontaneous π shift of the superconducting phase difference of the condensate wave functions on the sides of an SFS junction [8, 9, 19]. In particular, the transport properties of a tunnel junction in the π state can be described by the Josephson relation between the current and phase $J(\varphi) = I_C\sin(\varphi)$, in which the critical current I_C is negative.

It is interesting that, for SFIFS and SFS tunnel junctions (I stands for an insulator), it has been predicted [20–24] that the transition to the π state can occur even if the F layers are thin, that is, if there are no oscillations in the order parameter of an F layer. Moreover, while the π state arises if the layers are magnetized parallel, the critical tunneling current can even be enhanced for certain values of the exchange field if the magnetization vectors are antiparallel and the temperature is low [21–23]. The origin of this phenomenon is in induced magnetic correlations in the S layer and variations in the phase of the superconducting order parameter near the SF interface.

As was noted above, the π state in weak SFS links has been observed by several research groups [12–18]. The enhancement of the Josephson current in SFIFS junctions remains merely a theoretical prediction, and the theory should try to consider more realistic models. In particular, it is possible that spin-flip processes play a crucial part. These processes can be induced, for example, by spin–orbit interaction with the involvement of magnetic impurities. Another source of spin-flip transitions, particularly important for thin films, is the strong electric field appearing at the interface between different metals [25]. Spin-flip processes are special in that the electron spin is no longer conserved and reverses in a characteristic time τ_{SO}. The sign of the effective exchange field acting on a Cooper pair also reverses with the same characteristic frequency $1/\tau_{SO}$.

Spin–orbit scattering was discussed in [10, 26, 27], where the effect of this scattering was studied on the superconducting transition temperature of SF bilayers [10] and SF superlattices [26] and on the Josephson current flowing through an SF tunnel junction [10, 27]. In [10, 26], the temperature range in the vicinity of the superconducting transition temperature T_c was considered. In the present paper, we study the influence of spin–orbit scattering on the superconducting proximity effect and transport properties of an SFIFS junction using the microscopic theory of the proximity effect in SF bilayers in a low temperature range $T \ll T_c$. We consider an arbitrary state of the SF interface and calculate the critical current of an SFIFS junction; for certain special cases, we obtain analytical expressions. We demonstrate that spin–orbit scattering suppresses the effect of the exchange field in a nonlinear way and, for a fixed concentration of scattering centers, is determined by the SF interface resistance and the strength of the proximity effect. Preliminary results of this study were published in [27].

It is well known that, in order to study the tunneling properties of a junction whose sides consist of proximity-coupled layers, one must first determine the superconducting properties of the bilayers and then investigate the transport properties of the junction itself. The superconducting proximity effect for an SF bilayer with spin–orbit scattering is studied in Section 2. The influence of spin–orbit scattering on the critical current of an SFIFS junction is discussed in Section 3. In the appendix, we give a short derivation of the Uzadel equations for a system with spin–orbit scattering.

2. MODEL OF A JUNCTION AND PROXIMITY EFFECT INCLUDING SPIN–ORBIT SCATTERING

Let us consider the case where both the superconductor and the ferromagnet are dirty; that is, $\xi_{S,F} \gg l_{S,F}$. This case is of theoretical and practical interest. We also assume that the following conditions are satisfied: $d_S \gg \xi_S$ for an S layer, and $d_F \ll \min(\xi_F, \xi)$ for an F layer. Here, $\xi_S = (D_S/2\pi T_c)^{1/2}$, $\xi = (D_F/2\pi T_c)^{1/2}$, and $\xi_F = (D_F/2H_{ex})^{1/2}$ are the coherence lengths of S and F metals; l_S and l_F are the electron mean free paths in these metals; and d_S and d_F are the thicknesses and D_S and D_F the diffusion coefficients for S and F metals, respectively. Because of the restrictions imposed on the film thicknesses, we can neglect the reduction in the critical temperature of the SF bilayer as compared to that in the critical temperature of the superconductor. We assume that the F layer is a single-domain film with spin–orbit scattering centers and that there are no such centers in the S layer.

We suppose that the region $x \geq 0$ is filled by the S metal and the layer $-d_F \leq x < 0$ by the F metal and that the transverse dimensions of the junction are much smaller than the Josephson penetration depth; so all quantities depend only on the coordinate x along the normal to the interface. In this case, the superconducting properties of the SF bilayer are described by the well-known Uzadel equations [28, 29] for the normal (G) and anomalous (F) Green's functions. It is convenient to explicitly use the normalization condition $G^2 + F^2 = 1$ and, following [3], introduce the modified Uzadel function Φ defined by the relations $G_{S\sigma} = \omega_\sigma/\sqrt{\omega_\sigma^2 + \Phi_{S\sigma}\tilde{\Phi}_{S\sigma}}$ and $F_{S\sigma} = G_{S\sigma}\Phi_{S\sigma}/\omega_\sigma$. Here, the function $\tilde{\Phi}$ satisfies the relation $\tilde{\Phi}(\omega, H_{ex}) = \Phi^*(\omega, -H_{ex})$. In this case, the Uzadel equations for the S metal take the form

$$\Phi_{S\sigma} = \Delta_0 + \xi_S^2 \frac{\pi T_c}{\omega G_{S\sigma}} \partial_x (G_{S\sigma}^2 \partial_x \Phi_{S\sigma}). \quad (1)$$

Spin indices σ assume values ± 1, $\partial_x \equiv d/dx$, and the pairing potential is obtained from the self-consistency equation

$$\Delta_0 \ln\left(\frac{T}{T_c}\right) + 2\pi T \sum_\sigma \sum_{\omega > 0} \left(\frac{\Delta_0}{2} - \frac{G_{S\sigma}\Phi_{S\sigma}}{\omega}\right) = 0,$$

where $\omega = \omega_n = \pi T(2n + 1)$ is the Matsubara frequency. Without spin-flip processes in the S metal, the spin subbands with $\sigma = \pm 1$ are independent. This is not the case for the F metal, which is assumed to contain spin–orbit scattering centers. For this metal, the modified Uzadel equations take the form [see Eq. (A9)]

$$\Phi_{F\sigma} = \xi^2 \frac{\pi T_c}{\omega_\sigma G_{F\sigma}} \partial_x (G_{F\sigma}^2 \partial_x \Phi_{F\sigma}) + \alpha_{SO} G_{F-\sigma}\left(\frac{\Phi_{F-\sigma}}{\omega_{-\sigma}} - \frac{\Phi_{F\sigma}}{\omega_\sigma}\right), \quad (2)$$

and the subbands are coupled. Here, we introduce the notation $\omega_\sigma = \omega + i\sigma H_{ex}$ and $\alpha_{SO} = 2/3\tau_{SO}$, where τ_{SO} is the characteristic time of spin–orbit scattering. As usual, it is assumed that the "bare" order parameter for the normal F metal is $\Delta_F^0 = 0$, but $F_F \neq 0$ because of the proximity effect of the superconductor. If spin–orbit

scattering is absent, the spin-up and spin-down subbands do not mix and Eq. (2) reduces to the usual modified Uzadel equations for a ferromagnetic metal [19, 30].

Equations (1) and (2) have to be supplemented by boundary conditions for the functions Φ_S and Φ_F. Deep inside the S layer, we have

$$\Phi_S(\infty) = \Delta_S(\infty) = \Delta_0(T), \quad (3)$$

where $\Delta_0(T)$ is the order parameter of the bulk uniform superconductor at temperature T according to the BCS theory. At the interface of the ferromagnet and the insulator, we have $\partial_x\Phi_F(-d_F) = 0$. Assuming that spin-flip scattering is absent at the SF interface itself, the boundary conditions at this interface can be written as [19, 30]

$$\gamma\xi G_{F\sigma}^2\partial_x\Phi_{F\sigma}/\omega_\sigma = \xi_S G_{S\sigma}^2\partial_x\Phi_{S\sigma}/\omega, \quad (4)$$

$$\gamma_{BF}\xi G_{F\sigma}\partial_x\Phi_{F\sigma} = \tilde{\omega}_\sigma G_{S\sigma}(\Phi_{S\sigma}/\omega - \Phi_{F\sigma}/\omega_\sigma). \quad (5)$$

Here, $\gamma = \rho_S\xi_S/\rho\xi$ is the parameter characterizing the strength of the proximity effect; $\gamma_{BF} = R_B/\rho\xi$ is the parameter characterizing the interface transparency; ρ_S and ρ are the resistivities of the S and F metals, respectively; and R_B is the product of the interface resistance in the normal state multiplied by its area. Equation (4) expresses the continuity of a superconducting current passing through the SF interface with arbitrary transparency, and Eq. (5) describes the quality of the electric contact. These relations are true under the additional assumption that the exchange splitting of the subbands $p_F^\pm = \sqrt{2m}\sqrt{E_F + H_{ex}}$ is much smaller than the Fermi energy E_F; that is, $H_{ex} \ll E_F$. In this case, we can neglect the differences of the densities of states and the transparencies of the SF interface for electrons with opposite spins and assume the interface parameters (γ, γ_{BF}) to be the same for both spin subbands.

Since the F layer is thin, the proximity effect problem can be reduced to a boundary-value problem for the S layer, as is the case for an SN sandwich [3]. Assuming that $(d_F/\xi)^2 \ll \alpha_{SO} \ll d_F/\xi \ll 1$, we solve the differential equation (2) by iterations with $d_F\xi$ and α_{SO} as small parameters. In a first nontrivial approximation, using $\partial_x\Phi_F(-d_F) = 0$, we get

$$\partial_x\Phi_{F\sigma}(x) = \frac{\omega_\sigma}{\xi^2\pi T_c G_{F\sigma}(0)}\{\Phi_{F\sigma}(0) - \Xi_{F\sigma}(\alpha_{SO})\}(x + d_F), \quad (6)$$

where

$$\Xi_{F\sigma}(\alpha_{SO}) = \alpha_{SO}G_{F-\sigma}\left\{\frac{\Phi_{F-\sigma}(0)}{\omega_{-\sigma}} - \frac{\Phi_{F\sigma}(0)}{\omega_\sigma}\right\}.$$

Finding $\partial_x\Phi_{F\sigma}(x = 0)$ from Eq. (6) and substituting it into Eqs. (4) and (5), we get boundary conditions for $\Phi_{S,F\sigma}$:

$$\xi_S G_{S\sigma}^2\partial_x\Phi_{S\sigma}\big|_{x=0} = \gamma_M G_{F\sigma}\{\Phi_{F\sigma} - \Xi_{F\sigma}(\alpha_{SO})\}\big|_{x=0}, \quad (7)$$

$$G_{S\sigma}(\Phi_{S\sigma} - \omega\Phi_{F\sigma}/\omega_\sigma)\big|_{x=0} = \gamma_B\omega\{\Phi_{F\sigma} - \Xi_{F\sigma}(\alpha_{SO})\}\big|_{x=0}. \quad (8)$$

Here, $\gamma_M = \gamma d_F/\xi\pi T_c$ and $\gamma_B = \gamma_{BF}d_F/\xi\pi T_c$. In calculating the quantity $\Xi_{F\sigma}(\alpha_{SO})$, we use the values $G_{F\sigma}(0)$ and $\Phi_{F\sigma}(0)$ for $\tau_{SO} \longrightarrow \infty$, because this quantity is already on the order of $\sim\alpha_{SO}$. Using the results from [30], we can write $\Phi_{F\sigma}(0) = \left.\frac{G_{S\sigma}\Phi_{S\sigma}\omega_\sigma}{\omega(G_{S\sigma} + \gamma_B\omega_\sigma)}\right|_{x=0}$; therefore,

$$\Xi_{F\sigma}(\alpha_{SO})\big|_{x=0} \approx \left.\frac{2i\alpha_{SO}\sigma H_{ex}\gamma_B G_S\Phi_S}{\omega(G_S + \gamma_B\omega_\sigma)A_{-\sigma}}\right|_{x=0}, \quad (9)$$

where $A_\sigma = \sqrt{1 + 2\gamma_B G_S\omega_\sigma + \gamma_B^2\omega_\sigma^2}$. Substituting Eq. (9) into boundary conditions (8), we obtain an equation that relates the unknown value of $\Phi_{F\sigma}$ at the interface to the value of the function $\Phi_{S\sigma}$ for the S layer at this interface:

$$\Phi_{F\sigma}(0) = \left.\frac{G_{S\sigma}\Phi_{S\sigma}\omega_\sigma}{\omega(G_{S\sigma} + \gamma_B\omega_\sigma)}\left\{1 + \frac{2i\alpha_{SO}\sigma H_{ex}\gamma_B^2}{(G_S + \gamma_B\omega_\sigma)A_{-\sigma}}\right\}\right|_{x=0}. \quad (10)$$

The boundary conditions for $\Phi_{S\sigma}(x)$ are found by substituting Eq. (10) into Eq. (7):

$$\xi_S G_{S\sigma}\partial_x\Phi_{S\sigma}\big|_{x=0} = \frac{\gamma_M\omega_\sigma\Phi_{S\sigma}}{A_\sigma} \times \left.\left\{1 - \frac{2\alpha_{SO}\sigma i H_{ex}\gamma_B(1 + \gamma_B\omega_\sigma G_S)}{\omega_\sigma A_\sigma^2 A_{-\sigma}}\right\}\right|_{x=0}. \quad (11)$$

As a result, the proximity effect problem for the bulk superconductor and the thin ferromagnetic metal layer with spin–orbit scattering is reduced to solving the differential Uzadel equation for a semi-infinite superconductor with boundary conditions (3) and (11). The parameters γ_M and γ_B have a clear physical meaning [3, 19]. The parameter γ_M characterizes pair breaking near the interface, and its value depends on the quasiparticle density of states in the S and F metals. The value of γ_M is large if the density of states in the F metal is high. In this case, superconducting correlations quickly weaken at the SF interface. In the opposite limit ($\gamma_M \ll 1$), the influence of the S metal prevails and superconducting correlations in the F metal decay slowly with distance from the interface. The parameter γ_B describes the effective potential barrier at the SF interface. If $\gamma_B \ll 1$, then the S and F metals are in good electric contact; in the opposite limit, the interface has a large resistance.

In general, all equations for the modified functions $\Phi_{S\sigma}$ and $\Phi_{F\sigma}$ are linked via the boundary conditions and the problem can be solved only numerically. However, in the case where the proximity effect is weak or strong, it is possible to find analytical solutions. We are interested in the superconducting proximity effect and transport properties of an SFIFS junction at low temperatures $T \ll T_c$; the transparency of the SF interface (i.e., the value of γ_B) can be arbitrary.

2.1. Strong Proximity Effect

In the limit $\pi T_c\gamma_M \ll (1 + \pi T_c\gamma_B)$, it follows from Eq. (11) that, in the zero approximation in γ_M, we have $\partial_x\Phi_{S\sigma}(0) = 0$; i.e., the functions $\Phi_{S\sigma}(x)$ are spatially uniform: $\Phi_{S\sigma}(x) = \Delta_S(x) = \Delta_0$. In the next approximation in γ_M, using linearized Eq. (1) for $\Phi_{S\sigma}(x)$ and boundary conditions (3), we find the general solution in the form

$$\Phi_{S\sigma}(x) = \Delta_0 - C_0\exp(-\beta x/\xi_S),$$
$$\beta = [(\omega^2 + \Delta_0^2)^{1/2}/\pi T_c]^{1/2}. \quad (12)$$

Substituting this solution into boundary conditions (11), we find the coefficient C_σ to be

$$C_\sigma = \Delta_0\frac{\gamma_M\beta\omega_\sigma\pi T_c}{A_\sigma\omega + \gamma_M\beta\omega_\sigma\pi T_c} \quad (13)$$
$$\times\left\{1 - i2\sigma\alpha_{SO}\gamma_B H_{ex}\frac{(1 + \gamma_B\omega_\sigma\omega/\sqrt{\omega^2 + \Delta_0^2})}{A_\sigma A_{-\sigma}(A_\sigma\omega + \gamma_M\beta\omega_\sigma\pi T_c)\omega_\sigma}\right\}.$$

As follows from the obtained expressions, magnetism of the F layer is manifested in the preexponential factor and causes the spin-up and spin-down subbands of the S layer to become unequal. Superconductivity in the S layer is suppressed by the proximity effect over the characteristic length $\sim\xi_S/\beta$, which is independent of H_{ex}. In the limit $\tau_{SO} \longrightarrow \infty$, Eq. (13) reproduces the results from [30] for an SF bilayer without spin-flip scattering. Substituting $\Phi_{S\sigma}(x)$ at $x = 0$ given by Eq. (12) into Eq. (10), we can find the functions $\Phi_{F\sigma}(\omega, 0)$; however, the resulting expressions are too cumbersome to be shown here.

2.2. Weak Proximity Effect

In the limit of large values of γ_M [more precisely, at $\pi T_c\gamma_M \gg (1 + \pi T_c\gamma_B)$], we get for the S layer ($x < \xi_S$)

$$\Phi_{S\sigma}(0) = B(\gamma_B + 1/\tilde{\omega}_\sigma)/\gamma_M. \quad (14)$$

Here, the coefficient $B \equiv B(T)$ for all temperatures $T < T_c$ can be closely approximated by $B(T) = 2T_c[1 - (T/T_c)^2][7\zeta(3)]^{-1/2}$ [31], where $\zeta(3)$ is the Riemann ζ function. As before, because of the proximity effect, magnetic correlations of the F layer propagate into the S layer and make the spin-up and spin-down subbands unequal.

In the F layer, the modified Uzadel function for superconducting correlations is given by

$$\Phi_{F\sigma}(0) = \frac{B}{\gamma_M\omega}\left(1 + 2\alpha_{SO}\sigma\frac{i\gamma_B^2 H_{ex}}{(1 + \gamma_B\omega)^2 + \gamma_B^2 H_{ex}^2}\right). \quad (15)$$

So, because of the proximity effect, the superconducting and magnetic properties of the SF bilayer become coupled and the bilayer can be considered a unified system with strong superconducting and magnetic correlations. We will use these results to study the influence of spin–orbit scattering on the dc Josephson effect in tunnel junctions in which the contacts are formed by proximity-coupled layers.

3. EFFECT OF SPIN–ORBIT SCATTERING ON THE CRITICAL CURRENT

As mentioned above, the influence of spin-orbit scattering on the Josephson current through a weak SFS link near the superconducting transition temperature was discussed in [10]. In [27], we considered the influence of spin–orbit scattering centers on the transport characteristics of an SFIFS junction at low temperatures in the case where the proximity effect is strong ($\gamma_M \ll 1$). Here, we study the effects for an arbitrary state of the SF interface and for the strong and weak proximity effects and also present the results for asymmetric SFIFS junctions.

Suppose that both contacts of a tunnel junction are SF sandwiches and that the transparency of the insulating layer is so low that the influence of a superconducting current on the state of the contacts can be neglected. Then, the critical current of the symmetric SFIFS tunnel junction is given by

$$J_C = \frac{T}{T_c}\mathrm{Re}\sum_{\sigma,\,\omega>0} F_{S\sigma}^*|_L F_{S\sigma}|_R$$
$$= \frac{T}{T_c}\mathrm{Re}\sum_{\sigma,\,\omega>0}\frac{G_{F\sigma}^*\Phi_{F\sigma}^*}{\omega_\sigma}\Bigg|_L\frac{G_{F\sigma}\Phi_{F\sigma}}{\omega_\sigma}\Bigg|_R.$$

Let us consider the collinear configuration of the magnetic moments of the F layers.

3.1. Parallel Orientation of the Magnetization Vectors of the Ferromagnetic Layers

In the case where the resistance of the SF interface is significant ($\pi T_c\gamma_B > 1$), $\gamma_B H_{ex} \gg 1$, and γ_M is small, the critical current can be expressed as

$$J_C^{FM} \approx 2\frac{T}{T_c} \times \sum_{\omega>0} \frac{\omega^2 - H_{ex}^2 + 2\omega^2(3H_{ex}^2 - \omega^2)/\gamma_B\Omega(\omega^2 + H_{ex}^2)}{\gamma_B^2(\omega^2 + H_{ex}^2)^2\Omega^2} \times \left\{\Delta_0^2 - 8\alpha_{SO}\gamma_B^2\Omega^2\frac{\omega H_{ex}^2}{\omega^2 + H_{ex}^2}\right\}, \quad (16)$$

where $\Omega = (\omega^2 + \Delta_0^2)^{1/2}$. Analysis of Eq. (16) shows that the superconducting current is positive for small values of the exchange field H_{ex} and is negative for $H_{ex} \gg \omega \sim \pi T_c$. In other words, as the exchange field increases, the direction of the current flowing through the junction is reversed; i.e., the so-called transition from 0-phase to π-phase superconductivity takes place [22, 23]. In our case, when the thickness of the ferromagnetic layer is much smaller than the superconducting correlation length, the transition into the π state is induced by magnetism of the S layer, namely, by the additional phase shift accumulated over the junction [32]. For example, if the resistance of the SF interface is small ($\pi T_c\gamma_B < 1$) but, as before, $\gamma_B H_{ex} \gg 1$ and γ_M is small, then the critical current can be found to be

$$J_C^{FM} \approx -2\frac{T}{T_c}\sum_{\omega>0}(\gamma_B H_{ex}\Omega)^{-2}\left\{\Delta_0^2 + \frac{\Delta_0^2}{\gamma_B^2 H_{ex}^2\Omega^2} \times [\Delta_0^2 - 3\omega^2(1 + \gamma_B\Omega^2)] - 8\alpha_{SO}\gamma_B\Omega\omega(1 + \gamma_B\Omega)\right\}. \quad (17)$$

It can be seen that spin–orbit scattering (the terms containing $\sim\alpha_{SO}$) impedes the transition into the π state. In particular, for $\pi T_c\gamma_B = 2$, $T = 0.1T_c$, $\alpha_{SO} = 0.01\Delta_0$, and $H_{ex} = (3–5)\Delta_0$, the contribution of spin–orbit scattering can be as large as 3–4%.

In the case where $\pi T_c\gamma_M \gg (1 + \pi T_c\gamma_B)$, the critical current is given by

$$J_C^{FM} \approx 2\frac{T}{T_c}\sum_{\omega>0}\frac{B^2/(\gamma_M\omega)^2[B^2/(\gamma_M\omega)^2 + \omega^2 - H_{ex}^2 + A(\alpha_{SO})]}{[\omega^2 - H_{ex}^2 + B^2/(\gamma_M\omega^2)]^2 + 4\omega^2H_{ex}^2 + 2A(\alpha_{SO})B^2/(\gamma_M\omega)^2}, \quad (18)$$

where $A(\alpha_{SO}) = 8\alpha_{SO}\omega\gamma_B^2H_{ex}^2/[(1 + \gamma_B\omega)^2 + \gamma_B^2H_{ex}^2]$. As before, the critical current changes sign for a sufficiently strong exchange field ($H_{ex} > \pi T_c$) and the junction turns into the π state. Spin–orbit scattering attenuates the influence of the exchange field. For a junction with parameters $\pi T_c\gamma_M = 10$, $\pi T_c\gamma_B = 0.5$, $T = 0.1T_c$, $\alpha_{SO} = 0.01\Delta_0$, and $H_{ex} \approx \Delta_0$, the attenuation does not exceed 1%.

3.2. Antiparallel Orientation of the Magnetization Vectors of the Ferromagnetic Layers

If the interface resistance is low ($\pi T_c\gamma_B < 1$), $\gamma_B H_{ex} \gg 1$, and the density of states in the S metal is larger than that in the F layer (the proximity effect is strong), then the critical current is given by

$$J_C^{AF} = 2\frac{T}{T_c}\Delta_0\sum_{\omega>0}\frac{1 - 4\Delta_0^2\alpha_{SO}\omega(1 + \gamma_B\Omega)/\gamma_B\Omega H_{ex}^4}{\{[\omega^2(1 + \gamma_B\Omega)^2 + (\gamma_B\Omega H_{ex})^2]^2/\Delta_0^2 + 4\omega^2(1 + \gamma_B\Omega)^2\}^{1/2}}. \quad (19)$$

In this geometry, for the parameters of the bilayer $\pi T_c\gamma_B = 0.5$, $\alpha_{SO} = 0.1\Delta_0$, $H_{ex} \approx 5\Delta_0$, and $T = 0.1T_c$, the contribution from spin–orbit scattering to the critical current does not exceed 0.5%. In the case where the resistance of the SF interface is high ($\pi T_c\gamma_B > 1$), $\gamma_B H_{ex} \gg 1$, and $\pi T_c\gamma_M \ll 1$, the current amplitude is equal to

$$J_C^{AF} \cong 2\frac{T}{T_c}\sum_{\omega>0}\frac{\Delta_0^2}{\gamma_B^2(\omega^2 + H_{ex}^2)\Omega^2} \times \left\{1 - \frac{4\alpha_{SO}\Delta_0^2H_{ex}^2\omega}{\gamma_B^2\Omega^2(\omega^2 + H_{ex}^2)^3}\right\}. \quad (20)$$

An estimation of the second term in curly brackets for $\pi T_c\gamma_B = 2$, $T = 0.1T_c$, $\alpha_{SO} = 0.1\Delta_0$, and $H_{ex} \approx 2\Delta_0$ shows that the reduction in the critical current due to spin–orbit scattering is no greater than 1%. In the case where the superconducting proximity effect is weak [$\pi T_c\gamma_M \gg (1 + \pi T_c\gamma_B)$], calculations yield

$$J_C^{AFM} \approx 2\frac{T}{T_c}\sum_{\omega>0}\frac{B^2/(\gamma_M\omega)^2}{\{[\omega^2 - H_{ex}^2 + B^2/(\gamma_M\omega)^2]^2 + 4\omega^2H_{ex}^2 + 2A(\alpha_{SO})B^2/(\gamma_M\omega)^2\}^{1/2}}. \quad (21)$$

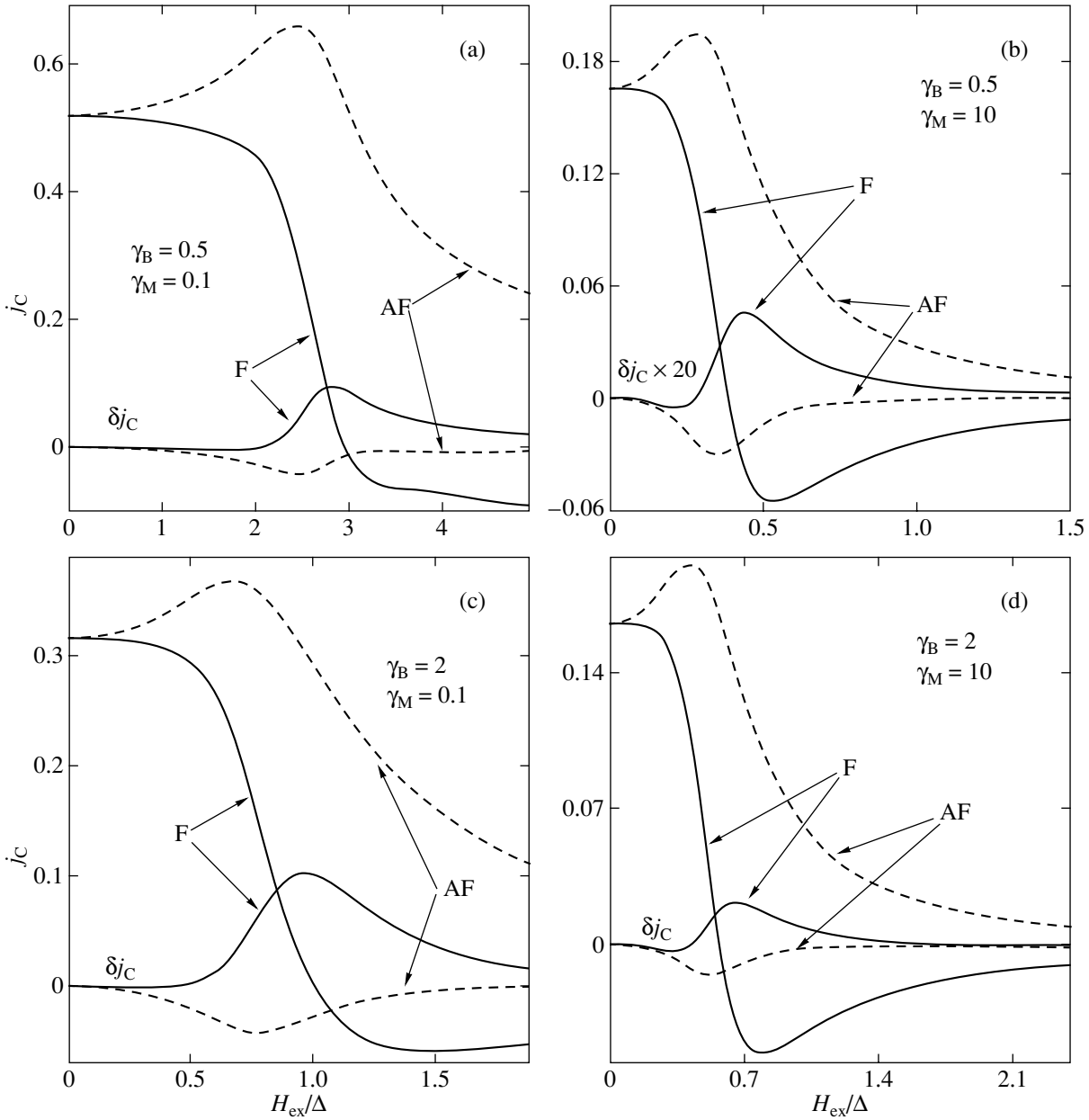

Fig. 1. Magnitude of the superconducting current j_C of an SFIFS junction as a function of the exchange field H_{ex} for parallel (solid lines) and antiparallel (dashed lines) orientation of the exchange fields of the F layers. The critical current of the junction without spin–orbit scattering and the additive correction δj_C due to spin–orbit scattering are shown. The junction temperature is $T/T_c = 0.1$. The spin–orbit scattering parameter is $\alpha_{SO}/\Delta = 0.1$. The parameter values of the SF layer are as follows: (a) $\pi T_c \gamma_B = 0.5$ and $\pi T_c \gamma_M = 0.1$; (b) $\pi T_c \gamma_B = 0.5$ and $\pi T_c \gamma_M = 10$; (c) $\pi T_c \gamma_B = 2$ and $\pi T_c \gamma_M = 0.1$; and (d) $\pi T_c \gamma_B = 2$ and $\pi T_c \gamma_M = 10$.

An analysis of the critical current as a function of the exchange field for the geometry in question shows that, for $\alpha_{SO} \longrightarrow 0$, there is a range of H_{ex} values in which the critical current increases [22, 23, 32]. The nature of the phenomenon is slightly different from that in the previous geometry. The exchange-field dependence is not related to the accumulated phase shift (the phase shifts on the opposite sides of the junction cancel each other) but instead is due to the shift and overlap of singularities in the quasiparticle density of states under the influence of the exchange field of the F layer [23]. Scattering (which does not conserve the electron spin) weakens the increase in the superconducting current.

Estimations based on Eqs. (16)–(21) show that contributions of spin–orbit scattering in the limit cases do not exceed a few percent. For more practical values of the bilayer parameters, analysis can be performed only numerically. The results of numerical calculations of the tunneling current through a symmetric SFIFS junction for parallel and antiparallel orientations of the

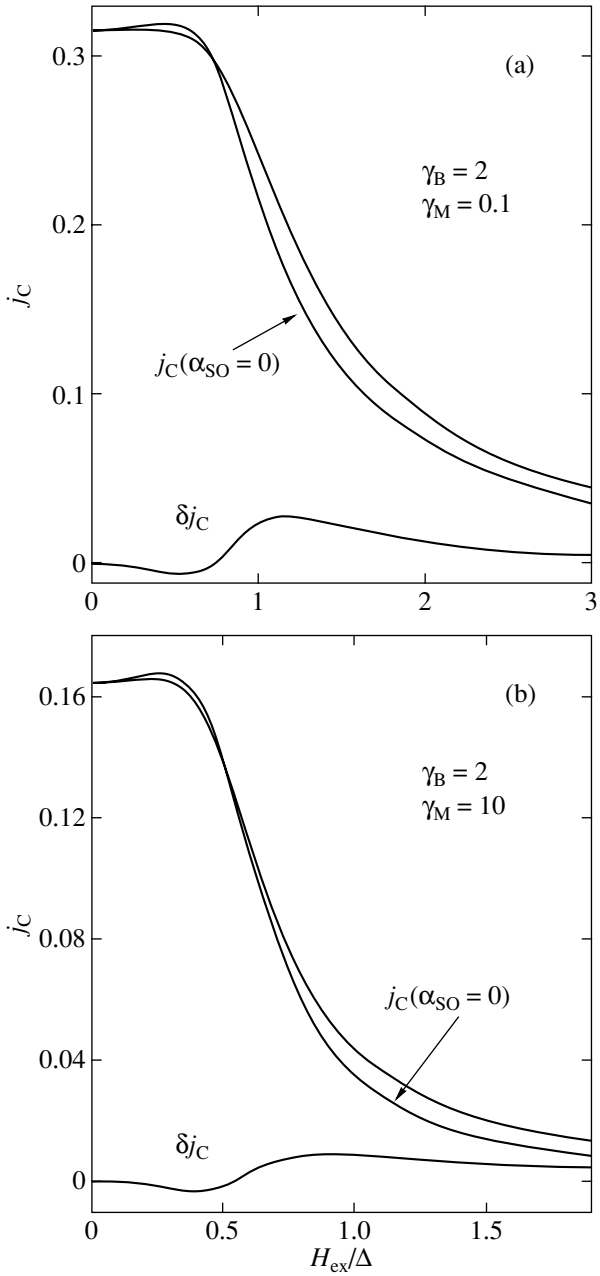

Fig. 2. Magnitude of the critical current j_C of an asymmetric SFINS junction as a function of the exchange field H_{ex} of the ferromagnetic layer. The critical current without spin–orbit scattering, the additive correction δj_C due to spin–orbit scattering, and the total current flowing through the junction are shown. The junction temperature is $T/T_c = 0.1$, and the spin–orbit scattering parameter is $\alpha_{SO}/\Delta = 0.1$. The parameter values of the bilayers are as follows: (a) $\pi T_c \gamma_B = 2$ and $\pi T_c \gamma_M = 0.1$, which corresponds to a strong proximity effect, and (b) $\pi T_c \gamma_B = 2$ and $\pi T_c \gamma_M = 10$, which corresponds to a weak proximity effect.

magnetization vectors of the F layers are shown in Fig. 1. The dependence of the superconducting current amplitude on H_{ex} for a small value of the effective pair-breaking parameter at the SF interface ($\gamma_M \ll 1$) is shown for a good (Fig. 1a) and poor (Fig. 1c) electric contact between the layers. The opposite limit of a junction with a large pair-breaking parameter at the SF interface ($\gamma_M \gg 1$) is shown in Figs. 1b and 1d for a good and poor electric contact between the S and F layers, respectively. As expected, the critical current of the junction strongly depends on H_{ex}, γ_M, and γ_B. It can be seen that, in the parallel geometry, the transition occurs between the zero-phase and π-phase states in a certain range of exchange fields. Spin–orbit scattering suppresses the tendency toward transition into the π state, and this suppression is nonlinear. The contribution of spin–orbit scattering to the critical current reaches a maximum near the transition to the π phase, when the main contribution to the superconducting current (zero-order approximation in α_{SO}) passes through zero and changes sign and the next-order corrections ($\sim\alpha_{SO}$) due to the mixing of states with opposite spins continue to grow. A further increase in the exchange field causes both the superconducting current and spin–orbit contribution to decrease rapidly.

For the antiparallel orientation of the magnetization vectors of the F layers, as well as in the parallel geometry, the critical current of the junction is governed by the parameters of the bilayer. The junction does not turn into the π state, but the superconducting current is enhanced in a certain range of the exchange fields. Spin–orbit scattering suppresses this enhancement according to its general tendency to impede exchange-field effects. The contribution of spin–orbit scattering to the critical current reaches a maximum in the region of the maximum boost to the current. This result becomes physically clear if we recall that, as mentioned above, the critical current is enhanced because of the overlap of two singularities in the quasiparticle density of states. In the limit $T \longrightarrow 0$, the singularities in the density of states $\sim\sqrt{\varepsilon}$ and the current diverges logarithmically [21, 23]. Spin–orbit scattering smears these singularities and effectively reduces the anomalous enhancement of the superconducting current. In this respect, the influence of spin-flip processes is similar to that of temperature: the thermal smearing is so strong that theory predicts enhancement of the superconducting current only for very low temperatures [21, 23, 33].

3.3. Asymmetric SFINS Junctions

The results of the previous section can easily be generalized to asymmetric $(SF)_L I(FS)_R$ junctions, including SFINS junctions with spin–orbit scattering in the F layer only. Skipping the analytical expressions, we present the results of numerical calculations for SFINS junctions for some limit cases.

The dependence of the magnitude of the Josephson current of an SFINS junction on the exchange field of the magnetic layer is shown in Fig. 2. Figure 2a corresponds to a small value of the effective pair-breaking parameter at the SF interface ($\gamma_M \ll 1$), and Fig. 2b corresponds to the opposite case ($\gamma_M \gg 1$). At first glance,

the influence of spin–orbit scattering in the F layer on the current in the SFINS junction is unusual: spin-flip scattering enhances the superconducting current. The reason for this is that spin-flip scattering, as mentioned before, causes the sign of the effective exchange field acting upon Cooper pairs to oscillate with the characteristic frequency $1/\tau_{SO}$. As a result, the pair-breaking influence of the field on pairs decreases and the current grows.

4. CONCLUSIONS

We have studied the influence of spin-flip scattering on the proximity effect of a bulk superconductor and a thin layer of a ferromagnetic normal metal. Spin-flip processes can arise due to spin–orbit interaction of conduction electrons with magnetic ions, to a strong electric field at the interface of the two metals, and to some other mechanisms. We have found the magnitudes of the superconducting order parameter for the case where both metals correspond to the dirty limit. The results obtained have been employed to calculate the critical current of tunnel SFIFS and SFINS junctions for the cases where the proximity effect is weak or strong and the quality of the electric contact between the S and F layers or between the S and N layers is arbitrary. The critical current was calculated as a function of the magnitude of the exchange field, the interface transparency, the magnitude of the proximity effect, and the intensity of spin-flip scattering. It has been demonstrated that spin–orbit scattering can significantly decrease the possible influence of an exchange field on the tunnel characteristics of SFIFS junctions.

APPENDIX

UZADEL EQUATIONS INCLUDING SPIN–ORBIT SCATTERING

Uzadel [28] (see also [29]) derived equations to describe the superconductivity of metals with a high concentration of nonmagnetic impurities. These equations are the isotropic limit of the Eilenberger equations. We generalize the Uzadel equations to dirty metals containing spin–orbit scattering centers. We follow [29] and start from the Eilenberger equations in the form

$$iv_0\mathbf{n}\nabla_R\zeta_\omega + [\bar{\omega}, \zeta_\omega], \tag{A1}$$

where square brackets denote a commutator, $\mathbf{n}$ is the unit vector in the direction of motion of an electron on the Fermi sphere, and $v_0 \approx v_F$. The matrix ζ_ω is composed of normal and anomalous Green's functions

$$\zeta_\omega = \begin{pmatrix} G & \tilde{F} \\ -F & -\tilde{G} \end{pmatrix},$$

which satisfy the normalization condition $G^2 - F\tilde{F} = -1/4$. Let us introduce an isotropic function $\zeta_\omega^0(R) = \int\zeta_\omega(\mathbf{R}, \mathbf{n})d\Omega/4\pi$, which depends on the coordinates of the center of a Cooper pair. We find the function $\zeta_\omega(\mathbf{R}, \mathbf{n})$ by calculating corrections to its isotropic part. In a first approximation, we have

$$\zeta_\omega(\mathbf{R}, \mathbf{n}) = \zeta_\omega^0(\mathbf{R}) + \mathbf{n}\bar{\Gamma}_\omega(\mathbf{R}), \tag{A2}$$

where $\bar{\Gamma}_\omega \ll \zeta_\omega^0$. For the matrix $\bar{\omega}_\pm$, we get

$$\bar{\omega}_\pm = i(\omega + iH_{ex})\sigma_Z - \hat{\Delta} - \frac{1}{\tau_0}\int\zeta_\pm(\mathbf{R}, \mathbf{n})\frac{d\Omega}{4\pi}$$
$$-\frac{3}{\tau_{SO}}\int\zeta_\mp(\mathbf{R}, \mathbf{n})\sin^2(\theta - \theta')\frac{d\Omega}{4\pi},$$
$$\hat{\Delta} = \begin{pmatrix} 0 & \Delta \\ -\Delta^* & 0 \end{pmatrix}, \quad \sigma_Z = \begin{pmatrix} 1 & 0 \\ 0 & -1 \end{pmatrix}.$$

The term proportional to $1/\tau_0$ describes scattering on nonmagnetic impurities and the term $\sim 1/\tau_{SO}$ describes the additional contribution from spin–orbit scattering. After integration using Eq. (A2), we get

$$\bar{\omega}_\pm = i(\omega + iH_{ex})\sigma_Z - \hat{\Delta}$$
$$-\frac{1}{\tau_0}\zeta_\pm^0 - \frac{1 + \cos^2\theta}{\tau_{SO}}\zeta_\mp^0 - \frac{3\pi}{16\tau_{SO}}\Gamma_\mp\sin 2\theta. \tag{A3}$$

Substituting Eqs. (A2) and (A3) into the Eilenberger equation (A1) and averaging over angles yields

$$\frac{iv_0}{3}(\nabla_R\bar{\Gamma}_\pm(\mathbf{R})) + [i(\omega + iH_{ex})\sigma_Z - \hat{\Delta}$$
$$-\frac{1}{\tau_0}\zeta_\pm^0 - \frac{4}{3\tau_{SO}}\zeta_\mp^0, \zeta_\pm^0\Big] - \frac{3\pi^2}{64\tau_{SO}}[\bar{\Gamma}_\mp, \bar{\Gamma}_\pm]. \tag{A4}$$

Next, we multiply Eq. (A1) by $\mathbf{n}$ and average over the corresponding solid angle to obtain

$$iv_0(\nabla_R\zeta_\pm^0(\mathbf{R})) + \Big[i(\omega + iH_{ex})\sigma_Z - \hat{\Delta}$$
$$-\frac{1}{\tau_0}\zeta_\pm^0 - \frac{8}{5\tau_{SO}}\zeta_\mp^0, \Gamma_\pm\Big] - \frac{9\pi^2}{64\tau_{SO}}[\bar{\Gamma}_\mp, \zeta_\pm^0]. \tag{A5}$$

In our case, it is assumed that $1/\tau_0 \gg \omega$, and $1/\tau_{SO}$. Therefore, it follows from Eq. (A5) that

$$\bar{\Gamma}_\pm = -2il\zeta_\pm^0\nabla_R\zeta_\pm^0. \tag{A6}$$

Substituting Eq. (A6) into Eq. (A4) gives an equation closed with respect to $\zeta_\pm^0$:

$$D\nabla_R\{\zeta_\pm^0(\nabla_R\zeta_\pm^0)\}$$
$$+\Big[i(\omega \pm iH_{ex})\sigma_Z - \hat{\Delta} - \frac{4}{3\tau_{SO}}\zeta_\mp^0, \zeta_\pm^0\Big], \tag{A7}$$

where $D = v_0 l/3$ is the diffusion coefficient. After the substitution $G \longrightarrow G/2i$, $F \longrightarrow F/2i$, $\tilde{F} \longrightarrow -\tilde{F}/2i$, and $\Delta \longrightarrow i\Delta$, Eq. (A7) becomes

$$\frac{D}{2}(F_\pm \nabla^2 G_\pm - G_\pm \nabla^2 F_\pm) + \omega_\pm F_\pm - \Delta^* G_\pm = \frac{2}{3\tau_{SO}}\{G_\pm F_\mp - G_\mp F_\pm\}. \quad \text{(A8)}$$

For $\tau_{SO} \longrightarrow \infty$, this set of equations turns into the usual Uzadel equations [29].

As mentioned above, it is convenient to use normalized Green's functions and introduce modified Uzadel functions. Passing over to these functions in Eq. (A8), we get

$$\frac{D}{2}\frac{1}{\omega_\pm G_\pm}\nabla(G_\pm^2 \nabla \Phi_\pm) = \Phi_\pm - \Delta^* - \frac{2}{3\tau_{SO}} G_\mp \left(\frac{\Phi_\mp}{\omega_\mp} - \frac{\Phi_\pm}{\omega_\pm}\right). \quad \text{(A9)}$$

This is the expression we used to describe the superconducting properties of a ferromagnetic metal containing spin–orbit scattering centers [see Eq. (2)].

REFERENCES

1. E. L. Wolf, *Principles of Electron Tunneling Spectroscopy* (Oxford University Press, Oxford, 1985).
2. A. A. Golubov and M. Yu. Kupriyanov, Zh. Éksp. Teor. Fiz. **96** (10), 1420 (1989) [Sov. Phys. JETP **69**, 805 (1989)].
3. A. A. Golubov, E. P. Houwman, J. G. Gisbertsen, M. Krasnov, J. Flokstra, H. Rogalla, and M. Yu. Kuprijanov, Phys. Rev. B: Condens. Matter **51** (2), 1073 (1995).
4. A. A. Golubov and M. Yu. Kupriyanov, Sov. J. Low Temp. Phys. **70** (1–2), 83 (1988).
5. T. Tokuyasu, J. A. Sauls, and D. Rainer, Phys. Rev. B: Condens. Matter **38** (13), 8823 (1988).
6. V. N. Krivoruchko and E. A. Koshina, Phys. Rev. B: Condens. Matter **66** (1), 014 521 (2002).
7. K. Halterman and O. T. Valls, Phys. Rev. B: Condens. Matter **69** (1), 014 517 (2004).
8. A. I. Buzdin, L. N. Bulaevskiĭ, and S. V. Panyukov, Pis'ma Zh. Éksp. Teor. Fiz. **35** (4), 147 (1982) [JETP Lett. **35** (4), 178 (1982)].
9. A. I. Buzdin and M. Yu. Kupriyanov, Pis'ma Zh. Éksp. Teor. Fiz. **53** (6), 308 (1991) [JETP Lett. **53** (6), 321 (1991)].
10. E. A. Demler, G. B. Arnold, and M. R. Beasley, Phys. Rev. B: Condens. Matter **55** (22), 15 174 (1997).
11. Yu. A. Izyumov, Yu. N. Proshin, and M. G. Khusainov, Usp. Fiz. Nauk **172** (2), 113 (2002) [Phys. Usp. **45** (2), 109 (2002)].
12. V. V. Ryazanov, V. A. Oboznov, A. Yu. Rusanov, A. V. Veretennikov, A. A. Golubov, and J. Aarts, Phys. Rev. Lett. **86** (11), 2427 (2001).
13. T. Kontos, M. Aprili, J. Lesueur, and X. Grison, Phys. Rev. Lett. **86** (2), 304 (2001).
14. V. V. Ryazanov, V. A. Oboznov, A. V. Veretennikov, and A. Yu. Rusanov, Phys. Rev. B: Condens. Matter **65** (2), 020501 (2002).
15. Y. Blum, A. Tsukernik, M. Karpovski, and A. Palevski, Phys. Rev. Lett. **89** (18), 187004 (2002).
16. T. Kontos, M. Aprili, J. Lesueur, F. Genet, B. Stephanidis, and R. Boursier, Phys. Rev. Lett. **89** (13), 137007 (2002).
17. W. Guichard, M. Aprili, O. Bourgeois, T. Kontos, J. Lesueur, and P. Gandit, Phys. Rev. Lett. **90** (16), 167001 (2003).
18. I. A. Garifullin, D. A. Tikhonov, N. N. Garifyanov, L. Lazar, Yu. V. Goyunov, S. Ya. Khlebnikov, L. A. Tagirov, K. Westerhold, and H. Zabel, Phys. Rev. B: Condens. Matter **66** (2), 020505 (2002).
19. A. A. Golubov, M. Yu. Kupriyanov, and E. Il'ichev, Rev. Mod. Phys. **76** (2), 411 (2004).
20. E. A. Koshina and V. N. Krivoruchko, Phys. Rev. B: Condens. Matter **63** (22), 224515 (2001).
21. F. S. Bergeret, A. F. Volkov, and K. B. Efetov, Phys. Rev. Lett. **86** (14), 3140 (2001).
22. V. N. Krivoruchko and E. A. Koshina, Phys. Rev. B: Condens. Matter **64** (17), 172511 (2001).
23. A. A. Golubov, M. Yu. Kupriyanov, and Ya. V. Fominov, Pis'ma Zh. Éksp. Teor. Fiz. **75** (3–4), 223 (2002) [JETP Lett. **75**, 190 (2002)].
24. A. Buzdin, Pis'ma Zh. Éksp. Teor. Fiz. **78** (9), 1073 (2003) [JETP Lett. **78** (9), 583 (2003)].
25. V. N. Lisin and B. M. Khabibullin, Fiz. Tverd. Tela (Leningrad) **17** (6), 1598 (1975) [Sov. Phys. Solid State **17** (6), 1045 (1975)].
26. S. Oh, Y.-H. Kim, D. Youm, and M. R. Bearsley, Phys. Rev. B: Condens. Matter **63** (5), 052501 (2000).
27. V. N. Krivoruchko and R. V. Petryuk, Phys. Rev. B: Condens. Matter **66** (13), 134520 (2002).
28. K. Uzadel, Phys. Rev. Lett. **25** (8), 507 (1970).
29. A. A. Svidzinskiĭ, *Spatially Inhomogeneous Problems in the Theory of Superconductivity* (Nauka, Moscow, 1982) [in Russian].
30. E. A. Koshina and V. N. Krivoruchko, Fiz. Nizk. Temp. (Kiev) **26** (2), 157 (2000).
31. M. Yu. Kupriyanov and V. F. Lukichev, Fiz. Nizk. Temp. (Kiev) **8** (10), 1045 (1982).
32. E. A. Koshina and V. N. Krivoruchko, Fiz. Nizk. Temp. (Kiev) **29** (8), 858 (2003).
33. X. Li, Z. Zheng, D. Y. Xing, G. Sun, and Z. Dong, Phys. Rev. B: Condens. Matter **65** (13), 134 507 (2002).

Translated by G. Tsydynzhapov

Physics of the Solid State, Vol. 47, No. 10, 2005, pp. 1823–1826. Translated from Fizika Tverdogo Tela, Vol. 47, No. 10, 2005, pp. 1754–1757.

SEMICONDUCTORS AND DIELECTRICS

Light-Emitting Si : Er Structures Prepared by Molecular-Beam Epitaxy: Structural Defects

V. I. Vdovin*, P. Verner, N. D. Zakharov**, D. V. Denisov***, N. A. Sobolev***, and V. M. Ustinov*****

** Institute for Chemical Problems of Microelectronics, B. Tolmachevskiĭ per. 5, Moscow, 109017 Russia*

*** Max Planck Institute of Physics of Microstructures, Halle/Saale, Germany*

**** Ioffe Physicotechnical Institute, Russian Academy of Sciences, Politekhnicheskaya ul. 26, St. Petersburg, 194021 Russia*

e-mail: nick@sobolev.ioffe.rssi.ru

Received November 29, 2004

Abstract—The structural defects in silicon layers grown by molecular-beam epitaxy and doped with erbium up to concentrations [Er] = 4×10^{19} cm^{-3} are studied using transmission electron microscopy and high-resolution electron microscopy. It is established that the main types of extended structural defects at erbium concentrations [Er] ≥ 2×10^{19} cm^{-3} are 4- to 25-nm Er spherical precipitates located at the "epitaxial layer–substrate" boundary and platelike $ErSi_2$ precipitates residing in the {111} planes throughout the thickness of the layer. © *2005 Pleiades Publishing, Inc.*

1. INTRODUCTION

Molecular-beam epitaxy has been widely used for fabricating light-emitting structures based on Si : Er single-crystal layers. The luminescence intensity of optically active centers containing erbium ions varies nonlinearly in epitaxial layers with increasing concentration of erbium atoms [Er] and passes through a maximum at values of [Er] substantially less than the limiting introduced erbium concentrations [1–5]. Analysis of the data available in the literature shows that the maximum intensity of luminescence is observed at different erbium concentrations depending on the type of doping impurity (oxygen, fluorine, carbon) and on the method of its introduction into the epitaxial layer: [Er] = 1.5×10^{19} [1] and 5.0×10^{19} cm^{-3} [2] when oxygen is introduced through a special capillary in the growth chamber, [Er] = 5.0×10^{19} cm^{-3} when oxygen is introduced by sublimation of Er_2O_3 [3], [Er] ~10^{19} cm^{-3} when fluorine is introduced by sublimation of ErF_3 [3], [Er] = 4.5×10^{19} cm^{-3} when carbon is introduced by sublimation from a graphite filament heated under an electric current [4], and [Er] = 1.5×10^{20} cm^{-3} when doping with oxygen is carried out by sublimation of ErO [5]. However, different erbium concentrations (2×10^{18} [6] and 2×10^{19} cm^{-3} [7]) corresponding to the maximum erbium luminescence have also been revealed in cases where doping impurities were not specially introduced. It is probable that such a large scatter in data is caused by specific features in the formation of structural defects in epitaxial layers depending on the conditions of their growth. As a rule, the observed decrease in the intensity of erbium luminescence at high concentrations [Er] has been associated with the formation of structural defects that either can act as effective centers of nonradiative recombination or can decrease the number of optically active Er^{3+} ions. To the best of our knowledge, the nature of the relevant structural defects formed in silicon epitaxial layers heavily doped with erbium has never been thoroughly studied. Efeoglu *et al.* [6] performed TEM investigations into the structure of silicon layers grown by molecular-beam epitaxy and doped with erbium at different levels. The structural defects observed were identified as $ErSi_2$ precipitates and platelike silicides. Unfortunately, those authors very arbitrarily determined the nature of the precipitates and did not present experimental evidence.

The purpose of this work was to elucidate the nature of the structural defects formed in Si : Er epitaxial layers during molecular-beam epitaxial growth.

2. SAMPLE PREPARATION AND EXPERIMENTAL TECHNIQUE

Samples were grown on a SUPRA-32 (RIBER) setup using *n*-Cz-Si(001) substrates with a resistivity of 4.5 Ω cm. The temperature of the substrate during epitaxial growth was maintained constant and equal to 600°C. The silicon flux was produced through electron beam evaporation of *n*-FZ-Si with a resistivity of 2 Ω cm. Doping of the growing layer with a rare-earth element was performed using an effusion cell with metallic erbium. At three temperatures of the effusion cell (740, 780, and 800°C), we grew epitaxial layers with concentrations [Er] = 8×10^{18}, 2×10^{19}, and 4×10^{19} cm^{-3}, respectively, according to the data on Rutherford backscattering of protons with an energy of 231 keV [7]. According to secondary ion mass spectrometry, the epi-

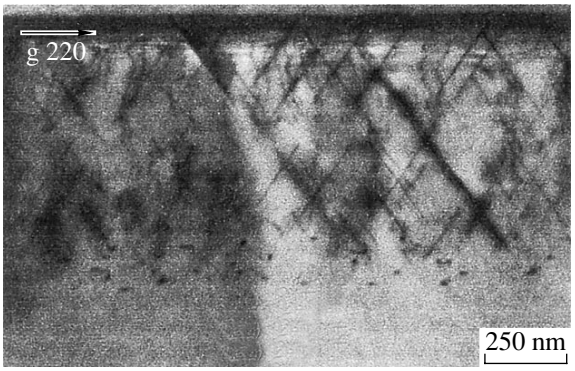

Fig. 1. TEM image of the cross section of the sample with an erbium concentration of 4×10^{19} cm^{-3}.

taxial layers contained impurities of oxygen and carbon at concentrations [O] $\approx 3 \times 10^{18}$ cm^{-3} and [C] $\approx 5 \times 10^{17}$ cm^{-3}. These concentrations depend on the pressure of residual gases ($\leq 8 \times 10^{-9}$ Torr) in the growth chamber during the growth and exceed the maximum solubility in bulk single crystals. The intensity of photoluminescence in the series of samples thus prepared increases by a factor of approximately 2 and reaches a maximum at [Er] = 2×10^{19} cm^{-3}, after which it decreases by more than one order of magnitude [7].

The structural investigations of the epitaxial layers were carried out on plan-view and cross sections of the samples with the use of transmission electron microscopy (TEM, JEM 200CX microscope) and high-resolution electron microscopy (HREM, JEM 4010 microscope).

3. RESULTS AND DISCUSSION

The developed defect structure was formed in the epitaxial layer at the highest concentration [Er] ~ 4×10^{19} cm^{-3}. The TEM image of the cross section of the sample in the (220) reflections is displayed in Fig. 1. Dislocations are not observed throughout the layer thickness (0.7 μm). Structural inhomogeneity of the epitaxial layer is represented by two types of precipitates of the second phase with different distributions over the layer depth. A strip of defects creating a contrast of dark spots is located in the region of the layer–substrate boundary. Under the conditions of absorption contrast, i.e., when strong reflections on the diffraction pattern are absent, the nature of the contrast on the defects remains virtually the same. This allows one to assume that these defects are precipitates. They have an approximately spherical form with diameters from 4 to 25 nm. The density of the precipitates is equal to $(5 \pm 2) \times 10^9$ cm^{-2}. Platelike precipitates are located in the {111} planes throughout the layer thickness. These precipitates with their ends exposed on the {110} foil surface are represented by straight inclined strips of dark contrast. Correspondingly, the precipitates lying in another pair of the {111} inclined planes are projected along the plane of their location and have the form of zigzag strips.

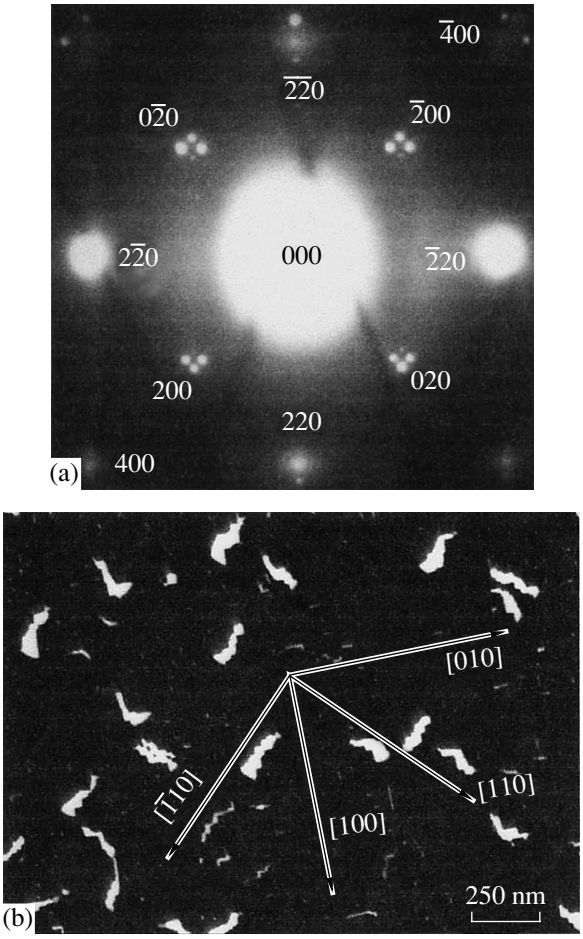

Fig. 2. (a) Electron diffraction pattern and (b) dark-field TEM image in extra reflections from the plan-view section of the same sample as in Fig. 1.

It can be seen from Fig. 1 that the formation of platelike precipitates is not immediately associated with the precipitates located at the "epitaxial layer–substrate" boundary. The electron diffraction patterns of the cross section contain extra reflections (these patterns are not shown). The dark-field images obtained in extra reflections exhibit platelike precipitates with their ends exposed on the foil surface, but the contrast on the precipitates in the region of the boundary remains dark. This points to the nature of these two types of precipitates of the second phase being different.

Figure 2 presents the results of examination of the plan-view section of the same epitaxial layer in the surface region with a thickness of about 0.3 μm. The electron diffraction pattern contains extra reflections (Fig. 2a), which are grouped near the main reflections from the silicon matrix and are arranged along the ⟨110⟩ directions. Such a specific location of extra reflections points to the fact that their appearance is due to the for-

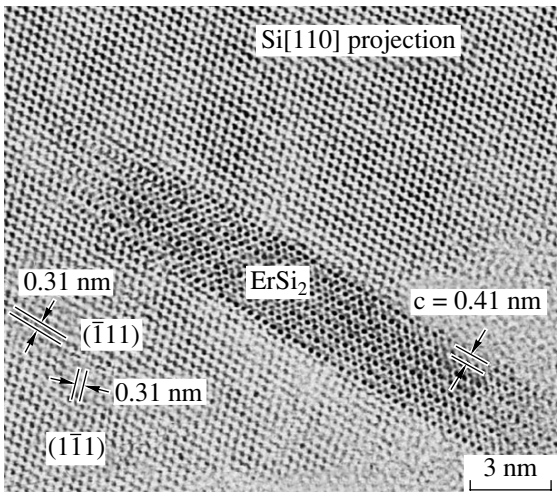

Fig. 3. HREM image of the platelike precipitate in the Si : Er epitaxial layer [the (110) cross section].

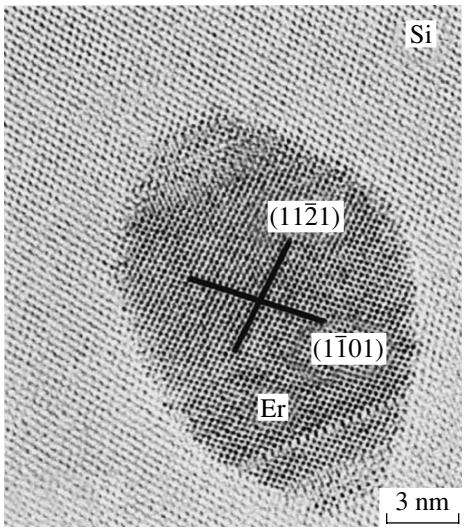

Fig. 4. HREM of the spherical precipitate in the region of the layer–substrate boundary [the (110) cross section].

mation of platelike precipitates lying in the {111} planes in the matrix of the layer. The strongest extra reflections are observed near the {200} reflections, even though formally the latter reflections are forbidden in a diamond-like lattice. The dark-field image obtained from a group of extra reflections near one of the {200} reflections clearly exhibits both large and very small platelike precipitates (Fig. 2b), which points to their nature being identical. The precipitates have a pronounced crystallographic orientation in the matrix of the layer. Small precipitates are located along the ⟨110⟩ crystallographic directions. These directions coincide with the fragments of zigzag contours of large precipitates, as well as with the lines along which the plane of precipitates is cut by the foil surface. The last finding confirms that platelike precipitates lie in the {111} inclined planes.

Similar defects of the crystal lattice are observed in the epitaxial layer with an erbium concentration [Er] ~ 2×10^{19} cm^{-3}. The only difference is the lower density of platelike precipitates. In the layer with a minimum concentration [Er] ~ 8×10^{18} cm^{-3}, platelike precipitates are not observed and the diffraction pattern of the epitaxial layer corresponds to single-crystal silicon.

The crystallographic structure of erbium-containing precipitates was determined using high-resolution electron microscopy on a sample with the highest atomic concentration of the rare-earth element. The HREM image of the platelike precipitate in the (110) cross section of the epitaxial layer is displayed in Fig. 3. Examination of the HREM image revealed that platelike precipitates are silicon disilicide, $ErSi_2$ (space group *P*6/*mmm*). It can be clearly seen from Fig. 3 that the (0001) atomic planes of the precipitate are aligned parallel to the (–111) atomic planes of the silicon matrix. Moreover, misfit dislocations are not observed, which suggests the absence of mechanical stresses between platelike precipitates and the silicon matrix. Figure 4 shows the HREM image of the spherical precipitate located in the region of the layer–substrate boundary. Analysis of the HREM image demonstrates that the crystal lattice of the precipitate corresponds to the metallic erbium phase.

The formation of two different erbium-containing phases in the epitaxial silicon layer and also the dependence of the possibility of their formation on the volume concentration of erbium indicate that, on the growth surface of the layer, there occur complex interactions between adsorbed erbium atoms, doping impurities (oxygen, carbon), and silicon. The consequence of these interactions is the formation of optically active erbium–oxygen (carbon) complexes and erbium disilicide precipitates. It should be noted that, taking into account the greater electric negativity of the doping impurities as compared to that of silicon, the rate of formation of erbium–oxygen (carbon) complexes should be higher than the rate of formation of $ErSi_2$. In this case, the formation should proceed only at the expense of excess erbium atoms on the surface of the growing layer, which are not captured by the erbium–oxygen (carbon) complexes. This assumption provides an explanation for the fact established in our study: the $ErSi_2$ precipitates are absent in the epitaxial layer at [Er] = 8×10^{18} cm^{-3}, which exceeds the limit of solubility of erbium in silicon [6], and are formed at [Er] = 2×10^{19} cm^{-3} or higher. It is quite possible that the formation of erbium precipitates in the near-boundary region of the layer is associated with the specific features of the physicochemical processes occurring on the surface of the growing layer at the initial stage of growth. It was demonstrated earlier in [7] that, in the Si : Er epitaxial layers at the boundary with the substrate,

there exists an intermediate region where a jump in the concentration profiles of erbium and impurities is observed.

In the case where the concentration of introduced erbium increases from 2×10^{19} to 4×10^{19} cm^{-3}, the density of $ErSi_2$ platelike precipitates increases to a substantially lesser degree as compared to the decrease in the intensity of photoluminescence. This allows one to assume that platelike precipitates are not effective channels of nonradiative recombination. This is also indicated by the sufficiently high intensity of luminescence in the epitaxial layer at [Er] = 2×10^{19} cm^{-3}. The formation of nonradiative-recombination channels is likewise not associated with extensive defects, which could be dislocations. It is unlikely that the observed decrease in the intensity of luminescence results from the decrease in the concentration of optically active centers, because the temperature of epitaxial growth is constant and the erbium concentration increases only twofold. It seems that the observed decrease in the intensity of luminescence is caused by effective channels of nonradiative recombination, which are formed at the expense of excess erbium atoms on the surface of the growing layer not participating in the formation of optically active centers and disilicide. It is interesting to note that any surplus component in the system of interacting erbium atoms, doping impurities, and silicon can be involved in the formation of nonradiative-recombination centers. For example, in [8], it was shown that additional implantation of oxygen ions into a Si : Er epitaxial layer at the erbium concentration [Er] = 2×10^{19} cm^{-3} and subsequent thermal annealing do not lead to an increase in the intensity of the Er^{3+} line or variation in the form of the luminescence spectrum. Only part of the introduced erbium governed by the concentration of doping impurities goes to the formation of optically active centers before oxygen implantation, and another ("superfluous") part goes to the formation of $ErSi_2$ precipitates. Therefore, implantation of oxygen ions and subsequent annealing do not give rise to additional erbium-containing optically active centers (due to the absence of erbium in the unbound state) and are accompanied by the formation of nonradiative-recombination centers. Efeoglu *et al.* [6] also concluded that the centers with deep-lying levels observed in the structures studied by them are more effective channels of nonradiative recombination than the structural defects.

4. CONCLUSIONS

The silicon layers grown by molecular-beam epitaxy and doped to the erbium concentration [Er] = 4×10^{19} cm^{-3} do not contain dislocations. The main types of defects in the crystal lattice of the epitaxial layer are 4- to 25-nm Er spherical precipitates located immediately at the layer–substrate boundary and $ErSi_2$ platelike precipitates lying in the {111} planes throughout the layer thickness. The nature of the precipitates has been established by high-resolution electron microscopy. Platelike precipitates are not formed in epitaxial layers at [Er] $\leq 8 \times 10^{18}$ cm^{-3}. When the erbium concentration is greater than or equal to 2×10^{19} cm^{-3}, the sizes and density of platelike precipitates vary in proportion to the concentration. The nucleation of platelike precipitates is not associated with erbium precipitates at the layer–substrate boundary. The rate of formation of optically active complexes is higher than the rate of formation of disilicide. The precipitates of disilicide are not effective channels of nonradiative recombination.

ACKNOWLEDGMENTS

This work was supported in part by the International Association of Assistance for the Promotion of Cooperation with Scientists from the New Independent States of the Former Soviet Union (project INTAS no. 2001-0194), the Russian Foundation for Basic Research (projects nos. 02-02-16374 and 04-02-16935), and the Department of Physical Sciences of the Russian Academy of Sciences within the framework of the scientific program "New Materials and Structures."

REFERENCES

1. R. Serna, J. H. Shin, M. Lohmeier, E. Vlieg, A. Polman, and P. F. A. Alkemade, J. Appl. Phys. **79** (5), 2658 (1996).
2. J. Stimmer, A. Reittinger, J. F. Nutzel, G. Abstreiter, H. P. Holzbrechter, and Ch. Buchal, Appl. Phys. Lett. **68** (23), 3290 (1996).
3. W.-X. Ni, K. B. Joelsson, C.-X. Du, I. A. Buyanova, G. Pozina, W. M. Chen, G. V. Hansson, B. Monemar, J. Cardenas, and B. G. Svensson, Appl. Phys. Lett. **70** (25), 3383 (1997).
4. M. Markmann, E. Neufeld, A. Sticht, K. Brunner, G. Abstreiter, and Ch. Buchal, Appl. Phys. Lett. **75** (17), 2584 (1999).
5. C.-X. Du, W.-X. Ni, K. B. Joelsson, F. Duteil, and G. V. Hansson, Opt. Mater. (Amsterdam) **14**, 259 (2000).
6. H. Efeoglu, J. H. Evans, T. E. Jackman, B. Hamilton, D. C. Honghton, J. M. Langer, A. R. Peaker, D. Perovic, I. Poole, N. Ravel, P. Hemment, and C. W. Chen, Semicond. Sci. Technol. **8**, 236 (1993).
7. N. A. Sobolev, D. V. Denisov, A. M. Emel'yanov, E. I. Shek, B. Ya. Ber, A. P. Kovarskiĭ, V. I. Sakharov, I. T. Serenkov, V. M. Ustinov, G. É. Tsirlin, and T. V. Kotereva, Fiz. Tverd. Tela (St. Petersburg) **47** (1), 106 (2005) [Phys. Solid State **47** (1), 113 (2005)].
8. N. A. Sobolev, D. V. Denisov, A. M. Emel'yanov, E. I. Shek, and E. O. Parsin, Fiz. Tverd. Tela (St. Petersburg) **47** (1), 110 (2005) [Phys. Solid State **47** (1), 117 (2005)].

Translated by O. Moskalev

Physics of the Solid State, Vol. 47, No. 10, 2005, pp. 1827–1830. Translated from Fizika Tverdogo Tela, Vol. 47, No. 10, 2005, pp. 1758–1761.

SEMICONDUCTORS AND DIELECTRICS

Exciton–Hole Scattering in ZnTe

V. S. Bagaev, V. V. Zaĭtsev, Yu. V. Klevkov, and V. S. Krivobok

Lebedev Physical Institute, Russian Academy of Sciences, Leninskiĭ pr. 53, Moscow, 119991 Russia

e-mail: bagaev@lebedev.ru

Received January 13, 2005

Abstract—Low-temperature luminescence of high-purity polycrystalline ZnTe was studied at various stationary excitation levels. It was found that edge luminescence spectra obtained at enhanced excitation levels are dominated by the radiation produced in exciton scattering from holes generated in Auger recombination of excitons bound to neutral acceptors (Cu). © *2005 Pleiades Publishing, Inc.*

1. INTRODUCTION

In real direct-gap semiconductor crystals containing shallow impurities, excitons localize efficiently at these impurities at low (liquid-helium) temperatures. Because of their large oscillator strengths, exciton–impurity complexes usually dominate edge radiation spectra within a broad range of excitation densities. This recombination channel in direct-gap semiconductors can be saturated only under pulsed excitation of a sufficiently high power. We present below the results of experiments which reveal the presence of high exciton densities in high-purity polycrystalline ZnTe at moderately high stationary pumping densities.

2. SAMPLE PREPARATION AND EXPERIMENTAL TECHNIQUES

[111]-patterned polycrystalline ZnTe samples 25 mm in diameter with an average grain size of 1.5–2 mm were prepared by free growth from the vapor phase in dynamic vacuum at a temperature of ~660°C. The starting charge was a purified ZnTe compound with the lowest possible deviation from stoichiometry. Plates cut from the starting samples were ground and annealed in liquid Zn at 680°C for 72 h. All photoluminescence (PL) measurements were conducted on freshly etched surfaces. The base concentration of substitutional impurities, as obtained from a chemical analysis, was $\sim 10^{14}$ cm^{-3}. The extended defects in the samples under study were, for the most part, grain boundaries and twins. The dislocation density did not exceed 10^2 cm^{-2}.

PL spectra were measured in He vapor at temperatures from 5 to 45 K. Optical excitation was effected with an Ar^+ laser (λ = 488.0 and 514.5 nm), whose radiation was focused to a spot ~70 μm in size. The highest possible excitation density was determined as overheating of the excitation region, which did not exceed 5 K. The enlarged image of the PL spot diaphragmed by an intermediate slit was focused onto the entrance slit of a DFS-24 double-grating monochromator. The PL spectra were recorded in the photon counting mode with a minimum resolution of 0.1 meV.

3. RESULTS AND DISCUSSION

Figure 1 displays a low-temperature PL spectrum of the samples under study obtained at a pump power density $W \sim 200$ W/cm^2. The spectrum obtained at this pumping density is dominated by the copper-bound exciton (A^0X Cu). The presence of this impurity is supported by the manifestation of a weak two-hole transition (2S Cu), as well as by the A^0X fine structure characteristic of this acceptor. The PL spectrum measured in the region of the exciton band bottom is a doublet structure produced by radiation of the upper polariton (UP) branch and the bottleneck region of the lower polariton (LP) branch. The long-wavelength region contains weak radiation ($Y1$, $Y2$) originating from extended defects. This radiation apparently can be attributed to the presence of a small concentration of dislocations near the grain boundaries.

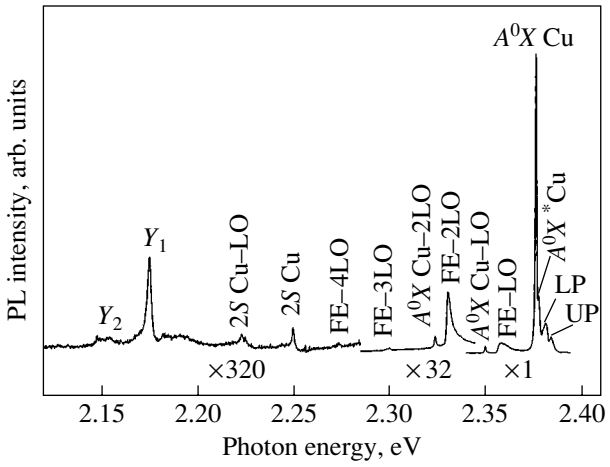

Fig. 1. General pattern of the PL spectrum obtained at a pump power density of 190 W/cm^2 at 4.2 K.

1063-7834/05/4710-1827$26.00 © 2005 Pleiades Publishing, Inc.

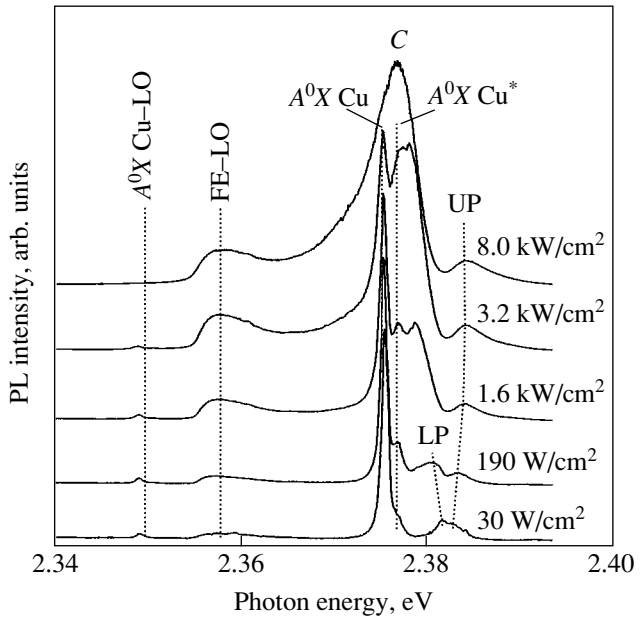

Fig. 2. PL spectra obtained at various pump power densities at ~4.2 K.

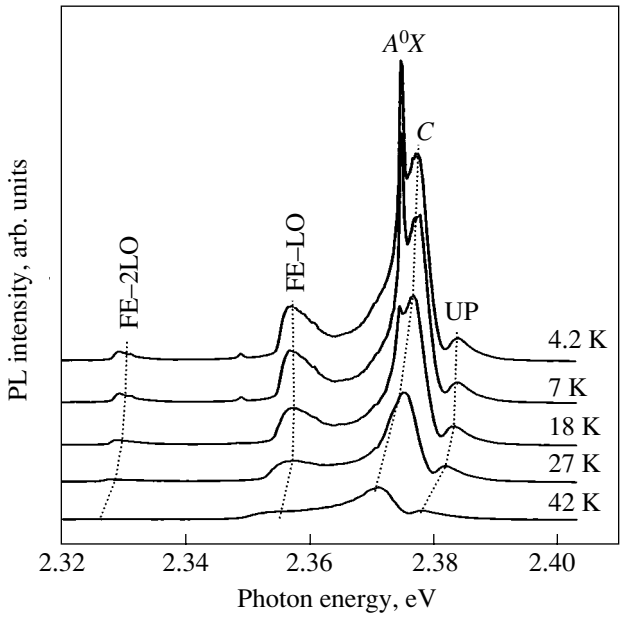

Fig. 3. Temperature dependence of PL spectra obtained at a pump power density of ~4 kW/cm^2.

Figure 2 shows the evolution of the PL spectrum in the excitonic region with increasing pump power density. At an excitation level $W \sim 30$ W/cm^2, the splitting between the LP and UP lines is not resolved, which indicates a short polariton relaxation time due to acoustic phonons. As W increases to 190 W/cm^2, the PL pattern changes to a classical polariton spectrum corresponding to the longitudinal–transverse exciton splitting ($\hbar\omega_{LT} \sim 2$ meV). The spectra near the exciton band bottom undergo the largest transformation for $W >$ 3 kW/cm^2. At these pump power densities, the exciton–impurity complex saturates and the spectrum becomes dominated by a broad C band (with a half-width markedly larger than kT); this band has a long-wavelength tail, and its maximum is located ~5 meV below the exciton band bottom. This fact suggests the onset of a new recombination process, which, as shown below, is mediated by exciton scattering from holes. Note that, according to our estimates [1], the lattice overheating at the spot center at $W = 8$ kW/cm^2 does not exceed 5 K.

Figure 3 plots the temperature dependence of PL spectra measured at a pump power density $W \sim$ 4 kW/cm^2. The spectra shown in this figure were obtained on a similar sample with a slightly higher acceptor concentration. We can see that an increase in temperature entails a noticeable lowering of the intensity of this band. The observed changes in the edge radiation spectra shown in Figs. 2 and 3 require separate analysis.

The effects associated with the transformation of spectra near the exciton band bottom were studied earlier in ZnTe and other direct-band semiconductors [2, 3] at fairly high pumping levels. A variety of processes occurring in systems with high exciton and nonequilibrium carrier concentrations were considered as candidates for interpretation of such effects. It was maintained in [2–4] that, at temperatures below 50 K, the processes in ZnTe are dominated by inelastic exciton–exciton scattering and, at higher temperatures, by scattering of excitons from holes. Inelastic exciton–exciton scattering should give rise to the formation of bands shifted to longer wavelengths by more than $(3/4)E_{ex} \approx$ 10 meV (E_{ex} is the exciton binding energy). Thus, the spectral positions of the lines produced in these processes do not fit our results. Therefore, in order to analyze the line shapes, we include the scattering of excitons by carriers. The theoretical treatment is based primarily on the data from [4, 5].

Exciton scattering on nonequilibrium carriers in direct-gap semiconductors (where excitons are coupled strongly to light) can be treated most conveniently in the so-called polariton basis. In the case where the valence band is nondegenerate, the polariton spectrum is determined by two (UP and LP) branches. The degeneracy observed in most crystals brings about a fairly complex structure of real polariton states. In ZnTe, the polariton dispersion is governed by three branches [6], namely, the UP, LP, and medium polariton (MP) branches. However, a rough description of exciton scattering by nonequilibrium carriers can be obtained by neglecting the MP branch on account of the low density of states. For the same reason, one can disregard the UP $\longrightarrow$ LP and UP $\longrightarrow$ UP scattering processes at the temperatures of interest here. Thus, the problem reduces to a study of two processes, namely, LP $\longrightarrow$ LP and LP $\longrightarrow$ UP.

The luminescence intensity deriving from scattering of the exciton polariton from an electron (hole) with the formation of a photonlike polariton of the upper or lower branch is given by [4]

$$I(\hbar\omega) = |c_{11}|^2|c_{12} - c_{14}|^2 \times \int_{-\infty}^{+\infty} C_{kK}\varphi_{e(h)}(k)\varphi_{ex}(K)d^3kd^3K\delta(\Delta E), \quad (1)$$

$$\Delta E = \frac{\hbar^2K^2}{2M} + \frac{\hbar^2k^2}{2m_{e(h)}} - \frac{\hbar^2q^2}{2m_{e(h)}} + (E_0 - \hbar\omega),$$

where E_0 is the exciton band bottom; $q = K + k$ is the electron (hole) momentum after the scattering event; $\delta(\Delta E)$ reflects the energy conservation law in scattering; K and k are the exciton and electron (hole) momenta before scattering, respectively; C_{kK} is the scattering probability of the exciton and electron (hole) in the (K, k) state into the $(0, K + k)$ state; c_{ij} are the Hopfield transformation coefficients [7]; and $\varphi_{e(h)}(k)$ and $\varphi_{ex}(K)$ are the electron (hole) and exciton distribution functions, respectively. We assume that C_{kK} depends only weakly on the momenta and that the functions $\varphi_{e(h)}(k)$ and $\varphi_{ex}(K)$ are Boltzmann distributions with effective temperatures T_e and T_{ex}, respectively. In this case, the PL intensity due to exciton–hole scattering can be found to be

$$I(\hbar\omega) = A_h\frac{(E_0 - \hbar\omega)^2}{((E_0 - \hbar\omega)^2 + \hbar\omega_{LT}E_0)^2} \times \exp\left(-\frac{|E_0 - \hbar\omega|}{2\kappa T_h M}\left(\sqrt{m_e^2 + 4\frac{T_h}{T_{ex}}m_hM} \mp m_e\right)\right) \times\left(1 + \frac{|E_0 - \hbar\omega|}{2\kappa T_h M}\sqrt{m_e^2 + 4\frac{T_h}{T_{ex}}m_hM}\right). \quad (2)$$

In Eq. (2), the minus sign corresponds to the LP ⟶ LP scattering and the plus sign, to the LP ⟶ UP scattering. The relation derived for the exciton–electron scattering is similar, with the only differences being that $m_e(m_h)$ should be replaced by $m_h(m_e)$, T_h by T_e, and the scaling parameter A_h by A_e (these parameters are different for the LP ⟶ LP and LP ⟶ UP processes). In Eq. (2), $M = m_e + m_h$ (m_h is the heavy-hole mass) and κ is the Boltzmann constant.

If the exciton system is in thermal equilibrium, the spectral shape of the exciton–phonon luminescence can be described by a general expression [8],

$$I_N(E) = \sqrt{E}\exp(-E/\kappa T_{ex})W_N(E), \quad (3)$$

where $W_N(E)$ is the probability of exciton–phonon emission of the order N for an exciton with kinetic energy E. This permits one to determine the exciton temperature T_{ex} from the shape of the LO phonon replicas. Figure 4 shows a typical fit using Eq. (3) (see inset). T_{LO} and T_{2LO} refer to the temperatures derived from the first and second LO replica, respectively. The C band was fitted with Eq. (2) by varying the hole (electron) temperature and the factors A_h and A_e. The best fit was found for $A_e/A_h \longrightarrow 0$; i.e., electrons are not involved in exciton scattering. Thus, one has to assume that, at high excitation densities, the concentration of nonequilibrium holes far exceeds that of nonequilibrium electrons. This may find explanation, besides in the direct hole generation in the photoexcitation of a semiconductor, in the existence of an additional channel associated with the so-called Auger process, in which annihilation of the exciton bound to a neutral acceptor generates a free hole [9]. This is suggested, in particular, by the temperature dependence of the C band presented in Fig. 3. The C band is seen to weaken rapidly at temperatures above 25 K, at which the exciton–impurity complex representing a copper-bound exciton thermally dissociates. The hole binding energy at this acceptor is ~148 meV, which is in substantial excess of the binding energy of a hydrogen-like acceptor in ZnTe [6]. It is known that the probability of the Auger recombination process in question is proportional to E_A^4, where E_A is the hole binding energy at the acceptor [9]. Thus, when the free-exciton concentration increases under stationary excitation, the rate of Auger-mediated hole generation in exciton–impurity complexes may become comparable to the rate of hole recapture by the acceptor, and this is what leads to the increase in the nonequilibrium hole concentration.

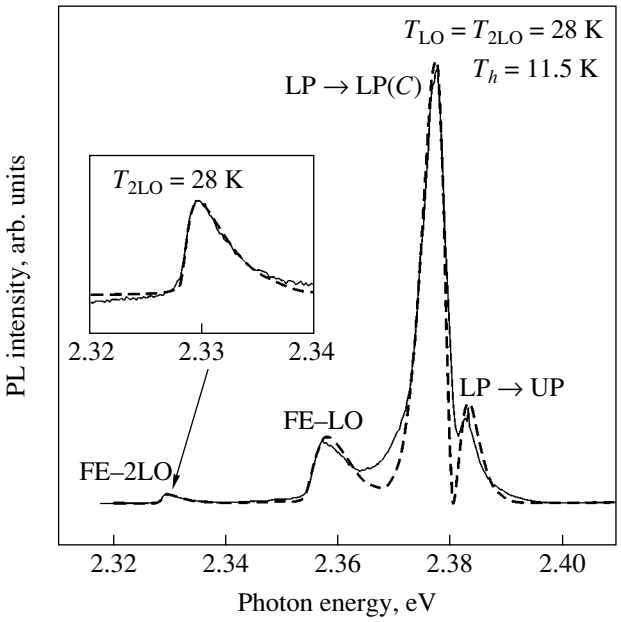

Fig. 4. Fitting of the C band and the free-exciton phonon replicas with Eqs. (2) and (3), respectively (dashed lines), with the following parameters: $T_{LO} = T_{2LO} = 28$ K and $T_h = 11.5$ K. The experimental curve was obtained for a temperature of 5 K and a pump power density of 8 kW/cm^2.

4. CONCLUSIONS

Our study of the PL spectra of high-purity ZnTe crystals has revealed the presence of excitons in high densities under stationary excitation. An analysis of PL spectra obtained at different temperatures and pump power densities suggests that this effect is related to exciton scattering from holes. The observation of exciton–hole scattering in our experimental conditions without any indication of exciton scattering from electrons should apparently be assigned to the existence of an additional channel of free-hole generation in the Auger recombination of exciton–impurity complexes. An efficient process of this kind may originate from the presence in the samples under study of residual copper, which is a deep acceptor for ZnTe.

ACKNOWLEDGMENTS

This study was supported by the Russian Foundation for Basic Research (project nos. 03-02-16854, 04-02-17078) and the foundation for support of leading scientific schools (project no. NSh1923.2003.2).

REFERENCES

1. V. S. Bagaev, T. I. Galkina, A. I. Sharkov, A. Yu. Klokov, V. P. Martovitskiĭ, V. V. Zaĭtsev, and Yu. V. Klevkov, Fiz. Tverd. Tela (St. Petersburg) **45** (11), 1941 (2003) [Phys. Solid State **45** (11), 2039 (2003)].
2. M. S. Brodin, V. M. Bandura, and M. G. Matsko, Fiz. Tverd. Tela (Leningrad) **24** (8), 2411 (1982) [Sov. Phys. Solid State **24** (8), 1369 (1982)].
3. C. F. Klingshirn, W. Maier, and B. Honerlage, Solid-State Electron. **21**, 1357 (1978).
4. C. F. Klingshirn and H. Haug, Phys. Rep. **70** (5), 315 (1981).
5. C. B. Guillaume, J. M. Debever, and F. Salvan, Phys. Rev. **177** (2), 567 (1969).
6. V. S. Bagaev, V. V. Zaĭtsev, Yu. V. Klevkov, V. S. Krivobok, and E. E. Onishchenko, Fiz. Tekh. Poluprovodn. (St. Petersburg) **37** (3), 299 (2003) [Semiconductors **37** (3), 283 (2003)].
7. J. J. Hopfield, Phys. Rev. **112** (5), 1555 (1958).
8. *Excitons*, Ed. by E. I. Rashba and M. D. Sturge (North-Holland, Amsterdam, 1982; Nauka, Moscow, 1985).
9. P. J. Dean and D. C. Herbert, in *Topics in Current Physics*, Ed. by K. Cho (Springer, Berlin, 1979), Vol. 14, p. 55.

Translated by G. Skrebtsov

Physics of the Solid State, Vol. 47, No. 10, 2005, pp. 1831–1836. Translated from Fizika Tverdogo Tela, Vol. 47, No. 10, 2005, pp. 1762–1767.

SEMICONDUCTORS AND DIELECTRICS

Ab Initio Studies of the Energy Characteristics and Magnetic Properties of Point Defects in GaAs

V. I. Baĭkov[1, 2], E. I. Isaev[1], P. A. Korzhavyĭ[2], Yu. Kh. Vekilov[1], and I. A. Abrikosov[3]

[1] *Moscow State Institute of Steel and Alloys, Leninskiĭ pr. 4, Moscow, 119049 Russia*
e-mail: eyvaz_isaev@yahoo.com
[2] *Royal Institute of Technology, Stockholm, SE-100 44 Sweden*
[3] *Linköping University, Linköping, SE-581 83 Sweden*

Received February 28, 2005

Abstract—The formation energies of intrinsic point defects and solution energies of transition metal impurities in gallium arsenide are determined on the basis of *ab initio* calculations using the method of a locally self-consistent Green's function, which is a generalization of the coherent potential approximation. Based on the calculated energies, the conclusion is made that the As_{Ga} antisite defect is the most common intrinsic defect in GaAs. Calculations showed that transition metal impurities, except for Ni, preferentially occupy gallium sites substitutionally. The magnetic moments of impurity atoms are calculated as a function of the chemical environment. It is shown that, in compensated GaAs, Mn atoms tend to form clusters. © *2005 Pleiades Publishing, Inc.*

1. INTRODUCTION

The distribution of impurity atoms over the sublattices in semiconductor compounds strongly affects their optical and transport properties. Impurity atoms can occupy interstitial and substitutional positions and also form defect complexes. Depending on the sublattice on which it is located, an impurity can act either as a donor or as an acceptor (which determines the type of impurity conduction). The concentration and location of defects are determined by the energies of defect formation and of dissolution of impurity atoms. To date, little is known about these energies and their dependence on the impurity type and position in the crystalline matrix.

Most of the studies of 3*d* metal impurities in GaAs deal mainly with the solution of two problems: determining the position and charge state of impurity atoms in the GaAs crystalline lattice and defining the position of the energy levels appearing in the band gap. The interest in these problems is due to the fact that impurities (e.g., Cr) can cause the appearance of deep energy levels in III–V compounds; these levels are necessary for the fabrication of semi-insulating crystals [1].

The distribution of an impurity over the GaAs sublattices has been studied both experimentally and theoretically [2–9]. EXAFS (extended x-ray absorption fine structure) studies on the local atomic environment in $(Ga_{1-x}Mn_x)As$ have shown that Mn atoms occupy Ga sites [2] and that the Mn–As bond length changes only slightly (by less than 3%). From electron spin resonance (ESR) and Mössbauer spectroscopy studies [3], it is known that Fe atoms in GaAs occupy Ga sites and, in the neutral charge state, have the $3d^5$ and $3d^6$ electronic configurations in the presence of a background of compensating donors; this conclusion is confirmed by acoustic paramagnetic resonance studies [4]. Recently, a crystal of the $Ga_{1-x}Fe_xAs$ magnetic semiconductor was grown and EXAFS studies confirmed that Fe atoms replace Ga [5]. Measurements of the Hall coefficient and electrical conductivity [3] have shown that an Fe impurity in gallium arsenide is an acceptor. Experimentally [6, 7], it has been shown that Cr impurities in GaAs occupy sites on the Ga sublattice. However, there are no reliable published results on the energy characteristics of these impurities in GaAs, which are necessary for analysis of the possible distribution of impurities over the other sublattices.

Since atoms of the elements of the Fe group with partially filled electronic shells have a nonzero intrinsic magnetic moment, the magnetic susceptibility of the crystal is expected to change. On the other hand, it is known [10] that the 3*d* metal ions in solids are strongly affected by the crystal field, which quenches the orbital angular momentum. Therefore, experimentally observed values of the magnetic moments of 3*d* metal ions in crystals usually differ from the corresponding values of the moments of free ions. Thus, studying the dependence of the magnetic moment of an impurity atom on its chemical environment in GaAs is of interest. This problem is directly related to the possibility of obtaining a magnetic semiconductor material with a high Curie temperature (of the order of room temperature). Numerous studies have dealt with this problem (see reviews [11, 12] and references therein); however, up to now, the problem has remained open.

In this study, we performed *ab initio* calculations of the electronic structure; the solution energy of impurity atoms of the transition metals (TMs) V, Cr, Mn, Fe, Co,

1063-7834/05/4710-1831$26.00

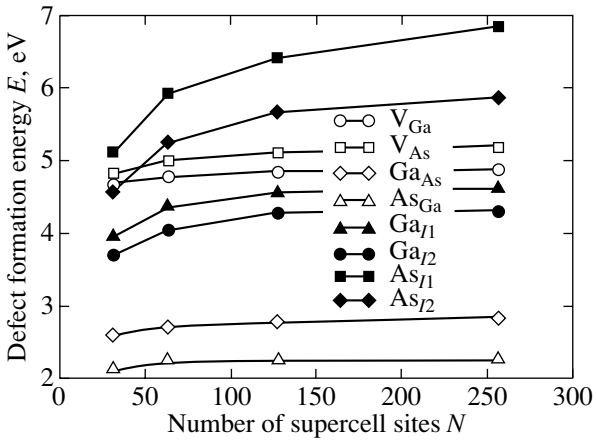

Dependence of the energy of formation of intrinsic point defects in GaAs on the number of atoms in a supercell. V_{As} and V_{Ga} are vacancies; Ga_{As} and As_{Ga} are antisite defects; and Ga_{I1}, As_{I1}, Ga_{I2}, and As_{I2} are interstitial atoms.

and Ni in different sublattices in gallium arsenide; and the energies of transition of impurities from one sublattice to the other. In addition, we calculated the formation energies for eight types of intrinsic point defects (vacancies V_{Ga}, V_{As}; antisite defects As_{Ga}, Ga_{As}; and interstitial defects As_{I1}, As_{I2}, Ga_{I1}, Ga_{I2}, where the tetrahedral positions $I1$ and $I2$ have Ga and As atoms at the vertices of the tetrahedron, respectively) and the magnetic moments of impurity atoms on different sublattices of GaAs. Using these quantities, we determined the preferred positions for the distribution of structural defects and impurity atoms in gallium arsenide for both stable and metastable states.

2. METHOD AND DETAILS OF THE CALCULATIONS

To calculate the energy characteristics of single point defects, we used cubic supercells based on the zinc blende (ZnS) structure with $N = 128$ sites ($2 \times 2 \times 2$) containing one defect per supercell. (Interstitial positions were simulated by empty spheres and were considered as additional lattice sites). To calculate the energies for pair defects, supercells with $N = 256$ ($2 \times 2 \times 4$) were used. As the number of sites per supercell increases, the computational expenses also increase. Therefore, it is preferable to apply the method of a locally self-consistent Green's function [13, 14], in which the scaling of the computation time with the number of sites is linear, in contrast to standard band structure methods, where this time is proportional to N^3.

Calculations were performed as follows. Each site in a supercell together with the first four coordination spheres of the atoms and empty spheres around this site was considered self-consistently as a local interaction zone of the method of a locally self-consistent Green's function embedded in an effective medium having the same symmetry as the original lattice. The parameters of the effective medium were chosen so that, on the average, they described the scattering properties of the system. The central diagonal block G_{LL}^{RR} of the Green's function matrix in the Korringa–Kohn–Rostoker (KKR) method, calculated in the atomic-sphere approximation (KKR–ASA), was used to construct the charge density inside an atomic sphere of radius vector R in the supercell. For all types of atoms and all empty spheres, the atomic radii were assumed to be equal to the average radius of the Wigner–Seitz sphere for the structure under study.

When calculating the total energy, we also took into account the nonspherical components of the electronic density within the framework of the linear response theory using a technique similar to that suggested in [15]. Integration of nonspherical components over an atomic sphere gives the multipole charges Q_L^R of the atomic spheres, which were used to define the multipole Madelung contributions to the one-electron potential and total energy

$$V_0^R = \frac{1}{S}\sum_{R',\,L'} M_{0,\,L'}^{R,\,R'} Q_{L'}^{R'}, \tag{1}$$

$$E_M = \frac{1}{2S}\sum_{R,\,L} Q_L^R \sum_{R',\,L'} M_{L,\,L'}^{R,\,R'} Q_{L'}^{R'}, \tag{2}$$

where $L \equiv (l, m)$ denotes the orbital and magnetic quantum numbers; $M_{L,\,L'}^{R,\,R'}$ is the multipole Madelung matrix, which is equivalent to the matrix of unscreened structural constants for the entire supercell; and S is the Wigner–Seitz radius.

The Green's function was calculated using the maximum orbital quantum number $l_{max} = 2$; accordingly, multipole components of the electronic density of up to $l = 4$ were taken into account. The total energy was calculated using the local density approximation for the exchange-correlation potential [16]. The volumes of the supercells were relaxed to a minimum of total energy; however, the local relaxation around point defects was not taken into account.

3. RESULTS AND DISCUSSION

The calculated formation energies of intrinsic point defects[1] in GaAs are shown in the figure, where it is seen that a satisfactory convergence for these energies is attained for 128 supercell sites (64 atoms and 64 empty spheres). In this study, the defect formation ener-

[1] It should be noted that we considered only neutral intrinsic point defects and, accordingly, compared the energies only for these defects.

Table 1. Formation energies of vacancies and antisite and interstitial defects in GaAs (in electronvolts)

Reference	Defect type							
	V_{Ga}	V_{As}	Ga_{As}	As_{Ga}	Ga_{I1}	Ga_{I2}	As_{I1}	As_{I2}
This study	4.89	5.21	2.85	2.27	4.63	4.32	6.85	5.89
[24]	4.55		2.74	2.50			6.14	
[25]	4.25	4.25	3.6	2.4	5.0	4.7	8.5	6.8
[19]	3.70			3.40			7.7[a]	7.0[a]
[20]	3.6			2.4				

Note: The first line is the results of our calculations.
[a] Without relaxation.

gies in GaAs are determined with respect to the stoichiometric compound using the formula

$$E_{def} = \left.\frac{\partial(\Delta E)}{\partial x_{def}}\right|_{P=0},$$

where ΔE is the formation energy of a compound containing defects of a certain type with concentration x_{def}. The calculated defect formation energies are given in Table 1. For comparison, data obtained by other authors are also listed. (In [17, 18], the defect formation energies are given for GaAs with an excess of As. Therefore, to compare them with the results of our calculations (Table 1), the defect formation energies obtained in [17, 18] were reduced to the definition used in this study, with regard to the energy $\Delta E = -0.8$ eV/atom of formation of the stoichiometric GaAs compound.) We note that, in most cases, our results are in agreement with the conclusions from previous studies. Above all, this statement applies to the conclusion that the antisite defect As_{Ga} (the so-called stable *EL*2 defect) is most favorable from the energy standpoint; this conclusion is confirmed both experimentally and theoretically [19–21]. Second, the large energy required for the creation of As_{I1} and As_{I2} defects explains why these defects have not been detected in ESR experiments, nor by electrical and optical methods [19]. In addition, the values of the calculated energies are in good agreement with the results of the *ab initio* calculations preformed by Northrup and Zhang [22] and Jansen and Sankey [23]. For tetrahedrally coordinated interstitial As defects, there is also good agreement with the results from [17], where the problem of the formation of intrinsic point defects in GaAs was studied using *ab initio* pseudopotentials and a large supercell containing 216 atoms. We note that the positions of the As_{I1} and As_{I2} defects were not relaxed in [17]. There are also some differences. For example, the formation energy of the vacancy V_{Ga} differs substantially from the values obtained in [18, 22]. This difference in the corresponding vacancy formation energies can be related to the use of different methods.

We also calculated the formation energies of pair defects in GaAs (Table 2). We note that, compared to the As_{Ga}–Ga_{As} defect, the energies required to create the other pair defects investigated are very large (even greater than that for interstitial As atoms). Therefore, those defects are unlikely to be observed experimentally in GaAs. Recently, using the molecular-dynamics method in the Car–Parinello formulation and *ab initio* norm-conserving pseudopotentials, Janotti *et al.* [24] showed that the formation energy of a neutral pair antisite As_{Ga}–Ga_{As} defect is equal to 2.62 eV (2.87 eV without relaxation). We believe that the difference in the obtained energies can be due to the following reasons. First, the integration over the Brillouin zone in [24] was performed using only one *k* point, namely, the Γ point. It was shown in [25] that this can result in substantial errors when calculating the defect formation energy. Second, the number of atoms in the supercell we used is twice smaller than that used in [24]. One more reason is the strongly nonspherical charge density distribution in semiconductors, which was taken into account in our method only approximately. Our method is intermediate between the atomic-sphere approximation and the total charge density approximation.

Now, let us discuss the results of the calculations for transition metal impurities (V, Cr, Mn, Fe, Co, Ni) in stoichiometric GaAs. The solution energies for these impurities are listed in Table 3. The calculations were performed starting from the calculated total energies of supercells (with one impurity atom per supercell) and defect creation reactions of the type

$$x \cdot TM + \mathrm{GaAs} \longrightarrow \mathrm{Ga}_{1-x}TM_x\mathrm{As} + x \cdot \mathrm{Ga}.$$

Table 2. Formation energies of intrinsic pair defects in stoichiometric GaAs (in electronvolts)

Pair defects	As_{Ga}–Ga_{As}	V_{Ga}–V_{As}	As_{I1}–V_{As}	Ga_{I2}–V_{Ga}	Ga_{I1}–V_{Ga}
Energy, eV	4.05	7.96	9.90	6.88	6.97

Table 3. Solution energies of Co, V, Fe, Mn, Cr, and Ni impurity atoms in different GaAs sublattices (in electronvolts)

Impurity	Sublattice			
	Ga	As	*I*1	*I*2
V	2.11	5.69	4.91	4.43
Cr	2.01	5.25	4.11	4.11
Mn	1.92	4.71	3.82	3.64
Fe	1.71	4.12	2.96	2.50
Co	2.52	4.10	3.14	3.00
Ni	2.98	3.67	2.10	2.15

Comparing these energies, we come to the conclusion that the substitution of TM atoms for Ga is energetically most favorable, in accordance with the results of experiments [2, 5, 26]. The Ni impurity, which prefers tetrahedrally coordinated interstitial sites, is an exception: the solution energy of Ni at interstitial positions is virtually the same as the solution energies of V, Cr, and Mn in the Ga sublattice. We also call attention to the smooth decrease in the impurity solution energy in the Ga sublattice from V to Fe in Table 3 and to the sharp jump for Co and Ni. This change in energy can be explained by the order of filling of the *d* states of impurity atoms. The valence electrons fill the spin-up *d* states of V, Cr, Mn, and Fe impurity atoms. This conclusion agrees with the calculated magnetic moments of impurity atoms on the gallium sublattice (Table 5). After complete filling of the spin-up *d* states (for Fe atoms), the filling of higher energy spin-down states begins. Accordingly, the solution energy increases and the impurity magnetic moment decreases.

However an impurity can also be in a metastable state on the other sublattice. For example, if a manganese impurity atom occupies an interstitial site during the crystal growth, then the impurity must spend an energy of about 1 eV to displace a Ga atom to an interstitial site in order to attain the stable state on the Ga sublattice. In other words, in the absence of Ga vacancies, the interstitial impurity will not stay in the metastable state (Table 4).

The equilibrium magnetic moment of impurities on different GaAs sublattices was calculated using the method of the "floating" magnetic moment, where a finite value of the magnetic moment is obtained by self-consistent calculations which is independent of the choice of the initial state. The calculated equilibrium magnetic moments for different chemical environments are listed in Table 5.

The magnetic moments of V, Cr, and Mn atoms in a Ga position are integers, and that of a Fe atom is not an integer (because of the filling of the spin-down *d* subband) and is dependent on the Fe–As tetrahedral-bond length (Table 6). Therefore, the relaxation of Fe atoms must have a strong effect on the thermodynamic and physical properties of Fe impurities in GaAs. These conclusions agree with the results from [27], where the Fe magnetic moment after relaxation was found to be equal to $1\mu_B$. For V, Cr, and Mn at Ga sites, a 8% increase in the bond length has no effect on the magnitude of the magnetic moment (Table 7). Hence, the V, Cr, Mn, and, possibly, Ni impurities do not destroy the tetrahedral symmetry (their relaxation is small) [28].

The interaction energy of pair defects is also of interest, since, based on this energy, a conclusion can be drawn as to the possible formation of defect clusters in GaAs. We calculated this energy for selected configurations of pair defects located in the first and second coordination spheres with respect to each other (Table 8). The interaction energy is evaluated from the energy of a supercell with defects at maximum distances from each other within the chosen supercell [$N = 256(2 \times 2 \times 4)$]. The calculations showed that As_{Ga} and Ga_{As} defects strongly attract each other in the first coordination sphere, but if they are the second nearest neighbors of each other, their interaction is repulsive. The interaction of the defects that form a (Mn_{As}–As_{Ga}) pair and are the

Table 4. Mn atom transition energies from one sublattice into the other (in electronvolts)

Transition	Energy	Transition	Energy	Transition	Energy
Ga ⟶ As	3.42	As ⟶ *I*1	3.30	*I*1 ⟶ *I*2	–0.17
Ga ⟶ *I*1	4.31	As ⟶ *I*2	3.35	*I*2 ⟶ Ga	0.92
Ga ⟶ *I*2	4.62	*I*1 ⟶ Ga	1.25	*I*2 ⟶ As	4.69
As ⟶ Ga	–0.18	*I*1 ⟶ As	4.75	*I*2 ⟶ *I*1	0.17
*I*2 ⟶ As	4.69	*I*2 ⟶ As	4.69		

Note: Ga ⟶ As denotes the Mn transition from the Ga into As sublattice. The corresponding reaction has the form $\left(\mathrm{TM}_{\frac{1}{32}}\mathrm{Ga}_{\frac{31}{32}}\right)\mathrm{As} \longrightarrow \longrightarrow \left(\mathrm{As}_{\frac{1}{32}}\mathrm{Ga}_{\frac{31}{32}}\right)\left(\mathrm{TM}_{\frac{1}{32}}\mathrm{As}_{\frac{31}{32}}\right)$.

Table 5. Magnetic moments of transition metal impurities (in Bohr magnetons μ_B) on different GaAs sublattices at the calculated equilibrium lattice parameters

Impurity	Sublattice			
	Ga	As	*I*1	*I*2
V	2	0	3.270	0
Cr	3	3	4	0
Mn	4	2	3	3
Fe	4.13	1.45	2	2
Co	2	0	1	1
Ni	0	0	0	0

Table 6. Magnetic moments of an Fe atom (in μ_B) on different GaAs sublattices for different values of the Wigner–Seitz radius R_{WS} (in atomic units)

R_{WS}	$\mu(Fe_{As})$	$\mu(Fe_{Ga})$	$\mu(Fe_{I1})$	$\mu(Fe_{I2})$
2.55	1.32	1.02	1.99	2.01
2.60	1.45	4.13	2.01	2.01
2.65	1.78	4.38	2.20	2.02
2.70	2.00	4.49		2.12
2.75	2.18	4.56		2.36

Table 7. Magnetic moments of a Cr atom (in μ_B) on different GaAs sublattices for different values of the Wigner–Seitz radius R_{WS} (in atomic units)

R_{WS}	$\mu(Cr_{As})$	$\mu(Cr_{Ga})$	$\mu(Cr_{I1})$	$\mu(Cr_{I2})$
2.55	3.00	3.00	3.91	0
2.60	3.00	3.00	4.05	0
2.65	300	3.00	4.51	0
2.70	3.00	3.00	4.83	0
2.75	3.00	3.00	4.88	4.80

Table 8. Calculated pair interaction energies between defects in GaAs (eV/atom)

Pair defect	For nearest neighbors of each other	For next-to-nearest neighbors of each other
$(As_{Ga}–Ga_{As})$	–1.24	0.07
$(Mn_{Ga}–As_{Ga})$	–0.16	–0.03
$(Mn_{Ga}–Mn_{Ga})$	–0.09	0
$(Mn_{Ga}–Mn_{Ga}) + As_{Ga}$	–0.22	–0.21

Note: Negative energy corresponds to attraction of defects to each other.

next-to-nearest neighbors of each other is attractive. The Mn_{Ga} impurity atoms in a pair interact with each other only if they are nearest neighbors. However, the most interesting result is the fact that, in the case of the more complicated defect complex $(Mn_{Ga}–Mn_{Ga}) + As_{Ga}$ (compensated semiconductor), the interaction energy of the defects forming the $(Mn_{Ga}–Mn_{Ga})$ pair is negative and is practically the same in the cases where these defects are the first and second nearest neighbors of each other. Thus, Mn impurity atoms tend to form clusters both in *p*-type GaAs and in a compensated semiconductor; in the latter case, this trend is expressed more strongly. This conclusion is in agreement with the results of recent studies, where it has been shown that Mn atoms can form small clusters both by replacing Ga atoms [29] and by occupying interstitial sites [30].

For these two types of defect complexes, we also determined the energy of magnetic ordering as a function of the distance between the Mn atoms (Table 9). The energy of magnetic ordering is defined here as the difference of the total energies between the configurations with antiferromagnetic (AFM) and ferromagnetic (FM) ordering of the moments of two impurity atoms in a supercell. In the case of a *p*-type semiconductor, the FM ordering is energetically more favorable. In a compensated semiconductor, the AFM configuration is most favorable. This result is in agreement with the results of recent experimental and theoretical studies [31]. For compensated GaAs, the local magnetic moment of a Mn atom is 5 μ_B, which corresponds to the Mn^{2+} $3d^5$ electronic configuration. This value of the magnetic moment agrees with the magnetic moment experimentally measured by the x-ray magnetic circular dichroism method (4.6 μ_B) [32] and with measurements of the saturation magnetization [26], according to which the average spin value is $S = 2.2$. The values of the Mn magnetic moment intermediate between 4 and 5 μ_B can be interpreted as being due to the presence of manganese atoms in two charge states, Mn^{+3} and Mn^{+2}.

Table 9. Magnetic ordering energy $\Delta E = E^{AFM} - E^{FM}$ (eV/Mn atom)

Defect configuration	$\frac{1}{2}\langle 110\rangle$	$\langle 100\rangle$	$\langle 200\rangle$
$\left(Ga_{\frac{62}{64}}Mn_{\frac{2}{64}}\right)As$	0.09	0.04	0.04
$\left(Ga_{\frac{62}{64}}Mn_{\frac{2}{64}}As_{\frac{1}{64}}\right)As$	–0.06	–0.03	–0.02

4. CONCLUSIONS

Using the method of a locally self-consistent Green's function, we have performed *ab initio* calculations of the formation energies of point defects in gallium arsenide. We have determined the equilibrium positions of impurity atoms in the crystal and the magnetic moments of transition metal impurities in various positions on the GaAs crystalline lattice. In some cases, the calculated defect formation energies appeared to be slightly overestimated, since the effects of local relaxation around the point defects were disregarded in our calculations. It has been found that, in contrast to all other 3*d* metal impurities, Ni atoms in GaAs preferably occupy interstitial sites. The formation of clusters of Mn atoms is shown to be possible.

ACKNOWLEDGMENTS

This study was supported by the Russian Foundation for Basic Research (project no. 04-02-16823), the Royal Swedish Academy of Sciences, and the Swedish Research Fund (VR, SSF).

REFERENCES

1. A. Partovi, A. M. Glass, D. N. Olson, G. J. Zydzik, H. M. O'Bryan, T. H. Chiu, and W. H. Knox, Appl. Phys. Lett. **62**, 464 (1993).
2. R. Shioda, K. Ando, T. Hayashi, and M. Tanaka, Phys. Rev. B: Condens. Matter **58**, 1100 (1998).
3. V. I. Fistul', L. Ya. Pervova, É. M. Omel'yanovskiĭ, E. P. Rashevskaya, N. N. Solov'ev, and O. V. Pelevin, Fiz. Tekh. Poluprovodn. (Leningrad) **8**, 485 (1974) [Sov. Phys. Semicond. **8**, 311 (1974)].
4. E. M. Ganapol'skiĭ, Fiz. Tverd. Tela (Leningrad) **15**, 368 (1973) [Sov. Phys. Solid State **15**, 269 (1974)].
5. Y. L. Soo, G. Kioseoglou, S. Huang, S. Kim, Y. H. Kao, Y. Takatani, S. Haneda, and H. Munekata, Phys. Rev. B: Condens. Matter **63**, 195 209 (2001).
6. E. M. Ganapol'skiĭ, Fiz. Tverd. Tela (Leningrad) **16**, 2886 (1974) [Sov. Phys. Solid State **16**, 1868 (1975)].
7. D. G. Andrianov, A. S. Savel'ev, N. N. Suchkova, E. P. Rashevskaya, and M. A. Filippov, Fiz. Tekh. Poluprovodn. (Leningrad) **11**, 1460 (1977) [Sov. Phys. Semicond. **11**, 858 (1977)].
8. K. V. Ponomarev, P. A. Korzhavyĭ, and Yu. Kh. Vekilov, Fiz. Tverd. Tela (St. Petersburg) **39**, 264 (1997) [Phys. Solid State **39**, 230 (1997)].
9. E. I. Isaev, V. I. Baykov, P. A. Korzhavyi, Yu. Kh. Vekilov, I. A. Abrikosov, B. Johansson, and O. Eriksson, J. Magn. Magn. Mater. **272–276**, 1961 (2004).
10. R. White, *Quantum Theory of Magnetism* (McGraw-Hill, New York, 1970; Mir, Moscow, 1976).
11. H. Ohno, J. Magn. Magn. Mater. **200**, 110 (1999).
12. T. Dietl, Semicond. Sci. Technol. **17**, 377 (2002).
13. I. A. Abrikosov, A. M. N. Niklasson, S. I. Simak, B. Johansson, A. V. Ruban, and H. L. Skriver, Phys. Rev. Lett. **76** (22), 4203 (1996).
14. I. A. Abrikosov, S. I. Simak, B. Johansson, A. V. Ruban, and H. L. Skriver, Phys. Rev. B: Condens. Matter **56** (15), 9319 (1997).
15. H. L. Skriver and N. M. Rosengaard, Phys. Rev. B: Condens. Matter **43** (12), 9538 (1991).
16. J. P. Perdew and Y. Wang, Phys. Rev. B: Condens. Matter **45**, 13 244 (1992).
17. J. T. Schick, C. G. Morgan, and P. Papulias, Phys. Rev. B: Condens. Matter **66**, 195 302 (2002).
18. A. A. Bonapasta and P. Giannozzi, Phys. Rev. Lett. **84**, 3923 (2000).
19. J. C. Bourgoin, H. J. von Bardeleben, and D. Stiévenard, J. Appl. Phys. **64**, R65 (1988).
20. J. Dabrowski and M. Scheffler, Phys. Rev. B: Condens. Matter **40**, 10 391 (1989).
21. R. M. Cohen, Mater. Sci. Eng., R **20**, 167 (1997).
22. J. E. Northrup and S. B. Zhang, Phys. Rev. B: Condens. Matter **47**, 6791 (1993).
23. R. W. Jansen and O. F. Sankey, Phys. Rev. B: Condens. Matter **39** (15), 3192 (1989).
24. A. Janotti, A. Fazzio, P. Piquini, and R. Mota, Phys. Rev. B: Condens. Matter **56**, 13 073 (1997).
25. M. J. Puska, S. Pöykkö, M. Pesola, and R. M. Nieminen, Phys. Rev. B: Condens. Matter **58**, 1318 (1998).
26. H. Ohno, A. Shen, F. Matsukura, A. Oiwa, A. Endo, S. Katsumoto, and Y. Iye, Appl. Phys. Lett. **69**, 363 (1996).
27. S. Mirbt and B. Sanyal, J. Phys.: Condens. Matter **14**, 3295 (2002).
28. D. G. Andrianov, N. N. Suchkova, A. S. Savel'ev, E. P. Rashevskaya, and M. A. Filippov, Fiz. Tekh. Poluprovodn. (Leningrad) **11**, 730 (1977) [Sov. Phys. Semicond. **11**, 426 (1977)].
29. M. van Schilfgaarde and O. N. Mryasov, Phys. Rev. B: Condens. Matter **63**, 233 205 (2001).
30. J. Blinowski and P. Kacman, Phys. Rev. B: Condens. Matter **67**, 121 204 (2003).
31. P. A. Korzhavyi, I. A. Abrikosov, E. A. Smirnova, L. Bergqvist, P. Mohn, R. Mathieu, P. Svendlindh, J. Sadowski, E. I. Isaev, Yu. Kh. Vekilov, and O. Eriksson, Phys. Rev. Lett. **88**, 187 202 (2002).
32. H. Ohldag, V. Solinus, F. U. Hillebrecht, J. B. Goedkoop, N. Finazzi, F. Matsukura, and H. Ohno, Appl. Phys. Lett. **76**, 2928 (2000).

Translated by I. Zvyagin

Physics of the Solid State, Vol. 47, No. 10, 2005, pp. 1837–1846. Translated from Fizika Tverdogo Tela, Vol. 47, No. 10, 2005, pp. 1768–1775.

SEMICONDUCTORS AND DIELECTRICS

Projection Technique for Population Analysis of Atomic Orbitals in Crystals

I. I. Tupitsyn*, R. A. Évarestov*, and V. P. Smirnov**

** Research Institute of Physics, St. Petersburg State University, Ul'yanovskaya ul. 1, Petrodvorets, St. Petersburg, 198904 Russia*

e-mail: evarest@hm.csa.ru

e-mail: tup@tup.usr.pu.ru

*** St. Petersburg State University of Information Technologies, Mechanics, and Optics, St. Petersburg, 197101 Russia*

Received December 28, 2004

Abstract—The one-electron density matrix of a crystal in the basis set of localized orbitals is calculated using two variants of the projection technique, namely, the projection of crystal orbitals onto the space of atomic orbitals (technique *A*) and the projection of atomic functions onto the space of crystal orbitals (technique *B*). A comparative analysis of the one-electron density matrices thus obtained is carried out, and a simplified version of technique *B* is proposed to avoid cumbersome calculations with a large number of vacant crystal orbitals. Both techniques are used to calculate the local characteristics of the electronic structure (atomic charges, atomic covalences, bond orders) for a number of crystals (Si, SiC, GaAs, MgO, cubic BN, TiO_2 rutile) in the framework of the density-functional theory within the generalized gradient approximation in the plane wave basis set with the norm-conserving pseudopotentials. It is revealed that both variants of the projection technique lead to close local characteristics of the electronic structure. The local characteristics of the electronic structure of the TiO_2 crystal with a rutile structure are determined by the projection technique and by constructing the Wannier-type atomic functions (WTAF) in the minimal valence basis set in the framework of the variational method with the crystal orbitals calculated in the linear combination of atomic orbitals (LCAO) approximation. It is demonstrated that, although the basis sets used for calculating the crystal orbitals differ significantly (plane waves in the projection technique, LCAO in the WTAF method), the local characteristics of the electronic structure are in good agreement. © *2005 Pleiades Publishing, Inc.*

1. INTRODUCTION

At present, the electronic structure of crystals, for the most part, has been calculated using the density-functional theory (DFT) in a plane wave basis set (see, for example, [1]). This approach is very efficient tool for optimizing the geometry of the atomic arrangement in a crystal and accounting for the atomic relaxation on the crystal surface or in the vicinity of a point defect.

However, the nature of the chemical bonding in solids has been analyzed either through direct use of the localized orbitals constructed in the basis set of one-electron states [2] or in the framework of local characteristics of the electronic structure (including the electron populations of atomic orbitals in a crystal and related quantities, such as the atomic charges, bond orders, electron bond populations, etc.) calculated in the basis set of atomic orbitals [3]. The one-electron Bloch functions (crystal orbitals) calculated in the plane wave basis set are delocalized over the crystal and do not allow one to calculate the local characteristics of the electronic structure. As a consequence, the functions of the minimal valence basis set for atoms in the crystal should be constructed from the aforementioned Bloch functions. There exist several approaches to this problem.

The most consistent approach is associated with the variational method for constructing the Wannier-type atomic functions (WTAF) localized at atoms with the use of the calculated Bloch functions [4, 5]. The Wannier-type atomic functions are related to the valence states of atoms forming the crystal, have symmetry of the corresponding atomic functions in the crystal [6], and can be obtained from the Bloch functions calculated in both the plane wave basis set and the basis set of linear combination of atomic orbitals (LCAO). In our earlier work [7], the Wannier-type atomic functions were used to calculate the local characteristics both for the bulk of crystals and for their surface.

Another approach to studying the local characteristics of crystals consists in using the technique for projecting the Bloch functions calculated in the plane wave basis set onto atomic orbitals of the minimal valence basis set for free atoms [8]. The method proposed for constructing quasi-atomic minimal basis orbitals (QUAMBO) in [9] is also closely related to the projection technique. Both variants of the projection technique were used for calculations of the local characteristics in the bulk of crystals [8–10] and, in a number of cases, led to results that are rather difficult to explain from the chemical standpoint (for example, the calcu-

lated charge of 0.76 for Mg atoms in the ionic crystal MgO [10]). Note that the construction of the Wannier-type atomic functions from the Bloch functions obtained in the plane wave basis set permitted us to derive almost ionic charges at atoms in the MgO crystal [11]. However, it should also be noted that comparison of the data available in the literature on different characteristics obtained by the projection technique is complicated because the crystal orbitals are calculated with different variants of the DFT method, different pseudopotentials for excluding the core electrons from consideration, different atomic basis sets, etc.

In order to interpret the results obtained by the projection technique, it is necessary to perform a comparative analysis of the density matrices (in the atomic orbital basis set) determined by the two aforementioned projection variants. No such analysis has been made to date. In the present work, this analysis is carried out for the first time. As is known, the one-particle density matrix of a crystal is determined only by the occupied crystal orbitals. However, the procedure proposed by Segall *et al.* [10] for constructing the QUAMBO and the subsequent population analysis were performed using a set of vacant states. In this paper, we will demonstrate that the above procedure can be substantially simplified and that its implementation enables one to avoid cumbersome calculations of a large number of vacant crystal orbitals. Thus, in both variants of the projection technique when the atomic orbital set for free atoms or free ions is assumed to be known, the population analysis can be carried out without invoking vacant crystal orbitals.

This paper is organized as follows. In Section 2, we briefly describe the procedure for population analysis of atomic orbitals in a crystal, which is used to calculate the local characteristics of the electronic structure. In Section 3, we elaborate the technique for projecting crystal orbitals onto the space of known atomic orbitals of the minimal basis set and derive the relationships for the one-electron density matrix in the basis set of Bloch sums of the atomic orbitals. Knowledge of this density matrix is sufficient for performing the population analysis of the atomic orbitals. The inverse procedure, i.e., the projection of the minimal basis set of the atomic orbitals onto the space of the crystal orbitals, is considered in Section 4. In Section 5, we describe the method for constructing quasi-atomic minimal basis orbitals and demonstrate that these orbitals can be obtained by using only the occupied Bloch one-electron states (the mathematical details of this consideration are presented in the Appendix). In Section 6, we derive the expression for the density matrix in the basis set of the Bloch sums of the QUAMBO and compare them with those obtained by the method of projecting onto the space of the atomic orbitals.

In Section 7, we discuss the results of calculating the local characteristics of the electronic structure for a number of crystals with a different nature of chemical bonding (Si with a diamond structure, SiC, GaAs, MgO, cubic BN, TiO_2 rutile) on the basis of the population analysis of the atomic orbitals in the crystal. The Bloch functions are calculated by the DFT method in the plane wave basis set with the CASTEP code [1]. A comparative analysis of the local characteristics is performed using both variants of the projection technique. Moreover, for the electronic structure of the TiO_2 rutile crystal, the local characteristics determined with the use of the WTAF method [5] are compared with those obtained by the projection technique.

2. POPULATION ANALYSIS OF ATOMIC ORBITALS IN A CRYSTAL

Hereafter, we will use a cyclic model of a crystal that consists of N_0 primitive cells with N_0 vectors $\mathbf{R}$ of the direct lattice. Let us assume that the crystal orbitals $\psi_{m\mathbf{k}}(\mathbf{r})$ are one-electron states of M energy bands, where $m = 1, 2, \ldots, M$ and the vector $\mathbf{k}$ takes on N_0 values in the Brillouin zone. The space spanned by these functions is designated as Ω_ψ. We will use the basis set of atomic or atomlike real orbitals $u_\mu(\mathbf{r} - \mathbf{R})$ (N atomic orbitals per primitive cell) and their Bloch linear combinations,

$$\chi_{\mu\mathbf{k}}(\mathbf{r}) = \frac{1}{\sqrt{N_0}}\sum_{\mathbf{R}} e^{i\mathbf{k}\mathbf{R}} u_\mu(\mathbf{r} - \mathbf{R}), \quad \mu = 1, \ldots, N, \quad (1)$$

which form the space Ω_χ. The functions $u_\mu(\mathbf{r} - \mathbf{R})$ constitute a nonorthonormal set with the overlap matrix

$$S_{\mu\nu}(\mathbf{R}) = \int u_\mu(\mathbf{r} - \mathbf{R}) u_\nu(\mathbf{r}) d\mathbf{r}. \quad (2)$$

The functions $\chi_{\mu\mathbf{k}}(\mathbf{r})$ with different vectors $\mathbf{k}$ are orthogonal, and those with identical vectors $\mathbf{k}$ form nonorthonormal sets with the nonorthogonality matrices

$$(S_\mathbf{k})_{\mu\nu} = \langle \chi_{\mu\mathbf{k}} | \chi_{\nu\mathbf{k}} \rangle. \quad (3)$$

The population analysis of the atomic orbitals in the crystal is performed using the density matrix in the basis set of the atomic orbitals $u_\mu(\mathbf{r} - \mathbf{R})$. It is assumed that M_0 occupied crystal orbitals $\psi_{m\mathbf{k}}(\mathbf{r})$ ($M_0 < M$) can be represented in the form of a linear combination of N Bloch sums (1); that is,

$$\psi_{m\mathbf{k}}(\mathbf{r}) = \sum_{\mu=1}^{N} C_{\mu m}(\mathbf{k}) \chi_{\mu\mathbf{k}}(\mathbf{r}). \quad (4)$$

The spinless one-particle density matrix in the coordinate representation can be obtained by summation over the occupied states:

$$\rho(\mathbf{r}, \mathbf{r}') = \frac{2}{N_0}\sum_{\mathbf{k}, m}^{\text{occ}} \psi_{m\mathbf{k}}(\mathbf{r}) \psi^*_{m\mathbf{k}}(\mathbf{r}') = 2\sum_{\mu\nu}\sum_{\mathbf{R}, \mathbf{R}'} P_{\mu\nu}(\mathbf{R}' - \mathbf{R}) u_\mu(\mathbf{r} - \mathbf{R}) u_\nu(\mathbf{r}' - \mathbf{R}'). \quad (5)$$

Here, the density matrix $P_{\mu\nu}(\mathbf{R})$ in the basis set of the atomic orbitals is defined as

$$P_{\mu\nu}(\mathbf{R}) = \frac{2}{N_0}\sum_{\mathbf{k}} e^{-i\mathbf{kR}}(P_{\mathbf{k}})_{\mu\nu}\omega_{\mu\nu}(\mathbf{R}) \quad (6)$$

and the elements $(P_{\mathbf{k}})_{\mu\nu}$ of the matrix density in the basis set of the Bloch sums are written in the form

$$(P_{\mathbf{k}})_{\mu\nu} = 2\sum_{m}^{\mathrm{occ}} C_{\mu m}(\mathbf{k})C^*_{\nu m}(\mathbf{k}). \quad (7)$$

The weighting function $\omega_{\mu\nu}(\mathbf{R})$ on the right-hand side of equality (6) appears as a result of the correct inclusion of the exchange upon summation over the Brillouin zone (see [3]).

The Mulliken populations [12] are analyzed with the use of the Mulliken density matrix:

$$\begin{aligned} P^M_{\mu\nu}(\mathbf{R}) &= \sum_{\mathbf{R}'}\sum_{\nu'} P_{\mu\nu'}(\mathbf{R}')S_{\nu'\nu}(\mathbf{R}-\mathbf{R}') \\ &= \frac{1}{N_0}\sum_{\mathbf{k}} e^{-i\mathbf{kR}}(P^M_{\mathbf{k}})_{\mu\nu}\omega_{\mu\nu}(\mathbf{R}), \end{aligned} \quad (8)$$

where

$$P^M_{\mathbf{k}} = P_{\mathbf{k}}S_{\mathbf{k}} \quad (9)$$

and $S(\mathbf{R})$ and $S_{\mathbf{k}}$ are the nonorthogonality matrices (2) and (3), respectively.

When analyzing the Mulliken populations, the atomic charge A is determined from the relationship

$$Q_A = Z_A - \sum_{\mu\in A} P^M_{\mu\mu}(0), \quad (10)$$

where Z_A is the nuclear charge (or the core charge in calculations with the pseudopotential) of the Ath atom.

The order of the bond between the Ath atom in the zeroth cell and the Bth atom in the cell $\mathbf{R}$ can be characterized either by the Mayer index [13]

$$M_{AB} = \sum_{\mu\in A}\sum_{\nu\in B} P^M_{\mu\nu}(\mathbf{R})P^M_{\nu\mu}(-\mathbf{R}) \quad (11)$$

or by the overlap population

$$P_{AB} = \sum_{\mu\in A}\sum_{\nu\in B} P_{\mu\nu}(\mathbf{R})S_{\nu\mu}(-\mathbf{R}). \quad (12)$$

The covalence C_A of the A atom can be defined as the sum of the orders of bonds between this atom and the other atoms in the crystal:

$$C_A = \sum_{B\neq A} M_{AB}. \quad (13)$$

Thus, the population of the atomic orbitals can be analyzed when the density matrix is determined in the basis set of these orbitals. For methods in which other functions (for example, plane waves) serve as the basis set, the problem of determining the density matrix calls for special consideration.

3. PROJECTION OF THE CRYSTAL ORBITALS ONTO THE SPACE OF BLOCH SUMS

Sanchez-Portal *et al.* [8] proposed the technique for projecting crystal orbitals onto the space of atomic orbitals. Subsequently, Segall *et al.* [10] used this technique for constructing the density matrix in the basis set of atomic orbitals and for analyzing populations. Hereinafter, it will be assumed that $M_0 < N < M$.

The operator

$$\hat{p}_{b\mathbf{k}} = \sum_{\mu\nu} |\chi_{\mu\mathbf{k}}\rangle(S^{-1}_{\mathbf{k}})_{\mu\nu}\langle\chi_{\nu\mathbf{k}}| \quad (14)$$

is the projector onto the space Ω_χ of the Bloch sums (1) because we have

$$\hat{p}^2_{b\mathbf{k}} = \hat{p}_{b\mathbf{k}}, \quad \hat{p}^+_{b\mathbf{k}} = \hat{p}_{b\mathbf{k}}. \quad (15)$$

By projecting the set of the crystal orbitals $\psi_{m\mathbf{k}}$ onto the space Ω_χ, we obtain the set of functions

$$\begin{aligned} \tilde{\psi}_{m\mathbf{k}} &= \hat{p}_{b\mathbf{k}}\psi_{m\mathbf{k}} = \sum_{\mu\nu} |\chi_{\mu\mathbf{k}}\rangle(S^{-1}_{\mathbf{k}})_{\mu\nu}\langle\chi_{\nu\mathbf{k}}|\psi_{m\mathbf{k}}\rangle \\ &= \sum_{\mu} (S^{-1}_{\mathbf{k}}T^+_{\mathbf{k}})_{\mu m}\chi_{\mu\mathbf{k}}, \end{aligned} \quad (16)$$

where the M-by-N matrix $T_{\mathbf{k}}$ with the matrix elements

$$(T_{\mathbf{k}})_{m\mu} = \langle\psi_{m\mathbf{k}}|\chi_{\mu\mathbf{k}}\rangle \quad (17)$$

is formed by the Fourier coefficients (located in columns) of expansion of the function $\chi_{\mu\mathbf{k}}$ in the orthonormal basis set of the crystal orbitals $\psi_{m\mathbf{k}}$.

Now, we introduce the M_0-by-N matrix $T_{0\mathbf{k}}$ with the matrix elements (17), where the subscript m numbers only the occupied bands. The projected occupied crystal orbitals $\tilde{\psi}_{m\mathbf{k}}$ ($m = 1, 2, \ldots, M_0$) constitute the nonorthonormal set with the M_0-by-M_0 nonorthogonality matrix $R_{0\mathbf{k}}$:

$$\begin{aligned} (R_{0\mathbf{k}})_{mn} = \langle\tilde{\psi}_{m\mathbf{k}}|\tilde{\psi}_{n\mathbf{k}}\rangle &= \sum_{\mu\nu}(S^{-1}_{\mathbf{k}}T^+_{0k})^*_{\mu m}(S_{\mathbf{k}})_{\mu\nu}(S^{-1}_{\mathbf{k}}T^+_{0\mathbf{k}})_{\nu n} \\ &= (T_{0\mathbf{k}}S^{-1}_{\mathbf{k}}T^+_{0\mathbf{k}})_{mn}. \end{aligned} \quad (18)$$

Note also that, in this case, the following relationship holds:

$$\langle\psi_{m\mathbf{k}}|\tilde{\psi}_{n\mathbf{k}}\rangle = \langle\psi_{m\mathbf{k}}|\hat{p}_{b\mathbf{k}}^2\psi_{n\mathbf{k}}\rangle = \langle\hat{p}_{b\mathbf{k}}\psi_{m\mathbf{k}}|\hat{p}_{b\mathbf{k}}\psi_{n\mathbf{k}}\rangle = \langle\tilde{\psi}_{m\mathbf{k}}|\tilde{\psi}_{n\mathbf{k}}\rangle. \quad (19)$$

The projected functions $\tilde{\psi}_{m\mathbf{k}}$ minimize the functional $\mathcal{S}_{\tilde{\psi}}$ in the space Ω_χ:

$$\mathcal{S}_{\tilde{\psi}} = \frac{1}{N_0}\sum_{\mathbf{k}}\frac{1}{M}\sum_{m}|\psi_{m\mathbf{k}}-\tilde{\psi}_{m\mathbf{k}}|^2 = 1-\frac{1}{N_0M}\sum_{\mathbf{k}m}|\tilde{\psi}_{m\mathbf{k}}|^2$$
$$= 1-\frac{1}{N_0M}\sum_{\mathbf{k}m}\sum_{\mu\nu}\langle\psi_{m\mathbf{k}}|\chi_{\mu\mathbf{k}}\rangle(S_{\mathbf{k}}^{-1})_{\mu\nu}\langle\chi_{\nu\mathbf{k}}|\psi_{m\mathbf{k}}\rangle \quad (20)$$
$$= 1-\frac{1}{N_0M}\sum_{\mathbf{k}}\mathrm{Sp}\,R_{0\mathbf{k}}.$$

Actually, this functional is the spilling parameter introduced in [8, 10] with the aim of assessing the quality of the projection.

The spinless density matrix in the basis set $\tilde{\psi}_{m\mathbf{k}}$ can be written in the form

$$\rho_{\mathbf{k}}(\mathbf{r},\mathbf{r}') = 2\sum_{m,n}^{\mathrm{occ}}\tilde{\psi}_{m\mathbf{k}}(\mathbf{r})(R_{0\mathbf{k}}^{-1})_{mn}\tilde{\psi}_{n\mathbf{k}}^*(\mathbf{r}')$$
$$= 2\sum_{\mu\nu}\chi_{\mu\mathbf{k}}(\mathbf{r})(S_{\mathbf{k}}^{-1}T_{0\mathbf{k}}^{+}R_{\mathbf{k}}^{-1}T_{0\mathbf{k}}S_{\mathbf{k}}^{-1})_{\mu\nu}\chi_{\nu\mathbf{k}}^*(\mathbf{r}'). \quad (21)$$

In the basis set of the Bloch sums, the N-by-N density matrix $P_{\mathbf{k}}$ [relationship (7)] has the form

$$P_{\mathbf{k}} = 2S_{\mathbf{k}}^{-1}T_{0\mathbf{k}}^{+}R_{0\mathbf{k}}^{-1}T_{0\mathbf{k}}S_{\mathbf{k}}^{-1}$$
$$= 2S_{\mathbf{k}}^{-1}T_{0\mathbf{k}}^{+}(T_{0\mathbf{k}}S_{\mathbf{k}}^{-1}T_{0\mathbf{k}}^{+})^{-1}T_{0\mathbf{k}}S_{\mathbf{k}}^{-1}. \quad (22)$$

Thus, in order to analyze the populations of the atomic orbitals in the crystal in the framework of the method under consideration, it will suffice to know only the M_0 occupied crystal orbitals $\psi_{m\mathbf{k}}$ and the set of N atomic Bloch sums.

4. PROJECTION OF THE BLOCH SUMS ONTO THE SPACE OF CRYSTAL ORBITALS

In the space of the Bloch functions $\psi_{m\mathbf{k}}$, the localized quasi-atomic functions $\tilde{u}_\mu$ can be constructed using a linear transformation $\hat{A}$ (for symmetry constraints, see [6]):

$$\tilde{u}_\mu = \sum_{\mathbf{k}}\sum_{m=1}^{M}(A_{\mathbf{k}})_{m\mu}\psi_{m\mathbf{k}}. \quad (23)$$

Unknown coefficients $(A_{\mathbf{k}})_{m\mu}$ can be determined from the maximum condition for the functional

$$\mathcal{F} = \sum_{\mu}|u_\mu-\tilde{u}_\mu|^2, \quad (24)$$

where $u_\mu(\mathbf{r})$ are the known atomic functions. The solution of this variational problem is provided by the Fourier coefficients:

$$(A_{\mathbf{k}})_{m\mu} = \langle\psi_{m\mathbf{k}}|u_\mu\rangle. \quad (25)$$

From the quasi-atomic orbitals u_μ and $\tilde{u}_\mu$, we can change over to the Bloch sums $\chi_{\mu\mathbf{k}}$ and $\tilde{\chi}_{\mu\mathbf{k}}$ with the use of formulas similar to expression (1); that is,

$$\tilde{\chi}_{\mu\mathbf{k}} = \sum_{m=1}^{M}\langle\psi_{m\mathbf{k}}|\chi_{\mu\mathbf{k}}\rangle\psi_{m\mathbf{k}} = \sum_{m=1}^{M}(T_{\mathbf{k}})_{m\mu}\psi_{m\mathbf{k}} = \hat{p}_{c\mathbf{k}}\chi_{\mu\mathbf{k}}, \quad (26)$$

where the projector $\hat{p}_{c\mathbf{k}}$ onto the M-dimensional space Ω_ψ of the crystal orbitals $\psi_{m\mathbf{k}}$ is given by

$$\hat{p}_{c\mathbf{k}} = \sum_{m=1}^{M}|\psi_{m\mathbf{k}}\rangle\langle\psi_{m\mathbf{k}}|. \quad (27)$$

Therefore, the Bloch sums $\tilde{\chi}_{\mu\mathbf{k}}(\mathbf{r})$ of the projected quasi-atomic functions $\tilde{u}_\mu(\mathbf{r})$ can be obtained by projecting the atomic Bloch sums $\chi_{\mu\mathbf{k}}(\mathbf{r})$ (1) onto the space Ω_ψ of the band functions $\psi_{m\mathbf{k}}(\mathbf{r})$.

The functions $\tilde{\chi}_{\mu\mathbf{k}}$ form nonorthonormal sets with the N-by-N nonorthogonality matrix $\tilde{S}_{\mathbf{k}}$ represented by the expression

$$(\tilde{S}_{\mathbf{k}})_{\mu\nu} = \langle\tilde{\chi}_{\mu\mathbf{k}}|\tilde{\chi}_{\nu\mathbf{k}}\rangle = (T_{\mathbf{k}}^{+}T_{\mathbf{k}})_{\mu\nu} = \langle\tilde{\chi}_{\mu\mathbf{k}}|\chi_{\nu\mathbf{k}}\rangle. \quad (28)$$

In the space Ω_ψ, the projected functions $\tilde{\chi}_{\mu\mathbf{k}}$ minimize the functional $\mathcal{S}_{\tilde{\chi}}$,

$$\mathcal{S}_{\tilde{\chi}} = \frac{1}{\mathcal{S}_0N_0}\sum_{\mathbf{k}}\frac{1}{N}\sum_{\mu}|\chi_{\mu\mathbf{k}}-\tilde{\chi}_{\mu\mathbf{k}}|^2$$
$$= 1-\frac{1}{\mathcal{S}_0N_0N}\sum_{\mu\mathbf{k}}|\tilde{\chi}_{\mu\mathbf{k}}|^2 = 1-\frac{1}{\mathcal{S}_0N_0N}\sum_{\mu\mathbf{k}}(T_{\mathbf{k}}^{+}T_{\mathbf{k}})_{\mu\mu} \quad (29)$$
$$= 1-\frac{1}{\mathcal{S}_0N_0N}\sum_{\mathbf{k}}\mathrm{Sp}\,\tilde{S}_{\mathbf{k}},$$

which can also be treated as the spilling parameter for assessing the projection quality. Here, we have

$$\mathcal{S}_0 = \frac{1}{N_0N}\sum_{\mu\mathbf{k}}|\chi_{\mu\mathbf{k}}|^2 = \frac{1}{N_0N}\sum_{\mathbf{k}}\mathrm{Sp}\,S_{\mathbf{k}}. \quad (30)$$

The populations in the basis set of the atomlike functions $\tilde{\chi}_{\mu\mathbf{k}}$ can be analyzed, as before, when the Bloch functions $\psi_{m\mathbf{k}}$ are projected onto the space of the

functions $\tilde{\chi}_{\mu\mathbf{k}}$. The expression for the density matrix $\tilde{P}_{\mathbf{k}}$ differs from expression (22) for the density matrix $P_{\mathbf{k}}$ in that the matrix $S_{\mathbf{k}}$ is replaced by the matrix $\tilde{S}_{\mathbf{k}}$; that is,

$$\begin{aligned}\tilde{P}_{\mathbf{k}} &= 2\tilde{S}_{\mathbf{k}}^{-1}T_{0\mathbf{k}}^{+}\tilde{R}_{0\mathbf{k}}^{-1}T_{0\mathbf{k}}\tilde{S}_{\mathbf{k}}^{-1}\\ &= 2\tilde{S}_{\mathbf{k}}^{-1}T_{0\mathbf{k}}^{+}(T_{0\mathbf{k}}\tilde{S}_{\mathbf{k}}^{-1}T_{0\mathbf{k}}^{+})^{-1}T_{0\mathbf{k}}\tilde{S}_{\mathbf{k}}^{-1}.\end{aligned} \tag{31}$$

It is evident that, at $M \longrightarrow \infty$, when the set of the Bloch functions $\psi_{m\mathbf{k}}$ becomes complete, we obtain the following limiting relationships: $\tilde{\chi}_{\mu\mathbf{k}} \longrightarrow \chi_{\mu\mathbf{k}}$ and $\tilde{u}_{\mu} \longrightarrow u_{\mu}$ for the functions, $\tilde{\mathcal{S}}_{\tilde{\chi}} \longrightarrow 0$ for the spilling parameter, and $\tilde{S}_{\mathbf{k}} \longrightarrow S_{\mathbf{k}}$ and $\tilde{P}_{\mathbf{k}} \longrightarrow P_{\mathbf{k}}$ for the matrices. Thus, at $M \longrightarrow \infty$, the population analysis considered in this section for the atomic orbitals is identical to that described in the preceding section. In the next section, we examine the modification of the method under investigation.

5. QUASI-ATOMIC MINIMAL BASIS ORBITALS (QUAMBO)

Lu *et al.* [9] proposed constructing the quasi-atomic minimal basis orbitals in a somewhat different manner. In the space Ω_{ψ}, we consider the subspace $\Omega^{(u)}$ composed of N orthonormal functions $\psi_{n\mathbf{k}}^{(u)}$, of which the first M_0 functions coincide with the occupied crystal orbitals $\psi_{n\mathbf{k}}$ and the next $(N - M_0)$ functions are obtained from the vacant crystal orbitals with the use of a linear transformation $\hat{U}_{\mathbf{k}}$; that is

$$\psi_{n\mathbf{k}}^{(u)} = \begin{cases}\psi_{n\mathbf{k}}, & n = 1, 2, \ldots, M_0\\ \sum\limits_{m=M_0+1}^{M}(U_{\mathbf{k}})_{mn}\psi_{m\mathbf{k}}, & n = M_0+1, \ldots, N.\end{cases} \tag{32}$$

The $(M - M_0)$-by-$(N - M_0)$ matrix $U_{\mathbf{k}}$ is orthogonal and normalized with respect to the columns ($U_{\mathbf{k}}^{+}U_{\mathbf{k}} = 1$).

The projector $\hat{p}_{\mathbf{k}}^{(u)}$ onto the space $\Omega^{(u)}$ of the orthonormal functions $\psi_{n\mathbf{k}}^{(u)}$ is defined by the relationship

$$\begin{aligned}\hat{p}_{\mathbf{k}}^{(u)} &= \sum_{m=1}^{N}|\psi_{m\mathbf{k}}^{(u)}\rangle\langle\psi_{m\mathbf{k}}^{(u)}|\\ &= \sum_{m=1}^{M_0}|\psi_{m\mathbf{k}}\rangle\langle\psi_{m\mathbf{k}}| + \sum_{m=M_0+1}^{N}|\psi_{m\mathbf{k}}^{(u)}\rangle\langle\psi_{m\mathbf{k}}^{(u)}|.\end{aligned} \tag{33}$$

Then, we project the atomic Bloch sums $\chi_{\mu\mathbf{k}}$ onto the space $\Omega^{(u)}$; that is,

$$\tilde{\chi}_{\mu\mathbf{k}}^{(u)} = \hat{p}_{\mathbf{k}}^{(u)}\chi_{\mu\mathbf{k}} = \sum_{n=1}^{N}(T_{\mathbf{k}}^{(u)})_{n\mu}\psi_{n\mathbf{k}}^{(u)}, \tag{34}$$

where $T_{\mathbf{k}}^{(u)}$ is the N-by-N matrix written in the form

$$(T_{\mathbf{k}}^{(u)})_{n\mu} = \langle\psi_{n\mathbf{k}}^{(u)}|\chi_{\mu\mathbf{k}}\rangle, \quad n, \mu = 1, \ldots, N. \tag{35}$$

By using expressions (32) and (35), the functions $\tilde{\chi}_{\mu\mathbf{k}}^{(u)}$ in the basis set of the functions $\psi_{m\mathbf{k}}$ in the space Ω_{ψ} can be represented in the form

$$\begin{aligned}\tilde{\chi}_{\mu\mathbf{k}}^{(u)} &= \sum_{m=1}^{M_0}(T_{0\mathbf{k}})_{m\mu}\psi_{m\mathbf{k}}\\ &+ \sum_{m=M_0+1}^{M}(U_{\mathbf{k}}U_{\mathbf{k}}^{+}\Delta T_{\mathbf{k}})_{m\mu}\psi_{m\mathbf{k}},\end{aligned} \tag{36}$$

where $\Delta T_{\mathbf{k}}$ is the $(M - M_0)$-by-N matrix with the elements

$$\begin{aligned}(\Delta T_{\mathbf{k}})_{m\mu} &= \langle\psi_{m\mathbf{k}}|\chi_{\mu\mathbf{k}}\rangle = (T_{\mathbf{k}})_{m\mu},\\ m &= M_0 + 1, \ldots, M.\end{aligned} \tag{37}$$

The spilling parameter for the projection of the functions $\chi_{\mu\mathbf{k}}$ onto the space $\Omega^{(u)}$ can be defined as follows:

$$\begin{aligned}\tilde{\mathcal{S}}^{(u)} &= \frac{1}{\mathcal{S}_0 N_0}\sum_{\mathbf{k}}\frac{1}{N}\sum_{\mu}\left|\chi_{\mu\mathbf{k}} - \tilde{\chi}_{\mu\mathbf{k}}^{(u)}\right|^2\\ &= 1 - \frac{1}{\mathcal{S}_0 N_0 N}\sum_{m\mathbf{k}}(T_{\mathbf{k}}^{(u)^{+}}T_{\mathbf{k}}^{(u)})_{mm}\\ &= 1 - \frac{1}{\mathcal{S}_0 N_0 N}\sum_{\mathbf{k}}\mathrm{Sp}\,\tilde{S}_{\mathbf{k}}^{(u)},\end{aligned} \tag{38}$$

where the N-by-N nonorthogonality matrix for the functions $\tilde{\chi}_{\mu\mathbf{k}}^{(u)}$ is written in the form

$$(\tilde{S}_{\mathbf{k}}^{(u)})_{\mu\nu} = \langle\tilde{\chi}_{\mu\mathbf{k}}^{(u)}|\tilde{\chi}_{\nu\mathbf{k}}^{(u)}\rangle = (T_{0\mathbf{k}}^{+}T_{0\mathbf{k}} + \Delta T_{\mathbf{k}}^{+}U_{\mathbf{k}}U_{\mathbf{k}}^{+}\Delta T_{\mathbf{k}})_{\mu\nu}. \tag{39}$$

The spilling parameter (38) can be minimized by using the arbitrariness in specifying the linear transformation $\hat{U}$. This is equivalent to searching for maxima of the expressions

$$\mathcal{F}_{\mathbf{k}}^{u} = \mathrm{Sp}(\Delta T_{\mathbf{k}}^{+}U_{\mathbf{k}}U_{\mathbf{k}}^{+}\Delta T_{\mathbf{k}}) = \mathrm{Sp}(U_{\mathbf{k}}^{+}\Delta T_{\mathbf{k}}\Delta T_{\mathbf{k}}^{+}U_{\mathbf{k}}). \tag{40}$$

The search for optimum coefficients U_{mn} is reduced to the determination of the $(N - M_0)$ greatest eigenvalues

and the corresponding eigenvectors of the $(M-M_0)$-by-$(M-M_0)$ matrix $\Delta T_{\mathbf{k}}\Delta T_{\mathbf{k}}^{+}$; that is,

$$(\Delta T_{\mathbf{k}}\Delta T_{\mathbf{k}}^{+})(U_{\mathbf{k}})_n = \lambda_{\mathbf{k}n}(U_{\mathbf{k}})_n. \quad (41)$$

Here, $(U_{\mathbf{k}})_n$ is the column of the matrix $U_{\mathbf{k}}$ with the number n ($n = 1, 2, \ldots, N-M_0$). It is this procedure [i.e., the diagonalization of the $(M-M_0)$-by-$(M-M_0)$ matrix] that was used in [9] to determine the coefficients $(U_{\mathbf{k}})_{mn}$.

In the Appendix, it will be shown that the optimum coefficients $(U_{\mathbf{k}})_{mn}$ can be expressed through the eigenvectors $(V_{\mathbf{k}})_n$ (A2) of the N-by-N matrix $\Delta\tilde{S}_{\mathbf{k}}$ (A1) with the use of relationship (A3). Furthermore, according to expression (A8), the Bloch sums $\tilde{\chi}_{\mu\mathbf{k}}^{(u)}(\mathbf{r})$ and the localized orbitals $\tilde{u}_{\mu}^{(u)}(\mathbf{r})$ can be obtained in the form of a linear combination of the occupied Bloch functions $\psi_{m\mathbf{k}}$ and the projected Bloch sums $\tilde{\chi}_{\mu\mathbf{k}}$ from the atomic orbitals $\tilde{u}_{\mu}(\mathbf{r})$. In order to determine the coefficients of this linear combination, it is sufficient to diagonalize the N-by-N matrices (N is the number of atomic functions in the minimal basis set per unit cell at each $\mathbf{k}$ and it is not necessary to diagonalize the M-by-M matrices ($N > N$ is the total number of Bloch states at each $\mathbf{k}$).

Let us now consider the limit $M \longrightarrow \infty$, when the basis set of the Bloch functions becomes complete. In this case, the following limiting relationships hold: $\tilde{\chi}_{\mu\mathbf{k}} \longrightarrow \chi_{\mu\mathbf{k}}$, $\tilde{u}_{\mu}(\mathbf{r}) \longrightarrow u_{\mu}(\mathbf{r})$, $\tilde{S}_{\mathbf{k}} \longrightarrow S_{\mathbf{k}}$, and $\Delta\tilde{S}_{\mathbf{k}} \longrightarrow \Delta S_{\mathbf{k}}$. Hence, the vacant bands can be excluded from consideration and, instead of relationship (A8), we obtain

$$\chi_{\mu\mathbf{k}}^{(u)} = \sum_{m=1}^{M_0}(T_{0\mathbf{k}})_{m\mu}\psi_{m\mathbf{k}} + \sum_{\nu=M_0+1}^{N}(V_{\mathbf{k}}V_{\mathbf{k}}^{+})_{\nu\mu}\Delta\chi_{\nu\mathbf{k}},$$
$$\Delta\chi_{\nu\mathbf{k}} = \chi_{\nu\mathbf{k}} - \sum_{m=1}^{M_0}(T_{0\mathbf{k}})_{m\nu}\psi_{m\mathbf{k}}. \quad (42)$$

The last equality completely determines the Bloch sums $\chi_{\mu\mathbf{k}}^{(u)}(\mathbf{r})$ of the localized orbitals $u_{\mu}^{(u)}(\mathbf{r})$ through the crystal orbitals $\psi_{m\mathbf{k}}(\mathbf{r})$ of the occupied bands and the Bloch sums $\chi_{\mu\mathbf{k}}(\mathbf{r})$ of the atomic functions $u_{\mu}(\mathbf{r})$. Here, the columns of the N-by-$(N-M_0)$ matrix $V_{\mathbf{k}}$ are eigenvectors that correspond to the $N-M_0$ greatest eigenvalues of the N-by-N positive definite matrix $\Delta S_{\mathbf{k}} = S_{\mathbf{k}} - S_{0\mathbf{k}}$.

6. POPULATION ANALYSIS IN THE QUAMBO SET

In order to analyze the populations in the QUAMBO set, it is necessary to construct the density matrix in this basis set. For this purpose, the occupied crystal orbitals $\psi_{n\mathbf{k}}$ are expressed through the Bloch sums $\chi_{\mu\mathbf{k}}^{(u)}$. Since the matrix $T_{\mathbf{k}}^{(u)}$ is a square matrix, equality (34) can be rewritten in the inverted form

$$\psi_{n\mathbf{k}} = \sum_{\mu}((T_{\mathbf{k}}^{(u)})^{-1})_{\mu n}\chi_{\mu\mathbf{k}}^{(u)}, \quad n = 1, \ldots, N. \quad (43)$$

Owing to the orthogonality of the Bloch functions, it is easy to derive the relationship for the one-particle density matrix in the coordinate representation:

$$\rho(\mathbf{r},\mathbf{r}') = 2\sum_{m}^{\mathrm{occ}}\psi_{m\mathbf{k}}(\mathbf{r})\psi_{m\mathbf{k}}^{*}(\mathbf{r}')$$
$$= \sum_{\mu\nu}\chi_{\mu\mathbf{k}}^{(u)}(\mathbf{r})((T_{\mathbf{k}}^{(u)})^{-1}W((T_{\mathbf{k}}^{(u)})^{-1})^{+})_{\mu\nu}\chi_{\nu\mathbf{k}}^{(u)*}(\mathbf{r}'), \quad (44)$$

where W is the diagonal matrix of the occupation numbers, i.e., $W_{mm} = w_m$ and $w_m = 2$ for occupied bands and $w_m = 0$ for vacant bands. Therefore, the density matrix $P_{\mathbf{k}}^{(u)}$ in the basis set of the Bloch sums $\tilde{\chi}_{\mu\mathbf{k}}^{(u)}$ of the QUAMBO has the form

$$P_{\mathbf{k}}^{(u)} = (T_{\mathbf{k}}^{(u)})^{-1}W((T_{\mathbf{k}}^{(u)})^{-1})^{+}. \quad (45)$$

For comparison with the projection technique considered in Section 3, we write the density matrix in a form similar to expression (22). This can be accomplished by using the matrix $S_{\mathbf{k}}^{(u)} = (T_{\mathbf{k}}^{(u)})^{+}T_{\mathbf{k}}^{(u)}$ as the nonorthogonality matrix and taking into account the relationship

$$\sum_{\mu}(T_{0\mathbf{k}})_{n'\mu}((T_{\mathbf{k}}^{(u)})^{-1})_{\mu n} = (T_{0\mathbf{k}}(T_{\mathbf{k}}^{(u)})^{-1})_{n'n}$$
$$= (I^{(u)})_{nn'} = \delta_{nn'}, \quad n' = 1, \ldots, M_0. \quad (46)$$

Here, $I^{(u)}$ is the M_0-by-N matrix, which satisfies the equalities $I^{(u)}(I^{(u)})^{+} = I_0$ and $2(I^{(u)})^{+}I^{(u)} = W$, where I_0 is the M_0-by-M_0 unit matrix. Then, we find

$$R_{\mathbf{k}}^{(u)} = T_{0\mathbf{k}}(S_{\mathbf{k}}^{(u)})^{-1}T_{0\mathbf{k}}^{+}$$
$$= (T_{0\mathbf{k}}T_{\mathbf{k}}^{(u)-1})(T_{0\mathbf{k}}(T_{\mathbf{k}}^{(u)})^{-1})^{+} = I_0. \quad (47)$$

From formulas (45) and (46), we have

$$P_{\mathbf{k}}^{(u)} = 2T_{\mathbf{k}}^{(u)-1}I^{(u)+}I^{(u)}T_{\mathbf{k}}^{(u)-1^{+}}$$
$$= 2S_{\mathbf{k}}^{(u)-1}T_{0\mathbf{k}}^{+}T_{0\mathbf{k}}(S_{\mathbf{k}}^{(u)})^{-1}. \quad (48)$$

As a result, we obtain the final expression

$$P_{\mathbf{k}}^{(u)} = 2(S_{\mathbf{k}}^{(u)})^{-1}T_{0\mathbf{k}}^{+}(R_{\mathbf{k}}^{(u)})^{-1}T_{0\mathbf{k}}(S_{\mathbf{k}}^{(u)})^{-1}$$
$$= 2(S_{\mathbf{k}}^{(u)})^{-1}T_{0\mathbf{k}}^{+}(T_{0\mathbf{k}}(S_{\mathbf{k}}^{(u)})^{-1}T_{0\mathbf{k}}^{+})^{-1}T_{0\mathbf{k}}(S_{\mathbf{k}}^{(u)})^{-1}. \quad (49)$$

A comparison of expressions (49) and (22) allows us to make the inference that the above two methods for constructing the density matrices and, correspondingly, the two approaches to the population analysis differ only in terms of the nonorthogonality matrices $S_{\mathbf{k}}$ and $S_{\mathbf{k}}^{(u)}$.

7. CALCULATIONS OF SPECIFIC SYSTEMS AND DISCUSSION OF THE RESULTS

In this section, we analyze the populations obtained by two different methods, namely, the projection technique [8] described in Section 3 and the QUAMBO technique [9] in the variant considered in Section 5. In what follows, these methods will be referred to as techniques *A* and *B*, respectively.

The objects of our investigation were crystals with a different nature of chemical bonding: Si with a diamond structure, SiC, GaAs, MgO, cubic BN, and TiO_2 with a rutile structure. The crystal orbitals were calculated by the DFT method in the plane wave basis set with the CASTEP code [1] in the generalized gradient approximation for the density functional. A set of special points **k** in the Brillouin zone for all the crystals was generated by the supercell method [14] with a $5 \times 5 \times 5$ diagonal symmetric extension, which corresponds to 125 points. In all cases, the pseudopotentials were represented by the norm-conserving optimized atomic pseudopotentials [15], which were also used to calculate the atomic orbitals of free atoms.

In the framework of both techniques (*A*, *B*), the population analysis was performed in the minimal atomic basis set; i.e., the basis set involved only occupied or partially occupied atomic orbitals of free atoms. It is well known that the inclusion of diffuse vacant atomic orbitals in the basis set can substantially change the results of the population analysis. For example, if the Mg 3*p* vacant atomic orbitals are included in the basis set, the charge calculated by technique *A* for the Mg atom in the MgO crystal decreases from 1.61 to 1.06. Consequently, the inclusion of the Mg 3*p* functions leads to a considerable decrease in the ionic component of the bonding and, correspondingly, to an increase in the covalence of atoms. Chemically, it is difficult to explain this high covalency of the bonding in the MgO crystal.

Table 1 presents the atomic charges Q_A [formula (10)] and the atomic covalences C_A [formula (13)] calculated by techniques *A* and *B* for the crystals. The spilling parameters, which characterize the accuracy of the projection of M_0 occupied crystal orbitals onto the space of the atomic orbitals (technique *A*) and the accuracy of the projection of *N* atomic orbitals onto the space of the *N* Bloch functions (technique *B*), are listed in columns 6 and 7 of Table 1. The calculated Mayer indices M_{AB} [expression (11)] and the overlap populations P_{AB} [expression (12)], which characterize the orders of bonds between atoms, are given in Table 2.

Table 1. Results of the Mulliken population analysis and spilling parameters $\mathcal{S}$ in the minimal atomic basis set

Atom in the crystal	Q_A		C_A		$\mathcal{S} \times 10^3$	
	A	*B*	*A*	*B*	*A*	*B*
Mg in MgO	1.609	1.607	0.630	0.632	14	11
B in BN	0.681	0.715	3.292	3.263	3.7	3.0
Ti in TiO_2	1.730	1.739	3.474	3.459	2.2	1.4
Si in Si	0	0	3.823	3.801	9.6	6.5
Si in SiC	1.260	1.284	3.497	3.472	8.9	5.3
Ga in GaAs	0.361	0.380	3.231	3.202	1.8	1.8

Note: *A* and *B* stand for the projection [8] and QUAMBO [9] techniques, respectively.

Table 2. Bond orders in the minimal atomic basis set

Crystal	R_{AB} (Å)	M_{AB}		P_{AB}	
		A	*B*	*A*	*B*
MgO	2.1067	0.112	0.113	0.095	0.096
BN	1.5653	0.804	0.800	0.709	0.700
TiO_2	1.9512	0.552	0.550	0.305	0.302
Si	2.3643	0.894	0.889	0.756	0.744
SiC	1.9009	0.831	0.827	0.760	0.751
GaAs	2.4509	0.768	0.765	0.636	0.629

Note: *A* and *B* stand for the projection [8] and QUAMBO [9] techniques, respectively.

The atomic charges obtained in this work by technique *A* can be compared with those calculated by Segall *et al.* [10] with the use of a similar method. The atomic charges and the spilling parameters presented in [10] are considerably smaller than those in our work. In our opinion, the main factor responsible for this disagreement is the difference between the atomic basis sets that are projected onto the crystal orbitals. This assumption is confirmed by the following fact noted in [10]. The removal of the Si *d* vacant orbital from the atomic basis set leads to an increase in the charge at the Si atom in the SiC crystal from 0.66 to 1.25 and an increase in the spilling parameter from 2×10^{-3} to 9×10^{-3}. It follows from Table 1 that, in our calculations in the minimal basis set (without the Si *d* function), these quantities are equal to 1.26 and 8.9×10^{-3}, respectively, which agrees well with the results obtained in [10] (without the Si *d* function).

It is evident that an increase in the size of the basis sets should result in a decrease in the spilling factor in

Table 3. Local characteristics of the electronic structure of the TiO_2 crystal

Method	Q_A	C_A	M_{AB}
A	1.79	3.36	0.51
B	1.80	3.34	0.51
LCAOM	1.78	3.30	0.52
LCAOL	1.04	4.29	0.66
WTAFM	1.98	3.16	0.51
WTAFL	1.92	3.23	0.52

Note: *A* is the projection technique (minimal basis set) [8], *B* is the QUAMBO technique (minimal basis set) [9], LCAOM is the Mulliken analysis (LCAO basis set) [5], LCAOL is the Löwdin analysis (LCAO basis set) [5], WTAFM is the Mulliken analysis (WTAF basis set) [5], and WTAFL is the Löwdin analysis (WTAF basis set) [5].

method *A*, because this is accompanied by an increase in the space of the atomic orbitals onto which the occupied crystal orbitals are projected. However, we believe that it is incorrect to decrease the spilling parameter in the population analysis of the atomic orbitals by increasing the atomic basis sets, as was actually done in [10]. For example, if the basis set of the atomic orbitals is increased to a complete set, the spilling coefficient can be reduced to zero; however, the occupation analysis of the atomic orbitals in this basis set loses all physical meaning.

For the purely covalent cubic Si crystal, the results obtained by technique *B* can be compared with the data reported in [9]. According to [9], the Mayer index for the Si–Si bond is $M_{AB} = 0.885$ and the Mulliken overlap population is $P_{AB} = 0.756$. As can be seen from Table 2, our results obtained by technique *B* ($M_{AB} = 0.889$, $P_{AB} = 0.744$) are very close to those given in [9]. The insignificant differences can be associated with the use of different variants of the DFT method in the plane wave basis set. Note that technique *B* is a simpler modified variant of the method proposed in [9] and does not deal with the vacant Bloch states.

One of the main objectives of this study was to compare the results obtained by techniques *A* and *B*. It can be seen from Tables 1 and 2 that the data calculated by the two techniques are in good agreement. It should only be noted that the ionic component of the bonding (Q_A) in technique *B* is somewhat larger than the analogous component in technique *A*. Correspondingly, the covalent component (C_A, M_{AB}, P_{AB}) is somewhat smaller in technique *B*. Moreover, the spilling parameters in technique *B* are regularly smaller in magnitude.

The local characteristics of the electronic structure determined for the TiO_2 crystal in this work with the use of the projection technique and those obtained in our earlier study [5] (in which the Wannier-type atomic functions of the minimal valence basis set of titanium and oxygen atoms were constructed by the variational method) are compared in Table 3. In [5], the Bloch functions were calculated by the DFT method in the LCAO approximation with the CRYSTAL code [16] and the atomic pseudopotentials taken from [17].

It follows from Table 3 that the local characteristics of the electronic structure of the TiO_2 crystal are close for two projection variants (techniques *A*, *B*) and differ only slightly from the results of the Mulliken population analysis performed in the basis set of the atomic orbitals at the LCAO level. When analyzing the populations in the WTAF basis set [18], the Löwdin orthogonalization of the basis set [18] leads to insignificant differences as compared to the results of the Mulliken population analysis (due to the localized character of the Wannier-type atomic functions). The Löwdin atomic charges and the atomic covalences correspond to a somewhat lower degree of ionicity. Note that the Löwdin population analysis with the initial LCAO basis set containing diffuse atomic functions leads to an overestimated covalency of chemical bonding.

8. CONCLUSIONS

The main results obtained in this study can be briefly summarized as follows.

(1) The one-electron density matrix of a crystal was calculated using two variants of the projection technique, namely, the projection of crystal orbitals onto the Bloch sums of atomic orbitals (technique *A*) [8] and the projection of Bloch sums of atomic functions onto the crystal orbitals (QUAMBO technique) [9]. A comparative analysis of the one-electron density matrices thus obtained was carried out, and a simplified version of technique *B* was proposed to avoid cumbersome calculations of a large number of vacant crystal orbitals.

(2) The projection technique was used for calculating the local characteristics of the electronic structure (atomic charges, atomic covalences, bond orders) for a number of crystals (Si, SiC, GaAs, MgO, cubic BN, TiO_2 rutile) in the framework of the DFT method within the generalized gradient approximation in the plane wave basis set with the use of the norm-conserving pseudopotentials. It was established that both variants of the projection technique lead to close local characteristics of the electronic structure.

(3) The local characteristics of the electronic structure, which were obtained by the projection technique and the WTAF variational method in the minimal valence basis set with the crystal orbitals calculated at the LCAO level, were compared for the TiO_2 crystal with a rutile structure. It was shown that, despite the use of substantially different basis sets for calculating the crystal orbitals (plane waves in the projection technique, LCAO in the WTAF method), the local characteristics of the electronic structure obtained within the two approaches are in good agreement.

APPENDIX

Apart from the $(M - M_0)$-by-N matrix $\Delta T_{\mathbf{k}} \Delta T_{\mathbf{k}}^{+}$, we consider the N-by-N matrix

$$\Delta T_{\mathbf{k}}^{+} \Delta T_{\mathbf{k}} = \Delta \tilde{S}_{\mathbf{k}} = \tilde{S}_{\mathbf{k}} - \tilde{S}_{0\mathbf{k}}. \tag{A.1}$$

Let us designate the eigenvectors and eigenvalues of this matrix as $(V_{\mathbf{k}})_n$ and $\lambda_{\mathbf{k}n}$, respectively. Then, we obtain

$$\Delta \tilde{S}_{\mathbf{k}} (V_{\mathbf{k}})_n = \lambda_{\mathbf{k}n} (V_{\mathbf{k}})_n, \quad \Delta \tilde{S}_{\mathbf{k}} V_{\mathbf{k}} = V_{\mathbf{k}} \Lambda_{\mathbf{k}}, \quad V_{\mathbf{k}}^{+} V_{\mathbf{k}} = I, \tag{A.2}$$

where the columns of the N-by-$(N - M_0)$ matrix $V_{\mathbf{k}}$ are formed by $N - M_0$ eigenvectors $(V_{\mathbf{k}})_n$ corresponding to the greatest eigenvalues of the matrix $\Delta \tilde{S}_{\mathbf{k}}$ and $\Lambda_{\mathbf{k}}$ is the $(N - M_0)$-by-$(N - M_0)$ diagonal matrix with the diagonal elements $(\Lambda_{\mathbf{k}})_{nn} = \lambda_{\mathbf{k}n}$.

It is well known that nonzero eigenvalues of the matrices $\Delta T_{\mathbf{k}} \Delta T_{\mathbf{k}}^{+}$ [formula (41)] and $\Delta T_{\mathbf{k}}^{+} \Delta T_{\mathbf{k}}$ [formula (A2)] coincide with each other. For the eigenvectors, we can write the relationship

$$U_{\mathbf{k}} = \Delta T_{\mathbf{k}} \Delta \tilde{S}_{\mathbf{k}}^{-1/2} V_{\mathbf{k}}. \tag{A.3}$$

The matrix $\Delta \tilde{S}_{\mathbf{k}}$ can be treated as the nonorthogonality matrix for the functions

$$\Delta \tilde{\chi}_{\mu\mathbf{k}} = \tilde{\chi}_{\mu\mathbf{k}} - \sum_{m=1}^{M_0} (T_{0\mathbf{k}})_{m\mu} \psi_{m\mathbf{k}} = \sum_{m=M_0+1}^{M} (\Delta T_{\mathbf{k}})_{m\mu} \psi_{m\mathbf{k}}. \tag{A.4}$$

The functions $\Delta \tilde{\chi}_{\mu\mathbf{k}}$ can also be interpreted as a set of functions obtained by orthogonalization of the functions $\tilde{\chi}_{\nu\mathbf{k}}$ with respect to the occupied band functions $\psi_{m\mathbf{k}}$.

If relationship (A3) for the coefficients $U_{\mathbf{k}}$ is used instead of relationship (32) for the functions $\psi_{\mathbf{k}}^{(u)}$, we obtain

$$\psi_{n\mathbf{k}}^{(u)} = \begin{cases} \psi_{m\mathbf{k}}, & n = 1, 2, \ldots, M_0 \\ \sum_{\mu=1}^{N} (\Delta \tilde{S}_{\mathbf{k}}^{-1/2} V_{\mathbf{k}})_{\mu n} \Delta \tilde{\chi}_{\mu\mathbf{k}}, & n = M_0 + 1, \ldots, N. \end{cases} \tag{A.5}$$

By using the hermicity of the matrices $S_{\mathbf{k}}^{1/2}$ and $\Lambda_{\mathbf{k}}^{1/2}$ and the expressions

$$\Delta \tilde{S}_{\mathbf{k}}^{-1/2} V_{\mathbf{k}} = V_{\mathbf{k}} \Lambda_{\mathbf{k}}^{-1/2}, \quad \Delta \tilde{S}_{\mathbf{k}}^{1/2} V_{\mathbf{k}} = V_{\mathbf{k}} \Lambda_{\mathbf{k}}^{1/2}, \quad V_{\mathbf{k}}^{+} S_{\mathbf{k}}^{1/2} = \Lambda_{\mathbf{k}}^{1/2} V_{\mathbf{k}}^{+}, \tag{A.6}$$

we find

$$\begin{aligned} U_{\mathbf{k}} U_{\mathbf{k}}^{+} \Delta T_{\mathbf{k}} &= \Delta T_{\mathbf{k}} \Delta \tilde{S}_{\mathbf{k}}^{-1/2} V_{\mathbf{k}} V_{\mathbf{k}}^{+} \Delta \tilde{S}_{\mathbf{k}}^{-1/2} \Delta T_{\mathbf{k}}^{+} \Delta T_{\mathbf{k}} \\ &= \Delta T_{\mathbf{k}} \Delta \tilde{S}_{\mathbf{k}}^{-1/2} V_{\mathbf{k}} V_{\mathbf{k}}^{+} \Delta \tilde{S}_{\mathbf{k}}^{1/2} = \Delta T_{\mathbf{k}} V_{\mathbf{k}} \Lambda_{\mathbf{k}}^{-1/2} \Lambda_{\mathbf{k}}^{1/2} V_{\mathbf{k}}^{+} \\ &= \Delta T_{\mathbf{k}} V_{\mathbf{k}} V_{\mathbf{k}}^{+}. \end{aligned} \tag{A.7}$$

Then, Eq. (36) for the functions $\tilde{\chi}_{\mu\mathbf{k}}^{(u)}$ takes the form

$$\begin{aligned} \tilde{\chi}_{\mu\mathbf{k}}^{(u)} &= \sum_{m=1}^{M_0} (T_{0\mathbf{k}})_{m\mu} \psi_{m\mathbf{k}} + \sum_{m=M_0+1}^{M} (\Delta T_{\mathbf{k}} V_{\mathbf{k}} V_{\mathbf{k}}^{+})_{m\mu} \psi_{m\mathbf{k}} \\ &= \sum_{m=1}^{M_0} (T_{0\mathbf{k}})_{m\mathbf{k}} \psi_{m\mathbf{k}} + \sum_{\nu=M_0+1}^{N} (V_{\mathbf{k}} V_{\mathbf{k}}^{+})_{\nu\mu} \Delta \tilde{\chi}_{\nu\mathbf{k}}. \end{aligned} \tag{A.8}$$

Instead of expression (39), the nonorthogonality matrix for the functions $\tilde{\chi}_{\mu\mathbf{k}}^{(u)}$ with the use of relationship (A3) can be written in the form

$$\begin{aligned} \tilde{S}_{\mathbf{k}}^{(u)} &= T_{0\mathbf{k}}^{+} T_{0\mathbf{k}} + \Delta T_{\mathbf{k}}^{+} \Delta T_{\mathbf{k}} \tilde{S}_{\mathbf{k}}^{-1/2} V_{\mathbf{k}} V_{\mathbf{k}}^{+} \Delta \tilde{S}_{\mathbf{k}}^{-1/2} \Delta T_{\mathbf{k}}^{+} \Delta T_{\mathbf{k}} \\ &= S_{0\mathbf{k}} + \Delta \tilde{S}_{\mathbf{k}}^{1/2} V_{\mathbf{k}} V_{\mathbf{k}}^{+} \Delta \tilde{S}_{\mathbf{k}}^{1/2}. \end{aligned} \tag{A.9}$$

REFERENCES

1. M. C. Payne, M. P. Teter, D. C. Allan, T. A. Arias, and J. D. Joannopoulos, Rev. Mod. Phys. **64**, 1045 (1992).
2. C. M. Zicovich-Wilson, A. Bert, C. Roetti, R. Dovesi, and V. R. Saunders, J. Chem. Phys. **116**, 1120 (2002).
3. R. A. Évarestov and I. I. Tupitsyn, Fiz. Tverd. Tela (St. Petersburg) **44,** 1582 (2002) [Phys. Solid State **44**, 1656 (2002)].
4. V. P. Smirnov, R. A. Evarestov, and D. E. Usvyat, Int. J. Quantum Chem. **88**, 642 (2002).
5. R. A. Évarestov, D. E. Usvyat, and V. P. Smirnov, Fiz. Tverd. Tela (St. Petersburg) **45**, 1972 (2003) [Phys. Solid State **45**, 2072 (2003)].
6. R. A. Evarestov and V. P. Smirnov, *Site Symmetry in Crystals: Theory and Applications* (Springer, New York, 1997), Springer Ser. Solid-State Sci., Vol. 108.
7. R. A. Evarestov, V. P. Smirnov, I. I. Tupitsyn, and D. E. Usvyat, Int. J. Quantum Chem. **104**, 110 (2005).
8. D. Sanchez-Portal, E. Artacho, and J. M. Soler, Solid State Commun. **95**, 685 (1995).

9. W. C. Lu, C. Z. Wang, T. L. Chan, K. Ruedenberg, and K. M. Ho, Phys. Rev. B: Condens. Matter **70**, 041101 (2004).
10. M. D. Segall, C. J. Pickard, R. Shah, and M. C. Payne, Mol. Phys. **89**, 571 (1996).
11. R. A. Evarestov, V. P. Smirnov, I. I. Tupitsyn, and D. E. Usvyat, Phys. Status Solidi B **241**, R35 (2004).
12. R. S. Mulliken, J. Chem. Phys. **23**, 1833 (1955).
13. I. Mayer, Int. J. Quantum Chem. **29**, 73 (1986).
14. R. A. Evarestov and V. P. Smirnov, Phys. Rev. B: Condens. Matter **70**, 233101 (2004).
15. J. S. Lin, A. Quteish, M. C. Payne, and V. Heine, Phys. Rev. B: Condens. Matter **47**, 4174 (1993).
16. R. Dovesi, V. R. Saunders, C. Roetti, M. Causa, N. M. Harrison, R. Orlando, and E. Apra, *Crystal 95 User's Manual* (Torino University Press, Torino, 1996).
17. P. Durand and J. C. Barthelat, Theor. Chim. Acta **38**, 283 (1975).
18. P. O. Löwdin, Adv. Quantum Chem. **5**, 185 (1970).

Translated by O. Borovik-Romanova

Physics of the Solid State, Vol. 47, No. 10, 2005, pp. 1847–1851. Translated from Fizika Tverdogo Tela, Vol. 47, No. 10, 2005, pp. 1776–1780.

SEMICONDUCTORS AND DIELECTRICS

Femtosecond Mechanisms of Electronic Excitations in Crystalline Materials

V. I. Baryshnikov and T. A. Kolesnikova

Research Institute of Applied Physics, Irkutsk State University, bul'v. Gagarina 20, Irkutsk, 664003 Russia
Irkutsk State University of Communications, Irkutsk, 664074 Russia
e-mail: vib@api.isu.ru

Received July 5, 2004; in final form, December 1, 2004

Abstract—The lattice dynamics of crystals is investigated in the course of high-power electronic excitation. It is revealed that, at $W_e < W_{eo}$, atoms and ions are displaced from their regular sites for 100–300 fs. Subsequent relaxation of the crystal lattice in response to a strong local electric field induced by the collisional displacement of ions occurs for 10–50 ns in an oscillatory manner with a period of 0.5–1.5 ps. © *2005 Pleiades Publishing, Inc.*

1. INTRODUCTION

Fast (<100 fs) broadband (UV–IR) stable (at 78–1500 K) luminescence excited by high-power electron beams in oxygen-containing, alkali-halide, and alkaline-earth crystals was revealed and investigated in our earlier works [1–3]. This luminescence is associated with the high probability of electronic radiative transitions in the broadened upper valence band formed by the *p* states of anions [1–3]. The degree of distortion of the *p* subbands is determined by the strength of short-lived disturbing electric fields in the vicinity of collision-displaced anions and depends on the electron beam energy W_e [1–3]. The energy of an electron in a beam is equal to its kinetic energy governed by the velocity of motion. Therefore, broadening of the cathodoluminescence spectra with an increase in the velocity and, hence, in the momentum of incoming electrons in crystals is caused by collisional excitation [1–3]. A numerical analysis of the threshold energies W_o for the generation of stable defects and the dependence of the broadening of the cathodoluminescence spectra on the electron beam energy W_e allowed us to determine the limiting (E_o) and current (E) strengths of the disturbing crystal fields in the region of collision-displaced anions [1, 2]. In particular, for Al_2O_3 crystals (W_0 = 70 eV, W_{eo} = 400 keV), the limiting strength E_o is of the order of 4×10^9 V/cm and the strength at W_e = 150–250 keV is estimated to be $E = (0.7–2.5) \times 10^7$ V/cm [1, 2]. However, the problems regarding the rate of ionic displacement and the rate of rise in the strength E as functions of the electron beam energy W_e, the lifetime of local disturbing fields after collisional displacements of ions from regular sites, and the mechanism of relaxation of collisionally excited ions in the crystal lattice remain to be solved.

In this work, we studied the dynamics of displacement and relaxation of regular lattice sites. Moreover, we analyzed the kinetics of rise and the lifetimes of strong local electric fields in the vicinity of collision-displaced ions during interaction of high-power electron beams with crystalline materials.

2. OBJECTS OF INVESTIGATION AND EXPERIMENTAL TECHNIQUE

The relative yield of broadband luminescence in alkali-halide, alkaline-earth, and oxygen-containing crystals is approximately equal to 10^{-3} [1, 4]. This broadband luminescence cannot be treated as an intense emission. For example, the broadband luminescence spectrum in Al_2O_3 crystals containing titanium impurities at a content of 10^{-2}–10^{-3} wt % is overlapped by the cathodoluminescence bands at 780 nm (Ti^{3+}) and 310 nm (Ti^{2+}) [5]. For this reason, investigations were performed using crystals and materials with high and nominal purities: the impurity concentrations were equal to 10^{-5}–10^{-6} wt % in oxygen-containing crystals and 10^{-4}–10^{-5} wt % in the other crystals. The samples for experiments were prepared in the form of plates ($5 \times 5 \times 0.02$ mm) cut from single crystals.

The crystals were irradiated with a picosecond (10, 1000 ps) high-current accelerator (W_e = 7–300 keV, j = 0.05–1000 kA/cm^2), in which uniform compression of the electron beam was provided by the interaction of accelerated electrons with the self-magnetic field [6]. The crystals were excited by pulses of a high-power (0.1–10 TW/cm^2) soft x-ray source (photon energy, 1–3 keV). The operation of the picosecond (10 ps) x-ray source is based on the use of radiation of a hot plasma generated upon high-rate energy input (>10^{13} A/s) into a high-current vacuum discharge [6]. In this case, the electron temperature of the plasma can be as high as 10^7 K. The fast photoluminescence of the crystals was investigated using three-photon excitation with the sec-

1063-7834/05/4710-1847$26.00

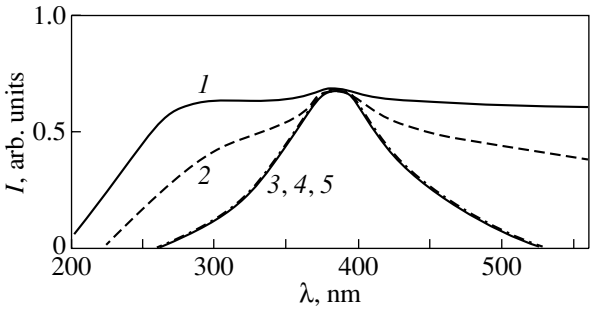

Fig. 1. Normalized spectra of (*1–3*) cathodoluminescence ($\tau < 10$ ps), (*4*) x-ray luminescence ($\tau < 1$ ns), and (*5*) photoluminescence ($\tau < 1$ ps) at electron beam energies of (*1*) 110, (*2*) 60, and (*3*) 7 keV. The measurement temperature is 300 K.

ond (360–450 nm), third (240–300 nm), and fourth (205–225 nm) harmonics of the high-power (1–10 GW) tunable femtosecond (110 fs) $Ti^{3+} : Al_2O_3$ laser.

The luminescence of the crystals was measured on a high-speed (resolution, 10 ps) VUV–IR (150–1200 nm) complex equipped with recording storage channels. A modified FÉU-31ÉLU-FM photomultiplier and a Tektronix TDS3032B oscilloscope are the key elements of the channel with a subnanosecond resolution (0.5 ns). Another channel is a unique high-sensitivity analog-to-digital converter based on a gated microchannel image tube connected to a CCD line or a CCD array through a wide-aperture lens. This system makes it possible to record the kinetics and spatial distribution of the spectra of single optical pulses with a resolution of 10 ns. The error in the measurement of the intensity and kinetics of luminescence did not exceed 5%. All pulse devices of the setup were synchronized with a nanosecond accuracy. Moreover, the kinetics of the photoluminescence spectra was studied using a high-speed (resolution, 1 ps) Hamamatsu Streak Camera C5680.

3. KINETICS OF CONVERSION OF ELECTRON IMPACT ENERGY IN CRYSTAL STRUCTURES

For alkali-halide (NaCl, KI, RbBr, CsI, CsBr) and alkaline-earth (BaF_2) crystals, a decrease in the electron beam energy W_e from 45 to 7 keV is accompanied by a gradual transformation of the broadband luminescence spectrum into a cathodoluminescence band ($\tau < 10$ ps) with maxima at 370 nm for NaCl, 360 nm for KI, 350 nm for RbBr, 650 nm for CsI, 250 and 350 nm for CsBr, and 220 and 310 nm for BaF_2 irrespective of the temperature (from 78 K to the melting point) and the current density (0.01–2.0 kA/cm^2) [3]. In oxide compounds, a similar phenomenon is observed with a decrease in the electron beam energy W_e from 100 to 15 keV [1, 2]. In alkali-halide, alkaline-earth, and oxide crystals, the cathodoluminescence spectra with $\tau < 10$ ps at $W_e = 7$ keV coincide with the initial densities of states in the *p* valence band [1–3]. This indicates that the above crystals can exhibit fast luminescence upon ionization of anions from deep-lying levels of the *p* valence shell. Actually, upon high-power picosecond electron excitation, x-ray excitation, and femtosecond laser excitation of Al_2O_3 single crystals, the cathodoluminescence ($\tau < 10$ ps), x-ray luminescence ($\tau < 1$ ns), and photoluminescence ($\tau < 1$ ps) spectra are identical to each other (Fig. 1). The three-photon excitation (16.6–18.2 eV) of these crystals results in selective ionization of anions from the 2*p* valence levels. Consequently, under radiation and high-power laser excitations, oxygen ions in oxides undergo 2*p* electron radiative valence transitions. Furthermore, the picosecond cathodoluminescence spectra of alkali-halide and alkaline-earth crystals at an electron energy of 7 keV [7] coincide with the photoluminescence spectra excited by high-power femtosecond laser pulses [8]. Therefore, fast radiative transitions in alkali-halide and alkaline-earth crystals, as in oxide crystals, proceed in the *p* valence shell of the ionized anions. The probability of these transitions does not depend on the temperature in the range 78–900 K. With allowance made for these features, the relationship $\Delta t \sim h/\Delta E$ is satisfied. The width of the fast luminescence spectra lies in the range $\Delta E = 1.0$–6.0 eV (Fig. 1) [3]. Therefore, the decay time ($\Delta t = \tau$) of broadband luminescence (cathodoluminescence), x-ray luminescence, and photoluminescence associated with the *p* valence electrons in alkali-halide, alkaline-earth, and oxide crystals does not exceed 100 fs.

The spectral parameters of the luminescence associated with the *p* valence electrons are related to the density of states in the *p* valence band. In turn, this density of states is determined by the density of *p* valence states of the initial crystal, the threshold energy W_o, the electron beam energy W_e, and, hence, the strength *E* of the disturbing crystal fields. Therefore, it is necessary to obtain an expression relating the field strength *E* to the energies W_o and W_e. This expression can be derived under the assumption of elastic collisions by using the law of conservation of momentum and the balance between the energy of an incoming electron and the energy of the disturbing electric field in the vicinity of a collision-displaced ion in the crystal. For oxide crystals, the condition providing the conversion of the impact energy through the elastic mechanism can be written in the form

$$-\Delta W_{O^{2-}} = \frac{m_e M_{O^{2-}}}{2(m_e + M_{O^{2-}})}\left(\sqrt{\frac{2W_e}{m_e}} - \sqrt{\frac{2W_e m_e}{M_{O^{2-}}^2}}\right)^2 (1 - k^2) = 0, \quad (1)$$

$$W_e < W_{eo}.$$

It follows from expression (1) that, at $k = 1$, we are dealing with an elastic collision. In this case, the change in the internal energy of the ion is determined to be $\Delta W_{O^{2-}} = 0$. In our experiments, it was established

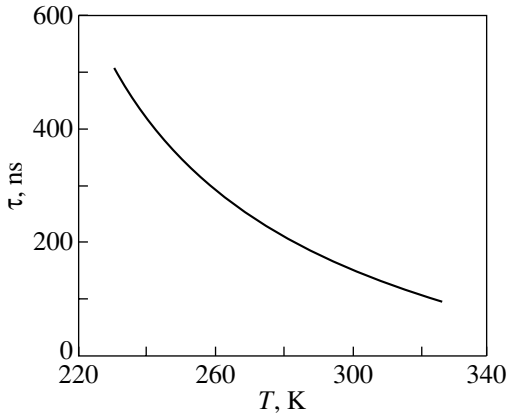

Fig. 2. Temperature dependence of the decay time of the intensity of the cathodoluminescence band at 310 nm for the Al_2O_3 crystal. The electron-beam current density is 0.05 kA/cm^2.

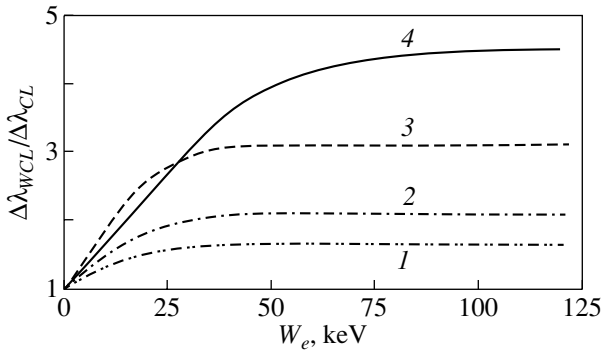

Fig. 3. Dependences of the broadening of the cathodoluminescence band ($\tau < 10$ ps) assigned to the *p* valence electrons on the energy of the exciting electron beam for (*1*) LiF, (*2*) RbBr, (*3*) KI, and (*4*) Al_2O_3 crystals. The measurement temperature is 300 K.

that, for the Al_2O_3 crystal, the intensity of the cathodoluminescence band at 310 nm decays with time constants $\tau = 220$ and 170 ns when the electron-beam current densities are equal to 0.05 ($W_e = 250$ keV, $\tau = 5$ ns) and 2 kA/cm^2, respectively. This means that the sapphire crystal is heated by $\Delta T = 18$–20 K per emitted pulse (Fig. 2). The relative fraction of the thermal energy released upon structural relaxation per collision-displaced O^{2-} ion is given by

$$\delta = \frac{emc\Delta T}{jW_eSt}(1-\eta), \qquad (2)$$

where *m*, *c*, and *S* are the mass, the specific heat capacity, and the surface area of the Al_2O_3 crystal, respectively; *j* is the current density; *t* is the electron-beam pulse width; *e* is the elementary charge; and η is the broadband luminescence yield. Substitution of the corresponding numerical parameters into expression (2) gives $\delta = 0.99$. As a result, we obtain $\Delta W_{O^{2-}} = Q_{O^{2-}}(1-\delta) \longrightarrow 0$ and, according to condition (1), $k = 1$. Consequently, the conversion of the electron impact energy occurs through the elastic mechanism. Then, according to the above technique, the dependence of the strength *E* of the disturbing crystal fields on the energies W_{eo} and W_e can be represented in the form

$$E = \frac{4\pi\varepsilon\varepsilon_0}{q^3}W_e^2\left(\frac{m_e}{m_i}\right)^2, \quad W_e < W_{eo}, \qquad (3)$$

where *q* is the effective ion charge, m_e is the electron mass, m_i is the ion mass, ε_0 is the permittivity of free space, and ε is the permittivity of the crystal. Since the threshold energies W_o for oxygen-containing crystals are higher than those for alkali-halide and alkaline-earth crystals, the strength *E* of short-lived disturbing fields in the vicinity of the collision-displaced anions in the former crystals is higher than that in alkali-halide crystals. In particular, we have $W_o = 6$–9 eV [9] ($W_{eo} = 30$–50 keV) for alkali-halide crystals and, at $W_e = 50$–250 keV, the field strength E_o in the vicinity of the collision-displaced ions is equal to 0.5×10^7 V/cm. Oxygen-containing crystals are characterized by the energies $W_o = 60$–75 eV ($W_{eo} = 350$–450 keV), and the field strength E_o at $W_e = 250$ keV can reach 2.5×10^7 V/cm. As a consequence, the degree of distortion of the subbands in the valence band in oxygen-containing materials is higher and the broadband luminescence spectrum is experimentally observed over a wider range than those in alkali-halide and alkaline-earth crystals.

The investigations revealed that, when the electron energy is higher than the threshold energy of the generation of stable interstitial species ($W_e > W_{eo} = 40$–50 eV), the width of the cathodoluminescence spectra ($\tau < 10$ ps) of alkali-halide crystals remains constant (Fig. 3). In this case, we can write the expression

$$t = \frac{A_o}{\sqrt{2W_o/m_i}}, \qquad (4)$$

where *t*, W_o, and A_o are the time, the threshold energy, and the magnitude of collisional displacement of ions, respectively. From this expression, we find that, at $W_o = 6$–8 eV, the collisional displacement of anions occurs for ~100 fs. This result, together with the obtained decay time (<100 fs) of broadband luminescence (cathodoluminescence), indicates that the time of rise of the local disturbing fields in the vicinity of the collision-displaced anions is approximately equal to 100 fs.

During the collisional displacement of lattice sites, there arise disturbing electric fields in their vicinity and, hence, quasi-elastic forces ($F_k = -ku$) act on the displaced ions. This implies that collisional subthreshold ($W_e < W_{eo}$) displacements of ions from regular sites necessarily lead to vibrational relaxation whose time corresponds to the recovery time of the crystal lattice.

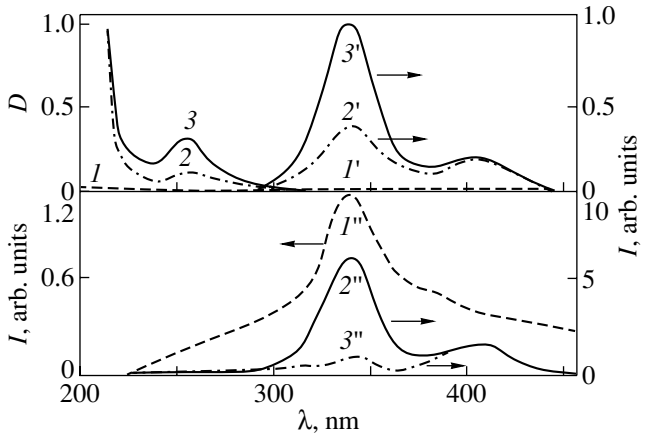

Fig. 4. Spectra of (*1*–*3*) absorption, (*1*'–*3*'), photoluminescence, and (*1*"–*3*") cathodoluminescence of sapphire crystals: (*1*) the special-purity crystal after electron bombardment, (*2*) sample *3* after F^+ illumination (4ω : YAG : Nd laser), and (*3*) an additively colored crystal. The measurement temperature is 300 K.

The vibrational process of recovering the regular sites of the ions is a decay process, because approximately 99% of the collision energy upon electron bombardment ($W_e < W_{eo}$) of the nominally pure crystals is converted into the internal energy of the lattice. Consequently, this vibrational mechanism should include the action of the resistance force ($F_r = -rdu/dt$) governed by the crystal properties. Therefore, the mechanism of vibrational relaxation of a collision-displaced site in an *N*-site lattice can be described by the classical system of equations

$$m_i\frac{d^2u_n}{dt^2} + r_n\frac{du_n}{dt} + k_nu_n = 0, \qquad (5)$$

where *k* is the quasi-elastic force coefficient, *r* is the resistance coefficient of the crystal lattice, and *u* is the ionic displacement vector. In order to construct the real system of equations (5) and to determine the kinetic parameters of damped vibrations of collision-displaced ions, we use the following approach. It is known that collisional excitations of oxygen-containing crystals at subthreshold energies induce the generation of short-lived defects, i.e., bound pairs in the form of electric dipoles $F^{2+}O^{2-}$ ("anion vacancy–displaced lattice site" pair). It is evident that the fields of short-lived electric dipoles are equivalent to the local disturbing crystal fields. During subthreshold electron bombardment of sapphire crystals, the generation and healing of short-lived defects (F^+O^{2-} pairs) are described by the following reaction [10]:

$$e \longrightarrow R \Rightarrow (F^+)^*O^{2-} \Rightarrow (h\nu_{F^+} + F^+O^{2-}) - e \Rightarrow R, \quad (6)$$

where *R* is the regular site, $(F^+)^*$ is the F^+ excited center, and $h\nu_{F^+}$ is the energy of the photon emitted by the F^+ center. The analysis of the cathodoluminescence, x-ray luminescence, and photoluminescence spectra depicted in Fig. 4 revealed that, during electron bombardment of special-purity sapphire crystals, the short-lived defects F^+O^{2-} are also formed through the excited state of F^+ centers [see reaction (6)]. The radiation pattern of the F^+ excited center is perpendicular to the dipole moment vector of the F^+ center, whose direction coincides with the dipole moment vector of the F^+O^{2-} dipole. The damped vibrations of the collision-displaced ions were experimentally examined using the luminescence method. The decay kinetics of the cathodoluminescence of the F^+ centers should be characterized by time components corresponding to the parameters of vibrations of the dipole moment vector of the F^+O^{2-} dipole along one of the coordinates of vibrations of the O^{2-} ion. Therefore, the system of equations (5) for vibrational relaxation of the collision-displaced site in the *N*-site lattice can be reduced to one equation of type (5) for the displacement coordinate that corresponds to vibrations of the dipole moment vector of the F^+O^{2-} dipole. The solution of this equation in the form

$$u = A_oe^{-\alpha t}\cos\omega t \qquad (7)$$

gives the desired set of parameters

$$\alpha = \frac{r}{2m_i}, \quad \omega_o = \sqrt{\frac{k}{m_i}},$$
$$\omega = \sqrt{\frac{k}{m_i} - \frac{r^2}{4m_i^2}} = \sqrt{\omega_o^2 - \alpha^2}. \qquad (8)$$

Here, A_o, α, and ω are the maximum amplitude (collisional displacement), the damping coefficient, and the angular frequency of damped vibrations of the ion, respectively; and ω_o is the natural frequency in the absence of resistance of the medium. These parameters can be determined by analyzing the quasi-elastic force and the force of lattice resistance to the vibrational motion of collisionally excited ions. Knowing the limiting values E_o [2] and W_o [11] and taking into account expression (3), we obtain the following relationship for the quasi-elastic force:

$$F_k = -ku = -qE_o = -\frac{W_o}{A_o} = -\frac{4\pi\varepsilon\varepsilon_o}{q^2}W_{eo}^2\left(\frac{m_e}{m_i}\right)^2, \qquad (9)$$
$$W_e < W_{eo}.$$

From relationship (9), at $u = A_o$, the quasi-elastic force coefficient *k* can be expressed in the form

$$k = \frac{q^2E_o^2}{W_o}. \qquad (10)$$

In order to determine the lifetime of short-lived pairs F^+O^{2-} and, hence, the damping coefficient α, we ana-

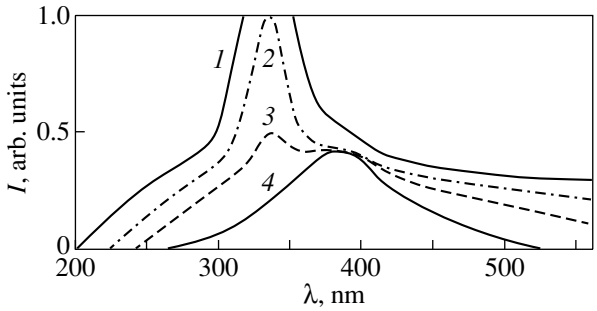

Fig. 5. Cathodoluminescence spectra of special-purity sapphire crystals at electron beam energies of (*1*) 250, (*2*) 60, (*3*) 30, and (*4*) 7 keV. The time resolution of cathodoluminescence pulses is 1 ns. The measurement temperature is 300 K.

lyzed the kinetic parameters of the cathodoluminescence of the F^+ centers as functions of the electron beam energy W_e for the Al_2O_3 crystals. It was experimentally found that, as the electron beam energy increases, the decay time of the cathodoluminescence of the F^+ centers (λ_{max} = 327 nm) increases from ~5 ns (Fig. 5, curve *3*) to 10 ns (Fig. 5, curve *2*) and becomes as long as 18–22 ns at W_e = 250–300 keV (Fig. 5, curve *1*). The decay time of the luminescence of the F^+ centers is 3.8 ns [12]. Therefore, we can make the inference that, at W_e = 250 keV, the lifetime of the short-lived pairs F^+O^{2-} induced by the electron impact in the Al_2O_3 crystals is equal to 15 ns. Consequently, the vibration amplitude of the collisionally excited O^{2-} ion in the sapphire crystal decreases by a factor of *e* in a time of 15 ns. Then, from expression (7), we obtain

$$e^{-\alpha t} = \left(\frac{A_o}{A(t)}\right)^{-1} = e^{-1}, \qquad (11)$$

where $\alpha t = 1$, $t = \tau = 15 \times 10^{-9}$ s, and $\alpha = 6.7 \times 10^7$ s^{-1}. Substitution of the experimental values W_o = 70 eV, $E_o = 4 \times 10^9$ V/cm, and $q = 6e$ into relationship (10) at $W_e = W_{eo}$ gives k = 1.3 N/cm for the sapphire crystal. With the use of formulas (8) and (11), we find the frequency of damped vibrations of the collisionally excited O^{2-} ions in the Al_2O_3 crystals: $\nu = \sqrt{\omega_o^2 - \alpha^2}/2\pi = 1.2 \times 10^{12}$ s^{-1}. As a result, the period of damped vibrations of the O^{2-} ions is estimated at ~800 fs and the time of their displacement from regular sites is approximately equal to 200 fs. In the Al_2O_3 crystals, the effective time of rise of the disturbing fields in the vicinity of the collision-displaced oxygen ions at $W_e < W_{eo}$ is approximately equal to 150 fs. The parameters of anions and crystal fields for sapphire and other crystals that belong to the groups of dielectrics and metals are such that, at $W_e < W_{eo}$, the times of collisional displacement of atoms and ions from regular sites fall in the range 100–300 fs, the times of their vibrational relaxation lie in the range 10–50 ns, and the vibrational periods are equal to 0.5–1.5 ps depending on the lattice type. Thus, during electron bombardment of alkali-halide, alkaline-earth, and oxide crystals, the strength of the disturbing fields in the vicinity of collision-displaced anions at $W_e < W_{eo}$ increases for 100–300 fs and then decays in an oscillatory manner with a period of 0.5–1.5 ps for 10–50 ns.

REFERENCES

1. V. I. Baryshnikov, L. I. Shchepina, T. A. Kolesnikova, and E. F. Martynovich, Fiz. Tverd. Tela (Leningrad) **32** (6), 1888 (1990) [Sov. Phys. Solid State **32** (6), 1103 (1990)].
2. V. I. Baryshnikov and T. A. Kolesnikova, Fiz. Tverd. Tela (St. Petersburg) **39** (2), 286 (1997) [Phys. Solid State **39** (2), 250 (1997)].
3. V. I. Baryshnikov, in *Proceedings of the VII All-Russia School–Workshop on Luminescence and Related Phenomena, Irkutsk, Russia, 2001* (Irkutsk, 2001), p. 56.
4. D. I. Vaĭsburd, B. I. Semin, É. G. Tavanov, S. B. Matlis, I. N. Balychev, and G. I. Gering, *High-Power Electronics of Solids* (Nauka, Novosibirsk, 1982) [in Russian].
5. V. I. Baryshnikov, T. A. Kolesnikova, and I. Kvapil, Fiz. Tverd. Tela (St. Petersburg) **36** (9), 2788 (1994) [Phys. Solid State **36** (9), 1524 (1994)].
6. V. I. Baryshnikov and V. L. Paperny, J. Phys. D: Appl. Phys. **28**, 2519 (1995).
7. V. I. Baryshnikov and T. A. Kolesnikova, in *Proceedings of the International Conference on Luminescence and Optical Spectroscopy of Condensed Matter, Osaka, Japan, 1999* (Osaka, 1999), PD1-22.
8. T. Sekikawa, T. Ohnj, Y. Nabekaw, and S. Watanabe, in *Proceedings of the International Conference on Luminescence and Optical Spectroscopy of Condensed Matter, Osaka, Japan, 1999* (Osaka, 1999), BO2-4.
9. Ch. B. Lushchik and A. Ch. Lushchik, *Decay of Electronic Excitations with the Formation of Defects in Solids* (Nauka, Moscow, 1989) [in Russian].
10. V. I. Baryshnikov, E. F. Martynovich, T. A. Kolesnikova, and L. I. Shchepina, Fiz. Tverd. Tela (Leningrad) **30** (5), 1505 (1988) [Sov. Phys. Solid State **30**, 868 (1988)].
11. G. P. Pells and D. C. Phillips, J. Nucl. Mater. **80**, 207 (1979).
12. E. D. Evans and M. Stapelbroek, Phys. Rev. B: Condens. Matter **18**, 7089 (1978).

Translated by O. Borovik-Romanova

Physics of the Solid State, Vol. 47, No. 10, 2005, pp. 1852–1853. From Fizika Tverdogo Tela, Vol. 47, No. 10, 2005, pp. 1781–1782.

SEMICONDUCTORS AND DIELECTRICS

Iodine Is a Covalent Crystal[1]

I. A. Stepanov

Institute of Physical Chemistry, University of Freiburg, Freiburg, 79104 Germany

e-mail: istepanov@email.com

Received October 5, 2004; in final form December 9, 2004

Abstract—Earlier it was supposed that the lattice energy of iodine is about 70 kJ/mol; therefore, it was considered to be a molecular crystal. In the present paper, it is shown that the lattice energy of iodine is at least 10 times larger and thus iodine is a covalent crystal. In previous works, the role of fluctuations was not taken into account. © *2005 Pleiades Publishing, Inc.*

1. INTRODUCTION

Earlier it was supposed that in molecular crystals, otherwise called van der Waals crystals, the molecules cohere for the most part through mutual van der Waals attraction, with this attraction being very weak. This was supported by the fact that the measured sublimation energies are approximately equal to the lattice energies calculated using the van der Waals potential [1, 2]. The sublimation energy of I_2 is equal to 63.7–74.2 kJ/mol [2–4], and the calculated energy is 71.4–74.2 kJ/mol [3, 4]. Iodine was considered to be a molecular crystal.

However, there is one disadvantage to calculating the lattice energies: fluctuations are not taken into account. One calculates the energy required to transfer the molecule from its equilibrium position to infinity, practically to r_{max}. Due to fluctuations, the molecule will rupture the intermolecular bond earlier than at r_{max}. But how much earlier?

2. THEORY

In the physics of strength of solids, it was proven long ago that more than 90% of the energy required to break an interatomic bond is provided by fluctuation and that the role of the external stretching force is less than 10%. This has been proven in the works of S.N. Zhurkov and coworkers [5–8] and references therein. If the depth of the potential well is decreased slightly, the probability of rupture fluctuation increases by tens of times because this probability depends exponentially on the depth U and temperature: $\exp(-U/kT)$. Max Born calculated the energy of the chemical bond in crystal (without taking fluctuations into account) and multiplied it by the number of molecules. The strength of a solid obtained like this is called the theoretical strength of a solid. The actual strength of solids is much less (by 1 to 2 orders of magnitude) than the theoretical strength predicted by crystal lattice theory [5, 6]. The physics of strength approach is justified in this paper because the mechanical failure energy U_0 is found to coincide with the sublimation energy Q, i.e., the interatomic binding energy [5, 6] (see table).

In [6], it was found that the breaking strength of a body under load is

$$\sigma_* = E\varepsilon_* - (\alpha ET/3)\ln\tau/\tau_0, \quad (1)$$

where E is the Young's modulus, α is the thermal expansion coefficient of the surface of the solid (which is several times greater than the bulk value [6]), T is temperature, ε_* is the relative elongation at which the interatomic bond becomes unstable and breaks, τ is the lifetime (i.e., the time during which the load is withstood), and τ_0 is the period of thermal oscillations of atoms. Experimental and theoretical estimates of the breaking strain of the interatomic bond give $\varepsilon_* \approx 0.2$ [6].

From Eq. (1) it is clear that the actual breaking strength consists of an athermal component $\sigma_0 = E\varepsilon_*$ and a component $\sigma_{T,\tau} = (\alpha ET/3)\ln\tau/\tau_0$, which depends on temperature and time. The athermal component is seen to be equal to the theoretical strength. The other component is responsible for the temperature and time dependence of the strength. One can interpret $\sigma_{T,\tau}$ as the local pressure due to anharmonically vibrating atoms. This fluctuating thermal pressure stretches the

The mechanical failure energy U_0 and the sublimation energy Q for some substances [5, 6]

Substance	U_0, kJ/mol	Q, kJ/mol
Zn	125	130
Al	217	230
Ag	259	284
Cu	326	334
Mo	752	669
Fe (steel-3)	418	405

[1] This article was submitted by the author in English.

1063-7834/05/4710-1852$26.00 © 2005 Pleiades Publishing, Inc.

interatomic bonds and contributes to their deformation and rupture caused by the external load. An estimate of the thermal fluctuation stress $\sigma_{T,\tau}$ shows that it is large [5, 6]. For instance, the theoretical strength of aluminum is 10^7 kPa, the thermal fluctuation stress $\sigma_{T,\tau} = 9.9 \times 10^6$ kPa, and the actual strength $\sigma_* = 10^5$ kPa. Therefore, according to the physics of strength, interatomic bond failure occurs when the bond is stretched by an external force and thermal fluctuation causes it to rupture.

To sublimate a crystal, one has to introduce a quantity of heat into it. The intermolecular distances increase, but the failure of the intermolecular bonds is caused by fluctuations. This quantity of heat is about 63.7–74.2 kJ/mol, but the theoretical energy of intermolecular bonds is more than ten times higher, i.e., greater than 640–740 kJ/mol. The cohesive energy of molecular crystals is of the order 0.1 eV/molecule, and that of covalent solids is of the order 10 eV/atom [1]. The quantity 64–74 kJ/mol is about 0.7–0.8 eV/molecule, so the energy of intermolecular bonds of iodine is greater than 7–8 eV/molecule. In [6], an interesting result was obtained:

$$Q = U_0 = \varepsilon_* C/\alpha, \quad (2)$$

where C is the atomic specific heat.

In iodine, the nearest and next-to-nearest neighbor distances are 3.50 and 3.93 Å [9]. They are noticeably less than the double van der Waals radius 4.3 Å [9] (the distance between the atoms in the molecule is 2.72 Å) and the distance of the next-to-nearest neighbor in the van der Waals crystal, which is about 4.6 Å. This is because there is covalent intermolecular interaction [4, 10–14]. This interaction is strong, about 40% of the energy of dissociation of the molecules [4]. So, one can make the following conclusion: the good agreement between the experimental and calculated sublimation energies of iodine is just an accident or a correlation.

Really, the previous point of view was suspect: the covalent forces play a major role in the interaction between molecules, but the cohesive energy of the crystal is as weak as the van der Waals one. Iodine crystals, although molecular, show interesting semiconducting properties, and it was found that the phenomenological behavior of iodine is not fundamentally different from other covalent or ionic crystals [15]. One can strongly suggest that iodine is a covalent crystal.

REFERENCES

1. J. M. Ziman, *Principles of Solid State Theory* (Cambridge University Press, Cambridge, 1971), pp. 110, 111.
2. K. Yamasaki, J. Phys. Soc. Jpn. **17**, 1262 (1962).
3. F. Vovelle and G. C. Dumas, Mol. Phys. **34**, 1661 (1977).
4. H. G. Drickamer, R. W. Lynch, R. L. Clendenen, and E. A. Perez-Albuerne, *Solid State Physics* (Academic, New York, 1966), Vol. 19, p. 135.
5. V. R. Regel, A. I. Slutsker, and E. E. Tomashevskii, *Kinetic Nature of the Strength of Solids* (Nauka, Moscow, 1974) [in Russian].
6. S. N. Zhurkov, Fiz. Tverd. Tela (Leningrad) **22**, 3344 (1980) [Sov. Phys. Solid State **22**, 1958 (1980)].
7. I. A. Stepanov, Materials Science **31**, 441 (1995).
8. I. A. Stepanov, J. Macromol. Sci., Part B: Phys. **36**, 117 (1997).
9. F. van Bolhuis, P. B. Koster, and T. Migchelsen, Acta Crystallogr. **23**, 90 (1967).
10. B. V. Shanabrook and J. S. Lannin, Solid State Commun. **38**, 49 (1981).
11. B. V. Shanabrook, J. S. Lannin, and J. S. Hisatsune, Phys. Rev. Lett. **46**, 130 (1981).
12. N. Orita, K. Niizeki, K. Shindo, and H. Tanaka, J. Phys. Soc. Jpn. **61**, 4502 (1992).
13. T. Itoh and K. Kambe, J. Phys. Soc. Jpn. **12**, 763 (1957).
14. H. A. Bent, Chem. Rev. **68**, 587 (1968).
15. A. A. Braner and R. Chen, J. Phys. Chem. Solids **24**, 135 (1963).

Physics of the Solid State, Vol. 47, No. 10, 2005, pp. 1854–1858. Translated from Fizika Tverdogo Tela, Vol. 47, No. 10, 2005, pp. 1783–1787.

SEMICONDUCTORS AND DIELECTRICS

Photoinduced Permittivity in Lead Molybdate

M. D. Volnyanskiĭ, A. Yu. Kudzin, S. N. Plyaka, and Z. Balasme

Dnepropetrovsk National University, Naukova ul. 13, Dnepropetrovsk, 49050 Ukraine

e-mail: Splyaka@ff.dsu.dp.ua

Received March 1, 2005

Abstract—The effect of illumination on the dielectric properties of lead molybdate ($PbMoO_4$) single crystals was studied. Illumination with intrinsic light gives rise to a substantial enhancement of low-frequency permittivity (the photodielectric effect, PDE). The PDE is dependent on temperature and reaches a maximum near 400 K. The permittivity reaches the steady state a long time after the light is turned on (off). The relaxation time and activation energy of the process were determined. The relation of the PDE to the photoconductivity of the crystal is discussed. A possible mechanism of the PDE in $PbMoO_4$ crystals is proposed. © *2005 Pleiades Publishing, Inc.*

1. INTRODUCTION

Crystals of lead molybdate and lead tungstate ($PbMoO_4$ and $PbWO_4$) are isomorphic, have a scheelite structure, feature similar physical properties, and hold promising application potential. Indeed, lead tungstate currently enjoys wide use as a material for scintillation detectors [1], while lead molybdate is used in acoustooptics [2]. Recent communications report on the possible usage of $PbMoO_4$ in Raman lasers and luminescent bolometers. Therefore, for a long time considerable attention has been focused on studying the properties and developing technologies for the preparation of high-quality lead molybdate and tungstate crystals. $PbMoO_4$ and $PbWO_4$ crystals are grown from a melt. As a result of the lead, molybdenum, and tungsten oxides having different vapor pressures, the crystals are usually off-stoichiometric. Their lattices contain a large number of defects whose concentration and charge state depend strongly on the composition of the charge and of the atmosphere in which the crystals are grown and annealed. Lattice defects affect almost all crystal parameters and practically dominate such properties as the electric and photoconductivity, color, and photoluminescence [3, 4]. Copious literature deals with the relation of physical properties to lattice defects [5, 6]. There are indications that intrinsic lattice defects are capable of forming associates, pair defects of various types. The formation of more complex, extended defects likewise cannot be excluded [7]. Thus, $PbMoO_4$ single crystals may be considered to be a partially disordered medium containing a large number of various (including extended) defects.

Intrinsic defects and impurities in $PbMoO_4$ crystals form a complex spectrum of electronic states in the bandgap. Localized electronic states are most pronounced in the optical absorption spectra of crystals. In particular, the characteristic yellow color of $PbMoO_4$ crystals owes its origin to intrinsic defects. Comprehensive studies of optical absorption spectra have revealed some features and a temperature dependence. The behavior of optical absorption follows the Urbach rule, which is attributed to a high density of localized states near the bandgap edges. The state of localized centers is strongly affected by various external factors. For instance, annealing of $PbMoO_4$ crystals in a reducing atmosphere or vacuum results in bleaching and annealing in an oxidizing atmosphere imparts a yellow color to the crystals. Lattice disorder determines the charge transport mechanism in lead molybdate crystals. Studies of the electrical conductivity of $PbMoO_4$ crystals show that below 700 K the transport is mediated by electrons (holes), while as the temperature is increased the ionic component of the current grows [8]. As follows from studies of the electrical conductivity in weak and strong dc and weak ac electric fields, the most probable mechanism of charge transport at temperatures below 600 K is hopping. Electrons (holes) can hop over extended clusters of finite size [9].

The permittivity of solids exhibiting photoconductivity and/or photoluminescence varies quite frequently under illumination; in other words, these solids exhibit the photodielectric effect (PDE). The PDE has long been studied intensely in crystal phosphors [10]. Two mechanisms are used most often to explain this effect: (i) the PDE being due to the photoconductivity in a nonuniform material and (ii) the PDE being due to a real variation of the polarizability of the medium through photoexcitation of certain centers. In addition to these two mechanisms, it was shown theoretically in [11] that the PDE can occur in disordered semiconductors.

As already mentioned, $PbMoO_4$ crystals represent a partially disordered medium exhibiting photoconductivity and photoluminescence. These features of the crystals suggest that illumination could affect their dielectric properties.

1063-7834/05/4710-1854$26.00

2. EXPERIMENT

The studies were carried out on lead molybdate crystals melt-grown by the Czochralski method. The charge was prepared using standard techniques, namely, by solid-state synthesis from thoroughly mixed lead and molybdenum oxides of extra-high purity taken in a ratio close to the stoichiometric ratio. The crystals were optically transparent, uniform, and yellow in color. They were used to prepare plane-parallel plate samples 1–3 mm thick, with the (001) plane as the major face (type 1 samples). Platinum electrodes were deposited on the polished sides of the samples. One of the electrodes was semitransparent with light transmission of ~20%. In addition, in some experiments, we used parallelepiped-shaped samples all of whose the sides were polished (type 2 samples). Solid platinum electrodes were evaporated on the (001) sides. The capacitance and conductivity of the samples were measured in a weak ac electric field by the bridge technique in the frequency range 200 Hz–20 kHz. The sample temperature was varied in the course of measurements from 300 to 450 K. The samples were illuminated by white or monochromatic light through a semitransparent electrode (for type 1 samples) or through a side face perpendicular to the electrodes (for type 2 samples). The illumination intensity was 5–7 $\mu W\ cm^{-2}$.

3. RESULTS AND DISCUSSION

Some of the results obtained in measurements of the effect of illumination on the permittivity of lead molybdate at several frequencies and temperatures are listed in the table. The permittivity of a sample in the dark (ε_d) is close to the value quoted in reference books; it is weakly dependent on temperature and on the measuring field frequency. Illumination of a sample with white light increases the low-frequency permittivity ε_l. The difference $\Delta\varepsilon = (\varepsilon_l - \varepsilon_d)$ is a few units at room temperature, but at close to 400 K $\Delta\varepsilon$ it exceeds the value of ε_d by more than twofold. Illumination affects ε only at low frequencies. Indeed, $\Delta\varepsilon$ is small at 1 kHz and becomes practically zero at frequencies above 2 kHz. Thus, lead molybdate crystals exhibit a low-frequency PDE. Illumination of a sample also changes its conductivity; i.e., $\Delta\sigma = \sigma_l - \sigma_d$ is nonzero, where σ_l and σ_d are the sample conductivities under illumination and in the dark, respectively.

Effect of illumination on the permittivity and electrical resistivity of $PbMoO_4$ crystals with d = 0.8 mm

F, Hz	300		500		1000	
T, K	300	400	300	400	300	400
ε_d	38	59	37	45	35	40
ε_l	45	168	39	89	36	47
$\Delta\varepsilon$	7	109	2	44	1	7
σ_d, $10^{-8}\ \Omega^{-1}\ cm^{-1}$		5.4		5.4		5.3
σ_l, $10^{-8}\ \Omega^{-1}\ cm^{-1}$		13.5		12.9		9.5
$\Delta\sigma$, $10^{-8}\ \Omega^{-1}\ cm^{-1}$		8.1		7.5		4.2

The magnitude of the PDE depends on the sample thickness, temperature, measuring field frequency, and illumination time, among other factors. The temperature dependence of $\Delta\varepsilon$ measured on samples of different thickness in close to stationary conditions ($\Delta\varepsilon \sim 0.8\Delta\varepsilon_{st}$) is displayed graphically in Fig. 1, which shows that the PDE grows with decreasing crystal thickness. At temperatures of ~400 K, $\Delta\varepsilon(T)$ passes through a broad maximum. $\Delta\varepsilon$ reaches the steady state a long time after the illumination is switched on (Fig. 2).

After the illumination is switched on, $\Delta\varepsilon$ varies in accordance with the relation $\Delta\varepsilon = \Delta\varepsilon_{st}(\gamma - \exp(-\tau/\tau_\varepsilon))$,

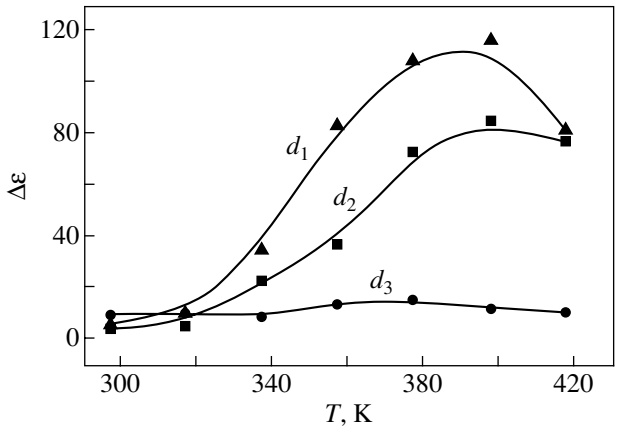

Fig. 1. Temperature dependence of the photodielectric effect in $PbMoO_4$ samples of various thicknesses: d_1 = 0.8 mm, d_2 = 1.5 mm, and d_3 = 2.7 mm. F = 300 Hz.

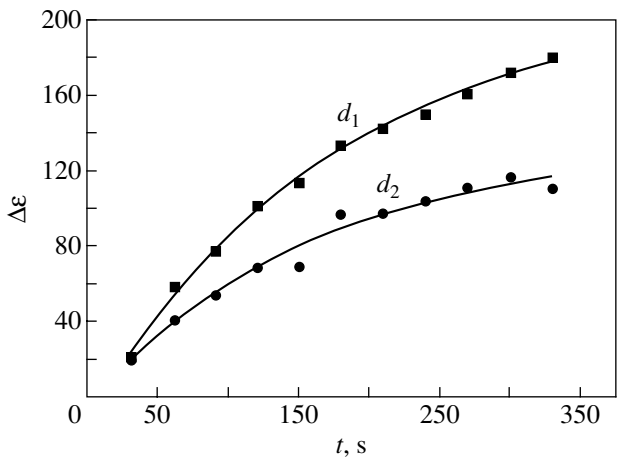

Fig. 2. Evolution of the permittivity with time after the illumination is switched-on measured on samples of different thicknesses: d_1 = 0.8 mm and d_2 = 1.5 mm. T = 100°C and F = 300 Hz.

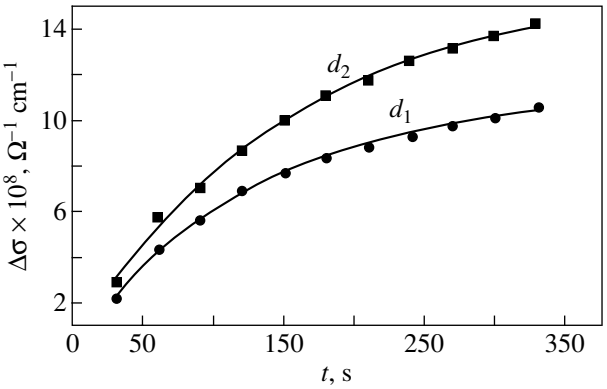

Fig. 3. Evolution of the electrical conductivity with time after the illumination is switched on. The samples and conditions of measurement are the same as those in Fig. 2.

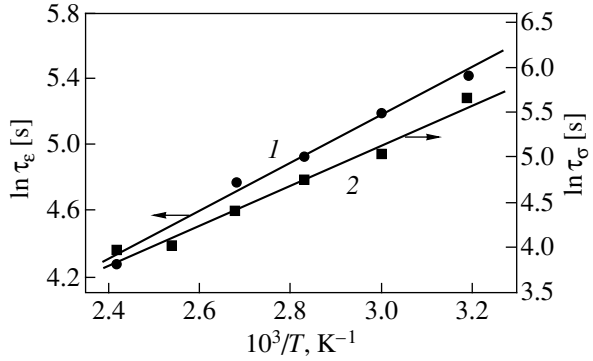

Fig. 4. Temperature dependence of the relaxation times of (*1*) the permittivity and (*2*) conductivity.

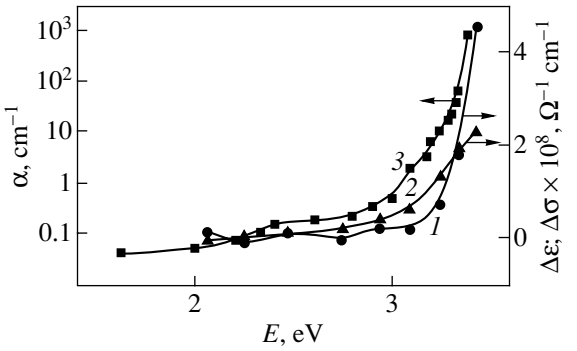

Fig. 5. Spectral dependences of the variation of (*1*) the permittivity, (*2*) electrical conductivity, and (*3*) light absorption coefficient (from [12]) of $PbMoO_4$ crystals.

where $\Delta\varepsilon_{st}$ is the steady-state value of $\Delta\varepsilon$ and τ_ε is the relaxation time. After the illumination is switched off, the recovery proceeds by the same exponential law with the same relaxation time. The value of γ depends on the sample and its prehistory and ranges from 1.1 to 1.2. The deviation of γ from unity may be caused (i) by the fact that the time dependence is not strictly exponential and (ii) by experimental errors due to nonuniform absorption of light in the crystal. We assume that the relaxation time is measured with the same accuracy as γ. The evolution of $\Delta\varepsilon$ and $\Delta\sigma$ with time is qualitatively the same. The kinetics of variation of $\Delta\varepsilon$ and $\Delta\sigma$ was studied on crystals of different thicknesses d (Figs. 2, 3). It was established that the relaxation times τ_ε are 180 ± 25 s and 170 ± 30 s and the relaxation times τ_σ are 130 ± 50 s and 160 ± 50 s for samples with $d_1 = 0.8$ mm and $d_2 = 1.5$ mm, respectively. In view of the fairly long time taken for a measurement and of the need to restore a sample to the equilibrium state before each repeated measurement (a procedure which is hard to monitor), one may assume the relaxation times τ_ε and τ_σ to be the same and independent of the crystal thickness. The relaxation times τ_ε and τ_σ fall off exponentially with increasing temperature. Figure 4 plots the log relaxation times of the photoconductivity (τ_σ) and of the PDE (τ_ε) vs reciprocal temperature. We see that these relations can be satisfactorily fitted by the expression $\ln\tau = \tau_0\exp(\Delta E/kT)$. Thus, the variation of the PDE and photoconductivity is an activated process with an activation energy ΔE (k is the Boltzmann constant). The temperature dependence of the relaxation times τ_ε and τ_σ permit estimation of the activation energy of these processes. The values of the activation energies of the PDE and conductivity obtained by averaging over three measurements are $\Delta E_\varepsilon = (0.14 \pm 0.03)$ eV and $\Delta E_\sigma = (0.17 \pm 0.04)$ eV. While these values coincide to within experimental error, the results obtained in different experiments seem to suggest that $\Delta E_\varepsilon < \Delta E_\sigma$.

The above observations of the effect of illumination on the properties of a crystal were obtained under illumination by white light through a semitransparent electrode. Figure 5 shows the spectral dependences of $\Delta\varepsilon$ and $\Delta\sigma$ in the visible and near UV regions. Also shown is the light absorbance α taken from [12]. The dependences of $\Delta\varepsilon$ and $\Delta\sigma$ on photon energy are seen to differ markedly for energies above 3 eV. One observes also a difference in the dependences of $\Delta\varepsilon$ and $\Delta\sigma$ on the illumination intensity. It was established that $\Delta\varepsilon$ scales proportionally to the square and $\Delta\sigma$ to the first power of the illumination intensity. The penetration depth of light causing a change in the conductivity and permittivity does not exceed 0.3 mm. Therefore, an illuminated sample may be considered a layered medium with the permittivity and conductivity distributed across the sample. This representation allows qualitative interpretation of the dependence of $\Delta\varepsilon$ and $\Delta\sigma$ on the crystal thickness. The above differences in the behavior of $\Delta\varepsilon$ and $\Delta\sigma$ suggest, however, that light acts simultaneously on ε and σ. The spectra of excitation and, hence, of the variation of σ and ε with depth are somewhat different, which considerably complicates analysis of the system.

Additional information on the nature of the PDE in lead molybdate can be derived from measurements of

the sample parameters performed in a different illumination geometry. Studies were therefore carried out under illumination of a sample side perpendicular to the electrodes. The temperature dependences of the variation of the capacitance ΔC and of the conductivity ΔG of a sample under illumination of a side of a sample are presented graphically in Fig. 6. The results of these measurements are in good qualitative agreement with those obtained in the transverse geometry. Special measures were taken to provide uniform illumination of the sample. In these conditions, the sample can be represented by a nonuniform layered structure with distributed conductivity and permittivity. An equivalent scheme of the sample consists of a capacitance and a resistance connected in parallel. Conductivity should not affect the sample capacitance noticeably. The results obtained provide an additional argument for the variation of permittivity under illumination being real.

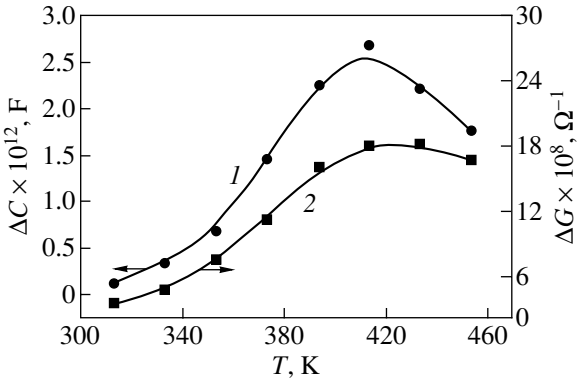

Fig. 6. Temperature dependence of the variation of (*1*) the capacitance and (*2*) conductivity of a $PbMoO_4$ sample under illumination of a side perpendicular to the electrodes. F = 500 Hz.

The permittivity of some complex oxides (for instance, perovskites) measured at low frequencies and comparatively high temperatures (above the Curie point in ferroelectrics) is known to be high [13]. An analysis of the possible cause for the high permittivity in these materials is given in [14]. As follows from that analysis, the complex conductivity of a spatially uniform medium does not contain an imaginary component for any mechanism of conduction (including hopping). If, however, the medium is an array of groups of potential wells separated by barriers of a certain height and the groups themselves are separated by higher potential barriers, then the complex conductivity of the medium will have an imaginary component. This model is similar in many respects to that of extended clusters of finite size; such a model is usually employed to describe hopping transport in partially disordered solids [15].

As already mentioned, $PbMo(W)O_4$ crystals are substantially disordered. They have, in addition to intrinsic point defects of various natures, complex associates of both paired and extended defects. The spatial distribution of these defects is nonuniform. The electronic levels of defects are localized near the edges of the bandgap, and the density of states increases as one approaches the bandgap edges. An interesting feature of these states is that the levels located near the lower edge of the conduction band are empty in the ground (nonexcited) state, while the levels in the proximity of the upper edge of the valence band are filled by electrons. Hence, just as in classical disordered solids, the density-of-states tails of these crystals extend into the bandgap [16]. Light-induced carrier excitation gives rise to the appearance of electrons in localized states near the conduction band and of holes near the valence band. Carrier hopping over localized states can mediate the electrical conductivity of crystals and contribute to permittivity. Intrinsic illumination of a crystal brings about an electron redistribution over localized states. It is conceivable that an electron absorbing a photon first transfers to the conduction band and then is captured into a localized state. In this model, the time required for the conductivity and permittivity to reach the steady state under illumination is actually the lifetime of electrons (holes) in these levels. We may assume the most probable mechanism responsible for the decrease in the concentration of captured carriers to involve their thermal excitation into the conduction or valence band followed by recombination. If this is so, the activation energy derived from the temperature dependence of the PDE relaxation time should characterize the depth of the localized states accounting for the permittivity variation.

The magnitude of the PDE should be determined by the concentration and occupancies of localized states before illumination. The results of measurements obtained in multiple dark-illumination cycles are reproducible. However, prolonged illumination by white light (solar light or a mercury lamp without a color filter) brings about darkening of the crystal. The absorbance increases throughout the visible range, while the sample remains spatially optically uniform. The specific mechanism responsible for the light-induced coloration of $PbMoO_4$ crystals is unknown. It is conceivable that room-temperature illumination does not give rise to the redistribution and formation of new lattice defects. The change in color may be caused only by electronic transitions. Our studies revealed that the PDE in crystals subjected to preliminary illumination is substantially larger, an effect that bears out the suggestion that defects play a dominant part in its onset.

REFERENCES

1. P. Lecoq, in *Proceedings of the International Conference on Inorganic Scintillators and Their Applications, SCIWT 95*, Ed. by P. Dorenbos and C. W. E. van Eik (Delft University Press, Delft, 1996), p. 52.
2. G. A. Coquin, D. A. Pinnow, and A. W. Warner, J. Appl. Phys. **42** (6), 2162 (1971).

3. I. M. Sol'skiĭ, A. S. Voloshinovskiĭ, R. V. Gamernik, A. S. Krochuk, and Z. A. Khapko, Ukr. Fiz. Zh. **46** (8), 881 (2001).
4. T. M. Bochkova, M. D. Volnyanskiĭ, D. M. Volnyanskiĭ, and V. S. Shchetinkin, Fiz. Tverd. Tela (St. Petersburg) **45** (2), 235 (2003) [Phys. Solid State **45** (2), 244 (2003)].
5. W. Bollmann, Krist. Tech. **15** (3), 367 (1980).
6. W. van Loo, Phys. Status Solidi A **28**, 227 (1975).
7. A. Ya. Neĭman, L. M. Fedorova, and A. A. Afanas'ev, Izv. Akad. Nauk SSSR, Neorg. Mater. **22** (5), 811 (1986).
8. A. Ya. Neĭman, E. V. Tkachenko, L. M. Fedorova, A. N. Petrov, V. T. Gabriélyan, and S. M. Karagezyan, Izv. Akad. Nauk SSSR, Neorg. Mater. **16** (11), 2025 (1980).
9. M. D. Volnyanskiĭ, A. Yu. Kudzin, S. N. Plyaka, and Z. Balasme, Fiz. Tverd. Tela (St. Petersburg) **46** (11), 1946 (2004) [Phys. Solid State **46** (11), 2012 (2004)].
10. R. H. Bube, *Photoconductivity of Solids* (Wiley, New York, 1960; Inostrannaya Literatura, Moscow, 1962).
11. V. L. Bonch-Bruevich and V. D. Iskra, in *Proceedings of the 6th International Conference on Amorphous and Liquid Semiconductors: Electronic Phenomena in Non-crystalline Semiconductors* (Leningrad, 1975), p. 182.
12. V. S. Shchetinkin and M. D. Volnyanskiĭ, Vest. Dnepropetr. Nats. Univ., Fiz. Radiof. **9**, 33 (2003).
13. R. Stumpe, D. Wagner, and D. Bauerle, Phys. Status Solidi A **75**, 143 (1983).
14. V. Hugo Schmidt, G. F. Tuthill, Chi-Shun Tu, T. V. Schogoleva, and S. C. Meschia, J. Phys. Chem. Solids **57** (10), 1493 (1996).
15. H. Bottger and V. V. Bryksin, Phys. Status Solidi B **133**, 9 (1982).
16. N. F. Mott and E. A. Davis, *Electronic Processes in Non-Crystalline Materials*, 2nd ed. (Clarendon, Oxford, 1979; Mir, Moscow, 1982), Vol. 1.

Translated by G. Skrebtsov

Physics of the Solid State, Vol. 47, No. 10, 2005, pp. 1859–1862. Translated from Fizika Tverdogo Tela, Vol. 47, No. 10, 2005, pp. 1788–1790.

DEFECTS, DISLOCATIONS, AND PHYSICS OF STRENGTH

Interpretation of the Optical and EPR Spectra of the Cr^{3+} Ion in a Lithium Niobate Crystal

A. M. Leushin* and E. N. Irinyakov**

** Kazan State University, Kremlevskaya ul. 18, Kazan, 420008 Tatarstan, Russia*

e-mail: Anatoly.Leushin@ksu.ru

*** Zavoĭskiĭ Physicotechnical Institute, Kazan Scientific Center, Russian Academy of Sciences, Sibirskiĭ trakt 10/7, Kazan 29, 420029 Tatarstan, Russia*

Received November 5, 2004

Abstract—The optical and EPR spectra of the Cr^{3+} γ-center in a lithium niobate crystal are interpreted, and the energy levels of the ground-state spin quadruplet and all the experimentally revealed doublet states are described. The parameters of the Coulomb Hamiltonian for the spin–orbit interaction of electrons and their interaction with an electrostatic field of the crystal are determined. It is found that the crystal field acting on the paramagnetic ion is relatively strong and has trigonal symmetry. The Cr^{3+} ion embedded in the crystal is characterized by considerable changes in the interactions associated with the excited configurations. © *2005 Pleiades Publishing, Inc.*

1. INTRODUCTION

Crystals of lithium niobate $LiNbO_3$ have found wide application in holography, electro-optics, nonlinear optics, optical information processing devices, and transmitter–receiver systems, etc. These crystals are readily doped with rare-earth and transition-metal ions [1], which has opened new opportunities for their use in quantum electronics [2]. In recent years, lithium niobate crystals doped with Cr^{3+} ions have been intensively studied using optical spectroscopy [3–6] and electron paramagnetic resonance (EPR) [7, 8].

An important feature of lithium niobate is that the composition of this compound in the crystal state considerably deviates from stoichiometry. This manifests itself in a deficit of lithium ions, which, in turn, leads to the formation of the so-called congruent structure [9]. The congruence of lithium niobate crystals and the necessity of compensating for an excess charge upon doping bring about the formation of a great variety of lattice defects and, consequently, different types of Cr^{3+} impurity centers [4, 8]. These impurity centers are easy to identify using the EPR method but are very difficult if not impossible to distinguish from the optical spectra. Nonetheless, in recent years, with the advent of new methods for growing stoichiometric lithium niobate samples, it has become possible to decrease significantly the number of impurity centers and even to prepare samples with a single γ-center due to the substitution of Cr^{3+} ions for Li^+ ions in the crystal lattice. The study of such samples makes it possible to interpret the observed EPR and optical spectra and to elucidate the specific features of the interactions between the impurity ion and the crystal. This is especially important because these features are responsible not only for the modification of the interactions of elections in a free ion but also for the formation of the crystal field.

2. EXPERIMENTAL DATA ON THE OPTICAL AND EPR SPECTRA OF IMPURITY CENTERS

At temperatures below the ferroelectric Curie point (T_C ~ 1480 K), lithium niobate crystals have trigonal symmetry with space group **R3c** ($\mathbf{C}_{3v}^6$) [9]. Owing to the oxygen network with a hexagonal closest packing motif, the Liion has a local environment with the symmetry of point group $\mathbf{C}_3$, which is slightly different from the symmetry of point group $\mathbf{C}_{3v}$. Nonetheless, the majority of experimental and theoretical studies are based on the use of a cubic crystal field acting on the impurity centers.

In particular, it has been established from the EPR spectra of the impurity centers under investigation that the splitting of the ground-state cubic spin quadruplet $^4A_2$ (in the notation of irreducible representations of point group $\mathbf{O}_h$) amounts to 0.773 cm^{-1} [8]. In this case, the location of two Kramers doublets ($E_{1/2}^T$ at the bottom and $E_{3/2}^{'T}$, $E_{1/2}^T$, and $E_{3/2}^{'T}$ at the top in the notation of irreducible representations of double point group $\mathbf{C}_{3v}^{'}$) is opposite to that for the Cr^{3+} ion in ruby. The luminescence spectrum exhibits a broad σ-polarized band with a maximum at a frequency of 11420 cm^{-1} and a bandwidth of 2285 cm^{-1} [3] and two zero-phonon lines [5] attributed to transitions from the energy levels at 13544 and 13570 cm^{-1} in the cubic representation $^4T_2$ to the ground-state spin quadruplet $^4A_2$. The excitation and luminescence spectra contain two *R* lines at somewhat higher frequencies of 13772 and 13810 cm^{-1} [5]. These lines correspond to transitions from the $^2E(E_{3/2}^{'T})$ and

Table 1. Parameters (cm^{-1}) of the crystal field and intraionic interactions of the Cr^{3+} ion in lithium niobate

B	C	ζ	α	B_{20}	B_{40}	B_{43}	B_{4-3}	Dq	ν	ν'
414	3054	155	214	–5106	–18475	–24631	24631	1471	–1511	1271

$^2E(E^T_{1/2})$ levels located in inverse order to their arrangement observed in ruby [1, 3]. Moreover, the excitation spectrum includes two broad bands $^4T_2$ and $^4T_1$ with maxima at frequencies of 15263 and 20849 cm^{-1} and bandwidths of 1561 and 2331 cm^{-1}, respectively, both of which display predominantly σ polarization [10]. The band $^4T_2$ is characterized by two relatively narrow lines at frequencies of 14053 and 14635 cm^{-1}, which are assigned to the transitions to the energy levels of the split cubic orbital triplet $^2T_1$ [5, 10]. The band $^4T_1$ also contains two lines at frequencies of 19238 and 20243 cm^{-1}, which are supposedly caused by the transitions to the energy levels of the split cubic orbital triplet $^2T_2$ [5, 10].

It is well known that the origin of the broad bands attributed to the transitions between the spin quadruplet states is primarily due to the interactions of electrons of the impurity centers with lattice vibrations [11], whereas their role in the formation of the zero-phonon lines and the lines assigned to the transitions from the ground-state quadruplet $^4A_2$ to the doublet states is not so important. Therefore, while not claiming to explain the location of the broad bands, we may try to interpret all the remaining features in the experimental spectra in terms of the theory of electronic transitions, which allows for the interactions of the electrons of the impurity center with each other and with the electrostatic field of the crystal.

3. INTERPRETATION OF THE Cr^{3+} EPR SPECTRA

In order to describe the observed spectra of the Cr^{3+} ion in the lithium niobate crystal, we constructed the Hamiltonian matrix

$$H = \sum_{i<j}\frac{e^2}{r_{ij}} + \zeta\sum_{i=1}^{3}(s_i l_i) + \alpha L(L+1) + \sum_{i=1}^{3}[B_{20}C_0^{(2)} + B_{40}C_3^{(4)} + B_{43}C_3^{(4)} - B_{4-3}C_{-3}^{(4)}]_{(i)} \quad (1)$$

for all 120 states of the $3d^3$ configuration included in the schematic diagram of the total angular momentum of the Cr^{3+} ion. In relationship (1), the first term describes the electrostatic repulsion between the electrons with the Racah parameters B and C. The second term accounts for the spin–orbit interaction of electrons, which depends on the one-electron parameter ζ. The third term is the Trees correction operator (where α is the Trees parameter and L is the magnitude of the total angular momentum of the Cr^{3+} ion), which takes into account the excited configurations and interactions of the orbit–orbit type [12, 13]. The last term in relationship (1) characterizes the interaction between the Cr^{3+} ion and the crystal field with the symmetry of point group $\mathbf{C}_{3v}$, which is written in the Wybourne notation [14] (where B_{20}, B_{40}, B_{43}, $B_{4-3} = -B_{43}$ are the Wybourne parameters and $C_q^{(k)}$ stands for the operators of the spherical functions). The matrix elements of the angle-variable-dependent operators were calculated by standard methods with the use of the genealogical coefficients and n–j symbols [14, 15], and the quantities B, C, ζ, α, and B_{kq} were treated as variable parameters.

For theoretical description of the spectrum, we developed a computer program. With this program, it is possible to make a self-consistent comparison of the theoretical energy levels E^T with the experimental values E^{exp} by minimizing the residual function $F(x_1, \ldots, x_n) = \sum_i W_i(E_i^T(x_1, \ldots, x_n) - E_i^{exp})^2$, where the parameters x_i act as variables and E_i and W_i are the energy and the weighting factor of the ith level, respectively. The program developed offers the best description of the location of the experimental energy levels and gives the best set of parameters, provided the experimental and theoretical energy levels are brought into one-to-one correspondence. In the situation we have been considering, it is not known which of the theoretically obtained Kramers doublets should correspond to the experimental locations of the energy levels of the $^2T_4$ and $^2T_2$ doublet groups. This uncertainty is further complicated by the lack of any information regarding the properties of the transformation of the states. In this respect, we had to first manually search for the theoretical levels which are best suited to the energy and only then carry out self-consistent calculations. The parameters of the crystal field and intraionic interactions obtained from this procedure are given in Table 1. This table also presents the parameters Dq, ν, and ν' usually used to describe the spectra of the iron group ions in the trigonal crystal field. The conformity of the theory to the experiments can be judged from Table 2, which lists the theoretical E_i^T and experimental E_i^{exp} levels. Since 22 of the 60 Kramers doublets in the $3d^3$ configuration of the Cr^{3+} ion fall into the transparent region of the crystal, Table 2 presents data for them only.

The results of calculating the spectrum of the Cr^{3+} γ-center in lithium niobate demonstrated that the Cr^{3+} ion is subjected to a strong crystal field of trigonal symmetry. It is this splitting of the $^4T_2$ cubic level by the strong

Table 2. Energy levels (cm^{-1}) of the Cr^{3+} ion in lithium niobate

Level number	Properties of the transformation of the states			Theory	Experiment	Dominant states
1	$^4A_2$	A_2^T	$E_{3/2}^{T}$	0	0	^4F
2			$E_{1/2}^T$	0.772	0.773	^4F
3	$^4T_2$	A_1^T	$E_{3/2}^{T}$	13525	13544	^2GDH
4			$E_{1/2}^T$	13584	13570	^2GDH
5	^2E	E^T	$E_{3/2}^{T}$	13788	13772	^2PGH
6			$E_{1/2}^T$	13796	13810	^2PGH
8	$^2T_1$	E^T	$E_{3/2}^{T}$	14057	14053	$^4F^2PH$
9			$E_{1/2}^T$	14058	–	$^4F^2PH$
12		A_2^T	$E_{3/2}^{T}$	14632	14635	$^4F^2PH$
20	$^2T_2$	E^T	$E_{3/2}^{T}$	19238	19238	^2DHGF
21			$E_{1/2}^T$	19251	–	^2DHGF
22		A_1^T	$E_{1/2}^T$	20244	20243	^2DHGF

trigonal crystal field that is responsible for the observed zero-phonon levels. The wave functions of these levels, as well as the wave functions of the ^2E levels, which give rise to the *R* lines, become both quadruplet and doublet in character due to the combined effects of the crystal field and the spin–orbit interaction and, hence, substantially impede the interpretation of the experimental spectrum. Consequently, all attempts to explain the experimental data in the cubic field approximation [4] cannot meet with success. The cubic component of the crystal field in lithium niobate is weaker than that in ruby. The sign of the parameter ν of the trigonal crystal field is opposite to that for ruby. The splitting of the cubic level $^2T_1$ in the trigonal crystal field turned out to be very small. The increased parameter α, as compared to its value for the free ion (70 cm^{-1}), indicates that the admixture of the excited configurations with the ground-state configuration $3d^3$ must be taken into account. According to the estimates obtained within the point charge model, the parameters of the odd crystal-field potential, which is responsible for this admixture, are sufficiently large in the case of the lithium niobate crystal.

ACKNOWLEDGMENTS

The authors would like to thank B.Z. Malkin, A.A. Kaplyanskiĭ, and S.A. Basun for their participation in discussions of the results and helpful remarks and Y.Y. Yeung (Hong Kong Polytechnic University) for kindly providing the Computer Package for Crystal Field Analysis of $3d^n$-ions program, which was used in the preliminary calculations and testing of the program we developed.

REFERENCES

1. G. Burns, D. F. O'Kane, and R. S. Title, Phys. Lett. **23** (1), 56 (1966).
2. T. Y. Fan, A. Gordova-Plaza, and R. L. Byer, *Spectroscopy of Solid-State Laser-Type Materials*, Ed. by B. Di Bartolo (Plenum, New York, 1987).
3. A. M. Glass, J. Chem. Phys. **50** (4), 1501 (1969).
4. P. I. Macfarlane, K. Holliday, J. F. H. Nicholls, and B. Henderson, J. Phys.: Condens. Matter **7** (49), 9643 (1995).
5. G. M. Salley, S. A. Basun, A. A. Kaplyanskii, R. S. Meltzer, K. Polgar, and U. Happek, J. Lumin. **87–89**, 1133 (2000).

6. S. A. Basun, A. A. Kaplyanskiĭ, A. B. Kutsenko, V. Dierolf, T. Troster, S. E. Kapphan, and K. Polgar, Fiz. Tverd. Tela (St. Petersburg) **43** (6), 1010 (2001) [Phys. Solid State **43** (6), 1043 (2001)].
7. D. J. Rexford, Y. M. Kim, and H. S. Story, J. Chem. Phys. **52** (2), 860 (1970).
8. G. Malovichko, V. Grachev, E. Kokanyan, and O. Schirmer, Phys. Rev. B: Condens. Matter **59** (14), 9113 (1999).
9. S. C. Abrahams and P. Marsh, Acta Crystallogr., Sect. B: Struct. Sci. **42** (1), 61 (1986).
10. G. M. Salley, private communication (2000).
11. K. K. Rebane, *The Elementary Theory of Vibrational Spectra of Impurity Centers in Crystals* (Nauka, Moscow, 1968) [in Russian].
12. R. E. Trees, Phys. Rev. **85** (2), 382 (1952).
13. B. G. Wybourne, J. Chem. Phys. **40** (5), 1457 (1964).
14. B. G. Wybourne, *Spectroscopic Properties of the Rare-Earths* (Wiley Interscience, New York, 1965).
15. B. R. Judd, *Operator Techniques in Atomic Spectroscopy* (McGraw-Hill, New York, 1963).

Translated by V. Artyukhov

Physics of the Solid State, Vol. 47, No. 10, 2005, pp. 1863–1868. Translated from Fizika Tverdogo Tela, Vol. 47, No. 10, 2005, pp. 1791–1795.

DEFECTS, DISLOCATIONS, AND PHYSICS OF STRENGTH

X-ray Diffraction Study of the Effect of Neutron Irradiation on the Defect Formation in Silicon Crystals Grown by the Czochralski Method and Annealed at High Temperatures

V. A. Makara, N. N. Novikov, and B. D. Patsaĭ

Taras Shevchenko National University of Kiev, Vladimirskaya ul. 64, Kiev, 03022 Ukraine

e-mail: pacaj@univ.kiev.ua

Received March 10, 2005

Abstract—The effect of x-ray scattering by neutron-irradiated and reference (unirradiated) silicon crystals grown by the Czochralski method and annealed at temperatures of 850–1050°C on the defect formation is comparatively investigated using triple-crystal x-ray diffractometry. The sizes and concentrations of clusters composed of point defects and dislocation loops formed during decomposition of an oxygen-containing solid solution and subsequent clusterization of the point defects are calculated. *© 2005 Pleiades Publishing, Inc.*

1. INTRODUCTION

It is known that, at high temperatures, the concentration of oxygen contained in the form of a solid solution in silicon single crystals grown using the Czochralski method (*Cz*-Si) can be as high as approximately 2×10^{18} cm^{-3}. Upon annealing of these crystals in the temperature range 600–1200°C, the solid solution gradually decomposes to form a large number of structural imperfections, primarily, in the form of dislocation loops and precipitates (clusters) of point defects, most probably, those of SiO_x molecules [1]. As the temperature and duration of annealing change, the sizes of defects can reach a submicrometer scale; i.e., they can be easily identified using x-ray diffraction methods. In our previous work [2], we studied silicon crystals heat-treated under the same conditions as were used by Bender [1] and demonstrated that triple-crystal x-ray diffractometry is an efficient tool for investigating x-ray scattering by such defects. The analysis of the results obtained was based on the dynamical theory of x-ray diffraction, which has been thoroughly described by researchers from the Institute for Metal Physics, National Academy of Sciences of Ukraine (Kiev, Ukraine) [3–6], as well as by other authors [7–11]. This analysis made it possible to estimate the sizes and concentration of scattering centers and to obtain valuable information regarding their nature. The data obtained are in good agreement with direct observations under an electron microscope [1].

It is also known that irradiation of silicon crystals brings about the formation of a great number of primary (for the most part, point) defects that can coagulate during subsequent annealing of the crystal to form dislocation loops and clusters. The nature of the related processes is rather complicated and depends both on the conditions of irradiation and subsequent annealing and on the type of impurity (which does not have to be an electrically neutral impurity) contained in the silicon crystal. Since a comprehensive analysis of the effect of irradiation on semiconductor materials is given in the monograph by Vavilov *et al.* [12] and the role played by oxygen in the formation of radiation-induced defects is considered in the monograph by Bolotov *et al.* [13], we will not describe the processes occurring in these cases. Note only that irradiation of crystals should have a profound effect on the decomposition of an oxygen-containing solid solution in the silicon crystal and, consequently, lead to substantial changes in the x-ray scattering pattern. In this respect, the purpose of the present work is to carry out an x-ray diffraction investigation into the effect of irradiation on the defect formation in silicon crystals grown by the Czochralski method and annealed under the same conditions as those used earlier in [1]. Note also that the purpose of this work is of interest especially because, to the best of our knowledge, similar studies have never been performed before.

2. SAMPLE PREPARATION AND EXPERIMENTAL TECHNIQUE

Experiments were carried out with *Cz*-Si(111) (KÉF-2.0) silicon crystals grown by the Czochralski method. Samples in the form of 0.7-mm-thick plates cut out and polished under industrial conditions were irradiated in a reactor with fast neutrons at a dose of 1.76×10^{16} neutrons/cm^2. Then, the samples were subjected to heat treatment according to the procedure described in [2]. At the first stage of heat treatment, the samples were annealed at temperatures of 850, 900, 950, and 1000°C for 5 h. At the second stage of heat treatment, these samples were annealed at a temperature of 1050°C for 24 h.

1063-7834/05/4710-1863$26.00

X-ray diffraction investigations were performed on a semiautomatic triple-crystal diffractometer consisting of an x-ray source, two GS-5 goniometers, a recording device, and a computer. The sample and the analyzer crystal had independent rotation axes (parallel to each other) and could be rotated manually through an angle of 360° in steps of 1″ with an absolute error of no larger than 1″. The analyzer crystal could be continuously rotated both automatically (at a rate of 0.3 arcsec/s) and manually. The measurements were carried out using a nondispersive triple-crystal scheme (*n*, –*n*, *n*) with single symmetric reflections from the Si(111) crystal. The monochromator, which was mounted on the case of the x-ray tube, and the analyzer crystal were cut from the silicon sample grown by crucibleless-zone melting along the [111] direction.

After each stage of heat treatment, the Bragg rocking curves were recorded on the semiautomatic triple-crystal diffractometer (CuK_{α_1} radiation) with symmetric reflections from the (111) surface of the samples upon their fixed rotation with respect to the Bragg position through an angle in the range from 10″ to 100″ in steps of 5″. The rocking curves were recorded in the course of automatic step-by-step rotation of the analyzer crystal together with the detector through an angle θ toward both the positive and negative directions with respect to the Bragg position. In all cases, the intensity of radiation incident on the sample was maintained at a constant value $I_0 \cong 10^5$ cps.

The integrated intensities $R_\Sigma(\alpha)$, the half-widths $w(\alpha)$, and the peak intensities $I(\alpha)$ obtained for all three (diffuse, subsidiary, and principal) maxima revealed in the x-ray diffraction patterns were automatically displayed on a computer screen and subsequently used for data processing according to the procedure described in [2].

The static Debye–Waller factors $E = e^{-L}$ were determined from the intensity of the principal maximum $I_M(\alpha)$, because, as is known from [2, 3], the intensity of a symmetric reflection from the Si(111) surface of the crystal obeys the relationship $I_M(\alpha) \sim Ae^{-2L}/\alpha^2$, where the proportionality factor A is a composite function of the reflection plane parameters and the intensity I_0 of radiation incident on the sample.

As follows from the basic relationships given in [2–4, 14], the integrated intensities of the diffuse maxima $R_\Sigma(\alpha)$ can be represented in the form

$$R_\Sigma(\alpha) = \frac{cC^2e^{-2L}m_0J(k_0)}{2\mu_0}, \qquad (1)$$

where c is the concentration of scattering centers, C is the polarization factor, $m_0 = 0.169$ cm^{-1} is the constant accounting for the reflection from the Si(111) surface, and μ_0 is the linear photoelectric absorption coefficient. Gavrilova *et al.* [3] and Bar'yakhtar *et al.* [4] considered two experimentally observed cases: (i) $k_m > |k_0|$ and (ii) $k_m < |k_0|$. Depending on the values of R and α, we deal either with the first inequality or with the second inequality. Here, $k_0 = \frac{2\pi}{\lambda}\alpha\sin 2\theta_B$ is the shortest distance from the Ewald sphere to the point of the reciprocal lattice, $k_m = \frac{2\pi}{R_0}$ is the parameter characterizing the boundary in the distribution of the diffuse scattering between the Huang region and the Stokes–Wilson region, and R_0 is the radius of the radiation-scattering defect [5].

For the most frequently used angles α (from approximately 20″ to 100″) and CuK_α radiation, the first inequality holds at $R_0 = 3$ μm in the region corresponding to $\alpha \approx 20''$ and at $R_0 = 0.6$ μm in the region corresponding to $\alpha \approx 100''$. When the radii R_0 of radiation-scattering defects are relatively large, we deal with the second inequality.

Molodkin *et al.* [15, 16] predominantly used prolonged annealing of silicon single crystals at high temperatures ($t \approx 10$ h, $T \approx 1100$°C) under conditions where the radii of scattering centers were of the order of 2 μm. Taking into account these conditions, it was not unfounded for those authors to believe that $k_m < |k_0|$. Hence, the integrated intensity of diffuse scattering R_Σ is proportional to k_m^2/k_0^2; i.e., $R_\Sigma \sim \alpha^{-2}$. In this case, the experimental results were conveniently represented in the $\ln\alpha$–$\ln R_\Sigma$ coordinates, which, as a rule, are used in similar works.

In our experiments, in which the annealing temperatures were relatively low and the annealing times were relatively short, we supposedly dealt with the first inequality; i.e., $k_m > |k_0|$. Here, $R_\Sigma \sim (R_0^2\alpha - \ln R_0 - \ln\alpha - b)$, where b is 17.183 for clusters and 16.835 for dislocation loops. For small values of R_0 and α, the first term in parentheses can be disregarded. In this case, the integrated intensity R_Σ is a linear function of $\ln\alpha$. Consequently, the results of measurements were represented in the $\ln\alpha$–R_Σ coordinates in the form of two straight lines with different slopes (Fig. 1). Note that the same data represented in double logarithmical coordinates had a different form from the expected straight lines with a slope of 2.

3. RESULTS AND DISCUSSION

Let us consider relationship (1). Here, $J(k_0) = B(aR_0^2\alpha^2 - \ln R_0\alpha - b)$, where $B = 3.4684 \times 10^{42}R_0^6$ and $a = 2.081 \times 10^{14}$ for scattering by clusters and $B = 4.1036 \times 10^{30}R_0^4$ and $a = 4.252 \times 10^{13}$ for scattering by dislocation loops [17, 18].

In the case where the quantities R_0 and α are small and the quadratic term in the expression for $J(k_0)$ is

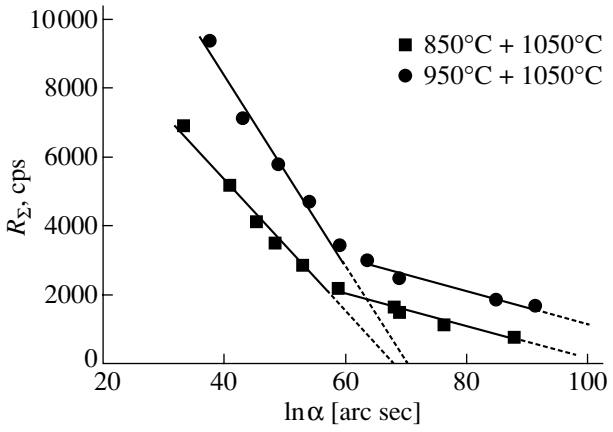

Fig. 1. Integrated intensity of the diffuse maximum as a function of the logarithm of the rotation angle for the samples subjected to primary annealing at temperatures of 850 and 950°C and secondary annealing at 1050°C.

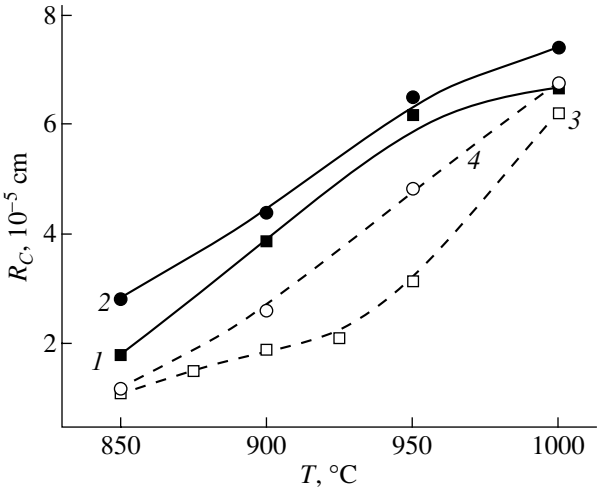

Fig. 2. Cluster size as a function of the annealing temperature for (*1*) the neutron-irradiated sample after primary annealing, (*2*) the neutron-irradiated sample after secondary annealing at 1050°C, (*3*) the unirradiated sample after primary annealing, and (*4*) the unirradiated sample after secondary annealing at 1050°C.

ignored, the integrated intensity R_Σ is a linear function of lnα. By extrapolating the dependences of the integrated intensity R_Σ on lnα to the point of intersection with the abscissa axis (lnα_0), we can calculate the effective radius of scattering centers from the expression

$$R_0 = e^{-(\ln\alpha_0 + b)}. \quad (2)$$

It should be noted that, for all the studied samples, the dependence of the integrated intensity R_Σ on lnα is characterized by two portions (Fig. 1). This suggests that the samples contain two types of defects, most probably, clusters and dislocation loops [1]. By using relationship (1) and assuming that the total scattering intensity is determined by the intensity of scattering from clusters and dislocation loops, we could calculate the effective radii of the scattering centers (Figs. 2, 3).

Taking into account that the integrated intensity of the diffuse maximum in the rocking curves is the sum of the intensities of x-ray scattering by clusters and dislocation loops ($R_\Sigma(\alpha) = R(\alpha)_C + R(\alpha)_D$ and that each of these terms is proportional to the concentration of defects c and depends exponentially on their size, the values of c_D/c_C can be determined by fitting in computer simulation experiments. The radii R_C and R_D as functions of the annealing temperature of the samples after the primary and secondary annealings are presented in Figs. 2 and 3, respectively. For comparison, these figures show the corresponding dependences for the samples cut from the same silicon ingot but not exposed to neutron radiation.

The static Debye–Waller factors L obtained from the intensity of the principal maximum are presented in Fig. 4 also in comparison with the corresponding data for the reference samples (not subjected to neutron irradiation). By assuming that the static Debye–Waller factor is determined by the sum of the root-mean-square deviations of the atoms from their equilibrium positions due to the presence of dislocation loops and clusters in the sample, we can write

$$L = L_D + L_C. \quad (3)$$

Then, according to [3, 19], we have

$$L = \frac{2c_D\Lambda_\sigma^2 C^2 m_0 J_D(0)}{\pi^2 \sin^2\theta_B R_D a_D} + c_C n_0 \eta^{\frac{3}{2}}, \quad (4)$$

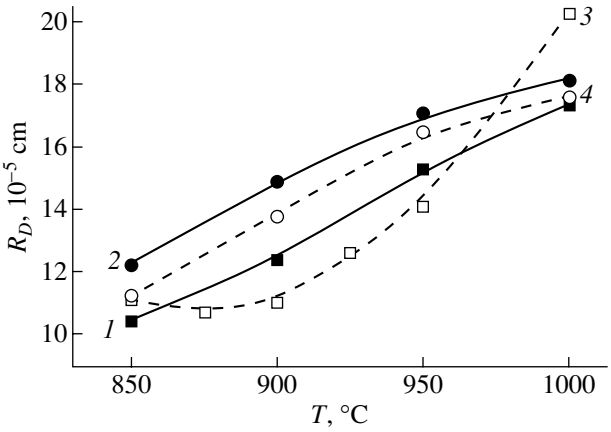

Fig. 3. Dislocation loop size as a function of the annealing temperature for (*1*) the neutron-irradiated sample after primary annealing, (*2*) the neutron-irradiated sample after secondary annealing at 1050°C, (*3*) the unirradiated sample after primary annealing, and (*4*) the unirradiated sample after secondary annealing at 1050°C.

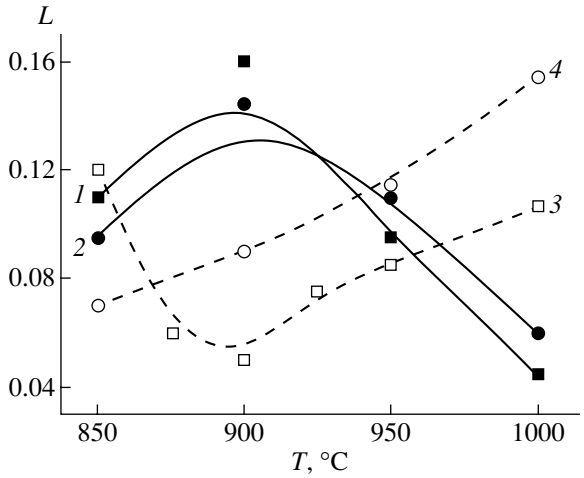

Fig. 4. Static Debye–Waller factor as a function of the annealing temperature for (*1*) the neutron-irradiated sample after primary annealing, (*2*) the neutron-irradiated sample after secondary annealing at 1050°C, (*3*) the unirradiated sample after primary annealing, and (*4*) the unirradiated sample after secondary annealing at 1050°C.

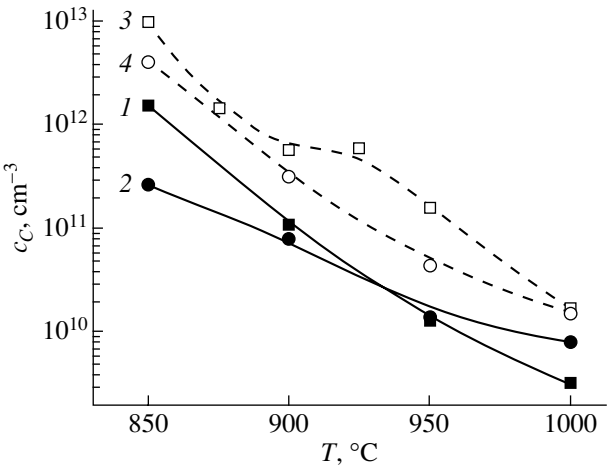

Fig. 5. Cluster concentration as a function of the annealing temperature for (*1*) the neutron-irradiated sample after primary annealing, (*2*) the neutron-irradiated sample after secondary annealing at 1050°C, (*3*) the unirradiated sample after primary annealing, and (*4*) the unirradiated sample after secondary annealing at 1050°C.

where Λ_σ is the extinction length; $J_D(0)$ is the function $J(k_0)$ at $\alpha = 0$; c_D and c_C are the concentrations of dislocation loops and clusters occupied by the precipitate, respectively; $a_D = -6.654 - \ln R_D$; $n_0 = V_P/\nu_c$ is the number of unit cells; $V_P = \pi R_C^2 h_p$; $\eta = \alpha_0 n_0^{1/3} a_0 H/2\pi$; $\alpha_0 = \Gamma\varepsilon(3\pi^2/4)^{1/3}$; $h_p = a_1 R_C (L/R_C)^{a_2}$; $a_1 = 3.96$; $a_2 = 0.597$; $\varepsilon = 0.0242$; a_0 is the lattice constant; $\Gamma \approx 0.6$; $H = 2 \times 10^8$ cm^{-1}; and R_D and R_C are the radii of dislocation loops and clusters, respectively.

In relationship (4), the first and second terms contain the defect concentrations c_D and c_C. Knowing the concentration ratio c_D/c_C, we can calculate their values. The concentrations c_C and c_D, as functions of the annealing temperature, are presented in Figs. 5 and 6, respectively.

Let us briefly analyze the results obtained. First and foremost, it is evident that the sizes of clusters in neutron-irradiated crystals (especially in the samples subjected only to primary annealing) are larger than those in the unirradiated samples by a factor of approximately 2 or 3. This difference reaches a maximum after primary annealing at a temperature of 900°C and somewhat (even though incompletely) levels off after secondary annealing at 1050°C. The sizes of dislocation loops in the neutron-irradiated and unirradiated crystals are almost identical, especially in the samples subjected to secondary annealing.

The static Debye–Waller factors for the neutron-irradiated samples are significantly larger than those for the unirradiated samples, especially after primary annealing at a temperature of 900°C.

An increase in the size of clusters naturally leads to a decrease in their concentration (Figs. 5, 6). This is most pronounced for the samples subjected to primary annealing. The variation in the concentration ratio of defects c_D/c_C due to heat treatment is noteworthy. For the unirradiated samples, the concentration ratio begins to increase rapidly at temperatures above 900°C. For the neutron-irradiated samples, the concentration ratio increases even at considerably lower temperatures. Such a behavior of the concentration ratio indicates a

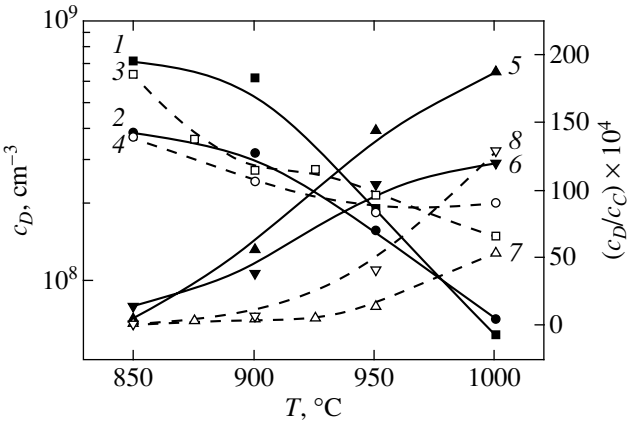

Fig. 6. (*1–4*) Concentration of dislocation loops as a function of the annealing temperature for (*1*) the neutron-irradiated sample after primary annealing, (*2*) the neutron-irradiated sample after secondary annealing at 1050°C, (*3*) the unirradiated sample after primary annealing, and (*4*) the unirradiated sample after secondary annealing at 1050°C. (*5–8*) Ratio c_D/c_C as a function of the annealing temperature for the neutron-irradiated sample after (*5*) primary and (*6*) secondary annealing and for the unirradiated sample after (*7*) primary and (*8*) secondary annealing.

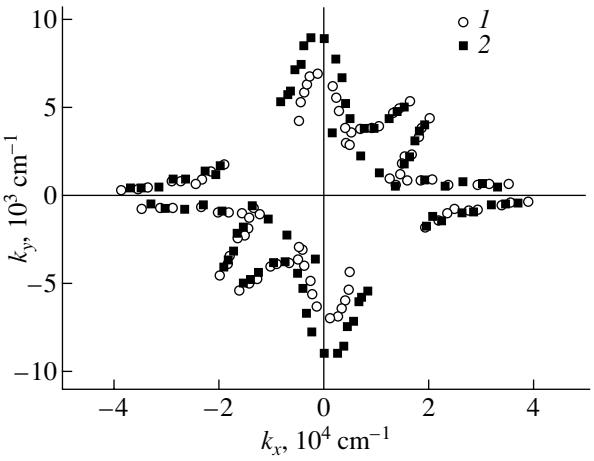

Fig. 7. Isointensity curves for X-ray scattering in the vicinity of the (111) point of the reciprocal lattice for (*1*) the unirradiated sample and (*2*) the samples subjected to neutron irradiation (I = 50 cps).

higher probability of formation of dislocation loops in neutron-irradiated samples, which, apparently, can be associated with the increase (especially pronounced in the temperature range 900–950°C) in the size of clusters in these samples and, hence, with the increase in the probability of displacement of dislocation loops by larger sized clusters. Although the concentration of dislocation loops increases rapidly at an annealing temperature of 1000°C or higher, it is apparently impossible, as follows from the results obtained, to prepare a structure consisting predominantly of dislocation loops through high-temperature treatment of oxygen-containing crystals.

It turned out that the characteristics of the defect structure in the neutron-irradiated and unirradiated samples subjected to primary annealing at temperatures close to 900°C differ most significantly. For this temperature, we constructed isointensity curves for x-ray scattering in the vicinity of the (111) point of the reciprocal lattice (Fig. 7) by using the relationships $k_x = \frac{2\pi}{\lambda}\theta\cos\theta_B$ and $k_y = \frac{2\pi}{\lambda}(2\alpha - \theta)\sin\theta_B$. These curves clearly demonstrate that the diffuse part of x-ray scattering in the neutron-irradiated samples increases, whereas the coherent part of x-ray scattering remains virtually unchanged.

4. CONCLUSIONS

In this work, we carried out a comparative analysis of the characteristics of the defects formed in the course of thermal decomposition of an oxygen-containing solid solution in neutron-irradiated and reference (unirradiated) silicon crystals grown by the Czochralski method and then subjected to heat treatment.

It was found that, in both cases, the decomposition of the oxygen-containing solid solution results in the formation of precipitates and dislocation loops. However, the sizes of the precipitates in the neutron-irradiated samples are considerably larger than those in the reference samples annealed under the same conditions. This can be associated with the coagulation of primary radiation defects formed under neutron irradiation. The sizes of the dislocation loops also somewhat, although less noticeably, increase upon heat treatment.

An increase in the precipitate size leads to a decrease in the precipitate concentration. As the annealing temperature of neutron-irradiated samples increases, the concentration ratio c_D/c_C begins to increase rapidly even at relatively low annealing temperatures. For unirradiated samples, this ratio increases only after annealing at temperatures above 900°C.

ACKNOWLEDGMENTS

We would like to thank P.G. Litovchenko, A.A. Groza, and L.A. Matveeva (Institute for Nuclear Research, National Academy of Sciences of Ukraine) for performing neutron irradiation of the samples used in this study.

REFERENCES

1. H. Bender, Phys. Status Solidi A **86** (1), 245 (1984).
2. N. N. Novikov and B. D. Patsaĭ, Metallofiz. Noveĭshie Tekhnol. **25** (2), 257 (2003).
3. E. N. Gavrilova, E. N. Kislovskiĭ, V. B. Molodkin, and S. I. Olikhovskiĭ, Metallofizika (Kiev) **14** (3), 70 (1992).
4. V. G. Bar'yakhtar, E. N. Gavrilova, V. B. Molodkin, and S. I. Olikhovskiĭ, Metallofizika (Kiev) **14** (11), 68 (1992).
5. M. A. Krivoglaz, *Diffuse Scattering of X-rays and Neutrons by Fluctuation Inhomogeneities in Imperfect Crystals* (Naukova Dumka, Kiev, 1984) [in Russian].
6. M. A. Krivoglaz, *X-ray and Neutron Diffraction in Imperfect Crystals* (Naukova Dumka, Kiev, 1983) [in Russian].
7. J. R. Schneider, R. Bouchard, H. A. Graf, and H. Nagasava, Acta Crystallogr., Sect. A: Found Crystallogr. **48** (6), 804 (1992).
8. H. Trinkaus, Phys. Status Solidi B **51** (1), 307 (1972).
9. P. Zaumseil and U. Winter, Phys. Status Solidi A **73** (2), 455 (1982).
10. B. C. Larson and W. Schmatz, Phys. Rev. B: Solid State **10** (6), 2307 (1974).
11. P. H. Dederichs, J. Phys. F: Met. Phys. **3** (2), 471 (1973).
12. V. S. Vavilov, N. P. Kekelidze, and L. S. Smirnov, *Effect of Radiation on Semiconductors* (Nauka, Moscow, 1988) [in Russian].
13. V. V. Bolotov, A. V. Vasil'ev, and N. N. Gerasimenko, *Physical Processes in Irradiated Semiconductors* (Nauka, Novosibirsk, 1977) [in Russian].

14. S. I. Olikhovskii, V. B. Molodkin, E. N. Kislovskii, E. G. Len, and E. V. Pervak, Phys. Status Solidi B **231** (1), 199 (2002).
15. V. B. Molodkin, S. I. Olikhovskiĭ, E. N. Kislovskiĭ, and T. P. Vladimirova, Metallofiz. Noveĭshie Tekhnol. **19** (12), 25 (1997).
16. V. B. Molodkin, S. I. Olikhovskiĭ, E. N. Kislovskiĭ, E. G. Len', and T. P. Vladimirova, Metallofiz. Noveĭshie Tekhnol. **22** (6), 3 (2000).
17. V. B. Molodkin, V. V. Nemoshkalenko, S. I. Olikhovskii, T. P. Vladimirova, O. V. Reshetnyk, G. E. Ice, and B. C. Larson, Metallofiz. Noveĭshie Tekhnol. **20** (11), 29 (1998).
18. M. M. Novikov and B. D. Patsaĭ, Metallofiz. Noveĭshie Tekhnol. **26** (2), 261 (2004).
19. V. B. Molodkin, S. I. Olikhovskii, E. N. Kislovskii, E. G. Len, and E. V. Pervak, Phys. Status Solidi B **227** (2), 429 (2001).

Translated by N. Korovin

Physics of the Solid State, Vol. 47, No. 10, 2005, pp. 1869–1871. Translated from Fizika Tverdogo Tela, Vol. 47, No. 10, 2005, pp. 1796–1798.

DEFECTS, DISLOCATIONS, AND PHYSICS OF STRENGTH

Influence of Structural Interfaces on the Statistics of Corrosion Microcracks

V. I. Vettegren*, A. Ya. Bashkarev, G. I. Morozov**, A. A. Lebedev**, E. Yu. Nefed'ev***, and M. A. Kryuchkov***

** Ioffe Physicotechnical Institute, Russian Academy of Sciences, Politekhnicheskaya ul. 26, St. Petersburg, 194021 Russia*

e-mail: Victor.Vettegren@mail.ioffe.ru

*** St. Petersburg State Polytechnical University, Politekhnicheskaya ul. 29, St. Petersburg, 195251 Russia*

**** OAO "Polzunov Scientific and Development Association on Research and Design of Power Equipment," St. Petersburg, 193167 Russia*

Received December 1, 2004

Abstract—The amplitude distributions of acoustic emission signals generated during the formation of corrosion microcracks in loaded welded joints connecting two corrosion-resistant steel tubes are studied. For acoustic emission signal amplitudes of less than 0.6 mV and a microcrack concentration of ~10 mm^{-3}, the distribution density of the signal amplitudes is described by a gamma function. For acoustic emission signal amplitudes exceeding 1.0 mV and a microcrack concentration of greater than or equal to 10^2 mm^{-3}, the distribution density of the amplitudes exhibits two maxima, whose shape is described by a Gaussian function. The mean amplitudes of acoustic emission signals differ by a factor of 3. The change in the amplitude distribution of acoustic emission signals is explained by the effect exerted by the weld–metal interface on the microcrack formation. © *2005 Pleiades Publishing, Inc.*

1. INTRODUCTION

Recent investigations have demonstrated that the size distribution of different objects (nanodefects [1–3] and corrosion pits [4] on a metal surface, microcracks at an interface [5], structural clusters in polymers [2, 6, 7], carbon black aggregates in resin, bacteria, fungi, protein molecules [2], etc.) can be adequately described by a gamma function. It is known [8] that the gamma distribution has a thermodynamically optimum form; i.e., in this case, the configurational entropy of the system is maximum. The existence of an "equilibrium" distribution in a nonequilibrium state is explained by the fact that the time it takes for any of the aforementioned objects to form is considerably shorter than the observation interval [2].

Earlier [9], it was established that the concentration and size of microcracks near the interfaces in metals are different from those in the bulk of the material. We were intrigued by the question of how the distribution of microcracks would change near the interfaces in the metal. In order to answer this question, we undertook an investigation into the distribution of corrosion microcracks inside a welded joint and in the surrounding region. It should be noted that, until recently, the statistics of corrosion microcracks had not been studied and the main efforts of researchers had been directed toward investigating the mechanism of corrosion cracking and protecting against it [10–12].

2. EXPERIMENTAL TECHNIQUE

Two tubes (08Cr18Ni10Ti stainless steel; inner diameter, 10 mm; working length, 100 mm; thickness, 1 mm) were connected by a welded joint ~ 1 mm wide. The tubes were filled with a process condensate (pH 9.5). The vapor pressure of the solution in the tubes was equal to 9 MPa at a temperature of 300°C. The specimens were loaded with a tensile stress of 290 MPa on an IP-4M tearing machine. The clutches of the tearing machine were equipped with two acoustic emission converters. Acoustic emission signals were recorded using an SDAÉ-8 automated system.

3. KINETICS OF ACCUMULATION OF MICROCRACKS

Figure 1 shows the time dependence of the number of acoustic emission signals for one of the studied specimens. The other specimens are characterized by similar curves. It can be seen from this figure that the number of acoustic emission signals increases nonmonotonically: periods of slow accumulation alternate with periods of fast accumulation of microcracks.

This dependence was conventionally divided into seven time intervals, as is shown in Fig. 1. We determined the locations of the microcracks and analyzed the amplitude distribution of acoustic emission signals in each time interval.

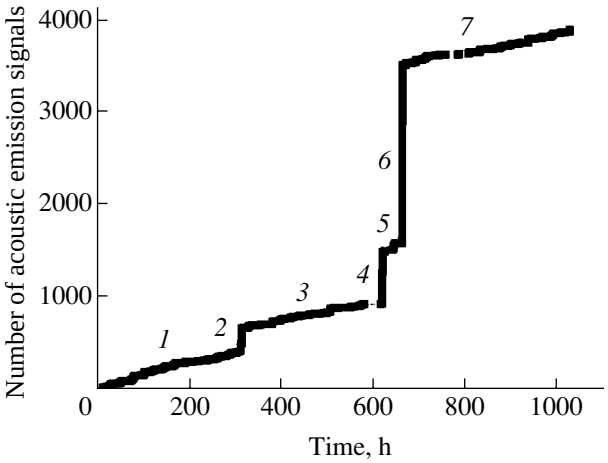

Fig. 1. Time dependence of the number of acoustic emission signals. Numerals near the curve denote time intervals in which the amplitude distributions of acoustic emission signals were calculated.

4. LOCATION OF MICROCRACKS IN A LOADED SPECIMEN

The table presents the ratio of the number of acoustic emission signals from a welded joint N_w to the number of acoustic emission signals from the surrounding region N_0. As follows from the table, the processes of crack formation in the welded joint and the surrounding region alternate: microcracks accumulate first in the vicinity of the joint, then inside the joint, then again in its vicinity, then again in the joint, etc.

The rate of accumulation of microcracks also depends on their location. For example, the rate of microcrack accumulation in the welded joint (time intervals *2*, *4*, *6*), is approximately four orders of magnitude higher than that in the surrounding region (time intervals *3*, *5*, *7*).

Ratio of the number of acoustic emission signals from the welded joint N_w to the number of acoustic emission signals from the surrounding region N_0

Time interval	N_w/N_0
1	0.2
2	2
3	0.5
4	24
5	0.05
6	110
7	0.3

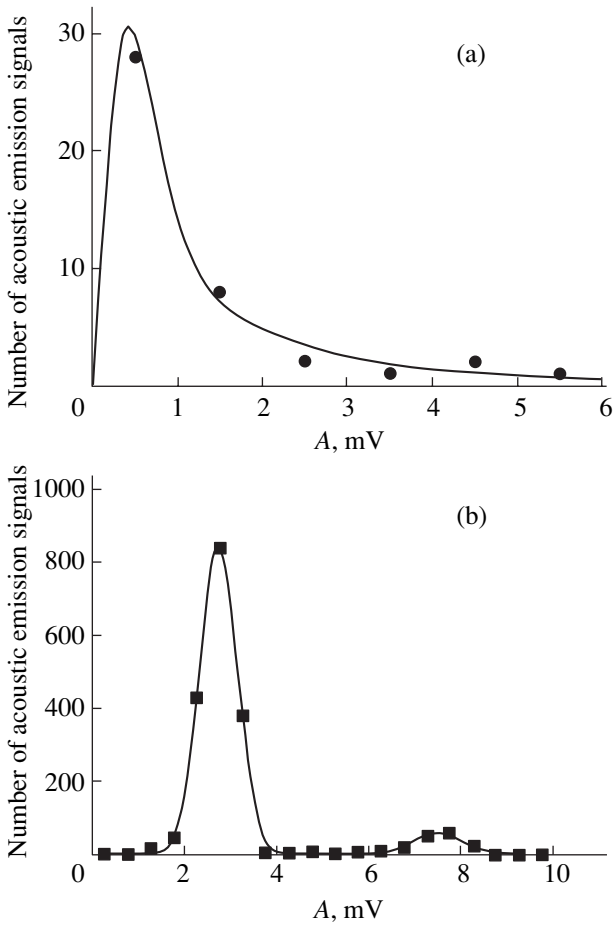

Fig. 2. Amplitude distributions of acoustic emission signals from the welded joint in time intervals (a) *2* and (b) *6*. The solid lines correspond to (a) the gamma distribution and (b) the Gaussian distribution.

5. AMPLITUDE DISTRIBUTION OF ACOUSTIC EMISSION SIGNALS FROM A WELDED JOINT

It turned out that the amplitude distribution of acoustic emission signals depends on their number and mean amplitude $\langle A \rangle$. For example, in time interval *2*, in which the mean amplitude $\langle A \rangle$ is approximately equal to 0.6 mV and the number of signals does not exceed several hundred, the amplitude distribution of acoustic emission signals can be described by the gamma function (Fig. 2a):

$$n(A) = n_0 A^2 \exp\left(-\frac{A}{\langle A \rangle}\right), \quad (1)$$

where A is the amplitude and n_0 is the normalizing factor.

A different situation takes place in other time intervals, in which the mean amplitude exceeds 0.6 mV and the number of acoustic emission signals is of the order of 10^3 (Fig. 2b). In this case, there are no acoustic emission signals with $A < 1$ mV and the amplitude distribu-

tion exhibits two maxima centered at ~2.5 and ~7.5 mV and is described by the Gaussian function

$$n(A) = n_0 \exp\left(-\frac{(A - \langle A\rangle)^2}{2\sigma^2}\right), \quad (2)$$

where σ is the variance.

The change in the distribution density of the acoustic emission signals can be explained by the effect exerted by the weld–metal interface on the microcrack formation. The fraction of the volume occupied by the microcracks reaches ~6–7%. In accordance with the concentration fracture criterion [13], when the fraction of the volume occupied by the microcracks reaches a critical value of ~5%, the interaction between the microcracks is drastically enhanced and they begin to enlarge. As was noted in [9], the concentration and sizes of microcracks change near the interfaces in metals. Probably, the interaction of microcracks is enhanced in the vicinity of the interfaces, which leads to a change in the size distribution of microcracks in the welded joint.

It is known [14] that the amplitude of acoustic emission signals is related to the microcrack size L by the following expression: $A \approx BL^{1.5}$. In our case, the proportionality coefficient B for the material of the welded joint is unknown. For a crude estimate of the microcrack sizes, we use the proportionality coefficient $B \approx 0.024$ mV/μm obtained in [14] for a spring steel. As a result, we obtain the mean size of microcracks $\langle L\rangle \approx 8.6$ μm for the mean amplitude $\langle A\rangle = 0.6$ mV, $L \approx 22.5$ μm for $\langle A\rangle = 2.5$ mV, and $L \approx 46$ μm for $\langle A\rangle = 7.5$ mV. Therefore, the mean sizes of microcracks differ by a factor of approximately 3. This ratio of the mean sizes is not an exception. Recent investigations into the amplitude distributions of acoustic emission signals in strained granites [5, 15, 16], as well as analyses of the sizes of nanodefects [1–3] and corrosion pits [4] on a metal surface and the sizes of structural clusters in polymers [2, 6, 7], have demonstrated that their mean values also differ by a factor of 3.

6. CONCLUSIONS

Thus, it was established that the amplitude distribution of acoustic emission signals from a welded joint depends on the size and concentration of the microcracks. When the mean amplitude of acoustic emission signals (which is approximately proportional to the microcrack size) reaches ~ 0.6 mV and the number of signals does not exceed several hundred, the distribution density of the signal amplitudes is described by a gamma function. When the mean amplitude reaches 2.5 mV and the number of acoustic emission signals is equal to 10^3, the distribution density is described by a Gaussian function. The change in the amplitude distribution with an increase in the size and concentration of microcracks is apparently due to a strong enhancement of their interaction near the interface between the welded joint and the metal. The mean sizes of microcracks in the welded joint differ by a factor of 3.

ACKNOWLEDGMENTS

This work was supported by the Russian Foundation for Basic Research (project no. 03-05-64831) and the joint grant from the Ministry of Education and Science and the Ministry for Atomic Energy of the Russian Federation (project no. 4.03-01).

REFERENCES

1. H. G. Kilian, V. I. Vettegren, and V. N. Svetlov, Fiz. Tverd. Tela (St. Petersburg) **42** (11), 4024 (2000) [Phys. Solid State **42** (11), 2083 (2000)]; Fiz. Tverd. Tela (St. Petersburg) **43** (11), 2107 (2001) [Phys. Solid State **43** (11), 2199 (2001)].
2. H. G. Kilian, M. Koepf, and V. I. Vettegren, Prog. Colloid Polym. Sci. **117**, 172 (2001).
3. A. Ya. Bashkarev, V. I. Vettegren', and V. N. Svetlov, Fiz. Tverd. Tela (St. Petersburg) **44** (7), 1260 (2002) [Phys. Solid State **44** (7), 1316 (2002)].
4. V. I. Vettegren, A. Ya. Bashkarev, and V. I. Morozov, Pis'ma Zh. Tekh. Fiz. **28** (13), 1 (2002) [Tech. Phys. Lett. **28** (7), 533 (2002)].
5. V. I. Vettegren, V. S. Kuksenko, N. G. Tomilin, and M. A. Kryuchkov, Fiz. Tverd. Tela (St. Petersburg) **46** (10), 1793 (2004) [Phys. Solid State **46** (10), 1854 (2004)].
6. S. V. Bronnikov, T. E. Sukhanova, and L. A. Laĭus, Vysokomol. Soedin., Ser. A **44** (5), 940 (2002).
7. S. V. Bronnikov and T. E. Sukhanova, Image Anal. Stereol. **20** (1), 105 (2001).
8. B. L. Lavenda, *Statistical Physics: A Probabilistic Approach* (Wiley, New York, 1997).
9. P. G. Cheremskoĭ, V. V. Slezov, and V. I. Betekhtin, *Pores in Solids* (Énergoatomizdat, Moscow, 1990) [in Russian].
10. M. Iovchev, *Corrosion of Thermal Power and Nuclear Power Equipment* (Énergoatomizdat, Moscow, 1988) [in Russian].
11. N. P. Zhuk, *A Course of the Theory of Corrosion and Protection of Metals* (Metallurgiya, Moscow, 1976) [in Russian].
12. L. Ya. Tomashov, *The Theory and Protection of Metals* (Akad. Nauk SSSR, Moscow, 1959) [in Russian].
13. V. S. Kuksenko, V. S. Ryskin, V. I. Betechtin, and A. I. Slutsker, Int. J. Fract. Mech. **11** (5), 829 (1975).
14. Yu. E. Nefed'ev, V. A. Volkov, S. V. Kudryashov, A. I. Lyashkov, and V. N. Savel'ev, Defektoskopiya, No. 3, 41 (1986).
15. V. Kuksenko, N. Tomilin, E. Damaskinskaja, and D. Lockner, Pure Appl. Geophys. **146** (1), 253 (1996).
16. N. G. Tomilin, E. E. Damaskinskaya, and V. S. Kuksenko, Fiz. Tverd. Tela (St. Petersburg) **36** (10), 3101 (1994) [Phys. Solid State **36** (10), 1649 (1994)].

Translated by V. Artyukhov

Physics of the Solid State, Vol. 47, No. 10, 2005, pp. 1872–1878. Translated from Fizika Tverdogo Tela, Vol. 47, No. 10, 2005, pp. 1799–1805.

DEFECTS, DISLOCATIONS, AND PHYSICS OF STRENGTH

X-ray Diffraction Study of Low- and High-Angle Misorientations in LiF Crystals during Creep

B. I. Smirnov, R. S. Chudnova, and V. V. Shpeĭzman

Ioffe Physicotechnical Institute, Russian Academy of Sciences, Politekhnicheskaya ul. 26, St. Petersburg, 194021 Russia

e-mail: shpeizm.v@mail.ioffe.ru

Received December 14, 2004

Abstract—Low- and high-angle lattice misorientations in LiF single crystals subjected to tensile deformation in the temperature range 573–973 K were studied using the following x-ray diffraction techniques: the ω-scanning method, the Laue method, and the Kossel and Fujiwara widely divergent beam (WDB) methods. The fraction of the high-angle misorientation is shown to be low at low temperature, where a block structure is absent, and at high temperature, where blocks are large (~100 μm). The high-angle misorientation increases with strain faster than the low-angle misorientation. The misorientations measured by different techniques can differ because of the different areas which are illuminated by an x-ray beam and over which the misorientations are averaged. The results obtained are compared with available data on the structure of deformed alkali-halide crystals. © *2005 Pleiades Publishing, Inc.*

1. INTRODUCTION

The number of studies dealing with deformation-induced lattice misorientations has recently increased due to particular interest in the structures that appear during severe plastic deformation of solids [1–3]. Low-angle misorientations take place in the initial deformation stages and then increase with deformation [1]. The lattice misorientation depends mainly on block, fragment, or grain boundaries, which occupy a relatively small volume as compared to the volume between the boundaries. In terms of dislocation theory, the so-called block boundaries, which form during deformation and consist of edge-dislocation walls with a predominant fraction of dislocations of the same sense, have the simplest structure of the boundaries between misoriented regions in a crystal [4]. Such boundaries have been repeatedly observed in electron-microscopic (EM) studies of deformed crystalline materials; the magnification used made it possible to determine the average interdislocation spacing and the misorientation angles at a relatively low dislocation density in these boundaries [5]. The authors of [6, 7] found that both low-angle (interblock) and high-angle (interfragment) misorientations appear in LiF and NaCl crystals during creep, and the latter misorientation can form both via the accumulation of correlated low-angle misorientations between blocks and via high-angle rotations of fragment boundaries. Two types of grain boundaries are distinguished in [1]: (i) geometrically necessary block (fragment) boundaries formed by regular dislocation or disclination [3] structures with misorientation angles that are specified by the difference in the orientation (rotation) of the lattices of neighboring fragments and (ii) incidental dislocation boundaries formed by a chaotic set of dislocations trapped by a boundary. When alkali-halide crystals are subjected to uniaxial loading along the [100] direction, two pairs of mutually perpendicular {110} planes are active. Therefore, regular boundaries of the first type are most likely to form during this loading. Moreover, at high temperatures and long holding times, restructuring can occur not only via dislocation slip but also via dislocation climb, which also favors a decrease in the boundary energy and boundary-structure ordering. If the slip geometry is such that two of the four competing slip systems are predominant, boundaries formed by either predominantly edge or screw dislocations can be detected in mutually perpendicular {100} faces [8].

In this work, we study the formation of high- and low-angle misorientations in LiF crystals subjected to tension under creep conditions and the dependences of these misorientations on the strain, stress, and temperature. The study was carried out using x-ray diffraction.

2. EXPERIMENTAL

We studied LiF single crystals containing no more than 0.002 wt % Mg. The single crystals were grown by the Kyropoulos technique, annealed at 1020 K for 48 h, and cooled at a rate of 5 K/h. Then, the crystals were cleaved along their {100} cleavage planes to form $1 \times 5 \times 10$ mm samples. The samples were subjected to uniaxial tension along the [100] direction under creep conditions at test temperatures of 573, 873, and 973 K and under stresses σ = 12, 5, and 2 MPa, respectively. To analyze block or fragment misorientations, we used the ω-scanning method, the Laue method, and the Kossel and Fujiwara widely divergent beam methods.

In the ω-scanning method [9, 10], a sample is placed in a holder so that the [100] tensile axis makes an angle

of 45° with the holder axis. The goniometer of the x-ray apparatus had a holder that could move in the vertical and horizontal directions with the use of fine adjustment screws. We examined a {200}-type reflection. The sample was moved along the [110] and $[1\bar{1}0]$ crystallographic directions in one face and along the [101] and $[10\bar{1}]$ directions in the other face and rotated about the vertical axis to determine the orientations of the regions that were parallel to the lateral faces of the sample and to determine their changes as the x-ray beam was scanned in given steps. The area of the regions to be measured was specified by the area of the incident x-ray beam. In our case, it was 0.07 mm^2 (the x-ray beam diameter was 300 μm). The measurements were performed at 7–15 points in each of the two mutually perpendicular crystal faces. In the wide face, the direction of motion from point to point was changed once after 7 to 8 measurements were made; in the narrow face, only two points to be measured could be located in one straight line. We used CuK_α radiation, and the rate of crystal rotation was 0.5 deg/min. The diffraction lines of the undeformed crystal were narrow and well resolved; after deformation, the lines shifted and split into several peaks. An example of such a line is given in Fig. 1 for a crystal subjected to creep at 873 K.

When Laue x-ray diffraction patterns are recorded from a deformed crystal with blocks, interference spots become broadened [11], which is mainly caused by the misorientation of crystal fragments. Therefore, the broadening of Laue spots can give information on the misorientation of the fragments illuminated by the x-ray beam. By measuring the spot broadening in the radial (Δr) and azimuthal (Δa) directions, we can determine the misorientations of the fragments ϑ_r and ϑ_a about the [010] and [001] axes, respectively, using the relations [11]

$$\Delta r = \frac{4L}{\cos^2 2\theta}\vartheta_r, \qquad \Delta a = \frac{4L\sin\theta}{\cos 2\theta}\vartheta_a, \tag{1}$$

where θ is the Bragg angle and L is the crystal–film distance. We recorded Laue x-ray diffraction patterns using CuK_α radiation and an RKV-86 x-ray camera. The crystal–film distance was 40 mm. We examined the (042) reflection at an x-ray beam diameter of ~1.8 mm. Therefore, we studied the misorientation averaged over an area $s \sim 2.5$ mm^2.

When we determined the misorientation using the Kossel method, we used a widely divergent x-ray beam with an external source, a film located parallel to the sample surface to be studied [12], and CuK_α radiation. The break in neighboring lines measured in terms of doublet spacing characterizes the misorientation of neighboring blocks (fragments) in the crystal.

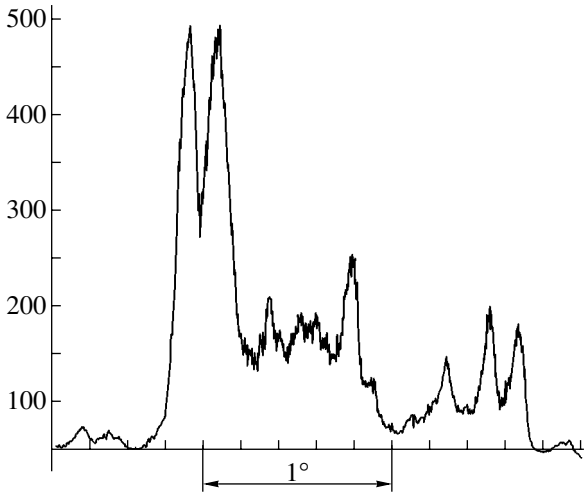

Fig. 1. Profile of the (002) diffraction line of a LiF crystal deformed to 80% at 873 K.

The Fujiwara method [13] uses the transmission geometry and a widely divergent polychromatic x-ray beam. After recording, the film contains a set of Laue spots with superimposed lines of a characteristic spectrum. Each interference spot reflects the topographic pattern of a crystal structure that is projected according to the orientation of the reflecting plane. If the crystal to be studied consists of misoriented blocks, interference spots in the x-ray diffraction pattern have a complex structure and consist of individual blocks. The misorientation angles are calculated from the widths of the boundary areas between the reflections of individual blocks and from the shifts in the characteristic lines in these reflections. The misorientation angles in the azimuthal and radial directions can be determined from the widths of the corresponding boundary bands using the relations [13]

$$\vartheta_a = \frac{m_a\cos 2\theta}{2L\sin\theta}, \qquad \vartheta_r = \frac{m_r\cos^2\theta}{L+R}, \tag{2}$$

where m_a and m_r are the widths of the boundary bands between reflections in the azimuthal and radial directions, respectively; θ is the Bragg angle for the reflecting plane generating the reflection to be studied; L = 150 mm is the crystal–film distance; and R = 100 mm is the x-ray tube–crystal distance. We used MoK_α radiation and studied the (331) reflection. In contrast to the Laue method, this method allows one to measure low-angle misorientations inside fragments illuminated by an x-ray beam.

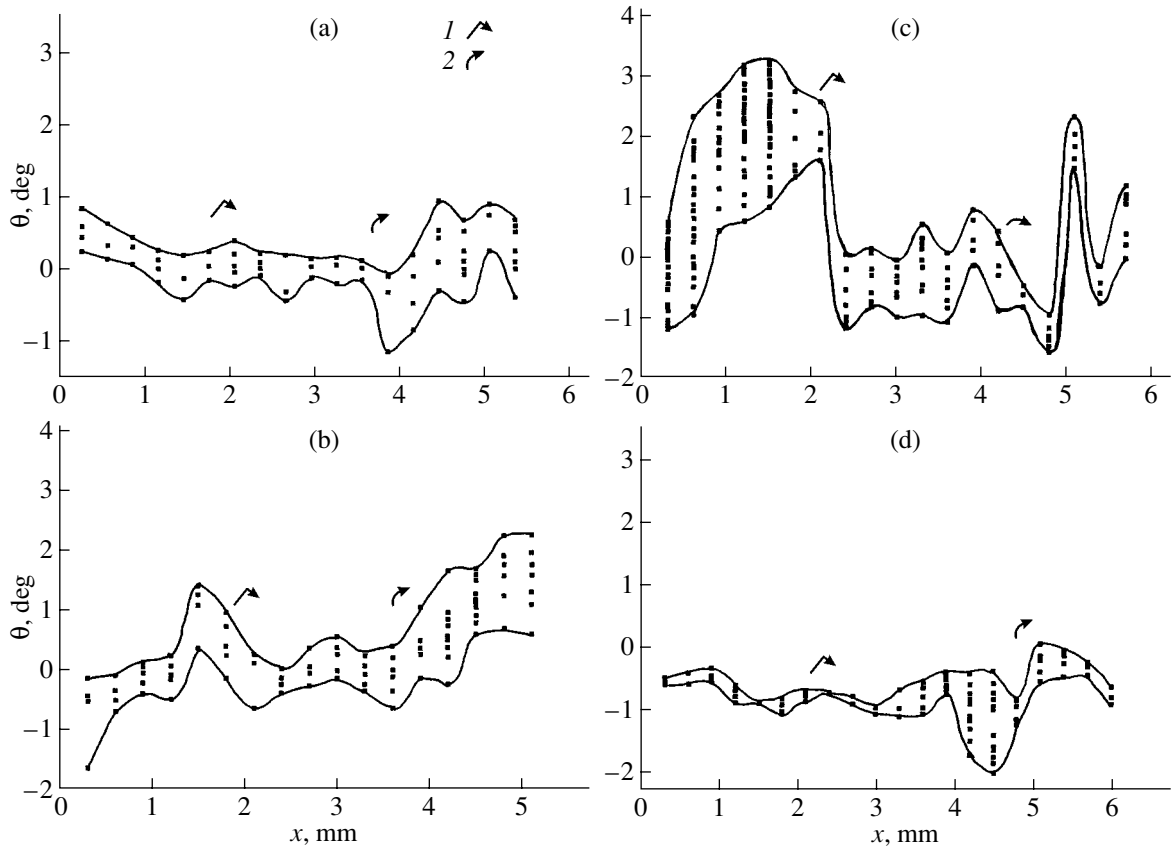

Fig. 2. Deviations of the maxima of the (002) and (020) lines of a deformed LiF crystal from their zero positions for an undeformed crystal as a function of the position of a point in the lateral surface of the sample. The direction of beam motion is along one of the {110} directions; arrow *1* shows 90° rotation, and arrow *2* indicates transition to the adjacent face. The deformation conditions are the following: the temperature T is (a) 573, (b, c) 873, and (d) 973 K and the strain ε is (a) 40, (b) 15, (c) 80, and (d) 50%.

3. RESULTS AND DISCUSSION

The misorientation angles of fragments in deformed LiF crystals as determined by the ω-scanning method are given in Figs. 2–4 and the table. Figure 2 shows the results of recording two lateral faces of the crystal deformed at various temperatures to different strains ε. The abscissa gives the position of a point on the surface. The ordinate of each point in the curves is the angular displacement of each peak in a split line with respect to the line of the undeformed sample. The point–point spacing on the sample surface is 300 μm along one of the <110> directions; 90° rotation and transition to an adjacent face are marked by arrows. Figures 3 and 4 show the change in the total line width and misorientation measured from the position of the middle of the line as a function of the point coordinate on the surface of the deformed sample. The results indicate that, apart from smooth changes in the misorientation, there are sharp jumps, which indicate that a high-angle grain boundary falls in the interval between the neighboring points to be measured (Fig. 2c). The average misorientation increases with strain (compare the data for T = 873 K at ε ~ 15 and 80%). The high-angle misorientation increases with temperature only to 873 K (from ~2.5° at T = 573 K to ~5° at T = 873 K); a further increase in temperature leads to a certain decrease in the fragment misorientation.

A more detailed analysis of the misorientation, based on the misorientation angle distributions as calculated from the ω-scanning data, demonstrates that high misorientation angles are virtually absent at T = 573 K (Fig. 5a); their fraction is also relatively low at 973 K (Fig. 5d). However, the distributions have a pronounced "tail" toward angles that are higher than the most probable angle. The second maximum appears in the distribution curves at T = 873 K at a low strain (Fig. 5b) and is most pronounced at ε = 80% (Fig. 5c).

The microstructural studies of the deformed samples indicate that, at T = 573 K, the block structure is absent and the misorientation is low and is created due to a nonuniform distribution of dislocations that are opposite in sign. At a higher temperature, block (fragment) boundaries mainly contribute to the misorientation and the fraction of high-angle grain boundaries increases with strain. As the temperature increases, the block size increases (from 40 μm at 873 K to 100 μm at 973 K) and high-angle grain boundaries either do not form or compensate for each other as the lattice orien-

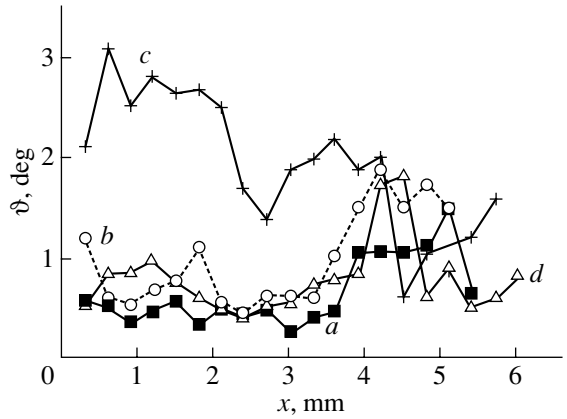

Fig. 3. Change in the total width of the (200) line of a deformed LiF crystal as a function of the position of a point in the lateral surface of the sample. The deformation conditions are the following: the temperature T is (a) 573, (b, c) 873, and (d) 973 K and the strain ε is (a) 40, (b) 15, (c) 80, and (d) 50%.

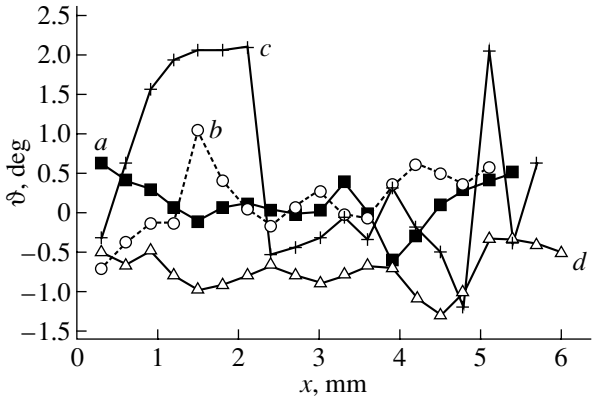

Fig. 4. Dependence of the position of the middle of the (002) or (020) line of a deformed LiF crystal as a function of the position of a point in the lateral surface of the sample. The deformation conditions are the following: the temperature T is (a) 573, (b, c) 873, and (d) 973 K and the strain ε is (a) 40, (b) 15, (c) 80, and (d) 50%.

tation is averaged over the x-ray beam area (which approximately corresponds to the area of ten blocks).

The results of studying the misorientation by the Kossel method support the presence of low- and high-angle boundaries in the LiF crystals deformed at T = 873 K and ε = 64%: two maxima (at 40′ and 2°30′) are detected in the misorientation-angle distributions of the 150 boundaries measured. The high misorientations were found to be formed by either one high-angle grain boundary or by the accumulation of sequential low-angle boundaries having orientations of the same sign [6].

The method of x-ray topography (Fujiwara method) gives the misorientation angles between neighboring regions in a crystal. The interference spots of the x-ray topographs of the deformed LiF crystals exhibit a fringe contrast. In a crystal deformed at T = 573 K, the misorientation corresponding to neighboring bands in the topograph is ~10′. Polygonization begins in the crystal. The diffraction spots in the topographs of crystals deformed at 873 and 973 K do not have a clear contour and consist of individual spots belonging to individual blocks. In the samples deformed at 873 K, 30- to 50-μm blocks with a ~40′ misorientation are dominant and mainly contribute to the misorientation. Unlike with the ω-scanning method and the Kossel method, no high-angle grain boundaries were detected with this method. This is likely due to the averaging of the contributions from low- and high-angle boundaries over the large area occupied by the x-ray beam. The samples deformed at 973 K consist of large similar blocks with a misorientation of 0.8°–1.5°. The results of analyzing the topographs are given in the table. As is seen, the

Misorientation angles in deformed LiF crystals measured by different x-ray diffraction techniques

Test conditions			Low-angle misorientation					High-angle misorientation		
			method					method		
T, K	σ, MPa	ε, %	Kossel WDB	ω scanning	Fujiwara WDB		EM	Kossel WDB	ω scanning	Laue
					ϑ_a	ϑ_r				ϑ_{max}
573	12.0	40		10′	10′	12′			54′	2°30′
673	13.0	70					12′			
773	7.0	80					24′			
873	4.0	64	40′					3°30′		
	4.5	73			37′	45′				4°54′
	5.0	15		49′					2°16′	
	5.0	80		1°12′			30′		3°48′	
973	2.0	33		51′					1°59′	
	2.0	50			1°10′	50′				4°26′

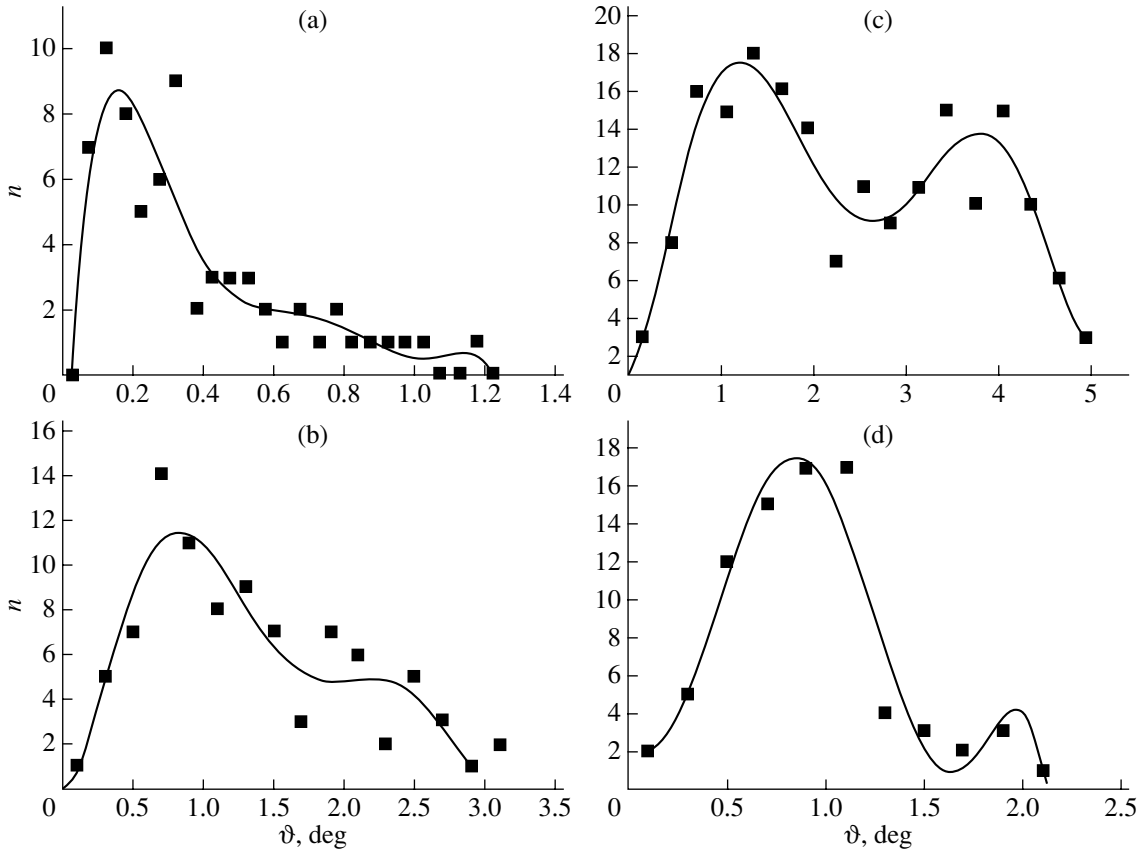

Fig. 5. Misorientation-angle distributions of illuminated regions in a deformed LiF crystal. The deformation conditions are the following: the temperature T is (a) 573, (b, c) 873, and (d) 973 K and the strain ε is (a) 40, (b) 15, (c) 80, and (d) 50%.

average low-angle misorientation between neighboring blocks increases with the deformation temperature (from ~10′ at T = 573 K to 1°10′ at T = 973 K).

The Laue x-ray diffraction patterns of the samples deformed at T = 573 K contain azimuthally broadened spots, and those of the samples deformed at 873 and 973 K exhibit asterism and fragmented spots, which indicates crystal fragmentation with azimuthal and radial misorientation of the fragments. The data obtained by the Laue method are also given in the table. As follows from the table, the high-angle misorientation in the LiF crystals deformed at various temperatures increases with temperature (from ~5° at T = 573 K to ~5° at T = 873 K). At T = 973 K, the misorientation of fragments is lower or equal to that at T = 873 K. The misorientation angles are higher than those determined by the other methods, which is likely due to the fact that the Laue method gives the maximum misorientations, which occur in a rather large area illuminated by the x-ray beam. The difference is most pronounced for nonuniform structures with strongly localized deformation (at low temperatures), and this difference is minimum for the structures with high-angle grain boundaries (deformed at 873 K).

The table gives the misorientations of blocks and fragments (determined using different x-ray methods) in the LiF crystals deformed by tension under creep conditions at various values of T and σ. For comparison, the table also lists electron-microscopic data [14].

The set of experimental data on the misorientations in deformed LiF crystals shows that, apart from low-angle misorientations between neighboring blocks, there are high-angle misorientations of fragments. As is seen, all methods of determining the misorientation between neighboring blocks give similar low-angle misorientations and this misorientation increases with the deformation temperature from ~10′ at T = 573 K to 1°10′ at T = 973 K. The low-angle misorientation remains virtually constant at the stage of steady-state creep for each deformation temperature. The values and character of the changes in the low-angle misorientation obtained for the LiF crystals agree well with the experimental data for metals [15]. The authors of [15] believe that a misorientation at the steady-state stage remains constant as a result of dynamic equilibrium between the processes of formation of new subgrain boundaries and annihilation of existing opposite-sign subgrain boundaries as they move in opposite directions. If low-angle boundaries meet isolated dislocations during motion, they either pass through them or

simultaneously absorb and emit a dislocation, since the misorientation remains the same. In [16], the passage of isolated dislocations through a low-angle boundary was experimentally observed in an electron microscope. The increase in the misorientation before the steady-state stage can be related to the absence of equilibrium in the processes of boundary formation and annihilation and to the fact that moving low-angle boundaries can reach high-angle grain boundaries and merge with them [15]. These factors can also explain the increase in misorientation with deformation temperature, since the velocity of block boundaries and, hence, the probability of their impingement and mergence increase under these conditions [17].

The high-angle misorientation increases with the deformation temperature only up to 873 K (from ~2° at 573 K to ~5° at T = 873 K). Conversely, a further increase in the deformation temperature to 973 K decreases it. This behavior is likely to be explained by a smaller number of blocks in the area illuminated by an x-ray beam at T = 973 K as compared to the case of T = 873 K, since the average block sizes are ~100 and 40 μm, respectively. If a high-angle misorientation occurs via sequential rotations in low-angle block boundaries in one direction and a localized rotation of a high-angle grain boundary in the opposite direction [6], then it is obvious that the number of blocks in a certain fixed area of the crystal at T = 873 K will be larger than that at T = 973 K. Therefore, the high-angle misorientation accumulated from low-angle rotations at T = 873 K is higher than that at T = 973 K. As the area illuminated by an x-ray beam increases, the measured difference in the orientations of crystal regions, i.e., the high-angle misorientation, should increase. Indeed, as this area increases from ~0.01 (Kossel method) to 0.07 mm^2 (ω-scanning method) at T = 873 K, the high-angle misorientation increases insignificantly, namely, from 3°30′ to 3°48′ (for high strains). However, a further increase in the beam area to 2.5 mm^2 (Laue method) leads to a significant increase in the misorientation (to 4°54′).

In the crystals deformed at T = 973 K, the effect of the illuminated area on the difference in the orientations of different crystal regions is stronger than for the case of T = 873 K: the misorientation is ~2° in the ω-scanning method and ~4.5° in the Laue method.

Figure 3b shows that a crystal can have 0.3×1.8 mm^2 regions that rotate via low-angle boundaries sequentially in one direction and then via a high-angle grain boundary in the opposite direction. This behavior is supported by the data obtained by the Kossel method. Large rotations can also be compensated when high-angle grain boundaries of opposite sign move at a spacing that is smaller than the x-ray beam diameter (300 μm). The maximum misorientation at this spacing (step) is ~3°. It should also be noted that, unlike the low-angle misorientation, the high-angle misorientation increases substantially with strain in the stage of steady-state creep.

A few modern theoretical models can explain the formation of high-angle misorientations. Computer simulation [18] as performed within the framework of the impinging-boundary model [15] has shown that the misorientations of some boundaries can rapidly increase if they impinge on an unmovable boundary. The authors of [19] considered the problem of the motion of a partial-dislocation dipole resulting in the separation of dislocation charges and in a ~1° misorientation inside a region of about block size. Applied stress–induced processes in the material lead to the accumulation of charges of one sign in a certain portion of the crystal and to the accumulation of charges of the opposite sign in another portion; that is, the charge separation is caused by forces. The elastic fields of the dislocation dipole favor further separation of the dislocation charges and, hence, growth of the misorientation region with strain.

Most modern theories [2, 3, 20, 21] try to explain the significant hardening and structural evolution (the appearance of micron and submicron fragments) during severe plastic deformation. The hardening is much higher than that achievable during tension of LiF crystals. However, the mechanisms of nucleation of low- and high-angle boundaries and the first stages of formation of fragmented structures can obviously be modeled on relatively simple (in the structural sense) alkali-halide crystals. Although the relative fraction of high-angle grain boundaries in these crystals is low, their role can be decisive in some processes, e.g., in fracture [22, 23].

4. CONCLUSIONS

Using different x-ray diffraction techniques, we have studied the nucleation and evolution of misoriented regions in deformed LiF crystals. Under certain conditions, the misorientation has been shown to be two-level, namely, low-angle and high-angle misorientations. The evolution of the misorientation with temperature and strain has been traced. The lattice misorientation mainly depends on fragment (block) boundaries, and the high-angle misorientation can either be accumulated by sequential rotations in one direction in low-angle boundaries or be realized with a high-angle grain boundary. When the lattice misorientation is determined by x-ray diffraction techniques, important factors are the size of the crystal area illuminated by an x-ray beam and the method of information analysis used, namely, the averaging of misorientations or an analysis of their extreme values. These factors are responsible for the differences in the misorientation angles determined by different techniques.

ACKNOWLEDGMENTS

This work was supported by the Russian Foundation for Basic Research, project no. 04-01-00887.

REFERENCES

1. D. A. Hughes and N. Hansen, Acta Mater. **48** (11), 2985 (2000).
2. I. J. Beyerlein, R. A. Lebensohn, and C. N. Tome, Mater. Sci. Eng., A **345** (1–2), 122 (2003).
3. A. A. Nazarov, N. A. Enikeev, A. E. Romanov, T. S. Orlova, I. V. Alexandrov, and I. J. Beyerlein, in *Proceedings of the NATO Advanced Research Workshop (ARW) on Nanostructured Materials by High Pressure Severe Plastic Deformation, Svyatogorsk, Donetsk oblast, Ukraine, 2004*, Ed. by Y. T. Zhu and V. Varyukhin (Kluwer, Dordrecht, 2005), NATO Sci. Ser., Ser. II: Math. Phys. Chem., Vol. 212.
4. S. Takeuchi and A. S. Argon, J. Mater. Sci. **7** (11), 1542 (1972).
5. M. M. Myshlyaev, Fiz. Tverd. Tela (Leningrad) **7** (2), 571 (1965) [Sov. Phys. Solid State **7** (2), 668 (1965)].
6. B. I. Smirnov, V. V. Shpeĭzman, S. A. Ivanov, K. V. Mal'chuzhenko, and R. S. Chudnova, Fiz. Tverd. Tela (Leningrad) **20** (12), 3730 (1978) [Sov. Phys. Solid State **20** (12), 2158 (1978)].
7. V. I. Betekhtin, V. I. Vladimirov, S. A. Ivanov, K. V. Mal'chuzhenko, and A. Yu. Razumovskiĭ, Fiz. Tverd. Tela (Leningrad) **24** (3), 843 (1982) [Sov. Phys. Solid State **24** (3), 475 (1982)].
8. B. I. Smirnov, *Dislocation Structure and Hardening of Crystals* (Nauka, Moscow, 1981) [in Russian].
9. D. M. Vasil'ev, *Diffraction Methods for Studying Structures* (Metallurgiya, Moscow, 1977) [in Russian].
10. D. M. Vasil'ev, S. A. Ivanov, and B. M. Tarakanov, Zavod. Lab. **40** (6), 685 (1974).
11. Yu. A. Bagaryatskiĭ, Kristallografiya **7** (6), 886 (1962) [Sov. Phys. Crystallogr. **7** (6), 721 (1962)].
12. D. M. Vasil'ev and S. A. Ivanov, Zavod. Lab. **37** (9), 1099 (1971).
13. Ya. S. Umanskiĭ, *X-ray Diffraction Analysis of Metals* (Metallurgiya, Moscow, 1967) [in Russian].
14. B. I. Smirnov, T. V. Samoĭlova, and T. G. Naryshkina, Fiz. Tverd. Tela (Leningrad) **11** (5), 1188 (1969) [Sov. Phys. Solid State **11** (5), 966 (1969)].
15. S. F. Exell and D. H. Warrington, Philos. Mag. **26** (5), 1121 (1972).
16. M. Brown, K. P. Hall, and R. Lagneborg, Scr. Metall. **7** (12), 1275 (1973).
17. B. I. Smirnov, R. S. Chudnova, and V. V. Shpeĭzman, Poverkhnost **6**, 143 (1982).
18. D. H. Warrington, in *Proceedings of the International Conference on Computer Simulation for Materials Applications, Gaithersburg, Maryland, USA, 1976*, Ed. by R. J. Arsenault, J. R. Beeler, and J. A. Simmons (National Bureau of Standards, Washington, DC, 1976), Vol. 20, Part 2, p. 672.
19. V. I. Vladimirov and A. E. Romanov, Fiz. Tverd. Tela (Leningrad) **20** (10), 3114 (1978) [Sov. Phys. Solid State **20** (10), 1795 (1978)].
20. Y. Estrin, L. S. Toth, A. Molinari, and Y. Brechet, Acta Mater. **46** (15), 5509 (1998).
21. G. A. Malygin, Fiz. Tverd. Tela (St. Petersburg) **46** (11), 1968 (2004) [Phys. Solid State **46** (11), 2035 (2004)].
22. B. I. Smirnov and T. N. Snezhkova, Fiz. Tverd. Tela (Leningrad) **19** (7), 2021 (1977) [Sov. Phys. Solid State **19** (7), 1182 (1977)].
23. V. V. Rybin, *Large Plastic Deformations and Fracture of Metals* (Metallurgiya, Moscow, 1986) [in Russian].

Translated by K. Shakhlevich

Physics of the Solid State, Vol. 47, No. 10, 2005, pp. 1879–1885. Translated from Fizika Tverdogo Tela, Vol. 47, No. 10, 2005, pp. 1806–1812.

MAGNETISM AND FERROELECTRICITY

Dynamic Systems of Concentric Ring Magnetic Domains in a Highly Anisotropic Garnet Ferrite Film in Magnetic Fields at Infrasonic Frequencies

G. S. Kandaurova, V. Kh. Osadchenko, and A. G. Pashko

Ural State University, pr. Lenina 51, Yekaterinburg, 620083 Russia

e-mail: gerta.kandaurova@usu.ru

Received September 27, 2004

Abstract—Dynamic domain structures in a garnet ferrite film with perpendicular anisotropy are investigated in magnetic fields at infrasonic frequencies for the first time. It is revealed that the multidomain film exists in the anger state and that stable dynamic structures with unusual properties are formed in ac magnetic fields at frequencies of 2–3 Hz. © *2005 Pleiades Publishing, Inc.*

1. It is known [1] that, in an ac magnetic field, the multidomain magnetic structure of films with perpendicular anisotropy can transform into a specific state, which is referred to as the anger state. In this state, a disordered dynamic ensemble of domains undergoes self-organization, which results in the formation of stable dynamic domain structures (DDSs) of a particular type. These are spiral domains and systems of concentric ring domains at frequencies of 10^2–10^4 Hz. Another specific feature of the anger state is that ordered dynamic domain structures arise, exist for a time, and disappear; then, again, arise, exist, and disappear; etc. Therefore, in order to describe the anger state, it is necessary to introduce not only the configuration parameters of the dynamic domain structure but also the dynamic parameters of this state, such as the lifetime T_g of an individual dynamic structure and the waiting time T_w for the appearance of similar structures in the studied region of the sample.

At present, dynamic spiral domains arising in the anger state of garnet ferrite films with perpendicular anisotropy in ac magnetic fields at frequencies $f = 10^2$–10^4 Hz and amplitudes $H_0 < H_S$ (where H_S is the static saturation field) have been experimentally and theoretically studied in sufficient detail (see, for example, [1–4]). In [5], it was demonstrated for the first time that the formation of stable ordered dynamic domain structures occurs in a limited amplitude–frequency region (H_0, f). As followed from graphic data and photographs of dynamic domain structures, dynamic spiral domains are observed in the frequency range 200–6000 Hz. However, it turned out that large stable dynamic systems of concentric ring domains rather than spiral domains are formed over a narrow frequency range 120–200 Hz. Like spiral domains, concentric ring domains exist, collapse, again arise, etc. The lifetime T_g and the waiting time T_w for domain structures of both types are of the same order of magnitude. Additional information on these concentric ring domains can be found in [6, 7]. However, the nature of the anger state has not been adequately investigated. Moreover, the question as to whether the anger state can exist in films at frequencies $f < 100$ Hz remains open.

In this work, we studied the dynamic domain structures in garnet ferrite films in ac magnetic fields at low frequencies, including infrasonic frequencies. The anger state and the formation of large, very stable dynamic systems of concentric ring domains in ac magnetic fields at a frequency of 2–3 Hz and at an amplitude considerably exceeding the static saturation field H_S were revealed in a highly anisotropic film. The first data on this effect are presented in our previous work [8].

2. We studied an $(YLuBi)_3(FeGa)_5O_{12}$ (111) garnet ferrite film (thickness, 8 μm; surface area, ~16 mm^2) with induced perpendicular anisotropy and the following parameters: the quality factor $Q \approx 80$, the static saturation field $H_S = 42$ Oe (determined from the hysteresis loops in an oscilloscope screen), and the coercive force $H_C \sim 1.5$ Oe (induced by the displacement of domain boundaries). The domain structure was examined using the magneto-optical Faraday effect over the area $S \approx 12$ mm^2. In the initial demagnetized state, stripe domains in the film had a labyrinth structure (Fig. 1a). The period P_0 of stripe domains in this structure (equal to twice the domain width) was 30 μm. The images of dynamic domains were recorded using the stroboscopic video micrographic technique [9] at an exposure time of 10^{-4} s with computer processing of the array of experimental data.

The film was placed at the center of a coil with an inner diameter of 6.5 mm and a height of 5 mm. An alternating current was passed through the coil. The

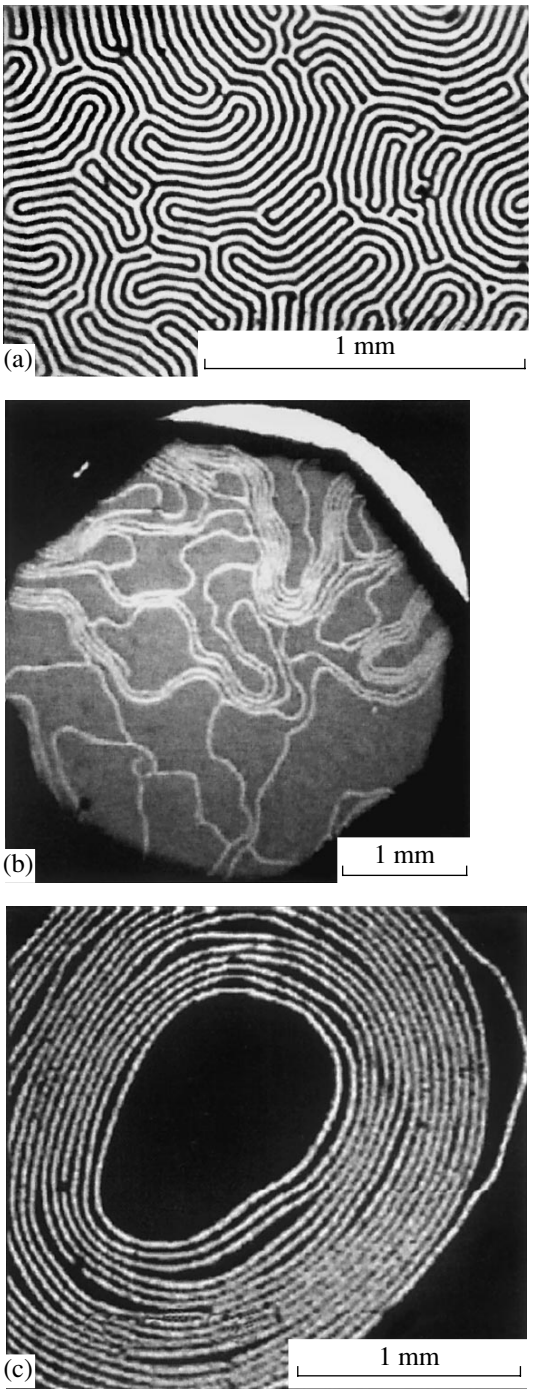

Fig. 1. Domain structures of the sample (a) in the initial state and (b, c) in ac magnetic fields at a frequency f = 2–3 Hz and amplitudes H_0 = (b) 35 and (c) 80 Oe. The magnetization vectors in bright and dark domains are directed "toward us" and "away from us," respectively.

current induced a magnetic field $H_\sim = H_0\sin(2\pi ft)$ at a frequency of 2–15 Hz and an amplitude of up to 170 Oe. The magnetic field was aligned with the easy-magnetization axis; i.e., it was directed perpendicular to the film. Thus, in the course of the experiment, the film was in a spatially uniform ac magnetic field.

3. Examination of the structure revealed that stripe domains chaotically move at amplitudes $H_0 < H_S$. The shape, size, and direction of motion of these domains vary over the period of the ac magnetic field and from period to period. Therefore, we are dealing here with an unstable disordered dynamic domain structure. This structure will be termed spatiotemporal dynamic domain chaos (or simply chaos), in which all domains are coupled through the long-range magnetostatic interaction. It should be noted that, among the stripe domains that appear for a moment, there arise bright single stripe domains from time to time. These domains differ in that their configuration is retained for several field periods; i.e., they are more stable.

4. An increase in the field amplitude to $H_0 \approx (1.1–1.5)H_S$ leads to a new previously unknown cooperative effect. The effect most clearly manifests itself at a frequency f = 2–3 Hz. In a continuously varying disordered ensemble of stripe domains, there arise systems of curved stripe domains ordered in parallel (for brevity, they will be referred to as bundles). The bundle configuration is retained for several (15–50) field periods. As a result, they are clearly seen in the DDS image (Fig. 1b) owing to the higher contrast. The bundle can contain three or more closely packed stripe domains. The period of these structures is close to the period of domain structures in the demagnetized state.

The aforementioned stable dynamic structure has no specific geometry but appears through the self-organization of the ensemble of domains, exists for a finite time ($T_g \approx$ 6–20 s), and then collapses. Over the period of time T_g, the stable initial bundle either accepts new stripe domains or, contrastingly, loses one or two boundary domains. The waiting time T_w for the appearance of these bundles is relatively short. For the above parameters of the field, these bundles are observed at virtually all times in the studied region of the sample. As a rule, the film structure simultaneously contains several systems of domains that are ordered in parallel and end in defects or sample boundaries.

The formation of bundles composed of stripe domains can be explained in the same manner as for the formation of dynamic spiral domains [10]. In an ac magnetic field, there arises a dynamic domain structure in which domain boundaries more rapidly reach their equilibrium positions. Over the half-period of the field, the domain boundaries move through a distance of ~0.2–1.0 mm in the dynamic domain structure surrounding bundles (Fig. 1b) and through a distance of less than 0.015 mm in the closely packed structure of stripe domains. The bundle stability is favored by the local decrease not only in the kinetic energy but also in the magnetostatic energy.

5. It should be noted that, in a magnetic field $H_0 > H_S$, sometimes (at instants of time corresponding to the

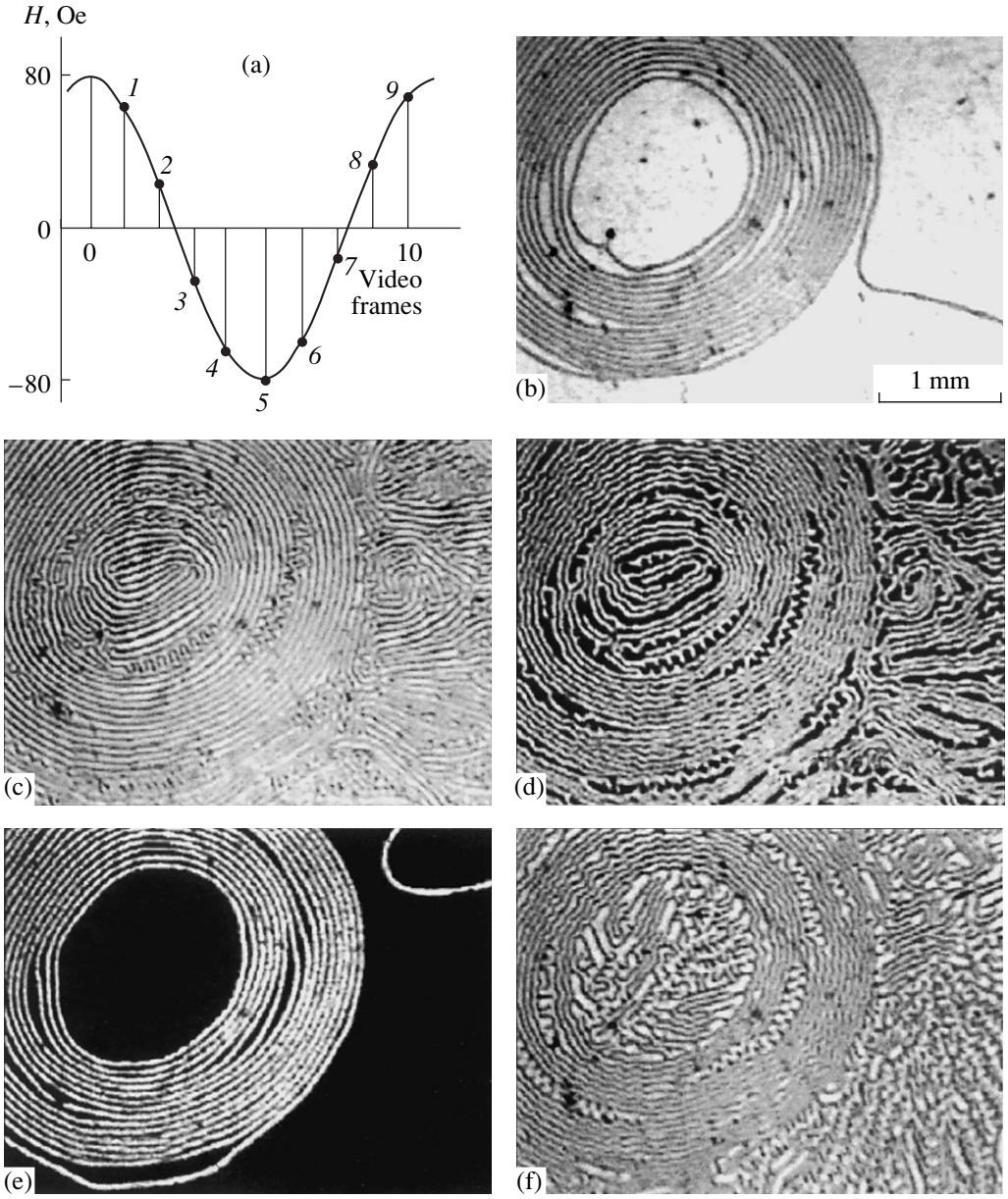

Fig. 2. (a) Sequential instants of time during one field period at which DDS images were recorded. (b–f) DDS images recorded at instants (b) *1*, (c) *3*, (d) *4*, (e) *5*, and (f) *9*.

decrease in the field strength from the amplitude value), spiral domains with a small number of turns twist from fragments of stripe domains of the reversed magnetic phase. These spiral domains exist for no more than the half-period $T/2$ and disappear during the half-period of the field opposite in sign. Most likely, this is associated with the action of the gyrotropic force on the end of the growing stripe domain. Two-arm, short-lived (half-period) spiral domains are formed according to a similar mechanism.

6. As the field amplitude increases to $H_0 = (2.0–2.8)H_S$, large systems of concentric ring domains are formed instead of the bundles of stripe domains ordered in parallel. One of these systems is shown in Fig. 1c. The distinctive features of this system are as follows: regular geometry, a large outer diameter comparable to the sample size, a large number of rings (N_r can reach 15–20), and a very large inner core (which, like the environment of the system of concentric ring domains, can be in a saturation state) (Fig. 1c). We succeeded in observing the transformation of the same system of concentric ring domains during one period of the ac magnetic field at $f = 2–3$ Hz and $H_0 = 80$ Oe. A series of video images is displayed in Fig. 2. The sequential instants of video filming of the dynamic domain structure are shown in the fragment of the sinusoid $H_\sim(t)$ for

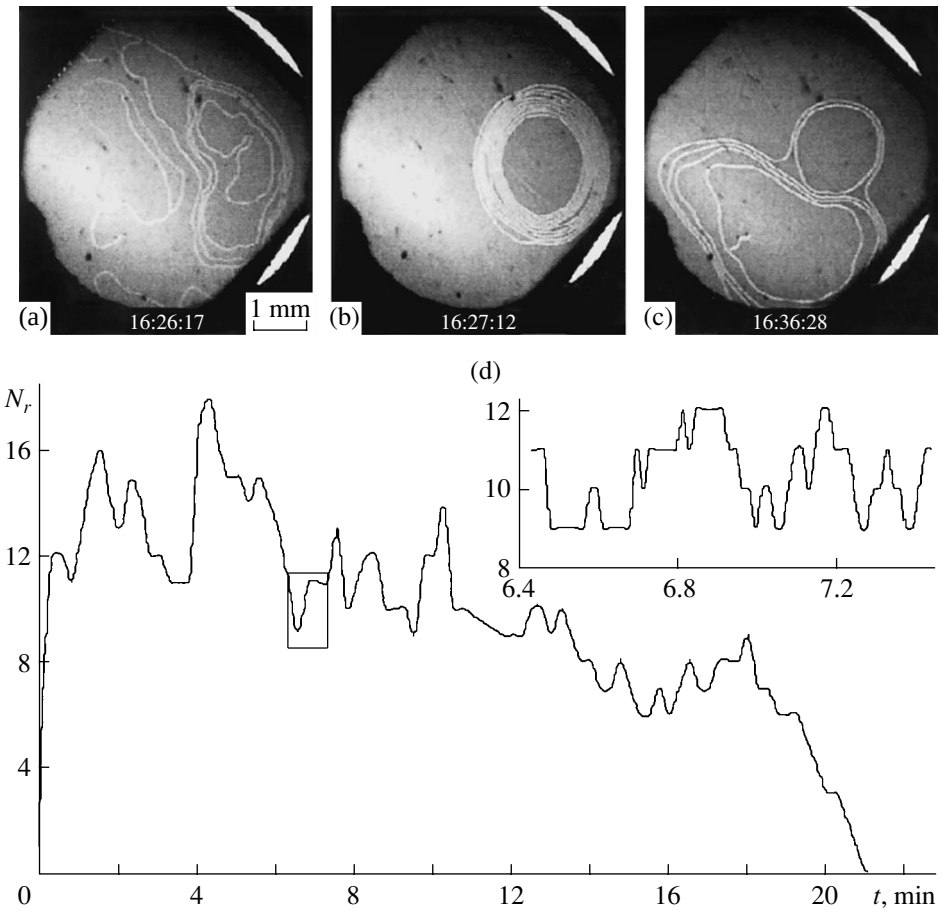

Fig. 3. Characteristic images of the system of concentric ring domains (a) at the initial stage of its life, (b) during its life, and (c) in the course of collapse. (d) Time dependence of the number of rings in one system of concentric ring domains during its life. The inset shows the dependence $N_r(t)$ on an enlarged time scale.

one field period (Fig. 2a). In the field close in strength to the amplitude value (instant of time *1*), the film exhibits one large system of concentric ring domains that has an outer diameter $D_{ex} \approx 2.5$ mm and an inner diameter $D_{in} \approx 1$ mm and consists of 16 dark and 16 bright thin stripe domains (Fig. 2b). The magnetization of the core of the system and the region surrounding the system of concentric ring domains has the opposite direction ("toward us"). Irregularities ("clear spaces") can be seen in the close packing of rings. With a decrease in the field (instant of time *2*), the film state and the DDS image remain unchanged. This indicates a large hysteresis loop associated with the delay of growth of magnetization reversal nuclei in bright regions in Fig. 2b.

As the field further decreases and changes sign (instant of times *3*, *4*), the dynamic domain structure changes in a jumpwise manner (Figs. 2c, 2d). The structure in Fig. 2c corresponds to a nearly demagnetized state. The core of the initial system of concentric ring domains and its environment are filled with stripe domains of various shapes (spiral, radial, disordered) and almost identical width. Judging from the wider dark domains in Fig. 2d, this dynamic domain structure corresponds to a state in which the magnetization is partially reversed.

After the field strength has reached a negative amplitude value (instant of time *5*), the film again exhibits one sole system of concentric ring domains with a uniformly magnetized ("away from us") dark core in the dark single-domain environment of the other region of the sample (Fig. 2e). This dynamic domain structure is retained for a long time with a decrease in the field (Fig. 2a, instant of times *6*, *7*). Then, as the field changes sign and increases in amplitude (Fig. 2a, instant of times *8*, *9*), the dynamic domain structure jumpwise transforms into a state with a partially reversed magnetization (Fig. 2f).

A comparison of the dynamic domain structures shown in Figs. 2d and 2f demonstrates that these structures are similar to each other. However, a larger area is occupied in Fig. 2f by bright domains with the magnetization directed toward us and in Fig. 2d by dark domains with the opposite orientation of the magnetization vector. As the field approaches the positive

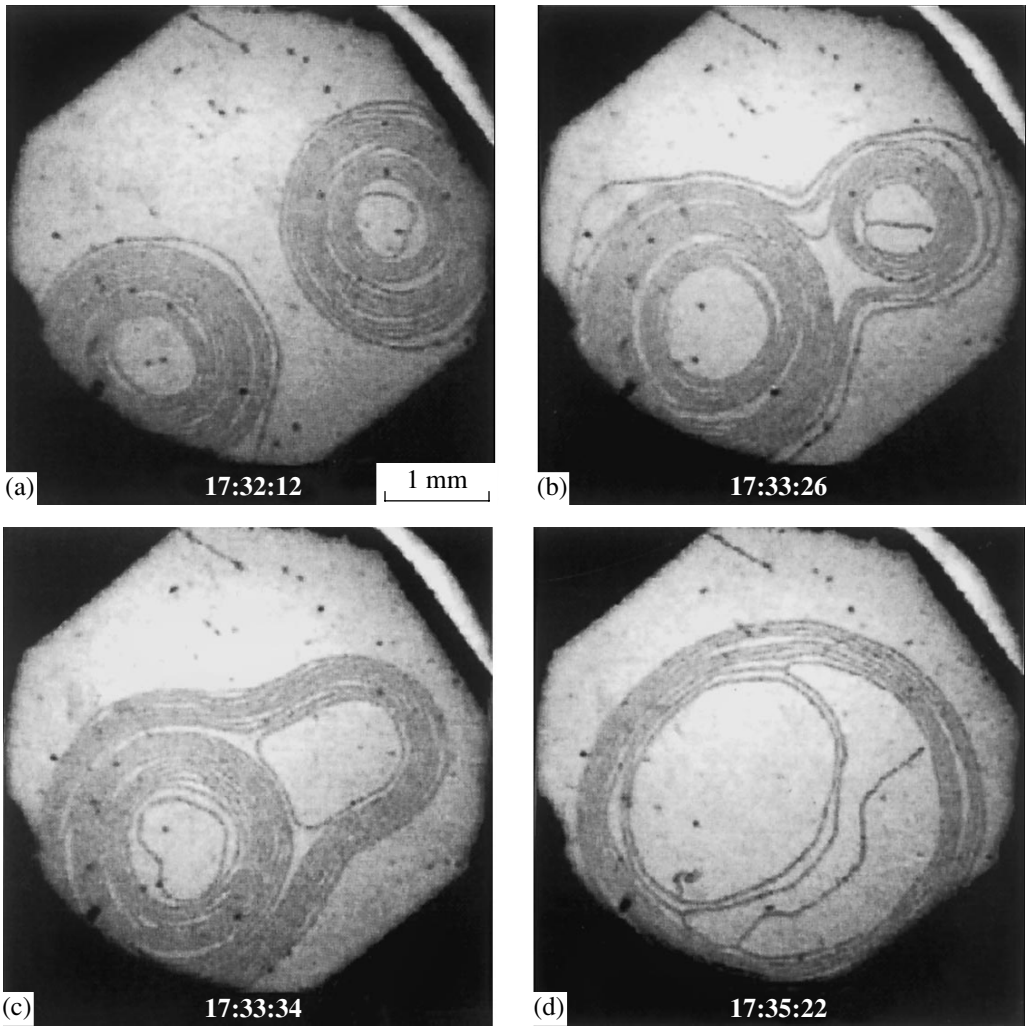

Fig. 4. Evolution of the dynamic domain structure due to the interaction between two systems of concentric ring domains. The time shown in the figure panels corresponds to the real time of observation of this dynamic domain structure.

amplitude value, the dynamic domain structure transforms into a structure similar to that shown in Fig. 2b.

As can be seen from Fig. 2, the transformation of the dynamic domain structure is characterized by a number of features. The ring domains in Figs. 2b and 2c have smooth undistorted boundaries, whereas wavy distortions of domains and their boundaries are clearly seen in Figs. 2d and 2f. Probably, this is a manifestation of the well-known effect of asynchronous motion of two boundaries of a ring domain with an increase (decrease) in the magnetic field [11, 12]. The observed periodic structures in dark (Fig. 2d) and bright (Fig. 2f) clear spaces can be associated with the growth of side arms of stripe domains surrounding a particular clear space.

7. The transformation of the dynamic domain structure with a stable system of concentric ring domains over one field period is shown in Fig. 2. For the most part, the core and the environment of the system of concentric ring domains undergo changes. The system itself changes only insignificantly. However, similar ring structures exist for several periods of the ac field. In this time (the lifetime T_g), they can undergo radical transformations, especially at the initial and final stages of the life of the system. The domain structures at the most important instants of life for one system of concentric ring domains are presented in Figs. 3a–3c. These images are typical of other similar systems.

Initially, a single stable ring is formed around a defect or a stripe domain nucleates at a defect, grows, and is curved into a ring. Then, stripe domains are added to the first ring from the surrounding chaos (Fig. 3a). The number of rings increases, and their shape becomes similar to a circle. This results in the formation of a stable system of concentric ring domains (Fig. 3b). Subsequently, this system can increase or decrease in diameter (with a change in the number N_r of rings) and move over the sample. The system of concentric ring domains is frequently separated into two concentric systems that can again coalesce into a single system. Sometimes, the concentricity of the systems

Comparison of the parameters of the anger state and dynamic systems of concentric ring domains (according to the data available in the literature)

Parameter	Reference	
	[5–7]	this work
Field type $H(t)$	Symmetric meander	$H_{\sim} = H_0 \sin 2\pi ft$
Frequency f, Hz	100–200	2–3
Amplitude H_0	$H_0 < H_S$	$H_0 > H_S$
Reduced amplitude range $\Delta H_0/H_S$	0.85–0.95	2.0–2.8
T_g, s	5–10	600–2500
T_g/T*	500, 1000–2000	1500–6000
D_{ex}, mm	0.8–1	1–4
D_{in}, mm	0.4–0.8	0.5–3

* T is the field period, and T_g/T is the number of field periods per lifetime of the ring domain structure.

can be disturbed. In the lifetime T_g, this process can repeat many times. At the end of its life, the system of concentric ring domains rapidly loses rings, especially if other ring domains are formed in the vicinity, as can be seen from Fig. 3c.

For one of the long-lived systems of concentric ring domains ($T_g \approx 21$ min), Fig. 3d presents detailed data on the measured number N_r of rings over the entire lifetime. It can be seen from this figure that the number of rings increases very sharply (jumpwise) at the initial stage of the system's life (seven rings are formed for 10 s). The number N_r of rings decreases rather rapidly at the end of its life. It follows from Fig. 3d that, during the life of the ring system, the number N_r of rings varies in an irregular fashion. The inset to Fig. 3d shows the dependence $N_r(t)$ on an enlarged time scale. As can seen from the inset, the jumps in the dependence $N_r(t)$ have a fractal character. Note also that, in a number of large systems of concentric ring domains, a drastic decrease in the number N_r of rings down to one ring was observed during the lifetime. However, these structures did not disappear, the number of rings began to decrease, and they continued to exist.

8. The above analysis was performed for single systems of concentric ring domains. However, the film can contain several similar systems simultaneously. These systems interact with each other in a specific manner. The interaction between two systems is illustrated in Fig. 4. The first structure nucleated and grew in the right part of the sample (Fig. 4a). Within 61 s, the second system of concentric ring domains appeared and grew in the left part of the sample and began to absorb the first system by accepting its rings on top of own rings (Fig. 4b).

After a time (shown in the panels in Fig. 4), only one distorted ring of the first system remained in the sample (Fig. 4c). Then, this ring disappeared and the second system transformed into a ring structure with a very large core. During the existence of the second system, its outer diameter increased to 3.2 mm and the number of rings decreased and increased in an irregular manner. Inside this system of concentric ring domains, systems of concentric rings with smaller sizes appeared and disappeared repeatedly.

9. As was noted above, large systems of concentric ring domains in garnet ferrite films were previously observed in fields at frequencies of 120–200 Hz [5–7]. Although these systems were poorly investigated, it is reasonable to compare the quantitative parameters (T_g, T_w) of the anger state and the ring systems from [5–7] with similar data obtained in the present work (table). It can be seen from the table that larger and considerably more stable ordered dynamic domain structures in the form of systems of concentric ring domains are formed in the infrasonic frequency range. Note that there are theoretical investigations of static and dynamic ring domain structures (see, for example, [11–16]). However, as far as we know, systems of dynamic concentric ring domains with the specific features described in the present work have not been considered to date.

10. Thus, the results of investigations into dynamic domain structures formed in a highly anisotropic garnet ferrite film in ac harmonic magnetic fields at infrasonic frequencies can be summarized as follows.

(1) The formation of the anger state was revealed in exciting fields at frequencies of 2–3 Hz. In this state, stable systems of dynamic stripe domains ordered in parallel are formed at field amplitudes smaller than the strength of the static saturation field ($H_0 < H_S$). The lifetime of a similar domain bundle can be as long as 20 s. Systems of concentric ring domains (containing up to 20 rings) with a large inner core, which is magnetized to saturation or filled with disordered dynamic domain structures, are formed at field amplitudes exceeding the static saturation field H_S by a factor of 2.0–2.8. The lifetime of these systems can reach 40 min. The maximum diameter of the systems of concentric ring domains can be close to the sample size (~4 mm).

(2) Approximately ten sequential video images that illustrate the evolution of the same system of concentric ring domains during one period of an ac field were recorded for the first time. It was clearly demonstrated that the large hysteresis loop of magnetization reversal in the film is associated both with the dynamic stability of the system of concentric ring domains at amplitude values of the field and with the delay of demagnetization in the core of the system of concentric ring domains and in the film region surrounding this system.

(3) Previously unknown mechanisms of transformation of a dynamic ordered structure during its lifetime were revealed. The system of concentric ring domains during the lifetime T_g can lose or accept ring domains

inside (or outside) and can also be separated to form an inner system of concentric ring domains with smaller diameters and the center displaced with respect to the center of the initial system. It is quite possible that a new system of smaller size is formed inside the system of concentric ring domains with a large core.

(4) The interaction between different systems of concentric ring domains was studied for the first time. It was established that the interaction of two systems of concentric ring domains is characterized by a number of specific features, such as "rewinding" of turns from one structure to another structure, the formation of rings joining both systems together, and the complete absorption of one system by another system.

ACKNOWLEDGMENTS

This work was supported in part by the US Civilian Research and Development Foundation for the Independent States of the Former Soviet Union (CRDF) (project no. EK-500-X1) and the Ministry of Education and Science of the Russian Federation (project no. E-3.4-258).

REFERENCES

1. G. S. Kandaurova, Usp. Fiz. Nauk **172** (10), 1165 (2002) [Phys. Usp. **45**, 1051 (2002)].
2. G. S. Kandaurova and V. Kh. Osadchenko, Fiz. Met. Metalloved. **97** (2), 38 (2004).
3. M. V. Logunov and M. V. Gerasimov, Fiz. Tverd. Tela (St. Petersburg) **44** (9), 1627 (2002) [Phys. Solid State **44** (9), 1703 (2002)].
4. V. N. Mal'tsev, G. S. Kandaurova, and L. N. Kartagulov, Fiz. Tverd. Tela (St. Petersburg) **45** (4), 658 (2003) [Phys. Solid State **45** (4), 691 (2003)].
5. G. S. Kandaurova and A. É. Sviderskiĭ, Pis'ma Zh. Tekh. Fiz. **14**, 777 (1988) [Sov. Tech. Phys. Lett. **47**, 346 (1988)].
6. G. S. Kandaurova and A. É. Sviderskiĭ, Zh. Éksp. Teor. Fiz. **97**, 1218 (1990) [Sov. Phys. JETP **70**, 684 (1990)].
7. A. É. Sviderskiĭ, Candidate's Dissertation (Ural State University, Yekaterinburg, 1994).
8. V. Kh. Osadchenko, G. S. Kandaurova, A. G. Pashko, and A. A. Shinkorenko, in *Proceedings of the XIX School–Workshop on New Magnetic Materials in Microelectronics, Moscow, Russia, 2004* (Moscow, 2004).
9. G. S. Kandaurova, V. Kh. Osadchenko, A. A. Rusinov, and E. A. Rusinova, Pis'ma Zh. Éksp. Teor. Fiz. **63** (6), 453 (1996) [JETP Lett. **63** (6), 478 (1996)].
10. G. S. Kandaurova and Yu. V. Ivanov, Fiz. Met. Metalloved. **76** (1), 49 (1993).
11. A. V. Antonov, A. M. Balbashov, V. A. Baltinskiĭ, and A. I. Chervonenkis, Fiz. Tverd. Tela (Leningrad) **14** (7), 1901 (1972) [Sov. Phys. Solid State **14**, 1649 (1972)].
12. F. A. de Jonge, W. F. Druyvesteyn, and A. G. H. Verhulst, J. Appl. Phys. **42**, 1270 (1971).
13. K. V. Lamonova, Yu. A. Mamalui, and Yu. A. Siryk, Fiz. Tekh. Vys. Davleniĭ **6** (4), 49 (1996).
14. A. F. Gal'tsev and Yu. I. Yalyshev, Fiz. Met. Metalloved. **85** (4), 5 (1998).
15. A. F. Gal'tsev and Yu. I. Yalyshev, Fiz. Met. Metalloved. **89** (3), 24 (2000).
16. V. N. Maltsev and G. S. Kandaurova, Phys. Met. Metallogr. **92** (Suppl. 1), 22 (2001).

Translated by O. Borovik-Romanova

Physics of the Solid State, Vol. 47, No. 10, 2005, pp. 1886–1891. Translated from Fizika Tverdogo Tela, Vol. 47, No. 10, 2005, pp. 1813–1817.

MAGNETISM AND FERROELECTRICITY

Specific Features of Magnetoacoustic Waves in Fe_3BO_6

V. D. Buchel'nikov*, N. K. Dan'shin, D. M. Dolgushin*, A. I. Izotov**, V. G. Shavrov***, L. T. Tsymbal**, and T. Takagi******

** Chelyabinsk State University, ul. Brat'ev Kashirinykh 129, Chelyabinsk, 454021 Russia*
e-mail: buche@csu.ru
*** Donetsk Institute of Physics and Technology, National Academy of Sciences of Ukraine, ul. Rozy Lyuksemburg 72, Donetsk, 83114 Ukraine*
**** Institute of Radio Engineering and Electronics, Russian Academy of Sciences, ul. Mokhovaya 18, Moscow, 125009 Russia*
e-mail: shavrov@cplire.ru
***** Institute of Fluid Science, Tohoku University, Sendai, 980-8577 Japan*
Received November 22, 2004

Abstract—The specific features of magnetoacoustic waves propagating in an orthorhombic antiferromagnet with weak ferromagnetism, namely, the Fe_3BO_6 orthoborate, are investigated experimentally in the vicinity of the spontaneous, first-order orientational phase transition. It is revealed that, at the phase transition point, the amplitude of active acoustic waves interacting with spin waves increases significantly. A phenomenological theory of magnetoelastic waves in orthoferrites is proposed. This theory allows for an intermediate domain structure existing in the range of a first-order orientational phase transition and offers a satisfactory explanation of the experimentally observed anomaly in the amplitude of active acoustic waves. © *2005 Pleiades Publishing, Inc.*

1. INTRODUCTION

The compound Fe_3BO_6 is an orthorhombic antiferromagnet with weak ferromagnetism. Like rare-earth orthoferrites $R FeO_3$ (R is a rare-earth ion), upon cooling, the Fe_3BO_6 orthoborate undergoes a spontaneous orientational $\Gamma_4(G_x, F_z)$–$\Gamma_2(G_z, F_x)$ phase transition, where **F** and **G** are the ferromagnetic and antiferromagnetic vectors in the two-sublattice approximation, respectively [1, 2]. In contrast to the phase transitions observed in rare-earth orthoferrites, the above transformation in the Fe_3BO_6 orthoborate occurs not through two consecutive second-order phase transitions involving the intermediate angular phase $\Gamma_{24}(G_{x,z}, F_{x,z})$ but through one first-order orientational phase transition [3]. The Fe_3BO_6 orthoborate is a unique orthorhombic compound in which the spin reorientation from one weakly ferromagnetic state to another weakly ferromagnetic state occurs through the first-order orientational phase transition.

In the present work, the temperature dependences of the velocity and attenuation of transverse acoustic waves transmitted through a sample of the Fe_3BO_6 compound were investigated experimentally in the vicinity of the spontaneous orientational $\Gamma_4(G_x, F_z)$–$\Gamma_2(G_z, F_x)$ phase transition. Moreover, we proposed a phenomenological theory of coupled magnetoelastic waves in orthoferrites at temperatures close to the first-order orientational phase transition. This theory offers a satisfactory explanation of the experimentally observed specific features of magnetoelastic waves propagating in the Fe_3BO_6 compound.

2. OBJECT OF INVESTIGATION AND EXPERIMENTAL TECHNIQUE

The velocity and attenuation of acoustic waves were measured on a pulsed ultrasonic spectrometer. Acoustic waves were excited by a resonant piezoelectric transducer (lithium niobate) at a frequency of 27.5 MHz. The attenuation of acoustic waves was measured in a continuous mode and registered on a recorder. The point-by-point measurements of the relative change in the acoustic velocity were performed using the phase-sensitive method. The number of reliably resolved ultrasonic echo pulses transmitted through the sample (more than ten) ensured a sufficiently high accuracy in determining the absolute velocity of acoustic waves in the crystal.

Since the temperature of the spontaneous phase transition in the studied sample of the Fe_3BO_6 compound was equal to 415 K, the working volume needed to be isolated from the piezoelectric sensors. For this purpose, the sample was placed between two Z-cut quartz delay lines each of a length of 4 cm. Acoustic contact of the delay lines with the sample was provided through a 7-μm-thick aluminum foil with the flat surfaces held down without the use of a lubricant. Acoustic contact of the delay lines with the piezoelectric sensors kept at room temperature was ensured through an aluminum foil with GKZh oil. The Fe_3BO_6 sample was prepared in the form of a single-crystal plane-parallel plate ($6.4 \times 3.1 \times 1.02$ mm in size) with the normal **n** to the sample plane aligned parallel to the **a** axis of the single crystal. The **a** axis and the normal **n** coincided accu-

rate to within 0.5°, and the plane of polarization of acoustic waves and the sample plane coincided accurate to within 3°.

A symmetry analysis demonstrates that, since the spontaneous $\Gamma_4(G_x, F_z)$–$\Gamma_2(G_z, F_x)$ reorientation is due to the disappearance of anisotropy in the *ac* plane, the acoustic modes with either $\mathbf{k} \parallel \mathbf{a}$ and $\boldsymbol{\varepsilon} \parallel \mathbf{c}$ or $\mathbf{k} \parallel \mathbf{c}$ and $\boldsymbol{\varepsilon} \parallel \mathbf{a}$ (where $\mathbf{k}$ is the wave vector and $\boldsymbol{\varepsilon}$ is the polarization vector) should be active (i.e., interact with spin waves) [1, 4]. The figure presents the results of measuring the amplitude of an ultrasonic wave transmitted through the sample ($\mathbf{k} \parallel \mathbf{a}$, $\boldsymbol{\varepsilon} \parallel \mathbf{c}$). It can be seen from the figure that, at the phase transition point, the amplitude of an active acoustic wave transmitted through the sample does not decrease (as is the case with all known orthoferrites [1]) but increases. This corresponds to a decrease in the attenuation of acoustic waves with vectors $\mathbf{k} \parallel \mathbf{a}$ and $\boldsymbol{\varepsilon} \parallel \mathbf{c}$ at the phase transition point. An anomaly with increasing temperature is observed against the background of a smooth variation in the amplitude of the acoustic wave transmitted through the sample. The measurements of the velocity of active acoustic waves with vectors $\mathbf{k} \parallel \mathbf{a}$ and $\boldsymbol{\varepsilon} \parallel \mathbf{c}$ revealed that, at the phase transition point, the velocity decreases insignificantly (the relative change in the acoustic velocity is estimated as $\Delta S/S \sim 0.2\%$).

The attenuation of acoustic waves with vectors $\mathbf{k} \parallel \mathbf{a}$ and $\boldsymbol{\varepsilon} \parallel \mathbf{b}$ also exhibits an anomaly of the resonance type. However, at temperature $T = 415$ K, the amplitude of acoustic waves of this type decreases. To within the limits of experimental error, no changes in the velocity of acoustic waves in this geometry of the experiment were determined.

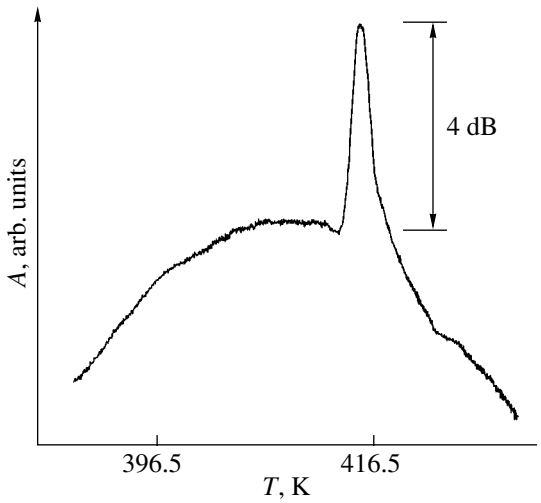

Temperature dependence of the amplitude of the active transverse acoustic wave in the Fe_3BO_6 compound in the temperature range of the spontaneous orientational Γ_2–Γ_4 phase transition.

3. THEORY. RESULTS AND DISCUSSION

The experimentally observed anomalous behavior of acoustic waves with vectors $\mathbf{k} \parallel \mathbf{a}$ and $\boldsymbol{\varepsilon} \parallel \mathbf{c}$ can be qualitatively explained as follows. It is known that, in the vicinity of the first-order phase transition in orthoferrites, there exists an intermediate domain structure [5]. Let us consider an orthoferrite sample in the form of a plate divided into domains of alternating phases, namely, the phases $\Gamma_2(G_z, F_x)$ and $\Gamma_4(G_x, F_z)$ separated by domain boundaries. In the domain boundaries, the antiferromagnetic vector $\mathbf{G}$ rotates from the $\mathbf{z}$ axis to the $\mathbf{x}$ axis, whereas the ferromagnetic vector $\mathbf{F}$ rotates from the $\mathbf{x}$ axis to the $\mathbf{z}$ axis. We consider only regions of the crystal that contain a sufficiently large number of domains of the phases $\Gamma_2(G_z, F_x)$ and $\Gamma_4(G_x, F_z)$ and whose sizes are small as compared to the acoustic wavelength. Therefore, during propagation through this crystal, an acoustic wave interacts not with the magnetization of each of these phases, $\Gamma_2(G_z, F_x)$ or $\Gamma_4(G_x, F_z)$, but with the average magnetization. If the crystal has a domain structure, the direction of the average magnetization coincides neither with the $\mathbf{x}$ axis nor with the $\mathbf{z}$ axis but is intermediate between these axes and dependent on the ratio between the volume fractions of the domains occupied by the phases $\Gamma_2(G_z, F_x)$ and $\Gamma_4(G_x, F_z)$. In turn, the volume fractions of the domains depend on the temperature. In this situation, the interaction of the acoustic wave with an intermediate domain structure in the vicinity of the first-order phase transition should be similar to the interaction of an acoustic wave with a magnetic subsystem of the orthoferrite in the angular phase $\Gamma_{24}(G_{x,z}, F_{x,z})$, in which the magnetization changes in direction from the $\mathbf{z}$ axis to the $\mathbf{x}$ axis, or vice versa. As was shown earlier by Dikshteĭn *et al.* [4], the attenuation of sound in orthoferrites due to the interaction of acoustic waves with a magnetic subsystem reaches a maximum at points of the $\Gamma_{24}(G_{x,z}, F_{x,z})$–$\Gamma_2(G_z, F_x)$ and $\Gamma_{24}(G_{x,z}, F_{x,z})$–$\Gamma_4(G_x, F_z)$ second-order phase transitions when the magnetization becomes parallel to the $\mathbf{x}$ axis or the $\mathbf{z}$ axis and vanishes when the angle the magnetization makes with the $\mathbf{x}$ axis or the $\mathbf{z}$ axis is equal to 45°. It is reasonable to assume that, in the situation where the orthoferrites with an intermediate domain structure undergo a first-order phase transition, the attenuation of sound exhibits a similar behavior. In actual fact, in the case when the volume fractions of the domains occupied by the phases $\Gamma_2(G_z, F_x)$ and $\Gamma_4(G_x, F_z)$ are equal to one another (i.e., at the point of the first-order phase transition), the direction of the average magnetization makes an angle of 45° with the $\mathbf{x}$ axis or the $\mathbf{z}$ axis. When the volume fraction of one of these phases is maximum, the direction of the average magnetization coincides either with the $\mathbf{x}$ axis or with the $\mathbf{z}$ axis. Therefore, with due regard for the aforementioned analogy, we can conclude that, in orthoferrites with an intermediate domain structure, the attenuation of sound should reach a minimum at the first-order phase transition point and a

maximum at points where the phases lose their stability, which is actually observed in the experiment.

Let us illustrate the above situation in terms of the phenomenological theory of coupled magnetoelastic waves in orthoferrites, which differs from the theories developed to date [1, 2, 4] in that it allows for the formation of an intermediate domain structure in an orthoferrite in the vicinity of the first-order orientational phase transition [5].

For this purpose, we consider a standard set of coupled equations, including the Landau–Lifshitz equations and the equations of elasticity theory, with allowance made for the attenuation of magnetoelastic waves in the magnetic subsystem [1, 2]:

$$\dot{\mathbf{F}} = -\frac{g}{2M_0}\left\{\left[\mathbf{F}, \frac{\partial W}{\partial \mathbf{F}}\right] + \left[\mathbf{G}, \frac{\partial W}{\partial \mathbf{G}}\right]\right\} + \frac{g}{2M_0}\mathbf{R}_\mathbf{F},$$

$$\dot{\mathbf{G}} = -\frac{g}{2M_0}\left\{\left[\mathbf{F}, \frac{\partial W}{\partial \mathbf{G}}\right] + \left[\mathbf{G}, \frac{\partial W}{\partial \mathbf{F}}\right]\right\} + \frac{g}{2M_0}\mathbf{R}_\mathbf{G}, \quad (1)$$

$$\rho\ddot{U}_i = \frac{\partial \sigma_{ik}}{\partial x_k}.$$

Here, g is the gyromagnetic ratio; $\mathbf{R}_\mathbf{F}$ and $\mathbf{R}_\mathbf{G}$ are the relaxation terms, which are written in the form [6]

$$\mathbf{R}_\mathbf{F} = -\lambda_0\frac{\partial W}{\partial \mathbf{F}} - \lambda_\perp \mathbf{G}^2\frac{\partial W}{\partial \mathbf{F}} - (\lambda_\perp - \lambda_\parallel)\mathbf{G}\left(\mathbf{G}, \frac{\partial W}{\partial \mathbf{F}}\right),$$

$$\mathbf{R}_\mathbf{G} = -\lambda_0\frac{\partial W}{\partial \mathbf{G}} - \lambda_\perp \mathbf{G}^2\frac{\partial W}{\partial \mathbf{G}} - (\lambda_\perp - \lambda_\parallel)\mathbf{G}\left(\mathbf{G}, \frac{\partial W}{\partial \mathbf{G}}\right);$$

M_0 is the magnetization of saturation of the sublattice at $T = 0$; W is the free energy density; ρ is the density of the magnet; $\mathbf{U}$ is the displacement vector; $\sigma_{ik} = \partial W/\partial U_{ik}$ is the stress tensor; U_{ik} is the strain tensor; and λ are the relaxation parameters. The relaxation terms $\mathbf{R}_{\mathbf{F},\mathbf{G}}$ are written in the approximation $F \ll G$. In the most general form, i.e., without this approximation, for two-sublattice antiferromagnets, the relaxation terms $\mathbf{R}_{\mathbf{F},\mathbf{G}}$ are given in [6] in the form of an expansion in terms of the effective fields $\partial W/\partial \mathbf{F}$ and $\partial W/\partial \mathbf{G}$. The parameters λ_0, $\lambda_\parallel$, and $\lambda_\perp$ separate out the contributions to the dissipation from the longitudinal and transverse vibrations with respect to the ferromagnetic and antiferromagnetic vectors. The free energy density has the form

$$W = \frac{1}{2}a\mathbf{G}^2 + \frac{1}{4}b\mathbf{G}^4 + \frac{1}{2}A\mathbf{F}^2 + \frac{1}{2}D(\mathbf{F}\mathbf{G})^2 + \frac{1}{2}D'\mathbf{F}^2\mathbf{G}^2$$
$$- 2M_0\mathbf{H}\mathbf{F} + \frac{1}{2}k_{ac}^0 G_z^2 + \frac{1}{2}k_{ab}^0 G_y^2 + \frac{1}{4}k_2 G_z^4 + \frac{1}{4}k_2' G_y^4$$
$$+ \frac{1}{2}k_2'' G_y^2 G_z^2 + d_1 F_x G_z - d_3 F_z G_x + 2[(B_{11}U_{xx}$$
$$+ B_{12}U_{yy} + B_{13}U_{zz})G_x^2 + (B_{21}U_{xx} + B_{22}U_{yy}$$
$$+ B_{23}U_{zz})G_y^2 + (B_{31}U_{xx} + B_{32}U_{yy} + B_{33}U_{zz})G_z^2 \quad (2)$$
$$+ B_{44}U_{yz}G_yG_z + B_{55}U_{xz}G_xG_z + B_{66}U_{xy}G_xG_y]$$
$$+ \frac{1}{2}(C_{11}U_{xx}^2 + C_{22}U_{yy}^2 + C_{33}U_{zz}^2) + C_{12}U_{xx}U_{yy}$$
$$+ C_{13}U_{xx}U_{zz} + C_{23}U_{yy}U_{zz}$$
$$+ 2C_{44}U_{yz}^2 + 2C_{55}U_{xz}^2 + 2C_{66}U_{xy}^2.$$

In this expression, the first five terms describe the energy of homogeneous exchange; the sixth term characterizes the energy of the magnet in an external magnetic field $\mathbf{H}$; and the subsequent terms account for the anisotropy energy (terms with coefficients k), the Dzyaloshinski–Moriya interaction energy (terms with coefficients d), the magnetoelastic energy (terms with coefficients B), and the elastic energy (terms with coefficients C). In expression (2), we used the standard designations accepted for orthoferrites [1, 2, 4].

As was noted above, in the range of the first-order orientational phase transition, there exists an intermediate domain structure consisting of domains of the phases $\Gamma_4(G_x, F_z)$ and $\Gamma_2(G_z, F_x)$. Therefore, the state of the magnet formed by domains of alternating phases Γ_2 and Γ_4 separated by the domain boundaries should be treated as the ground equilibrium state. In this state, the vectors $\mathbf{F}$ and $\mathbf{G}$ rotate in the xz plane and the angles between these vectors and the $\mathbf{z}$ axis depend on the y coordinate (taking into account the term characterizing the inhomogeneous exchange in the energy involved in expression (2)) [5]. For this state, it is necessary to obtain a linearized set of the equations of motion of magnetization (the Landau–Lifshitz equations) and elasticity, which will describe weak oscillations in the vicinity of the equilibrium. Then, this set of equations should be averaged over the volume containing a sufficiently large number of domains of the phases Γ_2 and Γ_4, whose linear sizes are however small as compared to the acoustic wavelength Λ. Upon averaging, in the linearized set of dynamic equations, the terms describing the inhomogeneous exchange can be disregarded. In this case, the surface waves localized at the domain boundaries are absent but the volume spin oscillations are retained. These volume spin oscillations are of special interest because it is precisely these oscillations that interact with acoustic vibrations of the aforementioned wavelengths. Within this approach, the problem of determining the spectrum of coupled magnetoelastic waves in the state with an intermediate domain structure becomes equivalent to the problem of determining the spectrum of these oscillations in the angular phase $\Gamma_{24}(G_{z,x}, F_{x,z})$, in which it is assumed that the vectors $\mathbf{G}$ and $\mathbf{F}$ depend implicitly on the y coordinate. This dependence disappears upon subsequent averaging (see below). It follows from relationship (2) that, in the state

$\Gamma_{24}(G_{z,x}, F_{x,z})$, the vectors **F** and **G** are determined by the equations

$$\begin{aligned}
\mathbf{F} &= 2M_0\chi_\perp[\mathbf{H} - D\chi_\parallel\mathbf{G}(\mathbf{HG}) + \mathbf{G}_d],\\
\chi_\perp^{-1} &= A + D\mathbf{G}^2, \quad \chi_\parallel^{-1} = A(D + D')\mathbf{G}^2,\\
\mathbf{G}_d &= \{D\chi_\parallel(d_1 - d_3)G_zG_x^2\\
&- d_1G_z, 0, D\chi_\parallel(d_1 - d_3)G_xG_z^2 + d_3G_x\},\\
&(a + b\mathbf{G}^2 + D'\mathbf{F}^2 + 4\Delta_1 - B_{55}^2G_z^2/C_{55})G_x\\
&+ D(\mathbf{FG})F_x - d_3F_z = 0,\\
&(a + b\mathbf{G}^2 + D'\mathbf{F}^2 + 4\Delta_3 + k_{ac}^0 + k_2G_z^2\\
&- B_{55}^2G_x^2/C_{55})G_z + D(\mathbf{FG})F_z + d_1F_x = 0,
\end{aligned} \tag{3}$$

where $\Delta_i = \sum_{p=1}^{3} B_{ip}U_{pp}^{(0)}$ and $U_{ik}^{(0)}$ stands for the equilibrium strains [1].

Let us now consider the case of wave propagation along the axis of a single crystal (i.e., $\mathbf{x} \parallel \mathbf{a}$), which was observed in the experiment. In order to linearize the set of coupled equations (1), all the variables should be represented in the form $\mathbf{Q} = \mathbf{Q}_0 + \mathbf{q}\exp(ikx - i\omega t)$, where $\mathbf{Q}_0$ is the quantity in the equilibrium state and **q** is a small deviation from the equilibrium state. Then, the obtained set of coupled equations should be averaged. For this purpose, all the coefficients in front of the variables **q** in the set of equations are represented in the following form [5]:

$$Q = Q(\Gamma_2)(1 - \xi) + Q(\Gamma_4)\xi, \tag{4}$$

where $Q(\Gamma_2)$ and $Q(\Gamma_4)$ are the coefficients for the phases $\Gamma_2(G_z, F_x)$ and $\Gamma_4(G_x, F_z)$ and $(1 - \xi)$ and ξ are the fractions of the domains of these phases, respectively. As was noted above, the correctness of this averaging is confirmed by the fact that the acoustic wavelength $\Lambda = S/\omega \approx 10^{-2}$ cm is considerably larger than the domain size in the intermediate state [5].

Finally, the total set of coupled equations takes the form

$$\begin{aligned}
&(i\omega - \lambda\omega_{fx})f_x - (1 - \xi)\omega_{cb}g_y + \xi\omega_{d3}f_y = 0,\\
&(i\omega - \lambda\omega_E)f_y - (1 - \xi)\omega_{ca}g_x + \xi\omega_{ac}g_z\\
&+ (1 - \xi)(\omega_{d3} - \omega_{d1})f_z - \xi\omega_d f_x\\
&+ \frac{\rho S_5^2\omega_{me5}}{B_{55}}(2\xi - 1)iku_z = 0,\\
&(i\omega - \lambda\omega_{fz})f_z - \xi\omega_{ab}g_y + (1 - \xi)\omega_{d1}f_y\\
&- \frac{\rho S_6^2\omega_{me6}}{B_{66}}\xi iku_y = 0,\\
&(i\omega - \lambda\omega_{gx})g_x + \frac{\omega_{d3}\omega_{ab}}{\omega_E}\xi g_y + (1 - \xi)\omega_E f_y\\
&+ \frac{\rho S_6^2\omega_{me6}\omega_{d3}}{B_{66}\omega_E}\xi iku_y = 0,\\
&(i\omega - \lambda\omega_{gy})g_y - \frac{\omega_{d3}\omega_{E1}}{\omega_E}\xi g_x\\
&- (1 - \xi)\frac{\omega_{d1}\omega_{E1}}{\omega_E}g_z - (1 - \xi)\omega_E f_x + \xi\omega_E f_z\\
&- \frac{\rho S_5^2\omega_{me5}}{\omega_E}\left[\frac{4B_{31}}{B_{55}}\omega_{d1}(1 - \xi) + \frac{4B_{11}}{B_{55}}\omega_{d3}\xi\right]iku_x = 0,\\
&(i\omega - \lambda\omega_{gz})g_z + \frac{\omega_{d1}\omega_{cb}}{\omega_E}(1 - \xi)g_y - \xi\omega_E f_y = 0,\\
&(\omega^2 - \omega_1^2)u_x + \frac{4ikB_{11}}{\rho}\xi g_x + \frac{4ikB_{31}}{\rho}(1 - \xi)g_z = 0,\\
&(\omega^2 - \omega_6^2)u_y + \frac{ikB_{66}}{\rho}\xi g_y = 0,\\
&(\omega^2 - \omega_5^2)u_z + \frac{ikB_{55}}{\rho}\xi g_z + \frac{ikB_{55}}{\rho}(1 - \xi)g_x = 0.
\end{aligned} \tag{5}$$

Here, we introduced the following designations:

$$\begin{aligned}
\omega_{fx} &= g[\chi_\perp^{-1}(1 - \xi) + \chi_\parallel^{-1}\xi + 16\pi M_0^2]/2M_0,\\
\omega_{fz} &= g[\chi_\parallel^{-1}(1 - \xi) + \chi_\perp^{-1}\xi]/2M_0,\\
\omega_{gx} &= g[2\xi b + (1 - \xi)(-k_{ac}^0 - k_2 - 4(\Delta_2 - \Delta_1)\\
&+ \chi_\perp d_1^2 + D\chi_\perp^2 d_1^2)]/2M_0,\\
\omega_{gy} &= \xi\omega_{ab} + (1 - \xi)\omega_{cb},\\
\omega_{gz} &= g[(1 - \xi)(2b + 2k_2 + \chi_\perp d_1^2)\\
&+ \xi(k_{ac}^0 + 4(\Delta_3 - \Delta_1) + \chi_\perp d_3^2)]/2M_0,\\
\omega_E &= g\chi_\perp^{-1}/2M_0, \quad \omega_{E1} = g\chi_\perp^{-1}[1 + 2\chi_\perp(b - D')]/2M_0,\\
\omega_{d3,1} &= gd_{3,1}/2M_0,\\
\omega_d &= g[d_3 - d_1 + 16\pi M_0^2\chi_\perp d_3]/2M_0,\\
\omega_{ab} &= g[k_{ab}^0 + 4(\Delta_2 - \Delta_1) + \chi_\perp d_3^2]/M_0,\\
\omega_{cb} &= g[k_{ab}^0 + k_2'' - k_{ac}^0 - k_2 + 4(\Delta_2 - \Delta_3) + \chi_\perp d_1^2]/2M_0,\\
\omega_{ca} &= g[-k_{ac} - k_2 - 4(\Delta_3 - \Delta_1) + \chi_\perp d_1(d_1 - d_3)]/2M_0,\\
\omega_{ac} &= g[k_{ac} + 4(\Delta_3 - \Delta_1) + \chi_\perp d_3(d_3 - d_1)]/2M_0,\\
\omega_i^2 &= S_i^2k^2, \quad S_i^2 = C_{ii}/\rho,
\end{aligned}$$

$$\omega_{mei} = \frac{gB_{ii}^2}{2M_0\rho S_i^2}, \quad \lambda = \lambda_0 + \lambda_\parallel.$$

Relationships (5) were derived using the condition $\lambda_\perp = \lambda_\parallel$ for the relaxation terms and ignoring the terms proportional to the small magnitude F. Moreover, it was assumed that, for the phases Γ_2 and Γ_4, the magnitude $G \approx 1$ and all the characteristic frequencies are considerably smaller than the exchange frequency ω_E.

The set of equations (5) is rather complicated to be used in analyzing the dispersion laws of coupled magnetoelastic waves. However, this set of equations can be substantially simplified without a loss in generality. In order to accomplish this simplification, we make the assumption that $B_{31} = B_{11} = 0$ and $d_3 = d_1 = 0$, which corresponds to disregarding both the interaction of longitudinal acoustic waves with the spin subsystem and the Dzyaloshinski–Moriya interaction. As a result, the set of coupled equations (5) is decomposed into two independent sets of equations in the variables f_y, g_x, g_z, u_z and g_y, f_x, f_z, u_y, respectively. In one of these sets, the transverse acoustic wave with polarization $\boldsymbol{\varepsilon} \parallel \mathbf{c}$ interacts with the spin subsystem. In the other set, the transverse acoustic wave with polarization $\boldsymbol{\varepsilon} \parallel \mathbf{b}$ interacts with the spin subsystem. By using the obtained sets of coupled equations, we can easily derive the dispersion relations for magnetoelastic waves:

$$\begin{aligned}
&\omega^5 + i\lambda(\omega_E + \omega_{gx} + \omega_{gz})\omega^4 - i\{\omega_5^2 + \omega_{1S}^2 \\
&+ \lambda^2[\omega_E(\omega_{gx} + \omega_{gz}) + \omega_{gx}\omega_{gz}]\}\omega^3 \\
&- i\lambda[\omega_5^2(\omega_E + \omega_{gx} + \omega_{gz}) + \omega_E\omega_{1rS}^2 + \lambda^2\omega_E\omega_{gx}\omega_{gz}]\omega^2 \\
&+ \omega_5^2\{\omega_{1S}^2 - \omega_E\omega_{me5}(2\xi - 1)^2 \\
&\times \lambda^2[\omega_E(\omega_{gx} + \omega_{gz}) + \omega_{gx}\omega_{gz}]\}\omega \\
&+ i\lambda\omega_5^2\omega_E[\omega_{1rS}^2 + \omega_{2rS}^2(2\xi - 1) + \lambda^2\omega_{gx}\omega_{gz}] = 0,
\end{aligned} \tag{6}$$

$$\begin{aligned}
&\omega^5 + i\lambda(\omega_{fx} + \omega_{gy} + \omega_{fz})\omega^4 - [\omega_6^2 + \omega_{2S}^2 \\
&+ \lambda^2(\omega_{fx}\omega_{gy} + \omega_{fx}\omega_{fz} + \omega_{gy}\omega_{fz})]\omega^3 \\
&- i\lambda[\omega_6^2(\omega_{fx} + \omega_{gy} + \omega_{fz}) + \omega_E\omega_{3rS}^2 \\
&+ \lambda^2\omega_{fx}\omega_{gy}\omega_{fz}]\omega^2 + \omega_6^2[\omega_{2S}^2 - \omega_E\omega_{me6}\xi^3 \\
&+ \lambda^2(\omega_{fx}(\omega_{gy} + \omega_{fx}\omega_{fz} + \omega_{gy}\omega_{fz}]\}\omega \\
&+ i\lambda\omega_6^2[\omega_E\omega_{3rS}^2 - \omega_E\omega_{fx}\omega_{me6}\xi^3 + \lambda^2\omega_{fx}\omega_{gy}\omega_{fz}] = 0,
\end{aligned} \tag{7}$$

where

$$\omega_{1S}^2 = \omega_E[\omega_{ca}(1-\xi)^2 + \omega_{ac}\xi^2],$$

$$\omega_{1rS}^2 = \omega_{gz}\omega_{ca}(1-\xi)^2 + \omega_{gx}\omega_{ac}\xi^2,$$

$$\omega_{2rS}^2 = \omega_{me5}[\omega_{gz}(1-\xi)^2 - \omega_{gx}\xi^2],$$

$$\omega_{2S}^2 = \omega_E[\omega_{cb}(1-\xi)^2 + \omega_{ab}\xi^2],$$

$$\omega_{3rS}^2 = \omega_{fz}\omega_{cd}(1-\xi)^2 + \omega_{fx}\omega_{ab}\xi^2.$$

From dispersion relations (6) and (7), we can determine the dispersion laws of coupled magnetoelastic waves. For $\lambda = 0$, we obtain the dispersion laws of continuous magnetoelastic waves:

$$\begin{aligned}
\omega_{\mathrm{I}}^2 &= \omega_{1S}^2 + \omega_5^2\omega_E\omega_{me5}(2\xi - 1)^2/\omega_{1S}^2, \\
\omega_{\mathrm{II}}^2 &= \omega_{2S}^2 + \omega_6^2\omega_E\omega_{me6}\xi^3/\omega_{2S}^2,
\end{aligned} \tag{8}$$

$$\begin{aligned}
\omega_{\mathrm{III}}^2 &= \omega_5^2[1 - \omega_E\omega_{me5}(2\xi - 1)^2/\omega_{1S}^2], \\
\omega_{\mathrm{IV}}^2 &= \omega_6^2[1 - \omega_E\omega_{me6}\xi^3/\omega_{2S}^2].
\end{aligned} \tag{9}$$

The first two branches of the spectrum correspond to quasi-spin waves, whereas the second two branches correspond to quasi-elastic waves. It is evident from dispersion relations (9) that the velocity of quasi-elastic waves $S_{\mathrm{III}} = \omega_{\mathrm{III}}/k$ with polarization $\boldsymbol{\varepsilon} \parallel \mathbf{c}$ decreases to the greatest extent at points of losses in stability of the phases Γ_2 and Γ_4, i.e., at $\xi = 1$ and 0, respectively. Under the assumptions used in our treatment, the velocity of quasi-elastic waves remains unchanged at the point of the orientational phase transition (this point corresponds to $\xi = 1/2$), which is in agreement with the experimental results (as was noted above, the relative decrease in the velocity of the quasi-elastic waves is estimated to be $\Delta S/S \sim 0.2\%$). The velocity of quasi-elastic waves with polarization $\boldsymbol{\varepsilon} \parallel \mathbf{b}$ decreases to the greatest extent only at the point of a loss in stability of the phase Γ_2. In the phase Γ_4, this acoustic wave does not interact with the spin subsystem absolutely.

By solving the set of equations (6) and (7) to first order in the attenuation parameter λ, we can determine the attenuation of acoustic waves $\Gamma = k''$, where k'' is the imaginary part of the wavenumber. This number is given by the formulas

$$\begin{aligned}
\Gamma_{\mathrm{III}} &= \frac{\lambda}{2}\frac{\omega_E\omega_{me5}(2\xi - 1)}{S_5\omega_{1S}^2(1-\zeta_5)^{3/2}} \\
&\times\left\{(\omega_{gz} - \omega_{gx})(\omega_{ca} + \omega_{ac})\xi^2(1-\xi)^2\right. \\
&\left.+ \frac{\omega^2}{\omega_{1S}^2}[(\omega_{gx} + \omega_E)\omega_{ca}(1-\xi)^2 + (\omega_{gz} + \omega_E)\omega_{ac}\xi^2]\right\},
\end{aligned} \tag{10}$$

$$\begin{aligned}
\Gamma_{\mathrm{IV}} &= \frac{\lambda}{2}\frac{\omega_E\omega_{me6}\xi^3}{S_5\omega_{2S}^4(1-\zeta_6)^{3/2}} \\
&\times[(\omega_{fx} - \omega_{fz})\omega_{cb}\omega_E(1-\xi)^2 + \omega^2(\omega_{gy} + \omega_{fz})],
\end{aligned} \tag{11}$$

where $\zeta_5 = \omega_E\omega_{me5}(2\xi - 1)^2/\omega_{1S}^2$ and $\zeta_6 = \omega_E\omega_{me6}\xi^3/\omega_{2S}^2$ are the parameters of magnetoelastic coupling.

Analysis of relationships (10) and (11) enables us to explain qualitatively the experimentally observed specific features of the propagation of acoustic waves in the Fe_3BO_6 compound. In particular, it follows from relationship (10) that, at the stability boundaries of the intermediate domain structure ($\xi = 0$ and 1), the parameter of magnetoelastic coupling ζ_5 is maximum, the frequency ω_{1S}^2 is minimum, and the attenuation of transverse acoustic waves Γ_{III} with orientations $\mathbf{k} \parallel \mathbf{a}$ and $\boldsymbol{\varepsilon} \parallel \mathbf{c}$ has maxima. However, at the phase transition point ($\xi = 1/2$), the attenuation of these acoustic waves becomes equal to zero and is determined only by the attenuation in the elastic subsystem, which was disregarded when deriving relationship (10). Therefore, at the point of the first-order orientational phase transition, the attenuation of active acoustic waves should actually have a minimum, which is observed in the experiment (see figure). It follows from relationship (11) that the attenuation Γ_{IV} of transverse acoustic waves with vectors $\mathbf{k} \parallel \mathbf{a}$ and $\boldsymbol{\varepsilon} \parallel \mathbf{b}$ should have one maximum corresponding to one boundary of existence of the intermediate domain structure ($\xi = 1$ is the point of loss in stability of the phase Γ_2). It is this situation that is observed in experiment [3].

It should be noted that one more hypothesis can be proposed to explain the acoustic anomaly in the Fe_3BO_6 compound, which was not observed in the experiment. According to this hypothesis, as the point of the orientational phase transition is approached, the absorption of active acoustic waves due to the strong magnetoelastic interaction increases to such an extent that these acoustic waves in the vicinity of the orientational phase transition point itself are of a purely relaxation nature [2]. As a result, the real part of the acoustic frequency vanishes and the absorption of acoustic waves should be minimum. However, this hypothesis is inconsistent with the fact that the relative change in the velocity of active acoustic waves in the vicinity of the orientational phase transition point is too small to cause a considerable increase in the attenuation of acoustic waves as the point of the orientational phase transition is approached.

REFERENCES

1. V. D. Buchel'nikov, N. K. Dan'shin, L. T. Tsymbal, and V. G. Shavrov, Usp. Fiz. Nauk **166** (6), 585 (1996) [Phys. Usp. **39** (6), 547 (1996)].
2. V. D. Buchel'nikov, N. K. Dan'shin, L. T. Tsymbal, and V. G. Shavrov, Usp. Fiz. Nauk **169** (10), 1049 (1999) [Phys. Usp. **42** (10), 957 (1999)].
3. L. T. Tsymbal, A. I. Izotov, N. K. Dan'shin, and K. N. Kocharyan, Zh. Éksp. Teor. Fiz. **105** (4), 948 (1994) [JETP **78**, 508 (1994)].
4. I. E. Dikshteĭn, V. V. Tarasenko, and V. G. Shavrov, Fiz. Tverd. Tela (Leningrad) **19** (4), 1107 (1977) [Sov. Phys. Solid State **19** (4), 644 (1977)].
5. V. G. Bar'yakhtar and V. A. Popov, *Problems of the Solid-State Physics* (Ural Research Center, USSR Academy of Sciences, Sverdlovsk, 1975) [in Russian].
6. A. A. Mukhin and A. S. Prokhorov, Tr. Inst. Obshch. Fiz. Akad. Nauk SSSR **25**, 162 (1990).

Translated by O. Moskalev

Physics of the Solid State, Vol. 47, No. 10, 2005, pp. 1892–1899. Translated from Fizika Tverdogo Tela, Vol. 47, No. 10, 2005, pp. 1818–1825.

MAGNETISM AND FERROELECTRICITY

Orientational Phase Transition into a Modulated Magnetic State in the Weak Ferromagnet $FeBO_3$: Mg

B. Yu. Sokolov

National University of Uzbekistan, Tashkent, 700174 Uzbekistan

e-mail: optic@nuuz.uzsci.net

Received November 24, 2004

Abstract—The transition from a homogeneous into a modulated magnetic state in the easy-plane weak ferromagnet $FeBO_3$: Mg is studied by a magnetooptic method. At $T < 135$ K, the application of a magnetic field in the basal plane of the crystal is shown to excite the modulation of its magnetic order parameter, which manifests itself in a periodic deviation of the local ferromagnetism vector from the magnetization direction. The conditions for the existence of a modulated magnetic superstructure in $FeBO_3$: Mg are studied, and its preferred orientation in the basal plane of the crystal is analyzed. A magnetic *H–T* phase diagram that shows the boundaries between the homogeneous and inhomogeneous magnetic states of this weak ferromagnet is constructed. The modulation period and the azimuthal angle specifying the local ferromagnetism vector direction in the structure are studied as a function of temperature and magnetic field. The results obtained are discussed in terms of the theory of magnetic ripple using the model of anisotropic magnetic centers appearing in a crystal doped by magnesium ions. © *2005 Pleiades Publishing, Inc.*

1. INTRODUCTION

Long-period modulated magnetic structures (MMSs) represent a widespread type of magnetic ordering in solids. The basic mechanisms of the appearance of MMSs are thought to be known. These mechanisms in magnetically ordered dielectrics are either the exchange interactions of different sign between the nearest and next-to-nearest atomic neighbors or the Dzyaloshinskiĭ–Moriya interaction [1]. Recently, Karaev *et al*. [2] demonstrated that an orientational phase transition from a homogeneous into a modulated magnetic state takes place in an easy-plane antiferromagnet having weak ferromagnetism, namely, in iron borate containing diamagnetic magnesium ions ($FeBO_3$: Mg). An MMS appeared when an external magnetic field **H** was applied along three preferred directions in the basal plane of the crystal. In this type of magnet, a field-induced MMS was detected for the first time and was to have several specific features. In particular, its appearance cannot be explained by the mechanisms mentioned above. For example, if the competition between exchange interactions in the nearest coordination shells is assumed to be responsible for the modulation of the order parameter in $FeBO_3$: Mg, the modulus of the wave vector **k** should be determined by the relation [3]

$$(ak)^2 \approx (J_1 - \xi J_2)/J_1,$$

where J_1 and J_2 are the exchange integrals between the nearest and next-to-nearest atomic neighbors, respectively; ξ is a numerical factor of the order of unity; and $a \approx 5$ Å is the lattice parameter of the $FeBO_3$ crystal in the basal plane [4]. Since the MMS period is $d = 2\pi/k \sim$ 100 μm, the relative accuracy for the compensation of the competing interactions should be $\sim 10^{-9}$, which seems unlikely. The Dzyaloshinskiĭ–Moriya interaction does not impose restrictions on the modulation period of the magnetic order parameter of a medium. However, in this case, an increase in the field *H* applied in the plane of rotation of the magnetic moments should be accompanied by a decrease in *k* [1], whereas experimentally $k(H)$ is an increasing function.

The unusual mechanism resulting in the modulation of the magnetic order parameter in $FeBO_3$: Mg stimulated further investigations into an MMS in this weak ferromagnet. The results of these investigations are presented in this work.

2. EXPERIMENTAL

We performed measurements on the single-crystal $FeBO_3$: Mg sample that was experimentally investigated in [2] (the developed plane of the sample coincides with the basal plane, the sample thickness is ≈60 μm, the cross-sectional dimension is ~3 mm, and the Mg content is ~0.1 wt %). The MMS was studied in the transparent region of the crystal with a polarizing microscope using the technique described in [2]: the incident light was normal to the sample plane, and a magnetooptic method was used to visualize the evolution of the domain structure (DS) of the sample induced by an applied magnetic field (in all experiments, the vector **H** lied in the basal plane of the crystal) and temperature. In contrast to [2], the experimental setup was equipped with a video camera connected to a computer. Since the DS of iron borate is sensitive to mechanical stresses [5,

6], the sample was mounted in a cryostat in a special holder to minimize the effect of the temperature deformations of the metallic parts of the cold conductor on the sample. (The results of studying the effect of nonuniform stresses on the magnetic state of $FeBO_3$ will be published in a later paper.)

To study the structure of a modulated magnetic state (i.e., the spatial distribution of the magnetic order parameter) in an easy-plane weak ferromagnet using a magneto-optic method, it is necessary to find the relation between the intensity of light passing through the polarizer–sample–analyzer system and the orientation of the ferromagnetism vector **m** (or the antiferromagnetism vector **l**) in the basal plane of the crystal. For light propagating along the C_3 (optical) axis and corresponding to the transparent region ($\lambda \sim 0.5$ μm), the main magneto-optic effects in iron borate are magneto-optic linear dichroism and the Faraday effect [7]. Therefore, we can represent the light intensity at the exit of the polarizer–sample–analyzer system in the form [2]

$$I = I_0[\cos^2(\varphi - \psi) + A(\delta)\cos\varphi + B\cos 3(\varphi + \varphi_0) + C\sin 2(\varphi - \varphi_1)], \quad (1)$$

where I_0 is the incident-light intensity; φ and ψ are the azimuths of the polarizer and analyzer transmission axes, respectively, with respect to the x axis of the laboratory coordinate system (the light direction coincides with the z axis); φ is the azimuth of the vector **m** with respect to the same axis in the plane that is normal to the z axis (we assume that $\mathbf{m}(Z) = \text{const}$); $A(\delta)$ and B are the magneto-optic coefficients characterizing the rotation of the plane of light polarization in the sample due to the Faraday effect; C is the magneto-optic coefficient characterizing the rotation due to magneto-optic linear dichroism; φ_0 is the angle between the x axis and the C_2 axis of the crystal; and $\varphi_1 = \varphi/2 + \psi/2$. Under typical experimental conditions that provide the maximum image contrast of a magnetic inhomogeneity in the sample (see below), we have $\varphi - \psi = \pi/2 + \Delta$, where $\Delta \approx 3°$.

Equation (1) takes into account the fact that the sample can be tilted a small angle δ with respect to the x axis; therefore, $I(\varphi)$ contains both the contribution from the Faraday effect that is caused by **m** periodically leaving the basal plane of the crystal and is maximum at $\mathbf{m} \parallel C_2$ [7] (the third term) and the contribution from the Faraday rotation due to the projection of the vector **m** on the light direction becoming nonzero when the sample is tilted (the second term). If the light direction coincides with the crystal optical axis, we have $A(\delta = 0) = 0$.

Our measurements showed that, in saturating fields ($H > 30$ Oe [2]), Eq. (1) describes well the orientation dependence of the magneto-optic signal I. Figure 1 shows the typical experimental $I(\varphi)$ curve recorded for the vector **H** rotated through an angle of 360° in the basal plane of $FeBO_3$: Mg at $T = 80$ K and $\delta \sim 1°$. Using this curve and the least squares method, we found the

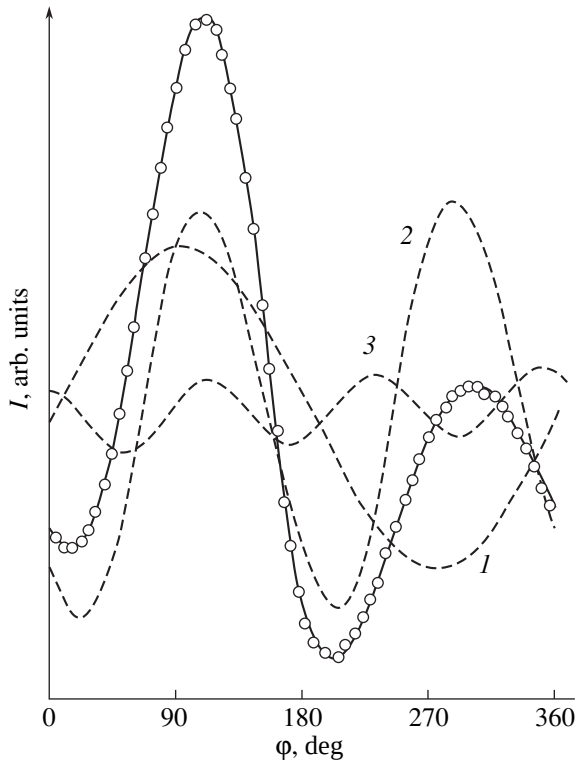

Fig. 1. Dependence of the magneto-optic signal I on the magnetic-field orientation in the basal plane of the $FeBO_3$: Mg crystal at $T = 80$ K and $H = 100$ Oe. The points stand for experiment, and the solid line shows the results of fitting by Eq. (1). (*1–3*) The first, second, and third signal harmonics, respectively.

harmonic amplitudes in Eq. (1) and determined the C_2 axis orientation. The ratios of the magneto-optic coefficients found from the results given in Fig. 1 are as follows: $A(\delta \sim 1°) : C : B \approx 5 : 6 : 1$. Thus, an analysis of the local characteristics of the luminous flux at the exit of the sample based on Eq. (1) can give information on the spatial variation of the magnetic order parameter in $FeBO_3$: Mg if the angle φ is taken to be a function of spatial coordinates.

Apart from visual observation of the evolution of a DS, we also studied hysteresis loops of the magneto-optic signal $I(H)$ detected under quasi-static magnetization conditions and the temperature dependence of the magneto-optic susceptibility dI/dH measured in an ac magnetic field with an amplitude of ~0.1 Oe and a magnetization reversal frequency of 25–100 Hz. For these studies, the sample was placed such that the angle of light incidence on the sample plane was ~10° and the polarizer transmission axis was oriented along the **H** direction (the vector **H** does not leave the sample plane and lies in the plane of incidence). As follows from Eq. (1), in this case (with allowance for the found relation between the magneto-optic coefficients), the magneto-optic signal I is specified almost completely by the term A, i.e., by the Faraday effect caused by the pres-

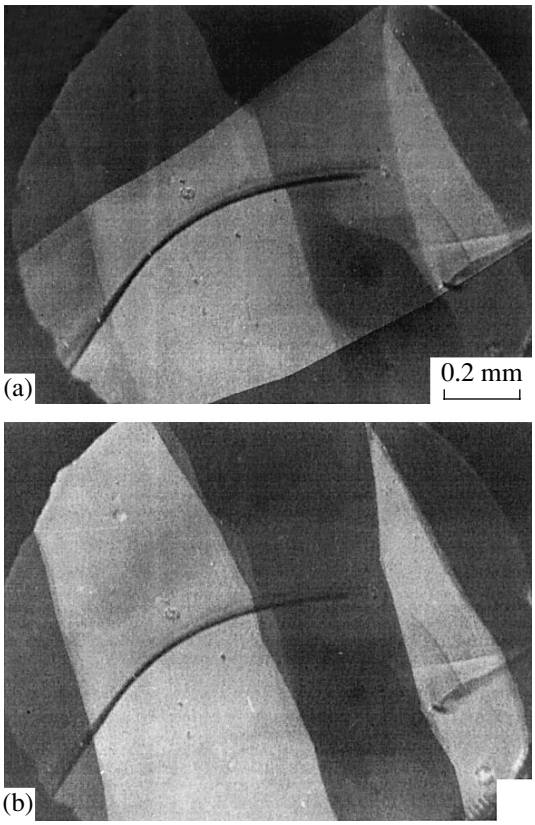

Fig. 2. Images of the domain structure of $FeBO_3$: Mg taken at temperatures of (a) 290 and (b) 80 K.

ence of the projection of the vector **m** on the light propagation direction. Hence, there is reason to believe that the $I(H) \approx A(H)$ and $dI/dH(T) \approx dA/dH(T)$ dependences obtained under these conditions reflect the run of the corresponding $M(H)$ and $dM/dH(T)$ dependences (M is the magnetic moment of the sample).

3. EXPERIMENTAL RESULTS

At room temperature, the sample has a two-layer DS that is typical of thin crystalline plates of iron borate free of stresses (see, e.g., [5, 6]): domain walls are oriented in the sample plane in directions close to the C_2 axes. As the temperature decreases to $T \approx 150$ K, the DS changes: it transforms jumpwise from a two-layer into a through structure, and this structure does not change down to the minimum experimental temperature (T = 80 K) (Fig. 2). To the best of our knowledge, investigations of the evolution of the DS of iron borate with temperature have not been performed; according to our observations, the DS of an impurity-free $FeBO_3$ crystal is virtually independent of T. Moreover, we also found that, at low temperatures, the $dA/dH(T)$ dependences of the magneto-optic susceptibilities of pure and magnesium-containing crystals differ substantially (Fig. 3).

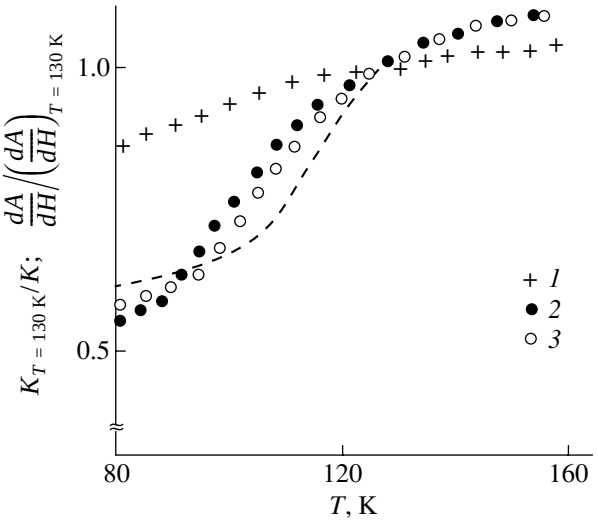

Fig. 3. Temperature dependence of the magneto-optic susceptibility normalized to its value at T = 130 K of (*1*) impurity-free and (*2*, *3*) magnesium-doped crystals. The frequency of the ac magnetic field is (*1*, *3*) 25 and (*2*) 95 Hz. The dashed line is the temperature dependence of K^{-1} normalized to its value at T = 130 K as calculated from Eq. (5).

The technical magnetization of the $FeBO_3$: Mg crystal is standard: as the field increases, the area of domains in which the vector **m** makes an acute angle with the vector **H** increases at the expense of domains with the opposite orientation of **m** until the crystal changes into a single-domain (homogeneous) state. However, below $T_k \sim 135$ K, when a magnetic field is applied in the sample plane in directions perpendicular to the C_2 axes, the crystal first becomes single-domain and then, as the field increases, bands with diffuse boundaries and different magneto-optic image contrasts appear in the sample image (Figs. 4a–4c). Unlike ordinary domain walls, a change in the applied magnetic field does not cause a smooth shift in the band boundaries with respect to each other; however, as the field increases (decreases), the number of bands increases (decreases) jumpwise. The banded structure exists in a certain T-dependent field range ΔH and disappears as the magneto-optic contrast between bright and dark bands gradually decreases. The conditions for the excitation and existence of the structure are slightly different for different directions: the ranges ΔH [2] and the values of T_k are different (T_k changed by about ±3 K).

When the vector **H** deviates by an angle <10° from these directions, the bands change: their spatial period changes, and they shift; however, their direction (which coincides with the direction of one of the C_2 axes) and their image contrast remain unchanged. A further deviation of the field from these directions leads to a jumpwise disappearance of the structure. As an example, Figs. 4b–4e show the image of an arising banded system observed in polarized light at T = 80 K.

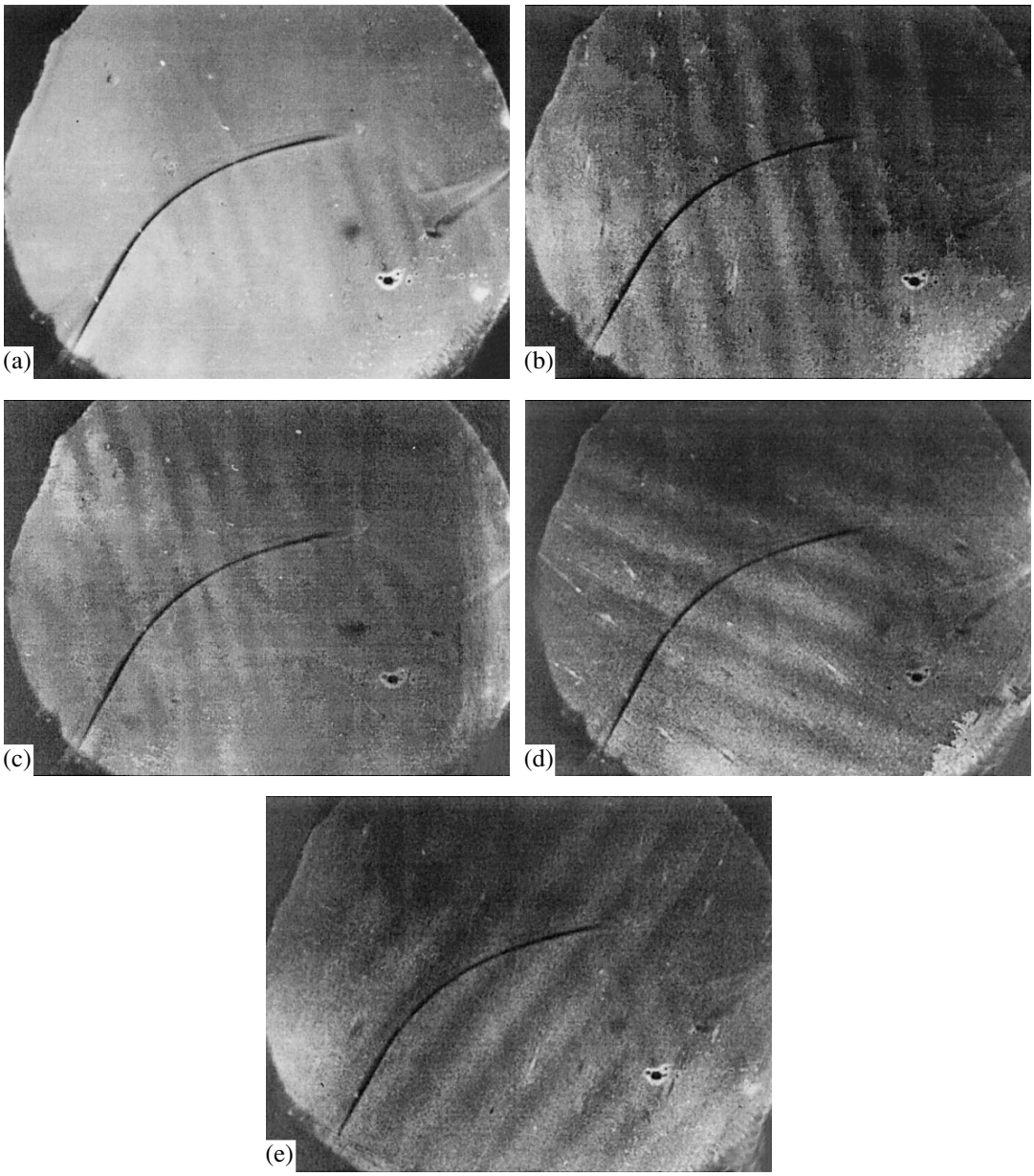

Fig. 4. Images of the crystal taken in polarized light at various field strengths and orientations. The field H is (a) 4.5, (b) 5, (c) 10, and (d, e) 6 Oe. T = 80 K. The vector **H** lies in the basal plane and is normal to the direction of structural bands.

It should be noted that, since the demagnetized sample has a 180° DS [5, 6], the contribution of linear dichroism [the term C in Eq. (1)] to I from neighboring domains is the same. Therefore, the DS images shown in Fig. 2 were mainly generated due to the Faraday effect [the term A in Eq. (1)]. The sample was rotated through ~10° about the horizontal axis lying in the sample plane. (When the angle between the direction of light propagation and the crystal optical axis is >10°, the contribution of natural birefringence to I becomes substantial, which degenerates the DS image contrast.) The sets of bands were detected most clearly for normal incidence of light on the sample plane (Fig. 4).

The appearance of a system of bands is accompanied by anomalous hysteresis loops of the magneto-optic signal $A(H)$. As is seen from Fig. 5, unlike the $A(H)$ curve recorded at T = 140 K, the $A(H)$ curve obtained at T = 80 K exhibits hysteresis in the range $5 < H < 20$ Oe (in addition to a significantly higher coercive force) and a break in its slope near $H = 0$.

The average spatial period d of the arising system of bands decreases with increasing H and increases with decreasing temperature. The period d varies with H and T jumpwise due to a jumpwise change in the interband distance induced by a change in the number of bands in the given length (the $d(H)$ dependence is given in [2],

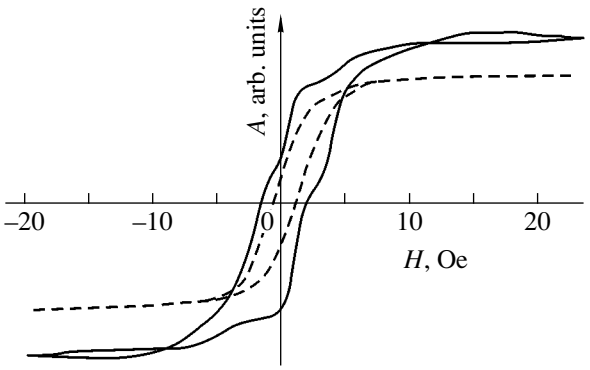

Fig. 5. Field dependences of the magneto-optic signal obtained at T = 80 K (solid line) and 140 K (dashed line). $\mathbf{H} \perp C_2$, and the field sweep time is ~15 s.

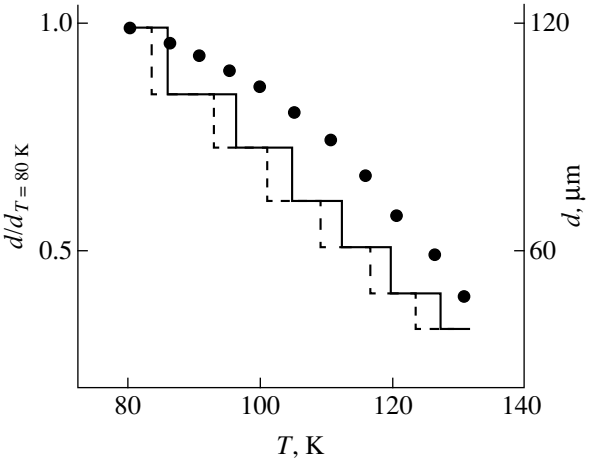

Fig. 6. Temperature dependence of the average spatial period of the system of bands recorded upon heating (solid line) and cooling (dashed line) of the sample. H = 6 Oe. $\mathbf{H} \perp C_2$. The points show the temperature dependence of the ratio $d/d_{T = 80\ \mathrm{K}}$ K as calculated from Eq. (3) at H = 6 Oe.

and the $d(T)$ dependence is shown in Fig. 6). The $d(T)$ dependences obtained upon heating and cooling of the sample differ only weakly, whereas the $d(H)$ dependence (see [2]) has a significant hysteresis (upon reverse magnetization, the average structure period is smaller than the period detected as H increases from zero).

The authors of [2, 8] related the appearance of the quasi-periodic system of bands having different magneto-optic image contrast to the transition of $FeBO_3$: Mg from a homogeneous magnetic state (with collinear local **m** vectors) into a ripple magnetic phase. In this phase, the dependence of the azimuthal angle of the vector **m** on the spatial coordinate along the magnetization direction has the form

$$\varphi = \varphi_A \cos kx, \qquad (2)$$

where φ_A is the amplitude of deviation of the local vector **m** from the **x** axis ($\mathbf{x} \parallel \mathbf{H} \perp C_2$) and **m** does not leave the basal plane of the crystal. According to Eq. (1), this transition should result in spatial modulation of signal I along the wave vector **k** of the structure, which manifests itself in a system of bright and dark bands with diffuse boundaries. The digitized image of the system of bands shown in Fig. 4 demonstrates that the intensity I modulation along the vector **k** is described well by a harmonic function of x. Therefore, the disappearance of the bands as a result of a gradual decrease in the structure image contrast (with increasing H and/or T) is specified by the corresponding $\varphi_A(H)$ and $\varphi_A(T)$ dependences.

Signal I contains contributions from several magneto-optic effects having different dependences on φ. Therefore, in general, it is difficult to experimentally find φ_A and to study the $\varphi_A(H, T)$ dependence by analyzing the local characteristics of the luminous flux at the exit of the sample. Methodically, it is easier to determine φ_A from the measured integrated light intensity $I(H, T)$ passing through the polarizer–sample–analyzer system using Eq. (1). Substituting Eq. (2) into Eq. (1) and integrating it with respect to x over the entire sample length in the vector **k** direction, we can obtain integral equations relating the measured value of $I(H, T)$ to the average amplitude of deviation of the vector **m** from the magnetization direction at the centers of neighboring bands. The normalizing factors in these equations were determined by measuring I at a given temperature in a saturating magnetic field H = 100 Oe ($\mathbf{H} \parallel \mathbf{k}$), i.e., when it is certain that $\varphi_A = 0$. The other parameters of the equations were determined using the relation between the coefficients A, B, and C found from the $I(\varphi)$ orientation dependence (Fig. 1), and the values of k were calculated from the $d(H)$ [2] and $d(T)$ dependences obtained experimentally. For calculations, the temperature dependence of the coefficients A, B, and C was assumed to be analogous to the I (H = 100 Oe, T) dependence (in the temperature range under study, I (H = 100 Oe) decreases by about 10% with increasing T). The field and temperature dependences of the angle φ_A obtained by this method are given in Fig. 7.[1]

Figure 8 shows the experimental H–T phase diagram that illustrates the boundaries between the homogeneous and inhomogeneous magnetic states of $FeBO_3$: Mg. The temperature and the field range ΔH of the MMS were determined by direct visual observation of the nucleation and disappearance of the system of bands. As follows from Fig. 8, the modulated magnetic state is intermediate between two phases of the crystal having homogeneous magnetization, with $\mathbf{m} \parallel C_2$ (phase I) and $\mathbf{m} \parallel \mathbf{H} \perp C_2$ (phase II). The characters of the $d(H, T)$ and $\varphi_A(H, T)$ dependences indicate that the I $\rightleftharpoons$ MMS

[1] According to the calculation, the maximum value of $\varphi_A(H$ = 6 Oe) is about 11.5° at T = 80 K, which is close to the angle φ modulation amplitude found in [8] by another method.

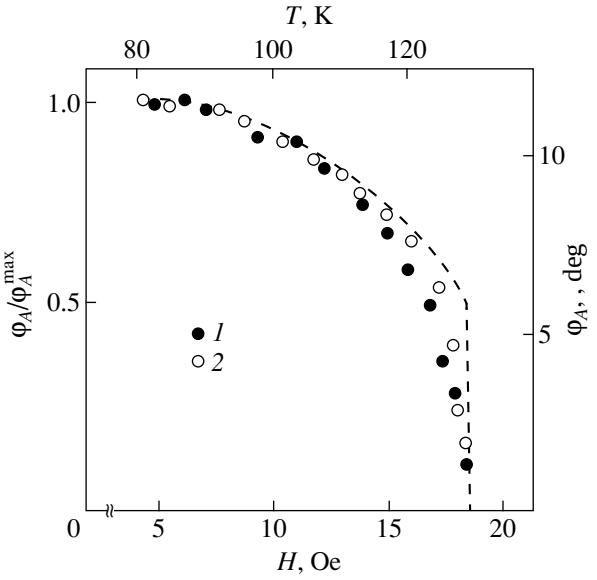

Fig. 7. (*1*) Field and (*2*) temperature dependences of the amplitude of deviation of the local ferromagnetism vector in the modulated magnetic structure from the applied-field direction: (*1*) $T = 80$ K and (*2*) $H = 6$ Oe, $\mathbf{H} \perp C_2$. The dashed line shows the temperature dependence of the angle φ_A normalized to its maximum value $\varphi_A^{\max}$ as calculated from Eq. (4) [for the calculation, we assumed that $K_a(T) \propto K(T)$].

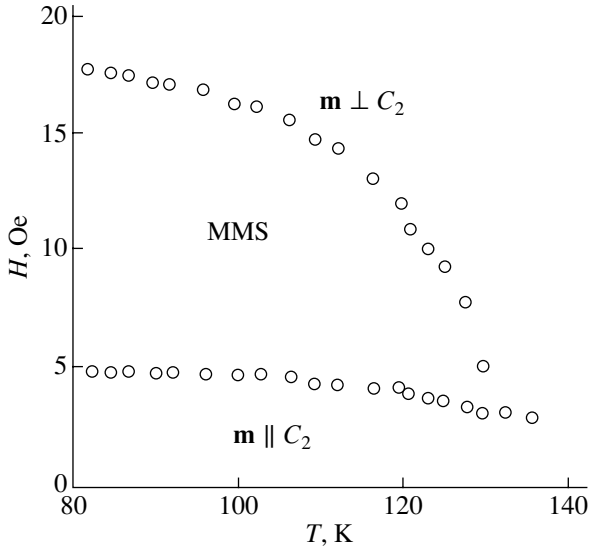

Fig. 8. Magnetic phase diagram of $FeBO_3$: Mg. MMS stands for modulated magnetic state.

transition is a first-order phase transformation and that the II $\rightleftharpoons$ MMS transition is a second-order phase transformation.

4. DISCUSSION OF THE RESULTS

In terms of its characteristic features, the MMS arising in $FeBO_3$: Mg resembles the well-known phenomenon of a magnetization ripple observed in polycrystalline permalloy films [9]. A magnetization ripple appears when a film is magnetized in its plane, and it is related to the transition of a permalloy into a magnetic phase in which the azimuth of the local magnetization vector oscillates about its value near the field direction. Like the MMS period in $FeBO_3$: Mg, the spatial modulation period decreases with increasing H. As was shown in [10], an equilibrium magnetic structure of the magnetization-ripple type appears due to the competition between random anisotropy (which is crystalline anisotropy in crystallites oriented randomly with respect to each other), uniaxial anisotropy induced by film texture, and an applied magnetic field. If the appearance of an MMS in $FeBO_3$: Mg is considered to be caused by analogous factors, we can assume that the crystal contains anisotropic magnetic centers with randomly oriented easy magnetization axes.

The local distortions of the crystal lattice of $FeBO_3$: Mg induced by the difference in the ionic radii of Mg and Fe lead to a strong crystalline magnetic anisotropy in a certain crystal region near impurities (due to an increase in the magnetoelastic energy). Therefore, the simplest model of anisotropic magnetic centers can be a complex consisting of a Mg ion (which substitutes for a Fe^{3+} matrix ion in $FeBO_3$) and the nearest surrounding iron ions. Since the central ion of the complex is diamagnetic (isotropic), the symmetry of this magnetic center (Mg–Fe center) does not differ from the hexagonal symmetry of the matrix. Therefore, there are six directions for stable orientation of the magnetic moment $\mathbf{M}_c$ of the center in the basal plane of the crystal. Since magnesium is divalent in $FeBO_3$ [6], we can assume that one of the iron ions in the complex is tetravalent in order to compensate for the charge. The presence of an Fe^{4+} ion should lead to certain spatial asymmetry of the Mg–Fe center, which will cause a preferred orientation of the vector $\mathbf{M}_c$ (the easy axis of the center). It is obvious that the orientations of the magnetic moments in the Mg–Fe centers in the crystal depend on two main orientational factors: the exchange field and the local anisotropy field. Therefore, in the case of strong local anisotropy, in general, the vectors $\mathbf{M}_c$ will not be directed along the total magnetization of the crystal.[2]

If we suppose that the impurity distribution in the crystal is sufficiently uniform and that the Fe ions in the nearest environment of a Mg ion can be in the Fe^{4+} state with the same probability, then we can assert that the presence of magnetic centers of the type described above does not change the hexagonal symmetry of the in-plane anisotropy of the doped crystal. Thus, the sym-

[2] Because the impurity concentration is small, it is natural to assume that the Mg–Fe centers do not interact with each other.

metry of the directions along which the MMS appears should reflect the hexagonal symmetry of the crystal in the basal plane, which corresponds to the experimental results (Figs. 4b–4d).

This model of magnetic centers explains the jumpwise change in the spatial MMS period with variation in the magnitude of the applied magnetic field (see [2]) and temperature. In the demagnetized crystal, the vectors $\mathbf{M}_c$ are symmetrically oriented with respect to the direction of the spontaneous magnetization $\mathbf{M}_s$ (the direction of domain walls). This symmetry in the distribution of directions of vectors $\mathbf{M}_c$ remains unchanged during the displacement of domain walls in the course of magnetization. However, when the field **H** applied in the basal plane is normal to the domain walls (i.e., $\mathbf{H} \perp C_2$), the magnetization $\mathbf{M}_s$ near saturation begins to rotate toward the field direction and the symmetry in the orientations of the vectors $\mathbf{M}_c$ is broken: under the action of the exchange field, the vectors $\mathbf{M}_c$ also rotate toward **H**. In this case, as H or T changes, the number of magnetic centers whose vector $\mathbf{M}_c$ deviates from **H** changes discretely due to the discrete azimuths of the easy axes of these centers. In turn, this change results in a jumpwise change in the ratio between the energies of the competing interactions responsible for the equilibrium magnetic state of the crystal. The difference between the $d(H)$ and $d(T)$ dependences described in the previous section is determined by the difference in the respective dependences of the concentration of centers with $\mathbf{M}_c \parallel \mathbf{H}$. At T = const, the difference in the number of centers with $\mathbf{M}_c \parallel \mathbf{H}$ for the direct (when the field increases from zero) and reverse magnetization process causes significant hysteresis of the $d(H)$ dependence [2]. This factor also causes hysteresis of the magneto-optic signal in fields $5 < H < 20$ Oe (Fig. 5).[3] The variation of d with T is specified by the temperature dependence of the anisotropy constant, which determines the direction of the magnetic moment of the Mg–Fe center. This leads to the absence of a substantial difference in the values of d measured upon heating and cooling of the sample. (The discrepancies in the temperatures of the jumps in d values in Fig. 6 are likely due to the error in determining T that appears as the heating and cooling conditions are switched because of the inertial process of establishing thermodynamic equilibrium in the crystal.)

If the assumptions regarding the causes that excite an MMS in $FeBO_3$: Mg are true, then we can use magnetic ripple theory and suppose (as follows from the theoretical model developed in [10]) that $K_a > K \gg K_a N^{-1/2}$, where K_a is the anisotropy constant specifying the direction of the magnetic moment of a center, N is the number of centers per unit volume, and K is the hexagonal anisotropy constant of $FeBO_3$: Mg (in [10], K was taken to be the induced uniaxial anisotropy constant). Then, the MMS period can be written as

$$d = 2\pi(A_{ex}/K)^{1/2}(M_s H/2K - 1)^{-1/2}, \quad (3)$$

where A_{ex} is a volume constant, and the amplitude of the angle of deviation of the local vector **m** from the applied-field direction is given by

$$\varphi_A = DK_a M_s^{-1/2}(M_s H - 2K)^{-3/8}, \quad (4)$$

where D is a constant dependent on the concentration of anisotropic magnetic centers (in [10], this constant depends on the crystallite size and the permalloy film thickness).

According to Eq. (3), an MMS appears under the condition

$$H > H_0 = 2K/M_s, \quad (5)$$

which makes it possible to determine the hexagonal anisotropy constant of $FeBO_3$: Mg. Using the MMS appearance field (H_0 = 5 Oe) and the known value of $M_s(T = 80\ \text{K}) \approx 17$ G [11]), we find $K \approx 42$ erg/cm^3 from Eq. (5). Note that, according to data from different studies, $K \sim 9$–13 erg/cm^3 in impurity-free $FeBO_3$ at liquid-nitrogen temperature [6, 12].

It is important that Eqs. (3) and (5) coincide with the corresponding expressions obtained in [2] from the consideration of the thermodynamic potential of a weak rhombohedral ferromagnet if we assume that $A_{ex} = \gamma$, $2K = -\alpha$, and $M_s = -\mu l q$. Here, γ, α, and μ are the coefficients of expansion of the thermodynamic potential of the crystal in powers of the order parameter; l is the modulus of the antiferromagnetism vector; and q is the sublattice magnetic moment.

Using Eq. (5), the experimental $H_0(T)$ dependence (Fig. 8), and the data on $M_s(T)$ [11], we can determine the temperature dependence of the constant K. The temperature dependence of K^{-1} thus calculated is shown in Fig. 3. It is known [6] that the initial magnetic susceptibility (which is associated with the reversible displacement of Néel domain walls) of $FeBO_3$ is specified by the rotation of the vector $\mathbf{M}_s$ in the basal plane and, hence, is proportional to the ratio M_s^2/K [13]. Therefore, during quasistatic magnetization reversal, the shape of the $dA/dH(T)$ dependence should depend on the temperature dependence of K^{-1} (since the change in M_s in the temperature range under study can be neglected). Indeed, as is seen from Fig. 3, the $\frac{dA}{dH}\Big/\left(\frac{dA}{dH}\right)_{T = 130\ \text{K}}$ and $K_{T = 130\ \text{K}}/K$ curves for $FeBO_3$: Mg are similar. As the frequency of the ac magnetic field decreases, the $\frac{dA}{dH}\Big/\left(\frac{dA}{dH}\right)_{T = 130\ \text{K}}$

[3] The break in slope of the hysteresis curve of the magneto-optic signal near $H \sim 5$ Oe (MMS appearance field) is likely related to a jump in the magnetic susceptibility as the crystal passes from the homogeneous into an inhomogeneous magnetic state; this jump is well known from the theory of magnetic phase transformations.

curve shifts toward the calculated $K_{T=130\,\mathrm{K}}/K$ dependence.

Substituting into Eq. (3) the parameters $A_{ex} = 2H_{ex}M_s c^2 \approx 2 \times 10^{-6}$ erg/cm (where $H_{ex} = 5.2 \times 10^6$ Oe [14] is the exchange field and $c \approx 10$ Å [4] is the lattice parameter along the C_3 axis), $K = 42$ erg/cm^3, $H = 6$ Oe, and $M_s = 17$ G, we find $d \approx 30$ μm. This value agrees with the experimental data only in order of magnitude (Fig. 6). Nevertheless, the temperature dependence of the ratio $d/d_{T=80\,\mathrm{K}}$ as calculated from Eq. (3) at $H = 6$ Oe using the found $K(T)$ dependence (for the calculation, A_{ex} was assumed to be independent of T) corresponds (without regard for the steps in the experimental $d(T)$ curve) to the variation in the MMS period with temperature (Fig. 6).

Unfortunately, the d hysteresis that appears during the magnetization reversal of the $FeBO_3$: Mg crystal [2] makes it impossible to directly compare Eq. (3) with the experimental $d(H)$ dependence. However, it is seen from the structure of Eq. (3) that, initially (at $H \geq H_0$), the $d(H)$ dependence exhibits a sharp decrease and then (at $H > 2H_0$) the modulation period changes only weakly. This behavior correlates with the experimental results from [2].

Therefore, we can conclude that Eq. (3) can qualitatively describe the experimentally detected change in the MMS period with variation in the applied field and temperature. As for Eq. (4), we would like to note that, first, comparison of the theoretical $\varphi_A(T)$ dependence with experiment would require knowledge of the temperature dependence of the constant K_a, which can hardly be determined experimentally. If the $K_a(T)$ temperature dependence is assumed to be close to the $K(T)$ dependence (as calculated from Eq. (5)), then Eq. (4) is seen to describe sufficiently well the detected variation in the angle φ_A with temperature (Fig. 7). Second, although Eq. (4) gives a decrease in the angle φ_A with increasing H, the run of the $\varphi_A(H)$ dependence does not correspond to the experimental curve. These circumstances do not allow us to calculate the temperature dependence in the field range of an MMS nor to compare the theoretical $\Delta H(T)$ dependence with the experimental H–T phase diagram of the crystal shown in Fig. 8.

The discrepancies between the magnetic ripple theory and the experimental behavior of the main MMS parameters are likely related to the fact that Eqs. (3) and (4) were obtained under the condition of a two-dimensional magnetic-inhomogeneity distribution (just as in polycrystalline permalloy films, where the sizes of the uniaxial magnetic centers (crystallites) are comparable to the film thickness). Obviously, the easy-axis directions of the Mg–Fe centers in $FeBO_3$: Mg are also scattered along the crystal thickness, which is not taken into account in the theoretical model developed in [10]. (In terms of the theoretical approach used in [10], the quantities d and φ_A cannot be represented in an analytical form in the three-dimensional case of a magnetic-inhomogeneity distribution). Nevertheless, on the whole, the magnetic ripple theory is consistent with the entire set of experimental results. This fact allows us to conclude that the proposed model for the appearance of an MMS in $FeBO_3$: Mg adequately describes the experimental situation.

REFERENCES

1. Yu. A. Izyumov, Usp. Fiz. Nauk **144** (3), 439 (1984) [Sov. Phys. Usp. **27**, 845 (1984)].
2. A. T. Karaev, B. Yu. Sokolov, and Yu. M. Fedorov, Fiz. Tverd. Tela (St. Petersburg) **42** (11), 2036 (2000) [Phys. Solid State **42** (11), 2097 (2000)].
3. Yu. M. Fedorov, A. F. Sadreev, and A. A. Leksikov, Zh. Éksp. Teor. Fiz. **93**, 2247 (1987) [Sov. Phys. JETP **66**, 1283 (1987)].
4. A. V. Postnikov, St. Bartkowski, M. Neumann, R. A. Rupp, E. Z. Kurmaev, S. N. Shamin, and V. V. Fedorov, Phys. Rev. B: Condens. Matter **50** (20), 14 849 (1994).
5. G. B. Scott, J. Phys. D: Appl. Phys. **7** (11), 1574 (1974).
6. D. E. Lacklison, J. Chadwick, and J. L. Page, J. Phys. D: Appl. Phys. **5** (4), 810 (1972).
7. Yu. M. Fedorov, A. A. Leksikov, and A. E. Aksenov, Fiz. Tverd. Tela (Leningrad) **26** (1), 220 (1984) [Sov. Phys. Solid State **26** (1), 128 (1984)].
8. B. Yu. Sokolov, Fiz. Tverd. Tela (St. Petersburg) **47** (2), 252 (2005) [Phys. Solid State **47** (2), 263 (2005)].
9. A. Baltz and W. D. Doyle, J. Appl. Phys. **35** (6), 1814 (1964).
10. H. Hoffman, J. Appl. Phys. **35** (6), 1790 (1964).
11. A. M. Kadomtseva, R. Z. Levitin, Yu. F. Popov, V. N. Seleznev, and V. V. Uskov, Fiz. Tverd. Tela (Leningrad) **14** (1), 214 (1972) [Sov. Phys. Solid State **14** (1), 172 (1972)].
12. J. Hisma and W. T. Stacy, J. Appl. Phys. **44** (7), 3367 (1973).
13. M. M. Farztdinov, *Physics of Magnetic Domains in Antiferromagnets and Ferrites* (Nauka, Moscow, 1981), p. 78 [in Russian].
14. Ch. G. Bogdanova, V. A. Golenishchev-Kutuzov, L. I. Medvedev, and M. M. Shakirzyanov, Fiz. Tverd. Tela (Leningrad) **33** (2), 379 (1991) [Sov. Phys. Solid State **33** (2), 219 (1991)].

Translated by K. Shakhlevich

Physics of the Solid State, Vol. 47, No. 10, 2005, pp. 1900–1908. Translated from Fizika Tverdogo Tela, Vol. 47, No. 10, 2005, pp. 1826–1833 .

MAGNETISM AND FERROELECTRICITY

Phase Separation and Anisotropy in the Electrical Properties of Weakly Doped Lanthanum Manganites

N. I. Solin, V. A. Kazantsev, L. D. Fal'kovskaya, and S. V. Naumov

Institute of Metal Physics, Ural Division, Russian Academy of Sciences, ul. S. Kovalevskoĭ 18, Yekaterinburg, 620219 Russia

e-mail: solin@imp.uran.ru

Received November 29, 2004

Abstract—Variations in the thermopower, electrical resistivity, magnetoresistance, thermal expansion coefficients, and their anisotropy with temperature were detected near room temperature in single crystals of weakly doped lanthanum manganites $La_{1-x}A_xMnO_3$ (A = Ca, Sr; x = 0.07–0.125) with orthorhombic structure. The results obtained are discussed in terms of a model of phase separation related to polaron anisotropy. Due to a gain in exchange and elastic energies in the lattice, small-radius magnetic polarons can merge to form polarons of a larger size, which would contain now not one but rather a few electrons (equal in number to the polarons in the cluster). As a result, short-range order in a cluster and phase separation set in at a temperature $T_{ps} \approx 250$–300 K, which is approximately equal to the Curie temperature T_C of conducting manganites with $x \approx 0.2$–0.3.

1. INTRODUCTION

Phase separation [1, 2] and the strong electron–phonon coupling [3] caused by the Jahn–Teller splitting of Mn^{3+} levels possibly account for the colossal magnetoresistance (MR) in the lanthanum manganites. Small-angle neutron scattering measurements performed on single crystals of weakly doped lanthanum manganites $La_{1-x}Ca_xMnO_3$ ($x \le 0.08$) at liquid-helium temperatures have revealed magnetic drops $2R_{cl} \approx 14$ Å in size [4] and their growth in size from $2R_{cl} \approx 7$–17 to 200 Å in $La_{1-x}Sr_xMnO_3$ as the Sr concentration is increased from 6 to 7% [5, 6], with the drops being anisotropic and shaped like flattened ellipsoids. In conventional magnetic materials, these drops (polarons) decay near the Curie temperature T_C [7]; therefore, the part played by phase separation is discussed in the region where antiferromagnetism exists. Some experiments performed on manganites could, however, be considered a manifestation of the onset of phase separation in the far paramagnetic region. Studies of the electrical resistivity, MR, thermopower, and magnetic susceptibility of $La_{0.92}Ca_{0.08}MnO_3$ and some weakly doped manganites [8] have argued for the onset of small-scale phase separation (the formation of magnetic clusters with dimensions of the order of 8–12 Å) in the paramagnetic region at temperatures below $T \approx 275$ K, which is about twice the Curie and Néel temperatures T_C and T_N, respectively, of the samples. The electric and magnetic properties of manganites [$(La_{1-y}Pr_y)_{0.3}Ca_{0.3}MnO_3$, $Pr_{0.71}Ca_{0.29}MnO_3$, $La_{0.08}Mg_{0.02}MnO_3$, etc.] in a broad paramagnetic temperature region are discussed [9] in the framework of the nonuniform state model developed in [10], and the results obtained are explained as being due to the presence of magnetic drops ≈30 Å in size.

Phase separation effects should manifest themselves most strongly in the properties of weakly doped manganites. Their properties have thus far been studied, however, too poorly to warrant a conclusion concerning the connection between the electrical properties and phase separation. Lattice distortions are one of the indications signaling the formation of magnetic clusters [11], and they could provide supportive evidence for phase separation at high temperatures. The orthorhombic structure and magnetic cluster anisotropy [5] of weakly doped lanthanum manganites give one grounds to expect their electrical properties to be anisotropic. The anisotropy of electrical resistivity (ρ) and MR of bulk manganites, unlike films [12], have remained practically unstudied to date. This communication reports on the detection of anisotropy in the electrical resistivity, MR, thermopower, and coefficients of linear expansion in $La_{0.93}Sr_{0.07}MnO_3$ single crystals, as well as of MR in some weakly doped lanthanum manganites. The anisotropy in the electrical properties of $La_{0.93}Sr_{0.07}MnO_3$ appears below the structural phase transition temperature $T_{OO'} \approx 440$ K and grows with decreasing temperature, to become strongest at about ≈300 K.

The anisotropy in the electrical properties is accounted for by an anisotropy in the carrier mobility, which originates from anisotropy in the polaron shape. Small-radius polarons form at high temperatures ($T >$ 300 K) in the paramagnetic region as a result of Jahn–Teller lattice distortions [3]. As the temperature decreases, the energy of the system decreases because

of the onset of short-range magnetic order near these polarons. Magnetic polarons of a larger size can form through the merging of smaller polarons due to the ensuing gain in the exchange and elastic energies in the lattice, and they contain not one but rather a few electrons (equal in number to the polarons in a cluster). As a result, short-range order in a cluster and phase separation occur at a temperature $T_{ps} \approx 250$–300 K, which is approximately equal to the Curie temperature T_C of conducting manganites with $x \approx 0.2$–0.3. The anomalies in the coefficients of linear and volume expansion observed at these temperatures are consistent with this model. It is expected that the polaron anisotropy favors phase separation.

2. SAMPLES AND TECHNIQUES

The $La_{0.93}Sr_{0.07}MnO_3$ sample[1] is a canted antiferromagnet with a canting angle $\theta \approx 25°$, $T_C = 128$ K, $T_N = 121$ K, and structural transition temperature $T_{OO'} \approx 450$ K [6]; the parameters of its orthorhombic lattice are $c = 7.753$ Å, $a = 5.58$ Å, and $b = 5.549$ Å [14]. Neutron measurements [6] show this $La_{0.93}Sr_{0.07}MnO_3$ single crystal to be, for the most part, single-domain, as $La_{0.94}Sr_{0.06}MnO_3$ [5], with the *c* axis aligned close to the crystal growth axis. X-ray measurements show $La_{0.93}Sr_{0.07}MnO_3$ single crystals to be single-phase at room temperature but reveal indications (traces) of a twin structure. $La_{0.9}Ca_{0.1}MnO_3$ and $La_{0.875}Ca_{0.125}MnO_3$ single crystals[2] are also canted antiferromagnets ($T_C = 138$ K, $T_N = 112$ K, and $T_{OO'} \approx 450$ K for the former crystal, and $T_C = 155$ K, $T_N = 112$ K, $T_{OO'} \approx 320$ K, and $T_{O'O''} \approx 80$ K for the latter) and were shown by neutron measurements [16] to have a twin structure.

The anisotropy in the electrical resistivity, MR, and thermopower of $La_{0.93}Sr_{0.07}MnO_3$ was measured on cylindrical samples with $d = 0.9$–1.5 mm and $L = 5$–7 mm, cut along the **b** and **c** axes. The current was directed along the cylinder axis, and a magnetic field was applied perpendicular to the cylinder axis. The MR anisotropy of the calcium samples was measured on the single crystals used earlier in neutron studies [4, 5, 16], which were in the shape of cylinders with a diameter $d \approx 4$ mm and length $L \approx 10$ mm. The samples were oriented by the x-ray technique. The dc electrical resistivity measurements were conducted by the conventional four-probe method. The thermopower was measured by the four-probe technique at a temperature difference of ≈4–8 K between the thermocouples. The sample was in vacuum, and the thermal gradient was directed along the **b** or **c** axis. The linear expansion coefficients of $La_{0.93}Sr_{0.07}MnO_3$ were studied on an ULVAC-SINKU RIKO dilatometer (Japan) in the temperature interval from 77 to 600 K in the dynamic mode at a temperature variation rate of 2 K/min. The sample was cube-shaped with $L \approx 5$ mm and oriented along the principal crystallographic directions. Magnetic measurements were performed at the Magnetometry Center of the Institute of Metal Physics (Ural Division, Russian Academy of Sciences) with a MPMS-5XL SQUID magnetometer (Quantum Design).

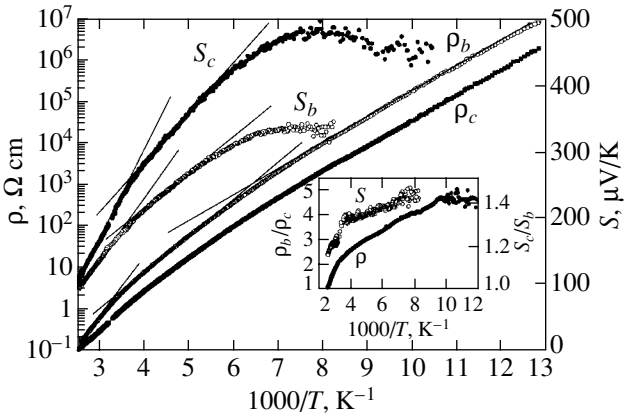

Fig. 1. Temperature dependences of the electrical resistivity (ρ_b, ρ_c) and thermopower (S_c, S_b) of a $La_{0.93}Sr_{0.07}MnO_3$ single crystal measured along the **b** and **c** axes. Inset shows the temperature dependences of the anisotropy in electrical resistivity ρ and thermopower *S* of $La_{0.93}Sr_{0.07}MnO_3$.

3. RESULTS

Studies of the thermopower of $La_{0.93}Sr_{0.07}MnO_3$ show it to be a *p*-type semiconductor. The values of the dc electrical resistivity ρ_0 and thermopower *S* of the $La_{0.93}Sr_{0.07}MnO_3$ single crystal measured at $T \approx 400$ K (close to the structural transition temperature $T_{OO'} \approx 440$ K) depend only slightly on the direction of the current and temperature gradient with respect to the crystallographic axes and become noticeably anisotropic with decreasing temperature (Fig. 1). The inset to Fig. 1 shows that, at $T \approx T_C = 128$ K, the electrical resistivity ρ_c along the **c** axis is approximately 4 times smaller than that along the **b** axis, while the thermopower S_c along the **c** axis is about 1.4 times larger than that along **b**. We see also that the anisotropy in the electrical resistivity ρ_b/ρ_c and that in thermopower S_c/S_b increase with decreasing temperature. A stronger change in the anisotropy of the properties occurs near ≈300 K. Within the interval $T = 400$–300 K, the thermopower and the electrical resistivity (Fig. 1) are fitted well by the activation relations characteristic of semiconductors [17]:

$$S = (k/e)(\Delta E_S/kT + S_0), \tag{1}$$

$$\begin{aligned}\rho_0(T) &= (1/\sigma^0)\exp(\Delta E_\rho/kT) \\ &= (1/\sigma^0)\exp[(\Delta E_S + W_1)/kT],\end{aligned} \tag{2}$$

[1] This sample was grown by Balbashov [13] at the Moscow Power Engineering Institute.

[2] Grown by L. Pinsard *et al.* [15] at the Laboratoire de Chimic des Solides, Universite Paris-Sud.

Activation energies for electrical resistivity ΔE_ρ, thermopower ΔE_S, and hopping W_1; the coefficient of conductivity σ^0; and thermopower S_0 of a $La_{0.93}Sr_{0.07}MnO_3$ single crystal measured along different crystallographic directions

T, K	Axis	ΔE_ρ, meV	σ^0, Ω^{-1} cm^{-1}	ΔE_S, meV	W_1, meV	S_0
$300 < T < 400$	*b*	275	18000	125	150	–2.4
	c	185	2000	95	90	–1.7
$175 < T < 270$	*b*	≈155	≈250	≈50	100	+0.1
	c	≈150	≈300	≈80	70	–0.4
$77 < T < 160$	*b*	130	10	–	–	–
	c	125	40	–	–	–

where e is the electronic charge, k is the Boltzmann constant, σ^0 is the prefactor of electrical resistivity, and S_0 is the kinetic coefficient. As seen from the table, the activation energies of the thermopower ΔE_S, electrical resistivity ΔE_ρ, and hopping W_1 are dependent on the crystallographic direction.

Below 270–300 K, the temperature dependences of the electrical resistivity and thermopower change in pattern in both directions. The values of ΔE_S, ΔE_ρ, σ^0, and S_0 (see table) undergo a jump near ≈300 K. The $\rho_0(T)$ and $S(T)$ relations follow a pattern characteristic of disordered (glassy) semiconductors and can be described by the quantities ΔE_S, ΔE_ρ, σ^0, and S_0 depending on the temperature and crystallographic direction (see table). The thermopower reaches a maximum near T_C and falls off with a further decrease in temperature.

The temperature dependence of the magnetic susceptibility χ_0 of $La_{0.93}Sr_{0.07}MnO_3$ in the paramagnetic temperature region 200–300 K can be roughly fitted with the Curie–Weiss law with an effective magnetic moment $\mu_{eff} \approx 5.75\ \mu_B$, which is larger than the theoretical value $\mu_{eff} = 4.80\ \mu_B$. The differential magnetic susceptibility χ_{ac} of $La_{0.93}Sr_{0.07}MnO_3$ measured in a 80-Hz ac magnetic field with an amplitude of 4 Oe follows about the same pattern as that of $La_{0.92}Sr_{0.08}MnO_3$ [8]. It is near $T_{ps} \approx 270$ K that the field dependence of there is sharp change in the character of the magnetic susceptibility; namely, at temperatures above ≈270 K, χ_{ac} is independent of the dc magnetic field, while below ≈270 K it is field-dependent (Fig. 2). For $T < 270$ K, χ_{ac} decreases strongly in weak magnetic fields down to $H_0 \approx 500$ Oe, after which it varies only weakly up to 3–5 kOe, to remain nearly constant in fields above ≈10 kOe. This behavior of χ_{ac} is usually observed for magnetic nanoparticles embedded in a paramagnetic medium [18].

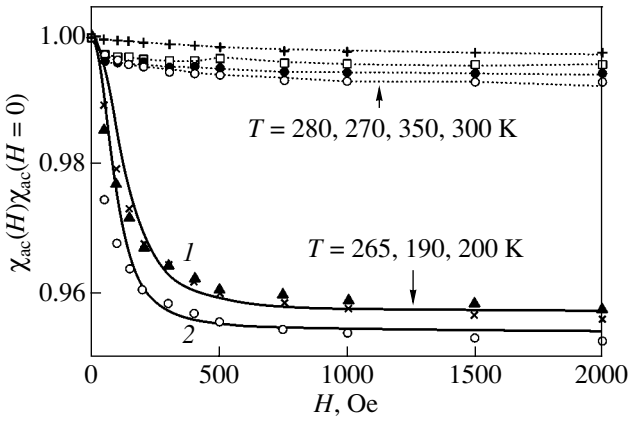

Fig. 2. Dependences of the relative differential magnetic permeability $\chi_{ac}(H)/\chi_{ac}(H = 0)$ of a $La_{0.93}Sr_{0.07}MnO_3$ single crystal on a dc magnetic field measured at various temperatures. Solid curves *1* and *2* are the calculated contributions to $\chi_{ac}(H)$ due to clusters with magnetic moments $M_{cl} = 10^4$ and $3 \times 10^4\ \mu_B$, respectively.

Note that we observed the same variations in the electrical properties (the activation energies of the electrical resistivity ΔE_ρ and thermopower ΔE_S, the prefactor of the electrical conductivity σ^0, and the Seebeck coefficient S_0; the onset of MR, etc.) in a number of single crystals of weakly doped $La_{1-x}A_xMnO_3$ (A = Ca, Ce, Sr; x = 0.07–0.1) manganites, including undoped $LaMnO_3$, at temperatures T = 270–300 K, which exceed the Curie and Néel temperatures ($T_C \approx T_N \approx$ 120–150 K) by about 2 times while being substantially below the points of structural transitions in these samples [19]. This shows that anomalies in physical characteristics near room temperature are a property common to weakly doped manganites.

Figure 3 displays the temperature dependences of the coefficients of volume, $\alpha_V = (\alpha_a + \alpha_b + \alpha_c)/3$, and linear, α_i ($i \equiv a, b, c$), expansion along the three orthorhombic axes. One clearly sees anomalies in three temperature domains:

(1) near the Curie and Néel temperatures, $T = T_C \approx T_N \approx$ 125–128 K;

(2) near the temperature of the structural transition of the orthorhombic O' to a pseudocubic phase, whose value for the sample under study can be assumed (from the temperature of the extremum in α_V) to be equal to $T_{OO'} \approx$ 440 K (heating above this temperature was observed to induce a hysteretic behavior in the temperature dependences of α_i and χ_{ac});

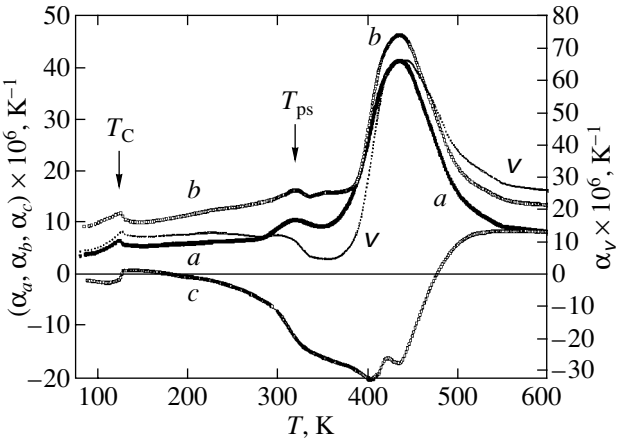

Fig. 3. Temperature dependences of the coefficients of volume (v) and linear (a–c) expansion along different crystallographic axes of the $La_{0.93}Sr_{0.07}MnO_3$ single crystal (for the sake of convenience, the values of α_b are increased by 5×10^{-6} K^{-1}).

(3) in the room temperature region, $T_{ps} \approx 300$ K.

The linear expansion coefficients in the **ab** plane are positive and close to one another throughout the temperature range studied (for the sake of convenience, the value of α_b is increased by 5×10^{-6} K^{-1}), which is consistent with the crystal symmetry. The values of α_c are negative within a broad temperature region, $\alpha_c < 0$; i.e., the sample dimension along the **c** axis decreases under heating. The values of $|\alpha_c|$ below ≈300 K are substantially smaller than those of α_a and α_b. Above ≈500 K, the values of α_i do not depend on the crystallographic direction. One clearly sees anomalies in α_i in the proximity of T_C, with the variation of the linear expansion coefficient here also being anisotropic; indeed, α_c grows, while α_a and α_b decrease near T_C. There is a jump in the coefficient of volume expansion at ≈300 K and then almost no variation down to T_C, below which the coefficient decreases with decreasing temperature.

A sharp growth in the dc magnetoresistance $MR_H \approx [\rho(H) - \rho(H = 0)]/\rho(H)$ of a $La_{0.93}Sr_{0.07}MnO_3$ single crystal near $T \approx 270$ K from $MR_H \approx -0.1\%$ to $MR_H \approx -(2.0 \pm 0.5)\%$ observed to occur in a field $H = 17$ kOe was reported earlier [8].

The MR was found to depend on the magnetic field orientation with respect to the crystallographic axes in $La_{0.93}Sr_{0.07}MnO_3$ below T_C in conditions where the current **j** is directed along the **b** axis and **H** ⊥ **b**. At 77 K, the dependence of the magnetoresistance $MR_H \equiv [\rho(H) - \rho(H = 0)]/\rho(H)$ on the magnetic field orientation in the **bc** plane is uniaxial in character and can be fitted by the expression MR ~ sin2θ (Fig. 4a), where θ defines the magnetic field direction in the **bc** plane. The maximum and minimum values of MR are apparently reached when the magnetic field is aligned with the **c** and **b** axes. When the current **j** is directed along the **c** axis and the field rotates in the **ab** plane (empty circles in Fig. 4b), the as-grown $La_{0.93}Sr_{0.07}MnO_3$ sample did not reveal any MR anisotropy. After the $La_{0.93}Sr_{0.07}MnO_3$ single crystal had been cooled from 500 K to room temperature at a **c**-aligned pressure of ≈25 kg cm^{-2}, a uniaxial-type anisotropy was observed along the **c** axis (filled circles in Fig. 4b).

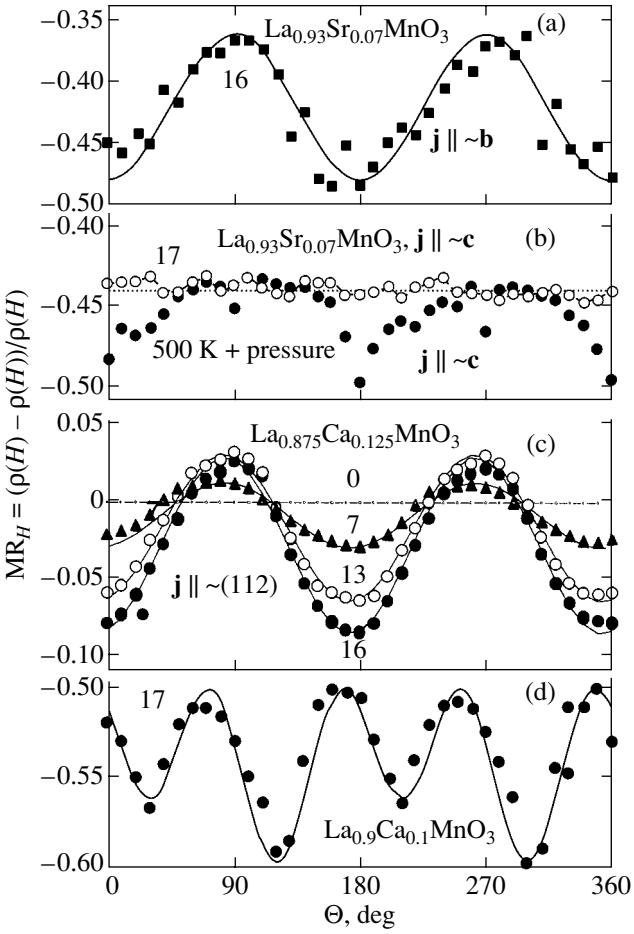

Fig. 4. Angular dependences of the transverse MR (**j** ⊥ **H**) of weakly doped single crystals of lanthanum manganites measured at 77 K. The figures on the curves are magnetic fields in kilooersteds. (a) The current is directed along the **b** axis, and the magnetic field rotates in the **bc** plane. The solid line is a plot of MR ~ cos2θ. (b) The current is directed along the **c** axis, and the magnetic field rotates in the basal plane **ab**. Empty circles are the MR of an as-grown single crystal. Filled circles are the MR of a single crystal precooled from 500 K down to room temperature under a pressure of 25 kg/cm^2 along the **c** axis. (c) The current is directed along an axis close to (112). The solid line is a plot of MR ~ cos2θ. (d) The solid curve is a plot of MR ~ K_1cos2Θ + K_2cos4Θ.

The transverse MR (**j** ⊥ **H**) was found to be anisotropic in other weakly doped manganites as well (Figs. 4c, 4d) and to also set in near T_C. This shows that the MR anisotropy originates from crystal magnetiza-

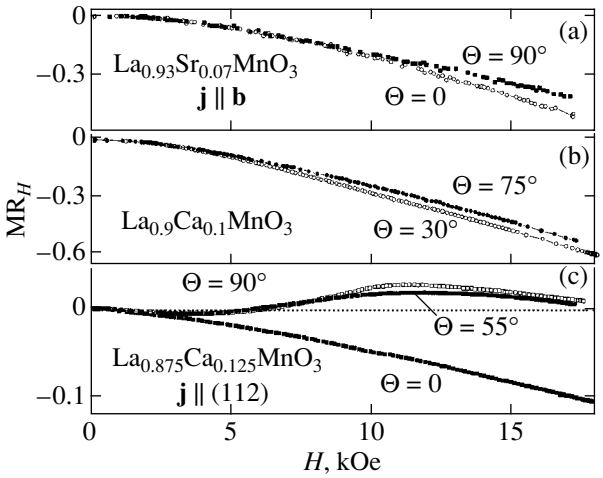

Fig. 5. Dependences of the MR of $La_{0.93}Sr_{0.07}MnO_3$, $La_{0.9}Ca_{0.1}MnO_3$, and $La_{0.875}Ca_{0.125}MnO_3$ single crystals on a magnetic field strength measured at 77 K for various orientations of the magnetic field with respect to the crystallographic axes. The angles indicated on the curves are the same as those in Fig. 4.

tion. In $La_{0.875}Ca_{0.125}MnO_3$, the MR decreases strongly below $T \approx 100$ K ($MR_H \approx -0.25$ at 100 K and $H =$ 17 kOe), reverses sign with magnetic field direction, and at 77 K follows a uniaxial pattern and can be described by the expression $MR \sim -K_1 + \cos 2\theta$, where $K_1 \approx 0.5$–0.55 (solid lines in Fig. 3c). This temperature is close to $T_B \approx 80$ K, where the transition to the quasicubic phase $T_{O'O}$ is believed [16] to take place. The anisotropy of the $La_{0.9}Ca_{0.1}MnO_3$ MR was found to have, besides a second-order symmetry contribution, a fourth-order contribution: $MR \sim K_1 \sin 2\theta + K_2 \sin 4\theta$ (the solid line in Fig. 3d plots the MR as calculated using this relation). In $La_{0.875}Ca_{0.125}MnO_3$, in addition to the "hard" direction, where the MR is small and positive ($\theta = 90°$ in Fig. 4), there is an intermediate direction ($\theta \approx 55°$–$60°$ and $120°$–$125°$ in Fig. 4), where the MR is nearly independent of the magnetic field strength.

At 77 K, the MR(H) of $La_{0.93}Sr_{0.07}MnO_3$ and $La_{0.9}Ca_{0.1}MnO_3$ as a function of magnetic field behaves in a similar manner in all directions; namely, MR_H grows monotonically with magnetic field in the two extreme (hard and easy) magnetic field directions with respect to the crystallographic axes (Figs. 5a, 5b). For $La_{0.875}Ca_{0.125}MnO_3$, the MR($H$) dependence follows a different pattern. Along the easy direction (Fig. 5c), the MR is seen to grow monotonically in magnitude with magnetic field, while along the hard direction it varies nonmonotonically. Along the intermediate direction, the MR is only weakly dependent on magnetic field, which may be assigned to a slightly incorrect orientation of the sample.

4. DISCUSSION

Anisotropy in the electrical resistivity (i.e., its dependence on the direction of the current with respect to the crystallographic axes) is inherent to some extent in all noncubic crystals. It is known that metals [19], semiconductors [20], and hexaferrites [21] exhibit a pronounced anisotropy in electrical resistivity. This anisotropy is usually attributed to an anisotropy in the carrier mobility (mass or relaxation time). Neutron and x-ray diffraction data show the samples studied to have a twin structure. Twinning originates from a phase transition to a state with lower symmetry occurring during growth. Obviously enough, with the domains distributed uniformly, there should be no anisotropy in the properties. The anisotropy observed in the properties of the samples under study suggests that a preferred growth of domains occurs in some directions due to a specific feature in the crystal preparation technology employed. In the $La_{0.93}Sr_{0.07}MnO_3$ crystal studied here, the **c** axis is oriented close to the crystal growth direction. In $La_{0.875}Ca_{0.125}MnO_3$, the crystal growth proceeded close to the (112) axis. In addition, the volumes of domains can be externally controlled to a certain extent. This is indicated by the appearance of a slight anisotropy in the (**ab**) plane in $La_{0.93}Sr_{0.07}MnO_3$ cooled under pressure (Fig. 4b).

The activated nature of the temperature dependences of the electrical resistivity and thermopower and the different activation energies of the electrical resistivity and thermopower along the same crystallographic directions in $La_{0.93}Sr_{0.07}MnO_3$ (see table) convincingly show [17] that nonlocalized carriers do not provide any contribution over the temperature region covered. The low conductivity of the sample at acceptor concentrations below the percolation threshold, $x < x_{per} \approx 0.16$, may be attributed to the fact that carriers either are captured in localized states in the valence band tail or become localized at the Mn^{4+} ion with the formation of polarons. Both mechanisms can account for the activated behavior of the electrical resistivity and thermopower described by Eqs. (1) and (2) [17, 22]. The polaron-mediated conductivity is argued for by the large values of the factor $\sigma^0 = (2\text{–}10) \times 10^3\ \Omega^{-1}\ cm^{-1}$ in Eq. (2) [22] and by the Debye-type losses characteristic of polaron-mediated conductivity, $\sigma(\omega) \sim \dfrac{\omega^2\tau}{1+\omega^2\tau^2}$, observed in the temperature [23] and frequency dependences of the ac conductivity [24] (ω is the current frequency, $1/\tau$ is the polaron hopping frequency) in $La_{1-x}Sr_xMnO_3$ single crystals ($x = 0.07$–0.075). The electron trapped at a Mn^{4+} ion binds six Mn^{3+} ions in its nearest environment to form a polaron with radius $R_{pol} = R_{Mn\text{–}Mn} = 1a \approx 4$ Å (a is the lattice parameter). The hopping activation energy W_1 characterizing the carrier mobility $\mu \sim (1/T)\exp(-W_1/kT)$ is governed primarily by the Coulomb potential [17] $W_1 = W_p/2 \approx e^2(2\varepsilon'_p R_{pol})$,

where $\varepsilon'_p \approx 10$ is the effective dielectric permittivity. Estimation of the polaron size from the hopping activation energy $W_1 \approx 100$–150 meV (see table) yields $R_{pol} = 4$–6 Å ≈ 1.0–$1.5a$. In an orthorhombic structure, this polaron is apparently an ellipsoid extended along the **c** axis. Therefore, along the **c** axis, the hopping activation energy W_1 is smaller (see table), the hole mobility is larger, and the electrical resistivity is lower than along the other axes. Thus, the nature of the anisotropy in the electrical resistivity may be intimately related to that of the polaron shape.

It was assumed in [8] that the formation of magnetic clusters in $La_{0.92}Ca_{0.08}MnO_3$ at ≈300 K would be accompanied by lattice distortions and, thus, could be considered to indicate the onset of phase separation in the paramagnetic region. Temperature studies of the coefficients of linear expansion of $La_{0.93}Sr_{0.07}MnO_3$ clearly reveal the presence of anomalies near 300 K and bear out this assumption. The small values of $\alpha_c \ll \alpha_a \approx \alpha_b$ obtained below 250 K can be accounted for by thermal expansion being compensated by magnetic clusters increasing in size. This assumption is consistent with the anisotropy in the electrical resistivity increasing with a decrease in temperature (Fig. 1).

The dependence of the differential magnetic susceptibility χ_{ac} on magnetic field (Fig. 2), the enhanced effective paramagnetic permeability μ_{eff}, and the specific features in the linear and volume expansion coefficients in the region of $T \approx 300$ K (Fig. 3), which is far from the points of magnetic and structural transitions in a sample but is close to the Curie temperature of heavily doped manganites with $x = 0.2$–0.3, can be explained as being due to the formation of magnetic clusters. The size of these magnetic drops can be roughly estimated from magnetic measurements. The magnetization of magnetic clusters in a paramagnetic matrix is described by the Langevin expression $L(x) \sim \coth x - 1/x$, where $x = M_{kl}H/kT$ [19]. The differential magnetic susceptibility of such a cluster is $\chi_{ac} \sim dL/dH \sim -\mathrm{cs\,ch}^2 x + 1/x^2$. The strong decrease in χ_{ac} observed in fields of up to 500 Oe at $T = 200$–250 K (Fig. 2) can be assigned to large magnetic moments M_{cl} of a cluster containing about $N_{cl} = 10^3$–10^4 Mn ions (the solid curves in Fig. 2 are plots of $\chi_{ac} \sim dL/dH$ calculated for $N_{cl} = 3 \times 10^3$ and 8×10^3 Mn ions in a cluster), which corresponds in a spherical model to clusters of radius $R_{cl} \approx 25$–50 Å $= 6$–$12a$. Assuming the increase in the effective moment μ_{eff} of $La_{0.93}Sr_{0.07}MnO_3$ by ≈1 μ_B from the theoretical value to be due to these clusters only, one can estimate their concentration from the expression for the magnetic susceptibility of magnetic clusters $\chi(T)$ [9] as $n \approx 10^{15}$ cm^{-3}. This concentration corresponds to cluster separation ≈10^3 Å. The slower variation of χ_{ac} up to fields of ≈5–7 kOe can be attributed to the presence of clusters of a smaller size, whose concentration can be estimated from data on μ_{eff} as 10^{19}–10^{20} cm^{-3}.

Thus, the results obtained on the magnetic and electrical properties and coefficients of linear and volume expansion of $La_{0.93}Sr_{0.07}MnO_3$ can be explained as being due to the formation for $T < \approx 300$ K of anisotropic clusters of a variety of sizes, with radii ranging from 4 to 50 Å. As follows from magnetic measurements, the larger the clusters, the lower their concentration and the larger their separation. As a result, the tunneling and hopping of carriers among large clusters are hampered. Therefore, in accordance with estimates based on the hopping activation energy, the electrical properties are affected more strongly by small drops (4–8 Å in size).

In the paramagnetic region, at high ($T > 300$ K) temperatures, small-radius polarons can form as a result of Jahn–Teller lattice distortions [3]. As the temperature decreases, the energy of a system can decrease due to phase separation, i.e., the formation of ferromagnetic drops near these polarons. Two causes for the formation of such drops can immediately be pointed out. With such a comparatively high concentration of Sr ions ($x = 7\%$), a purely statistical distribution of acceptors or specific features of the crystal growth technology may give rise to the formation of acceptor aggregates near which magnetic drops with $R_{cl} \approx 25$–40 Å and $T_C \approx 250$–300 K will appear.

The other (more likely) cause for the formation of magnetic drops is related to the anisotropy in the polaron shape. The average distance between the Sr acceptor ions in $La_{0.93}Sr_{0.07}MnO_3$ is less than 10 Å. Therefore, even a small (≈25%) polaron anisotropy is sufficient for overlap of adjacent polarons with $2R_{Mn–Mn} \approx 8$ Å. The ensuing gain in the exchange and elastic energies favor the merging of small-radius polarons into a large magnetic polaron with a few carriers. As a result, short-range order in the cluster and phase separation occur at a temperature $T_{ps} \approx 250$–300 K, which is approximately equal to the T_C of conducting manganites with $x \approx 0.2$–0.3.

Small-angle neutron scattering measurements revealed [16] that the size of clusters in $La_{0.9}Ca_{0.1}MnO_3$ at liquid-helium temperatures is larger than their separation and that they aggregate while retaining the semiconducting pattern of conductivity. It is apparently this pattern that is observed in $La_{0.93}Sr_{0.07}MnO_3$ at room temperature.

Phenomenological theories explaining the anisotropy in the MR and other even effects in ferromagnets [19] relate it to the dependence of the electrical resistivity tensor on strain. The relation between the current density j_i and electric field strength E_k for a conductor placed in an external magnetic field **H** can be written as [25]

$$j_i = \sigma_{ik} E_k, \tag{3}$$

where the conductivity tensor σ_{ik} is a function of magnetic field strength. The diagonal conductivity tensor

components σ_{ii}, which were measured in the experiment, are even functions of the magnetic field [25]:

$$\sigma_{ii} = \sigma_{ii}^{(0)} + \sum_{l, m = x, y, z} \beta_{iilm} H_l H_m + \ldots. \quad (4)$$

Analysis shows that expansion (4) yields the following relation for the MR in an orthorhombic system:

$$\mathrm{MR}_H \sim A_0 H^2 + A_1 H^2 \cos 2\Theta + A_2 H^4 \cos 4\Theta, \quad (5)$$

where Θ is the angle the magnetic field makes with the crystal axis. We readily see that the observed angular dependences of the MR (Fig. 4) are well fitted by Eq. (5). Note that some conducting tetragonal $La_{0.67}Ca_{0.33}MnO_3$ films also exhibit angular dependences of MR described by Eq. (5) [12]. In $La_{0.9}Ca_{0.1}MnO_3$, one observes (Fig. 4d) a near-cubic anisotropy of MR in place of the uniaxial pattern expected according to the actual crystal symmetry. The crystals studied have a twinned structure; therefore, in order to account for the observed MR, the specific features of the antiferromagnetic domain structure have to be considered. The proximity of the MR(θ) of $La_{0.93}Ca_{0.1}MnO_3$ to cubic symmetry suggests that in this case the MR(θ) apparently draws from contributions of two domains of about equal volume but tilted 90° relative to each other.

The observed anisotropy in the MR of $La_{0.9}Ca_{0.1}MnO_3$ and $La_{0.93}Sr_{0.07}MnO_3$ can be accounted for also by the effect of magnetic crystallographic anisotropy. For a uniaxial crystal, the anisotropy field can be written as $H_{A1} = 2K_1/M\cos 2\theta$ [19], where K_1 is the magnetic crystallographic anisotropy energy and M is the magnetization. The field dependence of the MR anisotropy in $La_{0.9}Ca_{0.1}MnO_3$ and $La_{0.93}Sr_{0.07}MnO_3$ along the different axes shown in Fig. 5 can be qualitatively explained if $H_{A1} \approx 1$–2 kOe. These values fit well the estimates of the anisotropy field made for manganites [26]. For $La_{0.875}Ca_{0.125}MnO_3$, however, this explanation does not apply; otherwise, one should assume very high anisotropy fields to account for the MR sign reversal. According to [27], below ≈100 K, $La_{0.875}Ca_{0.125}MnO_3$ undergoes charge ordering; i.e., Mn^{3+} and Mn^{4+} ions become ordered along certain crystallographic directions. This manifests itself in a decrease in orthorhombicity at this temperature [16]. The sharp decrease in MR and its positive values in some directions observed below 100 K are apparently connected with charge ordering in $La_{0.875}Ca_{0.125}MnO_3$.

Anisotropy in thermopower is a fairly rare phenomenon, and the conditions favoring its onset have been discussed in several papers [20, 28]. Thermopower anisotropy can appear in semimetals and semiconductors with carriers of one type and several scattering mechanisms characterized by an anisotropic relaxation time or with a single scattering mechanism and several types of carriers, as well as in the case of phonon drag. The nature of the thermopower anisotropy in $La_{0.93}Sr_{0.07}MnO_3$ is presently unclear. It may be appropriate to note here that tetragonal rutile TiO_2, whose conductivity was shown to be mediated by small-radius polarons, also exhibits anisotropy of both electrical resistivity and thermopower [29].

In concluding this section, we note that the variation of electrical resistivity with temperature originates not only from mobility but also from the carrier concentration. It is believed that, because of their large mass, polarons are pinned to impurities, i.e., localized [7]. As a result, the concentration of the carriers involved in conduction is considerably lower than that of the acceptors and is described by a relation of the type $n \sim \exp(-\Delta E_S/kT)$ [22]. It remains unclear at present at what impurities the polarons are localized and what determines the thermopower activation energy. Experiments performed on both $La_{0.9}Ca_{0.1}MnO_3$ [8] and $La_{0.93}Sr_{0.07}MnO_3$ (see table) suggest a decrease in ΔE_S upon the formation of magnetic clusters below 270 K. This shows that the onset of short-range magnetic order and an increase in cluster size reduce the polaron localization energy and bring about an increase in conductivity due to the increase in carrier concentration. Neutron measurements have shown [6] that an increase in doping from $x = 0.06$ to 0.07 in $La_{0.93}Sr_{0.07}MnO_3$ gives rise to a transition from a small-scale ($2R \approx 17$ Å) to a large-scale phase separation; at 4.2 K, the average linear size of magnetic clusters grows to $2R_{\mathrm{cl}} \approx 200$ Å, so that they occupy about 10% of the crystal volume. It is known that, in the region of hopping conduction, the thermopower is described by the Morin relation [30]

$$S = (k/e)Ln(N_0/n), \quad (6)$$

where N_0 is the electronic density of states and n is the number of carriers. We believe that the decrease in thermopower observed as one approaches T_C (Fig. 1) is a consequence of the onset of large-scale phase separation and corresponds, according to Eq. (6), to an increase in carrier concentration.

5. CONCLUSIONS

Thus, single crystals of weakly doped lanthanum manganites of orthorhombic symmetry exhibit a marked anisotropy in electrical properties. The electrical resistivity, magnetoresistance, thermopower, and linear expansion coefficients of $La_{0.93}Sr_{0.07}MnO_3$, as well as the MR revealed in single crystals of some weakly doped lanthanum manganites, depend on the direction of the current, the magnetic field, and the temperature gradient with respect to the crystallographic axes. The anisotropy in the electrical properties of $La_{0.93}Sr_{0.07}MnO_3$ sets in below the structural transition temperature $T_{OO'} \approx 440$ K and increases with decreasing temperature. The anisotropy in the MR of weakly doped manganites appears below the Curie temperature, and its angular dependence is fitted well, at a fixed

temperature and magnetic field, by the relation MR ~ $K_1\cos 2\Theta + K_2\cos 4\Theta$ derived from crystal symmetry considerations. Conduction at high temperatures ($T >$ 300 K) is explained in terms of the polaron mechanism. In manganites, polarons form in the paramagnetic region because of strong electron–phonon coupling and Jahn–Teller lattice distortions [3] and are apparently localized. The anisotropy in the electrical properties is assigned to that in the carrier mobility, which, in turn, originates from the polaron anisotropy.

Near room temperature, $T \approx$ 270–300 K, the magnetic properties (differential susceptibility χ_{ac}, paramagnetic effective permeability μ_{eff}), electrical properties (activation energies for electrical resistivity, thermopower, and hopping; MR; etc.), and lattice properties (linear and volume expansion coefficients) vary with temperature. These variations are believed to be due to the onset of short-range magnetic order and an increase in polaron size. The ensuing gain in exchange and elastic energies favor the merging of small-radius polarons into a large magnetic polaron with a few carriers. As a result, short-range order in a cluster and phase separation set in at a temperature $T_{ps} \approx$ 250–300 K, which is approximately equal to the Curie temperature T_C of conducting manganites with $x \approx$ 0.2–0.3. Magnetic measurements reveal the presence of fairly large clusters (about 30–50 Å in size), but conductivity in the paramagnetic temperature region is affected primarily (as follows from estimates based on polaron hopping activation energies) by clusters with $R_{cl} \approx$ 4–6 Å.

ACKNOWLEDGMENTS

The authors are indebted to A.V. Korolev for performing magnetic measurements; V.A. Sazonova for conducting x-ray studies and sample orientation; and to M. Hennion, L. Pinsard, and A. M. Balbashov for providing single crystals for the study.

This study was supported by the Russian Foundation for Basic Research (project no. 02-02-16429), the Department of Physical Sciences of the Russian Academy of Sciences (project no. 19490), and the Foundation for High-Priority Research Programs (project no. 40.012.1.1.1153).

REFERENCES

1. É. L. Nagaev, Usp. Fiz. Nauk **166** (6), 833 (1996) [Phys. Usp. **36** (8), 781 (1996)].
2. A. Moreo, S. Yunoki, and E. Dagotto, Science **283** (5410), 2034 (1999).
3. A. J. Millis, P. B. Littlewood, and B. I. Shraiman, Phys. Rev. Lett. **74** (25), 5144 (1995).
4. M. Hennion, F. Moussa, G. Biotteau, J. Rodrriguez, and L. Pinsard, Phys. Rev. Lett. **81** (9), 1957 (1998).
5. M. Hennion, F. Moussa, G. Biotteau, J. Rodrriguez, and L. Pinsard, Phys. Rev. B: Condens. Matter **61** (14), 9513 (2000).
6. S. F. Dubinin, V. E. Arkhipov, S. G. Teploukhov, V. D. Parkhomenko, N. N. Loshkareva, and N. I. Solin, Fiz. Tverd. Tela (St. Petersburg) **45** (12), 2192 (2003) [Phys. Solid State **45** (12), 2297 (2003)].
7. M. Yu. Kagan and K. I. Kugel', Usp. Fiz. Nauk **171** (6), 577 (2001) [Phys. Usp. **44** (6), 553 (2001)].
8. N. I. Solin, V. V. Mashkautsan, A. V. Korolev, N. N. Loshkareva, and L. Pinsard, Pis'ma Zh. Éksp. Teor. Fiz. **77** (5), 275 (2003) [JETP Lett. **77** (5), 230 (2003)].
9. K. I. Kugel, F. L. Rakhmanov, A. O. Sboychakov, M. Yu. Kagan, I. V. Brodsky, and A. V. Klaptsov, Zh. Éksp. Teor. Fiz. **125** (3), 648 (2004) [JETP **98** (3), 572 (2004)].
10. A. O. Sboychakov, A. L. Rakhmanov, K. I. Kugel', M. Yu. Kagan, and I. V. Brodsky, Zh. Éksp. Teor. Fiz. **122** (4), 869 (2002) [JETP **95** (4), 753 (2002)].
11. J. M. de Teresa, M. R. Ibarra, P. A. Algarabel, C. Ritter, C. Margulna, and Z. Arnold, Nature (London) **386** (3), 256 (1997); L. I. Koroleva, R. V. Demin, and A. M. Balbashov, Pis'ma Zh. Éksp. Teor. Fiz. **65** (6), 449 (1997) [JETP Lett. **65** (6), 474 (1997)].
12. J. N. Eckstein, I. Bozovic, J. O'Donnell, M. Onellin, and M. S. Rzchowski, Appl. Phys. Lett. **69**, 1312 (1996); B. I. Belevtsev, V. B. Krasovitsky, D. G. Naugle, A. Parasiris, S. Surthi, and M. Rom, Phys. Status Solidi A **188** (3), 1187 (2001).
13. A. M. Balbashov, S. G. Karabashev, and Ya. M. Mukovskii, J. Cryst. Growth **167**, 365 (1996).
14. N. N. Loshkareva, Yu. P. Sukhorukov, E. A. Neifel'd, V. E. Arkhipov, A. V. Korolev, V. S. Gaviko, E. V. Panfilova, V. P. Dyakina, Ya. M. Mukovskiĭ, and D. A. Shulyatev, Zh. Éksp. Teor. Fiz. **117** (1), 440 (2000) [JETP **90** (2), 389 (2000)].
15. F. Mussa, M. Hennion, J. Rodriguez-Carvajal, and L. Pinsard, Phys. Rev. B: Condens. Matter **54**, 15 149 (1996).
16. G. Biotteau, M. Hennion, F. Mussa, J. Rodrriguez, L. Pinsard, Y. M. Mukovskii, and D. Shulyatev, Phys. Rev. B: Condens. Matter **64**, 104 421 (2001).
17. N. F. Mott and E. A. Davis, *Electronic Processes in Non-Crystalline Materials*, 2nd ed. (Clarendon, Oxford, 1979; Mir, Moscow, 1982), Chap. 2–4, 6.
18. C. P. Bean and J. D. Divingston, J. Appl. Phys. **30S**, 120 (1959).
19. S. V. Vonsovskii, *Magnetism* (Nauka, Moscow, 1971; Wiley, New York, 1974).
20. P. I. Baranskiĭ, I. S. Buda, I. V. Dakhovskiĭ, *et al.*, *Electrical and Galvanomagnetic Phenomena in Anisotropic Semiconductors* (Naukova Dumka, Kiev, 1977) [in Russian].
21. K. Zaveta, Phys. Status Solidi **3** (11), 2111 (1963).
22. I. G. Austin and N. F. Mott, Adv. Phys. **18**, 41 (1969).
23. N. I. Solin and S. V. Naumov, Fiz. Tverd. Tela (St. Petersburg) **45** (3), 460 (2003) [Phys. Solid State **45** (3), 486 (2003)].

24. A. Seeger, P. Lunkenheimer, *et al.*, J. Phys.: Condens. Matter **11**, 3273 (1999).

25. L. D. Landau and E. M. Lifshitz, *Electrodynamics of Continuous Media* (Nauka, Moscow, 1982; Pergamon, Oxford, 1984).

26. A. V. Korolyov, V. Ye. Arkhipov, and V. S. Gaviko, J. Magn. Magn. Mater. **213**, 63 (2000); S. E. Loffland, V. Ray, P. H. Kim, S. Karabashev, Y. M. Mukovskii, D. Shulyatev, and A. Arsenov, J. Phys.: Condens. Matter **9**, L633 (1997).

27. V. E. Naĭsh, Fiz. Met. Metalloved. **92** (5), 16 (2001).

28. A. G. Samoĭlovich, I. S. Buda, and I. V. Dakhovskiĭ, Fiz. Tekh. Poluprovodn. (Leningrad) **7** (4), 859 (1973) [Sov. Phys. Semicond. **7** (4), 589 (1973)].

29. V. N. Bogomolov, E. K. Kudinov, and Yu. A. Firsov, Fiz. Tverd. Tela (Leningrad) **9** (11), 3173 (1967) [Sov. Phys. Solid State **9** (11), 2500 (1967)].

30. F. J. Morin, Phys. Rev. **93**, 1195 (1954); A. L. Éfros, Fiz. Tverd. Tela (Leningrad) **9**, 1152 (1967) [Sov. Phys. Solid State **9**, 1152 (1967)].

Translated by G. Skrebtsov

Physics of the Solid State, Vol. 47, No. 10, 2005, pp. 1909–1913. Translated from Fizika Tverdogo Tela, Vol. 47, No. 10, 2005, pp. 1834–1838.

MAGNETISM AND FERROELECTRICITY

Effect of Hydrogenation on the Magnetic and Magnetoelastic Properties of the $Tb_{0.27}Dy_{0.73}Fe_2$ and $Tb_{0.27}Dy_{0.73}Co_2$ Compounds with Compensated Magnetic Anisotropy

G. A. Politova*, I. S. Tereshina, S. A. Nikitin*, T. G. Sochenkova***, V. N. Verbetsky*, A. A. Salamova*, and M. V. Makarova***

** Moscow State University, Vorob'evy gory, Moscow, 119992 Russia*
e-mail: G_Politova@mail.ru
*** Baĭkov Institute of Metallurgy and Materials Science, Russian Academy of Sciences, Leninskiĭ pr. 49, Moscow, 117911 Russia*
**** State Research and Design Institute of the Less Common–Metal Industry, Moscow, 119017 Russia*

Received January 13, 2005

Abstract—The effect of hydrogenation on the magnetic ordering temperature and magnetostriction of the $Tb_{0.27}Dy_{0.73}Fe_2$ and $Tb_{0.27}Dy_{0.73}Co_2$ compounds with compensated magnetic anisotropy of the rare-earth sublattice was studied. It was established that the incorporation of hydrogen atoms into the crystal lattice of the compounds studied lowers the Curie temperature. It is shown that, in this case (i.e., for structures of the Laves phase type), the decrease in T_C results primarily from the change in the electronic structure of these compounds. An anomaly was found in the temperature dependence of thermal expansion of $Tb_{0.27}Dy_{0.73}Co_2$ and its hydride. It was established that hydrogenation brings about a substantial weakening of magnetostriction, which should be attributed to a change in the local electronic density induced by the incorporation of hydrogen atoms into the crystal lattice. © *2005 Pleiades Publishing, Inc.*

1. INTRODUCTION

Intermetallic compounds that are based on rare-earth (RE) and 3*d* transition metals, RT_2 (T = Fe, Co), and crystallize in a cubic crystal lattice of the $MgCu_2$ Laves phase type (space group $Fd3m$) are known to have high values of magnetostriction [1, 2]. In the $Tb_{0.27}Dy_{0.73}Fe_2$ alloy (terphenol), high magnetostriction is found to exist in comparatively weak fields because of the magnetic anisotropy of the RE sublattice being compensated, which should be attributed to the RE ions of terbium and dysprosium in these compounds having opposite signs of the single-ion magnetocrystalline anisotropy (MCA) constants [1, 2]. For concentrations of terbium $x = 0.27$ and of dysprosium $y = 0.73$, the first MCA constant is zero. Because the MCA single-ion constants retain their signs and values in the RT_2 Laves phases (where T is a 3*d* element) [1, 2], one may safely assume that the MCA of the RE sublattice in the $Tb_{0.27}Dy_{0.73}Fe_2$ and $Tb_{0.27}Dy_{0.73}Co_2$ compounds under study is likewise compensated.

It is known that these compounds react intensely with hydrogen to form stable hydrides under normal conditions [3, 4]. Depending on the 3*d* transition metal used, hydrogenation of different types of intermetallic compounds may give rise to an increase or, conversely, a decrease in the magnetic ordering temperature. The physical mechanisms responsible for the change in the magnetic ordering temperature have yet to find reasonable explanation. It is believed that one should take here into account the dependence of exchange integrals on the unit-cell volume, which changes when atoms of light elements are embedded into the crystal lattice. The magnetic ordering temperature may also be affected noticeably by a change in electron concentration in the 3*d* band and by hybridization of the 3*d* and 5*d* electron wave functions.

The present communication reports on a study of the common and distinguishing features of the effect of hydrogenation on the magnetic characteristics (magnetic ordering temperature and magnetostriction) of $Tb_{0.27}Dy_{0.73}T_2$ compounds (T = Fe, Co), which reveal compensated magnetic anisotropy of the RE sublattice.

2. SAMPLE PREPARATION TECHNOLOGY AND MEASUREMENT TECHNIQUE

$Tb_{0.27}Dy_{0.73}Fe_2$ and $Tb_{0.27}Dy_{0.73}Co_2$ alloys were prepared from the starting compounds in a vacuum arc furnace with a permanent tungsten electrode at a temperature T = 1480°C. The temperature in the furnace was controlled by properly varying the arc current and voltage. Melting was carried out in an argon atmosphere. The starting distillates of the RE metals and iron (or cobalt) taken in the ratio necessary to prepare an alloy of a specified composition were loaded into a water-cooled copper crucible in the chamber of the vacuum arc furnace. The chamber was sealed and evacuated

Structural and magnetic properties of the $Tb_{0.27}Dy_{0.73}(Fe, Co)_2H_x$ compounds (x = 0, 1, 3)

Compound	a, Å	V, Å^3	$\Delta V/V$, %	T_C, K	T_{comp}, K
$Tb_{0.27}Dy_{0.73}Fe_2$	7.325	393.03	–	686	–
$Tb_{0.27}Dy_{0.73}Fe_2H$	7.537	428.15	8.9	596	–
$Tb_{0.27}Dy_{0.73}Fe_2H_3$	7.959	504.19	28.3	290	110
$Tb_{0.27}Dy_{0.73}Co_2$	7.193	372.11	–	164	–
$Tb_{0.27}Dy_{0.73}Co_2H_3$	7.717	459.60	23.5	56	–

with a fore pump and a diffusion pump to a base pressure of 4.0×10^{-1} Pa, after which it was filled with argon to a pressure of 120 kPa. To make the alloy homogeneous, the starting components were remelted three times at a temperature of 1500–1600°C. Because the melting conditions in an arc furnace do not permit preparation of alloys with an equilibrium structure, the ingots were additionally annealed in a resistance furnace at 1100°C in vacuum for 10 h.

The polycrystalline samples thus obtained were hydrogenated at room temperature and a pressure of up to 0.66 Pa. Hydrogenation generated high internal stresses, which brought about spontaneous comminution of alloys to the powder state with an average grain size of about 50 μm. The amounts of absorbed hydrogen and nitrogen were calculated using the van der Waals equation

$$p(V - nb) = nRT,$$

where b is the van der Waals coefficient, equal to 26.6 cm^3/mol; R is the universal gas constant (82×10^6 cm^3 atm/mol K); p is the hydrogen pressure in the system (measured in atmospheres); V is the hydrogen volume (in cm^3); T is the temperature (in kelvins); and n is the amount of hydrogen per mole.

The Curie temperatures of the $Tb_{0.27}Dy_{0.73}Fe_2$ and $Tb_{0.27}Dy_{0.73}Co_2$ compounds and of their hydrides were determined by thermomagnetic analysis. The temperature dependences of magnetization were determined with a pendulum magnetometer in fields of up to 12 kOe in the 78- to 750-K temperature interval. For the $Tb_{0.27}Dy_{0.73}Co_2H_3$ compound, the temperature dependence of magnetic susceptibility in the temperature interval 4.2–100 K was also measured. The measurements were performed on polycrystals of the starting alloys and on powders of the hydrides placed in ceramic capsules.

Thermal expansion and magnetostriction were studied by means of wire strain gauges in the 77- to 300-K temperature interval and in magnetic fields of up to 12 kOe. The strain gauges employed in this study were made of strain-sensitive wire exhibiting no noticeable galvanomagnetic effect. The strain gauges had a base of 5 mm and a resistance of 340 or 390 Ω. The strain sensitivity coefficient was S = 2.15 throughout the temperature range covered. The magnetostriction and thermal expansion of the hydrides were measured on samples obtained by pressing a powder into pellets. All pellets were disk-shaped.

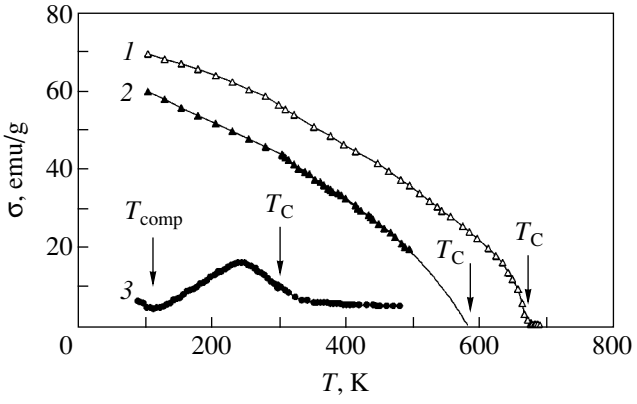

Fig. 1. Temperature dependences of the magnetization of (*1*) the $Tb_{0.27}Dy_{0.73}Fe_2$ compound and (*2*, *3*) its hydrides (*2*) $Tb_{0.27}Dy_{0.73}Fe_2H_1$ and (*3*) $Tb_{0.27}Dy_{0.73}Fe_2H_3$ measured in a field of 1 kOe.

3. EXPERIMENTAL RESULTS AND DISCUSSION

Structural studies and quality control of samples—both starting, $Tb_{0.27}Dy_{0.73}T_2$ (T = Fe, Co), and hydrogenated—were carried out on powder samples using a DRON-2 x-ray diffractometer. It was established that, while the $MgCu_2$-like cubic structure is not influenced by hydrogenation, $Tb_{0.27}Dy_{0.73}Co_2H_3$ exhibits broadening of the x-ray lines, which apparently implies that the hydride is structurally inhomogeneous. The lattice parameters for $Tb_{0.27}Dy_{0.73}Fe_2H_x$ (x = 0, 1, 3) and $Tb_{0.27}Dy_{0.73}Co_2H_x$ (x = 0, 3) are listed in the table (a is the lattice parameter, V is the unit-cell volume, $\Delta V/V$ is the relative change in the cell volume caused by hydrogenation). A cursory examination of the table reveals that the unit-cell volume of both Fe- and Co-containing compounds increases under hydrogenation, with the relative increase in volume observed for a hydrogen concentration x = 3 reaching higher than 20%.

Figure 1 displays the temperature dependences of the magnetization of the $Tb_{0.27}Dy_{0.73}Fe_2$, $Tb_{0.27}Dy_{0.73}Fe_2H_1$, and $Tb_{0.27}Dy_{0.73}Fe_2H_3$ compounds measured in a field H = 1 kOe. We see that the Curie

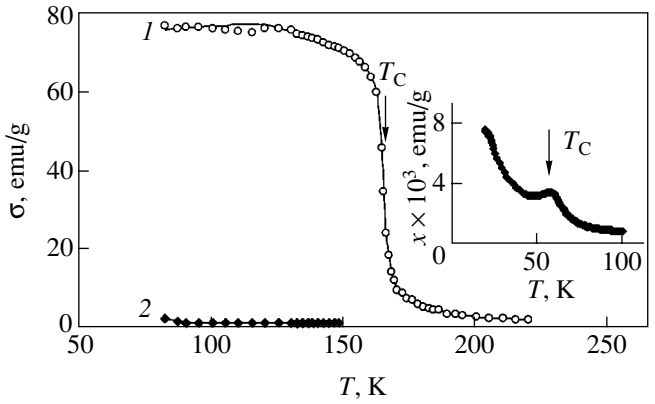

Fig. 2. Temperature dependences of the magnetization of (*1*) $Tb_{0.27}Dy_{0.73}Co_2$ and (*2*) its hydride $Tb_{0.27}Dy_{0.73}Co_2H_3$ measured in a field of 1 kOe. Inset: Temperature dependence of the magnetic susceptibility of the hydride $Tb_{0.27}Dy_{0.73}Co_2H_3$ in a field of 10 Oe.

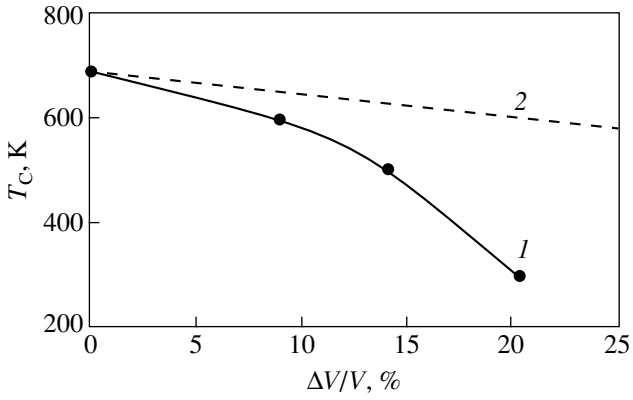

Fig. 3. (*1*) Curie temperature T_C of $Tb_{0.27}Dy_{0.73}Fe_2H_x$ plotted vs the relative increase in the unit-cell volume $\Delta V/V$ and (*2*) the expected variation in T_C in the hydrides as determined from literature data on the effect of pressure on the Curie temperature [11].

temperature T_C decreases strongly as the amount of incorporated hydrogen increases. Indeed, T_C decreases from 686 K for the starting composition $Tb_{0.27}Dy_{0.73}Fe_2$ to 596 and 290 K in the cases where one and three hydrogen atoms per formula unit are inserted, respectively. The magnetic ordering temperature was determined by the Belov thermodynamic method [5] for $Tb_{0.27}Dy_{0.73}Fe_2H_3$ and from the maximum of the derivative $d\sigma/dT$ for the other compounds (with $T_C > 300$ K). It was found that the temperature dependence of the magnetization of $Tb_{0.27}Dy_{0.73}Fe_2H_3$ has a minimum near $T_{comp} = 110$ K (curve *3* in Fig. 1), which apparently should be assigned to compensation of the magnetizations of the RE and Fe sublattices.

Figure 2 shows the temperature dependences of the magnetization of the $Tb_{0.27}Dy_{0.73}Co_2$ compound (curve *1*) and of its hydride $Tb_{0.27}Dy_{0.73}Co_2H_3$ (curve *2*) measured in a field $H = 1$ kOe. Note that the Curie temperature for $Tb_{0.27}Dy_{0.73}Co_2$ ($T_C = 164$ K) is markedly lower than that for $Tb_{0.27}Dy_{0.73}Fe_2$ ($T_C = 686$ K). The RT_2 intermetallics (*R* stands for heavy RE metals; *T* is a 3*d* transition element) are two-sublattice ferrimagnets with exchange interactions of three kinds: *R–R*, *R–T*, and *T–T*. Variation of the type of the *R* metal in RFe_2 compounds changes the Curie temperature very little [6]; therefore, the *T–T* interaction is strongest. In RCo_2, the Co magnetic moment (μ_{Co}) depends on the strength of the *R–T* exchange coupling because of the specific features of its band structure [7]. It was established that hydrogenation of $Tb_{0.27}Dy_{0.73}Co_2$, just as of $Tb_{0.27}Dy_{0.73}Fe_2$, lowers the magnetic ordering temperature substantially ($T_C = 57$ K). Such an effect of hydrogen on T_C is characteristic of Co-based intermetallic compounds [8] but is not typical, however, of all Fe-containing compounds, because hydrogenation increases T_C of compounds with a high Fe content, such as R_2Fe_{17} or $R(Fe,Ti)_{12}$ [9, 10], and decreases T_C of compounds with a low Fe content (RFe_2 Laves phases) [7].

Figure 3 displays the dependence of the Curie temperature of the $Tb_{0.27}Dy_{0.73}Fe_2H_x$ hydrides ($x = 0$, 1, 3) on the relative increase in the unit-cell volume. These compounds also have a crystal structure of the Laves phase type. From the standpoint of lattice expansion, incorporation of hydrogen is equivalent to the application of a negative hydrostatic pressure. The expected decrease in T_C in the above hydrides due to an increase in unit-cell volume as derived from literature data on the effect of pressure on the Curie temperature ($dT_C/dp \approx 5$ K/GPa for $ErFe_2$) [11] and compressibility ($\kappa = 10^{-2}$ GPa^{-1}) is plotted as a dashed line in Fig. 3. The rate of the decrease in T_C with increasing cell volume is calculated from the expression

$$\frac{d\ln T_C}{dp} = -\frac{\kappa}{T_C}\frac{dT_C}{d\ln V},$$

where $\kappa = -\dfrac{\Delta V/V}{p}$. We obtain $dT_C/d\ln V = dT_C/(dV/V) \approx$ 5 K per 1% of change in the atomic volume. The experimentally determined decrease in T_C is seen to be substantially larger than that expected from the increase in cell volume. One may therefore conclude that the main role is played here not by volume expansion but rather by the strong change in the electronic structure of $Tb_{0.27}Dy_{0.73}Fe_2$, and it is this change that accounts for the pronounced decrease in the Curie temperature under hydrogenation. By contrast, incorporation of hydrogen into compounds with a high concentration of iron and a low concentration of the RE element (R_2Fe_{17}) increases the Curie temperature [10], an effect that can be assigned to a unit-cell expansion in volume. The magnitude of this effect in Y_2Fe_{17} and Lu_2Fe_{17} can be

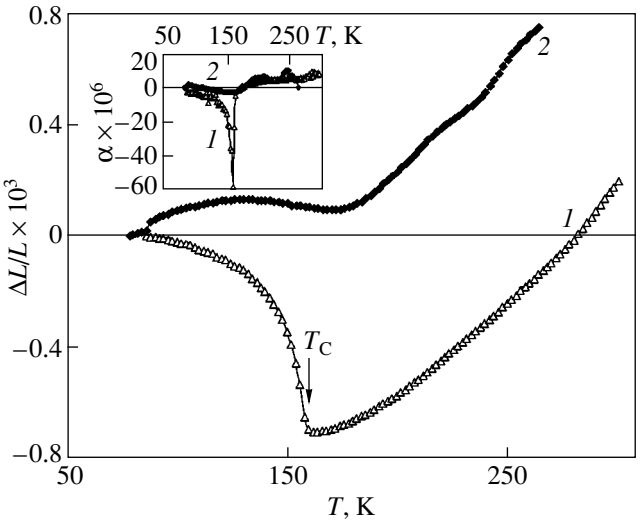

Fig. 4. Temperature dependence of thermal expansion and of the thermal expansion coefficient (inset) plotted for (*1*) $Tb_{0.27}Dy_{0.73}Co_2$ and (*2*) $Tb_{0.27}Dy_{0.73}Co_2H_3$.

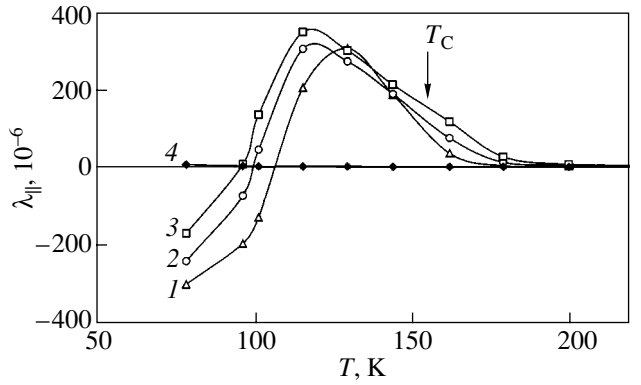

Fig. 5. Temperature dependence of the longitudinal magnetostriction of (*1–3*) $Tb_{0.27}Dy_{0.73}Co_2$ measured in fields of (*1*) 5, (*2*) 9.4, and (*3*) 11.8 kOe and (*4*) its hydride $Tb_{0.27}Dy_{0.73}Co_2H_3$.

derived using experimental data on the pressure dependence of the Curie temperature in these compounds [12].

Consider now thermal expansion near the magnetic ordering temperatures of the compounds under study. Figure 4 plots the temperature dependence of the thermal expansion of $Tb_{0.27}Dy_{0.73}Co_2$ and $Tb_{0.27}Dy_{0.73}Co_2H_3$. The graphs are clearly seen to be nonmonotonic. In the starting compound $Tb_{0.27}Dy_{0.73}Co_2$ (curve *1*), the relative elongation $\Delta L/L$ of the sample in thermal expansion is seen to decrease strongly in the temperature interval 78–160 K and exhibit a clearly pronounced minimum near T = 160 K, which is followed by a monotonic rise in $\Delta L/L$ with temperature. The temperature dependences of the linear coefficient of thermal expansion $\alpha(T)$ measured on the starting composition (curve *1*) and its hydride (curve *2*) are displayed in the inset to Fig. 4. The $\alpha(T)$ curve was obtained by numerical differentiation of the $\Delta L/L(T)$ dependence. The peak in $\alpha(T)$ (curve *1*) can be used to derive the Curie temperature. For $Tb_{0.27}Dy_{0.73}Co_2$, the result is T_C = 158 K, which agrees well with thermomagnetic data (to within 5%). The hydride $Tb_{0.27}Dy_{0.73}Co_2H_3$ exhibits a strong change in the pattern of the thermal expansion $\Delta L/L(T)$ curve and sign reversal of the linear thermal expansion coefficient α (curves *2* in Fig. 4).

The temperature dependence of longitudinal magnetostriction was measured on the samples used earlier to study thermal expansion. Figure 5 plots the temperature dependences of the longitudinal magnetostriction $\lambda_{\|}$ of $Tb_{0.27}Dy_{0.73}Co_2$. The measurements were performed in fields of 5, 9, and 12 kOe (curves *1–3*, respectively). We readily see that at T = 78 K the magnetostriction is negative, with its magnitude being 310×10^{-6} at 5 kOe. In the temperature interval 80–115 K, the magnetostriction decreases monotonically in magnitude and reverses sign (from negative to positive) near T = 100 K. The magnetostriction sign reversal should be attributed to the negative contribution of the cobalt sublattice being dominant at low temperatures. At $T \approx$ 115 K, the magnetostriction reaches a maximum value $\lambda = 355 \times 10^{-6}$ (at 12 kOe), to fall off thereafter sharply near the Curie temperature T_C = 164 K. The maximum in magnetostriction at $T \approx 120$ K is apparently caused by MCA compensation on the RE sublattice. Figure 5 also shows the temperature dependence of the longitudinal magnetostriction of the hydride $Tb_{0.27}Dy_{0.73}Co_2H_3$. Hydrogenation is seen to reduce the magnetostriction almost to zero.

Figure 6 displays the temperature dependences of the longitudinal magnetostriction $\lambda_{\|}$ of the hydride $Tb_{0.27}Dy_{0.73}Fe_2H_3$ measured in fields of 3.5, 8, and 12 kOe (curves *1–3*, respectively). Also shown for comparison is the temperature dependence of the longitudinal magnetostriction $\lambda_{\|}$ of the starting compound $Tb_{0.27}Dy_{0.73}Fe_2$ (curve *4*) determined at 12 kOe. It can be seen from Fig. 6 that hydrogenation lowers the room-temperature value of $\lambda_{\|}$ by about 100 times. It is seen also that the magnetostriction of the hydride $Tb_{0.27}Dy_{0.73}Fe_2H_3$ grows monotonically in the 80- to 270-K interval and reverses sign (from negative to positive) for all fields at $T \approx 118$ K, i.e., as the magnetic compensation point of magnetization T_{comp} is passed (curve *3* in Fig. 1). In the region of T = 270 K, the magnetostriction of the hydride reaches its maximum value $\lambda_{\|} = 18 \times 10^{-6}$ (in a field H = 12 kOe), to fall off sharply as the Curie temperature T_C = 290 K is approached. The magnetostriction of the starting compound $Tb_{0.27}Dy_{0.73}Fe_2$ at T = 78 K is $\lambda_{\|} = 180 \times 10^{-6}$ and grows monotonically in the range 80–240 K. In the region of T = 240 K, $Tb_{0.27}Dy_{0.73}Fe_2$ (just like its hydride) passes through a maximum in the temperature dependence of

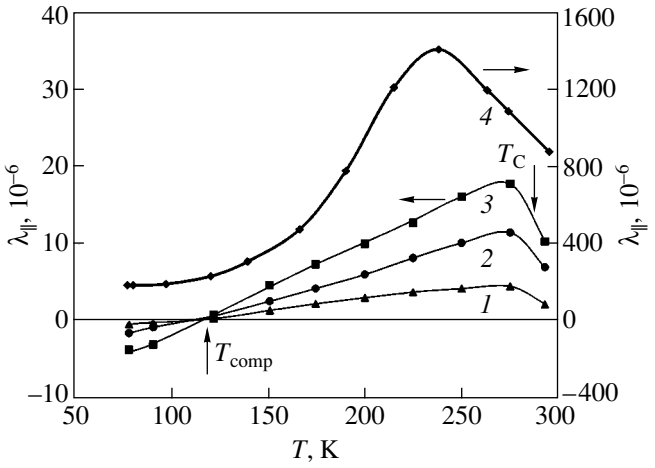

Fig. 6. Temperature dependence of the longitudinal magnetostriction of (*1–3*) $Tb_{0.27}Dy_{0.73}Fe_2H_3$ measured in fields of (*1*) 3.5, (*2*) 8, and (*3*) 12 kOe and (*4*) $Tb_{0.27}Dy_{0.73}Fe_2$ in a field of 12 kOe (right-hand scale).

magnetostriction ($\lambda_{\parallel} = 1400 \times 10^{-6}$), after which it decreases. The maxima of magnetostriction of these compounds, as well as those of $Tb_{0.27}Dy_{0.73}Co_2$, are apparently due to MCA compensation on the RE sublattice. The sharp decrease in the field-induced magnetostriction brought about by hydrogenation can find explanation in that hydrogen, in occupying lattice interstitial positions in the immediate vicinity of RE ions, exerts a considerable effect on the crystal field acting on the RE ions. At high hydrogen concentrations ($x > 3$), the hydrides RFe_2H_x exhibit rhombohedral distortions of the starting fcc structure (β phase) [7], which are assumed to be associated with hydrogen ordering in the crystal lattice. It is possible that the applied fields are small as compared to the local magnetic anisotropy field caused by hydrogen incorporation. Therefore, the magnetostriction of the starting compound $Tb_{0.27}Dy_{0.73}Fe_2$ originates primarily from the RE sublattice and that of the hydride $Tb_{0.27}Dy_{0.73}Fe_2H_x$ is due predominantly to the Fe sublattice. The magnetostriction of $LuFe_2H_{1.5}$ is due to the iron sublattice and remains positive over the range 4.2–300 K [7]. The magnetostriction constants of $LuFe_2H_{1.5}$ and $Tb_{0.27}Dy_{0.73}Fe_2H_x$ practically coincide for $T > 120$ K, making it possible to conclude that above 120 K the magnetostriction of $Tb_{0.27}Dy_{0.73}Fe_2H_x$ is also dominated by the Fe sublattice. Since the magnetostriction of $LuFe_2H_{1.5}$ is positive, the magnetostriction of $Tb_{0.27}Dy_{0.73}Fe_2H_x$ is also positive above T_{comp} and is negative below it, because an increase in the external field causes the projection of the Fe magnetic moment on the field direction to increase in the former case and to decrease in the latter case, i.e., at $T < T_{comp}$ (Fig. 6).

4. CONCLUSIONS

As follows from our studies, incorporation of hydrogen atoms into the crystal lattices of $Tb_{0.27}Dy_{0.73}Fe_2$ and $Tb_{0.27}Dy_{0.73}Co_2$ initiates a sharp decrease in the magnetic ordering temperature and in the magnitude of magnetostriction. The data obtained can be explained by a strong change in the local electronic density induced by hydrogenation, which entails a change in the magnitude of the exchange integrals and electrostatic crystal fields acting on the magnetic moments of the 4*f* and 3*d* ions.

ACKNOWLEDGMENTS

This study was supported by the Russian Foundation for Basic Research (project no. 02-02-16523a) and the federal program of support of leading scientific schools (project no. NSh-205.2003.2).

REFERENCES

1. A. E. Clark, in *Handbook on the Physics and Chemistry of Rare Earths*, Ed. by K. A. Gschneidner, Jr. and J. Eyring (North-Holland, Amsterdam, 1979), p. 231.
2. K. P. Belov, *Magnetostriction Phenomena and Their Technical Applications* (Nauka, Moscow, 1987) [in Russian].
3. A. V. Deryagin, V. N. Moskalev, N. V. Mushnikov, and S. V. Terent'ev, Fiz. Met. Metalloved. **57** (6), 1086 (1984).
4. F. Pourarian, Physica B (Amsterdam) **321**, 18 (2002).
5. K. P. Belov, *Magnetic Transitions* (Fizmatgiz, Moscow, 1959; Consultants Bureau, New York, 1961).
6. H. P. J. Wijn, E. Burzo, A. Chelkowski, and H. R. Kirchmayr, in *Landolt–Börnstein: New Series* (Springer, Berlin, 1990), Vol. III/19d2, p. 106.
7. N. V. Mushnikov, Doctoral Dissertation (Yekaterinburg, 2004).
8. G. Wiesinger and G. Hilscher, in *Handbook of Magnetic Materials*, Ed. by K. H. J. Buschow (Elsevier, Amsterdam, 1991), Vol. 6, Chap. 6, p. 511.
9. H. Fujii and H. Sun, in *Handbook of Magnetic Materials*, Ed. by K. H. J. Buschow (Elsevier, Amsterdam, 1995), Vol. 9, Chap. 3, p. 304.
10. S. A. Nikitin and I. S. Tereshina, Fiz. Tverd. Tela (St. Petersburg) **45** (10), 1850 (2003) [Phys. Solid State **45** (10), 1944 (2003)].
11. M. Brouda, K. H. J. Buschow, and A. R. Miedema, IEEE Trans. Magn. **MAG-10**, 182 (1974).
12. I. S. Tereshina, S. A. Nikitin, J. Stepien-Damm, L. D. Gulay, N. Yu. Pankratov, A. A. Salamova, V. N. Verbetsky, and W. Suski, J. Alloys Compd. **329**, 31 (2001).

Translated by G. Skrebtsov

Physics of the Solid State, Vol. 47, No. 10, 2005, pp. 1914–1921. Translated from Fizika Tverdogo Tela, Vol. 47, No. 10, 2005, pp. 1839–1845.

MAGNETISM AND FERROELECTRICITY

The Influence of Transverse Perturbations on the Propagation of Picosecond Acoustic Pulses in a Paramagnetic Crystal

A. N. Bugaĭ and S. V. Sazonov

Kaliningrad State University, Kaliningrad, 236041 Russia

e-mail: barab@newmail.ru

Received January 13, 2005

Abstract—The influence of transverse perturbations on the dynamics of a picosecond soliton-like acoustic pulse in a paramagnetic crystal in an external magnetic field is investigated. The nonlinear and dispersion effects are governed by the intrinsic properties of the crystal and the spin–phonon interaction. The effect of different nonlinear mechanisms and an external magnetic field on the stability against transverse perturbations is analyzed. It is shown that, in the absence of paramagnetic impurities, there can exist only a compression pulse that propagates in a defocusing regime. In the presence of paramagnetic ions in the crystal, there can arise rarefaction pulses that, under specific conditions, can propagate in self-focusing and self-channeling regimes.

1. INTRODUCTION

Nonlinear effects in optics have been investigated in parallel with those in acoustics, and the results of these studies complement each other [1, 2]. One of the latest trends in this direction is associated with research into the nonlinear propagation of the shortest possible pulses in different media. At present, femtosecond optical and picosecond acoustic pulses can be generated under experimental conditions. An important feature of pulses with these durations is that they have no carrier frequency. These pulses are referred to as ultimately short or video pulses (hereinafter, we will use both terms). Investigations into the soliton (soliton-like) regimes of propagation of ultimately short pulses are of special interest.

Despite the similarity between optical and acoustic solitons, there are two fundamental differences between them. First, optical solitons can be only transverse, whereas acoustic solitons can be longitudinal [3], transverse [4], and both longitudinal and transverse simultaneously [5–7]. Second, in the case of picosecond acoustic pulses (unlike femtosecond optical pulses), spatial dispersion effects are of particular importance. Actually, the spatial size of a pulse in the propagation direction can be estimated as $l_s \sim a\tau_p$, where a is the velocity of sound in the material and τ_p is the pulse duration. By assuming that $a \sim 5 \times 10^5$ cm/s and $\tau_p \sim 1$ ps, we obtain the spatial size of the pulse $l_s \sim 5 \times 10^{-7}$ cm, which is only one order of magnitude larger than the lattice spacing h (the distance between sites, i.e., between the nearest neighbors) [2, 8]. For a femtosecond optical pulse, the spatial size is estimated as $l_s' \sim c\tau_p \sim 5 \times 10^{-5}$ cm $\gg l_s$ and h. Therefore, spatial dispersion effects for optical pulses should be substantially less pronounced.

Paramagnetic impurities in a crystal can bring about additional nonlinear and dispersion effects associated with the spin–phonon interaction. Theoretical and experimental investigations have demonstrated that paramagnetic ions with an effective spin $S = 1$ interact most efficiently with lattice vibrations [9]. As an example, one can consider Fe^{2+} and Ni^{2+} ions in a MgO crystal matrix.

It should be noted that many aspects of the one-dimensional dynamics (in the propagation direction) of ultimately short acoustic pulses have been studied in sufficient detail [4, 5, 10–17]. However, this is not true for transverse effects. It is interesting to determine the conditions under which a pulse will undergo self-focusing and defocusing or will propagate in a self-channeling regime. Solving this problem is the main objective of the present work.

2. EQUATIONS OF MOTION

Let us consider a high-power longitudinal acoustic pulse traveling along the x axis. In our case, the x axis coincides with one of the fourfold axes of the cubic crystal containing paramagnetic impurities with effective spin $S = 1$. The crystal is in an external magnetic field $\mathbf{B}_0$ aligned with the axis perpendicular to the propagation direction.

The interaction of the acoustic pulse with paramagnetic impurities will be studied within a semiclassical approach according to which paramagnetic ions and the acoustic field are described in the framework of the quantum-mechanical and classical theories, respectively.

1063-7834/05/4710-1914$26.00

The Hamiltonian of the acoustic field can be represented in the form

$$H_a = \int \mathcal{H}_a d^3\mathbf{r},$$

where the Hamiltonian density is written as the sum of the linear ($\mathcal{H}_a^{(l)}$), nonlinear ($\mathcal{H}_a^{(nl)}$), and dispersive ($\mathcal{H}_a^{(\mathrm{dis})}$) parts; that is,

$$\mathcal{H}_a = \mathcal{H}_a^{(l)} + \mathcal{H}_a^{(nl)} + \mathcal{H}_a^{(\mathrm{dis})}. \quad (1)$$

Here, the linear and nonlinear parts of the Hamiltonian density are represented by the following expressions [18, 19]:

$$\mathcal{H}_a^{(l)} = \frac{p^2}{2\rho_m} + \frac{c_{11}}{2}\eta_{xx}^2 + 2c_{44}(\eta_{xy}^2 + \eta_{xz}^2), \quad (2)$$

$$\mathcal{H}_a^{(nl)} = \frac{c_{111}}{3!}\eta_{xx}^3 + \frac{c_{1111}}{4!}\eta_{xx}^4. \quad (3)$$

The strain tensor components are given by

$$\eta_{ij} = \frac{1}{2}\left(\frac{\partial u_i}{\partial x_j} + \frac{\partial u_j}{\partial x_i} + \frac{\partial u_l}{\partial x_i}\frac{\partial u_l}{\partial x_j}\right).$$

In expressions (2) and (3), p is the momentum density of local displacements in the crystal; ρ_m is the average density of the material; c_{11} and c_{44} are the linear elastic moduli; and c_{111} and c_{1111} are the nonlinear third-order and fourth-order elastic moduli, respectively.

Before writing the expression for the dispersive part of the Hamiltonian density $\mathcal{H}_a^{(\mathrm{dis})}$, we discuss expressions (2) and (3). The elastic wave is considered a purely longitudinal wave; i.e., only one component of the displacement vector $u_x \equiv u$ is nonzero. This assumption corresponds to the paraxial approximation (i.e., a small curvature of the wave front of the pulse); hence, we have $\partial u/\partial x \gg |\nabla_\perp u|$ (where $\nabla_\perp$ is the transverse gradient). It is clear that, for large curvatures, the pulse should be characterized by considerable velocity components forming large angles with the symmetry axis at the periphery. In this case, the wave cannot be considered purely longitudinal [20].

The relationship for the nonlinear part of the Hamiltonian density $\mathcal{H}_a^{(nl)}$ has the form of an expansion in powers of anharmonicity. Therefore, with due regard for the paraxial approximation, the terms containing the derivatives $\partial u/\partial x$ are retained, whereas the terms involving the derivatives $\partial u/\partial y$ and $\partial u/\partial z$ are omitted in expression (3).

Since the parameter h/l_s is small, the spatial acoustic dispersion effects are weak. The expression for the dispersive part of the Hamiltonian density $\mathcal{H}_a^{(\mathrm{dis})}$ can be obtained in terms of the discrete theory of lattice vibrations in the nearest neighbor approximation [8]. With allowance made for the paraxial approximation, the dispersive part of the Hamiltonian density contains only derivatives of the $\partial^2 u/\partial x^2$ type, whereas the second derivatives with respect to the transverse coordinates and mixed derivatives are omitted. Then, the expression for the dispersive part of the Hamiltonian density $\mathcal{H}_a^{(\mathrm{dis})}$ can be derived in the framework of a one-dimensional crystal model. In this case, the potential elastic energy in the nearest neighbor approximation has the form

$$\Pi_{\mathrm{lin}} = \sum_j \frac{\chi}{2}(u_{j+1} - u_j)^2,$$

where χ is the Hooke elastic constant and j is the ordinal number of the crystal site along the x axis. Next, we change over to the quasi-continuous model. Since $u_j = u(x)$, we have

$$u_{j+1} = u(x+h) \approx u(x) + h\frac{\partial u}{\partial x} + \frac{h^2}{2}\frac{\partial^2 u}{\partial x^2} + \frac{h^3}{6}\frac{\partial^3 u}{\partial x^3}.$$

By retaining the terms up to the fourth order in the lattice parameter h, we obtain

$$(u_{j+1} - u_j)^2 = \left(h\frac{\partial u}{\partial x} + \frac{h^2}{2}\frac{\partial^2 u}{\partial x^2} + \frac{h^3}{6}\frac{\partial^3 u}{\partial x^3}\right)^2$$

$$\approx h^2\left(\frac{\partial u}{\partial x}\right)^2 + h^3\frac{\partial u}{\partial x}\frac{\partial^2 u}{\partial x^2} + \frac{h^4}{4}\left(\frac{\partial^2 u}{\partial x^2}\right)^2 + \frac{h^4}{3}\frac{\partial u}{\partial x}\frac{\partial^3 u}{\partial x^3}.$$

It is evident that the first term in this expansion corresponds to the dispersionless limit and has already been included in expression (2).

In the expression for Π_{lim}, we change over from summation to integration: $\sum_j \longrightarrow \int n d\mathbf{r}$, where n is the average atomic density in the crystal. With integration by parts assuming that the crystal is infinite (i.e., $\partial u/\partial x = 0$ at $x \longrightarrow \pm\infty$, we find

$$\mathcal{H}_a^{(\mathrm{dis})} = -\frac{c_{11}h^2}{24}\left(\frac{\partial^2 u}{\partial x^2}\right)^2. \quad (4)$$

Here, we take into account that $n\chi h^2 = c_{11}$.

From expressions (1)–(4), taking into account the approximate relationships

$$\eta_{xx} = \frac{\partial u}{\partial x} + \frac{1}{2}\left(\frac{\partial u}{\partial x}\right)^2,$$

$$\eta_{xy} = \frac{1}{2}\left(\frac{\partial u}{\partial y} + \frac{\partial u}{\partial x}\frac{\partial u}{\partial y}\right) \approx \frac{1}{2}\frac{\partial u}{\partial y},$$

$$\eta_{xz} = \frac{1}{2}\left(\frac{\partial u}{\partial z} + \frac{\partial u}{\partial x}\frac{\partial u}{\partial z}\right) \approx \frac{1}{2}\frac{\partial u}{\partial z}$$

(the second terms in parentheses in the formulas for η_{xy} and η_{xz} are omitted with due regard for the paraxial approximation and the relatively weak nonlinearity) and retaining the terms up to the fourth order in the derivative $\partial u/\partial x$, we obtain the following formula for the Hamiltonian density of the acoustic field:

$$\mathcal{H}_a = \frac{p^2}{2\rho_m} + \frac{c_{11}}{2}\left(\frac{\partial u}{\partial x}\right)^2 + \frac{c_{44}}{2}(\nabla_\perp u)^2 - \frac{c_{11}h^2}{24}\left(\frac{\partial^2 u}{\partial x^2}\right) + \frac{1}{6}(c_{111} + 3c_{11})\left(\frac{\partial u}{\partial x}\right)^3 + \frac{1}{24}(c_{1111} + 6c_{111} + 3c_{11})\left(\frac{\partial u}{\partial x}\right)^4. \quad (5)$$

According to [21], the operator describing the interaction of the acoustic field with paramagnetic ions can be written in the form

$$\hat{H}_{\text{int}} = \sum_j G_{11}\hat{S}_x^{(j)^2}(u_{j+1} - u_{j-1}),$$

where G_{11} is the spin–phonon interaction constant and $\hat{S}_{x,y,z}^{(j)}$ are 3-by-3 matrices corresponding to the jth spin ($S = 1$) [9].

By changing over to the quasi-continuous approximation, we find

$$\hat{H}_{\text{int}} = \int n_s G_{11}\left(\frac{\partial u}{\partial x} + \frac{h^2}{6}\frac{\partial^3 u}{\partial x^3}\right)\hat{S}_x^2 d\mathbf{r}, \quad (6)$$

where n_s is the concentration of impurity paramagnetic ions.

The expression in parentheses accounts for the spatial nonlocality of the spin–phonon interaction [4, 5]. This nonlocality is significant for picosecond acoustic pulses and becomes negligible in the continuum limit.

If the crystal sites located not only along the x axis are taken into account in expression (4), after changing over to the quasi-continuous limit, expression (5) will contain terms with odd derivatives of u with respect to the variables y and z. Owing to the symmetry $y \longrightarrow -y$ and $z \longrightarrow -z$, these terms should not make contributions. The term proportional to $h^2(\Delta_\perp u)\partial u/\partial x$ in parentheses in expression (5) can be omitted within the paraxial approximation with allowance made for the weak effects of the spatial nonlocality of the spin–phonon interaction.

Expressions (5) and (6) can be supplemented by the operator of the interaction between the effective spin and the external magnetic field; that is,

$$\hat{H}_s = \int n_s \hbar \omega_0 \hat{S}_z d\mathbf{r}, \quad (7)$$

where $\omega_0 = 2g\mu_B B_0/\hbar$ is the frequency of splitting between the first and third levels of the Zeeman triple, g is the Landé factor, and μ_B is the Bohr magneton.

According to the semiclassical approach [5], the acoustic field can be described by the Hamiltonian equation

$$\frac{\partial p}{\partial t} = -\frac{\delta H}{\partial u}, \quad \frac{\partial u}{\partial t} = \frac{\delta H}{\delta p}, \quad (8)$$

where $H = H_a + \langle \hat{H}_{\text{int}} \rangle$, $\langle \hat{H}_{\text{int}} \rangle = \text{Sp}(\hat{\rho}\hat{H}_{\text{int}})$ is the quantum average of the interaction operator, and $\hat{\rho}$ is the operator of the effective spin density. The last operator obeys the equation of motion

$$i\hbar\frac{\partial \hat{\rho}}{\partial t} = [\hat{H}_s + \hat{H}_{\text{int}}, \hat{\rho}]. \quad (9)$$

By using expressions (7)–(9) and the explicit form of the operators $\hat{S}_x$, $\hat{S}_y$, and $\hat{S}_z$ [9], we obtain the self-consistent nonlinear system of equations describing the pulse dynamics and the quantum states of paramagnetic ions:

$$\frac{\partial^2 \varepsilon}{\partial t^2} - a^2\frac{\partial^2 \varepsilon}{\partial x^2} = -b_2\frac{\partial^2 \varepsilon^2}{\partial x^2} + b_3^a\frac{\partial^2 \varepsilon^3}{\partial x^2} + b^a\frac{\partial^4 \varepsilon}{\partial x^4} + \frac{2n_s G_{11}}{\rho_m}\left(\frac{\partial^2}{\partial x^2} + \frac{h^2}{6}\frac{\partial^4}{\partial x^4}\right)U + a_\perp^2\Delta_\perp\varepsilon, \quad (10)$$

$$\frac{\partial U}{\partial t} = -\omega_0 V, \quad \frac{\partial V}{\partial t} = \omega_0 U + \Omega W, \quad \frac{\partial W}{\partial t} = -\Omega V. \quad (11)$$

Here, $W = (\rho_{33} - \rho_{11})/2$ is the quantity characterizing the population inversion between the third and first (ground) Zeeman sublevels;

$$U = (\rho_{31} + \rho_{31}^*)/2, \quad V = (\rho_{31}^* - \rho_{31})/2i,$$

$$\Omega = \frac{2G_{11}}{\hbar}\left(\varepsilon + \frac{h^2}{6}\frac{\partial^2 \varepsilon}{\partial x^2}\right);$$

ρ_{jk} are the corresponding density matrix elements in the representation of the eigenfunctions of the operator $\hat{H}_s$; $\varepsilon = \partial u/\partial x$ is the linear component of the strain induced by the elastic pulse; and $a = \sqrt{c_{11}/\rho_m}$ and $a_\perp = \sqrt{c_{44}/\rho_m}$ are the longitudinal and transverse linear velocities of sound, respectively. The parameters $b_2 = 4a^2\Gamma$ and $b_3^a = (c_{1111}/6c_{11} - \Gamma - 1)a^2$ include contributions from the quadratic and cubic nonlinearities due to the anharmonicity of lattice vibrations. Here, $\Gamma = -3/2(1 + c_{111}/3c_{11})$ is the Grüneisen parameter. The term with the coefficient $b^a = a^2h^2/12$ accounts for the spatial dispersion associated with the discrete crystal structure. The terms in parentheses on the right-hand side of Eq. (10) take into account the spin–phonon

interaction. The constitutive equations (11) form the system of Bloch equations for the spin–phonon interaction [22] with allowance made for the spatial nonlocality of this interaction.

Let us assume that the pulse duration is $\tau_p \sim 10$ ps and the frequency of the Zeeman splittings is $\omega_0 \sim 10^{12}$ s^{-1}. Then, we obtain $(\omega_0\tau_p)^2 \gg 1$. In this approximation, with the use of relationships (11), the spin response can be expanded into a series allowing for nonlinearity and time dispersion [4, 23]; that is,

$$U = -\frac{W_\infty}{\omega_0}\Omega + \frac{W_\infty}{2\omega_0^3}\Omega^3 + \frac{W_\infty}{\omega_0^3}\frac{\partial^2\Omega}{\partial t^2}, \qquad (12)$$

where $W_\infty = W(t = -\infty)$.

In order for the spin–phonon interaction to affect the pulse propagation significantly, the initial difference W_∞ between the populations has to be considerable. In this case, the absolute temperature T must satisfy the condition $T < \hbar\omega_0/k_B$ [4, 5, 10], where k_B is the Boltzmann constant. For $\omega_0 \sim 10^{12}$ s^{-1}, we have $T < 10$ K, which holds at liquid-helium temperatures.

Now, we substitute expansion (12) into Eq. (10). Then, after renormalizing the velocity of sound $a_s = a\sqrt{1 + qW_\infty}$, the small terms of expansion in nonlinearity, dispersion, and transverse perturbations remain on the right-hand side of Eq. (10). In this situation, the wave equation in the slowly varying shape approximation can be reduced with respect to the derivatives by ignoring the reflected wave [24]. As a consequence, we obtain

$$\frac{\partial\varepsilon}{\partial t} - \beta_2\varepsilon\frac{\partial\varepsilon}{\partial\zeta} + \beta_3\varepsilon^2\frac{\partial\varepsilon}{\partial\zeta} + \beta\frac{\partial^3\varepsilon}{\partial\zeta^3} = -\frac{a_\perp^2}{2a}\Delta_\perp\int_{-\infty}^{\zeta}\varepsilon d\zeta, \qquad (13)$$

where

$$\beta_2 = b_2/a, \quad \beta_3 = 3b_3/2a, \quad \beta = b/2a,$$

$$b_3 = b_3^a + b_3^s, \quad b = b^a + b^s,$$

$$b^s = -a^2\frac{n_s W_\infty G_{11}^2}{c_{11}\hbar\omega_0}\left(\frac{a^2}{2\omega_0^2} - \frac{2h^2}{3}\right),$$

$$b_3^s = -a^2\frac{n_s W_\infty G_{11}^4}{C_{11}(\hbar\omega_0)^3}, \quad \zeta = z - at$$

(since $q \ll 1$, we set $a_s \approx a$).

From analyzing the coefficients of Eq. (13), it follows that the quadratic nonlinearity is associated only with the anharmonicity of the lattice vibrations. However, the cubic anharmonicity is governed by both the anharmonicity and the spin–phonon interaction.

For $a \sim 5 \times 10^5$ cm/s, $\omega_0 \sim 10^{12}$ s^{-1}, and $h \sim 10^{-8}$ cm, we find that the first term in parentheses in the relationship for the parameter b^s is considerably larger than the second term. Therefore, the normal time dispersion caused by the spin–phonon interaction is substantially larger than the anomalous dispersion due to the spatial nonlocality of this interaction. As a result, $b > 0$ and the total dispersion associated with the discrete crystal structure and the spin–phonon interaction is normal.

It can be seen from the derived expressions that the coefficients of the dispersion and the cubic nonlinearity are modified by the spin–phonon interaction. As a consequence, these coefficients depend on the external magnetic field strength.

In the one-dimensional case ($\Delta_\perp = 0$), Eq. (13) admits two types of one-soliton solutions,

$$\varepsilon_\pm = \frac{\pm 3b/b_2 l^2}{(\gamma/l^2 + 1)^{1/2}\cosh[(\zeta - ct)/l] \mp 1}, \qquad (14)$$

where l has the meaning of the pulse length, $c = \beta/l^2$, and $\gamma = 9bb_3/2b_2^2$.

Hereinafter, the plus and minus signs stand for the tensile and compressive strains, respectively.

It should be noted that Eq. (13) corresponds to two special cases. At $b_3 = 0$, Eq. (13) transforms into the Korteweg–de Vries equation. In this case, the nonsingular solution is represented only by the compression wave, which coincides with the Korteweg–de Vries soliton. At $b_2 = 0$, we have the modified Korteweg–de Vries equation. This equation can possess both solutions (14) coinciding with Korteweg–de Vries solitons of different polarity.

Let us now analyze the conditions under which pulses satisfying solutions (14) can exist. For this purpose, we estimate the characteristic strains by using the example of a MgO crystal. It is assumed that the external magnetic field is absent. Then, we have $b = b^a$ and $b_3 = b_3^a$. The constant b_3^a, which involves the fourth-order elastic modulus c_{1111}, can be estimated from the Morse interatomic interaction potential

$$\Pi_M = \Pi_0(e^{-2r/r_0} - e^{-r/r_0}),$$

where $r \equiv u_{j+1} - u_j$ are the relative displacements of sites, and r_0 and Π_0 are the effective width and depth of the potential, respectively. In the vicinity of the minimum, the Morse potential can be represented in the form of the expansion

$$\Pi_M = \Pi_0\left\{\frac{h^2}{r^2}\left(\frac{\partial u}{\partial x}\right)^2 - \frac{h^3}{r_0^3}\left(\frac{\partial u}{\partial x}\right)^3 + \frac{7h^4}{12r_0^4}\left(\frac{\partial u}{\partial x}\right)^4\right\}.$$

In our case, the interaction potential is given by

$$\Pi \sim \frac{c_{11}}{2}\left(\frac{\partial u}{\partial x}\right)^2 + \frac{1}{6}(c_{111} + 3c_{11})\left(\frac{\partial u}{\partial x}\right)^3 + \frac{1}{24}(c_{1111} + 6c_{111} + 3c_{11})\left(\frac{\partial u}{\partial x}\right)^4.$$

From the comparison of this relationship with the preceding expansion, we obtain the estimate $b_3^a = 7b_2^2/18a^2$. Note that the following relationships are satisfied: $\gamma/l^2 = 7h^2/48l^2 \ll 1$. Therefore, the relative displacements under tensile and compressive deformations are as follows: $|\varepsilon_+| \sim 3b/2b_2\gamma \sim a^2/b_2 \sim 1/4\Gamma$ and $|\varepsilon_-| \sim 3b/2b_2l^2 \sim h^2/32\Gamma a^2\tau_p^2$. For the MgO crystal, we have $a = 9 \times 10^5$ cm/s, $\Gamma = 6.8$, $h = 2.1 \times 10^{-8}$ cm, and the critical strain $\varepsilon \sim 3.8 \times 10^{-5}$ above which the elastic strain gives way to the plastic strain [3]. For the pulse duration $\tau_p \sim 10$ ps, we obtain $|\varepsilon_+| \sim 10^{-1}$ and $|\varepsilon_-| \sim 10^{-7}$. It is obvious that, in the given case, the solution can exist only in the form of the compression wave, which approximately coincides with the Korteweg–de Vries solution.

A decrease in the magnetic field strength (and, hence, in the frequency ω_0) leads to a decrease in the strain of the rarefaction wave. For example, we can assume that $n_s \sim 10^{19}$ cm^{-3}, $G_{11} \sim 10^{-13}$ erg [25], $\omega_0 \sim 10^{10}$ s, and $\tau_p \sim 300$ ps. In this case, the cubic anharmonicity and dispersion constants are determined primarily by the spin–phonon interaction, so we have the ratios $b^a/b^s \sim 10^{-7}$ and $b_3^a/b_3^s \sim 10^{-4}$ and the strains $|\varepsilon_+| \sim 10^{-5}$ and $|\varepsilon_-| \sim 10^{-6}$. Note also that $\gamma/l^2 \sim 1$ and the effective spin–phonon interaction can occur if the temperature of the sample is decreased to ~ 0.1 K. In this situation, there can exist both compression and rarefaction waves.

3. THE INCLUSION OF TRANSVERSE PERTURBATIONS

A further analysis of Eq. (13) will be performed using the variational method of an averaged Lagrangian [26]. The Lagrangian corresponding to Eq. (13) can be written in the form

$$L = \frac{1}{2}\frac{\partial u}{\partial \zeta}\frac{\partial u}{\partial t} - \frac{\beta_2}{6}\left(\frac{\partial u}{\partial \zeta}\right)^3 + \frac{\beta_3}{12}\left(\frac{\partial u}{\partial \zeta}\right)^4 - \frac{\beta}{2}\left(\frac{\partial^2 u}{\partial \zeta^2}\right) + \frac{a_\perp^2}{4a}(\nabla_\perp u)^2. \quad (15)$$

Here, we changed over from the strain field $\varepsilon = \partial u/\partial\zeta$ to the displacement field u. Taking into account relationship (14), the trial solution will be sought in the form

$$u_\pm = \pm\frac{6b}{b_2}\arctan\left(\frac{\sqrt{\theta^2 + 1} \pm 1}{\theta}\tanh[\theta(\zeta - \Phi)/2\sqrt{\gamma}]\right). \quad (16)$$

The inclusion of the non-one-dimensionality in the paraxial approximation suggests that the functions $\theta = \theta(t, \mathbf{r}_\perp)$ and $\Phi = \Phi(t, \mathbf{r}_\perp)$ in our case are slowly and rapidly varying functions of their arguments [27].

By substituting solution (16) into Lagrangian (15) and integrating the obtained expression over the fast variable ζ, we find the following averaged Lagrangians for the tensile and compressive strains:

$$\Lambda_\pm = \rho_\pm\frac{\partial\varphi_\pm}{\partial t} + \rho_\pm\frac{(\nabla_\perp\varphi_\pm)^2}{2} + \frac{b}{2\gamma}\left(\frac{\theta^3}{3} - \rho_\pm\right) + \frac{a_\perp^2\gamma(\nabla_\perp\theta)^2}{2\theta}d(\theta), \quad (17)$$

where

$$\varphi_\pm = -a\Phi_\pm, \quad \rho_- = \theta - \arcsin(1/\sqrt{1 + \theta^2}),$$
$$\rho_+ = \rho_- + \pi,$$
$$d(\theta) = -\rho^3/3\theta^4 + (3\theta^2 + \pi^2)\rho/3\theta^4 - (2\theta^2 + 5)/3\theta(\theta^2 + 1)^2.$$

From here on, the subscripts $\pm$ on the quantities ρ and φ will be omitted for brevity. For the quantities ρ and φ, with the use of expression (17), we write the Euler–Lagrange equations

$$\frac{\partial\rho}{\partial t} + \nabla_\perp(\rho\mathbf{V}_\perp) = 0, \quad \frac{\partial\varphi}{\partial t} + \frac{\mathbf{V}_\perp^2}{2} + \int\frac{dP}{\rho} = F_\perp, \quad (18)$$

where

$$\mathbf{V}_\perp = \nabla_\perp\varphi, \quad \int\frac{dP}{\rho} = \frac{b}{2\gamma}\theta^2,$$

$$F_\perp = a_\perp^2\gamma(1 + 1/\theta^2)[d(\theta)\Delta_\perp\theta + 0.5d'(\theta)(\nabla_\perp\theta)^2].$$

In the one-dimensional case ($\nabla_\perp = 0$), the system of equations (18) can be integrated easily. In this case, we have $\theta = \text{const}$ and $\Phi = b\theta^2 t/2\gamma a = \beta t/l^2$. Therefore, as could be expected, the trial solution coincides with the exact one-dimensional solution.

The functions $F_\perp$ describe the wave properties and account for the diffraction effects. This can be explained as follows. The relative diffraction effect can be described by the dimensionless parameter $\delta \sim \lambda/D$, where λ is the characteristic wavelength of the pulse and D is the characteristic size of transverse inhomogeneities induced in the medium by the pulse itself due to the nonlinearity. For the video pulse, the role of the wavelength is played by the spatial size of the pulse in

the propagation direction. Consequently, the following approximate equalities are satisfied: $\lambda \sim 1/l = \sqrt{\gamma}/\theta$ and $\Delta_\perp \sim 1/D^2$. In our case, we have $F_\perp \sim \delta^2$.

At the initial stage of bending of the front, we can disregard the wave properties and use eikonal (geometric) approximations when $F_\perp = 0$. Then, the system of equations (18) coincides in form with the equations for a potential flow of an ideal fluid (the continuity equation and the Cauchy integral for an unsteady flow, respectively). Here, the quantities φ, P, and ρ are analogs of the velocity potential $\mathbf{V}_\perp$, the pressure, and the density, respectively. The condition for the steady flow of fluids [described by equations of type (18)] $dP/d\rho > 0$ takes the form

$$b\rho(\theta^2 + 1)/\gamma\theta > 0. \tag{19}$$

Consequently, the pulses under consideration at the eikonal stage are stable against transverse perturbations.

Now, we assume that $F \neq 0$ in Eqs. (18). This corresponds to the inclusion of the diffraction of pulses in their transverse dynamics.

First, we examine small transverse perturbations. The functions θ and φ are represented in the form $\theta = \theta_0 + \theta_1$ and $\varphi = \varphi_0 + \varphi_1$, where $\varphi_0 = -b\theta_0^2 t/2\gamma$ and $\theta_0 = \theta(0)$. After linearizing the system of equations (18), we obtain

$$\begin{aligned} &\frac{\partial\theta_1}{\partial t} + \frac{\rho(\theta_0)(1+\theta_0^2)}{\theta_0^2}\Delta_\perp\varphi_1 = 0, \\ &\frac{\partial\varphi_1}{\partial t} + \frac{b\theta_0\theta_1}{\gamma} - \frac{a^2\gamma(1+\theta_0^2)d(\theta_0)}{\theta_0^2}\Delta_\perp\theta_1 = 0. \end{aligned} \tag{20}$$

The perturbations are chosen in the form of plane monochromatic waves $\theta_1\varphi_1 \sim \exp(i\omega t + i\mathbf{k}_\perp r_\perp)$. The quantities ω and $\mathbf{k}_\perp$ are related by the expression

$$\omega^2 = \mathbf{k}_2^2\frac{b\rho(\theta_0)(\theta_0^2+1)}{\gamma\theta_0}\left(1 + \frac{a^2\gamma^2 d(\theta_0)(\theta_0^2+1)}{b\theta_0^3}\mathbf{k}_\perp^2\right). \tag{21}$$

The pulse is stable against small perturbations if modes exponentially increasing with time are absent at any real value of $\mathbf{k}_\perp$. Consequently, in order for the pulse to be stable, the frequency ω must be real. For rarefaction waves, the inequality $d(\theta_0) > 0$ is satisfied and, hence, these waves are stable against small perturbations. In the case of compression waves, the inequality $d(\theta_0) > 0$ holds for $\theta_0 > 0.63$. Therefore, it follows from expression (21) that, when the duration of the compression pulses obeys the condition $\theta_0 < 0.63$, the frequency ω at $\mathbf{k}_\perp^2 > -b\theta_0^3/a^2\gamma^2 d(\theta_0)(1+\theta_0^2)$ becomes imaginary. This means that the compression pulses with a sufficiently long duration can be unstable against small perturbations.

Let us analyze the influence of nonlinear transverse perturbations. It is assumed that the strain field is axially symmetric. The function θ can be represented in the self-similar form

$$\theta = \theta_m(t)(1 - r^2/R_T^2(t)), \tag{22}$$

where R_T is the characteristic transverse size proportional to the pulse radius.

The function φ is written in the form of the expansion [28]:

$$\varphi = f_1(t) + f_2(t)r^2/2. \tag{23}$$

Substituting formulas (22) and (23) into the system of equations (18) gives

$$\begin{aligned} f_2 &= -\partial(\ln\rho(\theta_m))/\partial t, \\ R_T^2 &= C_0\theta_m^3/\rho^3(\theta_m)(1+\theta_m^2), \end{aligned} \tag{24}$$

where the constant C_0 is determined by the initial radius $R(0) = R_0$ and the length of the pulse. According to [1, 29], we use the paraxial approximation ($(r/R)^2 \ll 1$) and retain the terms up to the second order in the ratio r/R.

Now, we determine the time dependence of the transverse radius R of the pulse. The transverse intensity distribution is represented in the form $I_m = I_{\max}(t)(1 - r^2/R(t)^2)$, which is similar to formula (22). Since $I \sim \varepsilon^2$, we have $I_m^{(\pm)}(\theta) = I_0\theta^4/(\sqrt{1+\theta^2} \mp 1)^2$. Substituting formula (22) into the obtained relationship with due regard for expression (24), we find that the transverse radius of the pulse is given by the expression

$$R = R_0\sqrt{\psi(\theta)/\psi(\theta_0)},$$

where

$$\psi_\pm(\theta) = \frac{\theta^3(\sqrt{1+\theta^2} \mp 1)}{\rho^3(\theta^2 + 2 \mp 2\sqrt{1+\theta^2})\sqrt{1+\theta^2}}.$$

From expression (9), after equating the terms of the zeroth and second orders in r on the left- and right-hand sides, we obtain

$$f_1'(t) = -\frac{b}{2\gamma}\left(\theta_m^2 + \mu\frac{\psi(\theta_0)d(\theta_m)\rho(\theta_m)^3(1+\theta_m^2)}{\theta_m^2}\right), \tag{25}$$

$$\theta_m''(\tau) + k_1(\theta_m(\tau))\theta_m'(\tau)^2 + k_2(\theta_m(\tau), \theta_0, \mu) = 0, \tag{26}$$

where

$$\tau = t/t_c, \quad t_c = \sqrt{\gamma/bR_0}, \quad \mu = a_\perp^2\gamma^2/bR_0^2,$$

$$k_1 = 2(1 - \theta_m^5/\rho(\theta_m)^3)[\theta_m(1+\theta_m^2)]^{-1},$$

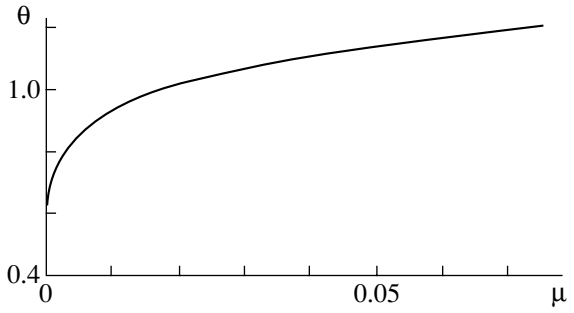

Fig. 1. Rarefaction pulse parameters corresponding to the self-channeling regime.

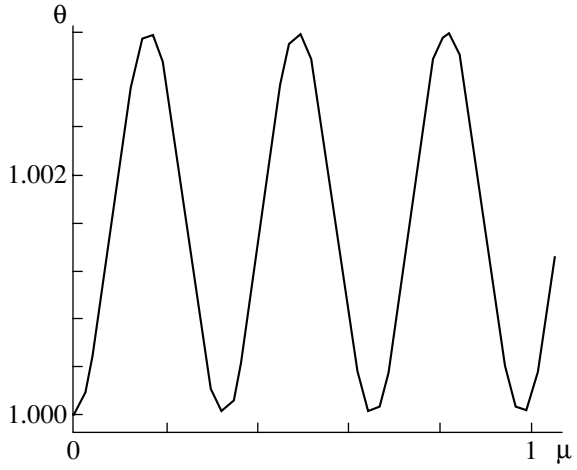

Fig. 2. Evolution of the quantity θ (proportional to the reciprocal of the pulse duration) for the rarefaction wave in the self-channeling regime for initial pulse parameters close to the stationary parameters ($\theta_0 = 1$, $\mu = 0.018$). The transverse pulse size oscillates in the antiphase with respect to the quantity θ.

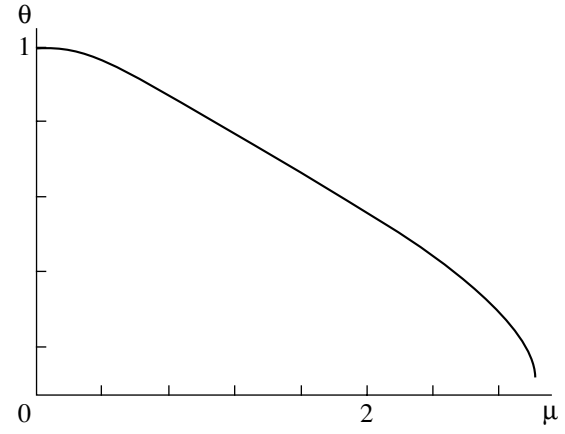

Fig. 3. Evolution of the quantity θ for the compression wave in the defocusing regime for initial pulse parameters $\theta_0 = 1$ and $\mu = 0.018$.

$$k_2 = 2\rho(\theta_m)^4(1+\theta_m^2)^2\theta_m^{-3}\psi(\theta_0)$$
$$\times\{1 + 2\mu\rho(\theta_m)^3(1+\theta_m^2)\theta_m^{-6}\psi(\theta_0)$$
$$\times[3\theta_m(1+\theta_m^2)d'(\theta_m) - 2d(\theta_m)]\}.$$

Under the assumption that the pulse coming into the material has a flat front, i.e., $f_2(0) = 0$ [see expressions (23), (24)], Eq. (26) is complemented by the initial conditions $\theta_m(0) = \theta_0 \equiv \sqrt{\gamma}/l(0)$ and $\theta_m'(0) = 0$.

The solution to Eq. (26) enables us to readily determine the time dependences of the pulse parameters (duration, radius, velocity, etc.).

The analysis of Eq. (26) for rarefaction pulses demonstrates that the equilibrium state is stable. Within the theory of dynamic systems, this corresponds to a stationary point of the center type. The stationary value θ_{st} is determined from the conditions

$$k_2(\theta_{st}, \mu_{st}) = 0, \quad \partial k_2(\theta, \theta_{st}, \mu_{st})/\partial\theta|_{\theta=\theta_{st}} > 0.$$

It is assumed that $\theta_0 = \theta_{st}$. The initial values of the parameters θ and μ at which the regime is stationary are presented in Fig. 1. The oscillations arising at small deviations from these parameters are shown in Fig. 2. These oscillations correspond to the regime of pulse self-channeling. Obviously, the period of small oscillations can be given by the expression $T_{osc} = 2\pi t_c(\partial k_2(\theta, \theta_{st}, \mu_{st})/\partial\theta|_{\theta=\theta_{st}})^{-1/2}$. At $\tau_p \sim 300$ ps and with allowance made for the material parameters estimated at the end of Section 2, we obtain $\theta \sim 1$. This value corresponds to the parameter $\mu \sim 0.01$. The transverse radius of the pulse is estimated as $R_0 \sim 1$ μm. In turn, the period of these oscillations is estimated as $T \sim 0.3t_c \sim 10^{-8}$ s $\sim 10^2\tau_p$. Since $\theta \sim \tau_p^{-1}$ and $\mu \sim R_0^{-2}$, an increase in the pulse duration leads to an increase in the average transverse radius in the case of the self-channeling regime (Fig. 1). In the case when the deviations from the stationary values of θ and μ are relatively large, the oscillations become nonlinear. When their amplitude is sufficiently large, the pulse radius can decrease significantly. This actually leads to self-focusing.

In the case of compression pulses, the equilibrium state is unstable. This corresponds to a stationary point of the saddle type. The value of θ_m can only decrease. This is accompanied by a spreading of the pulse and a decrease in the amplitude and velocity, i.e., by pulse defocusing (Fig. 3).

As was noted above, the generation of a rarefaction wave is associated with the strong cubic nonlinearity arising from the spin–phonon interaction. At the same time, the compression wave can be generated only in the presence of the quadratic nonlinearity. Similar calculations for ultimately short optical pulses demonstrated [28] that, if there is only a cubic nonlinearity, the influence of diffraction leads to focusing. In the situation where the medium is characterized by a quadratic

nonlinearity, the effect appears to be the opposite. If the pulse is defocused at the eikonal stage, the diffraction can lead to its self-channeling in the former case and only to an enhancement of defocusing in the latter case. In the problem under consideration, this is actually the case: channeling and defocusing are observed for rarefaction and compression waves, respectively.

4. CONCLUSIONS

Thus, we analyzed the propagation of ultimately short acoustic pulses in a paramagnetic crystal in a magnetic field. It was shown that paramagnetic impurities in the crystal are responsible for the appearance of additional nonlinear and dispersion effects, namely, the renormalization of the coefficients of fourth-order anharmonicity and acoustic dispersion. In the case where the process occurs only through the elastic mechanisms of nonlinearity (in the absence of paramagnetic impurities), the wave equation can possess only one type of soliton-like solution in the form of compression pulses. When the fourth-order anharmonicity is enhanced as a result of the spin–phonon interaction, there can arise another type of wave (rarefaction pulses).

The main objective of this work was to elucidate how transverse perturbations affect the pulse dynamics. At the eikonal stage, both types of waves are stable against transverse perturbations (self-focusing). The inclusion of the wave properties (diffraction) in the analysis leads to different propagation regimes. It was found that the compression pulses can undergo only defocusing. The self-channeling regime takes place when the initial duration and radius of the rarefaction pulse are close to stationary values. In this case, the soliton parameters oscillate. A considerable deviation of the initial duration and radius of the pulse from the stationary values can lead to a significant decrease in the pulse radius in the course of nonlinear oscillations. As a result, there occurs self-focusing.

In this work, the transverse effects were taken into account to a minimum extent (within the paraxial approximation). However, nonparaxial effects can turn out to be significant when the pulse front is strongly curved. This problem calls for further investigation.

ACKNOWLEDGMENTS

This work was supported by the Russian Foundation for Basic Research, project no. 05-02-16422a.

REFERENCES

1. S. A. Akhmanov, V. A. Vysloukh, and A. S. Chirkin, *Optics of Femtosecond Laser Pulses* (Nauka, Moscow, 1988) [in Russian].
2. V. É. Gusev and A. A. Karabutov, *Laser Optoacoustics* (Nauka, Moscow, 1991) [in Russian].
3. H.-Y. Hao and H. J. Maris, Phys. Rev. B: Condens. Matter **64**, 064 302 (2001).
4. S. V. Sazonov, J. Phys.: Condens. Matter **6** (31), 6295 (1994).
5. S. V. Sazonov, Zh. Éksp. Teor. Fiz. **118** (1), 20 (2000) [JETP **91** (1), 16 (2000)].
6. S. V. Voronkov and S. V. Sazonov, Zh. Éksp. Teor. Fiz. **120** (2), 269 (2001) [JETP **93** (2), 236 (2001)].
7. A. V. Gulakov and S. V. Sazonov, J. Phys.: Condens. Matter **16** (10), 1733 (2004).
8. Ch. Kittel, *Introduction to Solid State Physics*, 5th ed. (Wiley and Sons, New York, 1976; Nauka, Moscow, 1978).
9. J. W. Tucker and V. W. Rampton, *Microwave Ultrasonics in Solid State Physics* (North-Holland, Amsterdam, 1972; Mir, Moscow, 1975).
10. S. V. Sazonov, J. Phys.: Condens. Matter **4** (30), 6485 (1992).
11. S. V. Sazonov, Izv. Vyssh. Uchebn. Zaved., Fiz. **36** (7), 94 (1993).
12. S. V. Voronkov and S. V. Sazonov, Fiz. Tverd. Tela (St. Petersburg) **43** (11), 1969 (2001) [Phys. Solid State **43** (11), 2051 (2001)].
13. A. A. Zabolotskiĭ, Pis'ma Zh. Éksp. Teor. Fiz. **76** (10), 709 (2002) [JETP Lett. **76** (10), 607 (2002)].
14. A. A. Zabolotskii, Zh. Éksp. Teor. Fiz. **123** (4), 560 (2003) [JETP **96** (3), 496 (2003)].
15. A. A. Zabolotskii, Phys. Rev. E **67** (10), 066 606 (2003).
16. A. V. Gulakov and S. V. Sazonov, Fiz. Tverd. Tela (St. Petersburg) **46** (9), 1640 (2004) [Phys. Solid State **46** (9), 1693 (2004)].
17. A. A. Zabolotskii, Zh. Éksp. Teor. Fiz. **126** (1), 155 (2004) [JETP **99** (1), 133 (2004)].
18. L. K. Zarembo and V. A. Krasil'nikov, *Introduction to Nonlinear Acoustics* (Nauka, Moscow, 1966) [in Russian].
19. L. D. Landau and E. M. Lifshitz, *Course of Theoretical Physics*, Vol. 7: *Theory of Elasticity*, 4th ed. (Nauka, Moscow, 1987; Pergamon, New York, 1986).
20. V. A. Krasil'nikov and V. V. Krylov, *Introduction to Physical Acoustics* (Nauka, Moscow, 1984) [in Russian].
21. E. H. Jacobsen and K. W. H. Stevens, Phys. Rev. **129** (5), 2036 (1963).
22. N. S. Shiren, Phys. Rev. B: Solid State **2** (7), 2471 (1970).
23. É. M. Belenov, A. V. Nazarkin, and V. A. Ushchapovskiĭ, Zh. Éksp. Teor. Fiz. **100** (3), 762 (1991) [Sov. Phys. JETP **73** (3), 422 (1991)].
24. M. B. Vinogradova, O. V. Rudenko, and A. P. Sukhorukov, *The Theory of Waves* (Nauka, Moscow, 1979) [in Russian].
25. V. A. Golenishchev-Kutuzov, V. V. Samartsev, N. K. Solovarov, and B. M. Khabibulin, *Magnetic Quantum Acoustics* (Nauka, Moscow, 1977) [in Russian].
26. D. Anderson, Phys. Rev. A **27** (6), 3135 (1983).
27. S. K. Zhdanov and B. A. Trubnikov, *Quasi-Gaseous Unstable Media* (Nauka, Moscow, 1991) [in Russian].
28. S. V. Sazonov, Zh. Éksp. Teor. Fiz. **125** (6), 1419 (2004) [JETP **98** (6), 1237 (2004)].
29. N. V. Karlov and N. A. Kirichenko, *Oscillations, Waves, and Structures* (Fizmatlit, Moscow, 2001) [in Russian].

Translated by O. Borovik-Romanova

Physics of the Solid State, Vol. 47, No. 10, 2005, pp. 1922–1927. Translated from Fizika Tverdogo Tela, Vol. 47, No. 10, 2005, pp. 1846–1851.

MAGNETISM AND FERROELECTRICITY

Multilayer Metallization of Ferrite $Mg_{0.54}Zn_{0.46}Fe_2O_4$

Z. A. Samoĭlenko, V. S. Abramov, and N. N. Ivakhnenko

Galkin Donetsk Physicotechnical Institute, National Academy of Sciences of Ukraine, ul. R. Lyuksemburg 72, Donetsk, 83114 Ukraine

Received January 24, 2005

Abstract—The character of interatomic interaction in ferrite $Mg_{0.54}Zn_{0.46}Fe_2O_4$ was studied using the x-ray spectroscopy technique and theoretically. It was found that the electronic structure of samples is rearranged during annealing at high temperatures (1280°C, 0.5–0.8 h). The electronic structure rearrangement was shown to be associated with multilayered ferrite metallization in which alternating layers with metallic and ionic–covalent bonds form. © *2005 Pleiades Publishing, Inc.*

1. INTRODUCTION

Keen interest in magnetoresistive HTSC materials and ferrites has been generated by studies into the nature of magnetic and charge ordering in the electronic structure of these materials. Comprehensive information on atomic charges can be obtained from x-ray spectra [1]. According to earlier studies [2, 3], structural-chemical inhomogeneities in ferrites $Mg_{0.54}Zn_{0.46}Fe_2O_4$ change during high-temperature annealing (T = 1280°C, 0.5–0.8 h), which results in various sorts of ordering in solid solutions [4, 5], including magnetic (short-range), concentration (mesoscopic), and structural (matrix) ordering. This is what causes nonlinear changes in a range of parameters (including in the electric, magnetic, and structural parameters) [6]. Changes in electrical properties can be accompanied by multilayer metallization, which is to be studied in the present work.

2. EXPERIMENTAL

Like in the studies of variations in the interatomic interaction [7, 8], we studied FeK_β x-ray emission spectra (Fig. 1), in which the energy position of the FeK_{β_1} maximum is sensitive to the charge state of Fe ions. These spectra were analyzed using a theoretical model, which allowed the fine structure of the spectra to be revealed. The FeK_β band was considered a multiplet K_{ij} with theoretically predicted energy positions of the K_β lines (E_{ij}) corresponding to the transition energies between certain energy states (table, Fig. 1). Based on the experimentally measured intensities $I(E_{ij})$ of these lines for all samples, we chose the line with the maximum intensity (for example, K_{22} for an annealing time τ = 2 h), and the intensities of all lines were normalized to this maximum intensity. This normalization procedure makes it possible to obtain information both on the variation in the intensity of each separate line with annealing time τ and on a possible redistribution of intensities between the fine structural lines. The position of these lines is characterized by the energy $\Delta E = E_{ij} - E_{0\tau}$ (at a fixed value of τ) measured from the energy position of the center of gravity $E_{0\tau}$ of the FeK_β band. The energy $E_{0\tau}$ (measured in electronvolts) was calculated with respect to the standard Co$K_{\alpha 1}$ line, taking into account dispersion in the spectral region under study. The results of studying the evolution of the FeK_β lines carried out on zinc-magnesium ferrites are shown in Fig. 2. They characterize variations in population of the discrete energy states during high-temperature annealing.

3. THEORETICAL MODEL

Let us identify the lines in the observed K spectrum in terms of the theoretical model proposed in [9, 10]. The energy of the basic mode of the ${}_1Fe^0$–${}_4Fe^{2+}$–${}_3Fe^0$ chain is responsible for the energy positions of the β_1 and β' peaks. The quantum state of ${}_1Fe^0$ atoms (the electron configuration is $3d^8$; the spin and the orbital and total angular momenta of the electron shell are S = 1, L = 3, and J = 4, respectively; the nuclear spin is I = 1/2) and ${}_3Fe^0$ atoms (configuration $3d^7 4\bar{s}$, where $4\bar{s}$ means that the spin of the $4\bar{s}$ electron is opposite in direction to the total angular momentum of the $3d^7$ configuration; S = 1, L = 3, J = 4, I = 1/2) are described by the state vector $|F; m\rangle = |9/2; -1\rangle$ with the energy of the basic

Designations (K_{ij}) and calculated energy positions E_{ij} of K-spectral lines

K_{ij}	E_{ij}, eV	K_{ij}	E_{ij}, eV	K_{ij}	E_{ij}, eV	K_{ij}	E_{ij}, eV
K_{11}	7031.56	K_{21}	7064.02	K_{31}	7036.42	K_{41}	7065.32
K_{12}	7036.98	K_{22}	7058.62	K_{32}	7036.12	K_{42}	7059.49
K_{13}	7038.73	K_{23}	7056.82	K_{33}	7038.07	K_{43}	7057.54
K_{14}	7046.01	K_{24}	7049.62	K_{34}	7045.86	K_{44}	7049.76

1063-7834/05/4710-1922$26.00 © 2005 Pleiades Publishing, Inc.

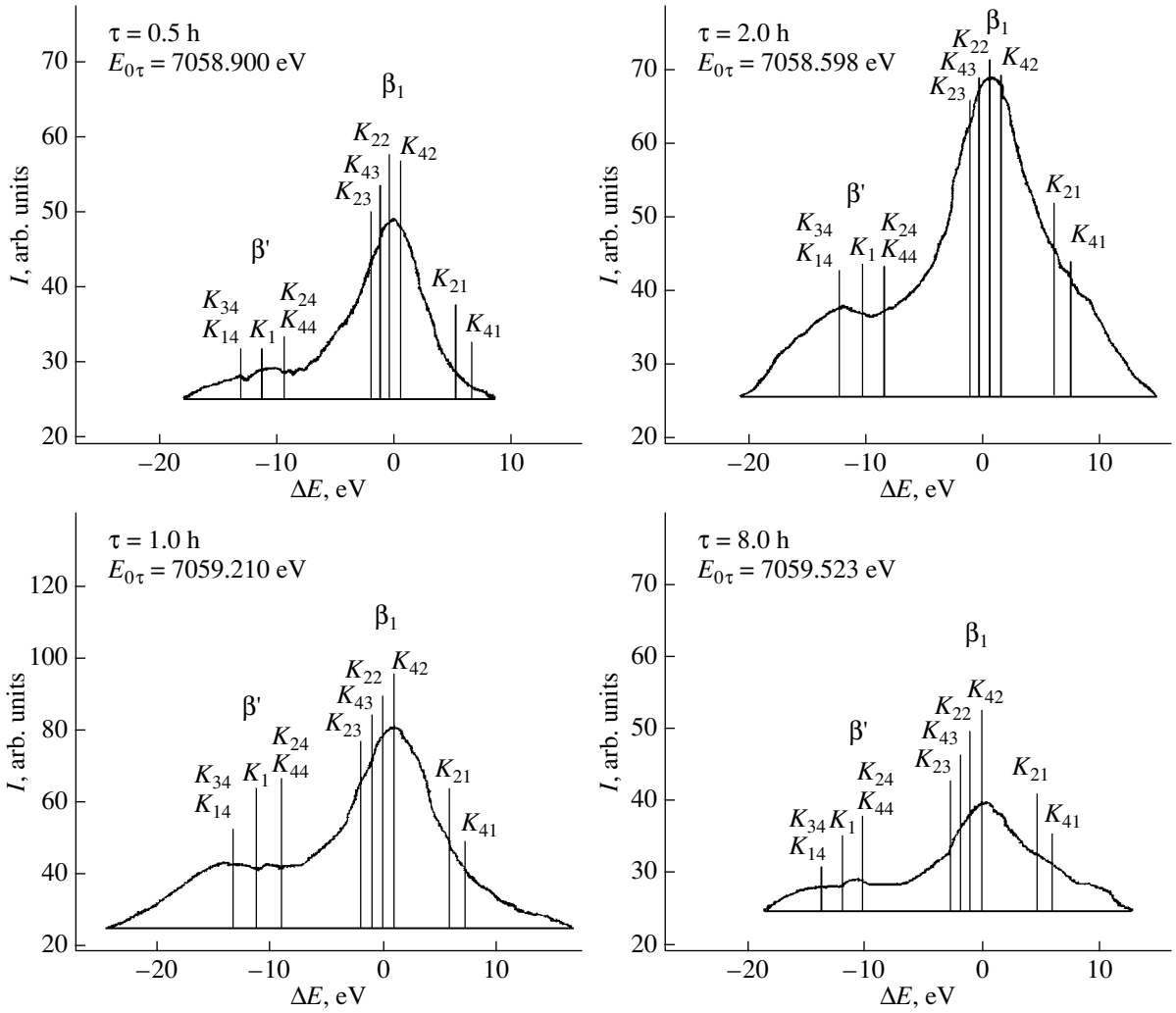

Fig. 1. Intensities I of the Fe $K_{\beta_1\beta'}$ lines plotted as a function of $\Delta E = E_{ij} - E_{0\tau}$ for ferrites $Mg_{0.54}Zn_{0.46}Fe_2O_4$. On the abscissa axis, point 0 is the origin of the energy coordinate reckoned from $E_{0\tau}$, where $E_{0\tau}$ is the energy position of the center of gravity of the β_1 line.

vibrational mode E = 302 keV. The quantum number F is obtained as the result of composition of the electron shell angular momentum and the nuclear spin. The crystallographic orientations of the valence bonds are described by the parameter $m = 3\cos^2\vartheta - 1$, where ϑ is the angle between the local Z axis and the local symmetry axis [9, 10]. Spontaneous deformation of the basic chain (corresponding to an order parameter $\Delta_q \neq 0$) accounts for the appearance of quasi-acoustic branches in the spectrum and, as a consequence, of the K_1 and K_2 spectral lines (with transition energies E_1 = 7047.81 eV and E_2 = 7393.29 eV, respectively). Further transformation of the spectrum is associated with a second order parameter $\Delta \neq 0$, corresponding to a soft mode of the additional chain $[{}_1O^- - {}_4Fe^{2+}] - {}_D Fe - [{}_3O^- - {}_4Fe^{2+}]$. The $[{}_1O^- - {}_4Fe^{2+}]$ and $[{}_3O^- - {}_4Fe^{2+}]$ complexes can exist in one of two possible states, $|1; -1\rangle$ or $|2; -1\rangle$, and are exchange-coupled through an intermediate ${}_D Fe$ ion. These ${}_D Fe$ ions can be ${}_4Fe^{2+}(1/2)$, ${}_3Fe^{3+}(1)$, ${}_2Fe^{4+}(3/2)$, and ${}_2Fe^{4+}(1/2)$ ions, which differ from each other in terms of their charge and magnetic state. (The figures in parentheses are the quantum number F of the intermediate ion state.) The additional chain causes further splitting of the spectral lines. Coupling between the basic and additional chains results in the formation of quasi-two-dimensional structures. The energies of the normal vibrational modes of these structures determine the energy positions of lines in the K spectrum. By comparing the experimental and calculated K spectra, information can be obtained on the possible electronic structure and its evolution during annealing. The table lists the designations and calculated energy positions of the additional lines in the K spectrum that derive from the basic K_1 line when the contribution from the second order parameter is taken into account. The K_{ij} lines with

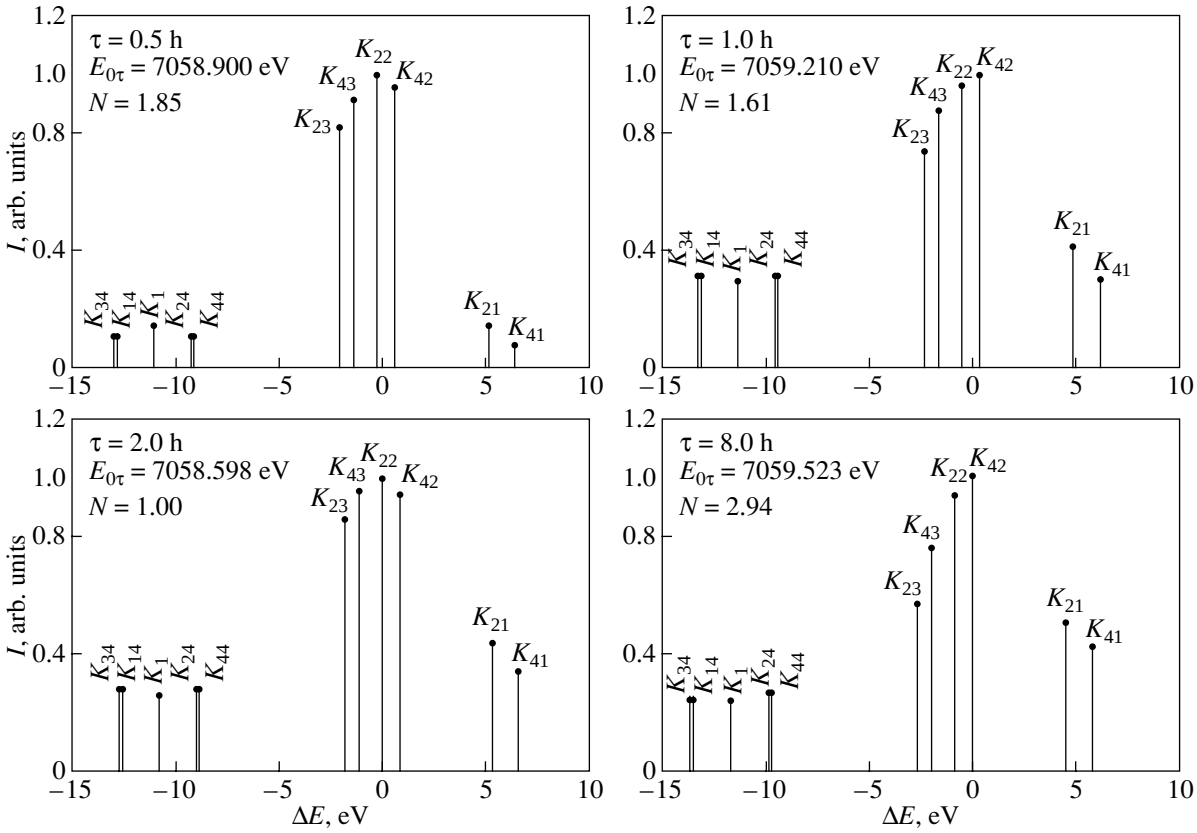

Fig. 2. Distribution of the Fe$K_{\beta_1\beta'}$ intensity over the multiplet components (*N* is the normalizing factor of the spectrum intensity).

i = 1 and 2 are related to the $|1; -1\rangle$ state, and those with i = 3 and 4 are related to the $|2; -1\rangle$ state of the oxygen–iron complexes of the additional chain. The second index (j = 1, 2, 3, 4) takes into account the contribution from the intermediate ions $_4Fe^{2+}(1/2)$, $_3Fe^{3+}(1)$, $_2Fe^{4+}(3/2)$, and $_2Fe^{4+}(1/2)$, respectively. In a real spectrum, the K_{11}, K_{12}, K_{13}, K_{31}, K_{32}, and K_{33} lines are not observed because of their weak intensity. The calculated energy positions of the lines derived from the second main line K_2 are not discussed here, because this energy region was not studied experimentally in the present work.

4. FINE STRUCTURE OF FeK_β X-RAY SPECTRA

Let us analyze experimental spectra in terms of the proposed theoretical model. It is known [11] that the 3*d* and 4*s* electrons of the elements from transition group VIII make the main contribution to transitions responsible for the occurrence of x-ray spectra. Oxygen does not have a core line, which could be used as a standard when studying variations in the population of its valence 2*p* shells. A comparison between the basic mode chain and the chain complexes associated with the soft mode shows that they contain the same iron ion ($_4Fe^{2+}$) in both cases. Consequently, the fine structure of the FeK_β line is determined by variations in the state of the soft mode of the additional chain. These changes are due to the intermediate $_D$Fe ions being of different types.

The formation of the β_1 peak in the experimental FeK_{β_1} spectrum is related to a group of lines K_{23}, K_{43}, K_{22}, and K_{42}. The high-energy slope of the β_1 peak (lines K_{21}, K_{41}) corresponds to metallic layers, whereas the low-energy slope of this peak (the β' peak, formed by the lines K_{34}, K_{14}, K_1, K_{44}, K_{24}) corresponds to layers with ionic–covalent bonding in which iron and oxygen ions (*p–d* coupling) are involved.

In the sample annealed for τ = 0.5 h, line K_{22} is closer to the maximum of the β_1 peak than lines K_{23}, K_{43}, and K_{42} The main contribution to its intensity is made by the soft mode in the state $|1; -1\rangle$. The shape of the β_1 line is smooth and symmetrical with respect to its center of gravity, which suggests that there is exchange coupling between the energy levels and that a quasi-equilibrium population distribution takes place. With an increase in annealing time (τ = 1 h), the β_1 peak shifts to the position of the K_{42} line, whose intensity is determined by the same soft mode as in the case of the

K_{22} line but in the state $|2; -1\rangle$. Thus, during annealing from $\tau = 0.5$ to 1 h, the observed shift of the β_1 peak and the redistribution of intensities of the K_{22} and K_{42} lines are caused by the soft-mode transition from the state $|1; -1\rangle$ to the state $|2; -1\rangle$. For the samples with $\tau = 1$–8 h, the β_1 line is asymmetrical (the Fano-like line profile is determined by interaction between a single excitation and a continuous background [12]), which can be interpreted as the result of partial charge carrier delocalization (metallization) and generation of free carriers. The fact that the line is broad and that the variation of its wings (peak β') is nonmonotonic for the samples annealed over time $\tau = 0.5$, 1, and 8 h gives evidence of nonuniform broadening of this line and possible rearrangement of the electronic structure.

Emphasis should be placed on the following discovered feature of the Fe$K_{\beta_1\beta'}$ spectra: the fine structure of the spectra is mobile, which manifests itself in a variation of the intensity ratios of multiplet lines with an increase in annealing time. Information on the variation in the population of the corresponding electronic states can be obtained not only from the fact that the spectrum broadens but also from the intensity redistribution over the lines (for example, K_{42}, K_{22}, K_{43}, K_{23}). Information on the electronic structure can be obtained from the energy position of individual lines of the spectrum. For example, the positions of the K_{34}, K_{14}, K_{44}, and K_{24} lines are determined by the energy of quantum transitions from the states with localized electrons in which the localization is due to indirect exchange via the intermediate soft-mode ${}_2Fe^{4+}(1/2)$ ion, whereas the positions of the K_{21} and K_{41} lines are determined by quantum transitions from the states with itinerant electrons in which the delocalization is due to exchange coupling via a ${}_4Fe^{2+}(1/2)$ ion. The distribution of itinerant electrons over the states (represented by the K_{21} and K_{41} lines) remains quasi-equilibrium during high-temperature annealing. The intensity of the K_{21} line is higher than that of the K_{41} line during annealing, $I(K_{21}) > I(K_{41})$; i.e., the difference in population between these states remains positive. However, the intensity of each line changes during annealing. In the low-energy group of lines during annealing over times $\tau = 0.5$, 2, and 8 h, we have $I(K_{14}) < I(K_{44})$ and $I(K_{34}) < I(K_{24})$, while for $\tau =$ 1 h, we have $I(K_{14}) > I(K_{44})$ and $I(K_{34}) > I(K_{24})$. Thus, an anomalous change in the intensity ratio is observed between the core lines K_{14} and K_{44} and between K_{34} and K_{24}. The difference in population between the localized electronic states corresponding to the K_{14} and K_{44} lines changes sign from minus (at $\tau = 0.5$ h) to plus (at $\tau =$ 1 h) and then again to minus (at $\tau = 2$ and 8 h). Similar behavior is observed for the states corresponding to the K_{34} and K_{24} lines. The position of the high-energy pair of lines K_{23} and K_{43} is determined by the energy of the quantum transition from a nonequilibrium metastable state with localized electrons where the localization is due to indirect exchange via an intermediate ${}_2Fe^{4+}(3/2)$ ion in the excited state with a quantum number $F = 3/2$. In this case, the difference in population between the localized electronic states corresponding to K_{23} and K_{43} remains negative during annealing. The position of the other high-energy pair of lines (K_{22}, K_{42}) is determined by the energy of the quantum transition from electronic states stabilized due to indirect exchange via an intermediate ${}_3Fe^{3+}(1)$ ion. The difference in population between the K_{22} and K_{42} states changes sign during annealing from plus at $\tau = 0.5$ and 2 h to minus at $\tau = 1$ and 8 h. This is evidence of rearrangement of the electronic structure during annealing and is a distinctive behavioral feature of the above-mentioned states.

Our theoretical and experimental data on the fine structure of the FeK_{β_1} line are consistent with the studied dependences of the integral parameters of peaks β_1 and β' on annealing time (Fig. 3). Figure 3a shows the experimental intensity of the β_1 and β' peaks plotted as a function of annealing time. The total intensity of these peaks was taken to be equal to 100 arbitrary units. The intensity of peak β_1 characterizes the distribution of the main group of electronic *d* states of iron ions in ferrite. Curves I_{β_1} and $I_{\beta'}$ vary only slightly for the samples annealed over $\tau = 0.5$, 2, and 8 h. However, for the sample annealed over $\tau = 1$ h, correlated variations in the electronic density of states are observed, which follows from the fact that a local maximum of intensity $I_{\beta'}$ and a local minimum of intensity I_{β_1} appear simultaneously. According to theoretical studies, the observed redistribution of the FeK_{β_1} and Fe$K_{\beta'}$ intensities is mainly due to the redistribution of population between the (K_{34}, K_{14}) and (K_{22}, K_{42}) states, which accompanies the rearrangement of the electronic structure. The increased intensity I_{β_1} for $\tau = 1$ h as compared to that for $\tau = 0.5$ h (Fig. 3a) is caused by the increase in population of the K_{34} and K_{24} states (Fig. 2).

Figure 3b shows the dependence of the asymmetry coefficient $\kappa = a/b$ of the FeK_{β_1} line on annealing time. This coefficient is determined as the ratio between the effective densities of states of itinerant electrons (high-energy region *a* of peak β_1) and localized electrons (low-energy region *b* of peak β_1). In the case where $\kappa \ll 1$, the contribution from ionic–covalent bonding is dominant and the electronic states are localized. In the opposite case of $\kappa \gg 1$, the bonds are metallic and there are free carriers in the material. In the intermediate case of $\kappa \approx 1$, the metallic and covalent bonds are equally significant and the itinerant and localized electronic states coexist in the structure. Therefore, the bonding can be switched from metallic to covalent and vice versa, which corresponds to the change in the sign of the parameter $\kappa - 1$ when the value $\kappa = 1$ is passed during annealing of a sample. Such variations in parameter

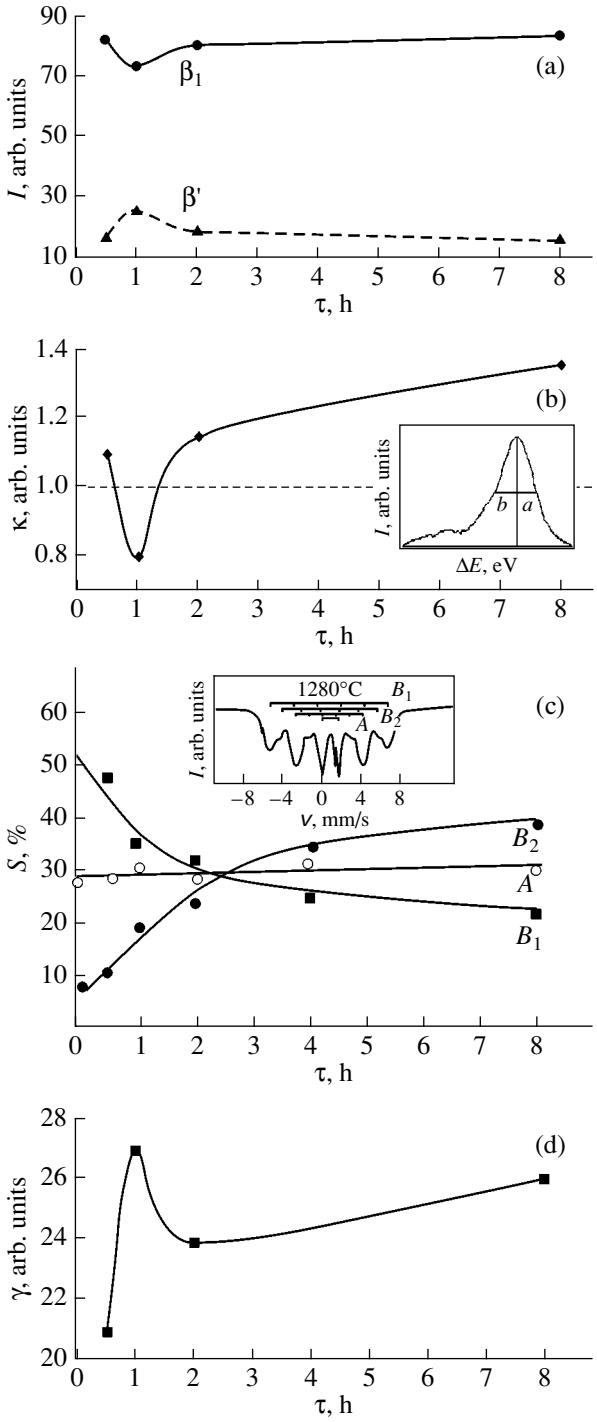

Fig. 3. Dependences of integral parameters of the β_1 and β' lines on the sample annealing time. (a) Intensities I_{β_1} and $I_{\beta'}$; (b) asymmetry coefficient $\kappa = a/b$ of the FeK_{β_1} line, where a and b are the half-widths of the β_1 line (inset exemplifies the determination of the parameters a and b from the x-ray spectrum for $\tau = 0.5$ h); (c) integrated intensities of the components of Mössbauer spectra (inset shows a Mössbauer spectrum); and (d) width $\gamma = a + b$ of the FeK_{β_1} spectral line.

κ are observed over the range from $\tau = 0.5$ to 2 h, with the parameter reaching a local minimum at $\tau = 1$ h. Additional arguments in favor of the change in the nature of bonding are the coincidence of the positions of the local extrema (at $\tau = 1$ h) observed in the time dependences of I_{β_1}, $I_{\beta'}$, κ, and γ (Figs. 3a, 3b, 3d) and the correlated variations in the integrated intensities I_{β_1} and $I_{\beta'}$ in the annealing time range indicated above (Fig. 3a).

As the annealing time increases from $\tau = 1$ to 8 h, the contribution from metallic bonding increases, which also manifests itself in an increased intensity of the high-energy states K_{21} and K_{41} (Fig. 2) and is consistent with the increased asymmetry coefficient κ (Fig. 3b).

5. MAGNETIC ORDERING FEATURES

In order to analyze the magnetic ordering [6], we studied the Mössbauer absorption γ spectra of ^{57}Fe in our samples. The spectra were obtained using ^{57}Co with an activity of 50 mCi in a chromium matrix as a source of γ rays. Figure 3c shows the dependence of the integrated intensities of the Mössbauer spectral components on annealing time for Mg–Zn ferrites. As is seen from Fig. 3c (curve *A*), during annealing at $T = 1280$°C, the integrated intensity S_A is almost constant as the annealing time increases from 0.5 h, which means that the concentration and ordering of magnetic Fe^{3+} ions in tetrahedral position *A* remain practically unchanged. However, the relative intensities S_{B1} and S_{B2} of sextets B_1 and B_2 change; these sextets are related to two nonequivalent octahedral positions, B_1 and B_2, of iron atoms in the magnetic structure of ferrite. The nonequivalence of these positions is due to the different nearest environments (consisting of magnetic ions) of the octahedral lattice sites. The intensity S_{B1} is determined by the concentration of magnetic Fe^{3+} ions in the B_1 position that are exchange-coupled to the 5 and 6 magnetic nearest neighbor atoms, and the intensity S_{B2} is determined by Fe^{3+} ions in the B_2 position that are exchange-coupled to the 3 and 4 magnetic nearest neighbor atoms [6]. If $\tau < 2$ h, we have $S_{B1} > S_{B2}$, while when $\tau > 2$ h, the inverse inequality $S_{B1} < S_{B2}$ is true. Consequently, as the point $\tau = 2$ h is passed, the magnetic long-range order ($S_{B1} > S_{B2}$) is replaced by magnetic short-range order ($S_{B2} > S_{B1}$).

It is known [13, 14] that a variation in the magnetic state of iron ions can cause a change in the spectral line width that is dependent on the spin–orbit coupling of *d*–*d* electrons: the stronger the coupling, the narrower the β_1 line. Therefore, it is interesting to compare the dependences of the magnetic parameters (Fig. 3c) and of the spectral line width (γ) of the main peak β_1 (Fig. 3d) on the annealing time. For example, at $\tau = 0.5$ h, there is magnetic order of iron ions (Fig. 3c) with characteristic deviations $S_{B1} - S_A \approx S_A - S_{B2}$ and the

spectral line width is minimum (Fig. 3d). At $\tau = 1$ h, the deviation $S_{B1} - S_A$ becomes smaller than $S_A - S_{B2}$ (i.e., the degree of disorder of the magnetic state increases), which is accompanied by an increase in the width of spectral line β_1 (the width reaches a maximum; Fig. 3d). At $\tau = 2$ h, the contributions from the intensities of sextets B_1 and B_2 become approximately equal to each other (Fig. 3c) and the spectral line width decreases in comparison with that at $\tau = 1$ h and reaches a local minimum (Fig. 3d). As the annealing time increases further to $\tau = 8$ h, the intensity of sextet B_2 becomes higher than that of B_1 (Fig. 3c) and the spectral line width increases monotonically (Fig. 3d). Thus, the most disordered magnetic state occurs at $\tau = 1$ h (Fig. 3c), where the spectral line width is maximum (Fig. 3d). In this case, the additional magnetic disordering appears before the subsequent magnetic phase transition (the change from the B_1 to B_2 magnetic quasiphase; Fig. 3c). A comparative analysis of all data (Figs. 1–3) shows that all the samples studied contain ferromagnetic domains with metallic electrical conductivity (Figs. 3b, 3c; lines K_{22} and K_{42} are sensitive to itinerant ferromagnetic ordering, Fig. 2) and antiferromagnetic domains with dielectric-type conductivity (Figs. 3b, 3c; lines K_{23} and K_{43} are sensitive to local antiferromagnetic ordering, Fig. 2). The volume ratio between these domains varies nonlinearly with annealing time (Figs. 3b, 3c). Ferromagnetic ordering is accompanied by metallization, whereas antiferromagnetic ordering is accompanied by localization of the electronic states.

6. CONCLUSIONS

Thus, it has been found that the fine structure of the FeK_β spectrum is determined by an additional chain of intermediate ions $_4Fe^{2+}(1/2)$, $_3Fe^{3+}(1)$, $_2Fe^{4+}(3/2)$, and $_2Fe^{4+}(1/2)$ (which differ in terms of their charge and magnetic state) via which indirect exchange coupling occurs between the $[_1O^- - _4Fe^{2+}]$ and $[_3O^- - _4Fe^{2+}]$ complexes.

During annealing of samples, there occurs a redistribution of populations between the electronic states involved in the formation of the Fe$K_{\beta_1\beta'}$ spectrum. This redistribution can cause the difference between the populations of certain states to change sign as the annealing time varies.

The samples studied contain domains with itinerant ferromagnetic ordering and metallic electrical conductivity and domains with antiferromagnetic ordering and dielectric-type conductivity.

Due to multilayer metallization, the fine structure of the Fe$K_{\beta_1\beta'}$ band in the x-ray emission spectra contains coexisting elements, some of which relate to the electronic structure with metallic coupling and others to ionic–covalent bonding. In this case, switching from metallic to covalent bonding and vice versa is observed during annealing.

REFERENCES

1. M. A. Blokhin and I. G. Shveĭtser, *Handbook of X-ray Spectroscopy* (Nauka, Moscow, 1982) [in Russian].
2. B. P. Ladgaonkar, P. N. Vasambekar, and A. S. Vaingankar, J. Magn. Magn. Mater. **210** (1–3), 289 (2000).
3. I. L. Dormann and M. I. Nogues, J. Phys.: Condens. Matter **2**, 1223 (1990).
4. Z. A. Samoĭlenko, N. N. Ivakhnenko, V. P. Pashchenko, O. V. Kopaev, B. K. Ostafiĭchuk, and I. M. Gasyuk, Zh. Tekh. Fiz. **72** (3), 83 (2002) [Tech. Phys. **47** (3), 364 (2002)].
5. Z. A. Samoĭlenko, V. P. Pashchenko, V. S. Abramov, and N. N. Ivakhnenko, Fiz. Tverd. Tela (St. Petersburg) **43** (8), 1496 (2001) [Phys. Solid State **43** (8), 1556 (2001)].
6. B. K. Ostafiychyk, J. V. Kopayev, and I. M. Gasyuk, Funct. Mater. **6** (4), 686 (1999).
7. Z. A. Samoĭlenko, V. S. Abramov, and N. N. Ivakhnenko, Pis'ma Zh. Éksp. Teor. Fiz. **72** (9), 679 (2000) [JETP Lett. **72** (9), 472 (2000)].
8. V. D. Okunev and Z. A. Samoĭlenko, Pis'ma Zh. Éksp. Teor. Fiz. **53**, 42 (1991) [JETP Lett. **53**, 44 (1991)].
9. V. S. Abramov and A. I. Linnik, Fiz. Tekh. Vys. Davleniĭ **8** (3), 90 (1998).
10. V. S. Abramov, V. P. Pashchenko, S. I. Khartsev, and O. P. Cherenkov, Funct. Mater. **6** (1), 64 (1999).
11. V. V. Nemoshkalenko and V. N. Uvarov, Metallofiz. Noveĭshie Tekhnol. **19** (3), 16 (1997).
12. Ch. Thomsen and M. Cardona, in *Physical Properties of High-Temperature Superconductors*, Ed. by D. I. Ginsberg (World Sci., Singapore, 1989; Mir, Moscow, 1990).
13. K. I. Narbutt, Izv. Akad. Nauk SSSR, Ser. Fiz. **40**, 355 (1976).
14. V. F. Demekhin, G. F. Lemeshko, and A. T. Shuvaev, Izv. Akad. Nauk SSSR, Ser. Fiz. **38**, 587 (1974).

Translated by E. Borisenko

Physics of the Solid State, Vol. 47, No. 10, 2005, pp. 1928–1936. From Fizika Tverdogo Tela, Vol. 47, No. 10, 2005, pp. 1852–1860.

MAGNETISM AND FERROELECTRICITY

The Lineshape of Inelastic Neutron Scattering in Relaxor Ferroelectrics[1]

M. A. Ivanov[1], M. Kozłowski[2], T. Piesiewicz[2], V. A. Stephanovich[3], A. Weron[4], and A. Wymysłowski[5]

[1] *Institute of Metal Physics, Ukrainian National Academy of Sciences, Kiev, Ukraine*
e-mail: ivanov@imp.kiev.ua

[2] *Institute of Power Systems Automation (IASE) and Laboratory for Interconnecting and Packaging Electronic Circuits, Wrocław University of Technology, Wrocław, Poland*
e-mail: Tomasz.Piesiewicz@pwr.wroc.pl

[3] *Opole University, Institute of Mathematics and Informatics, Opole, Poland*
e-mail: stef@math.uni.opole.pl

[4] *Hugo Steinhaus Center for Stochastic Methods, Wrocław University of Technology, Wrocław, Poland*
e-mail: weron@im.pwr.wroc.pl

[5] *Laboratory for Interconnecting and Packaging Electronic Circuits, Wrocław University of Technology, Wrocław, Poland*
e-mail: Artur.Wymyslowski@pwr.wroc.pl

Received November 4, 2004; in final form February 6, 2005

Abstract—We show that a microscopic reason for the steep drop of the optical phonon branch into an acoustic one (the so-called waterfall effect) in relaxor ferroelectrics may be the coupling of phonons with defects and impurities of different kinds, which is always present in relaxors. Namely, we do not specify the type of impurities but rather represent them as an ensemble of so-called two-level systems (TLS). This approach makes it possible to trace the evolution of the "waterfall" with temperature and the TLS concentration. To facilitate the planning of experiments on inelastic neutron scattering, we present a modification of the so-called Latin hypercube sampling method, which, based on some significance criteria, allows one to perform measurements that are highly significant for elucidating the physical nature of, e.g., phonon dispersion laws in relaxor ferroelectrics. © *2005 Pleiades Publishing, Inc.*

1. INTRODUCTION

The advantages of the neutron scattering method (as compared to, e.g., Raman spectroscopy) in the investigation of ferroelectrics and antiferroelectrics are well known [1, 2]. Since the wavelength of neutrons is equal (in order of magnitude) to the lattice constant of a solid and their energy and momentum are comparable to those of phonons, neutron scattering allows one to obtain information that is inaccessible with other (e.g., optical) methods. For instance, it is possible to obtain the dependence of the phonon energy on its momentum, known as its dispersion law. Inelastic neutron scattering makes it possible to obtain detailed information on the soft phonon mode (and actually any other phonon mode) dispersion throughout the entire Brillouin zone. Such investigations for the relaxor ferroelectric $PbMg_{1/3}Nb_{2/3}O_3$ have been performed, e.g., in [3]. It is also possible to study the thermal displacements of ions from their equilibrium positions in an elementary cell, also during a ferroelectric phase transition. Moreover, inelastic neutron scattering is free of the limitations imposed by optical selection rules.

Recently, much attention has been paid to the investigation of phonon dispersion in relaxor perovskites. The main peculiar (and puzzling) feature here is the so-called "waterfall effect" or very steep drop of the optic phonon branch into an acoustic one at some value q_{wf} of momentum transfer. This effect was first observed in [4], and q_{wf} was interpreted as a characteristic wave vector corresponding to the reciprocal size of so-called polar nanoclusters (in other words, short-range-ordered polar clusters), which prevent the optical phonons with $q < q_{wt}$ from propagating in a lattice.

In disordered ferroelectrics, the size of the above nanoclusters is defined by the so-called correlation radius. The latter quantity, being the characteristic length of the fluctuations of polarization, is a characteristic feature of any ferroelectric (antiferroelectric) substance (see, e.g., [5]). The correlation radius grows infinitely near the ferroelectric (antiferroelectric) phase transition temperature, knowledge of the soft mode dispersion law at different temperatures makes it possible to extract the temperature dependence of the correlation radius. Measurements of the correlation radius in the $PbMg_{1/3}Nb_{2/3}O_3$ (PMN) relaxor [6, 7] revealed a peculiar temperature dependence: a plateau at $T \le T_g$ (T_g is

[1] This article was submitted by the authors in English.

the freezing temperature of the dipole glass state) and another plateau at $T \geq 400$ K.

The waterfall effect was later observed in a number of relaxors [8] and described in terms of coupled optical and acoustic phonon branches in [9]. The authors of [9] based their explanation on a model suggested in an earlier work [10]. Their key assumption was a drastic increase in the damping of the "bare" (i.e., before coupling) optical phonon branch at $q \leq q_{wf}$. Another explanation of the waterfall effect was proposed in [11], which uses essentially the same approach as above (i.e., the mode coupling model) but does not attribute q_{wf} to the size of polar nanoclusters. In other words, the authors of [11] do not assume a sudden change in the optical mode damping at $q \leq q_{wf}$ but rather use a model of two coupled damped harmonic oscillators representing optic and acoustic branches. The coefficients of the corresponding bare dispersion laws, as well as of the damping, were taken phenomenologically from the best fit to experiments.

None of the above approaches takes into account the influence of the ensemble of defects and impurities (inherent to any disordered ferroelectric or relaxor in particular) on the phonon dispersion law. One of the aims of the present paper is to propose a formalism that permits this. The main physical idea is that impurities and defects of different kinds (for instance, impurity dipoles) interact with each other indirectly via one of the transversal optical phonon branches of a host dielectric. Due to this interaction, the above mode softens by itself (i.e., its frequency renormalized by the impurities becomes zero at some temperature and generally speaking wave vector q), so that the ferroelectric phase transition may occur. This mechanism has been shown to be the origin of ferroelectricity in incipient ferroelectrics [12]. The long wavelength dispersion of the soft phonon mode of this system was essentially renormalized by the impurities, as compared to the case of the host incipient ferroelectric. This renormalized dispersion law defines the width of the distribution function of random fields (created by the impurity ensemble [13]) that influences all observable physical quantities of disordered ferroelectrics. The static and dynamic properties of the disordered systems have been attributed to and expressed via the correlation radius of a host lattice (see, e.g., [5, 14, 15]). The host lattice is $KTaO_3$ in the case of $K_{1-x}Li_xTaO_3$ (KTL) [12] and is the Burns reference phase in the case of relaxor ferroelectrics [16].

The experimental investigations of relaxor ferroelectrics by inelastic neutron scattering are dependent on many parameters (see, e.g., [3, 6, 7]), such as temperature, the concentrations of different kinds of defects and impurities (sometimes called the degree of disorder), the vectors of the reciprocal lattice, etc. To draw the correct conclusions from anexperiment with such a multitude of factors, we need to know exactly which measurements (i.e., for which parameter values) give the most significant information for the system considered. An additional factor here is that neutron scattering experiments are quite costly and the required equipment can only be found in a very small number of laboratories. So, the best way to improve the effectiveness of neutron scattering experiments is to plan them in advance. Usually, planning for a multifactor experiment is performed using the so-called Latin hypercube sampling (LHS) method first introduced by McKay *et al.* [17]. In this method, the space of (n) experimental parameters is represented as n-dimensional Euclidean space, where the points correspond to each specific measurement performed with a certain set of the above parameters. In the standard LHS method, all the parameters are supposed to be of the same significance, so the number of possible experiments is too high to be performed in a reasonable time. Here, we present a modification of the LHS method, which, based on some significance criteria, makes it possible to perform measurements that are of great significance to elucidation of the physical nature of, e.g., phonon dispersion laws in relaxor ferroelectrics.

2. NEUTRON SCATTERING LINESHAPE OF A DISORDERED DIELECTRIC

It is well known (see, e.g., [2, 18]) that the differential cross section of neutron scattering is proportional to a Fourier image of the density–density correlation function:

$$S(\mathbf{K}, \omega) = \int \mathcal{P}(\mathbf{r}, t)\exp[i(\mathbf{K}\mathbf{r} - \omega t)]d^3r dt, \quad (1)$$

where

$$\mathcal{P}(\mathbf{r}, t) = \int \langle \rho(\mathbf{r}', 0)\rho(\mathbf{r}' + \mathbf{r}, t)\rangle d^3r. \quad (2)$$

Here, angular brackets indicate quantum-statistical averaging, $\hbar\mathbf{K}$ is a vector of a scattered neutron momentum, and $\hbar\omega = \hbar^2K^2/2m_k$ is its energy.

The scattering density $\rho(\mathbf{r}, t)$ can be expressed in the form

$$\rho(\mathbf{r}, t) = \sum_i b_i\delta(\mathbf{r} - \mathbf{r}_i(t)), \quad (3)$$

where b_i is the scattering length for the ith nucleus localized at the point

$$\mathbf{r}_i(t) = \mathbf{r}_{lk} + \mathbf{u}_{lk}(t), \quad (4)$$

where $\mathbf{r}_{lk}$ is the equilibrium position of the kth atom in the lth elementary cell and $\mathbf{u}_{lk}(t)$ is its displacement. If this displacement is due to lattice vibrations, we can expand it over the phonon normal coordinates in the following way:

$$\mathbf{u}_{lk}(t) = \left(\frac{\hbar}{2Nm_k}\right)^{1/2}\sum_{\mathbf{q}, j}\boldsymbol{\lambda}_{kj}(\mathbf{q})[Q_j(\mathbf{q}, t)\exp(i\mathbf{q}r_{lk}) + \text{c.c.}]. \quad (5)$$

Here, $Q_j(\mathbf{q}, t)$ is the normal coordinate of the phonon for the jth branch of the phonon spectrum, $\boldsymbol{\lambda}_{kj}$ is the polarization of the phonon, and $\mathbf{q}$ is its wave vector related (by virtue of the conservation of momentum) to the wave vector $\mathbf{K}$ of a scattered neutron

$$\mathbf{K} + \mathbf{q} = \boldsymbol{\tau},$$

where $\boldsymbol{\tau}$ is a reciprocal lattice vector. Note that, most often, the neutron scattering measurements in relaxors are performed for $\boldsymbol{\tau} = (2, 0, 0)$ and $(3, 0, 0)$ (see, e.g., [3, 8]). We will use this fact below for planning experiments by the LHS method.

The expression for $S(\mathbf{K}, \omega)$ assumes the following form with respect to relations (3)–(5):

$$S(\mathbf{K}, \omega) = N\sum_{\mathbf{q}j}|F_j(\mathbf{K})|^2\int\Phi(\mathbf{q}, t)\exp(i\omega t)dt, \quad (6)$$

where $F_j(\mathbf{K})$ is a structural factor of inelastic scattering and $\Phi(\mathbf{q}, t) = \langle Q_j(-\mathbf{q}, 0)Q_j(\mathbf{q}, t)\rangle$ is the phonon (of the jth branch) displacement correlation function.

Since the experimentally sensitive quantity is just the aforementioned correlator, we are not interested here in the precise form of $F_j(\mathbf{K})$. There are many ways to calculate the correlator. Here, in order to capture the waterfall effect, we will use the model of two coupled oscillators, which are the optical and acoustic modes. In this paper, in trying to keep everything as simple as possible, we assume that only the optical mode is coupled to the impurity ensemble and that this coupling is the source of its damping.

The fluctuation–dissipation theorem relates the function $S(\mathbf{K}, \omega) \equiv S(\mathbf{q}, \omega)$ to the imaginary part of the retarded phonon Green's function $\hat{G}(q, \omega)$, which in the case of two coupled oscillators will be a 2×2 matrix. More precisely,

$$S(q, \omega) = \frac{T}{\omega}\mathbf{F}(q)^*\mathrm{Im}[\hat{G}(q, \omega)]\mathbf{F}(q), \quad (7)$$

where $\mathbf{F}(q)$ is a structure factor,

$$\hat{G}^{-1}(1, \omega) = \begin{pmatrix} \omega^2 - \omega_{TA}^2 & \Delta \\ \Delta & \omega^2 - \omega_{TO}^2 - \Pi_1 - i\Pi_2 \end{pmatrix}, \quad (8)$$

and $\Pi^* = \Pi_1 + i\Pi_2$ is a self-energy, which we write in the customary form for the interaction of phonons with two-level systems (TLS) [19]; namely,

$$\Pi^* = \alpha_0\int_0^{\omega_m^2}\frac{P(\lambda)d\lambda}{\omega^2 + i\Gamma\omega - \lambda}. \quad (9)$$

Here, α_0 is a phonon-TLS coupling coefficient, Γ defines the damping of optical phonons due to their interaction with a TLS [23],[2] and $P(\lambda)$ is a TLS density of states. The value $\omega_m^2 = c\omega_D^2$ (ω_D is the Debye frequency) defines the width of the distribution function $P(\lambda)$ such that it is normalized by the condition

$$\int_0^{\omega_m^2} P(\lambda)d\lambda = c, \quad (10)$$

where $c = N_{TLS}/N$ is a dimensionless concentration of the TLS, defined as the ratio of the TLS number N_{TLS} to the host lattice particle number N, so that $0 < c < 1$. We take $P(\lambda)$ in a simple form,

$$P(\lambda) = \frac{c}{\ln 2}\frac{1}{\omega_m^2 + \lambda}. \quad (11)$$

To calculate the intensity $S(q, \omega)$, we should now evaluate integrals (9) with respect to (11) and substitute the dispersion laws for optical and acoustic phonons into inverse matrix (8). We take the dispersion laws in the long-wavelength limit

$$\begin{aligned} \omega_{TA}^2 &= s_0^2k^2, \\ \omega_{TO}^2 &= a(T - T_c) + bk^2, \end{aligned} \quad (12)$$

where we take $T_c \approx 400$ K from [3]. Now, integrals (9) can be easily evaluated. Their explicit form is quite cumbersome, so we do not give it here.

Specific calculations were performed for the following set of dimensionless variables:

$$\begin{aligned} y &= \frac{\omega}{\omega_D}, \quad y_{TA, TO} = \frac{\omega_{TA, TO}}{\omega_D}, \quad \tau = \frac{T}{T_c}, \\ \kappa &= \frac{aT_c}{\omega_D^2}, \quad q = \sqrt{\frac{b}{2}}\frac{k}{10\omega_D}, \quad s = \frac{10s_0\sqrt{2}}{\sqrt{b}}, \\ \alpha &= \frac{\alpha_0}{\omega_D^4}, \quad \gamma = \frac{\Gamma}{\omega_D}, \quad \delta = \frac{\Delta}{\omega_D^2}. \end{aligned} \quad (13)$$

Keeping in mind that in (12) $a(T - T_c) \propto 1/\chi$, χ is the dielectric susceptibility of a relaxor, it can be shown that $\kappa \sim 1$. Also, $s \sim 1$. We perform our specific calculations for the following set of values: $\alpha = 0.8$, $\kappa = 1$, $s = 2$, $\delta = 10q^2$, and $\gamma = 2$. The shape of the intensity profiles as functions of k and ω are qualitatively similar to those from [8]. The most interesting features are revealed in the dispersion curve $\omega(k)$ ($y(q)$ in dimensionless variables), which was obtained by the usual

[2] We do not consider here the imaginary part of Π^* (9) (namely, $\Pi^* = \alpha\int_0^{\omega_m^2}\frac{P(\lambda)d\lambda}{\omega^2 + i0 - \lambda}$ due to the Lifshitz tails of the density of states as it is much smaller then its intrinsic damping term.

procedure of taking the positions of maximum intensity (7) for several constant ω values.

The above curves $y(q)$ are reported in Fig. 1 for different temperatures. It is seen from Fig. 1 that, at temperatures close to T_c, the $y(q)$ curves rise almost vertically (with very small *s* shape) towards the corresponding (coupled with acoustic) optical branch. At higher temperatures, this jump is more *s*-shaped and at some temperature (around 1.61 in our case; see Fig. 1b) splits into two parts, one of them being close to the acoustic and the other to the optical mode. With a further increase in temperature, the acoustic part degenerates into a small segment, which disappears at $\tau \approx 1.71$. For higher temperatures, instead of the waterfall we have separate (although coupled by virtue of δ) acoustic and optical branches. It should be noted here that the parts of the *s*-shaped curves $y(q)$ where $dy/dq < 0$ correspond to the minimum of the corresponding constant energy curves. This means that two waterfalls (i.e., a sharp drop or increase in the corresponding dispersion curve) can be observed experimentally by increasing or decreasing the wave vector *q*. Possible experimental observation of such a waterfall hysteresis may be an argument in favor of the present model and, contrarily, absence of the effect would demonstrate that this feature is just an artifact. Note also that here we adjust the remaining parameters in such a way that the waterfall disappears around $T_0 \approx 1.6T_c = 640$ K, which corresponds to the Burns temperature for $PbMg_{1/3}Nb_{2/3}O_3$.

The above dispersion curves are also dependent on concentration. This dependence is shown in Fig. 2. It is seen that, while lowering the concentration, the waterfall behaves qualitatively similar to that while raising the temperature. Also, at very small concentrations, there are two distinct phonon branches without any waterfall effect. This is due to the simple fact that, at $c \longrightarrow 0$, $\Pi^* \equiv 0$, so there is no imaginary part in the matrix $\hat{G}$.

Curve *1* in Fig. 2 shows the curve $y(q)$ for different bare structural factors $F = (0.5, 0.5)$. It is seen that the position of the waterfall q_{wf} remains almost unchanged, while the *s* shape disappears. Our analysis shows that the *s* shape is regained at higher temperatures or at smaller concentrations, while q_{wf} will follow the corresponding value for $\mathbf{F} = (0.2, 0.8)$.

3. OPTIMIZATION OF PLANNING THE EXPERIMENT BY A MODIFIED LHS METHOD

To draw more specific conclusions about the vibrational spectra of relaxors, it is necessary to perform many experiments to extract reliable phonon dispersion curves from the above inelastic neutron scattering lineshapes. Here, we present a modified LHS method for planning such experiments.

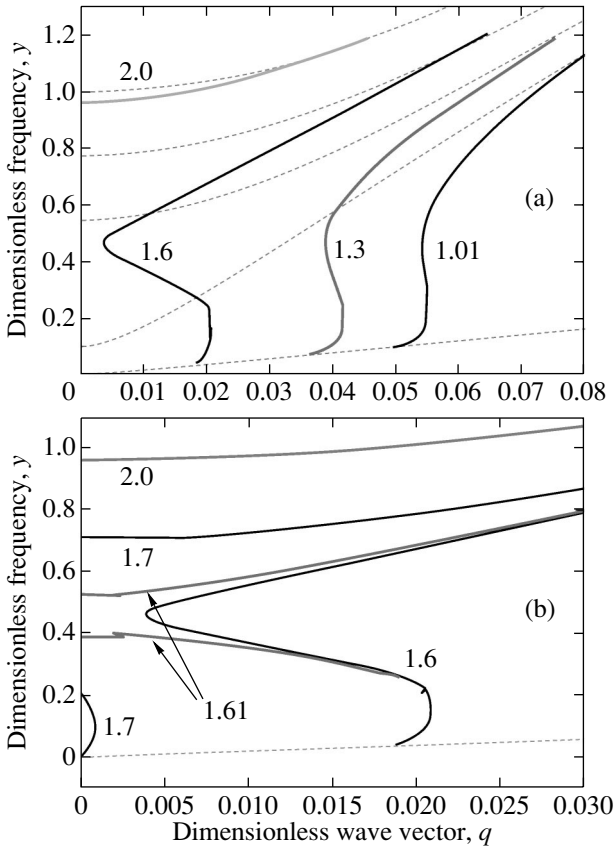

Fig. 1. Dispersion curves calculated for different temperatures (thick lines) for $\mathbf{F} = (0.2, 0.8)$ and $c > 0.4$. (a) General view for a larger temperature step and (b) detailed view showing the decay of the waterfall. Figures on the curves are values of the dimensionless temperature τ. Thin dashed lines correspond to the frequencies of coupled optical and acoustic modes for the corresponding temperatures.

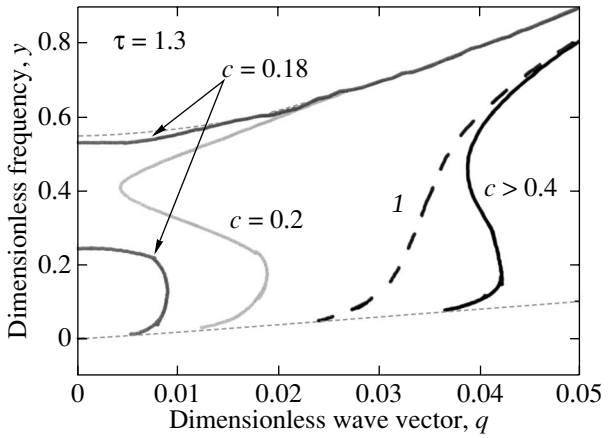

Fig. 2. Dispersion curves calculated for different *c*; $\tau = 1.3$ and $\mathbf{F} = (0.2, 0.8)$. Thin dashed lines are coupled optical and acoustic mode frequencies. Curve *1* corresponds to the same values (i.e., $c > 0.4$) and $\mathbf{F} = (0.5, 0.5)$.

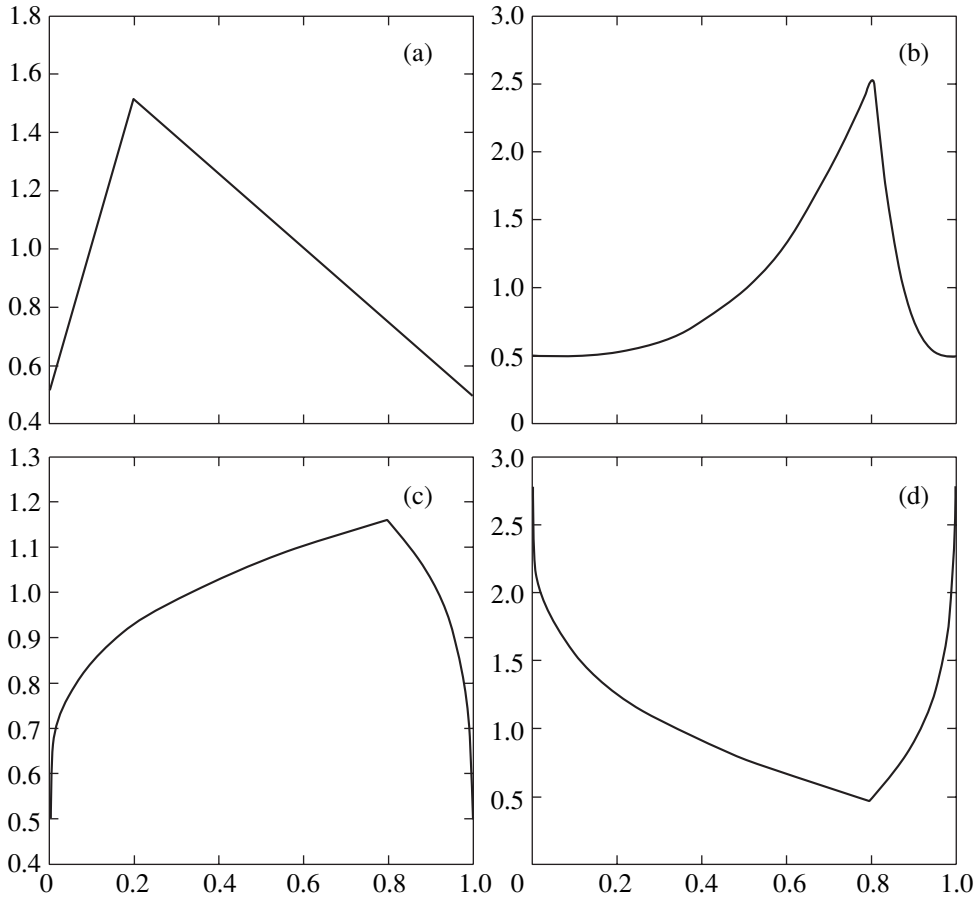

Fig. 3. Examples of the density function for various values of parameters *a*, *b*, and *p*: (a) $a = 0.2$, $b = 0.5$, and $p = 1$; (b) $a = 0.8$, $b = 0.5$, and $p = 3$; (c) $a = 0.8$, $b = 0.5$, and $p = 0.3$; (d) $a = 0.8$, $b = 2.8$, and $p = 0.3$.

In the LHS method (see, e.g., [17, 20–24]), the range of all *d* input variables (in our case, temperature, impurity concentrations, etc.) is divided into *n* intervals, with *n* being the number of sampling points. Each interval for each variable is randomly chosen only once with equal probability. A sampling point is chosen within each interval using the uniform probability density. This procedure prevents the formation of clusters of sampling points.

Formally, suppose that $x_{i,j}$ ($i = 1, \ldots, n$, $j = 1, \ldots, d$) is the *i*th value of the *j*th variable (i.e., experimental parameter), with *n* being the number of sampling points and *d* being the number of input variables. Let us define $p_{i,j}$ as the $n + d$ matrix, with each column being an independent random permutation of the set $(1\ldots n)$. Moreover, let $u_{i,j}$ be the $n + d$ values of the uniform [0, 1] independent random variables. The LHS points are defined as

$$x_{i,j} = \frac{1}{n}(p_{i,j} - u_{i,j}). \tag{14}$$

In this case, the points are well scattered and do not form clusters because observations are restricted within the respective interval. Moreover, it is possible to run the LHS procedure many times to maximize the minimal distance between two points in a generated sample.

Our modification of the LHS method is to apply probability density functions (PDF) to change the distribution of the parameters of the experiment. Suppose that $x_{i,j}$ is a standard Latin hypercube (LH) sample and $F_j(x)$ is a probability function (for the *j*th variable) corresponding to the probability density function (or distribution function) $f_j(x)$. We define the modified LH sample as

$$x_{i,j}^{\mathrm{mod}} = F_j^{-1}(x_{i,j}). \tag{15}$$

Our extensive numerical modeling of the LHS planning of experiments in different physical systems shows that very accurate adjustment of the experimental parameters can be accomplished by following the PDF of three parameters:

$$f(x) = \begin{cases} b + (1-b)(p+1)\left(\dfrac{x}{a}\right)^p, & x \in (0, a] \\ b + (1-b)(p+1)\left(\dfrac{1-x}{1-a}\right)^p, & x \in (a, 0), \end{cases} \tag{16}$$

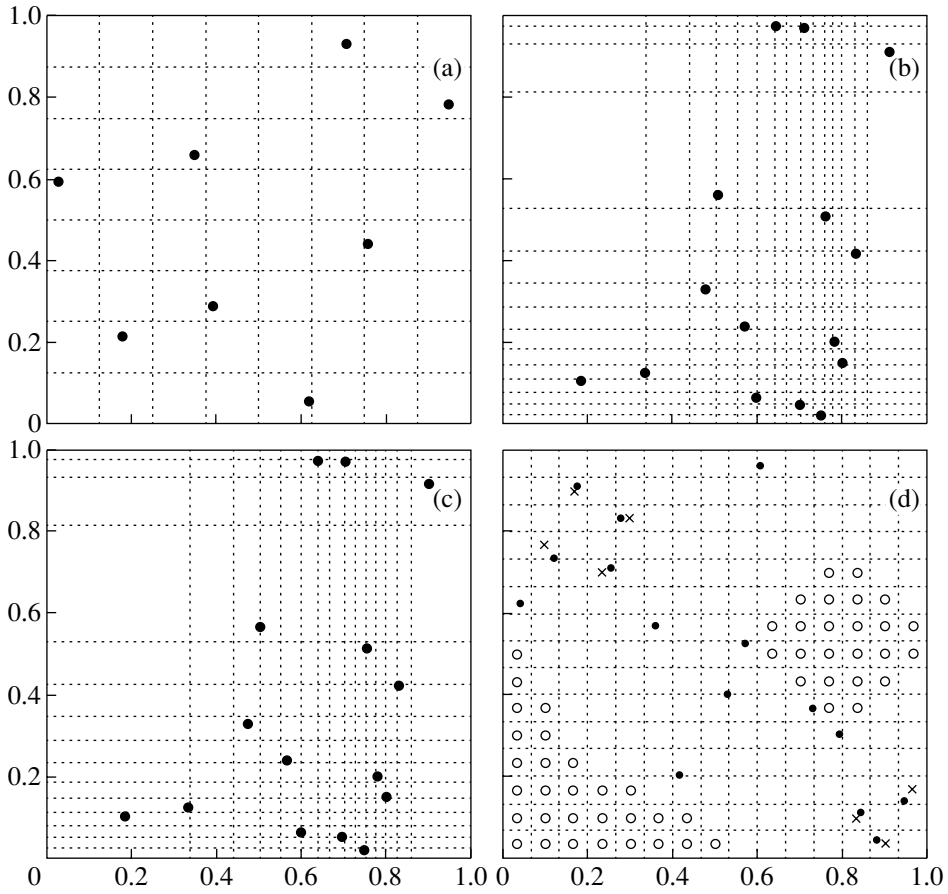

Fig. 4. Standard (a) and modified (b–d) LHS grids. For (a), $n = 8$ and $d = 2$, and for (b, c), $n = 15$, $d = 2$, and parameters a, b, and p are from Figs. 3b and 3d, respectively. Corresponds to the modified LHS grid with the expert matrix; the areas marked with crosses include sampling points and those marked with open circles are omitted in the sampling procedure.

where $a \in (0, 1)$ affects the position of the peak of function $f(x)$, $b \in [0, 1 + 1/p]$ affects the elevation of the peak, and $p \in [0, \infty)$ affects the strength of the curve. For $a = 0$ or $a = 1$, the $f(x)$ in Eq. (16) is undefined, so we have to use boundary PDF instead:

$$\begin{aligned} f(x) &= b + (1-b)(p+1)(1-x)^p, \quad a = 0, \\ f(x) &= b + (1-b)(p+1)x^p, \quad a = 1. \end{aligned} \tag{17}$$

For $b = 0.5$ and $p = 1$ (and any a), we have a standard triangle distribution. Increasing the parameter p causes a stronger concentration of PDF points in the area appointed by parameter a. Decreasing the parameter p weakens the concentration. If $b > 1$, we obtain the dispersion of PDF points rather then their concentration. For $b = 1$ or $p = 0$, Eq. (16) gives the standard uniform PDF in [0, 1], $f(x) = 1$. To visualize the above behavior of $f(x)$, we plot its shape for different parameter values in Fig. 3. Thus, adjusting the a, b, and p parameters allows us to modify the distribution of the points freely and therefore to include expert knowledge into the LHS method. Such knowledge in our case is, for example, the choice of the proper reciprocal lattice vector $\boldsymbol{\tau}$ (in [3], it is (3, 0, 0)) to clearly observe the soft mode. In particular, the authors of [3] have shown that observation of the soft phonon mode in PMN is much easier (as compared to previous results obtained in the Brillouin zone centered at (2, 0, 0)) in the [010] direction near the (3, 0, 0) reciprocal lattice vector.

The next modification we propose is to allow a researcher to indicate areas in which he/she wants to put a sampling point. On the other hand, it is possible to exclude certain areas from the sampling procedure. Including (excluding) areas is only allowed if there a possibility remains to generate a proper LH sample; e.g., it is forbidden to indicate more than one area in the same row or to exclude all columns. The information about all indicated areas is stored in a structure we call the expert matrix. After generating the LH sample (see Fig. 4), experiments should be performed to obtain the results. Then, the surface of the response parameters (response surface) is created by interpolating the results throughout the desired area. The surface is then used for further analysis, e.g., for optimization procedures.

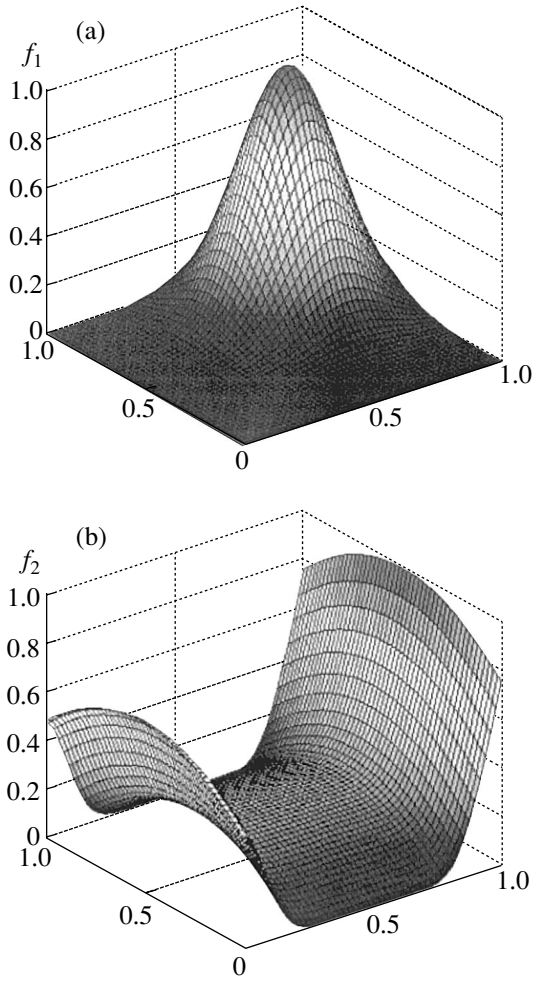

Fig. 5. Functions used in tests: (a) function f_1 with a single maximum and (b) function f_2 with two separate maxima.

Our comparison of the standard and modified LHS methods according to several criteria show that the modified LHS method substantially decreases the number of measurements necessary to achieve our goal. The latter method is especially useful when it is possible to take expert knowledge (see above) into consideration; see Appendix for details.

4. CONCLUSIONS

In the present paper, we have considered the possibilities of theoretical and experimental investigation of relaxor ferroelectrics by the inelastic neutron scattering method. We suggest a simple model which permits description of the peculiarities of inelastic neutron scattering lineshapes in ferroelectric relaxors. The essence of our model is to consider the interaction of the phonon subsystem of relaxor ferroelectrics with the ensemble of defects and impurities that are always present in such substances. This interaction has been taken into account in a quite general yet simple form without consideration of the detailed nature of defects and impurities. Our simple approach makes it possible to obtain temperature and concentrational dependences of the so-called waterfall effect, which recently has attracted much attention from scientists. Our dependences of the corresponding dispersion laws on temperature and the concentration of impurities are in qualitative agreement with available experimental data (see, e.g., [8, 9, 11]). Unfortunately, to make a more specific comparison, we need to take into account many additional factors, for instance, the acoustic phonon damping. Even in our simple model, the problem remains highly multiparametric; we have six model parameters in addition to temperature and concentration. A small variation of several of the above parameters may lead to very large differences in the behavior of the calculated $S(q, \omega)$. To have better parameters of our theory (such as κ, s_0, etc.), more experiments on relaxors aimed at obtaining, e.g., precise values of the coefficients in phonon dispersion laws need to be performed. Also, other complementary approaches can be used to calculate $S(q, \omega)$. One such approach is the so-called random field method, which has already been applied for calculation of the correlation radius in relaxors [5]. The latter calculation is also suitable for calculating the renormalized (by dipole impurities) dispersion law of the soft phonon mode in relaxors. Taking other types of impurities (such as elastic dipoles and point electric charges) into consideration will make it possible to estimate their partial contribution to the peculiarities of neutron scattering in relaxors, e.g., in the waterfall effect.

Also, we suggest that, to optimize (multifactor) experimental investigations into relaxor ferroelectrics by inelastic neutron scattering, one may use a modified Latin hypercube sampling method. The essence of this modification is the introduction of empirical PDF (16), which makes it possible to include the knowledge of an expert in the consideration.

We note finally that, to distinguish between different microscopic physical mechanisms leading to the appearance of peculiarities in neutron scattering in relaxors, such as the waterfall effect discussed above, experiments elucidating the specific features of a certain theoretical model (such as the presence or absence of *s* shape on the waterfall curve) would be highly desirable.

APPENDIX

In this paragraph, we will compare the standard and modified LHS methods according to several criteria. At first, we will generate a standard LH sample and a modified LH sample 10, 15, 20, 25, 30, 35, and 40 points in size. To properly count the errors of the response surface adjustment, we will take for our results an analytical function with a single extreme (f_1; see Fig. 5a) and, in the second case, a function with two separate max-

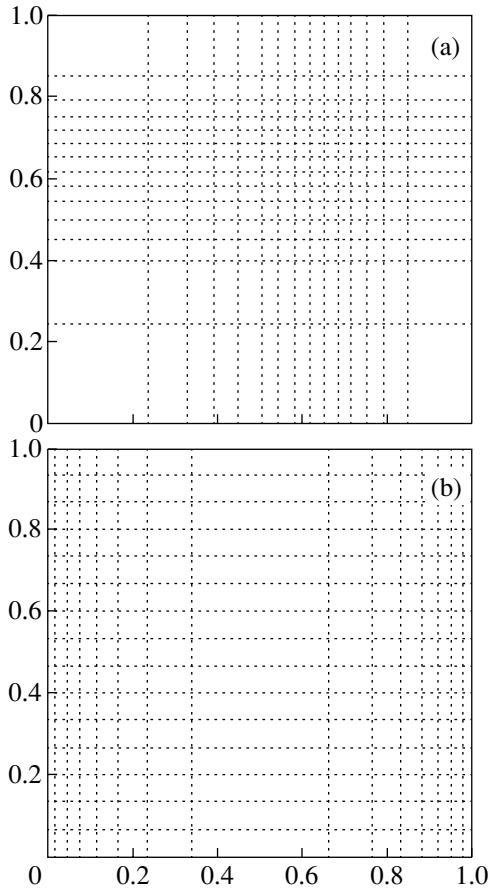

Fig. 6. Modified LHS design for (a) function f_1 and (b) function f_2.

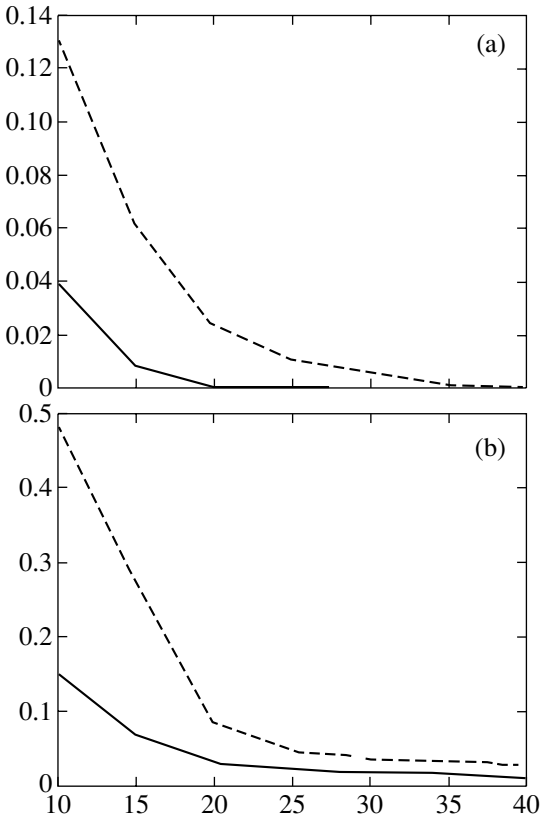

Fig. 7. Err$_d$ of standard (dashed) and modified (solid) LHS for (a) function f_1 and (b) function f_2.

ima located on the boundaries, with one of them being a bit higher than the other (f_2; see Fig. 5b).

As a response surface model, we will apply the widely used rigging interpolation method [25]. Then, we will compare the obtained surfaces according to the "hitting the target" criteria (i.e., the distance between the maximum of the function we are modeling and the maximum of the evaluated surface)

$$\mathrm{Err}_d = \sqrt{(x_1^{\max} - \hat{x}_1^{\max})^2 + (x_2^{\max} - \hat{x}_2^{\max})^2} \qquad \text{(A1)}$$

and the total mean square error of the surface adjustment

$$\mathrm{Err}_{\mathrm{MSE}} = \frac{1}{N^2}\sum_{i,j=1}^{N} (f(x_1^i, x_2^j) - \hat{f}(x_1^i, x_2^j))^2. \qquad \text{(A2)}$$

Considering the random character of the LHS design, we will repeat every experiment 100 times and take the average values of the calculated criteria as a result.

To simulate the knowledge of an expert suspecting nonlinearity in certain areas, we will modify the distribution of the LH sample points as shown in Fig. 6.

Criterion 1: Hitting the Target

This is a frequently encountered goal for experiments. Especially when dealing with optimization, it is required that the extremum of the function be properly indicated. In our experiment, we will focus on finding the location of the maxima of the test functions. As a measure, we will take the distance between the locations of real and evaluated maxima. As we can see in Fig. 7, the error of finding the maximum is significantly smaller (for both analyzed functions) if we use the modified LHS. Of course, it also decreases when we enlarge the size of the sample. Even so, it is higher for the standard LHS.

Criterion 2: Mean Square Error

In this case, we will focus on the overall adjustment of the response surface. The measure will now be the mean square error. For function f_1 (single maximum), we observe better adjustment of the response surface when using the modified LHS (see Fig. 8). On the other

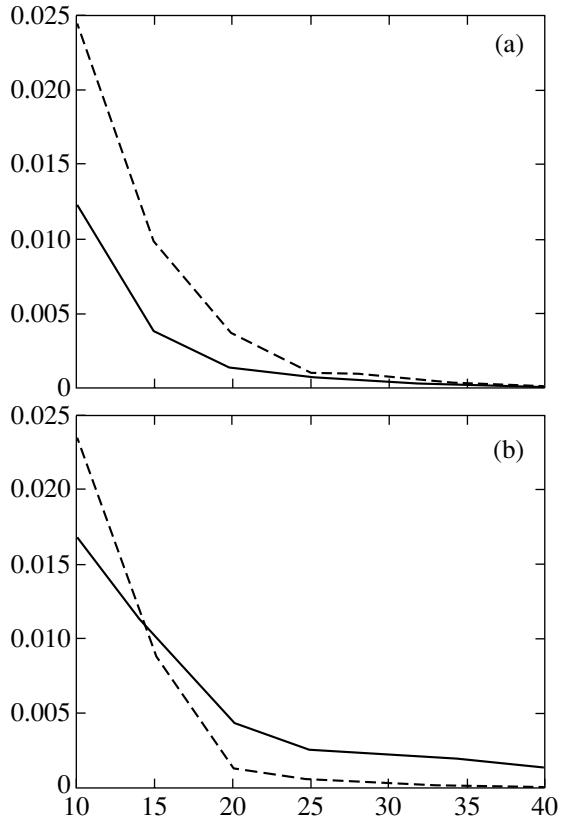

Fig. 8. $\mathrm{Err}_{\mathrm{MSE}}$ of standard (dashed) and modified (solid) LHS for (a) function f_1 and for (b) function f_2.

hand, the surface obtained when using the standard LHS is significantly better for function f_2. The reason is that striving for the better adjustment near the maxima of f_2 caused worse fitting in the area between.

ACKNOWLEDGMENTS

We are indebted to Bozena Hilczer for critical reading of the manuscript and attention to the work and to S. Vakhrushev for many helpful remarks.

This work was partially supported by the European Community 5th Framework Programme (MEVIPRO Project).

REFERENCES

1. V. G. Vaks, *Introduction to the Microscopic Theory of Ferroelectrics* (Nauka, Moscow, 1973) [in Russian].
2. R. Blinc and B. Zeks, *Soft Modes in Ferroelectrics and Antiferroelectrics* (Elsevier, New York, 1974).
3. S. B. Vakhrushev and S. M. Shapiro, Phys. Rev. B: Condens. Matter **66**, 214 101 (2002).
4. P. M. Gehring, S. E. Park, and G. Shirane, Phys. Rev. Lett. **84**, 5216 (2000).
5. M. D. Glinchuk, V. A. Stephanovich, E. A. Eliseev, E. V. Kirichenko, and L. Jastrabik, Appl. Phys. Lett. **80**, 646 (2002).
6. D. Viehland, J. F. Li, S. J. Jang, and L. E. Cross, Phys. Rev. B: Condens. Matter **43**, 8316 (1991).
7. E. V. Colla, E. Yu. Koroleva, N. M. Okuneva, and S. B. Vakhrushev, J. Phys.: Condens. Matter **4**, 3671 (1992).
8. P. M. Gehring, S. Wakimoto, Z.-G. Ye, and G. Shirane, Phys. Rev. Lett. **87**, 277601 (2001); D. La-Orauttapong, B. Noheda, Z.-G. Ye, P. M. Gehring, J. Toulouse, D. E. Cox, and G. Shirane, Phys. Rev. B: Condens. Matter **65**, 144101 (2002); S. Wakimoto, C. Stock, Z.-G. Ye, W. Chen, P. M. Gehring, and G. Shirane, Phys. Rev. B: Condens. Matter **66**, 224102 (2002).
9. P. M. Gehring, S. E. Park, and G. Shirane, Phys. Rev. B: Condens. Matter **63**, 224109 (2001).
10. J. Harada, J. D. Axe, and G. Shirane, Phys. Rev. B: Solid State **4**, 155 (1971).
11. J. Hlinka, S. Kamba, J. Petzelt, J. Kulda, C. A. Randall, and S. J. Zhang, Phys. Rev. Lett. **91**, 107 602 (2003); J. Phys.: Condens. Matter **15**, 4249 (2003).
12. B. E. Vugmeister and M. D. Glinchuk, Rev. Mod. Phys. **62**, 993 (1990).
13. M. D. Glinchuk and V. A. Stephanovich, J. Phys.: Condens. Matter **6**, 6317 (1994).
14. M. D. Glinchuk and V. A. Stephanovich, J. Phys.: Condens. Matter **10**, 11081 (1998).
15. M. D. Glinchuk and V. A. Stephanovich, J. Appl. Phys. **85**, 1722 (1999).
16. M. D. Glinchuk and R. Farhi, J. Phys.: Condens. Matter **8**, 6985 (1996).
17. M. D. McKay, R. J. Bechman, and W. J. Conover, Technometrics **21**, 239 (1979).
18. Ch. Kittel, *Quantum Theory of Solids*, 2nd ed. (Wiley, New York, 1987).
19. P. W. Anderson, B. I. Halperin, and C. M. Varma, Philos. Mag. **25**, 1 (1972).
20. R. L. Iman and W. J. Conover, Commun. Stat. Theory Methods A **9**, 1749 (1980).
21. J. Sachs, S. B. Schiller, and W. J. Welch, Technometrics **31**, 41 (1989).
22. B. Tang, J. Am. Stat. Assoc. **88**, 1392 (1993).
23. J. S. Park, J. Stat. Plan. Infer. **90**, 145 (1994).
24. K. Q. Ye, W. Li, and A. Sudianto, J. Stat. Plan. Infer. **90**, 145 (2000).
25. Noel A. C. Cressie, *Statistics for Spatial Data* (Wiley, New York, 1993).

Physics of the Solid State, Vol. 47, No. 10, 2005, pp. 1937–1943. Translated from Fizika Tverdogo Tela, Vol. 47, No. 10, 2005, pp. 1861–1866.

LATTICE DYNAMICS AND PHASE TRANSITIONS

Theory of Vibrational Excitations in a Solid Solution with the Inclusion of Their Scattering by Multi-Impurity Clusters

V. S. Vinogradov

Lebedev Institute of Physics, Russian Academy of Sciences, Leninskiĭ pr. 53, Moscow, 119921 Russia
e-mail: vvs@sci.lebedev.ru

Received November 10, 2004

Abstract—A theory of vibrational excitations in a solid solution is proposed. This theory allows for scattering of excitations by multi-impurity clusters and offers an adequate description of the complex spectra of the solid solution. The main feature of the theory is that the averaging and the Fourier transformation with respect to the coordinate of the impurity cluster as a whole are performed at the first stage, whereas the averaging over the distances between impurities in the cluster is carried out at the final stage. The calculations are performed in the approximation similar to the average *t*-matrix approximation and also the coherent-potential approximation. The theory is illustrated by calculating the spectra and dielectric functions of disordered linear chains with one and two atoms per unit cell. The calculated vibrational spectra are in good agreement with the computer calculations performed by Dean. © *2005 Pleiades Publishing, Inc.*

1. Description of the properties of elementary excitations (electrons, excitons, magnons, phonons) in a disordered medium still remains an important problem that has no satisfactory solution. The main obstacle to solving this problem is the difficulty associated with the correct inclusion of excitation scattering by multi-impurity complexes (clusters). This scattering has been described by different methods; however, none of them has led to results that are free of drawbacks. The method of a cluster embedded in an effective medium has been used in many studies (see the reviews [1, 2]). Spectra calculated with this method reflect a complex irregular structure of materials but in a very approximate fashion. The disagreement can be explained by the fact that the method breaks the symmetry of the initial lattice. Moreover, some variants of the cluster method lead to a nonanalytic frequency dependence of the spatially averaged Green's function. The traveling-cluster approximation in combination with the augmented space formalism used by Mills and Ratanavararaksa [3] and Kaplan *et al.* [4] is free of the above drawbacks. However, this approach does not give a clear and unique recipe for choosing summed diagrams [2]. Furthermore, the approach is extremely complicated for applications and has been used only for a cluster composed of a pair of nearest neighbor impurities. Jarrell and Krishnamurthy [5] used the dynamical cluster approximation. This method is more likely numerical than analytical. When calculating integrals over the Brillouin zone with this method, the zone is divided into cells and the wave vectors connecting points of different cells are replaced by wave vectors joining their centers. In the method, there are limitations imposed on the cluster symmetry. This symmetry must be in a certain correspondence with the symmetry of the Brillouin zone. The spectra calculated in the dynamical cluster approximation contain a larger number of features than those obtained in the traditional coherent-potential approximation CPA-1 (which accounts self-consistently for multiple excitation scattering by a single-impurity cluster). This was demonstrated for the case of a high impurity concentration $x = 0.5$. Unfortunately, spectra at low concentrations x, when fluctuations in the impurity distribution are significant and the spectra are the most irregular, are not reported in [5]. A comparison of these spectra with the spectra constructed using computer simulation would make it possible to elucidate how different approximations of the method affect its ability to reproduce fine spectral features.

The diagram technique is most attractive because it is illustrative, provides a means for properly evaluating and choosing diagrams, and allows one to generalize the results obtained. The relationships of the coherent-potential approximation [1, 2], which have found wide application, were derived with the diagram technique. However, when this technique was applied to clusters containing two or more impurities [6, 7], the expressions derived for the Green's function averaged over the impurity distribution were characterized by a nonanalytic frequency dependence [8]. This led to ambiguity, negative densities of states, and other nonphysical relationships for physical quantities. All these problems were described in detail in the reviews [1, 2]. As will be shown below, the above difficulties can be resolved by applying other approaches than those used in the previous works when averaging and taking the Fourier trans-

1063-7834/05/4710-1937$26.00

form of equations. This can be illustrated using the example of the simplest two-impurity cluster. First, the terms (diagrams) responsible for the scattering of excitations (for example, phonons) by an impurity pair are chosen in a perturbation series for the Green's function. Then, the terms of the series are averaged and rearranged with the aim of renormalizing the interaction and including the multiple-occupancy corrections. Finally, the Fourier transform is taken in order to obtain solvable equations. This transformation, as a rule, is performed with respect to the coordinate $\mathbf{R}_{ij}$, which is the distance between the ith and jth components of the pair. As a result, the derived equations possess the aforementioned drawbacks. Instead, we fix the distance between the components of the pair $\mathbf{R}_{ij} = \mathbf{R}_{i'j'} = \ldots$ and carry out the averaging and Fourier transformation with respect to the distance between different pairs $\mathbf{R}_{ii'}$ or, what is the same, the coordinate specifying the position of the cluster as a whole. This procedure takes into account the strongest resonant interactions between vibrational modes of distant identical clusters. The interaction of pairs with different coordinates $\mathbf{R}_{ij}$ in the approximation including only pair clusters is ignored because the averaging performed over the coordinate $\mathbf{R}_{ij}$ at the final stage of the calculations is an additive procedure. However, this weaker interaction can also be taken into account upon changing over to clusters consisting of a larger number of impurities. For example, a cluster formed by four impurities can be treated as a cluster composed of two pairs, in particular, with different coordinates $\mathbf{R}_{ij}$. An increase in the number of impurities in the clusters leads to rapidly convergent results, at least in the case of strong perturbations when there arise localized states. As follows from the computer calculations carried out by Dean [9], it is sufficient to take into account clusters consisting of five impurities.

The described procedure can be used in both the non-self-consistent and self-consistent approximations.

2. Specific calculations will be performed with a model of the crystal lattice. It is assumed that the replacement of a host atom by an impurity leads only to a change in the mass by Δm. The effect of this perturbation depends on the frequency ω. The appropriate relationships are conveniently transformed into a form that is independent of frequency. Then, the results obtained can be easily extended to electronic systems. For this purpose, we use the transformation proposed in [10].

The equation for lattice vibrations in the matrix form can be written as

$$CW = \omega^2[I + \delta\chi]W. \tag{1}$$

Here, W is the lattice displacement vector; $C \equiv C_{\alpha\beta}\begin{pmatrix} l & l' \\ k & k' \end{pmatrix}$ is the dynamic matrix for which the eigenvalue is represented by the square of the frequency $\omega_j(\mathbf{y})^2$ of lattice vibrations with the wave vector $\mathbf{y}$ and the jth branch; the index l characterizes the position of the unit cell; the index k characterizes the position of the atom in the unit cell; $\alpha, \beta = x, y, z$ stand for the displacement projections on the coordinate axes; I is the unit matrix; $\delta = \Delta m_{k_0}/m_{k_0}$ is the relative change in the mass of the k_0 atom upon substitution; $\chi \equiv \delta_{\alpha\beta}\delta_{ll'}\delta_{kk'}\delta_{kk_0}\eta(l)$; and $\eta(l) = 1$ and 0 in the presence and absence of the impurity in the lth cell, respectively.

Let us apply the operator $[I + \delta\chi]^{-1}$ to Eq. (1). Owing to the property $\chi^2 = \chi$, this operator is equal to $I - \Delta\chi$, where $\Delta = \delta/(1 + \delta)$. As a result, we obtain $[C - \omega^2 I]W = \Delta\chi CW$. The equation for the Green's function has the form

$$LG^{(0)} = I\Delta\chi CG^{(0)} + I, \tag{2}$$

where $L = C - \omega^2 I$. By applying the operator L^{-1} to Eq. (2), we find

$$G^{(0)} = g + g\Delta\chi CG^{(0)}, \tag{3}$$

where the Green's function g for the lattice without impurities obeys the equation $Lg = I$. Finally, we apply the operator C to Eq. (3) and obtain the basic equation

$$F = f + f\Delta\chi F, \tag{4}$$

where $f = Cg$ and $F = CG^{(0)}$. In the explicit form, we have

$$f_{\alpha\beta}\begin{pmatrix} l & l' \\ k & k' \end{pmatrix} = N^{-1}\sum_{\mathbf{y}j} w_\alpha\left(k\middle|\begin{matrix}\mathbf{y}\\ j\end{matrix}\right) w_\beta\left(k'\middle|\begin{matrix}\mathbf{y}\\ j\end{matrix}\right)^* \times f_j(\mathbf{y})\exp\left(2\pi i\mathbf{y}\mathbf{x}\begin{pmatrix} l & l' \\ k & k' \end{pmatrix}\right), \tag{5}$$

where $f_j(\mathbf{y}) = \omega_j(\mathbf{y})^2/[\omega_j(\mathbf{y})^2 - \omega^2]$, $w_\alpha\left(k\middle|\begin{matrix}\mathbf{y}\\ j\end{matrix}\right)$ are the eigenvectors satisfying the conditions

$$\sum_j w_\alpha\left(k\middle|\begin{matrix}\mathbf{y}\\ j\end{matrix}\right) w_\beta\left(k'\middle|\begin{matrix}\mathbf{y}\\ j\end{matrix}\right)^* = \delta_{\alpha\beta}\delta_{kk'},$$

$$\sum_{\alpha\beta} w_\alpha\left(k\middle|\begin{matrix}\mathbf{y}\\ j\end{matrix}\right) w_\alpha\left(k'\middle|\begin{matrix}\mathbf{y}\\ j'\end{matrix}\right)^* = \delta_{jj'},$$

and N is the number of unit cells in the periodically repeating volume. The expression for $g_{\alpha\beta}\begin{pmatrix} l & l' \\ k & k' \end{pmatrix}$ differs from the relationship for $f_{\alpha\beta}\begin{pmatrix} l & l' \\ k & k' \end{pmatrix}$ in that the quantity $\omega_j(\mathbf{y})^2$ is absent in the numerator of the summed expression.

The calculation of the permittivity requires knowledge of the Green's function G that obeys the equation $(L - \omega^2\delta\chi)G = I$ with the perturbation dependent on frequency. By using this equation, Eq. (2), and the properties of the operator χ, we find that the Green's functions G and $G^{(0)}$ are related by the expression

$$G = G^{(0)} - \Delta G^{(0)}\chi. \tag{6}$$

3. Let us now perform the iterations of Eq. (4) and change the type of summation over intermediate indices in the series obtained. We consider a cluster consisting of n unit cells of arbitrary shape and size in which impurities can be located at the k_0th site in the unit cell. Instead of the index l, each cell is numbered by the pair of indices (i, μ), where the index i characterizes the position of the cluster as a whole and the index μ characterizes the position of the cell in the cluster. It is also assumed that the origin of the coordinates of the ith cluster can be located at any lattice cell. In this case, upon summation over the index i, the number of cells corresponding to the cluster in the lattice appears to be n times larger than the number of cells existing in the lattice. In order to avoid error associated with multiple counting, each sum over the index i is multiplied by the factor $1/n$. Then, in the series for F, we choose and sum all the terms associated with the given cluster. As a result, we obtain

$$\begin{aligned} F\begin{pmatrix} l & l' \\ k & k' \end{pmatrix} &= f\begin{pmatrix} l & l' \\ k & k' \end{pmatrix} + n^{-1}\sum_i \bar{f}\begin{pmatrix} l \\ k \end{pmatrix} i\Big)\dot{t}(i)\,\bar{f}\Big(i\Big|\begin{matrix} l' \\ k' \end{matrix}\Big) \\ &+ n^{-2}\sum_{ij} \bar{f}\begin{pmatrix} l \\ k \end{pmatrix} i\Big)\dot{t}(i)\,\bar{f}'(ij)\dot{t}(j)\,\bar{f}\Big(j\Big|\begin{matrix} l' \\ k' \end{matrix}\Big) + \ldots. \end{aligned} \tag{7}$$

The bars over symbols indicate the rows, columns, and matrices in the cluster space. Specifically,

$$\bar{f}\begin{pmatrix} l \\ k \end{pmatrix} i\Big) \equiv f\begin{pmatrix} l \\ k \end{pmatrix} i\mu\Big), \quad \bar{f}\Big(i\Big|\begin{matrix} l' \\ k' \end{matrix}\Big) \equiv \Big(i\mu\Big|\begin{matrix} l' \\ k' \end{matrix}\Big)$$

are the row and column containing n elements ($\mu = 1, 2, \ldots, n$) and $\dot{t}(i) \equiv \Delta\bar{I}_\eta[\bar{I} - \Delta\bar{f}_\eta(ii)]^{-1}$, where $\bar{I} \equiv I\delta_{\mu\mu'}$, $\bar{I}_\eta(i) \equiv I\eta(i\mu)\delta_{\mu\mu'}$, and I is the diagonal matrix in the space of polarization indices. In particular, for a three-dimensional lattice, we have $I = \delta_{\alpha\beta}$; $\alpha, \beta = x, y, z$; $\bar{f}_\eta(ii) \equiv f(i\mu|i\mu')\eta(i\mu)\eta(i\mu')$; $\bar{f}(ij) \equiv f(i\mu|j\mu')$ ($\mu, \mu' = 1, 2, \ldots, n$); and $\bar{f}'(ij) = \bar{f}(ij)(1 - n\delta_{ij})$. In the space of dimensions $d = 2$ and 3, each matrix element of the type $f(i\mu|j\mu')$, in turn, is a matrix in the space of the polarization indices $f(i\mu|j\mu') \equiv f_{\alpha\beta}(i\mu|j\mu')$. In the above relationships, we omit the index characterizing the atomic position in the cell, because it is identical and equal to k_0. The factor $1 - n\delta_{ij}$ in the matrix $\bar{f}'(ij)$ forbids the repeated scattering by the ith cluster since it is completely included in the matrix $\dot{t}(i)$. The coefficient n appears in front of the δ function as this function removes one summation over the cluster coordinate. The matrix $\dot{t}(i)$ in relationship (7) describes the multiple scattering of the excitation by the ith cluster, and the matrix $\bar{f}'(ij)$ characterizes the translation of the excitation from the ith cluster to the jth cluster.

Let us average series (7) over the impurity distribution. The average of the product of the scattering matrices can be represented in the form

$$\langle\dot{t}(i)\dot{t}(j)\ldots\dot{t}(k)\rangle \cong \langle\dot{t}(i)\rangle\langle\dot{t}(j)\rangle\ldots\langle\dot{t}(k)\rangle.$$

The above approximation, which referred to as the average t-matrix approximation, provides the possibility of summing series (7). In the diagram method, this approximation corresponds to the rejection of diagrams of scattering by clusters containing more than n impurities and diagrams describing the "dressing" of the zero-order Green's function $f_{\alpha\beta}\begin{pmatrix} l & l' \\ k_0 & k_0 \end{pmatrix}$. These terms (diagrams) arise, for example, in the initial average when the indices of nonneighboring matrices $\dot{t}(i)$ coincide with each other, e.g., when $i = k$. The average of $\dot{t}(i)$ over the impurity distribution, $\bar{\tau} = \langle\dot{t}(i)\rangle$, is calculated from the formula

$$\begin{aligned} \bar{\tau} = &\sum_{\eta(i1)=0,1}\sum_{\eta(i2)=0,1} \\ \ldots &\sum_{\eta(in)=0,1} (1-x)^n[x/(1-x)]^{(\eta(i1)+\eta(i2)+\ldots+\eta(in))}\dot{t}(i), \end{aligned} \tag{8}$$

where x is the fraction of impurity atoms in the lattice ($0 \le x \le 1$).

By taking the Fourier transform of the averaged series (7)

$$\begin{aligned} &\left\langle F\begin{pmatrix} \mathbf{y} \\ k & k' \end{pmatrix}\right\rangle \\ &= \sum_{l-l'}\left\langle F\begin{pmatrix} l & l' \\ k & k' \end{pmatrix}\right\rangle \exp\left[-2\pi i\mathbf{y}\mathbf{x}\begin{pmatrix} l & l' \\ k & k' \end{pmatrix}\right], \end{aligned} \tag{9}$$

we obtain

$$\begin{aligned} \left\langle \bar{F}\begin{pmatrix} \mathbf{y} \\ k & k' \end{pmatrix}\right\rangle &= \bar{f}\begin{pmatrix} \mathbf{y} \\ k & k' \end{pmatrix} \\ &+ \bar{f}\begin{pmatrix} \mathbf{y} \\ k & k_0 \end{pmatrix}\bar{T}(\mathbf{y})\,\bar{f}\begin{pmatrix} \mathbf{y} \\ k_0 & k' \end{pmatrix}. \end{aligned} \tag{10}$$

Here,

$$\bar{T}(\mathbf{y}) = n^{-1}[\bar{\tau}_\phi^{-1} - n^{-1}\bar{f}'_\phi]^{-1}, \tag{11}$$

$\bar{f}_\phi' = f\left(\begin{array}{cc}\mathbf{y} & \\ k_0 & k_0\end{array}\right)\bar{E} - n\bar{f}_\phi(ii)$, $\bar{E}$ is an n-by-n matrix composed of identical elements I, $\bar{F}\left(\begin{array}{cc}\mathbf{y} & \\ k & k'\end{array}\right) = F\left(\begin{array}{cc}\mathbf{y} & \\ k & k'\end{array}\right)\bar{E}$, $\bar{f}\left(\begin{array}{cc}\mathbf{y} & \\ k & k'\end{array}\right) = f\left(\begin{array}{cc}\mathbf{y} & \\ k & k'\end{array}\right)\bar{E}$, and the matrices $\bar{f}_\phi(ii)$ and $\bar{\tau}_\phi$ are derived from the matrices $\bar{f}(ii)$ and $\bar{\tau}$ (8) using the replacement $f(i\mu|j\mu') \longrightarrow f(i\mu|j\mu')\exp(-i\phi_{\mu\mu'})$, where the quantity $\phi_{\mu\mu'} = 2\pi\mathbf{y}\mathbf{R}_{\mu\mu'}$ determines the change in the phase upon scattering, with $\mathbf{R}_{\mu\mu'} = \mathbf{R}_\mu - \mathbf{R}_{\mu'}$ being the vector connecting the μth and μ'th cells in the cluster.

The self-energy part $\bar{\Sigma}(\mathbf{y})$ can be defined by the equation

$$\left\langle \bar{F}\left(\begin{array}{cc}\mathbf{y} & \\ k & k'\end{array}\right)\right\rangle = \bar{f}\left(\begin{array}{cc}\mathbf{y} & \\ k & k'\end{array}\right) + \bar{f}\left(\begin{array}{cc}\mathbf{y} & \\ k & k_0\end{array}\right)\bar{\Sigma}(\mathbf{y})\left\langle \bar{F}\left(\begin{array}{cc}\mathbf{y} & \\ k_0 & k'\end{array}\right)\right\rangle. \quad (12)$$

From a comparison of relationships (10) and (12), we obtain

$$\bar{\Sigma}(\mathbf{y}) = n^{-1}[\bar{I} + \bar{\tau}_\phi\bar{f}_\phi]^{-1}\bar{\tau}_\phi, \quad (13)$$

where $\bar{f}_\phi \equiv \bar{f}_\phi(ii)$. Since all the elements of the matrix $\left\langle \bar{F}\left(\begin{array}{cc}\mathbf{y} & \\ k & k'\end{array}\right)\right\rangle$ are identical, Eq. (10) can be represented in the form

$$\left\langle F_{\alpha\gamma}\left(\begin{array}{cc}\mathbf{y} & \\ k & k'\end{array}\right)\right\rangle = f_{\alpha\gamma}\left(\begin{array}{cc}\mathbf{y} & \\ k & k'\end{array}\right) + f_{\alpha\beta}\left(\begin{array}{cc}\mathbf{y} & \\ k & k_0\end{array}\right)T_{\beta\delta}(\mathbf{y})f_{\delta\gamma}\left(\begin{array}{cc}\mathbf{y} & \\ k_0 & k'\end{array}\right), \quad (14)$$

where $T(\mathbf{y}) = \bar{u}'\bar{T}(\mathbf{y})\bar{u}$ and $\bar{u}'$ and $\bar{u}$ are the row and column consisting of n elements I, respectively. The matrix $T(\mathbf{y})$ can be rewritten in the form $T_{\beta\delta}(\mathbf{y}) = -d\ln(D(\mathbf{y}))/df_{\delta\beta}\left(\begin{array}{cc}\mathbf{y} & \\ k_0 & k_0\end{array}\right)$, where $D(\mathbf{y})$ is the determinant of the matrix $\bar{M}(\mathbf{y}) = \bar{\tau}_\phi^{-1} - n^{-1}\bar{f}_\phi'$. In the matrices f and T, we note the opposite order of the indices β and δ.

The function $\left\langle F_{\alpha\gamma}\left(\begin{array}{cc}\mathbf{y} & \\ k & k'\end{array}\right)\right\rangle$ can be expressed through the self-energy part $\Sigma(\mathbf{y})$; that is,

$$\left\langle F_{\alpha\gamma}\left(\begin{array}{cc}\mathbf{y} & \\ k & k'\end{array}\right)\right\rangle = f_{\alpha\gamma}\left(\begin{array}{cc}\mathbf{y} & \\ k & k'\end{array}\right) + f_{\alpha\beta}\left(\begin{array}{cc}\mathbf{y} & \\ k & k_0\end{array}\right)\Sigma_{\beta\delta}(\mathbf{y})\left\langle F_{\delta\gamma}\left(\begin{array}{cc}\mathbf{y} & \\ k_0 & k'\end{array}\right)\right\rangle. \quad (15)$$

From expressions (14) and (15), we find

$$\Sigma(\mathbf{y}) = T(\mathbf{y})\left[1 + f\left(\begin{array}{cc}\mathbf{y} & \\ k_0 & k_0\end{array}\right)T(\mathbf{y})\right]^{-1}.$$

Here, all the quantities are matrices in the space of polarization indices.

Thus, we derived Eqs. (14) and (15) accounting for the multiple coherent scattering of excitations by the n-impurity clusters and the strongest resonant interaction between vibrational modes of distant identical clusters.

4. Equations (14) and (15) and similar equations are obtained with due regard for scattering by n-impurity clusters in the non-self-consistent approximation. This approximation will be referred to as the modified average t-matrix approximation. In order to derive the equations within the self-consistent approximation, we use expression (13). Next, we introduce the designation $\bar{\sigma}(\bar{f}_\phi) = n\bar{\Sigma}$, which explicitly involves the dependence on the matrix $\bar{f}_\phi$ formed from the bare Green's function f. Equation (13) is equivalent to the series

$$\bar{\sigma}(\bar{f}_\phi) = \bar{\tau}(\bar{f}_\phi) - \bar{\sigma}(\bar{f}_\phi)\bar{f}_\phi\bar{\sigma}(\bar{f}_\phi) - \ldots, \quad (16)$$

where $\bar{\tau}(\bar{f}_\phi) \equiv \bar{\tau}_\phi$. This series can be interpreted as follows. The self-energy part $\bar{\sigma}(\bar{f}_\phi)$ is obtained if the corrections for multiple occupancy caused by the breaking apart of the interaction lines are subtracted from the bare self-energy part $\bar{\tau}(\bar{f}_\phi)$ [1, 2]. Figure 1 illustrates this procedure for the simplest diagram of scattering by a single-impurity cluster. The sums of all diagrams in the first and second columns are added to the expressions given in the first row of the table. The other columns (*2*, *3*, …) involve the diagrams of the multiple-occupancy corrections. The sum of the diagrams with two irreducible parts are added to $\bar{\sigma}(\bar{f}_\phi)\bar{f}_\phi\bar{\sigma}(\bar{f}_\phi)$, etc. In the self-consistent approximation, the self-energy part depends on the full Green's function; i.e., $\bar{\sigma}(\langle\bar{F}_\phi\rangle)$. Therefore, the diagrams with internal insertions of the type shown in column *1* of Fig. 2 are added to the diagrams depicted in Fig. 1. The terms of column *1* are rearranged to the left-hand side of the equality and are added to the terms of the left column. Owing to the

internal inserts, the argument in the function $\bar{\sigma}$ is replaced by the quantity $\bar{\Gamma}_\phi = [\bar{I} - \langle \bar{F}_\phi \rangle \bar{\sigma}(\bar{\Gamma}_\phi)]^{-1} \langle \bar{F}_\phi \rangle$. The arguments in the function $\bar{\sigma}$ in all the terms in the series are replaced in a similar manner. By performing the convolution of the series and returning to relationship of type (13), we find

$$\bar{\sigma}(\bar{\Gamma}_\phi) = [\bar{I} + \bar{\tau}(\langle \bar{F}_\phi \rangle) \langle \bar{F}_\phi \rangle]^{-1} \tau(\langle \bar{F}_\phi \rangle). \quad (17)$$

In order to determine the function $\bar{\sigma}$ $(\langle \bar{F}_\phi \rangle)$, the Green's function $\langle \bar{F}_\phi \rangle$ is expressed through the quantity $\bar{\Gamma}_\phi$. As a result, we have $\langle \bar{F}_\phi \rangle = \bar{\Gamma}_\phi [\bar{I} + \bar{\sigma}(\langle \bar{\Gamma}_\phi \rangle \bar{\Gamma}_\phi)]^{-1}$. Substituting the last expression into the right-hand side of expression (17) and making the substitution $\bar{\Gamma}_\phi \longrightarrow \langle \bar{F}_\phi \rangle$, we finally obtain

$$\bar{\Sigma}(\mathbf{y}) = n^{-1}[\bar{I} + \bar{\tau}(\bar{F}'_\phi)]^{-1} \bar{\tau}(\bar{F}'_\phi), \quad (18)$$

where $\bar{F}'_\phi = \langle \bar{F}_\phi \rangle [\bar{I} + n\bar{\Sigma}(\mathbf{y}) \langle \bar{F}_\phi \rangle]^{-1}$ and $\bar{\Sigma}(\mathbf{y}) \equiv \bar{\Sigma}(\bar{F}'_\psi)$. Thus, modified relationships of the *n*-impurity self-consistent coherent-potential approximation are obtained from relationships (13) for the *n*-impurity modified average *t*-matrix approximation using the replacement $\bar{f}_\phi \longrightarrow \bar{F}'_\phi$ on its right-hand side. At $n = 1$, formulas (18) transform into formulas for the single-impurity coherent-potential approximation [1, 6]. Note that relationships (18) of the *n*-impurity modified coherent-potential approximation and those of the *n*-impurity coherent-potential approximation [7] differ significantly, even though they were derived by similar methods. The expressions for the *n*-impurity coherent-potential approximation [7] relate clusters with different shapes and sizes, whereas the expressions for the *n*-impurity modified coherent-potential approximation relate clusters that differ only in translation. This renders them similar to clusters in the traveling-cluster approximation [3, 4].

In order to derive the final relationships for the Green's functions, these functions should be averaged over the distances $|\mathbf{R}_{\mu\mu'}|$ between impurities in the cluster. In this case, it is not necessary to take into account very large clusters. For example, the vibrational spectrum of an alloy can be adequately described with allowance made only for clusters of sizes that do not exceed the mean distance between impurities $|\mathbf{R}_{\mu\mu'}| \leq (a/x)^{1/d}$, where *a* is the lattice constant and $d = 1$, 2, or 3 is the space dimension.

5. For illustration, we calculate the density of vibrational modes for a linear monoatomic chain with allowance made only for two-impurity clusters. The averaging over the cluster size $|\mathbf{R}_{12}| = (r + 1)a$ is performed using the distribution function $P(r) = x(1 - x)^r$ $(\Sigma_{r = 0, \ldots, \infty} P(r) = 1)$, which has the meaning of the probability of finding a pair of impurities at a distance $(r + 1)a$ without other impurities between them. Then, we have

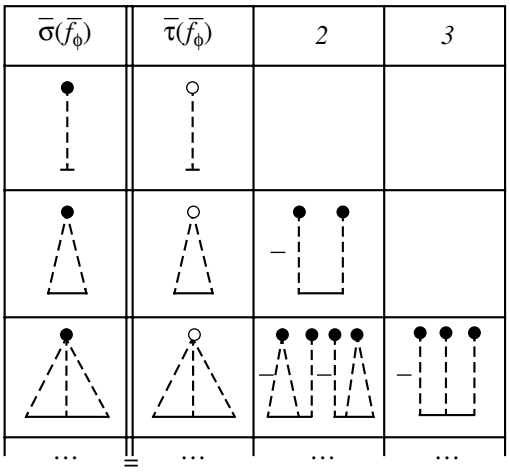

Fig. 1. Diagrams of the dressed (first column) and bare (second column) self-energy parts in the single-impurity non-self-consistent modified average *t*-matrix approximation. In columns *2*, *3*, …, the diagrams of the multiple-occupancy corrections containing *2*, *3*, … irreducible parts are given.

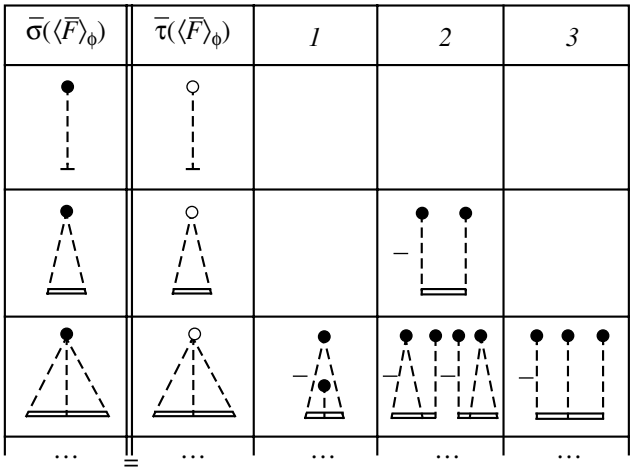

Fig. 2. The same as in Fig. 1 in the single-impurity self-consistent coherent-potential approximation. In column *1*, the diagrams with internal insertions are given.

$$\langle \langle F(\mathbf{y}) \rangle \rangle = \Sigma_{r = 0, \ldots, \infty} P(r) \langle F(\mathbf{y}, r) \rangle, \quad (19)$$

where the second angle brackets indicate the averaging over the distance R_{12}. Since the function $\langle F(\mathbf{y}, r) \rangle$ with an increase in *r* tends rapidly to the function $\langle F(\mathbf{y}) \rangle$ of the single-impurity cluster, sum (19) can be determined by calculating the function $\langle F(\mathbf{y}, r) \rangle$ at $r = 0, 1, \ldots, r_{\max}$, where $r_{\max} = 4$. With the use of expression (19), we obtain the density of vibrational modes $\rho(\omega^2) = (N\pi)^{-1} \mathrm{Im}(\Sigma_{\mathbf{y}} \langle \langle G^{(0)}(\mathbf{y}) \rangle \rangle)$, where $\langle \langle G^{(0)}(\mathbf{y}) \rangle \rangle = \langle \langle F(\mathbf{y}) \rangle \rangle / \omega(\mathbf{y})^2$. The results of calculations for $((m + \Delta m)/m = 1/3$ $(\Delta =$

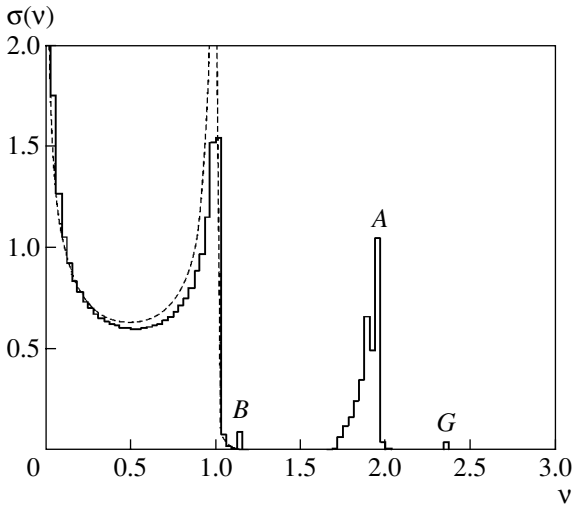

Fig. 3. Dimensionless spectral functions σ(ν) of the linear disordered chain for clusters containing *n* impurities at *n* = 0 (dashed line) and *n* = 1 and 2 (solid line). Conditions: the fraction of impurity atoms *x* = 0.1, the mass ratio of impurity and host atoms $(m + \Delta m)/m = 1/3$ (Δ = –2), the damping coefficient ε = 0.01, and $\nu = (\omega/\omega_0)$.

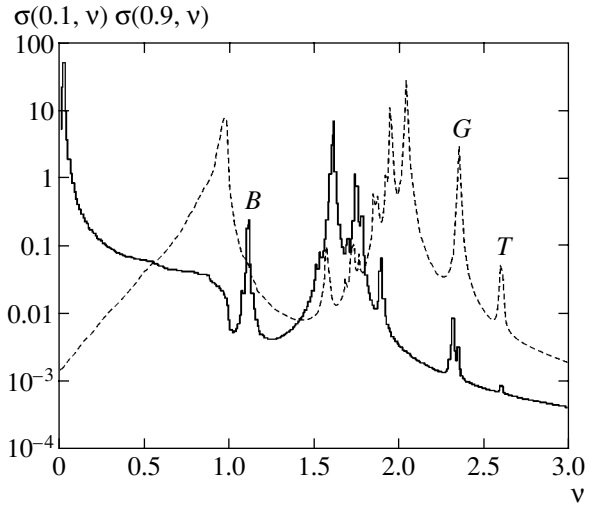

Fig. 4. Dependences of the imaginary parts of the Green's function σ(λ, ν) on the frequency $\nu = (\omega/\omega_0)^2$ for two magnitudes of the wave vector *y* for clusters *n* = 1–3 impurities at *x* = 0.2 and $\lambda \equiv 2ya = 0.1$ and 0.9: σ(0.1, ν) (solid line) and σ(0.9, ν) (dashed line). The other parameters are the same as in Fig. 3.

–2), *x* = 0.1, and the damping coefficient ε = $2\mathrm{Im}(\omega/\omega_0)^2 = 0.01$ are presented in Fig. 3. In this figure, the spectral function $\rho(\omega^2)$ in the dimensionless form, i.e., σ(ν), where $\nu = (\omega/\omega_0)^2$ and ω_0 is the maximum frequency in the lattice spectrum, is plotted along the ordinate axis. The function σ(ν) is normalized so that $\int_0^\infty \sigma(\nu)d\nu = 1$. Peaks *B* and *G* (according to the notation proposed in [9]) are assigned to the vibrational modes of pairs of the most closely spaced impurities (*r* = 0). The band at ν = 1.7–2.0 is attributed to the modes of single impurities (*A*) and impurity pairs with *r* > 0. The function σ(ν) with the same parameters but for a correlated impurity distribution was calculated in [11]. The positions of the peaks shown in Fig. 3 are in agreement with those obtained in [9] for one- and two-impurity peaks from direct computer calculations in the case of a disordered linear chain consisting of 8000 atoms.

Since the computer time it takes for the density of states for multi-impurity clusters (*n* > 2) to be calculated is sufficiently long, we calculate not the density of states but the function $\Delta(\mathbf{y}, \omega) = \pi^{-1}\mathrm{Im}(\langle\langle G(\mathbf{y}, \omega)\rangle\rangle)$ for different magnitudes of the wave vector **y**. The functions $\langle G\rangle$ are calculated from the matrix relationship $\langle G\rangle = \langle G^{(0)}\rangle - \langle G^{(0)}\rangle\Sigma$, which can be derived from expressions (6) and (15). The functions Δ(**y**, ω) in the dimensionless form σ(λ, ν) at *n* = 3, *x* = 0.2, and $\lambda \equiv 2ya = 0.1$ and 0.9 are depicted in Fig. 4. The other parameters are the same as in Fig. 3. The averaging over the distances between impurities $|\mathbf{R}_{1,2}| = (r + 1)a$ and $|\mathbf{R}_{2,3}| = (q + 1)a$ is performed using the distribution function $P(r, q) = P(r)P(q)$. The Green's functions $\langle G(y, r, q)\rangle$ are calculated at *r* = 0, 1, …, $r_{\max}$ and *q* = 0, 1, …, $q_{\max}$, where $r_{\max} = q_{\max = 4} = 4$. Peak *T* is associated with the three most closely spaced impurities. The other designations are the same as in Fig. 3. Knowing the spacings between the peaks in the curves σ(0.1, ν) and σ(0.9, ν), we can estimate the widths of the impurity bands of the corresponding modes.

With the Green's function $\langle G\rangle$, it is possible to calculate the dielectric function. This function for a cubic crystal and a linear chain that contains two ions with masses m_1 and m_2 per unit cell takes the form

$$\varepsilon(\omega) = \varepsilon_\infty + (\varepsilon_0 - \varepsilon_\infty)/\{1 - (\omega/\omega_0)^2 \times [1 - (m_2/(m_1 + m_2))\Sigma]^{-1}\}, \quad (20)$$

where ε_0 is the static permittivity, ε_∞ is the high-frequency permittivity, and ω_0 is the frequency of optically active vibrations of the lattice containing no impurities. The spectrum ε(ω) was also calculated for a linear chain. The number of specific features in this spectrum is smaller than those in the spectra σ(ν) and σ(λ, ν).

These calculations were carried out in the modified average *t*-matrix approximation. The use of the modified coherent-potential approximation requires considerably more computer time, and such calculations have not been performed to date. It should be noted that the *n*-impurity modified average *t*-matrix approximation makes it possible to describe adequately the spectra at *x* ~ 0.1–0.3, as can be judged from the comparison of our results with the data obtained by Dean [9]. Note also that the *n*-impurity modified average *t*-matrix approximation includes internal insertions (nested dia-

grams) which describe scattering by clusters containing $(n - 1)$ or less impurities.

6. Thus, a new method accounting for scattering of elementary excitations by multi-impurity clusters was proposed. This method allows one to describe complex spectra of these excitations in a disordered material. The theoretical relationships are free of the drawbacks specific to many previous theories (breaking of translational symmetry, nonphysical relationships for physical quantities). The expressions of the theory were derived within the non-self-consistent (average *t*-matrix) and self-consistent (coherent-potential) approximations. The theoretical results were illustrated by calculating the spectra of vibrational modes for one-dimensional models of solid solutions.

ACKNOWLEDGMENTS

This work was supported by the Russian Foundation for Basic Research, project no. 03-02-7110.

REFERENCES

1. R. J. Elliott, J. A. Krumhansl, and P. L. Leath, Rev. Mod. Phys. **46** (3), 465 (1974).
2. A. Gonis, *Green Functions for Ordered and Disordered Systems*, Ed. by E. van Groesen and E. M. De-Jager (North-Holland, Amsterdam, 1992), Ser. Studies Math. Phys.
3. R. L. Mills and P. Ratanavararaksa, Phys. Rev. B: Condens. Matter **18** (20), 5291 (1978).
4. T. Kaplan, P. L. Leath, L. J. Gray, and H. W. Diehl, Phys. Rev. B: Condens. Matter **21** (10), 4230 (1980).
5. M. Jarrell and H. R. Krishnamurthy, Phys. Rev. B: Condens. Matter **63** (12), 125 102 (2001).
6. R. N. Aiyer, R. J. Elliott, J. A. Krumhansl, and P. L. Leath, Phys. Rev. **181** (3), 1006 (1969).
7. B. G. Nickel and J. A. Krumhansl, Phys. Rev. B: Solid State **4** (12), 4354 (1971).
8. W. H. Butler and B. G. Nickel, Phys. Rev. Lett. **30** (9), 373 (1973).
9. P. Dean, Proc. R. Soc. London, Ser. A **260** (1301), 263 (1961).
10. A. M. Kosevich, *Fundamentals of Crystal Lattice Mechanics* (Nauka, Moscow, 1972) [in Russian].
11. V. S. Vinogradov, Kratk. Soobshch. Fiz., No. 2, 11 (2002).

Translated by O. Borovik-Romanova

Physics of the Solid State, Vol. 47, No. 10, 2005, pp. 1944–1947. Translated from Fizika Tverdogo Tela, Vol. 47, No. 10, 2005, pp. 1867–1870.

LATTICE DYNAMICS AND PHASE TRANSITIONS

Thermal Expansion of a $Ni_{2.14}Mn_{0.81}Fe_{0.05}Ga$ Alloy in Coarse-Grained, Submicron, and Nanocrystalline States

R. N. Imashev*, V. V. Koledov, Kh. Ya. Mulyukov***, I. Z. Sharipov**, and V. G. Shavrov****

**Institute for Metals Superplasticity Problems, Russian Academy of Sciences, ul. Khalturina 39, Ufa, 450001 Russia*
e-mail: ram79@mail.ru, Ramil_imashev@imsp.da.ru
***Institute of Radio Engineering and Electronics, Russian Academy of Sciences, ul. Mokhovaya 11-7, Moscow, 125009 Russia*
****Ufa State Aviation Technical University, ul. K. Marksa 12, Ufa, 450077 Russia*

Received December 9, 2004; in final form, December 23, 2004

Abstract—The physical properties of a $Ni_{2.14}Mn_{0.81}Fe_{0.05}Ga$ shape memory alloy in various structural states were studied using dilatometric data obtained in the region of first-order phase transitions. © *2005 Pleiades Publishing, Inc.*

1. INTRODUCTION

In Heusler Ni–Mn–Ga alloys, the first-order phase transition from the high-temperature bcc phase (spatial structure $L2_1$) to the low-temperature tetragonal phase (lattice parameter ratio, $c/a < 1$) is thermoelastic and can be accompanied by the shape memory effect [1, 2]. It should also be emphasized that, in samples with a nonstoichiometric composition, there can exist martensite phases with orthorhombic and monoclinic distortions due to martensite modulations along the [110] crystallographic direction. Intermartensite transitions (related to variations in the structural modulation period of the martensite) caused by the influence of both mechanical stresses and temperature are observed in some alloys [3–7]. It is known that thermoelastic martensite-to-austenite structural transitions are accompanied by significant strains in the crystal lattice. Moreover, it was shown in [8] that the strains in a $Ni_{52}Mn_{24.5}Ga_{23.5}$ single crystal caused by an intermartensite transition are even higher than those in the case of a martensite-to-austenite transition. Ni–Mn–Ga alloys are also unique because structural phase transitions take place in them in the ferromagnetic state. As a result, structural transitions in them are sensitive to magnetic fields [9, 10]. The structural transition temperatures depend, to a large extent, on the alloy composition [11, 12]. Notwithstanding the considerable research interest expressed in these alloys, so far there have been virtually no studies on the effect of grain size on the physical properties of these alloys in the region of phase transitions. In the present paper, we report on the results of studies of the effect of the structural state on phase transitions for three different states: initial coarse-grained (CG), nanocrystalline (NC), and intermediate (submicron) states, the last of which was obtained through recrystallization of an NC sample annealed at 773 K for 30 min in vacuum. The temperature dependence of thermal expansion (which makes it possible to detect structural phase transitions) is used as the main characteristic in our studies.

2. EXPERIMENTAL

Coarse-grained $Ni_{2.14}Mn_{0.81}Fe_{0.05}Ga$ was obtained using the technique described in [13]. Chemical analysis with a JSM-840A scanning electron microscope equipped with an x-ray microprobe analyzer indicated high homogeneity of the alloy chemical composition. In order to obtain the NC state, 0.5-mm-thich plates were cut from samples of the initial alloy using the electric-spark technique. The plates were then subjected to intense plastic deformation on Bridgman anvils at room temperature under a pressure of 7 GPa. The rotation angle of the moving part of the anvils was 10π. The microstructure of a CG sample was studied with an AXIOVERT-100A light metallographic microscope. The microstructure of the NC state was studied with a JEM-2000EX transmission electron microscope. The temperature dependence of thermal expansion was studied using a dilatometer containing a displacement transducer based on a differential transformer. Thermal expansion curves were recorded under heating in the range from liquid-nitrogen temperature to 380 K and then under cooling.

3. RESULTS AND DISCUSSION

The metallographic studies of a CG sample carried out with a light microscope showed that it is a polycrystal with a mean grain size of 0.5 mm (Fig. 1a; arrows indicate two mutually perpendicular directions in which thermal expansion was measured). Typical martensite plates are observed in the micrograph of the microstructure obtained at 283 K. Misorientations of

martensite plates in various grains show that the grain boundaries are high-angled. Figure 1b shows thermal expansion curves related to this CG structure. The lower branch of curve *1*, related to heating, shows that normal expansion of the sample occurs up to 268 K. In the range 270–273 K, an abrupt decrease in the sample length is observed, after which normal expansion again takes place up to 293 K. A more significant stepwise elongation by ~0.1% is observed later in the range from 294 to 297 K. Heating of the sample above 297 K is accompanied by an almost linear expansion. It should be noted that the reverse transition in the range 297–293 K under cooling is also accompanied by an abrupt sample expansion instead of contraction. However, the variation in the sample length observed in the range 270–273 K under heating is repeated only in the range 222–242 K under cooling. The complicated character of the temperature dependence of thermal expansion described above is apparently caused by the fact that a series of various phase transitions takes place in the CG sample. For example, the abrupt decrease in the sample length observed at 270 K under heating should be due to a change in the modulation period of the martensite structure [4, 7, 8], which, in turn, begins to convert into the high-temperature cubic phase (austenite) at 294 K, causing stepwise elongation at this temperature. But why is elongation of the sample again observed in the reverse transition under cooling? It is known that martensite transitions are accompanied by displacements of atomic planes. These displacements can, however, be either favored or impeded by various kinds of defects (stacking faults, dislocations). It is possible that a single preferable direction of martensite crystal nucleation arises after the first phase transition. Furthermore, this martensite phase becomes so stable that the reverse intermartensite modulating transformation becomes complete only at 222 K.

In order to study the anisotropy of thermal expansion during martensite transitions in the CG state, dilatometric measurements were carried out in two mutually perpendicular directions. Curve *2* in Fig. 1b shows an abrupt decrease in the sample length at 294 K, in contrast to the elongation observed in curve *1*. Indeed, when converting from the low-temperature phase (with the lattice-parameter ratio $c/a < 1$) into the high-temperature bcc phase, the crystal lattice should expand in the *c* direction and contract in the *a* and *b* directions, because the parameter *a* of the bcc lattice is smaller than the parameters *a* and *b* of the low-temperature phase. According to qualitative x-ray structural analysis data, the following series of phase transitions takes place under heating of the CG alloy under study: at 270 K, the orthorhombic martensite (a modulated 7M-type martensite in which each seventh plane (110) is not displaced) converts into a five-layer (5M) martensite, and then at 294 K the 5M phase converts into the bcc austenite. The reverse transition of the austenite to martensite under cooling proceeds irreversibly; it is again accompanied by expansion (curve *1*) or contraction (curve *2*) of the sample with a very small hysteresis of about 1 K. The intermartensite transition is, however, significantly delayed and occurs in a wider temperature range.

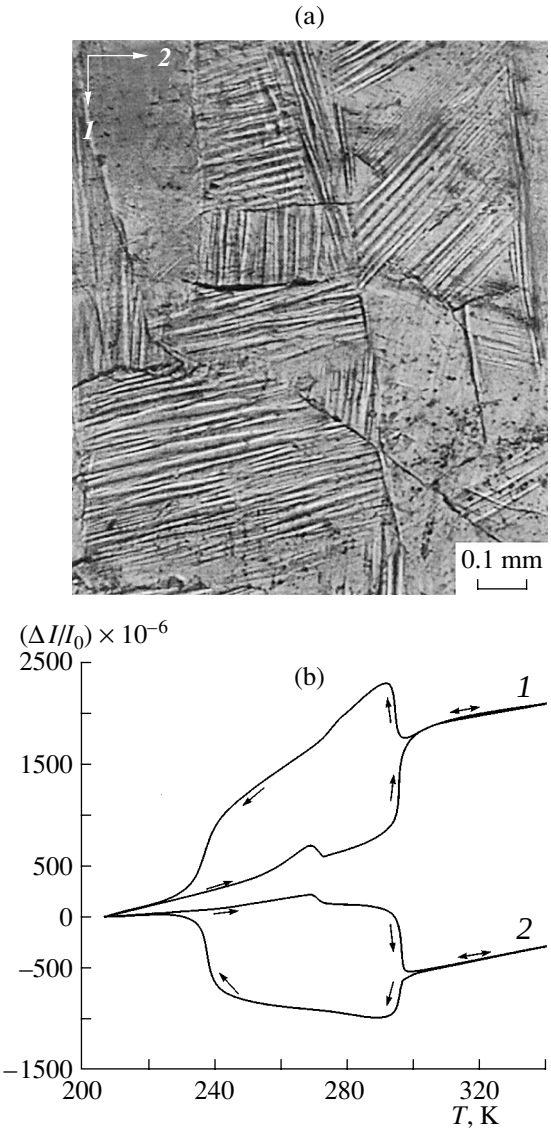

Fig. 1. (a) Microstructure of a CG sample (martensite phase) and (b) thermal expansion curve of this sample.

The fact that insignificant elongation of the sample is observed in curve *2* under cooling in the range of about 240–290 K is also surprising. This elongation can be caused by nonhomogeneous (diffuse) nucleation of the unmodulated martensite phase.

Figure 2 shows a micrograph of the microstructure of an NC sample and the corresponding thermal expansion curve. As is seen, the NC sample consists of very small crystallites without clearly distinguished boundaries between them. The mean size of the crystallites was estimated to be 10 nm. The diffraction pattern is a run of diffraction rings consisting of reflections that are

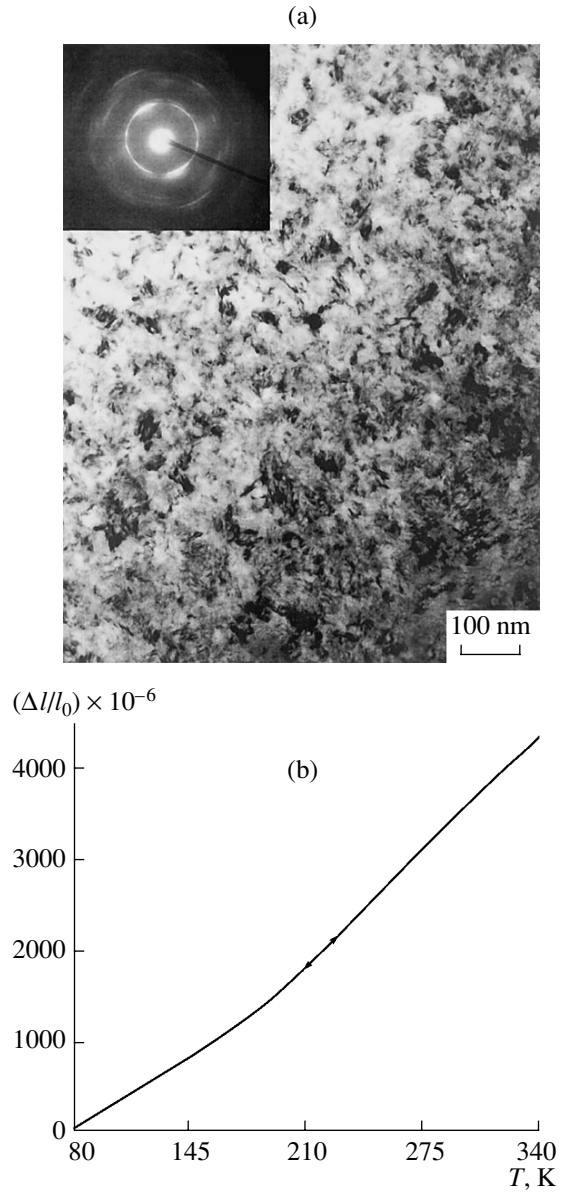

Fig. 2. (a) Microstructure and electron diffraction pattern of an NC sample and (b) the thermal expansion curve of this sample.

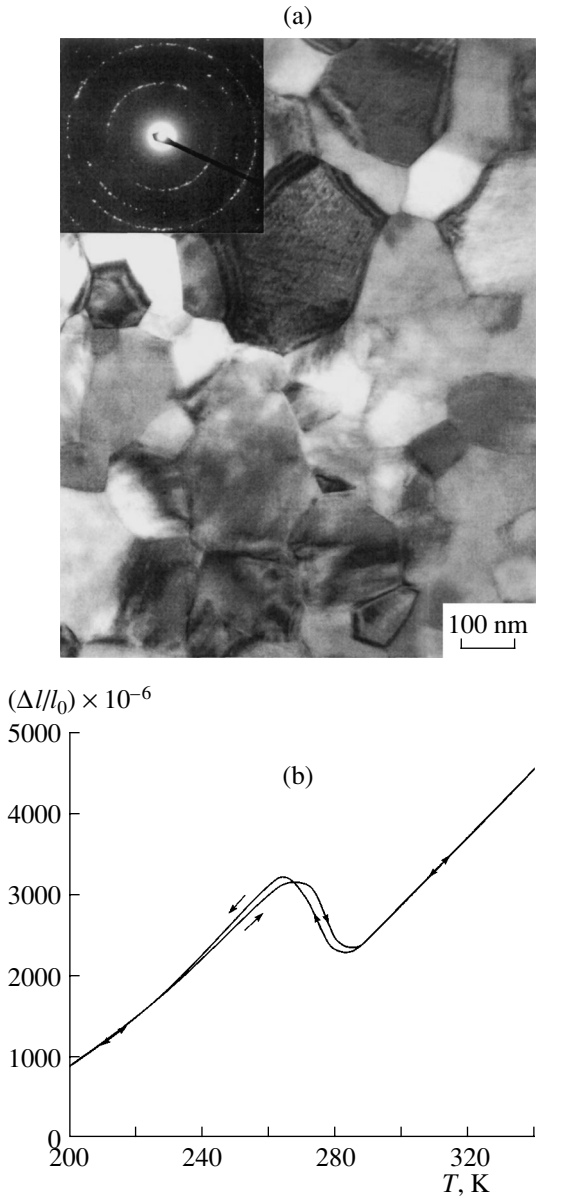

Fig. 3. (a) Microstructure and electron diffraction pattern of a recrystallized sample (austenite phase) and (b) the thermal expansion curve of this sample.

considerably blurred in the azimuth direction, which indicates strong internal stresses and high-angle mutual misorientations of the crystallographic axes of various crystallites. The $\Delta l/l(T)$ curve for the sample with an NC structure shows a monotonic reversible variation in the sample length, which indicates that phase transitions do not occur in the temperature range covered. This may be caused both by the small size of the crystallites and by the disordered structure of the compound in the NC state.

Annealing of the NC sample at 773 K results in significant changes in its structure (Fig. 3a). Well-defined boundaries appear between crystallites (with a mean size of 200 nm). Boundaries with a thickness extinction contrast are observed in some grains, which indicates that recrystallization has occurred. Color contrast between grains indicates misorientation. In the electron diffraction pattern obtained for an area of 0.5 μm^2, sharp reflections are observed, which indicates that the internal stresses are released. Figure 3b shows a thermal expansion curve of the alloy in the NC state. In contrast to the CG state, only one fairly abrupt change in the sample length (which takes place at lower temperatures, in the range 265–285 K) is observed both under heating and cooling. It is interesting to note that the strain due to the martensite-to-austenite transition

in this case is no smaller than that in the CG state and is approximately 0.1%. However, it should be noted that no intermartensite modulating transformation is observed in the annealed sample. It is also worth noting that, unlike the CG state, the martensite-to-austenite transition is essentially reversible. The martensitic transformation in the recrystallized sample is caused by crystallite grain growth and structural improvement due to annealing. The decrease in the temperature of the structural transition should be caused by the influence of grain size, because grain boundaries prevent transformation dislocations from motion and thereby limit their free paths, which decreases the martensitic transformation temperature [14, 15]. The broadening of the temperature range of the structural transition is explained by the fact that, in the recrystallized state, there is grain size dispersion, which causes the martensitic transition to occur in a wider temperature range. The absence of a martensitic transition is probably explained by internal stresses partially remaining in the annealed sample (it is known that the structural transitions in Ni–Mn–Ga alloys are sensitive to stresses) and by the small grain sizes.

4. CONCLUSIONS

It has been established that a $Ni_{2.14}Mn_{0.81}Fe_{0.05}Ga$ alloy in the CG state undergoes a series of structural phase transitions, including intermartensite and martensite–austenite transitions. The martensitic transition occurs with insignificant hysteresis and is irreversible, whereas the intermartensite transition occurs with significant hysteresis. It has been shown that, for these structural transitions in the CG state, the sign and magnitude of a sample dilatation depend on the crystallographic direction. It has also been established that no phase transitions take place in the NC state in the temperature range covered, but annealing at 773 K reverses the martensite–austenite transition, which, unlike the analogous transition in the CG state, is completely reversible. The effect of the structural state on the character of a phase transition has been demonstrated, which agrees well with the theories developed in [14, 15]. More comprehensive data on the dependence of the characteristic martensitic transition temperatures on grain size will be published in a later paper.

ACKNOWLEDGMENTS

This work was supported by the program "Prominent Scientific Schools" (project no. NSh-209.2003.8), the Russian Foundation for Basic Research (project no. 03-02-17443), the RFBR–SFNS of China (project no. 03-02-39006), and the Ministry of Education of the Russian Federation (project no. 202.01.01.054).

REFERENCES

1. P. J. Webster, K. R. A. Ziebeck, S. L. Town, and M. S. Peak, Philos. Mag. B **49** (3), 295 (1984).
2. V. V. Kokorin and V. A. Chernenko, Fiz. Met. Metalloved. **68** (6), 1157 (1989).
3. V. V. Martynov, J. Phys. IV **5** (C8), 91 (1995).
4. A. Sozinov, A. A. Likhachev, N. Lanska, and K. Ullakko, Appl. Phys. Lett. **80** (10), 1746 (2002).
5. I. K. Zasimchuk, V. V. Kokorin, V. V. Martynov, A. V. Tkachenko, and V. A. Chernenko, Fiz. Met. Metalloved. **69** (6), 110 (1990).
6. V. V. Martynov and V. V. Kokorin, J. Phys. III **2**, 739 (1992).
7. W. H. Wang, Z. H. Liu, J. Zhang, J. L. Chen, G. H. Wu, and W. S. Zhan, Phys. Rev. B: Condens. Matter **66** (5), 052 411 (2002).
8. W. H. Wang, G. H. Wu, J. L. Chen, S. X. Gao, W. S. Zhan, G. H. Wen, and X. X. Zhang, Appl. Phys. Lett. **79** (8), 1148 (2001).
9. A. N. Vasil'ev, A. D. Bozko, I. E. Dikshtein, C. V. Khovailo, V. D. Buchel'nikov, M. Matsumoto, S. Suzuki, V. G. Shavrov, T. Takagi, and J. Tani, Phys. Rev. B: Condens. Matter **59** (2), 1113 (1999).
10. I. E. Dikshteĭn, D. I. Ermakov, V. V. Koledov, L. V. Koledov, T. Takagi, A. A. Tulaĭkova, A. A. Cherechukin, and V. G. Shavrov, Pis'ma Zh. Éksp. Teor. Fiz. **72** (7), 536 (2000) [JETP Lett. **72** (7), 373 (2000)].
11. S. Wirth, A. Liethe-Jasper, A. N. Vasil'ev, and J. M. D. Coey, J. Magn. Magn. Mater. **167**, 7 (1997).
12. V. V. Khovailo, K. Oikawa, T. Abe, and T. Takagi, J. Appl. Phys. **93** (10), 8483 (2003).
13. A. A. Cherechukin, I. E. Dikshtein, D. T. Ermakov, A. V. Glebov, V. V. Koledov, D. A. Kosolapov, V. G. Shavrov, A. A. Tulaikova, E. P. Krasnoperov, and T. Takagi, Phys. Lett. A **291**, 175 (2001).
14. G. A. Malygin, Fiz. Tverd. Tela (St. Petersburg) **42** (8), 1469 (2000) [Phys. Solid State **42** (8), 1512 (2000)].
15. G. A. Malygin, Usp. Fiz. Nauk **171** (2), 187 (2001) [Phys. Usp. **44** (2), 173 (2001)].

Translated by E. Borisenko

Physics of the Solid State, Vol. 47, No. 10, 2005, pp. 1948–1957. Translated from Fizika Tverdogo Tela, Vol. 47, No. 10, 2005, pp. 1871–1880.

LOW-DIMENSIONAL SYSTEMS AND SURFACE PHYSICS

Eigenstate Statistics and Optical Properties of One-Dimensional Disordered Photonic Crystals

M. A. Kaliteevskiĭ*, V. V. Nikolaev*, and R. A. Abram**

**Ioffe Physicotechnical Institute, Russian Academy of Sciences, ul. Politekhnicheskaya 26, St. Petersburg, 194021 Russia*
e-mail: Valentin.Nikolaev@mail.ioffe.ru
***Department of Physics, University of Durham, Durham, DH1 3LE United Kingdom*
Received October 14, 2004

Abstract—Optical eigenstates in one-dimensional disordered photonic crystals were studied. The threshold disorder level was established below which the probability of appearance of an eigenstate at the photonic bandgap center is negligible. The threshold is reached when the relative fluctuation in the optical lengths of the structure periods becomes equal to the square root of one-third of the relative bandgap width. The dependence of the ensemble-averaged structure transmission coefficient on the fluctuation of the period optical length has a break corresponding to the threshold fluctuation. © *2005 Pleiades Publishing, Inc.*

1. INTRODUCTION

The interest in studies of the properties of disordered photonic crystals [1, 2] stems from two intimately related reasons. First, there is a need to develop for technical applications a photonic crystal with a photonic bandgap (PBG) that is not disorder-"contaminated" (i.e. not filled by states). Second, there is a possibility of light localization in photonic crystals [3].

Despite continual improvements in the technology of preparation of photonic crystals, their samples are disordered to some extent. In self-assembled photonic crystals, such as opals, the size of the spheres making up the crystal lattice varies. In addition, opals have vacancies and stacking faults. Photonic crystals obtained by lithography are not perfect because of the wall roughness and nonuniform etching in depth.

It is known that the presence of disorder in semiconductors may give rise to electron localization, which becomes manifest in a decrease in electrical conductivity [4, 5]. It has been repeatedly suggested that an analogous effect, light localization, could be observed in the corresponding dielectric structures as well [6]. Because the theory of electron localization in disordered solids has been developed to a sufficiently high level [7] and permits description of a sizable part of the experimentally observed phenomena, as well as due to the wave equations for light and carriers being similar, it appeared only natural to extend the results obtained for carriers to the photonic case.

However, despite the similarity of the wave equation for light

$$\nabla \times \nabla \times \mathbf{E}(\mathbf{r}) = \varepsilon(\mathbf{r})\frac{\omega^2}{c^2}\mathbf{E}(\mathbf{r}) \qquad (1a)$$

[where the spatial dependence of the dielectric permittivity $\varepsilon(\mathbf{r})$ includes a regular (for instance, periodic) and a random part, $\varepsilon(\mathbf{r}) = \varepsilon^{(0)}(\mathbf{r}) + \varepsilon_{\text{fluct}}(\mathbf{r})$] to the Schrödinger equation for the electron wave function

$$\frac{\hbar^2}{2m}\nabla^2\psi + V(\mathbf{r})\psi = E\psi \qquad (1b)$$

(where $V(r) = V^{(0)}(\mathbf{r}) + V_{\text{fluct}}(\mathbf{r})$ is the potential energy and E is the state energy), these two equations are essentially different. The potential $V(\mathbf{r})$ can be both positive and negative. In addition, $V(\mathbf{r})$ enters Eq. (1b) irrespective of E. The dielectric permittivity $\varepsilon(\mathbf{r})$ in nonabsorbing materials is a real positive quantity entering Eq. (1a) as a product with ω^2. An electron may be localized in wells of the $V(\mathbf{r})$ potential; by contrast, for photons, whose energy is positive, this possibility is ruled out. However, enhanced coherent backscattering (analogous to weak electron localization) [8–10], which is believed to be a precursor to "true" localization, is observed experimentally and manifests itself as an increase in scattered light intensity in a disordered medium in the direction opposite to that of the incident beam. This bears out the assumption that light localization is indeed possible in disordered photonic microstructures.

One more important difference between the cases of electrons and photons should be noted. Due to the electron–electron and electron–phonon coupling, for electrons one may introduce the concept of the coherence length [11]. In this sense, the electron is a particle rather than a wave and the extent to which the wave properties of the electron are essential is illustrated by the term "quantum corrections to conductivity." The interaction among photons is negligible (zero in the linear approximation), the photon scattering from phonons is

1063-7834/05/4710-1948$26.00

extremely weak, and the photon scattering by fluctuations (regular or random) in the dielectric permittivity is elastic. Thus, in nonabsorbing media, one cannot introduce for light the concept of the coherence length, which is a basic concept in "electronic" theories. Said otherwise, the coherence of the photonic state is not destroyed at distances of the order of the sample size. Whence it follows that the idea of photon propagation as a diffusion process described by a diffusion coefficient depending on sample size [12] is not fully applicable here. Moreover, description of the properties of optical eigenmodes should preferably take into account the sample boundaries.

It is appropriate to note also that the main subject of study in the electronic case is the effect of a factor of interest on conductivity. In the optical case, the corresponding counterpart is the transmission coefficient for light; the analogy is, however, incomplete. For systems characterized by conductivity, the average electron velocity varies and is proportional to the applied electric field. The velocity of photons is constant. In addition, conductivity is a quantity averaged over an ensemble of different electrons, whereas the transmission coefficient at a fixed frequency is a characteristic of one photon mode (or of a small number of them).

Electron localization brings about suppression of transport, i.e., a decrease in conductivity. Localization of light is possible in microcavities representing a single defect (for instance, a layer of half-wavelength thickness) in a photonic crystal (a Bragg reflector formed of a periodic sequence of quarter-wavelength-thick layer pairs) if the electromagnetic energy density ε for a microcavity eigenmode ε behaves as

$$\varepsilon(z) \propto \exp(-|z|/\xi), \qquad (2)$$

where ξ is the attenuation length. A localized state manifests itself in a transmission spectrum as a sharp peak (with the transmission coefficient becoming as high as unity); i.e., localization does not bring about suppression of transport.

Thus, one cannot extend the relations describing the behavior of electrons in disordered systems (in particular, the scaling theory of localization [13], sometimes called the scaling hypothesis [7]), to the "photonic" case.

Studies of light propagation in experimental samples of photonic crystals (which are all disordered to some extent) have revealed a dip in the light transmission spectra in the frequency region corresponding to the PBG, with the transmission coefficient falling off exponentially with increasing sample thickness but with the attenuation length being larger than it should be for an ideal structure [14–18].

Our understanding of disordered photonic microstructures gained considerably from the studies of John [3, 19, 20], who put forward a hypothesis by which light with a PBG frequency can be localized in photonic crystals even in the presence of a weak disorder. This hypothesis draws on the following considerations.

(1) The amplitude of the electric field of a propagating wave is, to good accuracy, a superposition of the fields of a free photon with wave vector **k** and of the same wave that suffered Bragg reflection and has wave vector **k**–**G**. As ω shifts into an allowed band, such a standing wave becomes modulated by an envelope whose wavelength is equal to $2\pi/q$, where q is the deviation of the vector **k** from the Bragg plane.

(2) A photonic state may be considered localized when the Ioffe–Regel criterion is satisfied [21]: $kl < 1$, where l is the mean free path. For photonic crystals, the Ioffe–Regel criterion should contain the envelope wavelength $\lambda_{env} = 2\pi/q$; so the criterion $2\pi l/\lambda_{env} \sim 1$ near the band edges is met automatically.

Obviously enough, assumption (1) is not valid. An electromagnetic field of a frequency beyond the PBG propagating in an ideal infinite photonic crystal is a Bloch wave of constant amplitude. If the frequency lies within the PBG, the electromagnetic field is an exponentially decaying Bloch wave. Application of the Ioffe–Regel criterion in assumption (2) appears somehow artificial; indeed, the original meaning of this criterion reads that "a section of a sine wave less than one wavelength long can no longer be considered a sine wave." In other words, modes satisfying the Ioffe–Regel criterion are not plane waves (which in no way implies that the modes are localized). Moreover, it is not clear what should one accept as the mean free path length l in a photonic crystal. The elements of a photonic crystal are scatterers, and for each of them one can calculate the scattering cross sections (or reflectance in the one-dimensional case) and, knowing their concentration, deduce the photon mean free path. The combined action of periodically positioned scatterers gives rise, however, not to scattering but rather to the formation of a Bloch wave, which propagates without scattering.

Therefore, substitution into the Ioffe–Regel criterion of a wavelength λ_{env} (whose physical meaning is far from clear) multiplied by a wave vector calculated in the effective medium approximation (which does not apply in the frequency domain of interest) does not permit the conclusion that light can be localized in photonic crystals.

One should bear in mind that the energy density can be modulated in photonic crystals of finite size [22]. The envelope of energy density is a half-wave corresponding to the sample size for the state closest to the bandgap edge, two half-waves for the second closest state to the edge, three half-waves for the third closest, and so on; this modulation is determined by the number of the state referenced to the PBG edge rather than by the deviation of the frequency of state from the PBG edge.

One of the most widely used theoretical methods of studying the behavior of an electromagnetic field in dis-

ordered photonic microstructures employs calculation of the "localization length of light" $\zeta = -L/\langle \ln T \rangle$, where T is the transmission coefficient and L is the sample size [23–27]. The point underlying this approach is that the field averaged over an ensemble of structures decays exponentially in disordered structures.

Exponential attenuation of a light wave does not imply, however, the existence of a localized state characterized by the corresponding attenuation length. Indeed, if the light frequency is within the PBG, light does decay exponentially, but there are no states of the electromagnetic field in this case.

The above theoretical approaches not only fail to provide a quantitative answer to the question of PBG stability against disorder in a photonic crystal, they do not offer a general physical picture of the observed phenomena either. The electron–electron and electron–phonon coupling in the electronic problem do not allow one to obtain an exact solution to the problem in a system of real size, and this justifies invoking the above theoretical methods. In the photonic case, the mode structure in a large system can be calculated exactly (by solving the Maxwell equations numerically).

In earlier numerical calculations of the refractive index for a one-dimensional disordered photonic crystal [28], it was shown that, if the parameter characterizing the disorder does not exceed a certain threshold value, the attenuation length at the PBG center averaged over an ensemble of structures does not grow substantially with increasing disorder. Similar results were obtained for the two-dimensional case as well [29, 30]. In this connection, a hypothesis was put forward that the filling of the PBG by photonic states starts only after the disorder in the structure has exceeded a certain threshold level.

This study is aimed at investigating the spectrum of optical eigenstates in one-dimensional disordered photonic crystals in the PBG frequency region, as well as at establishing the relation between the light transmission coefficient (an experimentally observable quantity) and the variations in the eigenmode spectrum induced by structure disorder.

2. RESULTS AND DISCUSSION

Consider a one-dimensional periodic structure represented as a sequence of layer pairs A and B of the same thickness d, whose refractive index is given by the relation

$$n_{A,B}^{(0)} = n_0 \pm g, \tag{3}$$

where g is the refractive index modulation and $n_0 = 2.0$ (Fig. 1a). The transfer matrix method yields for such a periodic structure the dispersion equation

$$\cos(KD^{(0)}) = \cos(n_A d\omega/c)\cos(n_B d\omega/c) - \frac{1}{2}\left(\frac{n_A}{n_B} + \frac{n_B}{n_A}\right)\sin(n_A d\omega/c)\sin(n_B d\omega/c), \tag{4}$$

where $D = 2d$ is the structure period and K is the Bloch wave vector. Solving Eq. (4) reveals that the mode spectrum of this structure has a PBG with a center frequency $\omega_0 = \pi c/(n_0 D)$ (Fig. 1b). The relative PBG width is $\Delta\omega/\omega_0 \approx 4g/(\pi n_0)$, and the light attenuation per period is $\mathrm{Im}(K_0 D) = D/\xi_0 = \ln|n_1/n_2| \approx 2g/n_0$ (where K_0 is the imaginary part of the Bloch wave vector at frequency ω_0 and ξ_0 is the bandgap center attenuation length) at the PBG center frequency directly proportional to the refractive index modulation g (Fig. 1c). Note that, for the chosen $n_0 = 2.0$, the light attenuation per period is $\mathrm{Im}(K_0 D) \approx g$.

For a structure of finite size, one can impose boundary conditions according to which light does not strike the structure from outside and, using the equation

$$A\begin{pmatrix} 1 \\ -n_f \end{pmatrix} = \hat{M}\begin{pmatrix} 1 \\ n_l \end{pmatrix}, \tag{5}$$

obtain the optical eigenmode spectrum of the structure. Here, n_f and n_l are the refractive indices of the semi-infinite media bounding the structure, $\hat{M}$ is the transfer matrix of the structure, and A is a constant. The eigenmode spectrum for a finite structure will be discrete (Fig. 2a), with the eigenfrequencies ω_i having a nonzero imaginary part due to the light leaking out through the structure boundaries. In other words, the lifetime of eigenstates $\tau = 1/\mathrm{Im}\,\omega_i$ will be finite. From the lifetime of a state, one can judge whether this state is localized or not. By the Thouless criterion, if a level width (inverse lifetime) is less than the level separation, the state is localized; otherwise, it is considered delocalized.

The light transmission spectra have a dip corresponding to the PBG, and the transmission coefficient at the minimum for a structure with a refractive index modulation $g = 0.025$ and a thickness of $200D$ is 2×10^{-4} (Fig. 3).

To study the properties of a disordered structure, let us introduce a random fluctuation of refractive indices such that, for each pair of layers, the refractive indices are defined as

$$n_{A,B} = n_0 \pm g + n_0 \delta P, \tag{6}$$

where the quantity P takes on random values in the interval from –1/2 to 1/2. Thus, the optical length of periods D_i in a disordered structure

$$D_i = dn_A + dn_B = 2dn_0(1 + \delta P) = D_0(1 + \delta P)$$

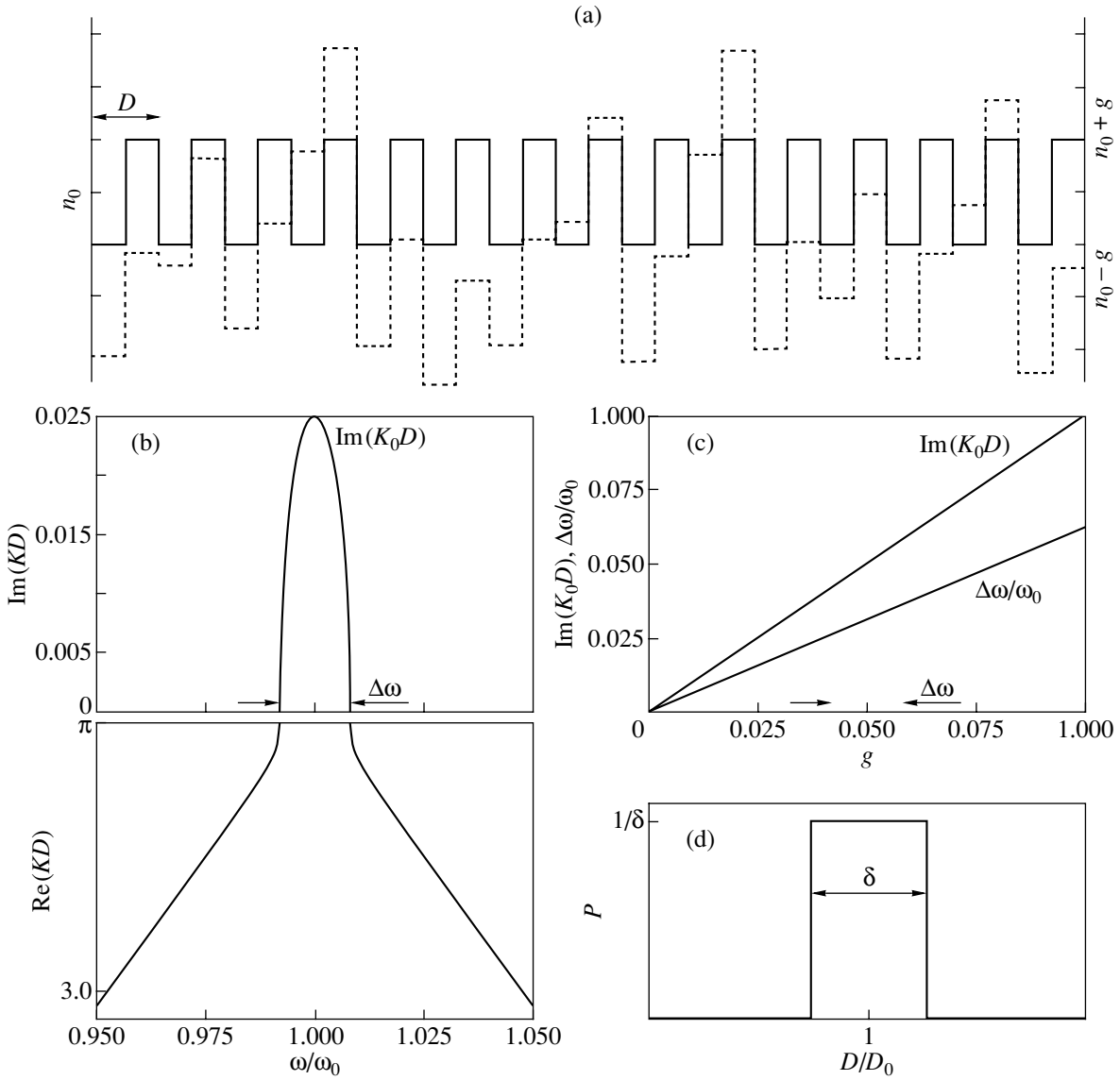

Fig. 1. Parameters of a model structure. (a) Refractive index profiles in ideal (solid line) and disordered (dashed line) structures; (b) dependence of the Bloch wave vector K on the frequency ω for an ideal structure with $g = 0.025$; (c) dependence of the relative PBG width $\Delta\omega/\omega_0$ and attenuation of light in one period $\mathrm{Im}(K_0D)$ at the PBG center frequency on the refractive index modulation g; and (d) distribution of the optical lengths of "structure periods" D_i in a disordered structure.

is characterized by a relative fluctuation δ (Fig. 1d). Figure 1a illustrates the refractive index profile of such a structure.

Figure 2a presents the density of states in the PBG region for an ideal structure (δ = 0), as well as the frequencies of the eigenstates and the corresponding lifetimes. The density of states shown in Fig. 2 for disordered structures is averaged over an ensemble of 3000 structures with a randomly disordered refractive index profile; these structures are characterized by a fluctuation δ = 0.035, 0.07, 0.1, and 0.15. The refractive index modulation of the structure is $g = 0.025$, and the thickness is $200D$; the structure is bounded on the outside by media with refractive indices of unity. The frequency interval between levels beyond the PBG in such a structure is of the order of $0.004\omega_0$. Strictly speaking, the relations shown in Fig. 2 are histograms, but the width of the discretization interval in frequency is sufficiently small (substantially less than the level separation) to warrant referring to these relations as densities of states. The only exception to this pattern is the ideal structure where in place of histogram bars of unit length there would be delta functions. We readily see that periodic modulation of the refractive index brings about an increase in the lifetime of states, this increase being the larger, the closer the state is to the bandgap edge. We shall call the states closest to the PBG the edge states. Such features in the eigenmode spectrum, first

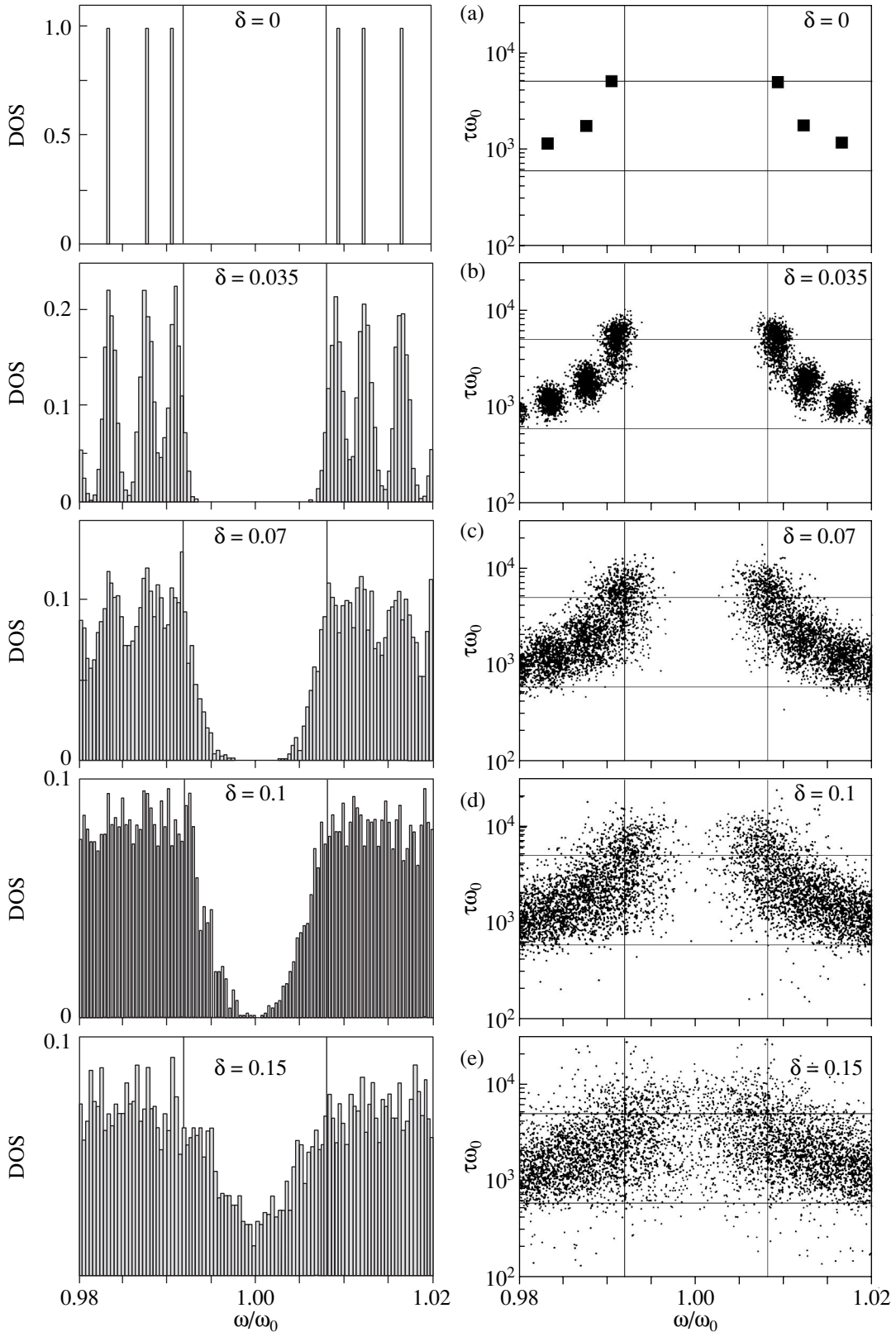

Fig. 2. Eigenfrequencies of an ideal and a disordered structure. (a) Left: the density of states for an ideal structure; right: frequencies $\mathrm{Re}\,\omega_i$ and lifetimes $\tau = 1/\mathrm{Im}\,\omega_i$ for an ideal structure ($\delta = 0$). (b–e) Left: the density of states averaged over an ensemble of 3000 structures with various values of δ; right: frequencies $\mathrm{Re}\,\omega_i$ and lifetimes $\tau = 1/\mathrm{Im}\,\omega_i$ of eigenmodes obtained by solving Eq. (5) for 1000 disordered structures with the same δ. The structure thickness is $L = 200D$, and the refractive index modulation is $g = 0.025$.

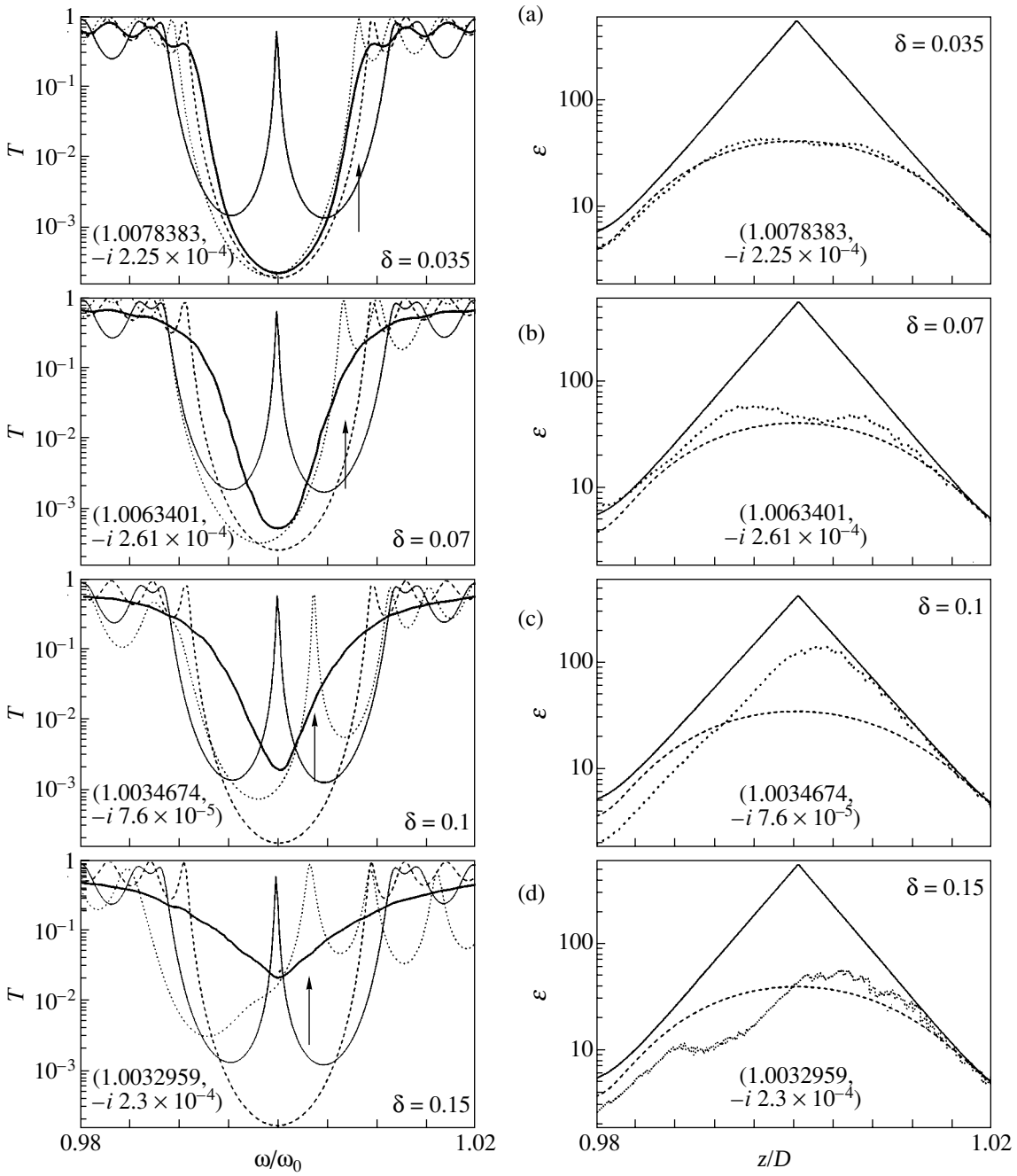

Fig. 3. Left: light transmission spectra for a single structure (dotted line) and those averaged over an ensemble of structures (bold solid line) drawn for different values of the fluctuation δ. The dashed line plots spectra for an ideal structure, and the thin solid line shows spectra for a half-wavelength microcavity based on an ideal structure. The structure thickness is $L = 200D$, and the refractive index modulation is $g = 0.025$. Arrows refer to frequencies for which electromagnetic-energy density profiles are shown on the right (dotted line). Shown for comparison on the right are the profiles of an edge state (dashed line) and of a microcavity eigenmode (solid line).

described in [22], are employed in distributed-feedback lasers.[1] Shown on the right in Figs. 2b–2e for each value of δ are the solutions to Eq. (5) ($\mathrm{Re}\,\omega_i$, $1/\mathrm{Im}\,\omega_i$) for 1000 disordered structures with various disorder configurations.

In accordance with the Thouless criterion, edge states in an ideal structure are localized; indeed, the level width $0.0002\omega_0$ (inverse lifetime) is nearly an

[1] The coupled-wave theory developed in [22] is a rough approximation (the second derivative of the wave amplitude with respect to the space coordinate is neglected) and, thus, is not applicable to an analysis of disordered systems.

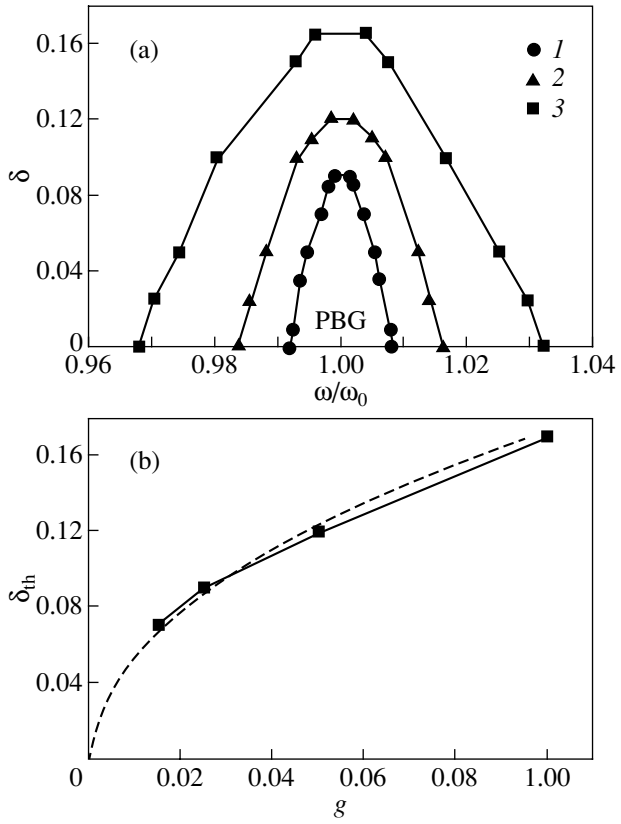

Fig. 4. Criterion for PBG stability against disorder. (a) PBG boundaries plotted vs fluctuation δ for structures with refractive index modulation g equal to (*1*) 0.025, (*2*) 0.05, and (*3*) 0.1. (b) Threshold value of the relative fluctuation of the period optical length δ_{th} plotted vs wave attenuation per period at the PBG center for an ideal structure, $\mathrm{Im}(K_0 D)$; the dashed line is a plot of $\delta_{th} = \sqrt{0.27g}$.

order of magnitude less than the level separation. Also, the electromagnetic-field energy-density profile falls off toward the edges of the structure more slowly than an exponential would. In the right-hand panels in Fig. 2, the top horizontal line ($\tau\omega_0 = 4800$) specifies the lifetimes of the edge states and the bottom horizontal line indicates the lifetimes of states in the structure with $g = 0$ (i.e., Fabry–Perot modes in a uniform structure, $\tau\omega_0 = 580$). The level width of such states is comparable to the interval between levels; so the states are not localized.

Is there an upper limit to the lifetime of an eigenstate in such a structure? If we place at the center of this structure a single defect, for instance, a layer of thickness $2d$ with a refractive index n_A (or n_B), or, said otherwise, form a microcavity, then the energy density profile of the microcavity eigenmode electromagnetic field will decay exponentially on both sides, as shown in Fig. 3. This mode will have the longest lifetime possible for this layered structure, about $19000/\omega_0$. The transmission spectrum of the structure has a sharp peak at the PBG center (Fig. 3).

As fluctuation δ increases to 0.035, the delta functions in the density of states graph are replaced by bell-shaped curves. While the tails in the density of states function now start to penetrate into the PBG, most of the PBG remains unfilled by states. The eigenmode frequencies $\mathrm{Re}\,\omega_i$ and eigenmode lifetimes τ fluctuate close to the values corresponding to the eigenmodes of an ideal structure; however, the lifetime fluctuation for an edge state is larger than that for the others. The energy density profile for a state within the PBG (see Fig. 3a) does not differ strongly from that for an edge state. This gives us grounds to maintain that edge states penetrate into the PBG. Eigenstates are identified by peaks in the transmission spectrum.

As the fluctuation δ increases to 0.07, edge states penetrate ever deeper into the PBG and the field profile of such states differs more strongly from that of an edge state. The PBG narrows while still remaining sufficiently broad.

With δ reaching 0.1, the probability of appearance of optical states at any point in the PBG becomes substantially different from zero. The fluctuation in the eigenstate lifetimes grows. The lifetime of certain states closely approaches the microcavity value. The field profile of such a state is shown in Fig. 3. We readily see that the profile of this state is close to that of a microcavity; i.e., it decays exponentially on both sides, although at a fluctuation $\delta = 0.1$ there are no single defects on which light could localize. Thus, as disorder increases, not only shifted edge states but also states localized at random microcavities characterized by long lifetimes appear in the PBG.

For δ of 0.15, the dip in the density of states becomes shallower, the lifetime fluctuation grows, and the probable lifetime in the PBG region decreases. As the disorder becomes still more pronounced, the effects associated with periodic modulation disappear.

In transmission spectra, eigenstates become manifest as peaks in the PBG region, which are sharper, the longer the lifetime. Ensemble-averaged transmission spectra exhibit a dip in the PBG region, but its depth decreases and shape changes as the fluctuation δ increases (Fig. 3).

As seen from Fig. 2, the PBG width decreases with increasing δ and, beyond a certain threshold value δ_{th}, the density of states at the PBG center becomes substantially different from zero. The lifetimes of the states suggest that most of the states, according to the Thouless criterion, are localized. Note that, judging from the lifetimes of some states, they are more likely delocalized than localized.

Figure 4a displays the variation of PBG boundaries in position with fluctuation δ for structures that differ in terms of their modulated refractive index ($g = 0.025$, 0.05, 0.1) and, hence, their bandgap width and attenuation length ξ_0. The PBG boundaries plotted in the δ–ω coordinates resemble parabolas. We see that, for a weak degree of disorder, the slope of the PBG boundary $\delta(\omega)$

is small (it may be that it is zero altogether; numerical modeling does not permit such a conclusion). The vertices of the parabolas correspond to the threshold value δ_{th}; as the refractive index modulation (and, hence, the PBG width) increases, the fluctuation threshold value δ_{th} also increases. Figure 4b plots the threshold fluctuation δ_{th} versus the refractive index modulation g. We readily see that δ_{th} is proportional to the square root of the refractive index modulation g and can be roughly described by the relation $\delta_{th} = \sqrt{0.27g}$.

Because the relative bandgap width and light attenuation per period are directly proportional to the refractive index modulation, the criterion for PBG filling by photonic states can be formulated as follows.

In a one-dimensional case, the probability of formation of an optical eigenmode at any point of the PBG becomes substantially different from zero when the relative fluctuation of the optical period length becomes approximately equal to one-fourth of the light attenuation per period of the structure

$$\delta_{th} \approx \sqrt{\mathrm{Im}(K_0 D)/4} \quad (7a)$$

or to one-third of the relative bandgap width

$$\delta_{th} \approx \sqrt{(\Delta\omega/\omega_0)/3}. \quad (7b)$$

The square root dependence of the threshold fluctuation on the bandgap width implies that, even for a very small refractive index modulation, the PBG is stable against disorder. This statement is at odds with the current concepts on the PBG becoming filled by localized states even under weak disorder [7].

The dependence of the transmission coefficient averaged over an ensemble of structures on the sample thickness L is presented graphically in Fig. 5. Within the PBG, the transmission coefficient falls off exponentially with increasing sample thickness:

$$\langle T\rangle = \exp(-L/\xi). \quad (8)$$

Note that the attenuation length ξ grows with δ. At a PBG edge and for small fluctuations δ, the transmission coefficient $\langle T\rangle$ behaves in a manner that is not so straightforward; indeed, it is determined in these conditions by the edge state frequency, which varies with increasing sample thickness L. As δ increases, the transmission coefficient $\langle T\rangle$ decays exponentially with increasing L.

Figure 6 shows the dependence of the ensemble-averaged transmission coefficient at the PBG center frequency $\langle T\rangle$, of $\ln\langle T\rangle$, and of the attenuation length $\xi = -L/\ln\langle T\rangle$ on the fluctuation δ for structures with refractive index modulation $g = 0.025$, 0.05, and 0.1. In all cases, the graphs exhibit a break. When the fluctuation δ is less than the threshold value, $\langle T\rangle$ grows slowly with increasing δ, while the attenuation length ξ remains practically constant. As δ_{th} is reached, a break

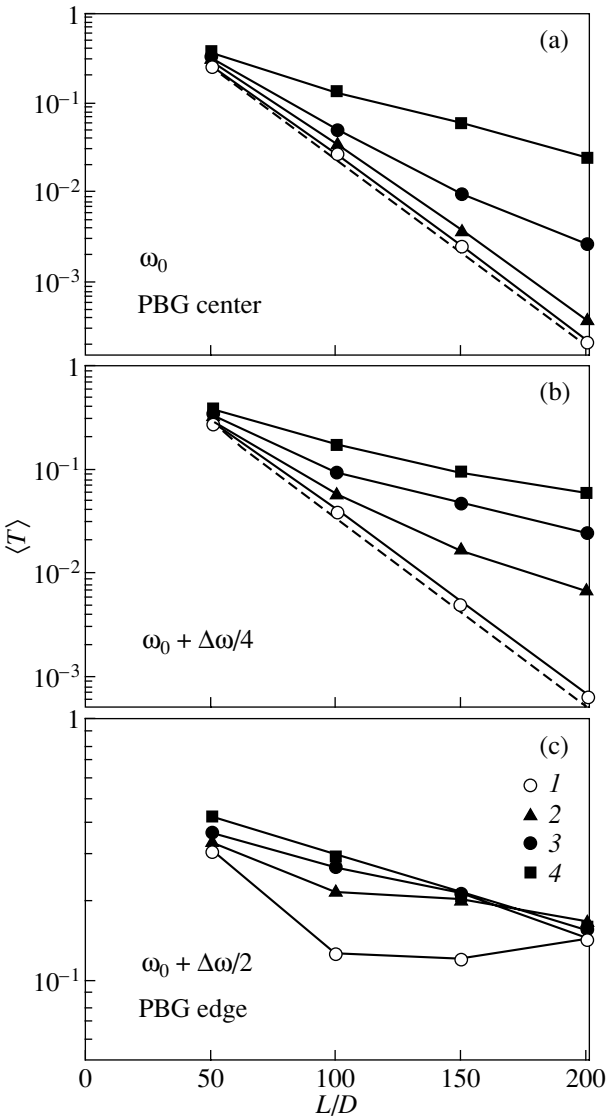

Fig. 5. Transmission coefficient averaged over an ensemble of structures [(a) at the PBG center frequency ω_0, (b) at frequency $\omega_0 + \Delta\omega/4$, (c) at the PBG edge frequency $\omega_0 + \Delta\omega/2$] as a function of the structure thickness L for various values of the fluctuation δ: (*1*) 0.35, (*2*) 0.7, (*3*) 0.1, and (*4*) 0.15. For comparison, the dashed line shows the corresponding graphs for an ideal structure. The refractive index modulation is $g = 0.025$.

appears in the $\langle T\rangle(\delta)$ dependence and $\langle T\rangle$ and ξ grow strongly with δ. This behavior allows a straightforward explanation. The increase in $\langle T\rangle$ is a consequence of the formation of sharp peaks corresponding to localized states in the transmission spectra of some structures (Fig. 3). For $\delta < \delta_{th}$, the increase in the transmission coefficient originates from the side regions of these peaks and, therefore, is small. For $\delta > \delta_{th}$, localized states and the corresponding peaks appear at the bandgap center and $\langle T\rangle$ grows rapidly with increasing δ. Note that, for a single structure, the transmission coef-

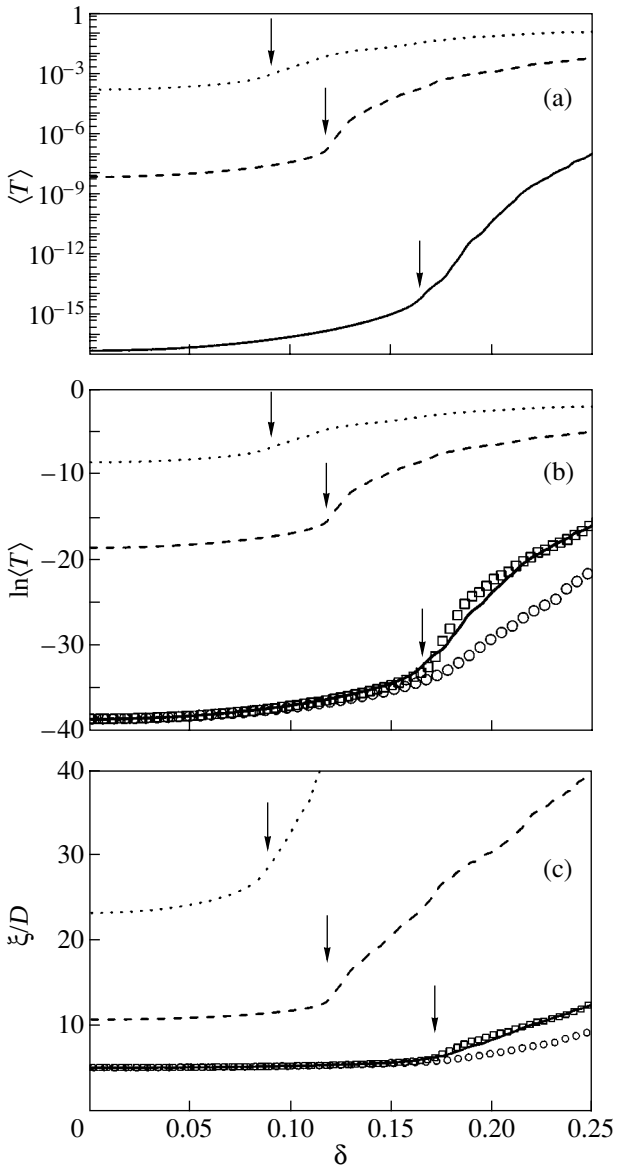

Fig. 6. Dependence of (a) the ensemble-averaged transmission coefficient at the PBG center frequency, (b) its logarithm, and (c) attenuation length on the fluctuation δ for structures with refractive index modulation g equal to 0.025 (dotted line), 0.05 (dashed line), and 0.1 (solid line). Symbols refer to relations obtained by transformations $\ln\langle T\rangle \longrightarrow \alpha\ln\langle T\rangle$ and $\delta \longrightarrow \sqrt{\alpha}\delta$ or $\xi \longrightarrow \xi/\alpha$ and $\delta \longrightarrow \sqrt{\alpha}\delta$ for structures with g equal to 0.025 (circles) and 0.05 (squares). α is the ratio of the inverse attenuation length for an ideal structure with $g = 0.025$ or 0.05 to the inverse attenuation length of a structure with $g = 0.1$. Arrows identify threshold values of δ. The structure thickness is $L = 200D$, and the refractive index modulation is $g = 0.025$.

ficient within the PBG may assume any value from zero to unity.

The square-root dependence of the threshold fluctuation δ_{th} on the refractive index modulation g suggests an interesting implication. Let α be the ratio of inverse attenuation lengths $\xi_0^{(1)}$ and $\xi_0^{(2)}$ for ideal structures with different refractive index modulations $g^{(1)}$ and $g^{(2)}$:

$$\alpha = \xi_0^{(2)}/\xi_0^{(1)} = g^{(1)}/g^{(2)} = \mathrm{Im}(K_0^{(1)}D)/\mathrm{Im}(K_0^{(2)}D). \quad (9)$$

Then, the dependence of the averaged transmission coefficient $\langle T\rangle$ (or of the attenuation length ξ) on the relative fluctuation δ of the optical period length can be derived through transformation:

$$\ln\langle T^{(2)}\rangle(\delta) = \alpha\ln\langle T^{(1)}\rangle(\sqrt{\alpha}\delta), \quad (10a)$$

$$\xi^{(2)}(\delta) \longrightarrow \xi^{(1)}(\sqrt{\alpha}\delta)/\alpha. \quad (10b)$$

In Fig. 6, squares refer to the results of transformation (10) applied to the $\langle T\rangle(\delta)$ or $\xi(\delta)$ relations for a structure with $g = 0.05$ and $\alpha = \xi_0(g = 0.05)/\xi_0(g = 0.1)$ and circles show the result of the corresponding transformation for a structure with $g = 0.025$ and $\alpha = \xi_0(g = 0.025)/\xi_0(g = 0.1)$. For structures with $g = 0.05$ and 0.1, transformation (10) relates the $\langle T\rangle(\delta)$ or $\xi(\delta)$ dependences with a very high precision. The structure with $g = 0.025$ and a value of δ above the threshold exhibits a deviation due to the fact that the attenuation length in such a structure is comparable to the size of the structure, which substantially increases the effect of boundaries.

Transformations (10), which reflect universal (independent of the PBG) behavior of the attenuation length in disordered photonic crystals, may serve as a key in developing an "analytical" theory of disordered photonic crystals.

3. CONCLUSIONS

There exists a threshold disorder below which the probability of formation of an eigenstate at the center of a photonic bandgap is negligible. The threshold is reached when the relative fluctuation in the optical lengths of the structure periods becomes equal to the square root of one-third of the relative bandgap width. The dependence of the attenuation length at the PBG center on the fluctuation of the optical period lengths of a structure has a break corresponding to the threshold fluctuation. As long as the disorder parameter is less than the threshold value, the attenuation length grows slowly with increasing fluctuation. After the disorder parameter has exceeded the threshold value, the attenuation length starts to grow rapidly. The dependences of the attenuation length on the disorder parameter reveal a universal behavior common for all widths of the bandgap.

REFERENCES

1. J. D. Joannopoulos, R. D. Meade, and J. N. Winn, *Photonic Crystals: Molding the Flow of Light* (Princeton University Press, Princeton, NJ, 1995).

2. K. Sakoda, *Optical Properties of Photonic Crystals* (Springer, Berlin, 2001).
3. S. John, Phys. Rev. Lett. **58**, 2486 (1987).
4. P. W. Anderson, Phys. Rev. **109**, 1492 (1958).
5. N. F. Mott, *Metal–Insulator Transitions* (Taylor and Francis, London, 1974).
6. *Photonic Band Gap and Localization*, Ed. by C. M. Soukoulis (Plenum, New York, 1993), NATO ASI Ser., Ser. B: Phys., Vol. 308.
7. V. F. Gantmakher, *Electrons in Disordered Media* (Fizmatlit, Moscow, 2003) [in Russian].
8. Y. Kuga and A. Ishimaru, J. Opt. Soc. Am. A **1**, 831 (1984).
9. M. P. van Albada and A. Lagendijk, Phys. Rev. Lett. **55**, 2692 (1985).
10. P. E. Wolf and G. Maret, Phys. Rev. Lett. **55**, 2696 (1985).
11. P. W. Anderson, D. J. Thouless, E. Abrahams, and D. S. Fisher, Phys. Rev. B: Condens. Matter **22**, 3519 (1980).
12. N. Garcia and A. Z. Genack, Phys. Rev. Lett. **66**, 1850 (1991).
13. E. Abrahams, P. W. Anderson, D. C. Licciaedello, and T. V. Ramakrishnan, Phys. Rev. Lett. **42**, 673 (1979).
14. *Photonic Band Gap Materials*, Ed. by C. M. Soukoulis (Kluwer, Dordrecht, 1996), NATO ASI Ser., Ser. E: Appl. Sci., Vol. 315.
15. T. F. Krauss, R. M. De La Rue, and S. Brand, Nature (London) **383**, 699 (1996).
16. Yu. A. Vlasov, V. N. Astratov, O. Z. Karimov, A. A. Kaplianskii, V. N. Bogomolov, and A. V. Prokofief, Phys. Rev. B: Condens. Matter **55**, 13 357 (1997).
17. A. V. Baryshev, A. V. Ankudinov, A. A. Kaplyanskiĭ, V. A. Kosobukin, M. F. Limonov, K. B. Samusev, and D. E. Usvyat, Fiz. Tverd. Tela (St. Petersburg) **44**, 1573 (2002) [Phys. Solid State **44**, 1648 (2002)].
18. A. V. Baryshev, A. A. Kaplyanskiĭ, V. A. Kosobukin, M. F. Limonov, K. B. Samusev, and D. E. Usvyat, Fiz. Tverd. Tela (St. Petersburg) **45**, 434 (2003) [Phys. Solid State **45**, 459 (2003)].
19. *Confined Electrons and Photons: New Physics and Applications*, Ed. by E. Burstein and C. Weisbuch (Plenum, New York, 1995), NATO ASI Ser., Ser. B: Phys., Vol. 340.
20. S. John, Phys. Today **44**, 32 (1991).
21. A. F. Ioffe and A. R. Regel, Prog. Semicond. **4**, 237 (1960).
22. H. Kogelnick and C. V. Shank, J. Appl. Phys. **43**, 2327 (1972).
23. L. I. Deych, D. Zaslavsky, and A. A. Lisyansky, Phys. Rev. Lett. **81**, 5390 (1998).
24. L. I. Deych, A. A. Lisyansky, and B. L. Altshuler, Phys. Rev. Lett. **84**, 2678 (2000).
25. V. A. Kosobukin, Fiz. Tverd. Tela (Leningrad) **32**, 227 (1990) [Sov. Phys. Solid State **32**, 127 (1990)].
26. V. A. Kosobukin, Fiz. Tverd. Tela (St. Petersburg) **45**, 1091 (2003) [Phys. Solid State **45**, 1145 (2003)].
27. A. R. McGurn, K. T. Christensen, F. M. Mueller, and A. A. Maradudin, Phys. Rev. B: Condens. Matter **47**, 13120 (1993).
28. Yu. A. Vlasov, M. A. Kaliteevskii, and V. V. Nikolaev, Phys. Rev. B: Condens. Matter **60**, 1555 (1999).
29. M. A. Kaliteevskii, J. M. Martinez, D. Cassagne, and J. P. Albert, Phys. Rev. B: Condens. Matter **66**, 113101 (2002).
30. M. A. Kaliteevskii, J. Manzanarez Martinez, D. Cassagne, and J. P. Albert, Phys. Status Solidi A **195**, 612 (2003).

Translated by G. Skrebtsov

Physics of the Solid State, Vol. 47, No. 10, 2005, pp. 1958–1963. Translated from Fizika Tverdogo Tela, Vol. 47, No. 10, 2005, pp. 1881–1885.

LOW-DIMENSIONAL SYSTEMS AND SURFACE PHYSICS

Multiphonon Absorption of Light in Quantum-Well Systems in Uniform Electric and Magnetic Fields

É. P. Sinyavskiĭ and R. A. Khamidullin

Taras Shevchenko Pridnestrovskiĭ State University, ul. Dvadtsat' Pyatogo Oktyabrya 128, Tiraspol, 3300 Moldova
e-mail: arusanov@mail.ru

Received June 28, 2004; in final form, December 14, 2004

Abstract—The effect of a transverse electric field on the multiphonon absorption of light in quantum-well systems in a uniform magnetic field aligned parallel to the spatial quantization axis is investigated. It is shown that, when the interaction of an electron with long-wavelength vibrations is taken into account, the half-width of the absorption line does not depend on the electric-field vector **E**. As the electric field strength increases, the maximum of the light absorption shifts toward the long-wavelength range and decreases. The effect of the electric field on the shape of the zero-phonon line and first vibrational satellites is analyzed with due regard for the interaction of charge carriers with optical phonons. It is demonstrated in particular that the half-width of the zero-phonon line substantially depends on the electric-field vector **E** and can reach several millielectron-volts at the electric field strength $E = 2 \times 10^4$ V/cm. © *2005 Pleiades Publishing, Inc.*

1. It is known that, in the case where the magnetic-field vector **H** is directed perpendicular to the surface of a quantum-well system, the spectrum of a free electron is completely quantized; i.e., it is quasi-zero-dimensional. It is this circumstance which is responsible for the fact that the shape of the absorption and luminescence bands is governed by multiphonon processes [1]. In the present paper, we analyze the specific features observed in the optical spectra of quantum-well systems in a magnetic field aligned with the axis of spatial quantization occurring in an electric field **E** oriented parallel to the surface of a quantum well. In the subsequent discussion, the exciton effects will be disregarded, because we will restrict our consideration to the special case of strong quantized magnetic fields in which the Coulomb interaction of an electron with a hole is weak as compared to the energy separation between the levels of transverse quantization. A detailed analysis and the criteria for the validity of this approximation are given in [2]. The absorption coefficient is calculated in the one-band approximation. This means that, at $\mathbf{E} \perp \mathbf{H}$, the strengths of the electric and magnetic fields satisfy the following condition [3, 4]: $cE/(SH) \ll 1$, where $S = \sqrt{\varepsilon_g/4m_c}$, ε_g is the band gap of the semiconductor material under investigation, m_c is the effective mass of the electron, and c is the velocity of light.

2. The Hamiltonian for electrons in state i at $\mathbf{H} \neq 0$ ($i = c$ for the conduction band and $i = v$ for the valence band) in the given orientation of the electric and magnetic fields in the Landau gauge $\mathbf{A}(-Hy, 0, 0)$ has the form

$$\hat{H}_i = \frac{1}{2m_i}\left(\hat{P}_x - \frac{eH}{c}y\right)^2 + \frac{\hat{P}_y^2}{2m_i} + \frac{\hat{P}_z^2}{2m_i} + U_i(z) + eEy. \quad (1)$$

Let E_{ni} be the quantum-well energy in the one-dimensional potential $U_i(z)$. In this case, the eigenvalues of the Schrödinger equation with Hamiltonian (1) can be determined from the relationship

$$\varepsilon^i_{n\nu k_x} = \hbar\omega_i(\nu + 1/2) + E_{ni} + eER^2K_x - \frac{e^2E^2}{2m_i\omega_i^2}, \quad (2)$$

where $\omega_i = eH/(m_ic)$ is the cyclotron frequency, ν is the quantum number of the Landau level, K_x is the projection of the electron wave vector, $R^2 = \hbar c/(eH)$, e is the elementary charge, and m_i is the effective mass of the charge carrier.

The wave functions of the problem under consideration are represented as the product of the wave function of the charge carrier in the one-dimensional potential multiplied by the wave functions of the electron in the crossed electric and magnetic fields [5].

According to the Kubo formula [6], the coefficient of interband absorption of light at a frequency Ω and a polarization $\boldsymbol{\xi}$ can be expressed through the correlation function of the dipole moments and, in the second quantization representation, has the form

$$K(\Omega) = \frac{8\pi e^2}{n_0c\hbar\Omega V}\left|\frac{\mathbf{P}_{cv}\boldsymbol{\xi}}{m_0}\right|^2 \sum_{\substack{\alpha\alpha_1\\ \beta\beta_1}} \langle\alpha^v|\alpha_1^c\rangle\langle\beta_1^c|\beta^v\rangle \times \int_{-\infty}^{\infty} dt \exp(i\Omega t)\langle\alpha_\alpha(t)a_{\alpha_1}(t)a^+_{\beta_1}\alpha^+_\beta\rangle. \quad (3)$$

Here, $a^+_\alpha(a_\alpha)$ and $\alpha^+_\alpha(\alpha_\alpha)$ are the operators of creation (annihilation) of an electron and of a hole, respectively;

$\alpha(m, k_x)$ stands for the set of quantum numbers characterizing the state of the charged particle ($m(\nu, n)$) is the smoothed wave function in state $|\alpha^{(i)}\rangle$; $\mathbf{P}_{cv}$ is the matrix element of the momentum operator in terms of the Bloch functions; V is the volume of the system; m_0 is the mass of the free electron; and n_0 is the refractive index. The averaging $\langle\ldots\rangle$ in expression (3) is carried out with the density matrix for the electron in the crossed electric and magnetic fields; that is,

$$\hat{A}(t) = \exp\left(\frac{it}{\hbar}\hat{H}\right)\hat{A}\exp\left(-\frac{it}{\hbar}\hat{H}\right). \quad (4)$$

The Hamiltonian for electrons and holes with allowance made for their interaction with lattice vibrations in the second quantization representation can be written in the following form:

$$\hat{H} = \sum_{\alpha}(\varepsilon_{\alpha}^{c} - \xi)a_{\alpha}^{+}a_{\alpha} + \sum_{\alpha}(\varepsilon_{\alpha}^{v} - \xi_1)\alpha_{\alpha}^{+}\alpha_{\alpha}$$
$$+ \sum_{\mathbf{q}}\hbar\omega_{\mathbf{q}}b_{\mathbf{q}}^{+}b_{\mathbf{q}} + \sum_{\alpha\alpha\mathbf{q}}C_{\mathbf{q}}^{c}V_{\alpha\alpha_1}^{c}(\mathbf{q})a_{\alpha}^{+}a_{\alpha_1}(b_{\mathbf{q}} + b_{-\mathbf{q}}^{+}) \quad (5)$$
$$+ \sum_{\alpha\alpha\mathbf{q}}C_{\mathbf{q}}^{v}V_{\alpha\alpha_1}^{v}(\mathbf{q})\alpha_{\alpha}^{+}\alpha_{\alpha_1}(b_{\mathbf{q}} + b_{-\mathbf{q}}^{+}),$$

where ξ is the chemical potential; $\xi_1 = -\xi + \varepsilon_g$; $b_{\mathbf{q}}^{+}(b_{\mathbf{q}})$ stands for the operators of creation (annihilation) of phonons with energy $\hbar\omega_{\mathbf{q}}$ and wave vector $\mathbf{q}$; and $C_{\mathbf{q}}^{i}$ is the coefficient function, which describes the interaction of the particle with phonons,

$$V_{\alpha\alpha_1}^{i}(\mathbf{q}) = \langle\alpha^{i}|e^{i\mathbf{qr}}|\alpha_1^{i}\rangle.$$

According to relationship (4), the equation of motion for the operator $a_{\alpha}(t)$ has the form

$$\dot{a}_{\alpha}(t) = -\frac{i}{\hbar}\left\{(\varepsilon_{\alpha}^{c} - \xi)a_{\alpha}(t)\right.$$
$$\left. + \sum_{\alpha_1\mathbf{q}}C_{\mathbf{q}}^{c}V_{\alpha\alpha_1}^{c}(\mathbf{q})(b_{\mathbf{q}}e^{-i\omega_{\mathbf{q}}t} + b_{-\mathbf{q}}^{+}e^{i\omega_{\mathbf{q}}t})a_{\alpha_1}(t)\right\}. \quad (6)$$

In expression (6), the effect exerted by the electrons on the phonon spectrum is disregarded; i.e., it is assumed that

$$b_{\mathbf{q}}(t) \approx b_{\mathbf{q}}e^{-i\omega_{\mathbf{q}}t}, \quad b_{\mathbf{q}}^{+}(t) \approx b_{\mathbf{q}}^{+}e^{i\omega_{\mathbf{q}}t}.$$

This approximation holds for nondegenerated semiconductors, because the corrections introduced into the spectrum of free phonons are determined by the polarization operator, which, to the lowest order in the electron–phonon interaction, is proportional to the concentration of electrons. The solution to Eq. (6) will be sought in the approximation diagonal with respect to the quantum numbers $m(\nu, n)$ (the validity of this approximation was discussed earlier in [1]). Within this approximation, the operator

$$\xi_{\alpha}^{c}(t) = \exp\left(\frac{it}{\hbar}(\varepsilon_{\alpha}^{c} - \xi)\right)a_{\alpha}(t) \quad (7)$$

satisfies the equation of motion

$$\dot{\xi}_{mK_x}^{c}(t)$$
$$= -\frac{i}{\hbar}\sum_{\mathbf{q}K_x'}C_{\mathbf{q}}^{c}\langle mK_x|e^{i\mathbf{qr}}|mK_x'\rangle(b_{\mathbf{q}}e^{-i\omega_{\mathbf{q}}t} + b_{-\mathbf{q}}^{+}e^{i\omega_{\mathbf{q}}t}) \quad (8)$$
$$\times\exp\left(\frac{it}{\hbar}eER^2(K_x - K_x')\right)\xi_{mK_x'}^{c}(t).$$

Making allowance for the equality $K_x - K_x' - q_x = 0$ [this equality immediately follows from the matrix element in expression (8)], the equation of motion for $\xi_{mK_x}^{c}(t)$ can be written in the form

$$\dot{\xi}_{mK_x}^{c}(t) = -\frac{i}{\hbar}\sum_{\mathbf{q}K_x'}C_{\mathbf{q}}^{c}\langle mK_x|e^{i\mathbf{qr}}|mK_x'\rangle$$
$$\times[b_{\mathbf{q}}\exp(-i\tilde{\omega}_{\mathbf{q}}t) + b_{-\mathbf{q}}^{+}\exp(i\tilde{\omega}_{\mathbf{q}}t)]\xi_{mK_x'}^{c}(t), \quad (9)$$

where

$$\tilde{\omega}_{\mathbf{q}} = \omega_{\mathbf{q}} - \frac{1}{\hbar}eER^2q_x.$$

The matrix element for the wave functions of the problem under investigation can be easily calculated from the expression

$$\langle mK_x|e^{i\mathbf{qr}}|mK_x'\rangle = V_m^{c}(\mathbf{q})\langle K_x|\exp(i\hat{A}_{\mathbf{q}})|K_x'\rangle. \quad (10)$$

Here,

$$V_m^{c}(\mathbf{q}) = \tilde{V}_n^{c}(q_z)L_{\nu}\left(\frac{1}{2}R^2(q_x^2 + q_y^2)\right)$$
$$\times\exp\left(-\frac{1}{4}R^2(q_x^2 + q_y^2)\right),$$

$$\hat{A}_{\mathbf{q}} = q_x x + q_y\frac{R^2}{\hbar}\hat{P}_x, \quad \hat{P}_x = -i\hbar\frac{\partial}{\partial x},$$

where $\tilde{V}_n^{c}(q_z)$ is the matrix element $\exp(iq_z z)$ for the wave functions of the one-dimensional potential well $U_c(z)$ and $L_{\nu}(z)$ is the Laguerre polynomial.

Taking into account relationship (10), expression (9) can be rewritten as

$$\dot{\xi}^c_{mK_x}(t) = -\frac{i}{\hbar}\sum_{\mathbf{q}K'_x} C^c_{\mathbf{q}} V^c_m(\mathbf{q})\langle K_x|e^{i\hat{A}_{\mathbf{q}}}|mK'_x\rangle \times [b_{\mathbf{q}}\exp(-i\tilde{\omega}_{\mathbf{q}}t) + b^+_{-\mathbf{q}}\exp(i\tilde{\omega}_{\mathbf{q}}t)]\xi^c_{mK'_x}(t). \quad (11)$$

It is a simple matter to demonstrate that the solution to Eq. (11) has the following form [1]:

$$\xi^c_{mK_x}(t) = \sum_{K'_x}\left\langle K_x\left|\exp\left\{\frac{it}{\hbar}\tilde{H}_0\right\}\exp\left\{-\frac{it}{\hbar}(\tilde{H}_0 + W^c_m)\right\}\right|K'_x\right\rangle \xi^c_{mK'_x}, \quad (12)$$

where

$$\tilde{H}_0 = \sum_{\mathbf{q}}\hbar\tilde{\omega}_{\mathbf{q}}b^+_{\mathbf{q}}b_{\mathbf{q}},$$

$$W^c_{\mathbf{q}} = \sum_{\mathbf{q}} C^c_{\mathbf{q}}V^c_m(\mathbf{q})e^{i\hat{A}_{\mathbf{q}}}(b_{\mathbf{q}} + b^+_{-\mathbf{q}}).$$

Therefore, according to expression (7), the time dependence $a_{mK_x}(t)$ can be represented by the relationship

$$a_{mK_x}(t) = \sum_{K'_x}\left\langle K_x\left|\exp\left\{\frac{it}{\hbar}\tilde{H}_0\right\}\exp\left\{-\frac{it}{\hbar}(\tilde{H}_0 + W^c_m)\right\}\right|K'_x\right\rangle \times \exp\left\{-\frac{it}{\hbar}((\varepsilon^c_{mK_x} - \xi))\right\}a_{mK'_x}. \quad (13)$$

A similar relationship holds for the dependence $\alpha_\alpha(t)$.

After substituting the functions $a_{mK_x}(t)$ and $\alpha_{mK_x}(t)$ into relationship (3), the absorption coefficient takes the form

$$K(\Omega) = \frac{8\pi e^2}{n_0 c\hbar\Omega V}\left|\frac{\mathbf{P}_{cv}\boldsymbol{\xi}}{m_0}\right|^2\sum_{mm_1K_xK'_x}\left|\langle m^v|m^c_1\rangle\right|^2 \times\int_{-\infty}^{\infty}dt\exp\left\{\frac{it}{\hbar}(\hbar\Omega - \varepsilon_g - \varepsilon^v_m - \varepsilon^c_{m_1})\right\} \times\left\{\left\langle K_x\left|\exp\left\{\frac{it}{\hbar}\tilde{H}_0\right\}\exp\left\{-\frac{it}{\hbar}(\tilde{H}_0 + W^v_m)\right\}\right|K'_x\right\rangle \times\left\langle K_x\left|\exp\left\{\frac{it}{\hbar}\tilde{H}_0\right\}\exp\left\{-\frac{it}{\hbar}(\tilde{H}_0 + W^c_{m_1})\right\}\right|K'_x\right\rangle\right\}_{\text{ph}}. \quad (14)$$

When writing expression (14), we took into account that the nondegenerated semiconductor systems satisfy the following approximate relationship:

$$\langle\alpha_\alpha a_{\alpha_1}a^+_{\beta_1}\alpha^+_\beta\rangle \approx \delta_{\alpha\beta}\delta_{\alpha_1\beta_1},$$

where $\{\ldots\}_{\text{ph}}$ denotes averaging over the system of free phonons.

The averaging in relationship (14) can be carried out using standard methods of the theory of multiphonon transitions [7], for example, the algebra of Bose operators [8]. Taking into account that averaging over the system of free phonons is performed independently for electrons and holes, we obtain the expression for the absorption coefficient:

$$K(\Omega) = K^{(0)}\sum_{mm_1}\left|\langle m^v|m^c_1\rangle\right|^2 \times\int_{-\infty}^{\infty}dt\exp\left\{\frac{it}{\hbar}(\hbar\Omega - \varepsilon_g - \varepsilon^v_m - \varepsilon^c_{m_1})\right\} \times\exp\{g^c_{m_1}(t) + g^v_m(t)\}. \quad (15)$$

Here, we introduced the following designations:

$$g^i_m(t) = \sum_{\mathbf{q}}\frac{1}{(\hbar\tilde{\omega}_{\mathbf{q}})^2}\left|C^i_{\mathbf{q}}V^i_m(\mathbf{q})\right|^2 \times\{it\tilde{\omega}_{\mathbf{q}} + (2N_{\mathbf{q}} + 1)[\cos\tilde{\omega}_{\mathbf{q}}t - 1] - i\sin\tilde{\omega}_{\mathbf{q}}t\},$$

$$K^{(0)} = \frac{4e^2}{n_0 c\hbar\Omega aR^2}\left|\frac{\mathbf{P}_{cv}\boldsymbol{\xi}}{m_0}\right|^2 \times\exp\left\{-\frac{1}{2}\left(\frac{eER^3}{\hbar^2}\right)^2(m_v + m_c)^2\right\}, \quad (16)$$

where $N_{\mathbf{q}}$ is the distribution function of equilibrium vibrations and a is the quantum-well width.

It should be noted that, in the absence of an electric field ($E = 0$), expression (15) transforms into the relationship derived in [1].

3. In the quasi-classical description of vibrations (this description is justified when the charge carriers interact with long-wavelength acoustic phonons), the function $g^i_m(t)$ can be expanded into a series with respect to t up to and including the terms t^2; that is,

$$g^v_m(t) + g^c_{m_1}(t) = -Bt^2.$$

In the case of rectangular quantum wells, we obtain the following expression for the lower magnetic quantum-well states [$m = m_1 = (0, 1)$]:

$$B = \frac{3kT(E^2_c + E^2_v)}{8\pi\hbar^2\rho v^2R^2a}. \quad (17)$$

Here, E_c and E_v are the deformation potentials for charge carriers in the conduction and valence bands, respectively; ρ is the density of the semiconductor material; v is the velocity of sound in the medium; and T is the temperature.

In the given case, the absorption line (as well as the luminescence line) can be adequately described by a Gaussian function and the electric field does not affect the half-width of the optical spectra and leads only to a shift in the maximum of the absorption (as the electric field strength E increases) toward the long-wavelength range and a decrease in the absorption coefficient. The strong effect of the electric field on the absorption line is observed when the electron interacts with optical vibrations at a frequency $\omega_{\mathbf{q}} = \omega_0$. If the electron–phonon interaction is relatively weak, the absorption spectrum (as well as the luminescence spectrum) is characterized by zero-phonon lines and vibrational satellites due to the absorption of the electromagnetic wave with the simultaneous absorption or emission of a vibrational quantum.

The quantum wells GaN/AlGaN and InGaN/InN are promising objects for the observation of zero-phonon lines and vibrational satellites in the fundamental absorption range. At present, it is these quantum systems that have been actively studied because of the need to increase the lifetime of ultraviolet lasers [9, 10] and to use these structures in the next generation of semiconductor electronic devices at high temperatures [11].

Vibrational satellites have been observed experimentally in both undoped and silicon-doped narrow quantum wells GaN/AlGaN [12]. In this respect, investigation into the optical properties of these quantum systems and elucidation of the mechanisms responsible, for example, for spontaneous emission in actual instrument structures [13] have been an important problem.

The specific features of the zero-phonon line in an electric field can be conveniently analyzed using the method developed in [14] and described in detail in [15]. For this analysis, we use the relationships

$$\left.\frac{1-\cos\tilde{\omega}_{\mathbf{q}}t}{\tilde{\omega}_{\mathbf{q}}^2}\right|_{|t|\to\infty} = \pi|t|\delta(\tilde{\omega}_{\mathbf{q}}) + \frac{P}{\tilde{\omega}_{\mathbf{q}}^2},$$

$$\left.\frac{\sin\tilde{\omega}_{\mathbf{q}}t}{\tilde{\omega}_{\mathbf{q}}^2}\right|_{|t|\to\infty} = \pi\delta'(\tilde{\omega}_{\mathbf{q}})\operatorname{sgn}t, \qquad (18)$$

where P is the principal value.

Then, we can write

$$g(t) = g^c(t) + g^v(t) \approx \frac{it}{\hbar}\tilde{\Delta} - M - \Gamma|t|. \qquad (19)$$

For simplicity, we disregard the second equality in relationships (18).

In the above relationships, we introduced the following designations:

$$\tilde{\Delta} = \sum_{\mathbf{q}} V_{\mathbf{q}}\frac{P}{\hbar\tilde{\omega}_{\mathbf{q}}}, \quad M = \sum_{\mathbf{q}} V_{\mathbf{q}}(2N+1)\frac{P}{(\hbar\tilde{\omega}_{\mathbf{q}})^2},$$

$$\Gamma = \sum_{\mathbf{q}} V_{\mathbf{q}}(2N+1)\frac{\pi}{\hbar^2}\delta(\tilde{\omega}_{\mathbf{q}}),$$

$$V_{\mathbf{q}} = \left|C_{\mathbf{q}}^c V_m^c(\mathbf{q})\right|^2 + \left|C_{\mathbf{q}}^v V_{m_1}^v(\mathbf{q})\right|^2,$$

$$N = \left[\exp\left(\frac{\hbar\omega_0}{kT}\right) - 1\right]^{-1}.$$

Now, we take into account relationship (18) and the interaction of the electron with acoustic vibrations. After integration with respect to the variable t in relationship (15), the expression describing the zero-phonon line takes the following form (in this case, we consider the optical transition in rectangular quantum wells between the lowest lying magnetically dimensional ith states):

$$K(\Omega) = K^{(0)}\omega_0 e^{-M}\sqrt{\frac{\pi}{4B}}\left\{\exp\left(\frac{1}{4B}(\Gamma + i\Delta)^2\right)\right.$$
$$\left.\times\left[1 - \Phi\left(\frac{1}{2\sqrt{B}}(\Gamma + i\Delta)\right)\right] + \text{h.c.}\right\}, \qquad (20)$$

where

$$\Delta = \frac{1}{\hbar}\left[\hbar\Omega - \varepsilon_g - \hbar\omega_c/2 - \hbar\omega_v/2 - E_{1c} - E_{1v}\right.$$
$$\left. + \frac{c^2E^2}{2H^2}(m_c + m_v) + \tilde{\Delta}\right],$$

and $\Phi(z)$ is the probability function.

It follows from relationship (20) that, in the case when $\Gamma/\sqrt{4B} > 1$, the zero-phonon line can be described by a Lorentzian curve with the half-width $2\hbar\Gamma$. For $\Gamma/\sqrt{4B} < 1$, the zero-phonon line can be described by a Gaussian curve with the half-width $2\hbar\sqrt{B\ln 2}$.

For a rectilinear quantum well with infinitely high walls at $(a/R)^2 = \pi^2\hbar\omega_c/(2E_{1c}) \ll 1$ [for quantum wells with standard parameters, this inequality is satisfied to high accuracy; for example, for $a = 100$ Å and $H = 1$ T,

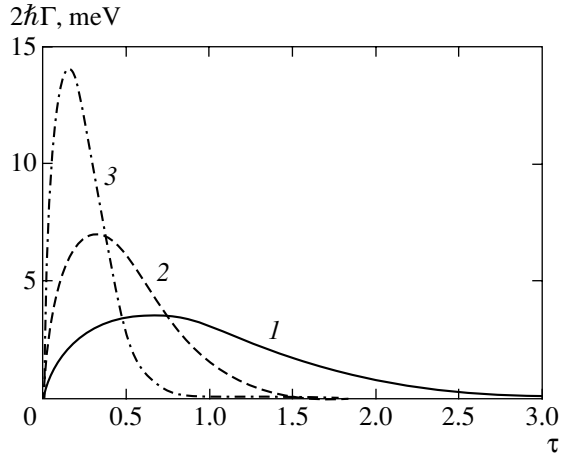

Fig. 1. Dependences of the half-width of the zero-phonon line on the electric field strength $\tau = \frac{\hbar\omega_0}{2eER_0}$ ($R_0 = 2.56 \times 10^{-6}$ cm is the magnetic length in a magnetic field of 1.0 T) for different magnetic field strengths H: (*1*) 0.25, (*2*) 1.0, and (*3*) 4.0 T.

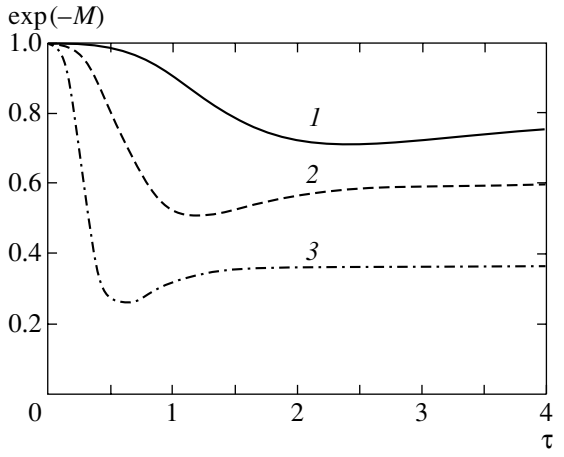

Fig. 2. Dependences of exp(–M) (the intensity of the zero-phonon line attributed to the electron–phonon interaction) on the electric field strength $\tau = \frac{\hbar\omega_0}{2eER_0}$ ($R_0 = 2.56 \times 10^{-6}$ cm) for different magnetic field strengths H: (*1*) 0.25, (*2*) 1.0, and (*3*) 4.0 T.

we have $(a/R)^2 \sim 10^{-1}$], the parameters Γ and M can be calculated directly from the following expressions [16]:

$$\Gamma = \Gamma_0 \tau e^{-\tau^2} K_0(\tau^2),$$

$$M = M_0 \tau^3 e^{-\tau^2} [I_0(\tau^2) - I_1(\tau^2)],$$

$$\Gamma_0 = \frac{e^2 c_0 (2N+1)}{2\hbar R}, \quad M_0 = \frac{4\pi e^2 c_0 (2N+1)}{\hbar\omega_0 R}, \quad (21)$$

$$\tau = \frac{\hbar\omega_0}{2eER}, \quad c_0 = \frac{1}{\varepsilon_0} - \frac{1}{\varepsilon_\infty},$$

where ε_0 and ε_∞ are the static and high-frequency permittivities, respectively; $I_\nu(z)$ is the modified Bessel function; and $K_0(z)$ is the Macdonald function with the zero index.

Figure 1 shows the dependences of the half-width of the zero-phonon line on the electric field strength. It can be seen from this figure that an increase in the electric field strength leads to an increase in the half-width of the zero-phonon line ($\Gamma/\sqrt{4B} > 1$). Therefore, the dominant contribution to the intensity of the zero-phonon line arises when the energy acquired by the electron as a function of the magnetic length is of the order of the limiting energy of the optical phonon: $eER \approx \hbar\omega_0$. Taking into account the universally accepted parameters for rectangular quantum wells (for the GaN/AlGaN quantum well at $H = 1$ T, $c_0 = 0.09$, $N = 0.5$, and $\hbar\omega_0 = 0.03$ eV, we have $E \approx 2 \times 10^4$ V/cm), the half-width of the zero-phonon line is of the order of 7 meV. Figure 2 presents the dependences of exp(–M) (i.e., the contribution to the intensity of the zero-phonon line associated with the electron–phonon interaction) on the electric field strength. It can be seen from Fig. 2 that, when $E < 10^4$ V/cm ($\tau > 2$), the quantity exp(–M) is virtually independent of the electric field strength. Consequently, the parameters of the zero-phonon line are determined only by the dependence of the quantity $K^{(0)}$ on the electric field strength E.

In order to investigate the frequency dependence of the vibrational satellite in relationship (15), we expand the exponent into a series in terms of $g(t)$ and, for the first vibrational satellites, restrict our treatment to the terms describing the single-phonon processes. As a result, we obtain

$$K_{ps}(\Omega) = K^{(0)} \frac{2\tau e^2 c_0}{R\hbar\omega_0 q_0^2} \{(N+1)\exp(-\tau^2(q_0+1)^2) \times K_0[\tau^2(q_0+1)^2] + N\exp(-\tau^2(q_0-1)^2) \times K_0[\tau^2(q_0-1)^2]\}, \quad (22)$$

where $q_0 = \Delta/\omega_0$.

In relationship (22), the first term describes the absorption of light with emission of an optical vibrational quantum and the second term characterizes the absorption of the electromagnetic wave with subsequent absorption of a nondispersive phonon. When $q_0 = \pm 1$, i.e., at the maximum of the vibrational satellite, there arise logarithmic divergences $K_0(x) \sim \ln(2/x)$, $x \ll 1$) [16]. These divergences can be eliminated if one takes into account the interaction of the electrons with acoustic phonons (as was done in the analysis of the zero-phonon line). In this case, the maxima of the absorption of the vibrational satellites are determined

by the parameter B, i.e., by the deformation potential and temperature.

REFERENCES

1. É. P. Sinyavskiĭ and E. I. Grebenshchikova, Zh. Éksp. Teor. Fiz. **116** (6), 2069 (1999) [JETP **89** (6), 1120 (1999)].
2. L. V. Butov, A. Zrenner, and M. Shayegan, Phys. Rev. B: Condens. Matter. **49** (19), 14054 (1994).
3. A. I. Ansel'm, *Introduction to the Theory of Semiconductors* (Nauka, Moscow, 1978) [in Russian].
4. A. G. Aronov and G. E. Pikus, Zh. Éksp. Teor. Fiz. **51** (3), 505 (1966) [Sov. Phys. JETP **24**, 339 (1966)].
5. B. Lax, *Proceedings of the 7th International Conference on Physics of Semiconductors, Paris, France, 1964* (Dunod, Paris, 1964), p. 253.
6. R. Kubo, J. Phys. Soc. Jpn. **12**, 570 (1957).
7. Yu. E. Perlin, Usp. Fiz. Nauk **80** (4), 553 (1963).
8. W. H. Louisell, *Radiation and Noise in Quantum Electronics* (McGraw-Hill, New York, 1964; Nauka, Moscow, 1972).
9. S. Nakamura, M. Senoh, S. Nagahama, N. Iwasa, S. Yamada, T. Matsushita, H. Kiyoku, and Y. Sugimoto, Appl. Phys. Lett. **68**, 3269 (1996).
10. L. Akasaki, S. Sota, H. Sakai, T. Tanaka, M. Koike, and H. Amano, Electron. Lett. **32**, 1105 (1996).
11. S. K. Islam, F. C. Jain, G. Zhao, and E. Heller, Int. J. Infrared Millimeter Waves **19**, 1633 (1998).
12. K. C. Zeng, J. Y. Lin, H. X. Jiang, A. Salvador, G. Popovici, H. Tang, W. Kim, and H. Morkos, Appl. Phys. Lett. **70** (10), 1368 (1997).
13. A. V. Andrianov, V. Yu. Nekrasov, N. M. Shmidt, E. E. Zavarin, A. S. Usikov, N. N. Zinov'ev, and M. N. Tkachuk, Fiz. Tekh. Poluprovodn. (St. Petersburg) **36** (6), 679 (2002) [Semiconductors **36** (6), 641 (2002)].
14. M. A. Krivoglaz, Fiz. Tverd. Tela (Leningrad) **6** (4), 1707 (1964) [Sov. Phys. Solid State **6** (4), 1340 (1964)].
15. Yu. E. Perlin and B. S. Tsukerblat, *Effect of Electronic–Vibrational Interaction in Optical Spectra of Impurity Paramagnetic Ions* (Shtiintsa, Kishinev, 1974) [in Russian].
16. I. S. Gradshteĭn and I. M. Ryzhik, *Tables of Integrals, Sums, Series, and Products* (Gos. Izd. Fiz. Mat. Lit., Moscow, 1962) [in Russian].

Translated by O. Moskalev

Physics of the Solid State, Vol. 47, No. 10, 2005, pp. 1964–1971. Translated from Fizika Tverdogo Tela, Vol. 47, No. 10, 2005, pp. 1886–1893.

LOW-DIMENSIONAL SYSTEMS AND SURFACE PHYSICS

Tamm Interface States in ZnSe/BeTe Periodic Heterostructures

A. S. Gurevich*, V. P. Kochereshko*, A. V. Platonov*, B. A. Zyakin*, A. Waag, and G. Landwehr*****

**Ioffe Physicotechnical Institute, Russian Academy of Sciences, ul. Politekhnicheskaya 26, St. Petersburg, 194021 Russia*
e-mail: alexei.gurevich@mail.ioffe.ru
***Braunschweig Technical University, Braunschweig, 38106 Germany*
****Physikalisches Institut der Universität Würzburg, Würzburg, 97074 Germany*

Received December 16, 2004

Abstract—The spectral response of the lateral optical anisotropy of periodic undoped type-II ZnSe/BeTe heterostructures with nonequivalent interfaces was studied by ellipsometry. The spectra revealed two types of features corresponding to optical transitions with energies lying in the bandgap. The position of features of the first type does not depend on the heterostructure period. Features of the second type shift toward lower energies with decreasing period of the heterostructure. This behavior is explained in terms of a model taking into account the existence of electronic and hole interface states and of a mixed-type interface state. *© 2005 Pleiades Publishing, Inc.*

1. INTRODUCTION

As far back as 1932, Tamm predicted the existence of carrier states localized on the surface of a semiconductor crystal [1]. Such states are characterized by one-dimensional localization along the surface normal and by an energy falling into the bandgap of a bulk semiconductor. Seventeen years later, the existence of similar states in the proximity of a sharp interface separating two different semiconductor materials was first conjectured [2]. Like a surface, the interface between two different semiconductors is a strong perturbation of the periodic crystal potential.

The possible existence of electronic states localized on a heterointerface and with an energy inside the bandgap was theoretically substantiated in [3] in the tight binding approximation without inclusion of spin–orbit coupling. Hole interface states localized on the InAs/AlSb type-II heterointerface were studied theoretically in [4], likewise in the tight-binding approximation but with inclusion of the spin–orbit interaction. In order to account for the temperature dependence of the carrier concentration and the anomalously high electron mobility in InAs/AlSb quantum wells (QWs), Kroemer *et al.* [5] postulated the existence of localized states of carriers with a high lateral mobility at the heterointerfaces bounding the QWs.

Heterointerfaces may considerably affect not only the transport but also optical properties of semiconductor structures. It is an established fact that the lowered point symmetry of an interface separating two zinc-blende semiconductors gives rise to lateral anisotropy in the optical properties of semiconductor heterostructures [6]. In the case of ZnSe/BeTe periodic structures with nonequivalent interfaces, this becomes manifest in a difference between the effective refraction coefficients of the heterostructure as a whole in the [110] and $[1\bar{1}0]$ crystallographic directions. The difference between both the real and imaginary parts of these refractive indices was found to be the largest in the spectral region corresponding to spatially direct excitonic transitions in such structures [7].

This communication reports on an ellipsometric study within a broad spectral range of the dependence of the lateral optical anisotropy on the period of ZnSe/BeTe heterostructures with nonequivalent interfaces. Two types of features corresponding to optical transitions with energies within the bandgap were found to exist in the spectral response of the optical anisotropy. Measurements showed that features of the first type remain practically in the same position when the heterostructure period is reduced from 345 to 45 Å. By contrast, features of the second type undergo a monotonic displacement (ranging up to 110 meV) toward lower energies with decreasing heterostructure period. The observed behavior suggests the presence in the structures under study of carrier states localized on the ZnSe/BeTe heterointerfaces.

2. EXPERIMENT

We studied ZnSe/BeTe periodic heterostructures with type-II band offsets, grown by molecular beam epitaxy on GaAs substrates in the [001] direction. The band diagram of the heterostructures is shown in Fig. 1. The heterostructures studied had 20 periods each. The ZnSe/BeTe layer thicknesses were 230/115, 100/50, 40/20, and 30/15 Å. Due to the reasonably chosen thickness ratio of the ZnSe and BeTe layers (2 : 1), as well as to the small difference in the lattice constants between ZnSe, BeTe, and GaAs (within 0.4%), these

heterostructures have almost no strain. The samples were not intentionally doped.

The bandgap of ZnSe at the Γ point is E_g^{Γ}(ZnSe) = 2.8 eV [8], and the ZnSe bandgap associated with the *X* valley is E_g^{X}(ZnSe) = 4.6 eV [9]. The corresponding values for BeTe are E_g^{Γ}(BeTe) = 4.5 eV [10] and E_g^{X}(BeTe) = 2.6 eV [11]. BeTe is an indirect-gap semiconductor.

There are three types of optical interband transitions in the heterostructures under study (Fig. 1): spatially direct transitions in ZnSe layers (DT), spatially direct transitions connecting valence band states with states in the *X* valley of BeTe (DxT), and spatially indirect transitions (IT) between electrons in ZnSe layers and holes in the BeTe layers mediated by the wave-function overlap of the carriers penetrating under the barriers.

Unlike a bulk semiconductor of T_d point symmetry with zinc-blende structure, an ideal interface and, hence, a single heterojunction has point symmetry C_{2v}. In a heterostructure with a ZnSe QW surrounded by BeTe barriers and possessing nonequivalent interfaces of the type Zn–Te on the left (right) of the QW and Be–Se on the right (left) of the QW, the C_{2v} lowered symmetry is retained for the QW and, hence, for the heterostructure as a whole [12]. As shown by direct ellipsometric measurements of the optical constants, this gives rise to a natural anisotropy of the effective dielectric permittivity of ZnSe/BeTe heterostructures in the blue-green region of the spectrum [7]. The optical anisotropy induced by the low symmetry of the interfaces was used in the present study of carrier states localized on the heterointerfaces separating ZnSe from BeTe.

An ellipsometer with a rotating compensator was employed to measure the spectral response of the lateral optical anisotropy of ZnSe/BeTe heterostructures with nonequivalent interfaces [13]. The measurements were performed at a sample temperature of 77 K. The spectral response of the ratio of the Fresnel complex amplitude reflectances [14]

$$\rho(E) = \frac{r_p}{r_s} \equiv \rho_{\text{abs}}(E)\exp[i\Delta(E)] \qquad (1)$$

was measured at a fixed angle of incidence of light on the sample for a fixed orientation of the [110] and $[1\bar{1}0]$ crystallographic axes relative to the plane of incidence (specified by the rays striking the sample and reflected from it). Next, the sample was rotated through 90° about the heterostructure growth axis and the spectral response of the Fresnel coefficient ratio was measured again with all the other conditions kept unchanged. In Eq. (1), r_p and r_s are the Fresnel complex amplitude reflectances for the *p* and *s* polarized waves, respectively; ρ_{abs} is the modulus of the Fresnel coefficient ratio showing the extent to which the *p* wave is reflected more weakly than is the *s* wave; Δ is the argument of the Fresnel coefficient ratio actually representing the phase shift between the *p* and *s* waves generated in reflection; and *E* is the photon energy. Because the period of the ZnSe/BeTe heterostructures studied is much smaller than the wavelength of light in the spectral interval covered, these structures can be treated as a uniform, optically anisotropic film whose interaction with light can be described by a permittivity tensor [15].

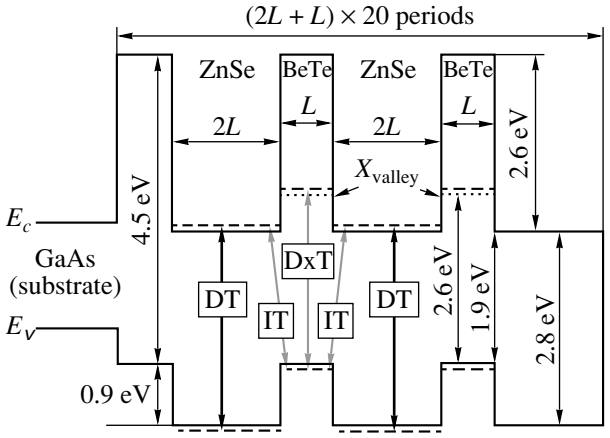

Fig. 1. Band diagram of ZnSe/BeTe periodic heterostructures with type-II band offsets. All the structures studied contained 20 ZnSe/BeTe periods. The BeTe layer thicknesses *L* of the heterostructures were 115, 50, 20, and 15 Å. In the diagram: DT refers to spatially direct optical transitions in ZnSe layers, DxT to spatially direct optical transitions involving BeTe valence band and *X* valley states, and IT to spatially indirect optical transitions between electrons in ZnSe layers and holes in BeTe layers, which are made possible by wave-function overlap of the carriers penetrating under the barriers.

Figure 2 displays the spectral dependences of ρ_{abs} and Δ measured at an angle of incidence θ_0 = 53.40°. These dependences were measured with the $[1\bar{1}0]$ crystallographic axes of the samples set perpendicular to the plane of incidence of light. Filled circles refer to measurements made on a ZnSe/BeTe heterostructure with a period of 345 Å (the total thickness of the heterostructure is 6900 Å), and empty circles refer to a heterostructure with a period of 45 Å (the total heterostructure thickness is 900 Å). The plots exhibit a periodic variation in ρ_{abs} and Δ with increasing photon energy, which fits the pattern of interference of light waves reflected from the boundaries between the heterostructure and the external medium and between the heterostructure and the substrate. At photon energies corresponding to spatially direct optical transitions in the ZnSe layers, the pattern of reflection from the samples under study changes. For the thickest heterostructure with the 230/115 Å layer thicknesses, one observes a sharp variation of ρ_{abs} and Δ due to strong absorption of the light wave reflected from the heterostructure–substrate interface (DT feature). For the structure with the 30/15 Å

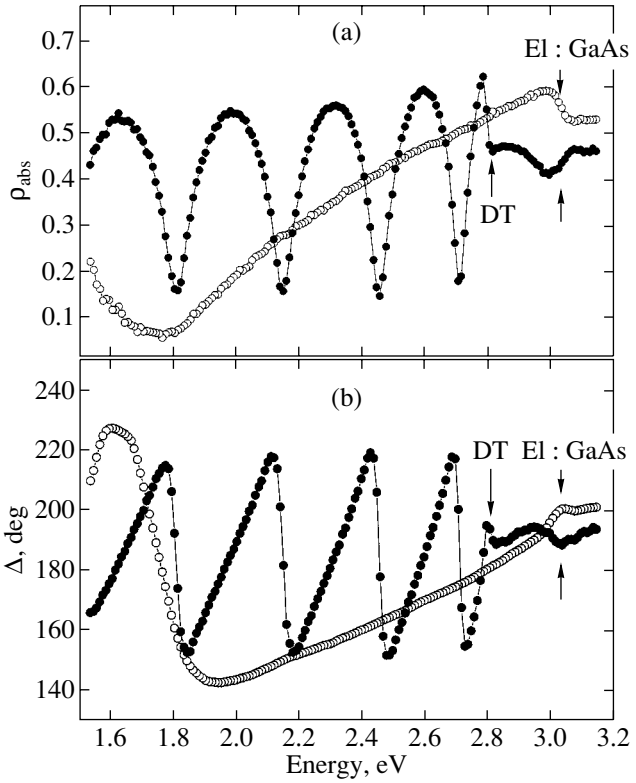

Fig. 2. Spectral responses of ρ_{abs} and Δ measured on ZnSe/BeTe heterostructures with periods of 345 (filled circles) and 45 Å (empty circles). The symbol DT identifies features associated with spatially direct optical transitions in the ZnSe layers, and El : GaAs is the manifestation of a feature in the GaAs substrate refractive index. The measurements were conducted at an angle of incidence of light on the sample $\theta_0 = 52.95°$ and a sample temperature of 77 K.

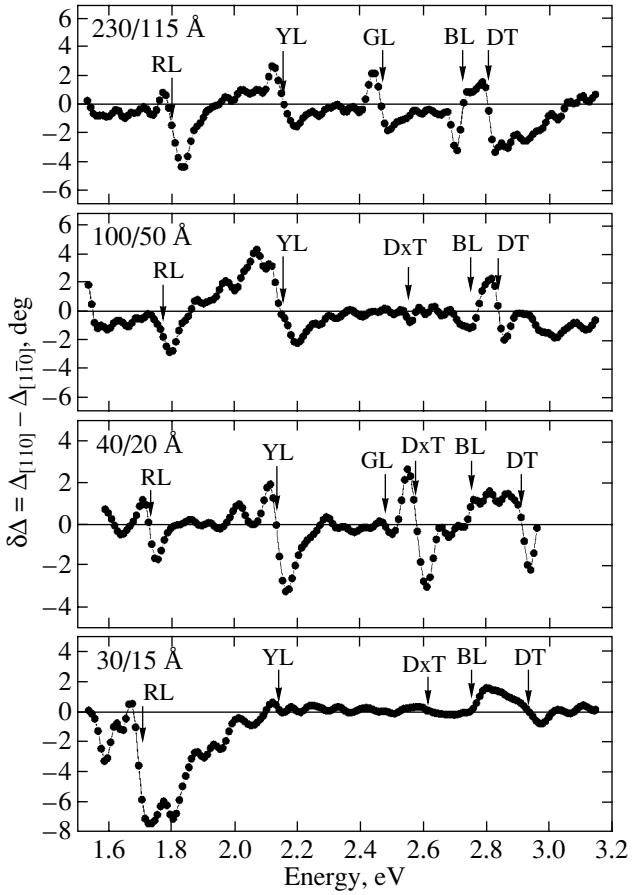

Fig. 3. Spectral response of the lateral optical anisotropy measured on four periodic heterostructures with ZnSe/BeTe layer thicknesses of 230/115 Å, 100/50 Å, 40/20 Å, and 30/15 Å, respectively. Symbols DT and DxT denote the features characteristic of the heterostructures under study that correspond to spatially direct interband transitions in ZnSe and BeTe layers, respectively. Symbols RL, YL, GL, and BL denote features whose energies lie in the bandgap and which have not been observed earlier. Angle of incidence $\theta_0 = 52.95°$. The sample temperature is 77 K.

layer thicknesses, the features corresponding to spatially direct transitions are obscured by those caused by the strong variation of the substrate refraction coefficient (E_1 : GaAs feature). This feature originates from interband optical transitions involving the states in the GaAs *L* valley [16].

In the case where light is reflected from the anisotropic-layer–isotropic-substrate system, the quantities ρ_{abs} and Δ are determined, in particular, by the orientation of the permittivity tensor axes in the layer relative to the plane of incidence. Therefore, the nonzero quantity

$$\delta\Delta = \Delta_{[1\bar{1}0]} - \Delta_{[110]} \quad (2)$$

describes the anisotropy of optical constants in the plane of the heterostructures under study. In Eq. (2), $\Delta_{[1\bar{1}0]}$ is the reflection-induced phase difference between *p*- and *s*-polarized waves measured in the case where the $[1\bar{1}0]$ crystallographic axis of the sample is perpendicular to the plane of incidence and $\Delta_{[110]}$ is the analogous quantity measured in the case where the $[1\bar{1}0]$ axis is parallel to the plane of incidence (i.e., after the sample has been rotated through 90° about the growth axis).

3. EXPERIMENTAL RESULTS

Figure 3 presents the spectral dependences of δΔ characterizing the lateral optical anisotropy. These dependences are measured on four periodic heterostructures with layer thicknesses 230/115, 100/50, 40/20, and 30/15 Å, respectively.

These spectral responses exhibit two groups of lines that shift toward higher energies with decreasing heterostructure period. In the energy interval E = 2.80–2.93 eV, all samples exhibit DT features related to spatially direct excitonic transitions in ZnSe layers. Such transitions are characterized, first, by a shift toward higher energies with decreasing ZnSe layer thickness (which corresponds to an increase in the carrier size

quantization energy) and, second, by a distinct sign reversal of the signal, which is caused by the difference in the sign of the lateral optical anisotropy between optical transitions involving light and heavy holes [7]. The second group of lines, DxT, which shifts to shorter wavelengths with decreasing heterostructure period, is related to spatially direct transitions in the BeTe layers. This semiconductor is an indirect-gap material, and the observed features should be assigned to transitions between valence band states and states in the X valley in BeTe [10].

In addition, the above plots exhibit three groups of features whose spectral positions remain practically unchanged as compared to the spatially direct transitions in the ZnSe and BeTe layers. We introduce the notation for these features according to the color of the spectral interval in which they are located. At an energy $E \approx 2.75$ eV, all samples produce a blue-line (BL) feature whose width increases with decreasing heterostructure period. In ZnSe/BeTe samples with layer thicknesses 230/115 and 40/20 Å at an energy $E \approx 2.47$ eV, green-line (GL) features are observed whose amplitude, just as in the case of DxT transitions, reveals a dependence on the angle of incidence of light. At $E \approx 2.15$ eV, in all samples are detected one more group, namely, yellow lines (YL), whose spectral position likewise does not change noticeably when the heterostructure period decreases from 345 to 45 Å.

Finally, at energies below 1.80 eV, all samples produce a red line (RL) that undergoes a monotonic shift to lower energies. This shift ranges up to 110 meV in the ZnSe/BeTe heterostructure period range studied, a figure comparable to the increase in interband transition energy resulting from quantum confinement.

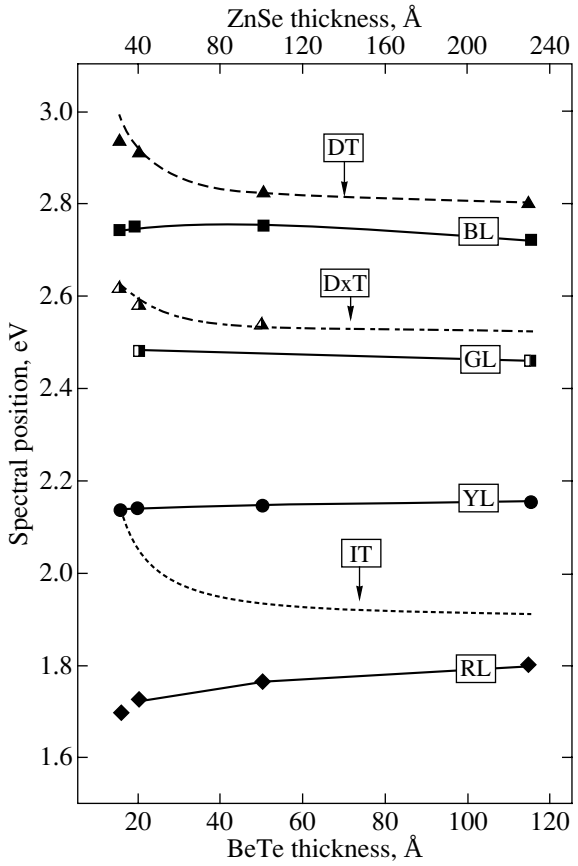

Fig. 4. Spectral position of features in the optical anisotropy spectra plotted vs. the ZnSe/BeTe heterostructure period. The filled and half-filled triangles denote characteristic features corresponding to spatially direct optical transitions in the ZnSe and BeTe layers, respectively. The dashed and dash-dotted curves display the energies of these transitions (DT and DxT, respectively) calculated in the effective mass approximation. The dotted line corresponds to calculated energies for spatially indirect transitions (IT). RL, YL, GL, and BL refer to features not observed earlier and falling into the bandgap region.

4. INTERPRETATION OF THE EXPERIMENTAL RESULTS

Figure 4 plots the spectral positions of the observed features versus the ZnSe and BeTe layer thickness (period) of the heterostructures studied. Filled and half-filled triangles denote features corresponding to spatially direct transitions in the ZnTe and BeTe layers, respectively (i.e., the DT and DxT features). The dashed and dash-dotted curves refer to the energies of spatially direct optical transitions in ZnSe and BeTe layers, respectively, calculated in the effective mass approximation. The dotted curve relates to the energies of spatially indirect interband optical transitions (IT in Fig. 1). Because of the small overlap (~5 Å) of the wave functions of electrons and holes penetrating under the barriers and, hence, of the weak oscillator strength, such transitions manifest themselves only weakly at liquid-nitrogen temperature in the spectral response of $\delta\Delta$ [see Eq. (2)].

The calculation of the interband optical transition energies versus the layer thickness in the heterostructures was based on the following estimates of the carrier effective masses. For ZnSe, the effective masses of electrons and heavy holes at the Γ points (expressed in free electron masses) were assumed to be m_e^* (ZnSe) = 0.16 and m_{hh}^* (ZnSe) = 0.70, respectively [8]. The effective electron mass in an X valley of BeTe was taken to be m_X^* (BeTe) = 6.0 [10]. The other carrier masses were chosen using the empirical rule of the effective carrier mass being proportional to the bandgap of the material: m_e^* (BeTe) = 0.25, m_{hh}^* (BeTe) = 1.15, and m_X^* (ZnSe) = 3.80. The ground-state energy of a heavy hole localized on the ZnSe barrier was calculated according to [17].

In Fig. 4, filled squares, half-filled squares, and filled circles denote the BL, GL, and YL features, whose positions remain practically unchanged as the layer thickness in the heterostructures decreases. The diamonds trace the spectral position of the RL feature,

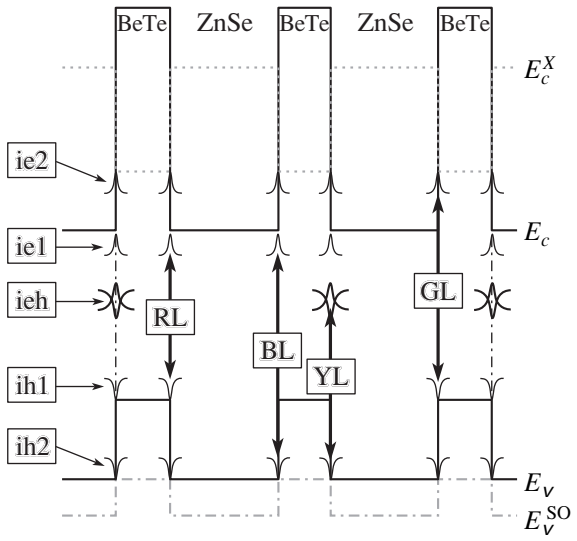

Fig. 5. Energy positions of interface states in ZnSe/BeTe heterostructures. The electron-type interface states ie1 and ie2 are due to conduction-band-level discontinuities at the Γ point (E_c, solid broken line) and in the *X* valley (E_c^X, dashed broken line), respectively. The hole interface states ih1 and ih2 are connected with the offsets of the valence band of light and heavy holes (E_v, solid broken line) and of the spin–orbit-split valence band (E_v^{SO}, dash-dotted, broken line), respectively. The ieh symbol refers to a mixed-type interface state. Bold vertical arrows specify observed optical transitions between the RL, YL, GL, and BL interface states.

which is seen to undergo a noticeable low-energy shift with decreasing heterostructure period.

The four types of spectral features (BL, GL, YL, RL) observed in the spectral dependences of the lateral optical anisotropy cannot be accounted for by interband optical transitions, first, because of their spectral positions and, second, because they do not undergo a high-energy shift with a decrease in the ZnSe and BeTe layer thicknesses. In addition, the amplitudes of the BL, GL, YL, and RL features in the optical-anisotropy spectra are of the same order of magnitude as those of the features associated with spatially direct transitions. (Note also that these features are not seen in the spectral responses of ρ_{abs} and Δ against the background of spatially direct interband transitions; see Fig. 2.)

Finally, the observed features cannot be assigned to the structural properties or defects of any concrete heterointerface, because this effect was observed on more than one heterostructure, each containing a sufficiently large number (20) of interfaces. This behavior suggests the existence of Tamm interface states in the structures under study, i.e., of carrier states strongly localized on heterointerfaces as a result of a sharp jump in the parameters of the crystal periodic potential.

The energy positions of the observed features, as well as theoretical results obtained in the tight-binding approximation [3, 4], which provide information on the energy positions of interface states, suggest the following pattern of optical transitions between interface states in the heterostructures studied here (Fig. 5). To interpret the results obtained, one has to take into account the electronic and hole interface states (IS) associated with the conduction and valence band offsets at the heterointerfaces, respectively. The electronic interface state (IS) ie1 originates from the conduction band offset at the Γ point. The electronic IS ie2 is connected with the conduction-band *X* valley discontinuity (dotted broken line in Fig. 5). In turn, the hole IS ih1 is related to the heavy and light hole valence band discontinuity and the hole IS ih2, to the spin–orbit-split valence band offset (dash-dotted broken line). The offsets of the corresponding bands were taken from [9, 10].

This approach identifies the RL features observed in the spectral dependences of heterostructure optical anisotropy with optical transitions between the electronic ie1 and hole ih1 interface states (Fig. 5). The GL features originate from optical transitions between electronic ie2 IS and hole ih1 IS. Finally, the BL features should be assigned to optical transitions connecting the electronic ie1 IS with the hole ih2 IS.

Taking into account the above four ISs does not explain the YL feature. To understand the origin of this feature, one has to take into account the ieh IS, which, because of its energy position, is apparently a mixed-type IS (Fig. 5). The possible existence of states of this type was mentioned in [18], a study of the generalized boundary conditions at heterointerfaces performed in terms of the many-band smooth-envelope method. By introducing a mixed ieh IS, one can assign the observed YL feature to optical transitions between the ieh IS and the hole ih2 IS.

Considered within this model, the dependence of the spectral position of the observed features on the heterostructure layer thickness can be interpreted in the following way. As follows from the general properties of the Schrödinger equation, imposing a boundary condition on the wave function of a particle and its derivative with respect to the particle coordinate is equivalent to adding a zero-dimensional potential to the Hamiltonian at the same point in space [19]. This approach is applicable to an electron in a semiconductor crystal as well. According to [20], the effect of boundary conditions associated with a sharp heterointerface can be included in crossing over from a multiband effective-mass method to a single-band approximation by adding a point potential of the type $\gamma\delta(x - x_0)$ to the Hamiltonian, where x_0 is the heterointerface coordinate and γ is the potential strength. With the above boundary conditions, we consider a state localized on two heterointerfaces, namely, a state localized in a one-dimensional potential symmetric with respect to the origin

$$U(x) = U_{QW}(x) - \gamma[\delta(x + a) + \delta(x - a)]. \quad (3)$$

Here, a is one-half of the distance between the interfaces, γ is a positive parameter determining the strength of the δ function, and $U_{QW}(x)$ describes the potential energy in a single QW with finite barriers of height U_0 and width $2a$ (Fig. 6). The corresponding one-dimensional Schrödinger equation has the form

$$-\frac{\hbar^2}{2m}\frac{d^2\psi}{dx^2} + U_{QW}(x)\psi - \gamma[\delta(x+a) + \delta(x-a)]\psi = E\psi. \quad (4)$$

The ground-state wave function can be represented as

$$\psi(x) = \begin{cases} A\exp(\eta_0 x) & x < -a \\ A\dfrac{\exp(-\eta_0 a)}{\cosh(q_0 a)}\cosh(q_0 x) & -1 < x < a \\ a\exp(-\eta_0 x) & x > a. \end{cases} \quad (5)$$

Here, η_0 is the particle wave vector in the region of space $x < -a$ and $a < x$, q_0 is the particle wave vector in the region of space $-a < x < a$, and A is a constant found from the normalization condition. In Eq. (4) and henceforth, m is the particle effective mass. Figure 6 presents the probability distribution for a particle with the wave function defined by Eq. (5). The absolute value of the energy of the state E_0 and the relation connecting the quantities η_0 and q_0 are given by

$$E_0 = \frac{\hbar^2 q_0^2}{2m}, \quad \eta_0^2 - q_0^2 = \frac{2mU_0}{\hbar^2}. \quad (6)$$

The continuity condition imposed on the first derivative of the wave function with respect to the coordinate at points $x = \pm a$ yields a transcendental equation for the wave vector and, hence, the particle ground-state energy:

$$\tanh(q_0 a) = \frac{2m\gamma}{\hbar^2}\frac{1}{q_0} - \sqrt{\frac{2mU_0}{\hbar^2 q_0^2} + 1}. \quad (7)$$

This equation has a solution only if the condition

$$\gamma^2 > \frac{\hbar^2 U_0}{2m} \quad (8)$$

is met. The physical meaning of this condition can be formulated as follows: the force acting on a particle due to the δ-function potential and attracting this particle to the interface must be stronger than the force caused by the potential step, which tends to repel the particle away from the interface. Figure 7 displays the dependences of the left- and right-hand sides of Eq. (7) on wave vector q_0 (for the case where condition (8) is satisfied). In the case where the distance between the interfaces far exceeds the characteristic localization length of a particle at a single δ-function QW

$$a \gg L, \quad L \approx \frac{\hbar^2}{m\gamma}, \quad (9)$$

the left-hand side of Eq. (7) can be replaced by unity. This yields the energy of the state (its magnitude):

$$E_0 = \frac{m\gamma^2}{2\hbar^2} - \frac{U_0}{2}\left(1 - \frac{U_0\hbar^2}{4m\gamma^2}\right). \quad (10)$$

A decrease in the distance between the interfaces will not bring about a noticeable change in the IS energy or,

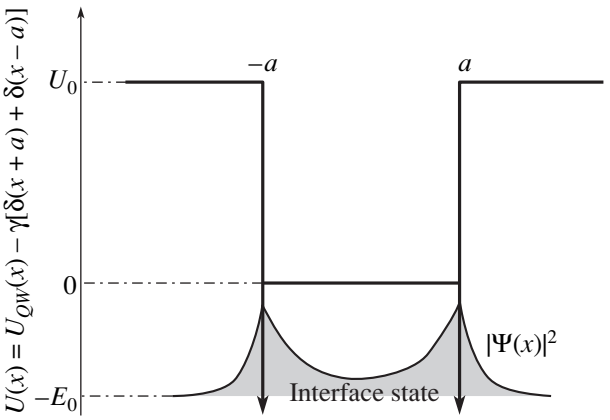

Fig. 6. Carrier localization on two interfaces.

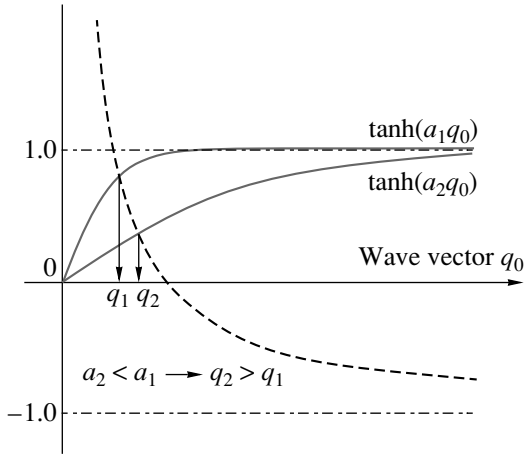

Fig. 7. Explanatory graph to the calculation of the wave vector of a carrier localized on two interfaces. Solid curves represent the left-hand side of Eq. (7) for different interface separations. The dashed curve represents the right-hand side of Eq. (7). As the interface separation decreases, the wave vector and the absolute value of the energy of the interface state grow, implying that the energy of the optical transition connecting the electronic and hole interface states decreases.

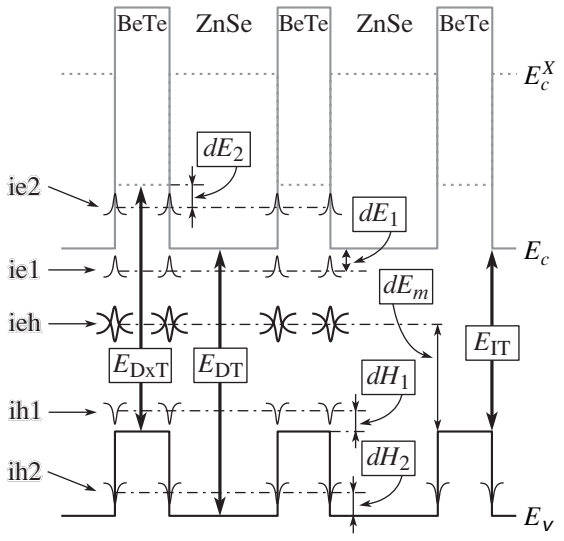

Fig. 8. Explanatory graph to the estimation of the energy position of interface states with respect to the ZnSe and BeTe band edges. The dotted broken line is the conduction-band *X*-valley level. Solid broken lines: E_c is the conduction band level at the Γ point and E_v is the heavy and light hole valence-band level.

hence, in the energies of the optical transitions between them. This situation is observed for the BL, GL, and YL optical transitions (Fig. 5), whose spectral positions do not change markedly as the heterostructure period decreases (Fig. 4).

The situation changes when the distance between the interfaces is comparable to the characteristic length L. As seen from Fig. 7, as a decreases, the wave vector q_0 corresponding to the solution of Eq. (7) increases. Hence, the absolute value of the energy of a localized particle defined by Eq. (6) will grow and the energies of the optical transitions between the ISs will decrease. This situation applies to the RL transitions (Fig. 5), whose low-energy shift ranges up to 110 meV in the heterostructure period range studied (Fig. 4).

The present study relates to heterostructures with nonequivalent interfaces of the Zn–Te and Be–Se type. The corrections to the above model for this nonequivalence can be included within perturbation theory by introducing into the Schrödinger equation (3) a perturbing potential of the kind $V(x) = \beta[\delta(x + a) - \delta(x - a)]$. This will not, however, affect the pattern of the dependence of the ground-state energy on interface separation. Depending on the actual relative magnitude of the interface separation and characteristic length L (as the interfaces are brought closer to one another), the absolute value of the ground-state energy either will not change noticeably or will increase, thus decreasing the energies of the optical transitions connecting the interface states.

Let us estimate the range within which the IS energy levels lie (Fig. 8). For the longest period structure with layer thicknesses 230/115 Å, the IS energies will be closest to those of the corresponding ISs on a single interface. We can write

$$\begin{cases} dE_1 + dH_1 \\ = E_{IT} - E_{RL} \approx 1.90\ \text{eV}–1.80\ \text{eV} \approx 100\ \text{meV}, \\ dE_1 + dH_2 \\ = E_{DT} - E_{BL} \approx 2.80\ \text{eV}–2.75\ \text{eV} \approx 50\ \text{meV}, \\ dE_2 + dH_1 \\ = E_{DxT} - E_{GL} \approx 2.55\ \text{eV}–2.47\ \text{eV} \approx 80\ \text{meV}. \end{cases} \quad (11)$$

Here, dE_1 and dE_2 are the energy levels of the electronic ie1 and ie2 ISs reckoned from the ZnSe conduction band and BeTe *X* valley edges, respectively (Fig. 8); dH_1 and dH_2 are the energy levels of the hole ISs reckoned from the ZnSe and BeTe heavy and light hole valence band edges, respectively; E_{RL}, E_{BL}, and E_{GL} are the optical transition energies between the electronic and hole ISs ie1–ih1, ie1–ih2, and ie2–ih1, respectively; E_{DT} and E_{DxT} are the energies of spatially direct interband optical transitions in the ZnSe and BeTe layers; and E_{IT} is the energy of spatially indirect interband transitions in the heterostructures studied. Equations (11) can be easily transformed to

$$\begin{aligned} dH_1 - dH_2 &= 50\ \text{meV}, \\ dE_1 - dE_2 &= 20\ \text{meV}, \\ dE_1 + dH_2 &= 50\ \text{meV}. \end{aligned} \quad (12)$$

Allowing for the quantities introduced by us earlier being nonnegative, Eqs. (12) yield the ranges of possible values of the IS localization energies in the system studied:

$$\begin{cases} 20 < dE_1 < 50\ \text{meV} \\ 50 < dH_1 < 80\ \text{meV} \\ dE_2 < 30\ \text{meV} \\ dH_2 < 30\ \text{meV}. \end{cases} \quad (13)$$

The energy dE_m of the ieh IS reckoned from the top of the BeTe heavy and light hole valence band (Fig. 8) is given, in turn, by the relation

$$E_{YL} = dE_m + \delta E_v - dH_2. \quad (14)$$

Here, E_{YL} is the energy of optical transitions between the ieh and the hole ih2 ISs, δE_v is the heavy and light hole valence band offset in the heterostructures studied, and dH_2 is the energy of the hole ih2 IS. It follows from Eqs. (13) and (14) that the ieh state energy is confined in the interval

$$1.25 < dE_m < 1.28\ \text{eV}.$$

Note that this energy level lies comparatively close (90 meV lower) to halfway between the centers of the ZnSe and BeTe bandgaps and far away from the band edges of these materials. This suggests that this state is apparently of mixed type, unlike the ie1, ie2, ih1, and ih2 ISs, which are satellites of the conduction band and valence band of the semiconductors making up the heterostructures under study.

5. CONCLUSIONS

We have reported on an ellipsometric study of the low-temperature spectral relations governing lateral optical anisotropy of the ZnSe/BeTe periodic heterostructures with nonequivalent interfaces. The heterostructures studied have various periods. The spectra of the lateral optical anisotropy revealed two types of features corresponding to optical transitions with energies in the bandgap. Unlike interband optical transitions, the spectral position of features of the first type does not depend on the period of the heterostructures studied. As the heterostructure period decreases, features of the second type undergo a monotonic shift toward lower energies comparable to the increase in interband optical transition energy induced by size quantization. The observed behavior can be interpreted within a model allowing for the existence of two types of electronic and two types of hole Tamm interface states, as well as of a mixed-type interface state. The localization of such states along the heterostructure growth axis is accounted for by the discontinuity in the properties of the periodic crystal potential at a heterointerface. By using the effective mass approximation, with the interface represented by a δ-function attractive potential, the energy of optical transitions between interface states has been shown to decrease with decreasing heterostructure period. By analyzing the energies of optical transitions connecting interface states, the range of interface state energy levels has been determined.

ACKNOWLEDGMENTS

This study was supported by the Russian Foundation for Basic Research, project no. 04-02-16674-a. A.S.G. and A.V.P acknowledge partial support of the work by the program of support for leading scientific schools (project no. 2199.2003.2).

REFERENCES

1. I. Tamm, Phys. Zs. Sowjetunion **1**, 733 (1932).
2. H. M. James, Phys. Rev. **76**, 1611 (1949).
3. A. A. Gorbatsevich and I. V. Tokatly, Pis'ma Zh. Éksp. Teor. Fiz. **67** (6), 393 (1998) [JETP Lett. **67** (6), 416 (1998)].
4. M. O. Nestoklon, Int. J. Nanosci. **2** (6), 411 (2003).
5. H. Kroemer, C. Nguyen, and B. Brar, J. Vac. Sci. Technol. B **10** (4), 1769 (1992).
6. O. Krebs and P. Voisin, Phys. Rev. Lett. **77** (9), 1829 (1996); A. V. Platonov, V. P. Kochereshko, E. L. Ivchenko, G. V. Mikhailov, D. R. Yakovlev, M. Keim, W. Ossau, A. Waag, and G. Landwehr, Phys. Rev. Lett. **83** (17), 3546 (1999).
7. A. S. Gurevich, V. P. Kochereshko, A. V. Platonov, A. Waag, D. R. Yakovlev, and G. Landwehr, Fiz. Tverd. Tela (St. Petersburg) **46** (4), 759 (2004) [Phys. Solid State **46** (4), 780 (2004)].
8. H. J. Lozykowsky and V. K. Shastri, J. Appl. Phys. **69** (5), 3235 (1991).
9. J. R. Chelikowsky and M. L. Cohen, Phys. Rev. B: Solid State **14** (2), 556 (1976).
10. M. Nagelstraβer, H. Dröge, H.-P. Steinrück, F. Fischer, T. Litz, A. Waag, G. Landwehr, A. Fleszar, and W. Hanke, Phys. Rev. B: Condens. Matter **58** (16), 10 394 (1998).
11. A. Fleszar and W. Hanke, Phys. Rev. B: Condens. Matter **62** (4), 2466 (2000).
12. E. L. Ivchenko, A. A. Toropov, and P. Voisin, Fiz. Tverd. Tela (St. Petersburg) **40** (10), 1925 (1998) [Phys. Solid State **40** (10), 1748 (1998)].
13. P. S. Hauge, Surf. Sci. **96** (1), 108 (1980).
14. M. Born and E. Wolf, *Principles of Optics*, 4th ed. (Pergamon, Oxford, 1969; Nauka, Moscow, 1970).
15. E. L. Ivchenko and G. E. Pikus, *Superlattices and Other Heterostructures: Symmetry and Optical Phenomena* (Springer, Berlin, 1997).
16. P. Lautenschlanger, M. Garriga, S. Logothetidis, and M. Cardona, Phys. Rev. B: Condens. Matter **35** (17), 9174 (1987).
17. H. Luo, N. Dai, F. C. Zhang, N. Samarth, M. Dobrowolska, J. K. Furdyna, C. Parks, and K. Ramdas, Phys. Rev. Lett. **70** (9), 1307 (1993).
18. A. V. Rodina, A. Yu. Alekseev, Al. L. Efros, M. Rosen, and B. K. Meyer, Phys. Rev. B: Condens. Matter **65**, 125302 (2002).
19. A. I. Byaz', Ya. B. Zel'dovich, and A. M. Perelomov, *Scattering, Reactions, and Decays in Relativistic Quantum Mechanics* (Nauka, Moscow, 1971) [in Russian].
20. É. E. Takhtamirov and V. A. Volkov, Zh. Éksp. Teor. Fiz. **116** (5), 1843 (1999) [JETP **89**, 1000 (1999)].

Translated by G. Skrebtsov

Physics of the Solid State, Vol. 47, No. 10, 2005, pp. 1972–1979. Translated from Fizika Tverdogo Tela, Vol. 47, No. 10, 2005, pp. 1894–1900.

LOW-DIMENSIONAL SYSTEMS AND SURFACE PHYSICS

Quantum Corrections to the Conductivity of a Natural $Nd_{2-x}Ce_xCuO_4$ Superlattice

G. M. Min'kov*, A. I. Ponomarev*, A. A. Sherstobitov*, S. G. Novokshonov*, and A. A. Ivanov**

** Institute of Metal Physics, Ural Division, Russian Academy of Sciences, ul. S. Kovalevskoĭ 18, Yekaterinburg, 620219 Russia*

e-mail: grigori.minkov@usu.ru

*** Moscow Institute of Engineering Physics, Kashirskoe sh. 31, Moscow, 115410 Russia*

Received October 12, 2004; in final form, February 2, 2005

Abstract—Temperature and magnetic field dependences of the resistivity and Hall coefficient in layered single-crystal $Nd_{2-x}Ce_xCuO_4$ ($x = 0.12$) films are experimentally investigated and analyzed. It is shown that this material clearly exhibits quantum effects characteristic of 2D semiconductor structures: negative magnetoresistance caused by suppression of the interference quantum correction by a magnetic field, a near-logarithmic temperature dependence of the conductivity, and a temperature dependence of the Hall coefficient related to *e–e* interaction. It is shown that, when analyzing experimental data, it is necessary to take interlayer transitions into account. Such an approach provides quantitative agreement between experiment and the standard theory of quantum corrections. © *2005 Pleiades Publishing, Inc.*

1. INTRODUCTION

The $Nd_{2-x}Ce_xCuO_4$ compound occupies a special place among the oxide superconductors with a perovskite structure. Standard high-temperature superconductor materials contain conducting CuO_2 layers with oxygen pyramids (YBaCuO, BiSrCaCuO) or octahedra (LaSrCuO), whereas optimally annealed NdCeCuO crystals contain CuO_2 layers without apical oxygen atoms; i.e., the CuO_2 layers form quasi-two-dimensional (2D) planes at a distance of $a = 6$ Å from each other. Therefore, a NdCeCuO single crystal can be considered a selectively doped system of quantum wells (CuO_2 layers) separated by barriers doped by cerium (buffer NdO layers). This statement is based on the fact that macroscopic 3D-crystals of layered high-temperature superconductor materials exhibit strongly pronounced 2D properties of charge carriers.

Undoped Nd_2CuO_4 compounds are insulators. Doping Nd_2CuO_4 by cerium and lowering the content of oxygen down to the stoichiometric value produces *n*-type conduction in the CuO_2 layers of a $Nd_{2-x}Ce_xCuO_4$ crystal. As excess electrons pass to the CuO_2 planes, charged Ce^{4+} impurity centers randomly distributed over the lattice produce an electric field in the buffer layer between these planes and scattering by this field determines, apparently, the charge carrier mobility.

Calculations of the NdCeCuO band structure [1] have shown that the Fermi level is located in the $pd\sigma$ band formed by $3d(x^2 - y^2)$ orbitals of copper and $p\sigma(x, y)$ orbitals of oxygen. This $pd\sigma$ band has a pronounced 2D character, with almost no dispersion in the *c* direction perpendicular to the conducting CuO_2 planes (*ab* planes). Because of low transition probabilities between the planes, the conductivity of NdCeCuO crystals in the normal phase is highly anisotropic, $\sigma_{ab}/\sigma_c \geq 10^3$ [2–4]. Due to the quasi-2D nature of charge carriers, the temperature and magnetic field dependences of σ_{ab} of NdCeCuO crystals are determined substantially by quantum corrections to the Drude conductivity. There are two types of quantum corrections to the conductivity: (i) corrections produced by the interference of electron waves propagating in opposite directions along closed trajectories [weak localization (WL)] and (ii) corrections produced by electron–electron (*e–e*) interaction, which can be separated into corrections in the diffusion channel (the Altshuler–Aronov term) and corrections in the Cooper channel (also known as corrections due to superconducting fluctuations). These corrections increase in magnitude with decreasing temperature or with increasing disorder and basically determine the transport in 2D systems at low temperatures.

There are a few publications reporting on the observation and study of the effects due to quantum corrections to the conductivity σ_{ab} of $Nd_{2-x}Ce_xCuO_4$ crystals. For example, a linear dependence of the resistivity on $\ln T$ (one of the signatures of 2D weak localization) has been observed at $T < T_c$ in a $Nd_{2-x}Ce_xCuO_4$ sample with $x = 0.15$, where the superconducting state is suppressed by a magnetic field [5]. Highly anisotropic negative magnetoresistance in fields $\mathbf{B} \parallel CuO_2$ and $\mathbf{B} \perp CuO_2$, which is also characteristic of 2D weak localization, has been observed in nonsuperconducting

$Nd_{2-x}Ce_xCuO_4$ samples with $x = 0.11$ [6], 0.15 [7], and 0.18 [8]. Furthermore, in analyzing the negative magnetoresistance in a magnetic field perpendicular to the *ab* planes, the authors of [7] estimated the spin relaxation time to be $\tau_{so} > 5 \times 10^{-11}$ s and showed that this time is much greater than the phase relaxation time τ_φ. By processing negative-magnetoresistance curves, the authors of [6] found the temperature dependence of the phase relaxation time τ_φ to be $1/\tau_\varphi \sim T^{0.4}$. The authors of [9] used the theory of quantum corrections to conductivity both in the Cooper [10] and diffusion [11, 12] channels, and their results are in qualitative agreement with the experiment performed on $Nd_{2-x}Ce_xCuO_4$ single-crystal films. In [13], the $\rho_{ab}(T, H)$ dependences were studied for a series of $Nd_{2-x}Ce_xCuO_4$ single-crystal films with $x = 0.12$–0.18 and $k_F l = 2$–150 (k_F is the Fermi quasimomentum, l is the mean free path) and all three signatures of 2D weak localization were observed: a logarithmic temperature dependence of resistivity, negative magnetoresistance in a magnetic field perpendicular to the *ab* plane, and anisotropy of magnetoresistance in fields $\mathbf{B} \parallel CuO_2$ and $\mathbf{B} \perp CuO_2$.

From the above short survey of the studies of quantum corrections to the conductivity of layered high-temperature superconductor materials, we see that those studies are mainly fragmentary. For example, there is no understanding as to the reason for the unusual temperature dependence of the phase relaxation time $1/\tau_\varphi \sim T^{0.4}$, the contribution of the *e*–*e* interaction in the diffusion channel, and the role played by interlayer transitions. Moreover, in spite of the numerous studies of quantum corrections for 2D semiconductor structures, such as GaAs/AlGaAs and Ge/GeSi, there are no reliable data on the role of the *e*–*e* interaction in the Cooper channel. This is not surprising, since the contribution of this interaction is determined by the parameter $(T - T_c)$ and must be important at temperatures close to the temperature of the superconducting transition, which is absent in usual 2D semiconductor structures. In this respect, the study of quantum corrections to the conductivity of layered high-temperature superconductors is of special interest, since, by changing the material composition and oxygen content, it is possible to change T_c over a wide range and, therefore, to perform experiments at a known and controllable value of the parameter $(T - T_c)$. In our opinion, in order to clarify the role of the *e*–*e* interaction in the Cooper channel, it is necessary to understand well (not only qualitatively but also quantitatively) the role of the interference contribution and the contribution due to the *e*–*e* interaction in the diffusion channel in nonsuperconducting structures. It is to this problem that the present study is devoted. We analyze the temperature and magnetic field dependences of the conductivity and the Hall coefficient in nonsuperconducting $Nd_{2-x}Ce_xCuO_{4+\delta}$ ($x = 0.12$).

In this study, we show that a three-dimensional $Nd_{2-x}Ce_xCuO_4$ crystal clearly exhibits quantum effects characteristic of 2D semiconductor structures, namely, negative magnetoresistance due to suppression of the interference quantum correction by a magnetic field, a near-logarithmic temperature dependence of the conductivity, and a temperature dependence of the Hall coefficient related to *e*–*e* interaction. We also show that interlayer transitions result in an apparent saturation of the phase relaxation time with a decrease in temperature, in small values of the magnetoresistance prefactor, and in a weaker temperature dependence of the conductivity and its deviation from a logarithmic dependence.

2. SAMPLES

Epitaxial $Nd_{2-x}Ce_xCuO_{4+\delta}$ films were synthesized by the method of pulsed laser sputtering. The technological process may be divided into two stages.

(i) Epitaxial film growth in vacuum. The original ceramic target was sputtered by a focused laser beam with subsequent deposition of the material of the target onto a heated single-crystal (100)-oriented $SrTiO_3$ substrate 5×10 mm in size. The substrate temperature was 800°C, the pressure during sputtering was 0.8 mm Hg, the residual gas was air, and the target was a sintered ceramic $Nd_{2-x}Ce_xCuO_{4+\delta}$ pellet of given composition.

In the single-crystal films prepared in this way, the CuO_2 planes (the *ab* plane) are parallel to the plane of the substrate. $Nd_{2-x}Ce_xCuO_{4+\delta}$ samples 120-Å thick with a fixed cerium content of $x = 0.12$ were synthesized.

(ii) Film annealing in vacuum. To obtain the stoichiometric composition, samples were subjected to heat treatment (annealing) at $T = 780$°C at a pressure $p = 10^{-2}$ mm Hg over 60 min.

According to the data from x-ray structural studies, single-crystal $Nd_{2-x}Ce_xCuO_{4+\delta}$ films deposited on $SrTiO_3$ substrates are epitaxial (001)-oriented films.

Using photolithography, samples were obtained in the form of a double cross with a 1-mm-wide central strip and with potential contacts separated by a distance of 3 mm. After etching, silver contacts were deposited on the samples by laser sputtering in vacuum. The resistivity ρ_{ab} was measured using the standard four-probe method, and the Hall coefficient was measured for two directions of the electric current and magnetic field.

3. EXPERIMENTAL RESULTS AND DISCUSSION

The temperature dependences of the resistivity, the magnetoresistance, and the Hall coefficient of single-crystal $Nd_{2-x}Ce_xCuO_4$ films with $x = 0.12$ were studied in the range $1.5 \le T \le 40$ K. The temperature dependences of the conductivity and of the change in the conductivity $\sigma(B) - \sigma(0) \equiv 1/\rho_{xx}(B) - 1/\rho(0)$ in a field perpendicular to the plane of a sample ($\mathbf{B} \perp ab$) are shown

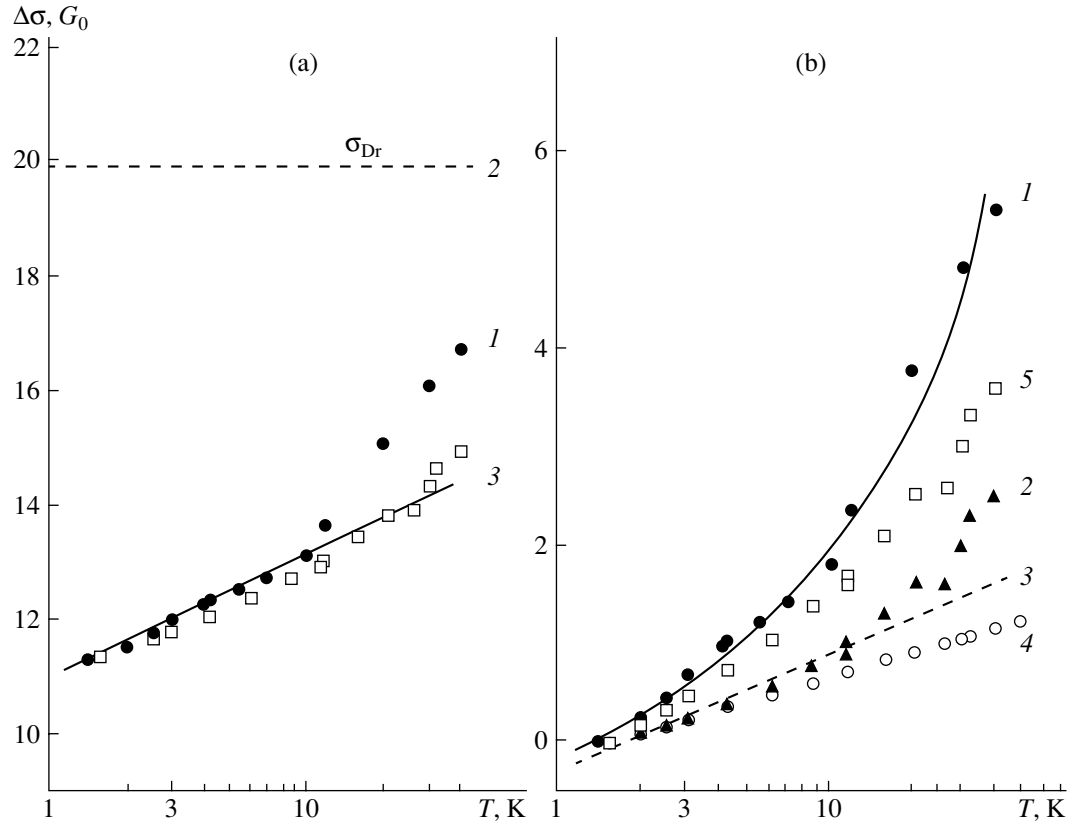

Fig. 1. (a) Temperature dependence of the conductivity (measured in units of $G_0 = e^2/\pi h = 1.23 \times 10^{-5}\ \Omega^{-1}$) at $B = 0$; (*1*) the experimental dependence of the conductivity, (*2*) the Drude conductivity (see text), and (*3*) the calculated temperature dependence of $\sigma(T) = \sigma(1.5\ \text{K}) - \Delta\sigma^{WL}(T) - \Delta\sigma^{ee}(T)$ with the parameters determined from the analysis of the magnetoresistance and Hall effect. (b) Temperature dependence of $\Delta\sigma(T) = \sigma(T) - \sigma(1.5\ \text{K})$; (*1*) experiment, (*2*) the interference correction to the conductivity $\Delta\sigma^{WL}(T)$–$\Delta\sigma^{WL}(1.5\ \text{K})$, (*3*) the $\sigma(T) \approx a + 0.5\ln(T)$ dependence, (*4*) the *e*–*e* interaction correction $\Delta\sigma^{ee}(T)$–$\Delta\sigma^{ee}(1.5\ \text{K})$, and (*5*) the quantity $\Delta\sigma(T)$–$\Delta\sigma(1.5\ \text{K})$ including the WL correction and correction due to the *e*–*e* interaction.

in Figs. 1 and 2 (in these figures, the conductivity is recalculated per layer and measured in units of $G_0 = e^2/\pi h = 1.23 \times 10^{-5}\ \Omega^{-1}$). We see in Figs. 1 and 2 that the $\sigma(T)$ dependence is almost logarithmic over a rather wide temperature range from 1.5 to 10 K (Fig. 1a) and that the magnetoresistance is negative (Fig. 2).

As noted previously [5–9, 13], the conductivity of layered high-temperature superconducting cuprates at temperatures $T < 30$–40 K is determined to a large degree by quantum corrections. We first analyze the negative magnetoresistance. As a first approximation, we assume that the contributions from each of the CuO_2 layers to the conductivity are the same and independent; i.e., we neglect the transitions between the layers. In this case, the magnetoresistance of one layer related to the suppression of the interference quantum correction to the conductivity by a magnetic field is described by the known expression [14]

$$\Delta\sigma(B) = \sigma(B) - \sigma(0) = \alpha G_0 \text{Hi}(x),$$
$$\text{Hi}(x) = \psi\left(\frac{1}{2} + \frac{1}{x}\right) + \ln(x), \quad x = \frac{B}{B_\varphi}, \qquad (1)$$

where ψ is the digamma function; $B_\varphi = \dfrac{\hbar}{4eD\tau_\varphi}$, $D = \sigma_{Dr}/e^2 N_F$ is the diffusion coefficient; N_F is the density of states at the Fermi level, which is equal to $N_F = m^*/\pi\hbar^2$ in the 2D case; τ_φ is the phase relaxation time; σ_{Dr} is the Drude conductivity; and α is a numerical factor (prefactor), which is unity in the theory of weak localization. The reasons for introducing a factor $\alpha < 1$ into Eq. (1) will be discussed below. Expression (1) is obtained in the diffusion approximation, where $\tau_\varphi/\tau_p \gg 1$, $B \ll B_{tr} = B_\varphi\tau_\varphi/\tau_p$, and τ_p is the momentum relaxation time. The physical parameters of the sample are determined from the conductivity and Hall coefficient at $T = 30$ K, where the quantum corrections to the conductivity are small. We obtain $\tau_p = 3.7 \times 10^{-15}$ s, an electron concentration per layer $n_s = 2.5 \times 10^{14}\ \text{cm}^{-2}$, and an electron mean free path $l = 1.6 \times 10^{-7}$ cm. The effective mass is set equal to the free electron mass ($m^* = m_0$).

When fitting formula (1) to experimental dependences, we use two fitting parameters, α and τ_φ. The theoretical $\Delta\sigma(B)$ dependences obtained using this procedure and the temperature dependences of the fitting

parameters τ_φ and α are shown in Figs. 2 and 3. We note that $\tau_\varphi/\tau_p > 2 \times 10^2$ and $B \ll B_{tr} = 120$ T; so the condition of applicability of the diffusion approximation is reliably satisfied. We see that the magnetoresistance calculated from Eq. (1) (Fig. 2) agrees very well with the experimental curves but only for values of α that are appreciably smaller than unity (Fig. 3b). The temperature dependence of the fitting parameter τ_φ is close to the theoretical dependence $\tau_\varphi \sim 1/T$ at high temperatures and deviates from it appreciably at $T < 8$–10 K (Fig. 3a). A similar behavior of $\tau_\varphi(T)$ in nonsuperconducting $Nd_{2-x}Ce_xCuO_4$ was observed in [6]. Before discussing the behavior of $\tau_\varphi(T)$, we consider the reasons for the low values of α.

We can indicate at least two reasons for a decrease in the prefactor α: (i) the contribution of the *e*–*e* interaction in the Cooper channel and (ii) the transitions between the layers.

First, let us discuss the role of the *e*–*e* interaction in the Cooper channel. As shown in [11], two terms contribute to the magnetoresistance in low magnetic fields:

$$\begin{aligned} \Delta\sigma_1(B) &= -\beta(g)G_0\varphi_1(B), \\ \Delta\sigma_2(B) &= -g(T)G_0\varphi_2(B). \end{aligned} \qquad (2)$$

The first term (known as the Maki–Thompson correction) has the same field dependence as the interference correction in Eq. (1); i.e., $\varphi_1(B) = \mathrm{Hi}(B)$. The function $\beta(g)$ is always positive, does not depend on the sign of the "bare" constant $g(T)$, and depends only on its magnitude. The second term (density-of-states term) has somewhat different field and temperature dependences (the function $\varphi_2(B)$ can be found in [12]). The constant $g(T)$ is positive (negative) for effective repulsion (attraction) between electrons. In order to estimate to what extent the contributions $\Delta\sigma_1$ and $\Delta\sigma_2$ can change the prefactor α, we calculated the total change in conductivity $\Delta\sigma(B) = G_0\mathrm{Hi}(B) + \Delta\sigma_1(B) + \Delta\sigma_2(B)$ for various values of $g(1.5\ \mathrm{K})$ and the value of τ_φ given in the caption to Fig. 2 for $T = 1.5$ K. Describing this magnetoresistance, as well as the experimental $\Delta\sigma(B)$ dependences, by expression (1) and using α and τ_φ as fitting parameters, we can also obtain good agreement in this case. If the quantity $g(T)$ is negative, the value of the prefactor appears to be close to unity and is virtually independent of temperature, in contradiction with experiment. This circumstance is related to the fact that, in low magnetic fields ($B \ll B_{tr}$), the corrections $\Delta\sigma_1$ and $\Delta\sigma_2$ almost completely compensate each other. At a positive value $g(1.5\ \mathrm{K}) = 0.34$, the prefactor decreases to a value close to the experimental value $\alpha = 0.45$ but becomes very strongly temperature-dependent. For example, already at $T = 5$ K, the prefactor decreases to $\alpha = 0.07$, in disagreement with the experimental results shown in Fig. 3b. Thus, the low value of the prefactor α is not related to the contribution of the *e*–*e* interaction in the Cooper channel.

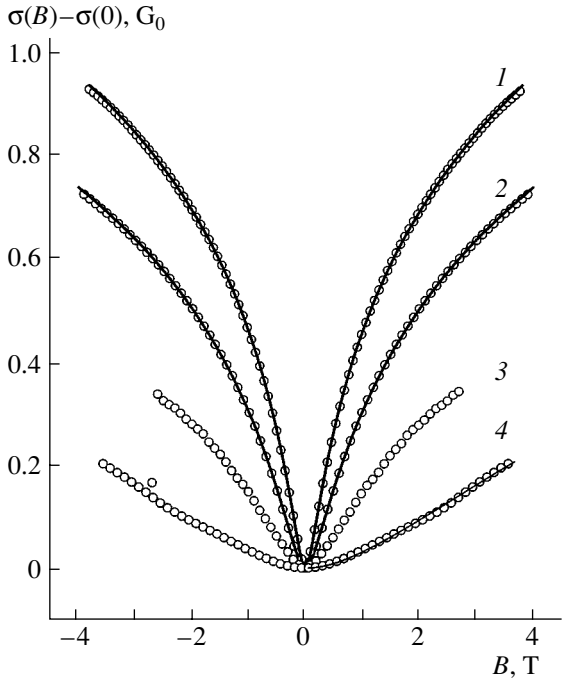

Fig. 2. Magnetic field dependence of the change in conductivity (magnetoconductivity) at various temperatures. Points represent experimental data, and solid lines are theoretical dependences (disregarding the interlayer transitions) calculated from Eq. (1) for various values of the parameters α and τ_φ. (*1*) $T = 1.5$ K, $\alpha = 0.42$, and $\tau_\varphi = 6.9$ ps; (*2*) $T = 4.2$ K, $\alpha = 0.41$, and $\tau_\varphi = 4.1$ ps; (*3*) $T = 11.5$ K, $\alpha = 0.42$, and $\tau_\varphi = 2.2$ ps; and (*4*) $T = 30$ K, $\alpha = 0.60$, and $\tau_\varphi = 0.51$ ps.

Another possible reason for the low value of α and for the deviation of the temperature dependence of τ_φ^{-1} from a linear function can be the nonzero probability of carrier transitions between the layers, which we disregarded in the preliminary data processing. The effect of transitions between the layers in multilayer structures and intersubband transitions in structures with several filled quantum-confinement subbands on the interference correction to the conductivity has been considered in several studies (see, for example, [15–18]).

Qualitatively, the effect of transitions between the layers can be easily explained using the following model. When moving in a field of random scatterers, an electron has a nonzero probability of returning to the starting point. The electron can pass along the corresponding closed path both clockwise and counterclockwise. If, during the motion of the electron along this path, the phase of the wave function is not broken, the interference of these paths is constructive and results in an increase in the backscattering probability, i.e., in a decrease in the conductivity. Thus, the total interference correction is proportional to the probability of an electron returning to the starting point in a time smaller than the phase-breaking time τ_φ. For example, let us consider a structure consisting of two parallel layers. If

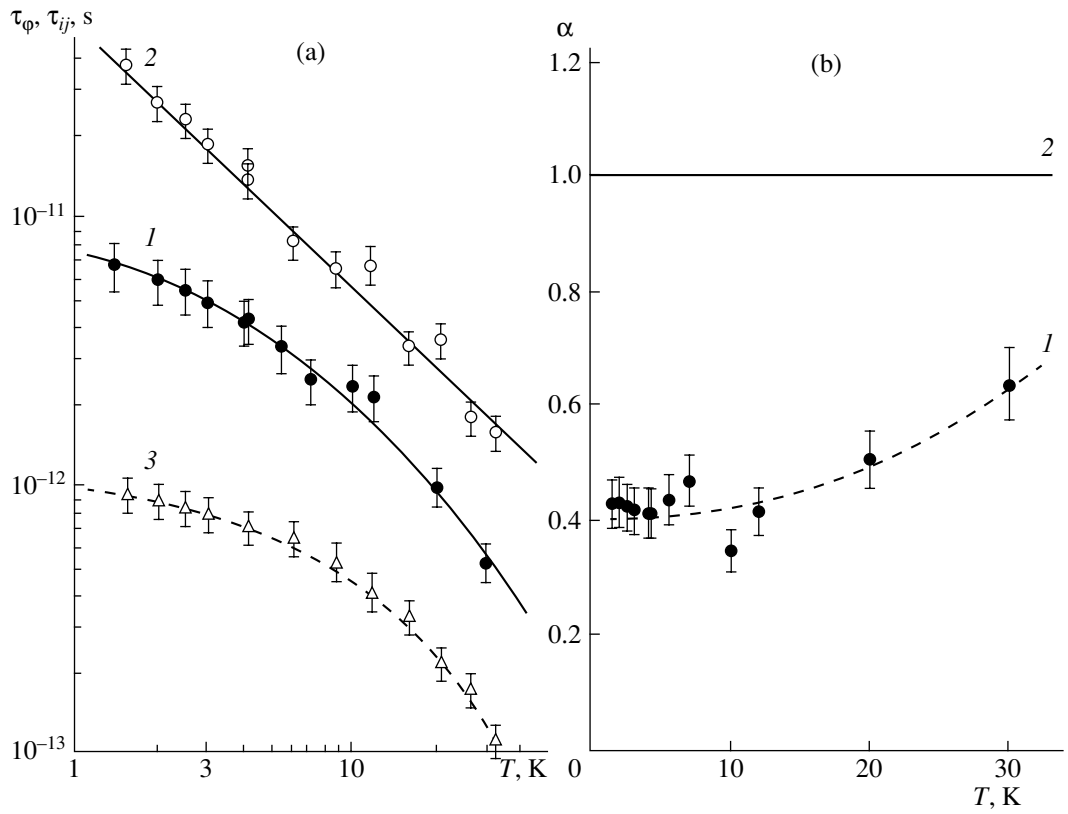

Fig. 3. (a) Temperature dependences (*1*, *2*) of the phase relaxation time $\tau_\varphi(T)$ and (*3*) of the interlayer transition time; (*1*) calculation from Eq. (1) disregarding the interlayer transitions and (*2*) calculation from Eq. (3) with allowance for interlayer transitions; the solid straight line corresponds to the function T^{-1}. (b) (*1*) Temperature dependence of the prefactor α obtained by fitting Eq. (1) to the experiment and (*2*) the theoretical $\alpha = 1$ line in the absence of interlayer transitions.

there are no transitions between the layers, each of them gives the correction $-G_0\ln(\tau_\varphi/(\tau_p)$ to the conductivity and the total correction to the conductivity of this two-layer structure is $-2G_0\ln(\tau_\varphi/(\tau_p)$. What is the effect of the transitions between the layers?

If the time τ_{ij} of the transition from one layer to the other is comparable to the phase-breaking time τ_φ, then, instead of returning to the starting point, the electron can appear in the neighboring layer with the same coordinates x, y but with a different value of z (x, y are the coordinates in a CuO_2 plane, z is the coordinate in the direction perpendicular to the CuO_2 planes). Clearly, such paths no longer contribute to the interference and the magnitude of the correction is smaller than $-2G_0\ln(\tau_\varphi/(\tau_p)$. This effect not only reduces the magnitude of the total interference correction but also changes the shape of the negative magnetoresistance curve.

The role played by interlayer transitions in multilayer structures has been considered theoretically in two limiting cases corresponding to different values of the interlayer transition time: $\tau_{ij} < \tau_p$ and $\tau_{ij} > \tau_p$ [15, 16, 18]. The physical meaning of these limiting cases is clear: $\hbar/\tau_{ij}$ characterizes the width of a miniband in the superlattice, and $\hbar/\tau_p$ is the damping of the states. Therefore, if $\tau_{ij} < \tau_p$, there is a three-dimensional (propagative) Fermi surface and the quantum corrections for such a structure can be considered in the same way as for a three-dimensional anisotropic conductor. In the opposite case of $\tau_{ij} > \tau_p$, there is no three-dimensional Fermi surface (the Fermi surface is diffusive) and the behavior of the quantum corrections is closer to that in the two-dimensional case. Since the conductivity of the material under study is highly anisotropic, $\sigma_{ab}/\sigma_c \geq 10^3$, it is natural to assume that $\tau_{ij} > \tau_p$. In this case, the magnetoresistance (more exactly, magnetoconductivity) ($\Delta\sigma^{WL}$) caused by the suppression of the interference correction to the conductivity and the temperature dependence of this correction are described by the expressions [15]

$$\Delta\sigma^{WL}(B) = -G_0F(\delta, \delta'),$$

$$F(\delta, \delta') = \sum_{n=0}^{\infty}[(n + 1/2 + \delta)(n + 1/2 + \delta')]^{-1/2} - 2\ln[(n + 1 + \delta)^{1/2} + (n + 1 + \delta')^{1/2}] + 2\ln[(n + \delta)^{1/2} + (n + \delta')^{1/2}], \quad (3)$$

$$\delta = \frac{B}{B_\varphi}, \quad \delta' = \frac{B}{B_\varphi} + \frac{B}{B_\varphi}2\left(\frac{\tau_\varphi}{\tau_{ij}}\right),$$

$$\Delta\sigma^{\mathrm{WL}}(T) = -G_0\ln\left(\frac{\tau_\varphi}{\tau_p}\right) + G_0\ln\left(\frac{1}{2}+\left(\frac{1}{4}+\frac{1}{2}\frac{\tau_\varphi}{\tau_{ij}}\right)^{0.5}\right). \quad (4)$$

Using only τ_{ij} and τ_φ as fitting parameters (without introducing the prefactor α), we compare the experimental dependence of the magnetoresistance with expression (3) (Fig. 4). We see that, at low temperatures and high fields, the agreement is somewhat worse than for the magnetoresistance described by expression (1) for a purely 2D case with a small prefactor. However, on the whole, the agreement is satisfactory. The temperature dependences of the parameters τ_φ and τ_{ij} obtained by fitting expressions (3) to the experiment are plotted in Fig. 3a. We see that the temperature dependence of τ_φ is close to T^{-1} over the entire temperature range, as predicted from theory for the case where the phase relaxation is determined by the inelastic *e–e* interaction [11].

In Fig. 3a, we see that the interlayer transition time τ_{ij} decreases with increasing temperature; this time is smaller than τ_φ but is much greater than τ_p. This relation between the times τ_{ij} and τ_p agrees with the large anisotropy of the conductivity in the material, because

$$\frac{\sigma_{ab}}{\sigma_c} = \left(\frac{l}{a}\right)^2\frac{\tau_{ij}}{\tau_p}.$$

At $T = 1.5$ K, we obtain $\sigma_{ab}/\sigma_c = 1.9\times10^3$, and at $T = 32$ K we have $\sigma_{ab}/\sigma_c = 2.5\times10^2$, in agreement with the results from [2–4].

Now, let us analyze the temperature dependence of the conductivity $\sigma(T)$ (Fig. 1). In the case where this dependence is determined by quantum corrections to the conductivity for a 2D system, we can write [11]

$$\sigma(T) = \sigma_{\mathrm{Dr}} + G_0\ln\left(\frac{\tau_p}{\tau_\varphi}\right) + G_0K_{ee}\ln\left(\frac{k_{\mathrm{B}}T\tau_p}{\hbar}\right), \quad K_{ee} = 1+3\left(1-\frac{\ln(1+F_0^\sigma)}{F_0^\sigma}\right), \quad (5)$$

where the second term is the interference correction to the conductivity, the third term is the correction due to the *e–e* interaction in the diffusion channel, and F_0^σ is the Fermi-liquid interaction constant. In the presence of interlayer transitions, the temperature dependence of $\sigma(T)$ including only the interference correction is given by Eq. (4). The temperature variation of the interference correction $\Delta\sigma^{\mathrm{WL}}(T) - \Delta\sigma^{\mathrm{WL}}$ (1.5 K) for the above values of the parameters τ_φ and τ_{ij} is shown in Fig. 1b (curve *2*). This variation does not differ strongly from logarithmic in the investigated temperature range but has a slope of approximately 0.5 rather than 1 as expected from Eq. (5); this slope is appreciably smaller

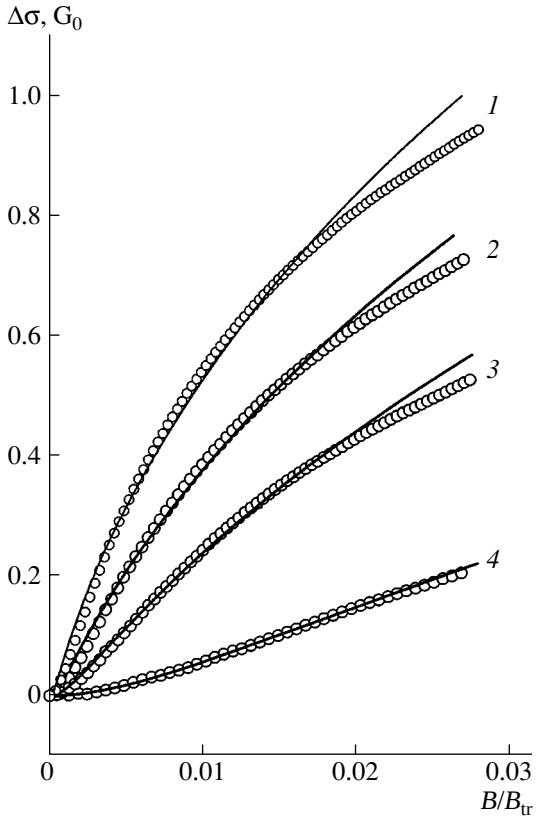

Fig. 4. Comparison of the magnetoresistance (magnetoconductivity) curves calculated from Eq. (3) with regard to interlayer transitions with the experiment. The values of the fitting parameters at various temperatures are (*1*) $T = 1.5$ K, $\tau_{ij} = 9.1\times10^{-13}$ s, and $\tau_\varphi = 3.7\times10^{-11}$ s; (*2*) $T = 4.2$ K, $\tau_{ij} = 6.9\times10^{-13}$ s, and $\tau_\varphi = 1.4\times10^{-11}$ s; (*3*) $T = 8.7$ K, $\tau_{ij} = 5.0\times10^{-13}$ s, and $\tau_\varphi = 0.65\times10^{-11}$ s; and (*4*) $T = 26.6$ K, $\tau_{ij} = 1.7\times10^{-13}$ s, and $\tau_\varphi = 0.18\times10^{-11}$ s.

than the experimentally observed slope of $\sigma(T)$ at $T <$ 10 K. This difference can be related to the contribution from the *e–e* interaction to the conductivity. It should be noted that this contribution gives a correction to the component σ_{xx} of the conductivity tensor but not to the component σ_{xy} [11]. For this reason, there appears a correction to the Hall coefficient,

$$\frac{\Delta R_H}{R_H} = \frac{-2\Delta\sigma_{xx}^{ee}}{\sigma_{xx}} = \frac{-2G_0K_{ee}\ln\left(\frac{k_{\mathrm{B}}T\tau_p}{\hbar}\right)}{\sigma_{xx}}. \quad (6)$$

Thus, by measuring the temperature dependence of the Hall coefficient $R_H(T)$, we can estimate the contribution of the *e–e* interaction to the conductivity.

Figure 5 shows the results of measurements of $R_H(T)$. The appreciable scatter of experimental points is related to the properties of the material under study: a high carrier concentration and, therefore, a small magnitude of the Hall coefficient; a rather low conductivity;

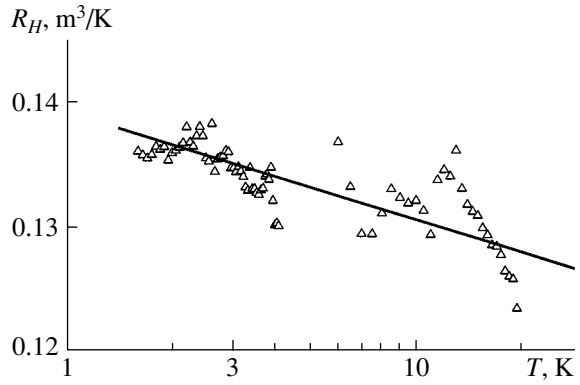

Fig. 5. Temperature dependence of the Hall coefficient. The slope of the $R_H(\ln T)$ plot corresponds to $K_{ee} = 0.25$ [see Eq. (5)].

and a strong temperature dependence of the resistivity. Due to all these factors, despite the fact that the potential of the Hall contacts is only slightly nonuniform, the Hall voltage appears to be much smaller than the spurious voltage. Nevertheless, we reliably observe in Fig. 5 that the Hall coefficient decreases with increasing temperature; this decrease can be attributed to the contribution of *e–e* interaction. The slope of the $R_H(\ln T)$ curve corresponds to $K_{ee} = 0.25 \pm 0.15$ in Eq. (5). From this value, the Fermi-liquid interaction constant can be determined to be $F_0^\sigma = -0.37 \pm 0.06$. The contributions to the temperature dependence of the conductivity from the *e–e* interaction, $\Delta\sigma^{ee}(T)$–$\Delta\sigma^{ee}(1.5\ \mathrm{K})$, and from all quantum corrections are shown in Fig. 1b. We see that the variation in the conductivity with increasing temperature at $T < 10$ K is described well if the quantum corrections are taken into account. At higher temperatures, the conductivity increases more sharply. The reason for this behavior still remains unclear.

Let us estimate the total magnitude of quantum corrections. From expressions (4) and (5) at $T = 1.5$ K, we obtain $\Delta\sigma^{\mathrm{WL}} = -6.1G_0$ and $\Delta\sigma^{ee} = -2.5G_0$. The magnitude of the Drude conductivity is $\sigma_{\mathrm{Dr}} = \sigma(1.5\ \mathrm{K}) - \Delta\sigma^{\mathrm{WL}} - \Delta\sigma^{ee} \approx 19.9G_0$. We note that the sum of quantum corrections is not small: at $T = 1.5$ K, it is almost one-half of the Drude conductivity and the interference correction is approximately 2.5 times greater than the correction for the *e–e* interaction.

4. CONCLUSIONS

In this study, we have consistently analyzed the temperature and magnetic field dependences of the conductivity and of the Hall coefficient in perfect single-crystal nonsuperconducting $Nd_{2-x}Ce_xCuO_4$ films.

(1) We have proved that the transverse magnetoresistance is determined by the suppression of the quantum interference correction to the conductivity.

(2) When quantitatively analyzing the negative magnetoresistance, it is necessary to take interlayer transitions into account; in this case, the determined τ_{ij}/τ_p ratio agrees with the anisotropy of the conductivity σ_{ab}/σ_c.

(3) We have established that the temperature dependence of the phase relaxation time is close to T^{-1}, in accordance with the prediction from the standard theory for the "dirty" limit in the case where the main mechanism of phase relaxation is inelastic *e–e* interaction.

(4) We have estimated the correction to the conductivity due to the *e–e* interaction; the Fermi-liquid interaction constant was found to be $F_0^\sigma = -0.37 \pm 0.06$.

(5) We have shown that, at $T < 10$ K, the temperature dependence of the conductivity in the absence of a magnetic field can be described if the corrections for both the *e–e* interaction and interference are included.

ACKNOWLEDGMENTS

This study was supported by the Russian Foundation for Basic Research (project nos. 03-02-16150, 02-02-16942), RFBR-Ural (project no. 04-02-96084), and state contract no. 40.012.1.1.1146 (subcontract 12/04).

REFERENCES

1. S. Massida, N. Hamada, J. Yu, and A. F. Freeman, Physica C (Amsterdam) **157**, 571 (1989).
2. Z. Z. Wang, T. R. Chian, N. R. Ong, J. M. Tarascon, and E. Wang, Phys. Rev. B: Condens. Matter **43** (4), 3020 (1991).
3. A. I. Ponomarev, V. I. Tsidilkovski, K. R. Krylov, T. B. Charikova, and L. I. Leonyuk, J. Supercond. **9** (1), 27 (1996).
4. T. Ito, Y. Nakamura, H. Takagi, and S. Uchida, Physica C (Amsterdam) **185–189**, 1267 (1991).
5. Y. Hidaka, Y. Tajima, K. Sugiyama, F. Tomiyama, A. Yamagishi, M. Date, and M. Hikita, J. Phys. Soc. Jpn. **60** (4), 1185 (1991).
6. S. J. Hagen, X. Q. Xu, W. Jiang, J. L. Peng, Z. Y. Li, and R. L. Green, Phys. Rev. B: Condens. Matter **45** (1), 515 (1992).
7. A. Kussmaul, J. S. Moodera, P. M. Tedrow, and A. Gupta, Physica C (Amsterdam) **177**, 415 (1991).
8. S. Tanda, M. Honma, and T. Nakayama, Phys. Rev. B: Condens. Matter **43** (10), 8725 (1991).
9. V. F. Gantmakher, S. N. Ermolov, G. E. Tsydynzhapov, A. A. Zhukov, and T. I. Baturina, Pis'ma Zh. Éksp. Teor. Fiz. **77** (8), 498 (2003) [JETP Lett. **77** (8), 424 (2003)].
10. V. M. Galitski and A. I. Larkin, Phys. Rev. B: Condens. Matter **63**, 174 506 (2001).
11. B. L. Altshuler, A. G. Aronov, and D. E. Khmelnitsky, J. Phys. C: Solid State Phys. **15**, 7367 (1982); B. L. Altshuler and A. G. Aronov, in *Electron–Electron Interaction in Disordered Systems*, Ed. by A. L. Efros and M. Pollak (North-Holland, Amsterdam, 1985).

12. B. L. Al'tshuler, A. G. Aronov, and D. E. Khmel'nitskiĭ, Pis'ma Zh. Éksp. Teor. Fiz. **36**, 157 (1982) [JETP Lett. **36**, 195 (1982)].

13. G. I. Harus, A. N. Ignatenkov, A. I. Ponomarev, L. D. Sabirzyanova, N. G. Shelushinina, and N. A. Babushkina, Pis'ma Zh. Éksp. Teor. Fiz. **70** (2), 93 (1999) [JETP Lett. **70** (2), 97 (1999)]; G. I. Harus, A. N. Ignatenkov, A. I. Ponomarev, L. D. Sabirzyanova, N. G. Shelushinina, and A. A. Ivanov, Zh. Éksp. Teor. Fiz. **116** (5), 1723 (1999) [JETP **89** (5), 933 (1999)].

14. S. Hikami, A. Larkin, and Y. Nagaoka, Prog. Theor. Phys. **63**, 707 (1980).

15. A. Cassam-Chenai and D. Mailly, Phys. Rev. B: Condens. Matter **52** (3), 1984 (1995).

16. N. S. Averkiev, L. E. Golub, and G. E. Pikus, Solid State Commun. **107**, 757 (1998).

17. G. M. Minkov, A. V. Germanenko, O. E. Rut, O. I. Khrykin, V. I. Shashkin, and V. M. Danil'tsev, Phys. Rev. B: Condens. Matter **62** (24), 17 089 (2000).

18. W. Szott, C. Jedrzejek, and W. P. Kirk, Phys. Rev. B: Condens. Matter **40**, 1790 (1989); Phys. Rev. B: Condens. Matter **45** (7), 3565 (1992).

Translated by I. Zvyagin

Physics of the Solid State, Vol. 47, No. 10, 2005, pp. 1980–1985. Translated from Fizika Tverdogo Tela, Vol. 47, No. 10, 2005, pp. 1901–1906.

LOW-DIMENSIONAL SYSTEMS AND SURFACE PHYSICS

Interaction of Cobalt Atoms with an Oxidized Si(100)2 × 1 Surface

M. V. Gomoyunova*, I. I. Pronin*, D. E. Malygin*, N. R. Gall'*, D. V. Vyalykh, and S. L. Molodtsov****

**Ioffe Physicotechnical Institute, Russian Academy of Sciences, ul. Politekhnicheskaya 26, St. Petersburg, 194021 Russia*

e-mail: Marina.Gomoyunova@mail.ioffe.ru

***Institut für Oberflächen- und Mikrostrukturphysik, Technische Universität Dresden, Dresden, D-01062 Germany*

Received January 17, 2005

Abstract—The initial stages of oxidation of a Si(100)2 × 1 surface and the interaction of cobalt atoms with it were studied by core-level photoelectron spectroscopy. The study was carried out with cobalt coverages of up to 8 ML. Computer modeling of the spectra of photoexcited electrons revealed Co atom penetration under the silicon oxide layer, an effect observed even at room temperature. This process was shown to give rise to the disappearance of silicon interface phases at the oxide-layer–silicon boundary and to the formation of a more complex phase involving atoms of Co, O, and Si. After completion of the process, a Co–Si solid solution forms at the interface. © *2005 Pleiades Publishing, Inc.*

1. INTRODUCTION

Forming and studying nanosized objects on the surface of a solid (clusters, thin films, etc.), which possess unusual properties, is of fundamental significance for science and nanoelectronics. Intense research interest is focused on nanosized objects formed from cobalt and its compounds, which can exhibit anomalous magnetic properties and can have an atomically sharp interface with the substrate. Among such objects are, in particular, ultrathin layers of cobalt disilicide on a Si(100)2 × 1 surface, which are widely used as Ohmic and barrier contacts in semiconductor electronics. Available literature data on the initial stages of their formation are, however, contradictory. It was reported in [1], for instance, that cobalt grows on silicon at room temperature as an epitaxial film. However, other authors insist that cobalt atoms incident on a surface immediately begin to react chemically with silicon to form cobalt silicides [2]. These differences are apparently due to the fact that the interaction of Co atoms with silicon depends on a variety of factors that are difficult to control, which seriously complicates the reproducible formation of acceptable $CoSi_2$ layers on the silicon (100) face.

The presence of oxygen noticeably affects the process of solid-phase epitaxy of cobalt disilicide on the surface of a crystal. For instance, a thin oxide layer may improve the morphological properties of growing silicide films [3–5]. The mechanism of this effect was not, however, established in the above references. We have succeeded recently in obtaining experimental data which suggest that cobalt deposited on an oxidized silicon surface, rather than staying on it, penetrates down to the SiO_x/Si interface [6]. Therefore, the improvement in the quality of grown $CoSi_2$ layers may be due to a solid-phase reaction proceeding under the oxide layer, which spatially confines the region involved in the reaction and inhibits large-scale atomic rearrangement. These conclusions were drawn, however, only from a qualitative analysis of the photoelectron spectra obtained.

We report here on a more comprehensive study of the interaction of cobalt atoms with the oxidized Si(100)2 × 1 surface by core-level photoelectron spectroscopy under synchrotron irradiation [7] and on computer modeling of the Si 2*p* spectra. It was shown that cobalt adatoms do indeed penetrate through the oxide layer at room temperature. This powerful method permitted reproduction of the totality of the atomic processes occurring in this system during cobalt deposition. Early stages of silicon oxidation were also investigated in considerable detail, which is important from a more general standpoint, because SiO_2/Si structures enjoy wide use in present-day solid-state electronics and this problem is still being actively discussed in the literature [8–12].

2. EXPERIMENTAL TECHNIQUE

Measurements were conducted using the Russian–German synchrotron beam line of the BESSY II storage ring (Berlin). The instrument used in the experiment was an ultrahigh vacuum photoelectron spectrometer, whose total energy resolution, including the monochro-

mator and the analyzer, was 130 meV. The spectrometer detected photoelectrons ejected within a cone aligned with the surface normal. The main measurements were conducted at a photon energy $h\nu = 130$ eV, corresponding to the maximum surface sensitivity under Si 2*p* core-level excitation. The silicon samples studied were fabricated from KÉF-1 single-crystal silicon plates. Their surface misalignment relative to the (100) face was less than 0.1°. Before being loaded into the spectrometer chamber, the samples were chemically treated by the Shiraki method [13]. After this, they were heated for a short time in ultrahigh vacuum to 1200°C and cooled slowly at a rate not exceeding ~50°C/min. This procedure provided a Si(100)2 × 1 reconstructed surface free of carbon and oxygen contaminations. The elemental composition of the sample surface was monitored by photoelectron spectroscopy.

The surface of the silicon single crystals was oxidized at room temperature by exposure to an oxygen environment at a pressure of $\sim 10^{-5}$ Pa. The exposure was varied from a few L to 10^4 L, the level of saturated surface coverage by oxygen. Cobalt was deposited on the surface of a substrate maintained at room temperature from a thoroughly degassed source, in which the material to be evaporated (a rod of extra-high purity cobalt) was heated by electron bombardment. The cobalt deposition rate was ~1 ML/min. One monolayer (ML) of cobalt coverage was identified with 6.8×10^{14} at/cm^2, which is the silicon atom concentration on the substrate surface. All measurements of the photoelectron spectra were performed at room temperature in vacuum at a pressure not exceeding 1.2×10^{-8} Pa.

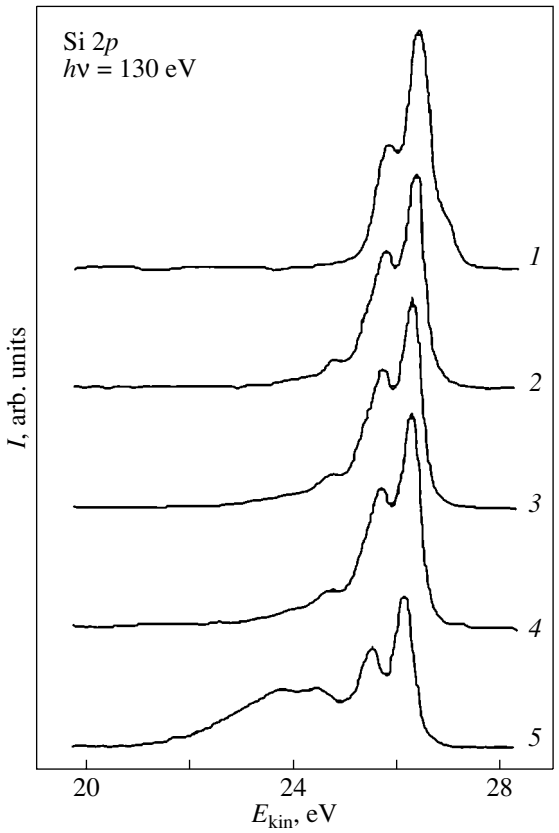

Fig. 1. Spectra of silicon 2*p* photoelectrons measured at $h\nu = 130$ eV in the course of room-temperature oxidation of the Si(100)2 × 1 surface. (*1*) Initial Si(100)2 × 1 surface. The sample exposure in the oxygen environment is (*2*) 3, (*3*) 15, (*4*) 100, and (*5*) 10^4 L.

3. RESULTS AND DISCUSSION

3.1. Silicon Oxidation

Figure 1 shows typical Si 2*p* spectra obtained from a clean Si(100)2 × 1 surface and during its oxidation at room temperature. These spectra do not contain a background of inelastically scattered electrons, which was eliminated using polynomial approximation of the spectral regions without lines and the Shirley method [14]. As seen from Fig. 1, interaction of oxygen with the Si(100)2 × 1 surface changes the pattern of the spectra substantially. In particular, the intensity of the $2p_{3/2}$ and $2p_{1/2}$ doublet of pure silicon decreases and the shoulder on the right-hand side of the $2p_{3/2}$ line (the substrate up-dimer atom mode [15–18]) disappears. In addition, the dip between the $2p_{3/2}$ and $2p_{1/2}$ sublevels (in the region of the second-layer atom mode of the reconstructed surface) grows markedly. The main changes in the spectrum originate, however, from the appearance of new components having positive energy shifts. The range over which they can be seen broadens with increasing exposure and is about 4-eV wide. As follows from literature data [8–12], these modes are due to oxide phases of silicon with valences varying from +1 to +4 determined by the number of oxygen atoms that surround a silicon atom and with which it interacts. The above changes in the spectra indicate rearrangement of the near-surface region of the crystal and the formation of a SiO_x oxide layer of complex composition on its surface.

The spectra obtained were numerically simulated to gain more comprehensive information on the structure of this layer. Each spectrum was assumed to be the sum of a bulk and of a number of surface spin–orbit doublets with a splitting of 608 meV between the $2p_{3/2}$ and $2p_{1/2}$ sublevels. The line intensity ratio of these sublevels was assumed to be two, in accordance with their population. All the spectral modes were represented by Voigt functions customarily used for this purpose [15]. These functions are essentially convolutions of Lorentzians (taking into account the hole lifetime in the core level) with Gaussians describing the phonon-induced line broadening and the energy resolution of the instrument. Decomposition of a spectrum into its constituent parts was performed under variation of the width, energy position, and intensity of the lines.

The results obtained are illustrated by data pertaining to a surface covered by oxygen to saturation

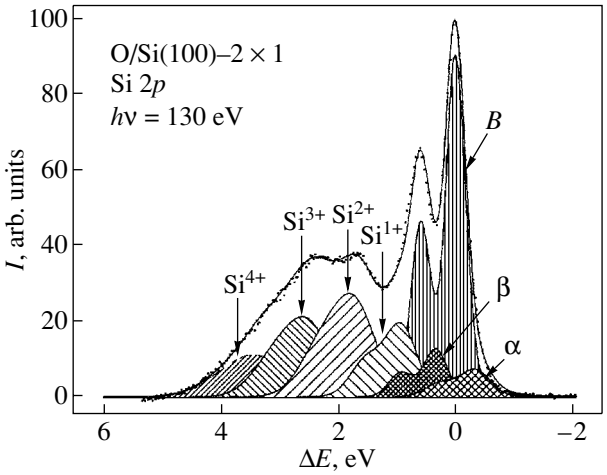

Fig. 2. Computer-simulated decomposition of a Si 2*p* spectrum of a Si(100)2 × 1 surface saturated by oxygen at room temperature.

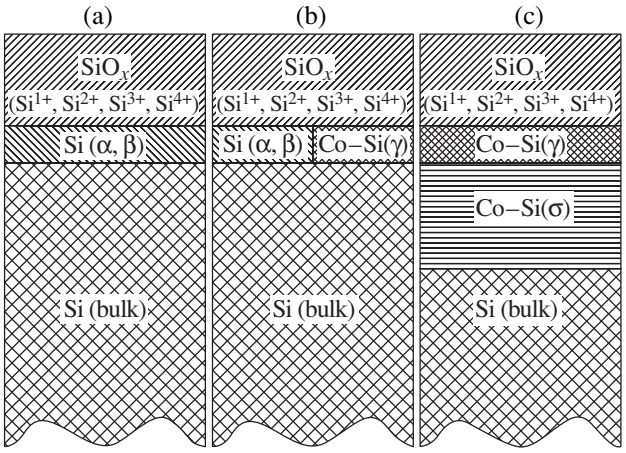

Fig. 3. Schematic representation of the structure of the near-surface region (a) in an oxidized silicon crystal and (b, c) in this crystal coated by (b) 2 and (c) 8 ML of cobalt.

(Fig. 2). The spectrum is seen to be contributed by the pure-silicon bulk mode (*B*), four oxide modes (Si^{1+}, Si^{2+}, Si^{3+}, Si^{4+}), and two additional modes (α, β), without which calculations could not be fitted well enough to experimental data. Note that oxidized-silicon spectrum components similar to the latter two modes were detected in other studies as well [9, 11, 19, 20], where they were related to the formation of the SiO_x/Si interface. These modes can be assigned to silicon atoms being located in the second coordination shell rather than being in direct contact with oxygen atoms. The energy shifts Δ*E* obtained by us for the above modes, as well as their FWHMs, are presented in the table; they also compare well with literature data [8–12].

The structure of the near-surface region of oxidized silicon is shown schematically in Fig. 3a. The thickness of the oxide layer *d* as estimated from damping of the bulk mode of pure silicon is no less than ~3 Å. According to the literature data, this layer is nonuniform in depth; indeed, the low-valency phases (Si^{1+}, Si^{2+}) are in direct contact with the silicon crystal, while the Si^{3+} and Si^{4+} phases are localized in close proximity to the surface of an oxidized sample [21]. Decomposition of the spectra obtained by us at lower exposures of the crystal to oxygen (3–100 L) support this conclusion, because in the earliest stages of silicon oxidation at room temperature the Si^{3+} and Si^{4+} modes are not seen at all. Note that high-temperature oxidation of silicon is characterized by a different dynamics of spectral changes. In this case, the intensity ratio of different oxide modes does not vary in the course of oxidation, with only their linear growth being observed. This behavior can be attributed to the formation on the silicon surface of oxide spots which include all four oxide phases from the very onset and to the subsequent lateral growth of these spots with increasing exposure of the sample to oxygen [19].

Our results suggest a different scenario of the silicon oxidation process at room temperature. In our case, as seen from a comparison of curves *1* and *2* in Fig. 1, the silicon up-dimer atom mode on the low-energy side of the $2p_{3/2}$ line disappears in the earliest stages of oxidation. It thus follows that the process encompasses practically the whole crystal surface. This may be assigned to the fact that the migration of oxygen atoms over the surface at room temperature is inhibited and the surface turns out to be more uniform than in the case of high-temperature oxidation.

3.2. Cobalt Deposition on an Oxidized Si(100)2 × 1 Surface

Figure 4 displays experimental data obtained with cobalt evaporated on the surface of oxidized silicon. We readily see that the shape of the spectral lines changes as the dose of the deposited metal increases, which implies interaction of cobalt atoms with silicon. Also, unlike the oxidation stage described above, the oxide modes of the spectrum, on the whole, change very little,

Energy shifts Δ*E* of various Si 2*p* spectral modes and their half-widths (FWHM)

Parameter	*B*	Si^{1+}	Si^{2+}	Si^{3+}	Si^{4+}	α	β	γ	σ
Δ*E*, eV	0	0.94	1.73	2.52	3.29	0.35	−0.32	0.38	−0.28
FWHM, eV	0.35	0.60	0.80	0.85	1.08	0.44	0.57	0.55	0.41

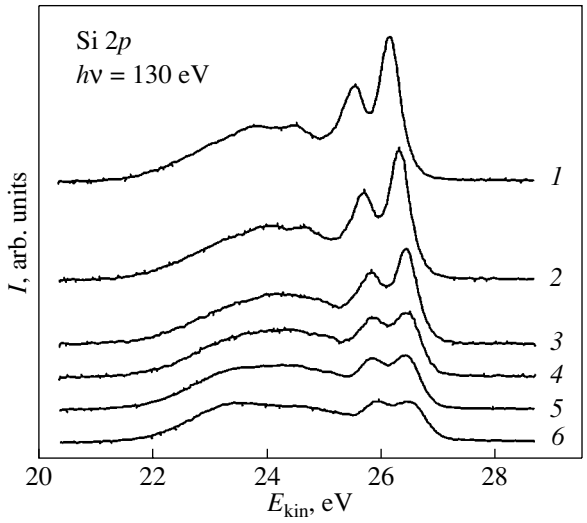

Fig. 4. Silicon 2*p* photoelectron spectra measured at $h\nu$ = 130 eV after deposition of increasing cobalt doses onto an oxidized silicon surface. (*1*) Starting oxidized silicon surface. The Co dose is (*2*) 0.7, (*3*) 2, (*4*) 4, (*5*) 6.5, and (*6*) 8 ML.

with major changes observed in the region of the lines of pure silicon. They become manifest, first, in a strong intensity drop of the whole 2*p* doublet and, second, in a leveling off of the intensities of the maxima located in the region of the $2p_{3/2}$ and $2p_{1/2}$ sublevels. The latter effect is particularly clearly pronounced in the spectrum measured after the deposition of 8 ML of cobalt (curve *6* in Fig. 4). This dynamics of spectral variation gives us grounds to suggest that the cobalt atoms deposited on the sample surface, rather than condensing on it, diffuse under the oxide layer [6]. If this were not so, the cobalt film forming on the surface would have strongly screened the oxide layer signal, an effect not observed in experiment. Note that the intensity of the oxide phases could weaken slightly also in the case where three-dimensional cobalt islands form. In this situation, however, the bulk mode intensity of pure silicon should not vary strongly; in actual fact, it undergoes, as already mentioned, the strongest changes of all.

To verify the conclusion that evaporated cobalt atoms penetrate under the oxide layer, we carefully studied the totality of the measured spectra by unfolding them into constituent parts. We did this by the same curve-fitting procedure as in the simulation of the Si 2*p* spectra of oxidized silicon. The results obtained are illustrated in Fig. 5, which presents data for three increasing cobalt doses (2, 4.5, and 8 ML). Evaporation of 2 ML of cobalt is seen to bring about a drop in the intensity of the silicon bulk mode *B*, a noticeable decrease of the interface modes α and β in intensity, and the appearance of a new mode γ with a positive energy shift of ~0.4 eV. This variation of the spectral modes can be interpreted only if we assume that cobalt atoms incident on the surface penetrate into the region

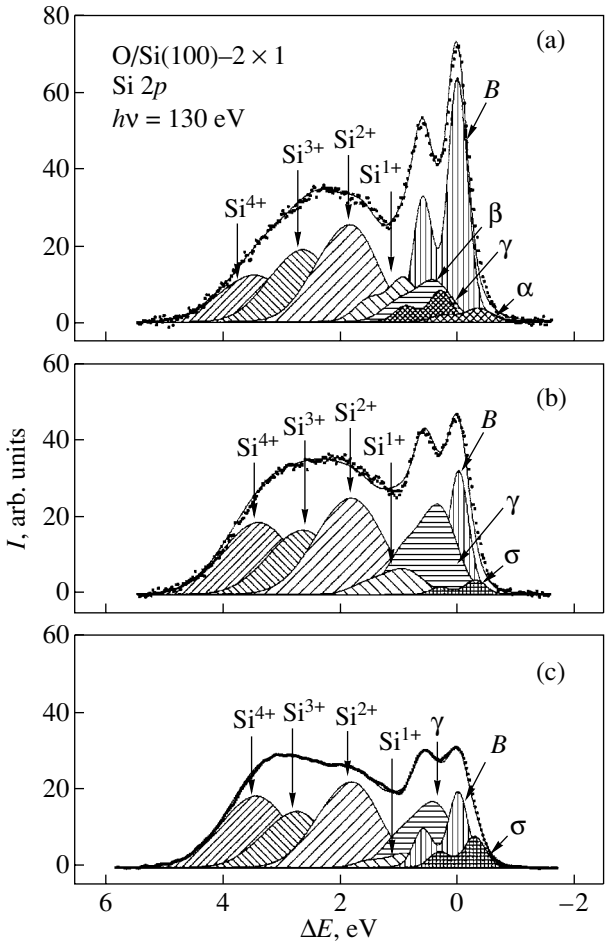

Fig. 5. Computer simulation of the Si 2*p* spectrum of an oxidized Si(100)2 × 1 surface atop which increasing cobalt doses were evaporated. The Co dose is (a) 2, (b) 4.5, and (c) 8 ML.

of the oxide-layer–silicon interface and modify it into a new interface phase γ whose properties are now determined by three components, namely, Si, O, and Co.

Because deposition of 2 ML of cobalt does not bring about complete decay of the α and β modes, the new phase forming in the region of the interface grows by the island pattern. The structure of the near-surface region of the sample in this stage of the process is shown schematically in Fig. 3b.

After deposition of 4.5 ML of cobalt, the α and β phases are no longer seen, while the γ component grows noticeably in intensity (Fig. 5b). This suggests that the new interface in this ternary system has already formed. In addition, there appears one more new mode (σ) with a negative energy shift of ~0.3 eV, which corresponds to the shift of the Co–Si solid solution mode [22–26]. It is known that deposition of cobalt on a clean Si(100)2 × 1 surface gives rise to the formation of a film of a Co–Si solid solution [22–26]. As the thickness of this film grows, the silicon atom concentration near the surface decreases, until at doses of above 6–7 ML a film of pure

metal forms. Observation in our case of the σ mode with such a shift gives us grounds to maintain that, after the formation of the new intermediate layer characterized by mode γ, a Co–Si solid solution starts to form under it too. This is in accord with the further growth in the mode σ intensity with increasing cobalt dose. As is evident from Fig. 5c, mode σ does indeed grow after the deposition of 8 ML of cobalt. As for the γ mode, its intensity varies only weakly in the process. The structure of the near-surface region after the deposition of 8 ML of cobalt is shown schematically in Fig. 3c. It should be stressed that only deconvolution of the spectra into constituent parts permitted us to detect the stage of formation of a Co–Si solid solution under the oxide layer.

Deposition of cobalt also brings about a change in the oxide mode intensities. As seen from Fig. 5, these changes are most clearly pronounced for the Si^{1+} mode, whose intensity decreases with increasing cobalt dose. Because the silicon atoms responsible for this mode are in direct contact with the silicon crystal, it may be suggested that a cobalt atom penetrating under the oxide layer enters the Si–O bond to form the O–Co–Si block, which becomes incorporated into the new interface. One can see also a slight increase in the Si^{4+} mode intensity, which indicates a slight change of the top layer in the oxide film as well.

The buildup of cobalt atoms in the proximity of the SiO_x/Si interface is apparently due to its being energetically favorable for them to reside under the oxide layer. One may ask how Co atoms get under it. We believe that this process is most probably related to discontinuities (pinholes) in the oxide layer. In this case, an adsorbed atom first migrates over the oxide surface, reaches a defect, and penetrates through it under the layer. Note that the absence in the 2*p* spectrum of the oxidized silicon surface of the up-dimer atom mode characteristic of a reconstructed Si(100)2 × 1 surface would seemingly indicate the formation of a solid oxide layer on the crystal surface. This conclusion can be drawn, however, only within the sensitivity of the method used. Recalling that this mode is weak, this sensitivity turns out to be fairly poor. Assuming the migration activation energy to be 0.6–0.8 eV, one can estimate the number of migration hops made by an atom per second [27]. This number turns out to be more than 100. Therefore, if there is even 1 defect per 100 surface atoms, a Co adatom can certainly reach a defect in 1 s and after that penetrate under the thin oxide layer.

4. CONCLUSIONS

Based on the decomposition of Si 2*p* spectra, we have proved the existence of a fairly nontrivial effect of the penetration of cobalt adatoms under a thin (~3-Å-thick) SiO_x layer of complex composition that forms on a Si(100)2 × 1 surface. This effect is observed at room temperature and results in the buildup of cobalt at the SiO_x/Si interface and in the disappearance of the α and β interface phases, which existed at the boundary between the oxide layer and silicon. These phases are replaced by a new phase γ characterized by a spectral mode with a positive energy shift, whose formation involves atoms of silicon, cobalt, and oxygen. On completion of the formation of this phase, a film of a Co–Si solid solution forms under it, exactly as in the case of pure silicon.

ACKNOWLEDGMENTS

This study was supported by the Russian Foundation for Basic Research (project no. 04-02-17651) and the bilateral program "Russian–German Laboratory at BESSY."

REFERENCES

1. W. S. Cho, J. Y. Kim, N. G. Park, I. W. Lyo, K. Jeong, S. S. Kim, D. S. Choi, S. N. Whang, and K. H. Chae, Surf. Sci. **453**, L309 (2000).
2. U. Starke, W. Weiss, G. K. Heinz, Th. Fauster, and G. R. Castro, Surf. Sci. **352**, 89 (1996).
3. T. R. Tung, Appl. Phys. Lett. **68** (24), 3461 (1996).
4. T. R. Tung, Jpn. J. Appl. Phys., Part 1 **36** (3B), 1650 (1997).
5. Y. Hayashi, M. Yoshinaga, H. Ikeda, S. Zaima, and Y. Yasuda, Surf. Sci. **438**, 116 (1999).
6. M. V. Gomoyunova, I. I. Pronin, N. R. Gall', S. L. Molodtsov, and D. V. Vyalykh, Pis'ma Zh. Tekh. Fiz. **30** (20), 17 (2004) [Tech. Phys. Lett. **30** (20), 850 (2004)].
7. M. V. Gomoyunova and I. I. Pronin, Zh. Tekh. Fiz. **74** (10), 1 (2004) [Tech. Phys. **49** (10), 1249 (2004)].
8. G. Hollinger and F. J. Himpsel, Phys. Rev. B: Condens. Matter **28** (6), 3651 (1983).
9. Y. Hoshino, T. Nishimura, T. Nakada, H. Namba, and Y. Kido, Surf. Sci. **488**, 249 (2001).
10. P. Morgen, T. Jensen, C. Gundlach, L.-B. Taekker, S. V. Hoffman, and K. Pedersen, Comput. Mater. Sci. **21**, 481 (2001).
11. H. W. Yeom and R. Uhrberg, Jpn. J. Appl. Phys., Part 1 **39** (7B), 4460 (2000).
12. A. Mascaraque, C. Ottaviani, M. Caposi, M. Pedio, and E. G. Michel, Surf. Sci. **377–379**, 650 (1997).
13. A. Ishizaka and Y. Shiraki, J. Electrochem. Soc. **133** (4), 666 (1986).
14. D. A. Shirley, Phys. Rev. B: Solid State **5** (12), 4709 (1972).
15. E. Landemark, C. J. Karlsson, Y.-C. Chao, and R. I. G. Uhrberg, Phys. Rev. Lett. **69** (10), 1588 (1992).
16. T.-W. Pi, I.-H. Hong, C.-P. Cheng, and G. K. Wertheim, J. Electron Spectrosc. Relat. Phenom. **107**, 163 (2000).
17. H. Koh, J. W. Kim, W. H. Choi, and H. W. Yeom, Phys. Rev. B: Condens. Matter **67** (7), 073 306 (2003).

18. M. V. Gomoyunova, I. I. Pronin, N. R. Gall', S. L. Molodtsov, and D. V. Vyalykh, Pis'ma Zh. Tekh. Fiz. **29** (12), 25 (2003) [Tech. Phys. Lett. **29** (6), 496 (2003)].
19. T.-W. Pi, J.-F. Wen, C.-P. Ouyang, R.-T. Wu, and G. K. Wertheim, Surf. Sci. **478**, L333 (2001).
20. F. Jolly, F. Rochet, G. Dufour, C. Grupp, and A. Taleb-Ibrahimi, J. Non-Cryst. Solids **280**, 150 (2001).
21. J. H. Oh, H. W. Yeom, Y. Hagimoto, K. Ono, M. Oshima, N. Hirashita, M. Nywa, A. Toriuma, and A. Kakizaki, Phys. Rev. B: Condens. Matter **63** (20), 205 310 (2001).
22. F. Boscherini, J. J. Ruckman, and J. H. Weaver, Phys. Rev. B: Condens. Matter **35** (9), 4216 (1987).
23. J. M. Gallego, R. Miranda, S. Molodtsov, C. Laubcshat, and G. Kaindl, Surf. Sci. **239**, 203 (1990).
24. G. Rangelov, P. Augustin, J. Stober, and Th. Fauster, Phys. Rev. B: Condens. Matter **49** (11), 7535 (1994).
25. G. Rangelov and Th. Fauster, Surf. Sci. **365**, 403 (1996).
26. M. V. Gomoyunova, I. I. Pronin, N. R. Gall', S. L. Molodtsov, and D. V. Vyalykh, Fiz. Tverd. Tela (St. Petersburg) **45** (8), 1519 (2003) [Phys. Solid State **45** (8), 1596 (2003)].
27. M. Roberts and C. McKee, *The Chemistry of the Metal–Gas Interface* (Clarendon, Oxford, 1978; Mir, Moscow, 1981), pp. 306–312.

Translated by G. Skrebtsov

Physics of the Solid State, Vol. 47, No. 10, 2005, pp. 1986–1992. Translated from Fizika Tverdogo Tela, Vol. 47, No. 10, 2005, pp. 1907–1913.

LOW-DIMENSIONAL SYSTEMS AND SURFACE PHYSICS

Molecular Dynamics Simulation of the Interaction of Low-Energy Ar and Xe Ions with Copper Clusters on a Graphite Surface

G. V. Kornich*, G. Betz, V. I. Zaporojtchenko***, F. Faupel***, and L. I. Lozovskaya***

** Zaporozhye National Technical University, Zaporozhye, 69063 Ukraine*
e-mail: gkornich@zntu.edu.ua
*** Institut für Allgemeine Physik, Technische Universität Wien, Wien, A-1040 Austria*
**** Technische Fakultät, Christian-Albrechts Universität, Kiel, 24143 Germany*
Received February 22, 2005

Abstract—A molecular-dynamics simulation of sputtering of isolated clusters consisting of 13, 27, and 195 Cu atoms from the (0001) graphite surface by 200-eV Ar and Xe ions is carried out. The angular and energy parameters of sputtered Cu atoms and scattered ions are discussed. © *2005 Pleiades Publishing, Inc.*

1. INTRODUCTION

Studying metallic nanometer clusters on various substrates, including carbon-containing surfaces [1–9], is of particular interest due to the development of new materials in electronics, atomic engineering, and the chemical and biological industries. Over the past decade, the following composing elements and processes relating to cluster/substrate systems have been simulated: carbon structures [10–13]; metallic clusters, including their sputtering onto atomic surfaces [14–18]; surface sputtering by atomic clusters [19–23]; and sputtering mechanisms of materials in the form of clusters [24] and molecular fragments [25]. However, simulations of sputtering of nanometer metallic clusters from substrates have not been carried out, except for rough estimations made (using classical molecular dynamics (MD) [26]) for copper cluster sputtering from a graphite surface [27].

In this study, we carried out MD simulation of the bombardment of isolated copper clusters consisting of various numbers of atoms on the (0001) graphite substrate by 200-eV Ar and Xe ions. Comparing the results of the interaction of Ar and Xe ions with surface clusters makes it possible to separate manifestations of many-body interaction of Xe ions with lighter cluster atoms. Analogous interaction effects have already been considered within the MD model with many-body atomic potentials for smooth metal surfaces as a target [28, 29].

2. MOLECULAR DYNAMICS MODEL

Substrates with the hexagonal atomic structure were simulated by two atomic layers arranged in the (0001) plane, each consisting of 792, 960, and 1500 carbon atoms for clusters consisting of 13 (13 Cu), 27 (27 Cu), and 195 (195 Cu) Cu atoms, respectively. Cluster–substrate systems were created by relaxation of copper clusters (initially isolated in space and minimized in energy) on the (0001) graphite surface [19, 24]. After 20- to 40-ps relaxation of the cluster–substrate systems, the highest kinetic energy of Cu atoms in the surface clusters did not exceed 0.02 eV/atom. The position of the graphite atomic layers with respect to the normal to the substrate surface was assumed to remain unchanged, in contrast to the model [27], where the substrate during relaxation of a binary system was free and its surface was slightly deformed. Simulation of the second atomic layer in the substrate allowed more comprehensive consideration of collisions in the target, which resulted in a 5–10% increase in the cluster sputtering coefficient. A further increase in the number of substrate atomic layers had no effect on the cluster sputtering coefficient.

Copper atoms separated by a distance of 1.3–5.5 Å interacted with each other via a many-body potential in the Gades–Urbassek representation [30], which yields reasonable sublimation energies for small atomic clusters, in particular, 2.64 eV for the Cu–Cu dimer [31]. In this model, the potential from [30] was immediately joined to the Born–Mayer pair repulsive potential describing high-energy atomic collisions [32] in the range 0–1.3 Å. The interaction of carbon atoms was described by the Tersoff many-body potential with a cutoff radius of 2.1 Å [33], which was joined to the Ziegler–Biersack–Littmark pair repulsive potential [32] using a coupling function in the form of a fifth-degree polynomial in the range of 0.5–0.98 Å. The shortest distance between carbon atoms in the (0001) plane was 1.46 Å, and the interplane distance was 3.35 Å. The Cu–C interaction at distances of 1.946–3.75 Å was described by the Lennard–Jones pair potential [34] with a mini-

mum Cu–C interaction energy of –0.11 eV at an interatomic distance of 2.34 Å. The Lennard–Jones potential was joined to the Ziegler–Biersack–Littmark potential using a coupling function that was likewise in the form of a fifth-degree polynomial in the range 1.2–1.946 Å. Periodic boundary conditions [26] were imposed, and a dissipative layer [35] was assumed to be at the perimeter of the graphite atomic layers. Equations of motion of particles were solved using the Verlet method [26, 32]. The interaction of Ar and Xe ions with carbon and copper atoms was described by the Ziegler–Biersack–Littmark potential with a cutoff radius of 5 Å. The largest time integration step did not exceed 4 fs. The simulated time of a single collision cascade development was 2 and 3 ps for Ar and Xe ions, respectively. The energy conservation law in each model cascade was satisfied with an accuracy of better than 1%. For each cluster, 2000 tests were carried out. Each new test was performed for the initial cluster–substrate system. The initial ion coordinates were chosen using random numbers; so the highest possible ion interaction energy with at least one Cu atom approaching a cluster was no lower than 37 eV.

3. RESULTS AND DISCUSSION

3.1. Energy Loss of Bombarding Ions and Their Scattering

Figure 1a shows the model distributions of the probability that bombarding Ar and Xe ions occur in copper clusters and substrate atomic layers after tests. The probability of reflection of bombarding Ar ions to range 1 (Fig. 1a) is slightly higher than that of Xe ions. There are no bombarding particles in copper clusters already 0.5 ps after a collision evolution, because only the Cu–ion repulsive interaction is included. Taking into account the possibility that Ar and Xe ions can be in range 2, the probabilities of Ar and Xe ions occurring above the substrate after interacting with the target differ insignificantly. An appreciable difference in the probabilities of Ar and Xe ions occurring in the first atomic layer of the substrate is due to the significantly larger mass of the Xe ion in comparison with those of the Cu, C, and Ar ions. The probabilities that Ar and Xe ions occur in other target regions differ insignificantly.

Figure 1b shows the distributions (averaged over the number of tests) of the elastic energy loss of bombarding Ar and Xe ions in clusters and in atomic layers of the substrate. We can see that the average energies of the reflected Xe ions are lower than those of the reflected Ar ions by a factor of 3–4 for all the clusters under consideration. For both types of bombarding ions, elastic losses in copper clusters are dominant; they can be as large as 60–70% of the initial energy for Xe ions and 50–55% for Ar ions and tend to increase with cluster size. In substrate atomic layers, elastic energy losses of Ar and Xe ions decrease in a similar way.

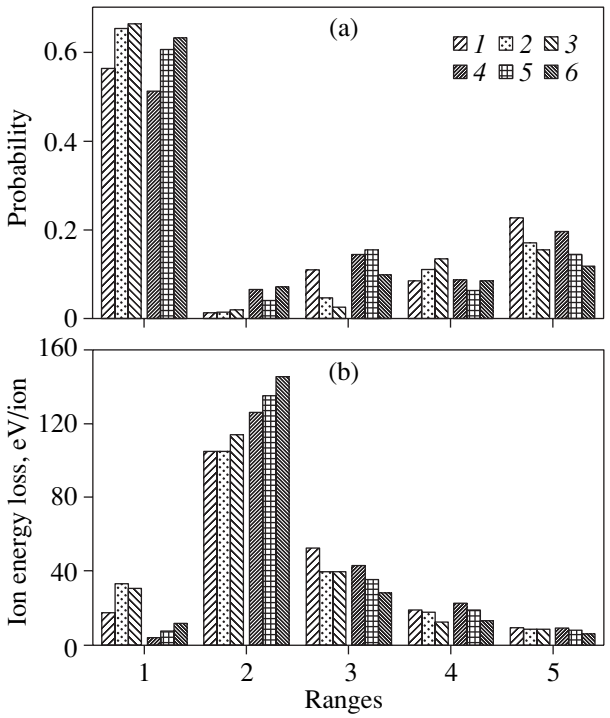

Fig. 1. Distributions of (a) the probability of finding 200-eV bombarding ions and (b) their average elastic energy losses for Ar and Xe ions in various simulated target ranges. Ar ions: (*1*) (13 Cu), (*2*) (27 Cu), and (*3*) (195 Cu). Xe ions: (*4*) (13 Cu), (*5*) (27 Cu), and (*6*) (195 Cu). Target ranges: (*1*) backscattered ions; (*2*) surface cluster; (*3*, *4*) first and second substrate atomic layers, respectively; and (*5*) space behind the substrate.

Figure 2 shows the polar-angular distributions of scattered Ar and Xe ions. The polar angle was measured from the outward normal to the substrate surface. For both ion types and all clusters under consideration, the main maximum of the distributions is in the angular range 60°–80°. In the case of Xe, the maximum clearly tends to shift to larger polar angles as the cluster size increases. The maximum at angles of 60°–80° is caused by the overlapping of two reflected ion intensities: one of the ions that preliminarily interact with a cluster and then are reflected from the substrate and one of the ions that are reflected from clusters without significant interaction with the substrate (see Subsection 3.2). A number of local maxima [such as those in the range 90°–105° in the case of cluster (195 Cu) bombarded by Ar ions] arise as a manifestation of the geometrical features of the cluster/substrate model systems under consideration.

3.2. Angular Distributions of Intermediate-Energy Scattered Ions

Figure 3 shows the polar angular dependences of intermediate-energy scattered Ar and Xe ions. The maximum in the polar-angle range 50°–85° is characteristic of all cases and approximately coincides in

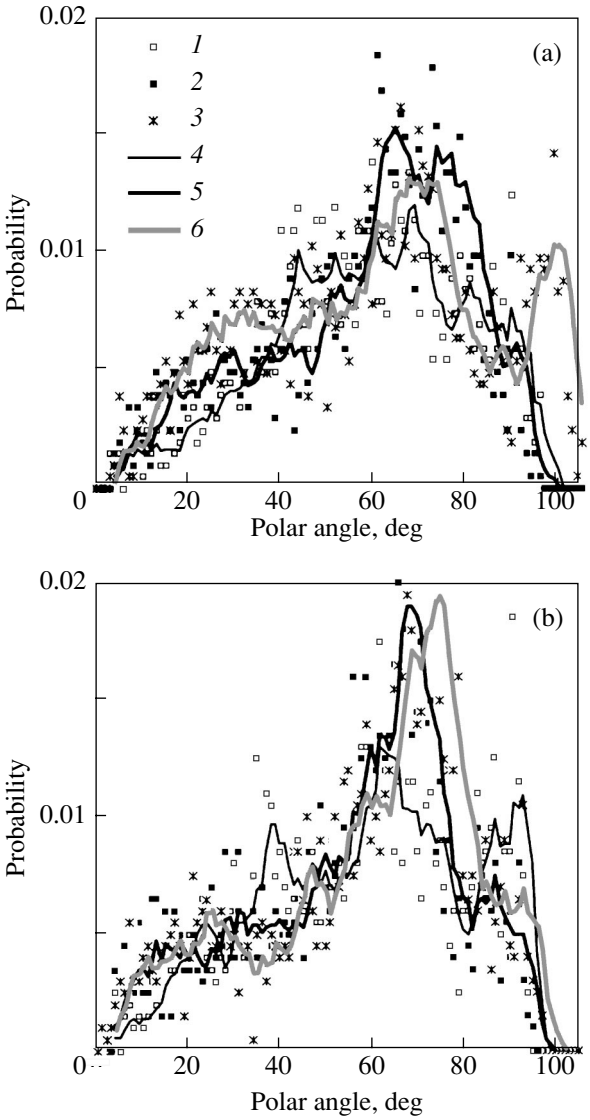

Fig. 2. Polar-angle distributions (with a resolution of 1°) of the probability of (a) Ar and (b) Xe ion scattering by various clusters: (*1*, *4*) (13 Cu), (*2*, *5*) (27 Cu), and (*3*, *6*) (195 Cu). Curves *4–6* are piecewise linear five-point approximations.

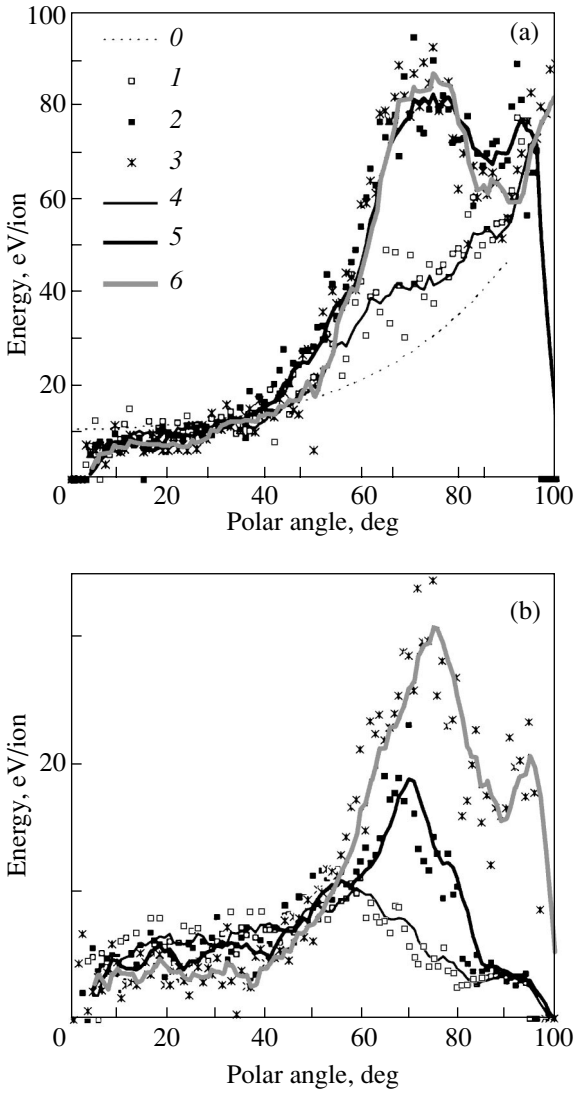

Fig. 3. Distributions of the average energy of (a) Ar and (b) Xe ions scattered by (*0*) one Cu atom and (*1–6*) various clusters (*1*, *4*) (13 Cu), (*2*, *5*) (27 Cu), and (*3*, *6*) (195 Cu) over the emission polar angles (with a resolution of 1°). Curves *4–6* are piecewise linear five-point approximations.

position with the main maximum of the probability distribution of ion scattering in Fig. 2. Thus, the main maximum of the ion scattering probability is mostly formed due to high-energy reflected ions. Figure 3a (dashed line) shows the analytically calculated energy of the Ar ion after its interaction with a free Cu atom in the case where the initial ion energy is 200 eV. It follows from this dependence that the general tendency toward an increase in the average energy of the scattered Ar ions with an increase in the scattering angle is caused by the Ar–Cu pair interaction, which is responsible for the second maximum in the angular range 90°–105°. Significant many-body interaction in the scattering angle range 50°–85° is superimposed on the pair interaction. The many-body interaction consists of Ar ion scattering by cluster atoms and, in many cases, subsequent ion interaction with the substrate. The many-body and multiple interactions of the Ar ion with cluster copper atoms consist of simultaneous and successive interactions, respectively, with a few Cu atoms, which results in a higher retained ion energy in comparison with the energy of a scattered ion moving in the same direction after interacting with a single Cu atom. When ions are scattered by clusters in directions with polar angles larger than 90°, the ions are secondarily scattered by the substrate (if they fall within the model substrate); the latter process also has a many-body character. When an ion is incident on the substrate at a large angle, the ion loses a small fraction of its kinetic energy and is finally scattered from the substrate also at

a large polar angle. As a result, a characteristic peak of the average energy of scattered Ar ions arises in the polar-angle range 50°–85° (Fig. 3a). In the case of the (13 Cu) cluster, the peak in the angular range 50°–85° is the least pronounced due to the limited probability of many-body or multiple interactions of the Ar ion with Cu atoms.

At small scattering angles of Ar ions, low reflection energies dominate, because the Ar–Cu interaction is predominantly pair interaction, which is confirmed by the insignificant difference between the scattering energies at polar angles of 10°–40° and the pair interaction energies shown in Fig. 3a. The role of the graphite substrate during these interactions remains insignificant, although secondary low-energy reflections from the substrate can occur. However, in the case where the ion retains a high energy after interacting with a cluster and the polar angle of incidence on the substrate is large, the ion, as a rule, is introduced into the graphite. When the ion energy after interaction with a cluster is 50–150 eV, the critical polar angle of the Ar ion incidence on the substrate, with its damage and possible ion penetration into the substrate, is 130°–160°. These data agree with the experimental results from [36], where the threshold energy for the penetration of normally incident Ar ions through the (0001) surface into the graphite layer was determined to be 43.5 eV.

We can see in Fig. 1b that the difference between the average energies of scattered Ar and Xe ions is due to the mechanisms of reflection of bombarding Ar and Xe ions being different, which also manifests itself in much different behaviors of the average reflection energies at polar angles of 85°–105°. Xe ions are reflected from a cluster due to the mechanism of collective reflection of a heavy particle by a group of lighter Cu atoms. At polar scattering angles of up to 50°, the average energies of the reflected Xe ions are rather low (Fig. 3b) and differ only slightly for different clusters. This counts in favor of the mechanisms of collective reflection of heavy ions by 3 to 4 cluster atoms at small angles being identical. When an energy of 50–150 eV is retained after interaction with a cluster at polar angles of motion greater than 135°, Xe ions (as tests showed) damage the surface atomic layer of the graphite. In this case, the ions lose most of their energy and, as a rule, penetrate into the substrate. It should be noted that, even in the case where the polar angle of incidence on the (0001) graphite surface is 115°–120°, Ar and Xe ions lose approximately half their energy in reflection from the substrate. The dependence shown in Fig. 3b is similar to that in Fig. 2b; namely, the polar angle corresponding to the maximum of the average energy of reflected Xe ions increases with cluster size.

3.3. Polar and Azimuthal Distributions of Sputtered Cu Atoms

Figure 4 shows the polar angular dependences of the differential sputtering coefficient $dY/d\varphi$ (where φ is the polar angle) for isolated copper atoms (disregarding sputtered dimers, trimers, etc.) knocked out of the (13 Cu), (27 Cu), and (195 Cu) clusters by Ar and Xe ions with a primary energy of 200 eV. We can see that the $dY/d\varphi$ distribution maximum is near the normal polar angle for both ion types, irrespective of the cluster size. There is no principal difference between the polar distributions of $dY/d\varphi$ of sputtered atoms for Ar and Xe ions. There are at least two sputtering mechanisms for both ion types: (1) the recoil mechanism (1 to 2 collisions of Cu atoms) with random and focused emission directions of particles sputtered from clusters in the entire range of polar angles and (2) the mechanism of

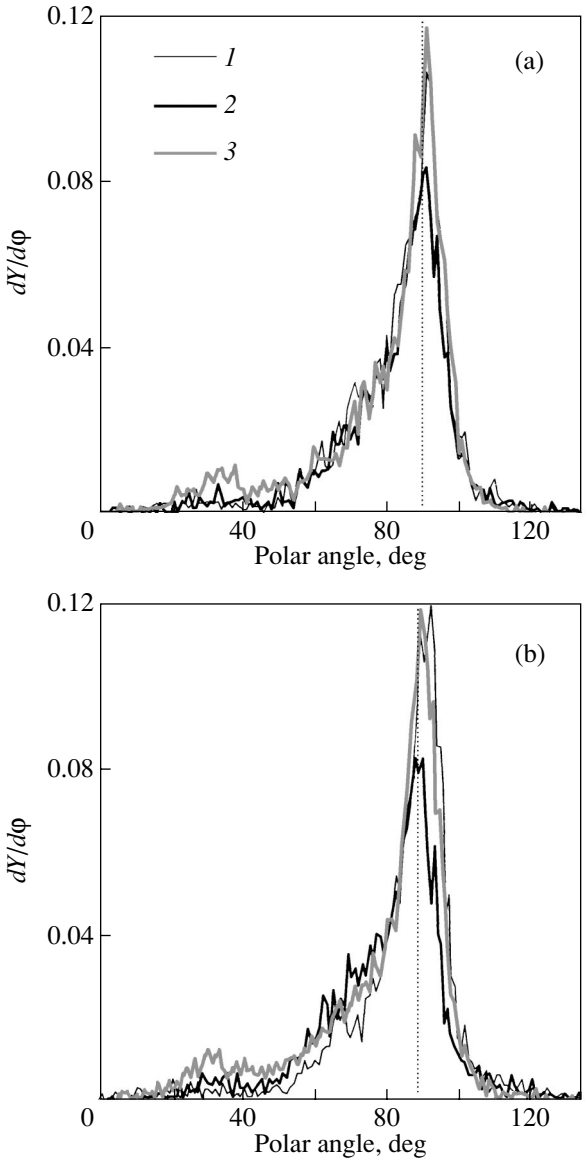

Fig. 4. Dependence of the differential coefficient of sputtering of Cu atoms by (a) Ar and (b) Xe ions on the polar angle of atom emission (with a resolution of 1°). Curves *1–3* correspond to the clusters (13 Cu), (27 Cu), and (195 Cu), respectively.

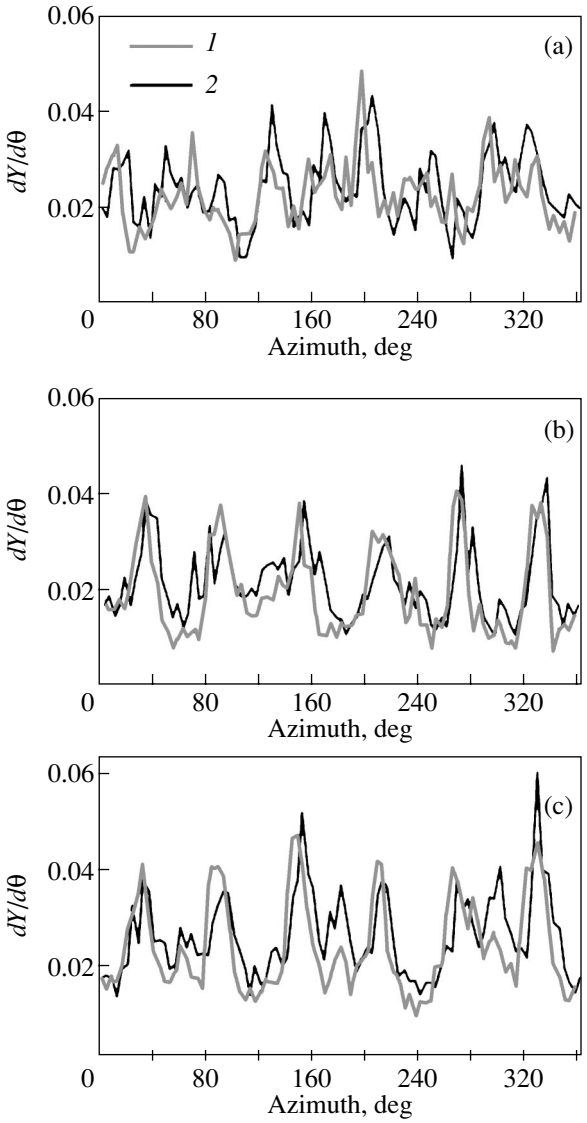

Fig. 5. Dependence of the differential coefficient of sputtering of Cu atoms from (a) (13 Cu), (b) (27 Cu), and (c) (195 Cu) clusters by Ar ions (curve *1*) and Xe ions (curve *2*) on the azimuthal angle of atom emission (with a resolution of 4°).

successive collisions [2 to 4 collisions of Cu atoms in the (27 Cu) and (195 Cu) clusters], some of which are focused. The second mechanism is efficient if there is a free surface area on the cluster side faces, through which emission occurs of most of the sputtered copper atoms and of straight atomic chains (parallel to the substrate; 3 to 6 Cu atoms) in clusters. As is evident from Fig. 4, there is no direct relation between the shape of the polar distribution and the atomic structure of a cluster, since there are no qualitative differences between the polar distributions for the (13 Cu) cluster, on the one hand, and the (27 Cu) and (195 Cu) clusters, on the other, despite the fundamental differences in their atomic structures. In the case of the (13 Cu) cluster, the first mechanism controls sputtering in the entire range of polar angles. A certain number of sputtered atoms leave clusters in directions with polar angles greater than 90°. We can see in Fig. 4 that some of these atoms are not reflected from the model substrate since the substrate is bounded in space.

Figure 5 shows the azimuthal angular dependences of the differential sputtering coefficient $dY/d\theta$ (θ is the azimuthal angle of emitted Cu atoms) for isolated atoms in the case of the (13 Cu), (27 Cu), and (195 Cu) clusters bombarded by Ar and Xe ions. The azimuthal angle was measured counterclockwise from the [1000] direction in the (0001) graphite surface. The characteristic components of the distributions correspond to each other in the case of Ar and Xe ions for all clusters (although they can differ in terms of their intensities), which suggests that the mechanisms of cluster sputtering by different types of ions are similar.

For the (13 Cu) cluster in Fig. 5a, there is no angular azimuthal periodicity in the distributions of sputtered particles. In Figs. 5b and 5c, the differential sputtering coefficients for the (27 Cu) and (195 Cu) clusters, respectively, have maxima in sectors near 30°, 90°, 150°, 210°, 270°, and 330° for both ion types. The preferential sputtering directions of Cu atoms in the azimuth for the (27 Cu) and (195 Cu) clusters are almost coincident with the ⟨1100⟩ directions of the graphite substrate. The largest openness of atomic structures of these surface clusters was observed in the ⟨1100⟩ directions, along which parallel chains of 3 to 6 Cu atoms (oriented in the azimuth along the (0001) atomic plane of graphite) are arranged. Thus, preferential sputtering of the (27 Cu) and (195 Cu) copper surface clusters in the ⟨1100⟩ directions is caused by the occurrence of 2 to 4 focused atomic collisions in the clusters. For the (13 Cu) cluster, the absence of azimuthal periodicity of the sputtering intensity is due to the small number of Cu atoms and to its atomic structure being different from that of large clusters. The (13 Cu) cluster remains an almost perfect cubic octahedron even on the substrate.

We can see in Figs. 5b and 5c that, when the (27 Cu) and (195 Cu) clusters are bombarded by Xe ions, additional maxima arise in some cases near the main sputtering peaks (which coincide in azimuth with the peaks characteristic of Ar ions). For example, for the (195 Cu) cluster, two peaks arise near azimuthal angles of 180° and 300°. In the case of Ar ions, insignificant spikes in the sputtering intensity are also observed at these azimuthal angles; however, they are weak in comparison with the main maxima. Presumably, Xe ions incorporated into the cluster increase its atomic structure openness, which brings about an increase in the sputtering intensity in the directions that are less open under bombardment by Ar ions.

3.4. Sputtering Coefficients

Figure 6 shows the sputtering coefficients taking into account isolated atoms, dimers, trimers, etc., for

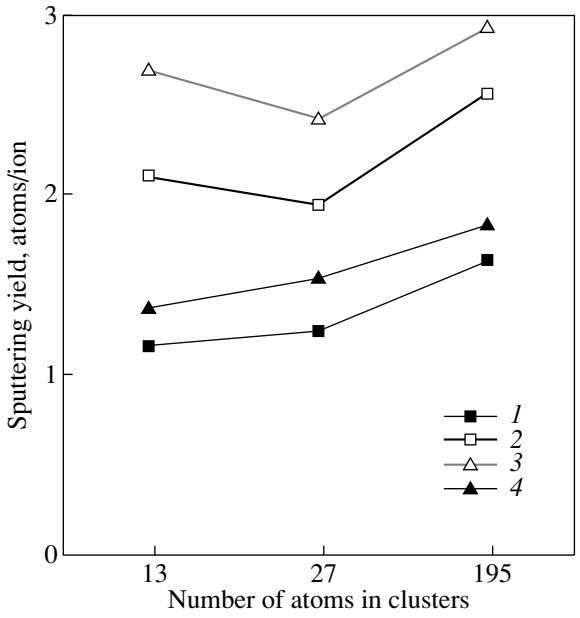

Fig. 6. Sputtering coefficients of the (13 Cu), (27 Cu), and (195 Cu) clusters for the emission of Cu atoms at polar angles of up to 90° (curves *1* and *4* correspond to Ar and Xe, respectively) and at all polar angles (curves *2* and *3* correspond to Ar and Xe, respectively) at a primary ion energy of 200 eV.

the clusters bombarded by Ar ions (curves *1*, *2*) and Xe ions (curves *3*, *4*). The total number of atoms in sputtered multiatomic Cu particles accounts for 10–20% of all sputtered Cu atoms. In the case of Ar ions, this number is 10% for (13 Cu) and 20% for (195 Cu); in the case of Xe ions, this number is ~20% for all clusters The difference between the model sputtering coefficients for Cu particles emitted from clusters at polar angles of up to 90° [curves *1* (Ar) and *4* (Xe)] and for Cu particles emitted at all polar angles [curves *2* (Ar) and *3* (Xe)] can be as large as 50%. Since some sputtered cluster atoms can adhere to the substrate in the case where they are emitted from the cluster at polar angles greater than 90°, the actual values of the sputtering coefficient lie between the total sputtering coefficient of Cu atoms and that for angles smaller than 90°. The values of the puttering coefficient for Xe ions are larger than those for Ar ions in all cases under consideration. This difference is likely due to the difference between the elastic energy losses of Ar and Xe ions in clusters (see Subsection 3.1). The total sputtering coefficients of surface clusters have insignificant minima for the (27 Cu) cluster and maxima for the (195 Cu) cluster for both ion types. The sputtering coefficient of graphite for Ar and Xe ions with an energy of 200 eV is negligible and is not considered in this paper.

Energy and dimensional parameters of clusters

Cluster parameters	(13 Cu)	(27 Cu)	(195 Cu)
U_{sub}, eV	2.57	2.65	3.08
U_{coh}, eV	2.58	9.89	22.65
N_a	3	14	32
H_n, Å	5.8	5.9	14.2

The table lists the energy and dimensional parameters of simulated clusters. The sublimation energy U_{sub} of clusters slightly increases with the number of atoms composing the cluster. The cohesion energy (U_{coh}) of model clusters to the substrate is proportional to the number N_a of Cu atoms at the copper–graphite interface (see Section 2). The cluster height H_n was determined as the distance from the graphite substrate to a cluster atom at the longest distance from it. The smaller total sputtering coefficient of the (27 Cu) cluster in comparison with (13 Cu) is obviously caused by a change in the type of cluster attachment to the substrate as the cluster size increases, which is evident from the values of the parameters N_a and U_{coh}. An increase in N_a promotes a more efficient transfer of the energy introduced by a bombarding ion from the cluster to the substrate, which decreases the ion energy fraction expended on cluster sputtering. The heights H_n of the (13 Cu) and (27 Cu) clusters are almost identical; therefore, their difference has no effect on changing the sputtering coefficient. The larger sputtering coefficient of the (195 Cu) cluster in comparison with that of (27 Cu) is caused by a significantly larger height of the (195 Cu) cluster. The ion energy transferred to upper atoms of this cluster (which consists of more than three atomic layers) does not reach the substrate for a characteristic sputtering time, which is of the same order as the period of lattice atom vibrations (~10^{-13} s). Therefore, the role of the copper–graphite interface area in sputtering is insignificant for clusters with a large height H_n, which is evident from the data given in the table and Fig. 6.

4. CONCLUSIONS

A molecular-dynamics simulation of the interaction of Ar and Xe ions having a primary energy of 200 eV with copper surface clusters consisting of 13, 27, and 195 Cu atoms has been carried out. It has been shown that the coefficients of reflection of Ar and Xe ions from copper clusters differ insignificantly, although the energies of the reflected Xe ions are much lower than those of Ar ions. The cluster sputtering coefficients for Xe ions are larger than those for Ar ions. Two cluster sputtering mechanisms have been identified. With these mechanisms, the sputtering intensity is maximum at incident directions close to the normal and the maxima in the azimuthal distributions of the sputtering intensity are periodic with a period of 60°. The azimuthal periodicity in cluster sputtering is dictated by the most open ⟨1100⟩ directions in the cluster atomic structure, which arise due to the interaction of surface clusters with the (0001) graphite substrate.

ACKNOWLEDGMENTS

One of the authors (G.V.K.) is grateful to the Technische Universität, Wien, and the Christian-Albrechts Universität, Kiel, for their support during his work at the Institut für Allgemeine Physik and Lehrstuhl für Materialverbund.

This study was supported by the Ministry of Education and Science of Ukraine (grant DB 04314), Wien Technical University (grant UT8/058-04), and Kiel University (grant 405/1033976).

REFERENCES

1. W. F. Egelhoff, Jr. and G. G. Tibbetts, Phys. Rev. B: Condens. Matter **19**, 5028 (1979).
2. I. Jirka, Surf. Sci. **232**, 307 (1990).
3. S. Di Nardo, L. Lozzi, M. Passacantando, P. Picozzi, S. Santucci, and M. de Crescenzi, Surf. Sci. **307–309**, 922 (1994).
4. P. Marcus and C. Hinnen, Surf. Sci. **392**, 134 (1997).
5. D.-Q. Yang and E. Sacher, Appl. Surf. Sci. **195**, 187 (2002).
6. V. Zaporojtchenko, K. Behnke, T. Strunskus, and F. Faupel, Surf. Interface Anal. **30**, 439 (2000).
7. Y. Tai, J. Murakami, C. Majumder, V. Kumar, H. Mizuseki, and Y. Kawazoe, J. Chem. Phys. **117** (9), 4317 (2002).
8. J. Lehmann, M. Merschdorf, W. Pfeiffer, A. Thon, S. Voll, and G. Gerber, J. Chem. Phys. **112** (12), 5428 (2000).
9. R. Anton and I. Schneidereit, Phys. Rev. B: Condens. Matter **58** (20), 13874 (1998).
10. R. Smith and K. Beardmore, Thin Solid Films **272**, 255 (1996).
11. K. Nordlund, J. Keinonen, and T. Mattila, Phys. Rev. Lett. **77** (4), 699 (1996).
12. R. P. Webb and I. H. Wilson, Nucl. Instrum. Methods Phys. Res., Sect. B **202**, 217 (2003).
13. Z. Y. Pan, Z. Y. Man, and M. Hou, Z. Phys. D: At., Mol. Clusters **41**, 275 (1997).
14. H. Rafii-Tabar, H. Kamiyama, and M. Cross, Surf. Sci. **385**, 187 (1997).
15. J. W. Kang and H. J. Hwang, Comput. Mater. Sci. **23**, 105 (2002).
16. F. J. Palacios, M. P. Iniguez, M. J. Lopez, and J. A. Alonso, Comput. Mater. Sci. **17**, 515 (2000).
17. D. Pantelios and G. A. Evangelakis, Comput. Mater. Sci. **25**, 493 (2002).
18. G. W. Wu and K. Y. Chan, Surf. Sci. **365**, 38 (1996).
19. G. Betz and W. Husinsky, Nucl. Instrum. Methods Phys. Res., Sect. B **122**, 311 (1997).
20. I. Yamada, J. Matsuo, and N. Toyoda, Nucl. Instrum. Methods Phys. Res., Sect. B **206**, 820 (2003).
21. Z. Insepov, L. P. Allen, C. Santeufemio, K.S. Jones, and I. Yamada, Nucl. Instrum. Methods Phys. Res., Sect. B **202**, 261 (2003).
22. X. M. Wang, H. Chen, L. Shao, J. R. Liu, and W. K. Chu, Nucl. Instrum. Methods Phys. Res., Sect. B **196**, 100 (2002).
23. M. Henkel and H. M. Urbassek, Nucl. Instrum. Methods Phys. Res., Sect. B **145**, 503 (1998).
24. G. Betz and W. Husinsky, Nucl. Instrum. Methods Phys. Res., Sect. B **102**, 281 (1995).
25. Z. Postawa, K. Ludwig, J. Piaskowy, K. Krantzman, N. Winograd, and B. J. Garrison, Nucl. Instrum. Methods Phys. Res., Sect. B **202**, 168 (2003).
26. J. M. Haile, *Molecular Dynamics Simulation—Elementary Methods* (Wiley Interscience, New York, 1992).
27. G. V. Kornich, G. Betz, V. I. Zaporojtchenko, and A. I. Bazhin, Pis'ma Zh. Tekh. Fiz. **29** (22), 33 (2003) [Tech. Phys. Lett. **29** (11), 938 (2003)].
28. G. V. Kornich, G. Betz, and A. I. Bazhin, Fiz. Tverd. Tela (St. Petersburg) **43** (1), 30 (2001) [Phys. Solid State **43** (1), 29 (2001)].
29. G. V. Kornich, G. Betz, A. I. Bazhin, and V. G. Kornich, Izv. Akad. Nauk, Ser. Fiz. **66** (1), 89 (2002).
30. H. Gades and H. M. Urbassek, Nucl. Instrum. Methods Phys. Res., Ser. B **69**, 232 (1992).
31. G. Betz, R. Kirchner, W. Husinsky, F. Rüdenauer, and H. M. Urbassek, Radiat. Eff. Defects Solids **130–131**, 251 (1994).
32. W. Eckstein, *Computer Simulation of Ion-Solid Interactions* (Springer, Berlin, 1991; Mir, Moscow, 1995).
33. J. Tersoff, Phys. Rev. B: Condens. Matter **39**, 5566 (1989).
34. S. Dorfman, K. C. Mundim, D. Fuks, A. Berner, D. E. Ellis, and J. van Humbeeck, Mater. Sci. Eng., C **15**, 191 (2001).
35. H. J. Berendsen, J. P. M. Postma, W. F. V. Gunsteren, A. Di-Nola, and J. R. Haak, J. Chem. Phys. **81**, 3684 (1984).
36. D. Marton, H. Bu, K. J. Boyd, S. S. Todorov, A. H. Al-Bayati, and J. W. Rabalais, Surf. Sci. Lett. **326**, L489 (1995).

Translated by A. Kazantsev

Physics of the Solid State, Vol. 47, No. 10, 2005, pp. 1993–1997. Translated from Fizika Tverdogo Tela, Vol. 47, No. 10, 2005, pp. 1914–1918.

FULLERENES AND ATOMIC CLUSTERS

C_{60} Heat Capacity Anomaly at the Orientational Phase Transition

V. M. Egorov*, B. I. Smirnov*, V. V. Shpeĭzman*, R. K. Nikolaev, and N. S. Sidorov****

**Ioffe Physicotechnical Institute, Russian Academy of Sciences, ul. Politekhnicheskaya 26, St. Petersburg, 194021 Russia*
e-mail: V.Egorov@mail.ioffe.ru

***Institute of Solid State Physics, Russian Academy of Sciences, Chernogolovka, Moscow oblast, 142432 Russia*

Received December 9, 2004

Abstract—An orientational phase transition in C_{60} crystals was studied by differential scanning calorimetry with the highest resolution provided by this method. The temperature dependence of the specific heat $\Delta C_p(T)$ was found to have a double peak in the range 250–270 K. An analysis of the temperature dependences of heat capacity in the region of the peaks revealed that the lower temperature peak follows a power law of the type $\Delta C_p = A/(T - T_0)^{1/2}$ characteristic of order–disorder second-order phase transitions, while the high-temperature peak can be identified with a diffuse Λ-shaped first-order phase transition. © *2005 Pleiades Publishing, Inc.*

1. INTRODUCTION

The phase transition in the C_{60} fullerene occurring near 260 K has been sufficiently studied by a variety of physical methods. This transition is assigned to an orientational transition originating from the onset of an additional orientational order of rotating C_{60} molecules below the phase transition point, which is assumed to account for a change in the crystal symmetry, more specifically, to the transition from the face-centered cubic (fcc) to a simple cubic (sc) lattice. It has been established that in this transition the positions of the C_{60} molecules preserve the fcc structure and that the additional orientational order stems from the fact that to each sc lattice site now corresponds a tetrahedron formed by four molecules with fixed orientations along four different directions [1, 2].

The temperature dependence of the heat capacity of polycrystalline samples measured in the 259- to 270-K interval exhibits a fairly sharp asymmetric peak (endothermal on heating and exothermal on cooling) [1, 3], which shows a ~1- to 3-K hysteresis in the heating–cooling cycle [4]. The peak shape depends strongly on the technology of preparation used and on the mechanical prehistory of the sample [5]. C_{60} powders, as well as fullerene samples subjected to preliminary hydrostatic compression, revealed a double rather than a single peak [6]. The dependence of the thermodynamic parameters of the phase transition and of the macroscopic properties of C_{60} crystals on the quality of the starting samples and on the thermal [7] and mechanical [8–11] prehistory accounts for the discrepancies between the calorimetric data (temperature, enthalpy) obtained by different researchers.

The present communication reports on an experimental DSC determination of the thermodynamic parameters of the orientational phase transition in the most perfect C_{60} crystals under conditions providing the highest possible resolution of the method.

2. EXPERIMENTAL TECHNIQUE

The heat capacity of C_{60} crystals was studied by DSC on a DSC-2 Perkin–Elmer calorimeter in a nitrogen environment at heating and cooling rates variable in the range 5–0.3 K/min. The temperature scale was calibrated against the melting points of ice (273.1 K) and indium (429.7 K), and the heat flow scale was calibrated using the sapphire specific heat. The characteristics determined for the C_{60} samples studied were the temperatures of the maximum of the endothermal peak T_{max} under heating and of the minimum of the exothermal peak T_{min} under cooling, as well as the temperature dependence of the specific heat, $C_p(T)$, in the range 220–280 K.

C_{60} single crystals were prepared by a modified technique [12] of vapor phase crystal growth [13] in which the starting material used consisted of small C_{60} crystals purified preliminarily by repeated sublimation in vacuum. The weight of the samples intended for calorimetric measurements by DSC was ~3 mg. The samples were well-faceted plane-parallel platelets measuring $0.5 \times 2 \times 2$ mm, which shape provided the smallest thermal resistance of samples of this weight.

3. EXPERIMENTAL RESULTS AND DISCUSSION

Figure 1 presents DSC curves obtained under heating and cooling of C_{60} samples at scanning rates of 0.31 to 5 K/min which exhibit endo- and exothermal phase

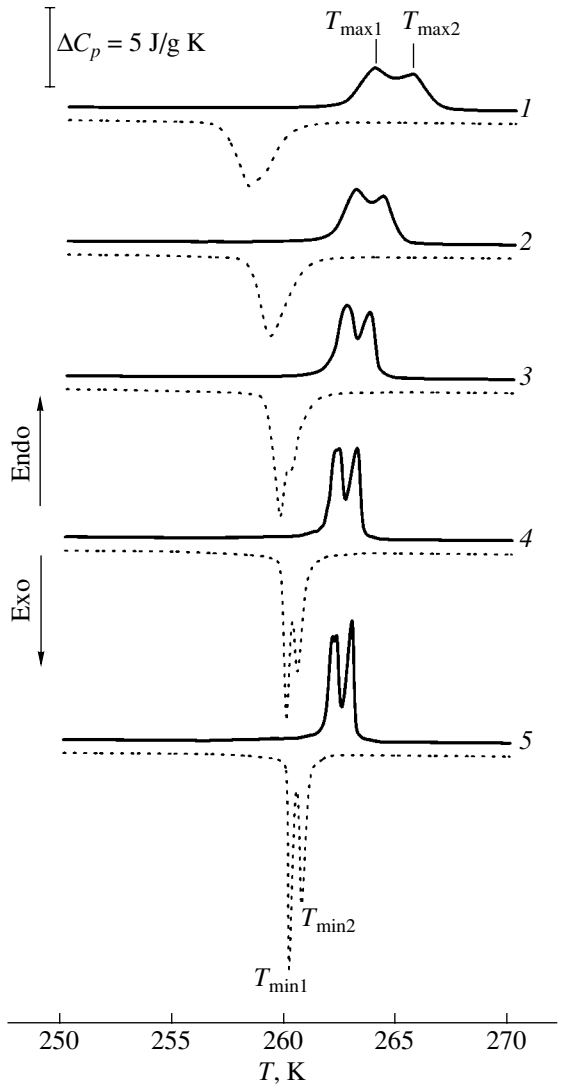

Fig. 1. DSC curves of a C_{60} sample obtained under heating (solid lines) and cooling (dashed lines) at a rate of (*1*) 5, (*2*) 2.5, (*3*) 1.25, (*4*) 0.62, and (*5*) 0.31 K/min.

transition peaks. The pattern observed at a high heating rate (curves *1*, *2*) fits, on the whole, the results reported in available publications; namely, one clearly sees an asymmetric peak with a well-pronounced temperature hysteresis in the heating–cooling cycle. At lower scanning rates, however (curves *3*–*5*), the direct and reverse evolution of the phase state of C_{60} crystals occurs in two stages; indeed, in place of one peak, the DSC curves obtained both under cooling and heating exhibit a doublet. To understand the physical nature of the observed transitions, one has to elucidate the situation where the peaks do not coincide in temperature, i.e., where hysteresis occurs. As seen from Fig. 1, the maxima of both the endo- and exothermal peaks of the doublet obtained in the heating and cooling DSC cycles shift in relative position (i.e., $T_{max1} - T_{min1}$ and $T_{max2} - T_{min2}$ are non-

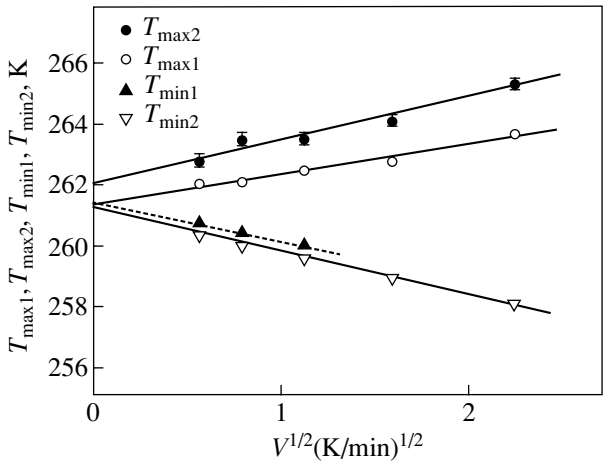

Fig. 2. Phase transition temperatures plotted vs the scanning (heating–cooling) rate for C_{60} samples.

zero). It was found that these shifts (the so-called hysteresis effect) are of different natures for each of the doublet peaks, which can be traced to both methodological and physical causes.

It is known [14] that the temperature parameters of the heat capacity peaks (including T_{max} and T_{min}) as determined by DSC contain a methodological error ΔT, which doubles in the heating and cooling cycle to produce a semblance of a temperature hysteresis, the so-called apparent hysteresis. The absolute value of ΔT depends on the scanning rate and sample mass. For samples ~10–20 mg in mass and with the customarily used scanning rates of 5–10 K/min, this error can amount to 5–7 K. In the present study, this error was removed by employing a special procedure [15] in which the experimental data obtained at different scanning (heating or cooling) rates V are used to construct $T_{max, min} = f(V^{1/2})$ graphs. In the absence of any structural transformations, these graphs should be linear. Extrapolation of these linear relations to $V \longrightarrow 0$ yields the true phase transition temperatures not distorted by methodological errors.

Figure 2 displays such graphs obtained in heating–cooling runs on the C_{60} samples studied. It was found that the extrapolated (true) phase transition temperatures are $T_{max1} = T_{min1} = T_{min2} = 261.6$ K and $T_{max2} = 262.2$ K. These data suggest that in actual fact the lower temperature peaks have no hysteresis in the heating–cooling cycles at all and that the difference in their positions in the experimental DSC curves stems from the methodology employed. The absence of hysteresis assigns this peak in the doublet directly to a second-order phase transition. If, rather than resorting to the $T_{max, min} = f(V^{1/2})$ extrapolation as done in this study, one chooses to use the data obtained at one scanning rate in temperature (which seem to suggest an apparent hysteresis), these peaks cannot be attributed to second-order transitions.

Elimination of the methodological error through extrapolation permitted us to establish a hysteresis of ~0.6 K for the higher temperature peaks and to assign this phase transition to the first order.

The enthalpy of the transition ΔH_{exp} is defined by the expression $\Delta H_{exp} = \int \Delta C_p(T)dT$ and can be found without having to resort to extrapolation, because the area bounded by the heat capacity peak in the DSC curve depends on neither the thermal resistance nor the scanning rate. The total enthalpy of the transition (the doublet) was found to be equal to $\Delta H_{exp} = 10.9$ J/g.

The absence of a temperature hysteresis and the specific λ shape of the low-temperature peak are signatures of a second-order phase transition of the order–disorder type, for which the temperature dependence of the specific heat $C_p(T)$ is described by a power-law function [16]

$$\Delta C_p(T) = A(T_{01} - T)^{-\alpha}, \quad (1)$$

where A, T_{01}, and α are constants. T_{01} has the meaning of the true temperature of a second-order phase transition. A good fit of the calculations to the experimental $\Delta C_p(T)$ relation for the low-temperature shoulder in the λ-shaped peak was obtained with $A = 1.1$, $\alpha = 0.5$, and $T_{01} = 261.6$ K (circles in Fig. 3a), which convincingly supports our interpretation of this phase transition to be of the order–disorder type [17].

This is insufficient, however, for experimental determination of the entropy and of the heat of transition, because the peaks in the doublet overlap and isolation of the low-temperature peak based only on Eq. (1) for the low-temperature branch does not appear possible. One can try to use the difference between the experimental $C_p(T)$ relation (for the doublet) and the isolated high-temperature peak to resolve the low-temperature feature.

It is well known [17] that the presence or absence of a temperature hysteresis in a physical property, including peaks in the temperature dependence of the heat capacity, is a signature of the first- and second-order phase transitions, respectively. To characterize thermodynamic transitions in calorimetric measurements, information on the peak shape is also appropriate. Ideal first-order transitions are associated with a δ-function peak with a zero temperature interval and a discontinuity in the $C_p(T)$ relation at the phase transition point. In real crystals, interaction of the interface (the presence of an interface is an essential feature of a first-order transition) with structural defects, as well as the presence of compositional fluctuations, gives rise to a nonzero temperature width of the transition and a diffuse peak shape. Such transitions are called diffuse first-order transitions [18], and they are characterized by a symmetric Λ-shaped peak and a nonzero temperature interval. The hysteresis observed in this study, the finite temperature width of the peak, and its Λ-shaped profile permit its assignment to a first-order transition.

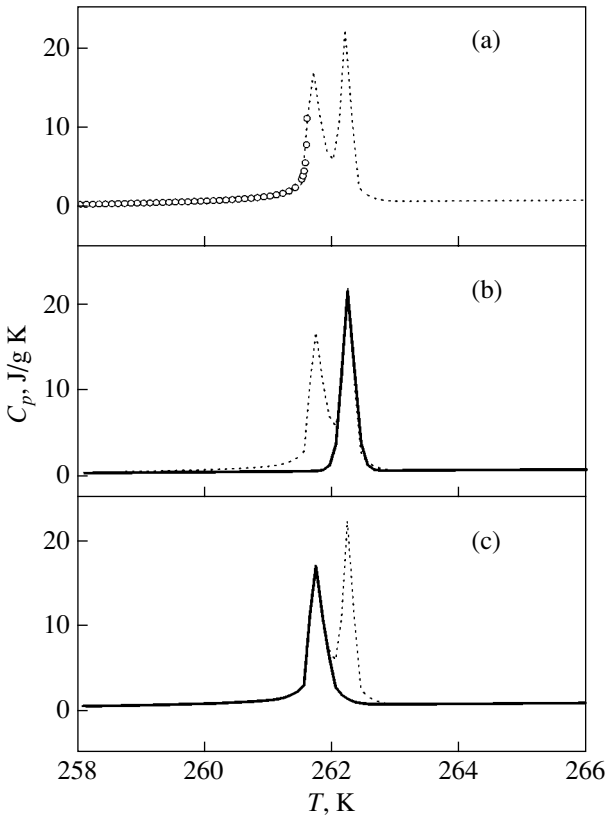

Fig. 3. DSC curve obtained by heating a C_{60} sample at a rate of 0.31 K/min (dashed lines). The circles in panel (a) plot the temperature dependence of the second-order phase-transition specific heat calculated from Eq. (1). The solid line in panel (b) is a plot of the first-order phase-transition specific heat calculated from Eq. (2). The solid line in panel (c) is the specific heat for the second-order phase transition obtained by subtracting the first-order phase transition specific heat from the experimental data.

The temperature dependence of the specific heat associated with a diffuse Λ-shaped first-order phase transition can be written as [19]

$$\Delta C_p(T) = 4\Delta C_m F(T)/[1 + F(T)]^2, \quad (2)$$

where $F(T) = \exp[B(T - T_{02})/T_{02}]$, T_{02} is the first-order phase transition temperature and ΔC_m is the maximum value of the specific heat at $T = T_{02}$. Figure 3b plots the specific heat calculated from Eq. (2) using the known values $\Delta C_m = 21.9$ J/gK and $T_{02} = 262.2$ K. The best fit of the calculated to experimental relation was found with $B = 4200$. The parameter B contains the most interesting information on the physical nature of a phase transition, because it is related [19] to the height of the specific-heat peak ΔC_m ($\Delta C_m = qB/4T_{02}$, where q is the heat of transition) and to the elementary volume of transformation ω ($B = \omega q/kT_{02}$, where k is the Boltzmann constant). The first relation yields for the specific

heat (enthalpy) of the transition $q = \Delta H_2 = 5.25$ J/g (for the C_{60} crystal density $\rho = 1.62$ g/cm^3 [20], the volume specific heat of transition is $q = 8.5$ J/cm^3), and the second relation gives the elementary volume of the transformation $\omega = (kT_{02}/q)B \approx 1.8 \times 10^{-18}$ cm^{-3}. Using the lattice parameter of the C_{60} crystal $a = 1.41$ nm, the number of molecules involved in a correlated transformation event in this case can be found to be $n \approx \omega/a^3 \approx 640$.

The elementary volume of transformation obtained is of a mesoscopic scale and does not compare to known microscopic transformation volumes, for instance, to the volume of a tetrahedron formed by four C_{60} molecules ($n = 4$) or to the volumes of transformation of the orientational transition in C_{60} ($n \approx 20$) measured in neutron studies [21, 22]. On the mesoscopic scale, this volume may be compared to the volume of the Känzig region (~10^{-18}–10^{-17} cm^3) [23, 24]. The latter volume represents a structure-sensitive parameter characterizing regions of new-phase nucleation in materials undergoing a diffuse first-order phase transition.

Using the first, low-temperature peak, one can find the thermodynamic parameters of the corresponding phase transition. For instance, the enthalpy ΔH_1 can be determined from the difference $\Delta H_1 = \Delta H_{exp} - \Delta H_2 = 10.9 - 5.25 = 5.65$ J/g. To learn the entropy of the λ-shaped transition, one needs to know the temperature dependence of the specific heat $\Delta C_{p1}(T)$. The good fit between the calculated, $\Delta C_{p2}(T)$, and experimental, $\Delta C_{exp}(T)$ temperature dependences of the specific heat for the high-temperature peak permits one to isolate $\Delta C_{p1}(T)$ from the doublet using the difference $\Delta C_{p1}(T) = \Delta C_{exp}(T) - \Delta C_{p2}(T)$ (Fig. 3c). The entropy of the transition ΔS_1 as derived from the relation $\Delta S_1 = \int \Delta C_{p1}(T) d(\ln T)$ was found to be $\Delta S_1 = 0.0238$ J/gK.

It is well known [16, 25] that the variation of the heat capacity due to an order–disorder transition originates from the change in the configurational entropy, whose limiting value upon completion of the phase transition is $\Delta S_c = R\ln 2 = 5.73$ J/mol K. By comparing ΔS_1 with ΔS_c one can determine the mass of one mole of building blocks involved in the phase transition; if $\Delta S_1 = 0.0238$ J/g K and $\Delta S_c = 5.73$ J/mol K, then 1 mole = 240 g. Therefore, the relevant building block consists of $n \approx 3.4$ C_{60} molecules (for C_{60}, 1 mole = 72 g). This result suggests that the building blocks involved in the order–disorder phase transition are close in mass to tetrahedra. Thus, our estimate is consistent with the interpretation of the phase transition according to which the additional orientational order is accounted for by each site of the sc lattice being identified with a tetrahedron formed by four C_{60} molecules.

4. CONCLUSIONS

Experimental DSC data obtained under variation of the heating and cooling rates have permitted us to eliminate methodological errors and determine the true values of the thermodynamic parameters of phase transitions in C_{60}, in particular, the order–disorder transition temperature ($T_{max1} = T_{min1} = 261.6$ K) and the temperatures and hysteresis of the diffuse first-order transition ($T_{max2} = 262.2$ K, $T_{min2} = 261.6$ K). The good fit between the theoretical and experimental dependences of the heat capacity on temperature for the Λ-shaped transition made it possible to isolate the peak corresponding to the order–disorder solid-phase transition and to estimate the elementary volume of transformation, which turned out to be comparable to the volume of the Känzig region. A comparison of the experimental entropy with the calculated entropy of the order–disorder transition has revealed that the phase transition involves building blocks close in mass to tetrahedra.

ACKNOWLEDGMENTS

The authors are indebted to G.A. Malygin for helpful discussions of the work.

This study was supported by the Ministry of Education and Science of the Russian Federation.

REFERENCES

1. P. A. Heiney, J. E. Fisher, A. R. McChie, W. J. Romanov, A. M. Denenstein, J. P. McCauley, A. B. Smith, and D. E. Cox, Phys. Rev. Lett. **66** (22), 2911 (1991).
2. O. Gunnarsson, S. Satpathy, O. Jepsen, and O. K. Andersen, Phys. Rev. Lett. **67** (21), 3002 (1991).
3. B. V. Lebedev, K. B. Zhogova, T. A. Bykova, B. S. Kaverin, V. L. Karnatsevich, and M. A. Lopatin, Izv. Akad. Nauk, Ser. Khim. **60** (9), 2229 (1996).
4. V. M. Egorov, I. N. Kremenskaya, B. I. Smirnov, and V. V. Shpeĭzman, Fiz. Tverd. Tela (St. Petersburg) **37** (11), 3493 (1995) [Phys. Solid State **37** (11), 1919 (1995)].
5. A. V. Markin, N. N. Smirnova, B. V. Lebedev, A. G. Lyapin, M. V. Kondrin, and V. V. Brazhkin, Fiz. Tverd. Tela (St. Petersburg) **45** (4), 761 (2003) [Phys. Solid State **45** (4), 802 (2003)].
6. V. M. Egorov, V. V. Shpeĭzman, and I. N. Kremenskaya, Pis'ma Zh. Tekh. Fiz. **19** (19), 49 (1993) [Tech. Phys. Lett. **19**, 621 (1993)].
7. V. M. Egorov, R. K. Nikolaev, B. I. Smirnov, and V. V. Shpeĭzman, Fiz. Tverd. Tela (St. Petersburg) **42** (9), 1716 (2000) [Phys. Solid State **42** (9), 1766 (2000)].
8. V. M. Egorov, V. I. Nikolaev, R. K. Nikolaev, B. I. Smirnov, and V. V. Shpeĭzman, Fiz. Tverd. Tela (St. Petersburg) **41** (3), 550 (1999) [Phys. Solid State **41** (3), 494 (1999)].
9. V. M. Egorov, B. I. Smirnov, V. V. Shpeĭzman, and R. K. Nikolaev, Fiz. Tverd. Tela (St. Petersburg) **38** (7), 2214 (1996) [Phys. Solid State **38** (7), 1219 (1996)].

10. V. V. Shpeĭzman, N. N. Peschanskaya, V. M. Egorov, V. I. Nikolaev, R. K. Nikolaev, and B. I. Smirnov, Fiz. Tverd. Tela (St. Petersburg) **41** (6), 1115 (1999) [Phys. Solid State **41** (6), 1017 (1999)].
11. V. V. Shpeĭzman, N. N. Peschanskaya, V. M. Egorov, V. I. Nikolaev, R. K. Nikolaev, and B. I. Smirnov, Fiz. Tverd. Tela (St. Petersburg) **42** (9), 1721 (2000) [Phys. Solid State **42** (9), 1771 (2000)].
12. N. P. Kobelev, R. K. Nikolaev, Ya. M. Soĭfer, and S. S. Khasanov, Fiz. Tverd. Tela (St. Petersburg) **40** (1), 173 (1998) [Phys. Solid State **40** (1), 154 (1998)].
13. M. Tachibana, M. Michiyama, and H. Sakuma, J. Cryst. Growth **166**, 883 (1996).
14. V. A. Bershtein and V. M. Egorov, *Differential Scanning Calorimetry of Polymers: Physics, Chemistry, Analysis, and Technology* (Ellis Horwood, New York, 1994).
15. K. Illers, Eur. Polym. J. **10**, 911 (1974).
16. M. Fisher, *The Nature of Critical Points* (University of Colorado Press, Boulder, 1965; Mir, Moscow 1973).
17. L. D. Landau and E. M. Lifshitz, *Course of Theoretical Physics*, Vol. 5: *Statistical Physics*, 2nd ed. (Nauka, Moscow, 1964; Pergamon, Oxford, 1980).
18. G. A. Malygin, Usp. Fiz. Nauk **171** (2), 187 (2001) [Phys. Usp. **44** (2), 173 (2001)].
19. G. A. Malygin, Fiz. Tverd. Tela (St. Petersburg) **43** (10), 1911 (2001) [Phys. Solid State **43** (10), 1989 (2001)].
20. V. D. Blank, A. A. Nuzhdin, V. M. Prokhorov, and R. Kh. Bagramov, Fiz. Tverd. Tela (St. Petersburg) **40** (7), 1387 (1998) [Phys. Solid State **40** (10), 1261 (1998)].
21. B. Sundqvist, Adv. Phys. **48** (1), 1 (1999).
22. L. Pintschovius, S. L. Chaplo, G. Roth, and G. Heger, Phys. Rev. Lett. **75** (15), 2843 (1995).
23. V. Kanzig, *Ferroelectrics and Antiferroelectrics* (Academic, New York, 1957; Inostrannaya Literatura, Moscow, 1960).
24. V. Ya. Fritsberg, Izv. Akad. Nauk SSSR, Ser. Fiz. **47** (4), 696 (1983).
25. L. A. Nikolaev and V. A. Tulupov, *Physical Chemistry* (Khimiya, Moscow, 1967) [in Russian].

Translated by G. Skrebtsov